



**Department of Mechanical Engineering  
College of Engineering, Design and Physical Sciences  
Brunel University London  
London, United Kingdom**

**Metal and Oxide Nanoparticles: Green Biosynthesis  
using Portobello Mushroom Spores (PMS) for  
Nanocomposites and Replicas,  
Properties and Applications**

**A thesis submitted to Brunel University in Partial Fulfilment of the  
Requirements for the Degree of  
DOCTOR OF PHILOSOPHY**

**By**

**Iman Abdullah Jaaffer AL-Timimi**

**Supervised by  
Professor Paul A. Sermon  
2018**

## DECLARATION

I declare that this thesis is my own work and is submitted for the first time to the Post-Graduate Research Office. The study was originated, composed and reviewed by myself and my supervisor in the Wolfson Centre, Department of Mechanical Engineering, College of Engineering, Design and Physical Sciences, Brunel University London UK and under the supervision of Professor Paul A. Sermon to fulfil the requirement of the University of Brunel PhD in Chemistry (Bio-medical inorganic nanomaterials). All the information derived from other works has been properly referenced and acknowledged.

Iman Abdullah Jaaffer AL-Timimi

Student No. 1137132

Brunel university London

31 July /2018

I confirm that the above information is correct.

Professor Paul A. Sermon

Professor of Nanomaterials

Wolfson Center

Brunel university London

- **Email:** [paul.sermon@brunel.ac.uk](mailto:paul.sermon@brunel.ac.uk)
- **Tel:** +44 (0)1895 265877
- [College of Engineering, Design and Physical Sciences](#)
- [Institute of Materials and Manufacturing](#)
- [Materials Characterisation and Processing](#)

## ACKNOWLEDGMENTS

The author must give huge thanks to her country (Iraq), the martyrs, orphans, widows, her family and all Iraqi people. She would also like to thank her sponsor, the Iraqi Ministry of Higher Education and Scientific Research (MOHESR), Department of Missions and Cultural Relations and the Iraqi Cultural Attaché in London. She would also like to thank University of Basrah for giving her this opportunity to complete her PhD study. She would like to thank her colleagues who assistance her in carrying out Biological tests: Afrodet A. Salih for DNA tests, Sameerah A. Zearah for LD<sub>50</sub> test and cytotoxicity, Ahmed A. Burghal and Inaam M. N. Alrubaya for anti-microbial activity in the College of Science at University of Basrah.

She wishes to express her sincere gratitude to her supervisor Professor Paul A. Sermon, who always supported, advised and encouraged her; a huge thank you for his patient approach and guidance to help her succeed in her work, for sharing his immense knowledge and allowing her the opportunities to achieve the pinnacle of her ability, especially during the challenging times in her PhD. Moreover, she will never forget the moral support and consideration given in her research. She could not have hoped for a better mentor and teacher for her Ph.D. study. Thank you for helping her to mature into the scientist she is today, from teaching her the basics of nanoscience in lab practices to continuous encouragement throughout the past 4 years and even before she began her PhD, when she was in the English course. She wishes him more brilliant scientific progress in his life.

She must also extend her appreciation to her second supervisor, Professor Jack Silver (Executive Director for Materials Processing) for his words of encouragement and give special thanks support for Mandy Sermon for her invaluable help. She would like to give a big thank you to the Wolfson Centre for support during all her PhD study especially, Dr. Lesley Hanna and Dr. Daksha Parekh. Also, she would thank all those who work in Experimental technique centre (ETC) for helping her in experimental techniques: Dr. Alan Reynolds, Abdul Ghaffar Ghani (TGA), Dr. Ashley Howkins (TEM and SEM), Nita Verma (SEM), Dr. Lorna Anguilano (XRD and SEM), Dr. Jesus Javier Ojeda (micro-FTIR), Dr Nico Nelson (Raman) and Dr. Safiyeh Haghani (SEM).

The author would like to give special thanks to Brunel University language centre, student centre, graduate school and postgraduate research office. She would also like to thank her friends in the Wolfson Centre who helped and supported her: Jean-Charles Eloi who was always willing to help and answer every question, Uchechukwu for her on-going support, encouragement and all the fun time spent together, Virginia with her permanent smile, Sam, Mohmad Fathullah and Myles for their help and all Iraqi students at Brunel University and in the UK.

## LIST OF SYMBOLS AND ABBREVIATIONS

<b>AMR</b>	Anti-Microbial Resistance
<b>ARB</b>	Anti-biotic-Resistance Bacteria
<b>ABG</b>	Antibiotic-Resistant Genes
<b>AA</b>	Ascorbic Acid
<b>AMR</b>	Anti-Microbial Resistance
<b>ATR</b>	Attenuated Total Reflection
<b>Bio-Oss</b>	Commercial Hydroxy Apatite
<b>CVD</b>	Chemical Vapor Deposition
<b>E</b>	Lattice strain
$\Sigma$	Tensile stress or lattice deformation stress
<b><math>\mu</math>-FTIR</b>	Micro-FTIR
<b>D</b>	Crystallite size
<b>DLS</b>	Dynamic Light Scattering
<b>EEO</b>	Electroendosmosis
$E_{hkl}$	Elastic Modulus
<b>EDX</b>	Energy Dispersive X-ray
<b>EM</b>	Electron Microscopy
<b>ETC</b>	Experimental technique centre
<b>FCC</b>	Face Centred Cubic
<b>FFT</b>	Fast Fourier Transform
<b>FTIR</b>	Fourier Transform Infrared Spectroscopy
<b>FWHM</b>	Full Width at Half-Maximum
<b>nHAp</b>	Nano Hydroxy Apatite
<b>Nano</b>	Commercial Nano Hydroxy Apatite
<b>Hb</b>	Hemoglobin
<b>In</b>	Insulin
<b>IPA</b>	Isopropanol, 2-propanol
<b>kV</b>	kilovolts
<b>NaBH<sub>4</sub></b>	Sodium borohydride
<b>NADH</b>	Nicotinamide adenine dinucleotide
<b>NPs</b>	Nanoparticles
<b>PDAm</b>	Plant Derived Antimicrobial
<b>PBS</b>	Phosphate Buffer Saline
<b>Pg</b>	Picogram
<b>PVA</b>	Polyvinyl Alcohol
<b>PLGA</b>	Poly Lactic-co-Glycolic Acid
<b>PVD</b>	Physical Vapor Deposition
<b>PM</b>	Portobello Mushroom
<b>PMS</b>	Portobello Mushroom Spores
<b>RMM</b>	Relative Molecular Mass
<b>RT</b>	Room Temperature
<b>ROS</b>	Reactive Oxides Species
<b>SBF</b>	Simulated Body Fluid
<b>SE</b>	Secondary Electron
<b>SEM</b>	Scanning Electron Microscopy
<b>SAED</b>	Selected Area Electron Diffraction
<b>SGF</b>	Simulated Gastric Fluid
<b>SIMS</b>	Secondary Ion Mass Spectrometer

<b>SPIE</b>	Society of Photographic Instrumentation Engineering
<b>TAE</b>	Tris-acetate-EDTA
<b>TBE</b>	Tris-borate-EDTA
<b>TEM</b>	Transmission Electron Microscopy
<b>TGA</b>	Thermal Gravity Analysis
<b>TSC</b>	Tri-sodium citrate
<b>TON</b>	Turnover Numbers
<b>XRD</b>	X-Ray Diffraction
<b>XRDLB</b>	X-Ray Diffraction Line Broadening
<b>W-H</b>	Williamson-Hall approach

## ABSTRACT

This thesis describes novel research using Portobello mushroom spores (PMS) as a biotemplate and reducing agent that may be used to produce nanocomposites and replicas with societal benefits.

First, the use of PMS as a green eco-friendly bioreagent for the biosynthesis of Ag, Au and TiO<sub>x</sub> nanoparticles (NPs) and their hybrids is described. These have been characterised using SEM, TEM, XRD, FTIR, UV, SIMS, DLS and TGA (where a full list of acronyms is to be found on page iv). The spherical shape, location and mean diameter of the PMS-held (5-30nm) Ag and Au NPs were confirmed. PMS functional groups are comparable with those in plant sources and allow them to act as reducing/capping/stabilising agents.

Second, the sequential biosynthesis of PMS-held Ca<sup>2+</sup>, CaCO<sub>3</sub> and nanohydroxyapatite (nHAp) is described where surface nucleation and growth are facilitated by biotemplate surface hydrophilic polar groups (-OH and -COO<sup>-</sup>). XRD and HRTEM suggest that the nHAp so formed has lower crystallinity and greater directed growth in the (002) direction than commercial nHAp (e.g. Bio-Oss), making PMS-routes useful for the delivery of artificial bone (after subsequent PMS removal). Furthermore, PMS-held nHAp showed more rapid *in-vitro* mineralization in simulated body fluid (SBF).

Third, it is shown that ascorbic acid (AA), haemoglobin (Hb) and insulin (In) can be loaded into/released by PMS through its cell walls faster than with synthetic hydrogels (PVA); the transdermal use of PMS nanocomposites is considered in the context of drug delivery nanotechnology, avoiding size-dependent toxicity.

Fourth, it is shown by traditional diffusion and novel methods that the antimicrobial activity especially of Ag/PMS, but also TiO<sub>x</sub>/PMS and Ag-TiO<sub>x</sub>/PMS (but not Au/PMS) is good in the inhibition of the growth of *E.coli* and *S.aureus* bacteria. The highest activity of Ag/PMS is attributed to Ag<sup>x+</sup> release.

Fifth, the synthesis of NPs/PMS and biomimetic TiO<sub>x</sub>/PMS has shown to lead to good photocatalysis for the removal of coloured organic pollutants (e.g. methyl orange) from water, with faster rates of removal in molecules/mg/s and turnover numbers (TON) (s<sup>-1</sup>) than commercial anatase-rutile TiO<sub>2</sub> (P25) possibly as the texture of the titania replicas raises the number of multiple reflections of light.

## List of publications

Biosensing and Nanomedicine, Proc. of SPIE

- 1- Biomimetic TiO<sub>2</sub> formation from interfacial sol-gel chemistry leading to new photocatalysts.

The surfaces of Portobello mushroom spores (PMS) have been used to produce Au and Ag nanoparticles, which are held thereon. They have then been overcoated with TiO<sub>x</sub>. These adsorbed more methyl orange (MO) pollutant from water than commercial P25 TiO<sub>2</sub>. After calcination they form biomimetic TiO<sub>2</sub> (PMS) and removal of the biotemplate, they catalyse faster rates of MO from water (molecules/mg/s) than P25 anatase-rutile. Other biotemplates are now anticipated that will yield biomimetic photocatalysts with higher turnover number (s<sup>-1</sup>) removal of endocrine disrupters from water.

- 2- Nanoengineering the antibacterial activity of biosynthesized nanoparticles of TiO<sub>2</sub>, Ag and Au and their nanohybrids with Portobello mushroom spores (PMS) (TiO<sub>x</sub>/PMS, Ag/PMS and Au/PMS) and making them optically self-indicating.

Nanoparticles (NPs) can be biosynthesized at room temperature on the reductive and chelating surfaces of Portobello mushroom spores (PMS). Using this green approach TiO<sub>x</sub>, Ag, Au, Ag-TiO<sub>x</sub> and Au-TiO<sub>x</sub> NPs have been prepared. These were characterized by TEM, SIMS and FTIR-FTIR. TiO<sub>x</sub>/PMS, Ag-TiO<sub>x</sub>/PMS, Au-TiO<sub>x</sub>/PMS and Ag/PMS were active in bacterial inhibition towards *Escherichia coli* and *Staphylococcus aureus*, but Au/PMS was not active (suggesting a strong Au-PMS interaction). TiO<sub>x</sub>/PMS, Ag/PMS and Ag-TiO<sub>x</sub>/PMS were equally active in an antibacterial and an antifungal sense when tested against *Asperillus.spp* and *Candide.spp*. All samples (except Ag-TiO<sub>x</sub>/PMS and Au-TiO<sub>x</sub>/PMS) showed an interesting interaction with DNA. We report on the process of fine-tuning these antibacterial properties, progress on making these nanomaterials optically self-indicating and movement towards optical control of their antibacterial activity. Au-TiO<sub>x</sub>/PMS shows a surface plasmon resonance (SPR) with a maximum at 518nm that might be useful in following its anti-bacterial properties (i.e. making the bionanomaterial self-indicating). The future of such green bio-nanomaterials is strong.



## Table of Contents

Chapter 1: General introduction .....	1
1.1 Biomimetic material .....	1
1.2 Nanotechnology.....	3
1.2.1 Definitions of nanotechnology .....	3
1.2.2 The importance of the nanoscale .....	4
1.2.3 Types of nanotechnology.....	6
1.2.4 Synthesis of metal NPs .....	6
1.2.5 Preparation of NPs .....	7
1.3 Green chemistry.....	8
1.3.1 Bio-Reducing agents .....	9
1.3.2 Capping agent.....	10
1.4 Properties of gold and silver .....	11
1.4.1 Surface Plasmon Resonance (SPR) .....	12
1.4.2 Sol-gel method .....	12
1.5 Antibacterial activity .....	13
1.5.1 Plant derived antimicrobial (PDAm).....	13
1.5.2 Ag NPs .....	15
1.5.3 Au NPs .....	15
1.6 Photocatalysis .....	18
1.6.1 Semiconductor (SC) materials .....	18
1.6.2 TiO <sub>2</sub> NPs .....	20
1.6.3 TiO <sub>2</sub> and hybrid system.....	23
1.6.4 Surface plasmon resonance (SPR) and TiO <sub>2</sub> NPs.....	24
1.7 Green chemistry and photocatalysis .....	25
1.8 Aims of present research .....	26
Chapter 2: PMS and Related Works .....	27
2.1 Introduction .....	27
2.2 Biosynthesis of NPs.....	27
2.2.1 Green synthesis of NPs and antimicrobial resistance (AMR) .....	28

2.3	Toxicology and NPs .....	28
2.4	Related works .....	29
2.4.1	<i>Ag NPs</i> .....	29
2.4.2	<i>Au NPs</i> .....	30
2.4.3	<i>TiO<sub>2</sub> NPs</i> .....	31
2.4.4	<i>HAp biotemplate</i> .....	32
2.4.5	<i>Drug delivery</i> .....	33
2.4.6	<i>Cytotoxicity</i> .....	35
2.4.7	<i>NPs and natural photocatalysts</i> .....	35
Chapter 3: Experimental Techniques.....		37
3.1	Electron microscopy (EM) .....	37
3.1.1	<i>Scanning electron microscopy (SEM)</i> .....	40
3.1.2	<i>Transmission electron microscope (TEM)</i> .....	44
3.2	X-Ray Diffraction (XRD).....	46
3.2.1	<i>Determination of crystal size using the Scherrer Equation</i> .....	47
3.2.2	<i>Determination of crystallite size (D) and lattice strain (<math>\epsilon</math>) using the Williamson-Hall approach</i> .....	49
3.3	Secondary ion mass spectrometer (SIMS).....	51
3.4	Fourier transform infrared spectroscopy (FTIR) and micro-FTIR.....	53
3.5	NanoDrop-UV spectroscopy.....	55
3.5	Electrophoresis .....	56
3.7	White light interferometry (WLI) .....	57
3.3	Conclusions.....	58
Chapter 4: Materials and preparative methods .....		60
4.1	Materials .....	60
4.2	Preparative Methods .....	61
4.2.1	Preparation of TiO <sub>2</sub> NPs/PMS .....	62
4.2.2	Preparation of Ag NPs/PMS .....	62
4.2.3	Preparation of Au NPs/ PMS .....	63
4.2.4	<i>Preparation of nanohybrids/PMS</i> .....	64
4.2.5	nHAp/PMS.....	66

4.2.6 Bioactivity studies .....	67
1. <i>In vitro</i> bioactivity evaluation .....	67
2. <i>In vitro</i> dissolution evaluation.....	68
4.2.7 Methods of Assessing the Uptake and Release of AA, Hb Protein and Insulin .....	68
4.2.8 Cytotoxicity test.....	69
4.2.9 Study of the effects of NPs/PMS on DNA .....	70
1. Samples collection DNA extraction.....	70
.2 Detection of DNA by agarose gel electrophoresis .....	71
3. Migration of DNA on agarose gel and NPs/PMS .....	71
4. Visualizing DNA on a UV transilluminator.....	71
5. The effect of prepared NPs/PMS on human genomic DNA .....	71
4.2.10 Determination of Median Lethal Dose (LD <sub>50</sub> ).....	72
1. Animal and experimental design .....	72
1. Dose preparation and administration.....	72
4.2.11 Antimicrobial Measurements.....	72
4.2.12 Biotemplate TiO <sub>x</sub> overcoating and addition of Au/Ag NPs .....	73
4.2.13 Biotemplate TiO <sub>2</sub> replica formation .....	74
4.2.14. Photocatalytic activity .....	74
Chapter 5: Characterization results for Portobello mushroom spores (PMS) .....	76
5.1 Introduction.....	76
5.1.1 Mushroom spores .....	77
5.1.2 Comparison between spores, pollen and seeds.....	77
5.1.3 Sporopollenin.....	79
5.1.4 Cell Walls Structure of Spores .....	79
5.1.5 Portobello Mushroom.....	81
5.2. Results and discussion .....	82
5.2.1 SEM and TEM analysis .....	83
5.2.2 SIMS.....	90
5.2.3 FTIR and $\mu$ - FTIR .....	91
5.2.4 Optical Microscopy .....	94
5.2.5 Thermal gravity analysis (TGA).....	97

5.3	Conclusions .....	98
Chapter 6: Green biosynthesis of TiO <sub>2</sub> , Ag, Au NPs and nanohybrids using the spores of edible Portobello mushroom as biotemplates .....		
6.1	Introduction.....	99
6.1.1	Metal nanoparticles.....	99
6.1.2	Nanohybrids.....	100
6.2	NPs and biological properties .....	102
6.2.1	TiO <sub>2</sub> NPs .....	102
6.2.2	Ag NPs.....	103
6.2.3	Au NPs.....	103
6.3	Characterization Results .....	104
6.3.1	NPs/PMS.....	104
1-	TiO <sub>x</sub> /PMS .....	104
2.	Ag and Au NPs coated PMS .....	108
□	Ag NPs/PMS .....	109
□	Au NPs coated PMS.....	110
6.3.2	SEM and TEM of Ag and Au NPs/PMS .....	111
6.3.3	DLS analysis of Ag NPs .....	119
6.3.4	FTIR.....	121
6.3.5	UV-Vis.....	122
6.3.6	TGA .....	123
6.3.7	<i>Au and Ag nanohybrids with PMS</i> .....	124
□	Method No.1 (described in section 4.2.4) .....	124
□	Method No.3 (described in section 4.2.4) .....	129
□	Factors affecting nanohybrids formation with PMS using SEM .....	135
6.4.	Conclusions.....	137
Chapter 7: Biosynthesis of nHAp/PMS microspheres for medical applications .....		
7.1	Introduction.....	138
7.1.1	Bone structure .....	139
7.1.2	The crystalline structures .....	141
7.1.3	Nano and hollow spheres of HAp.....	142

7.2 Methods of Analysis .....	143
7.2.1 General approach .....	143
7.3 Results and Discussion .....	146
7.3.1 Uptake of Ca and phosphate ions on PMS surfaces .....	146
7.3.2 nHAp/PMS.....	148
7.3.3 nHAp/PMS-PVA hydrogel film .....	149
7.3.4 SEM and TEM .....	149
1. nHAp/PMS .....	149
2. CaCO <sub>3</sub> /PMS .....	154
3. nCa/PO <sub>4</sub> <sup>3-</sup> -Ag/PMS .....	155
4. Bio-Oss.....	158
7.3.5 X-ray diffraction (XRD) .....	159
7.3.6 FTIR.....	166
7.3.7 TGA .....	168
7.3.8 <i>The mechanism of nucleated nHAp-PMS</i> .....	168
7.4 Conclusions.....	169
Chapter 8: The bioactivity studies of nHAp/PMS .....	170
8.1 Introduction.....	170
8.1.1 Types of methods.....	171
8.2. Results.....	172
8.2.1 bioactivity study.....	172
8.2.2 Dissolution studies.....	177
8.3 Conclusions.....	183
Chapter 9: The drug delivery and protein adsorption by hollow microsphere by Portobello mushroom spores (PMS) using ascorbic acid (AA) hemoglobin (Hb) and insulin as model therapeutic agents.....	184
9.1 Introduction.....	184
9.1.1 Ascorbic Acid .....	184
9.1.2 Hemoglobin .....	186
9.1.3 Drug Delivery and Nanomaterials .....	187
1. Insulin.....	187

2. Oral Delivery of Insulin (In) .....	188
9.2 Results and discussion .....	189
9.2.1 Uptake Studies .....	189
1. Ascorbic Acid.....	189
2. Hemoglobin (Hb) Absorbed on PMS Surface.....	191
9.2.2 AA, Hb and In Drug release .....	192
1. Ascorbic Acid.....	193
2. Hemoglobin.....	193
3. Insulin Swelling Study .....	201
9.3 Conclusions.....	207
Chapter 10 : Nanoengineering the antibacterial activity of biosynthesized nanoparticles of TiO <sub>2</sub> , Ag and Au and their nanohybrids with Portobello mushroom spores (PMS) (TiO <sub>x</sub> /PMS, Ag/PMS and Au/PMS) making them optically self-indicating .....	208
10.1 Introduction.....	208
10.2 Anti-microbial and Anti-Fungal Activity Results .....	211
10.2.1 Novel SEM- EDX and White-light interferometry analysis .....	213
10.2.2 The antimicrobial mechanism for NPs/PMS .....	215
10.3. Conclusions.....	218
Chapter 11: Nanocytotoxicity and genotoxicity of TiO <sub>x</sub> , Ag and Au NPs/PMS in human blood and nucleic acid for future medical applications .....	219
11.1 Introduction.....	219
11.1.1 Cytotoxicity .....	219
11.1.2 Median lethal dose.....	225
11.2.2 Effect of NPs/PMS nanohybrids on nanocytotoxicity.....	230
11.2.3 Median Lethal Dose (LD <sub>50</sub> ).....	231
11.3 Conclusions.....	233
Chapter 12: Biomimetic TiO <sub>2</sub> formation from interfacial sol-gel chemistry leading to new photocatalysts.....	234
12.1 Introduction.....	234
12.1.1 Adsorption and photocatalytic activity towards methyl orange (MO).....	235
12.2 Characterization Results .....	237
12.2.1 Absorbance edges and extents of methyl orange adsorption.....	237

12.2.2 Photocatalytic and temperature effect .....	239
12.2.3 Turnover Frequency (TOF) .....	242
12.3 Conclusions.....	243
Chapter 13: Discussion on importance and novelty of research and future work .....	244
13.1 The aims.....	244
13.2 Extent of Achieving the above Goals .....	244
13.2.1 Achievements and novelty.....	245
13.3 Future work.....	247
13.4 Errors, uncertainties and Novel Analytical Approaches.....	248
References.....	249

## **Chapter 1: General introduction**

---

In this chapter, a brief review is undertaken of the concepts of biomimicry, nanotechnology, nanoparticles (NPs) of Ag, Au and TiO<sub>2</sub>, their properties and their applications as antimicrobials and in photocatalysis. Finally, the aims of the proposed PhD research are considered.

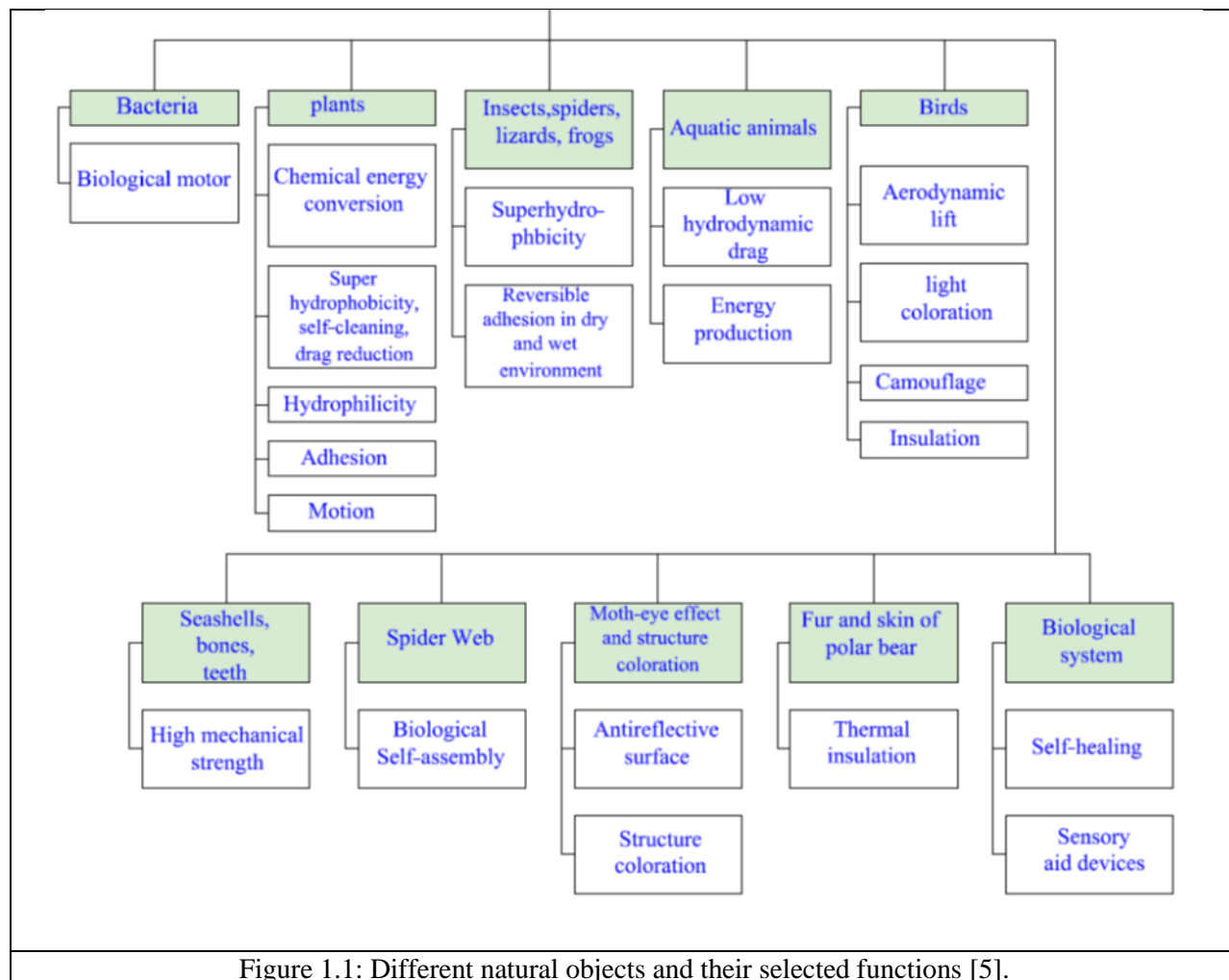
### **1.1 Biomimetic material**

In the 1950s Otto Schimdt described biology/technology transfers as biomimetic. Organic syntheses were the initial realm of biomimetic chemistry, but its impact has progressed to bio-inorganic interfaces with benefits to materials design. With biomimetic evolution, many living plant and animal species have constructed species-specific biocomposite-structures that have nano-architectures. In biomimetic materials, researchers learn from (and replicate) nature's three-dimensional self-assembled biotemplates (whether there be 8.7 million or 20 million species on Earth) through transformation of hybrid nanostructures to develop novel inorganic nanostructures. Nanochemistry aims thereby to extend the traditional length scales of synthetic chemistry. Applying lessons from nature allows the synthesis bio-inspired, biomimetic and biominerals materials of evermore fascinating complexity and properties [1]. Nature has different objects and processes with different function from macro- to nano- scale. Understanding these processes, can lead to imitation and production of them at a nano-scale. Biological materials derived from nature are biomimetic. Many terms are used such as biomimicry, biognosis and bionics. The field of biomimetics is a multidisciplinary science that refers to human-made processes, substances, devices or systems that imitate nature or that take their inspiration from models in nature and aims thereby to solve human problems. Biomimetic approaches to materials chemistry relate to the supply of new methods for the synthesis and assembly of nanomaterials [2].

Biomimetic science is when systems that have several functions learned and copied from Nature. It is the study of the structure and function of biological substances materials (i.e. enzymes and



silk) [3], biological mechanisms and processes (e.g. protein synthesis and photosynthesis) used in engineering, chemistry design and electronics [4].



Nano-chemistry has been developed to take advantages of chemistry and physical properties of biomolecules for progress towards the next generation of nanoscale materials [6]. Recently, scientists and researchers have shifted their thinking in the field of nanotechnology to ensure that we learn from nature [7]. For example, studies of the surface of lotus leaves (that emerge pristine and clean from muddy waters) suggested this is a result of their surface filaments with inherent surface roughness and structure/chemical anisotropy; this led to a ‘lotus leaf’ (due to superhydrophilic surface), paint surface that is antibiotic, self-cleaning and pollution controlling. All biological materials contain water at some concentration, which is critical to organization, functioning and hierarchy and can provide a biomimetic solution to engineering materials. All

interactions between living species and their environment takes place at their surfaces or interfaces [8]. There are various materials from nature that serve as the inspiration of technology development [5] (see Fig. 1.1).

## **1.2 Nanotechnology**

In 1959, the physicist Richard Feynman was the first scientist who proposed the concepts of nanotechnology and described molecular machines built with atomic precision. He said, “there’s plenty of room at the bottom” [9]. At that time, he discussed the benefits of manipulating materials at a small scale. In 1974, Professor Norio Taniguchi (Tokyo University of Science) defined nanotechnology and used it as a scientific field at first time; his paper was ‘Taniguchi, N. (1974) On the Basic Concept of Nanotechnology; Proceedings of the International Conference on Production Engineering, Tokyo, 18-23’. From 1980, nanotechnology developed for many applications in medicine and industry when the first paper published in 1980 by K. Eric Drexler [9]. Nanotechnology entered a more public arena in 2001 when President Clinton brought worldwide attention to nanotechnology [10]. In recent years, nanotechnology has become one of the more significant and exciting new fields at the interface of chemistry, physics, engineering and biology [11]. There are many new branches of nanotechnology emerging such as nanomedicine, nano-biotechnology, nanoelectronics [10] and nanofibers [12] etc.

### ***1.2.1 Definitions of nanotechnology***

Nanotechnology means any technology that has applications on a nanoscale. It can be defined in many ways: (i) as the design and application realised by controlling size and shape at nanoscale and using materials (atomic/molecular), devices and machines, making use of unique properties that occur for such structures at these small dimensions [13]; (ii) the broad-based science involving electrons, protons, atoms and neutrons which can be manipulated by different methods to generate new materials that can be used to solve many problems in different fields [14]; (iii) it is the study and application of small-scale (materials) across many fields as (e.g. in chemistry, physics, biology and material science) [15]. ‘Nanotechnology is the principle of atom manipulation atom by atom, through control of the structure of matter at the molecular level. It

entails the ability to build molecular systems with atom-by-atom precision, yielding a variety of nanomachines' [16].

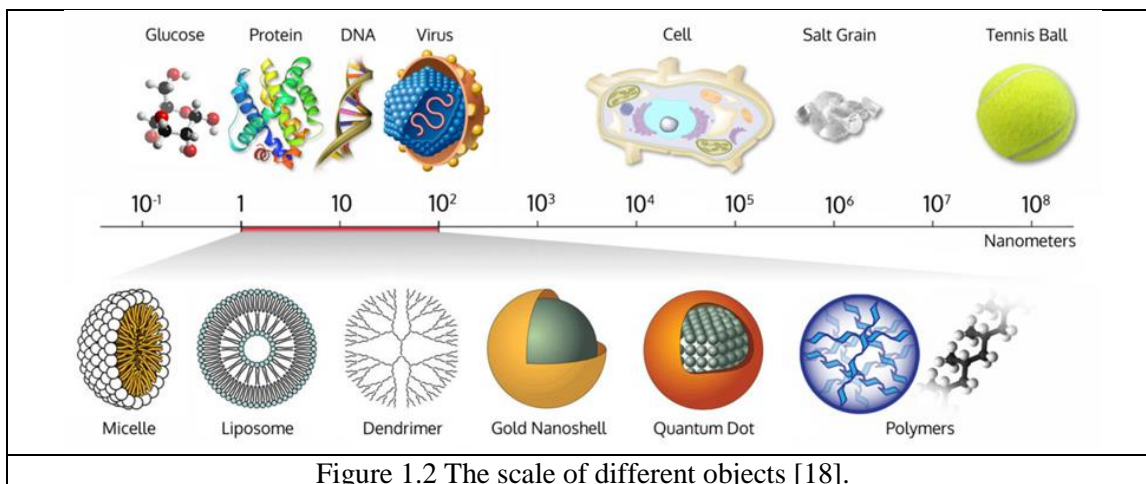
- **Important definitions**

- 1- Bio-nanotechnology is the science that combines the principles of biology with chemical and physical methods to generate nanoparticles (NPs) with specific functions [11].
- 2- Nanomaterials possess unique material characteristics; they are nanoscale and manufactured by design to exhibit novel characteristics, compared to the same material without nanoscale [13].
- 3- Nanoparticles are particles of any shape with dimensions in the size range  $1 \times 10^{-9}$  and  $1 \times 10^{-7}$ cm ( $1\text{nm} = 10^{-9}\text{m}$ ) [17].
- 4- Nanoscience is the study of nanomaterials whose properties differ from those of large scale materials.
- 5- Nanomedicine is the use of nanomaterials to improve medicine and drug delivery, and
- 6- Nano-toxicity is the study of toxic effects of nanomaterials on human health and the environment.

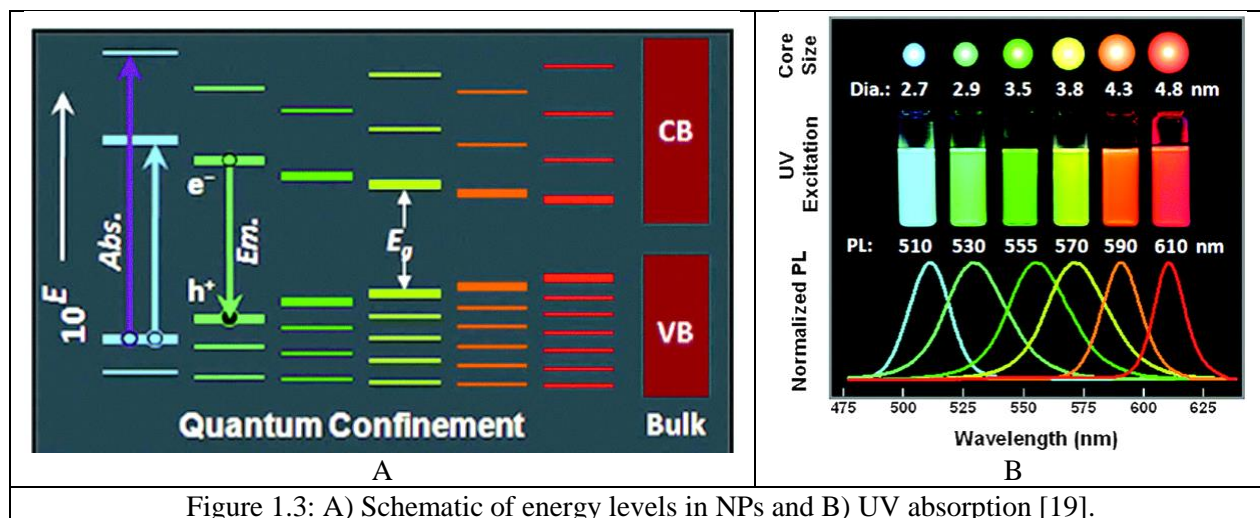
### ***1.2.2 The importance of the nanoscale***

Nanotechnology deals by definition with dimensions below 100 nm ( $10^{-9}\text{m}$ ). Such a nanoscale is very important [18]. For instance, bulk gold is not active; therefore, it is used as jewellery. However, at a nanoscale, gold clusters become very active and are used in catalysis and medicine for cancer treatment [19].

Figure 1.2 shows examples of objects on different scales and nanoscales (such as a virus of about 200 nm size, protein molecules which are nearly 1-10nm in size, DNA 10nm (each base pair DNA =0.34nm) and a red blood cell 7000nm in size). The properties of adjacent molecules can be changed by their proximity to nanomaterials that have a comparatively large surface area per unit/volume, when compared to the same mass of material produced in microscopic form. This can make these molecules more chemically reactive [19].



Nanoscale materials (nanomaterials) or nanoparticles (NPs) exhibit unique properties, which differ from bulk materials: physical, chemical, biological, optical, thermal and mechanical properties. These properties come precisely from their nano-size, size distribution and shape. From another perspective, NPs can act as bridge between molecules or atoms and bulk materials due to their nm size. Their surface area to volume ratio increases when bulk materials become sufficiently small. This affects their chemical and physical properties [20].



Some materials can be produced that are nanoscale in one, two or three dimensions as very thin surface coatings (semiconductor, metal, carbon), nanowires and nanotube or nanoparticles [13]. With their small size NPs are excited leading to increasing band gap energy and lower

wavelength. (Quantum confinement is change of electronic and optical properties when the material sampled is small size typically 10nm or less, see Fig. 1.3). Quantum dots improve the efficiency by generating multiple exciton (e-hole pairs) after collision with one photon.

### ***1.2.3 Types of nanotechnology***

There are three types of nanotechnology: (i) *dry* nanotechnology which involves chemistry, physics, the surface science and gives significant fabrication of structure for inorganic materials, (ii) *wet* nanotechnology deals with enzymes, cellular components and membrane for biological systems, and (iii) computational nanotechnology involving simulation and modelling of the complex nanometer scale structures. All these can inter-relate with each other [21].

### ***1.2.4 Synthesis of metal NPs***

There are two methods of nanomaterial processing: *top-down* and *bottom-up*. A unit can be designed to self-assemble (which is similar to self-organization where a material grows layer by layer) [22].

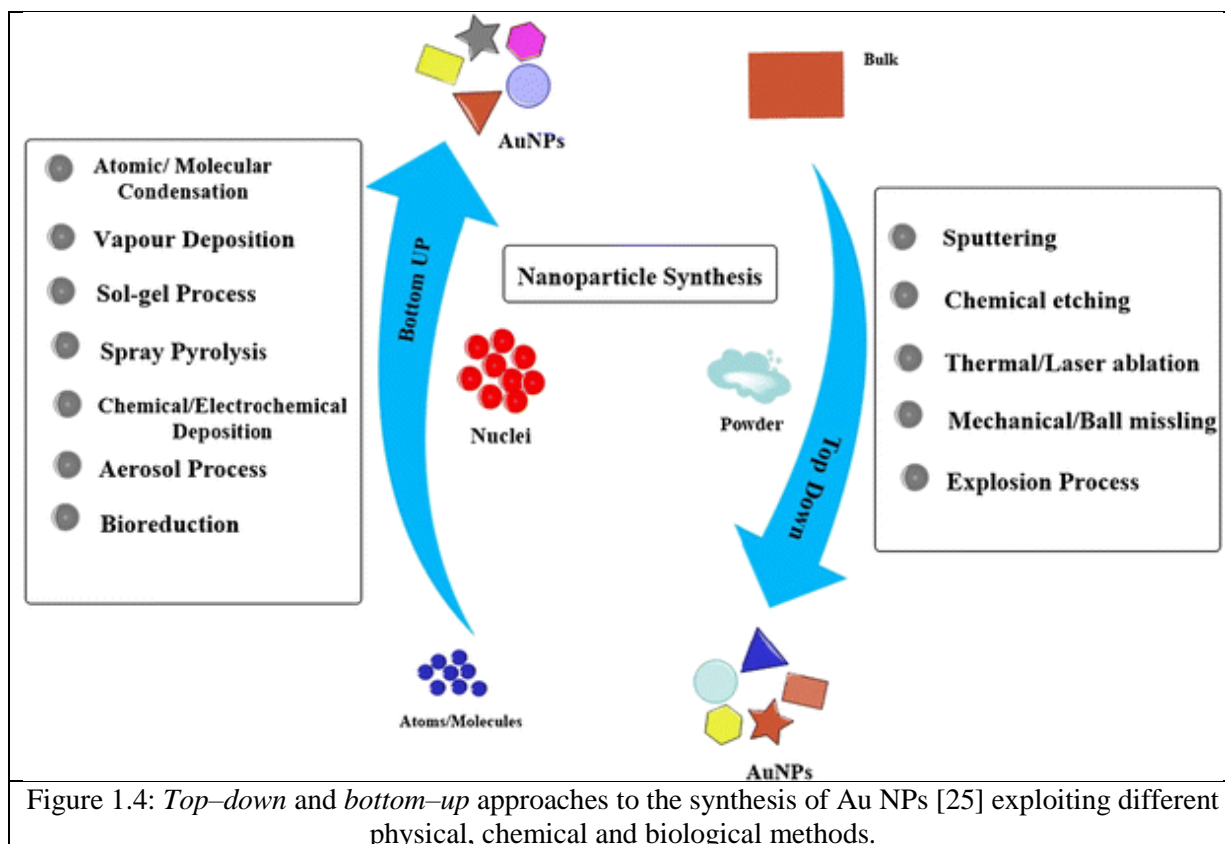
- ***Top-down approach***

The *top-down* approach is a simple and fast technique for engineering a nano-structure. It involves the breakdown or fabrication of the bulk materials or device structure via monolithic to nano-sized particles. It is inherently simple and depends on removal or division of bulk material to produce the desired nano-structure with appropriate properties. The *top-down* approach is used in the electronic industry and includes as chemical vapor deposition (CVD) and physical vapor deposition (PVD) [11] sputtering, grinding and milling [23] and laser ablation. The generation of a biomimetic plant surface includes a top-down approach in which the structure is applied to a material by moulding. [7].

- ***Bottom-up approach***

In contrast, with *bottom-up* approach, the required structure is produced from molecules or ions using chemistry. Thus, the bottom-up approach produces the desired nano-structure by building it up from small units (single molecules or ions). This approach assembles structure from atom-to-atom, molecule-to-molecule, and cluster-to-cluster interactions say at the surface of a base substrate to give a bigger structure. In this case, the nanoparticles grow in size by self-assembly

or by chemical reactions. Chemical self-assembly utilizes the selective attachment of units to a specific surface or specific functional group. Here, the bonding between the atoms or molecules producing self-assembly is covalent or non-covalent; it can produce metal (e.g. Au and Ag) or metal oxide [24] (e.g. TiO<sub>2</sub> overcoats) aggregates and NPs (see Fig 1.4).



### 1.2.5 Preparation of NPs

Many approaches have been used to prepare metal NPs: (i) chemical (including chemical and photochemical reduction, hydrolysis, thermal decomposition co-precipitation and (ii) physical laser ablation and vapor deposition. Functionalization of NPs can include: (i) electrostatic adsorption (of positive charged adsorbate), (ii) chemisorption (e.g. thiols have an affinity noble metals and covalent binding of bifunctional linkers occurs on metals and (iii) affinity-based functionalization of NPs (with affinity sites in the biomolecules [26]). Self-assembly can be used to produce nanostructures by selective attachment of molecules to specific surfaces via covalent and non-covalent binding [27]. Nature exploits self-organization of soft materials in many ways, to produce cell membranes, biopolymer fibers and viruses [28]. Principles drawn from biology

have helped in understanding the fundamentals of self-assembly, and have stimulated the development of new strategies and new applications such as base pairs in DNA [29]. Self-assembly is the step after NP nucleation in a mixture and growth-stable agglomeration. Here, larger NPs may be thermodynamically blocked and also biomolecules can help the NP self-assembly and aggregation. The particle shape are defined in this stage [20].

### 1.3 Green chemistry

Phytochemicals (which found in many different plant sources) have been used in green chemistry. The conventional chemical routes to NPs can be hazardous (using toxic reagents or chemicals). This has driven researchers to develop alternative methods for NPs synthesis that are safer, more eco-friendly, simpler, readily, available and more efficient one-step processes. Biological synthesis has therefore been preferred universally for the synthesis of NPs using microorganisms and plants (bacteria, fungi, algae and others). Others use vitamin C, chitosan, glycerol, starch, Ca-alginate, honey, sponge and diatoms. Phytochemistry is considered a major mechanism of green synthesis for plants assisting reduction ions. Recently, the combination between green chemistry and nanotechnology has created new NPs. The mechanism of green synthesis of NPs involves the significant use of plants as reducing, capping and stabilizing agents (see Fig. 1.5) [25].

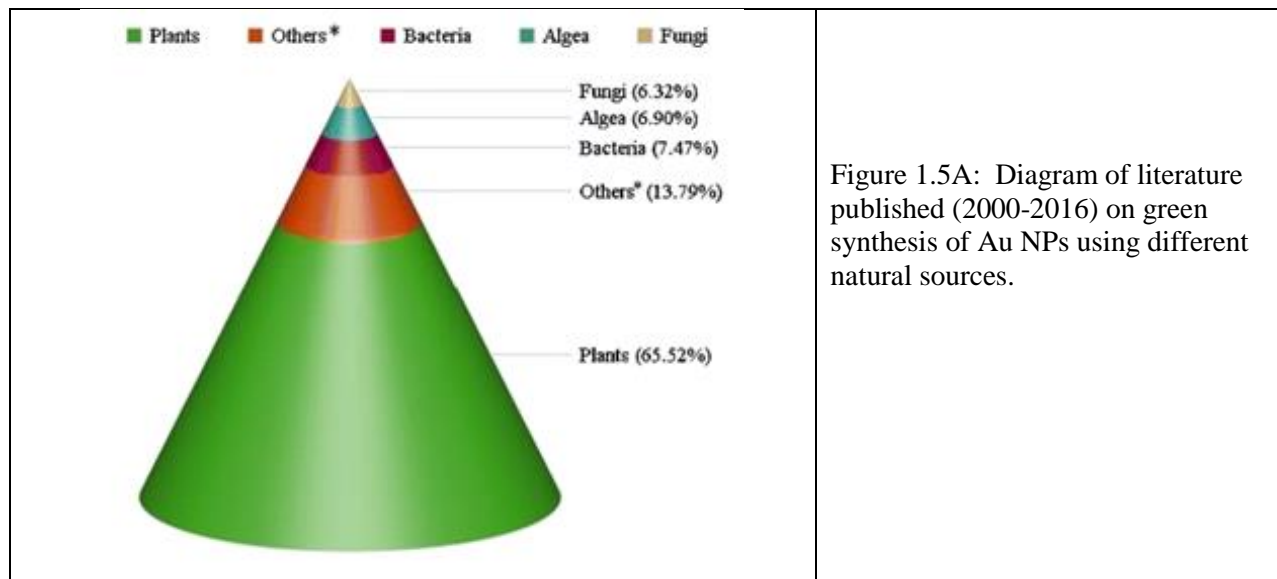


Figure 1.5A: Diagram of literature published (2000-2016) on green synthesis of Au NPs using different natural sources.

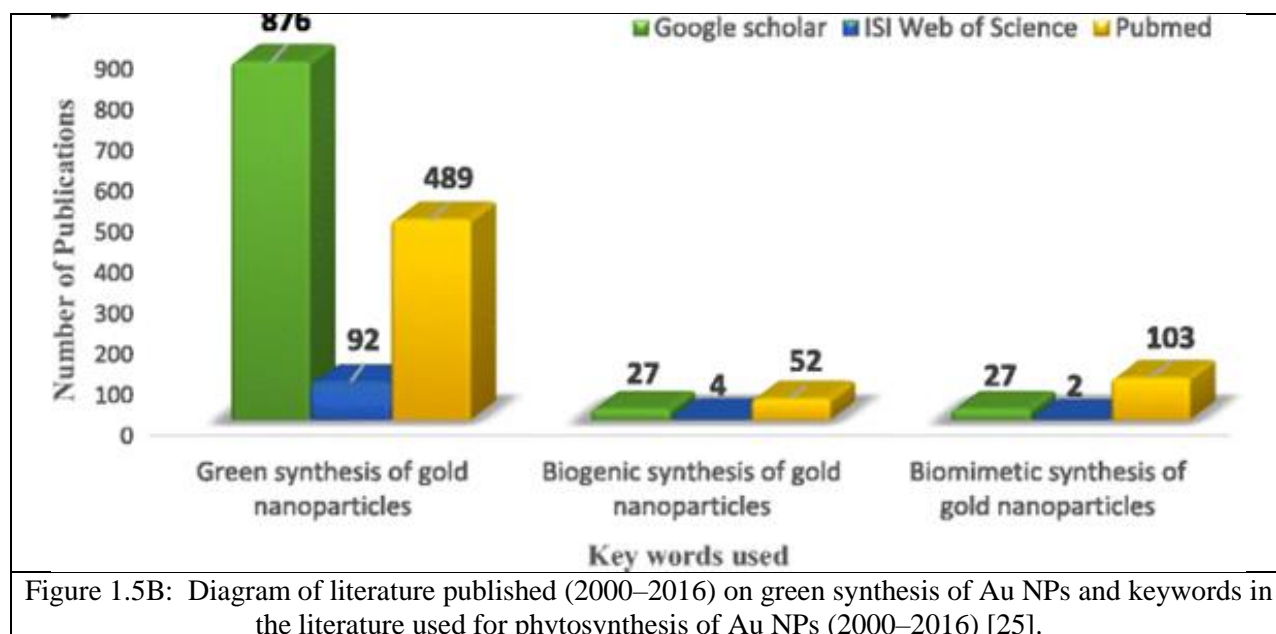
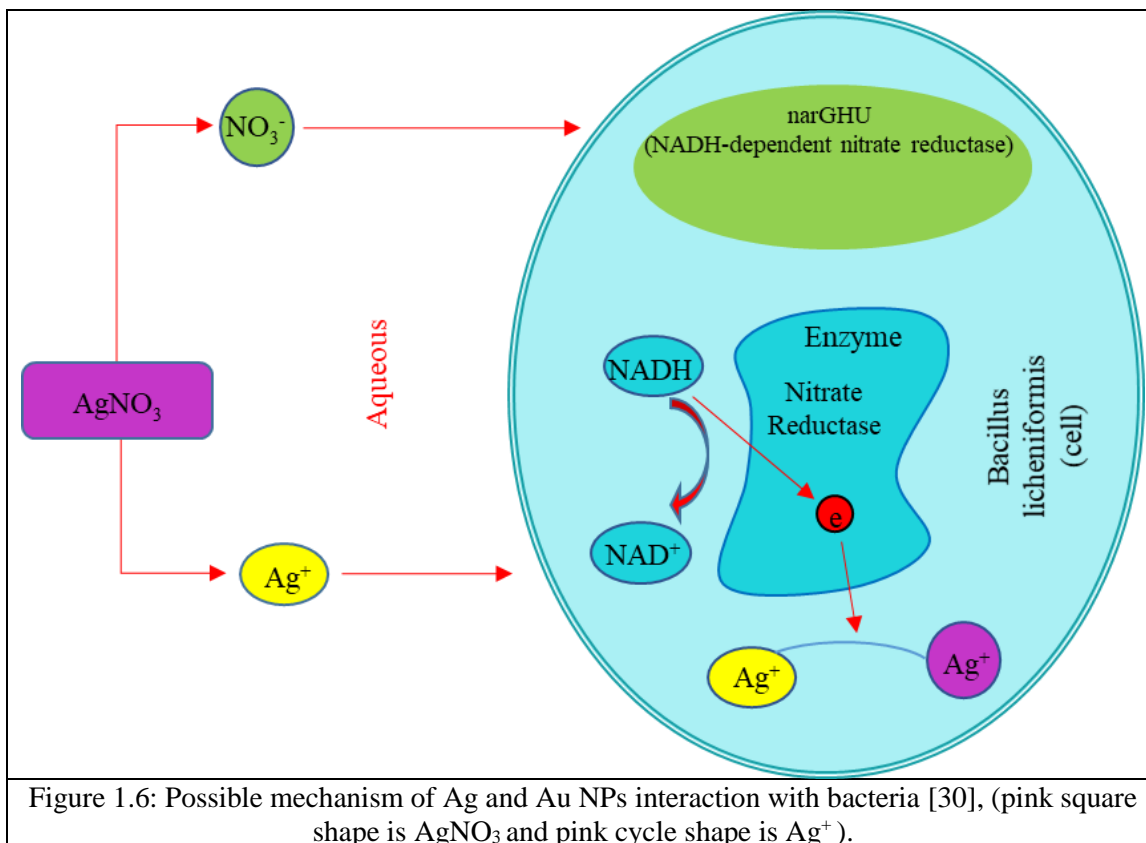


Figure 1.5B: Diagram of literature published (2000–2016) on green synthesis of Au NPs and keywords in the literature used for phytosynthesis of Au NPs (2000–2016) [25].

### 1.3.1 Bio-Reducing agents

The bio-reduction to give NPs uses a combination of biomolecules, which are present in plants and enzymes (proteins and amino groups, acids, polysaccharide and vitamins). For example, synthesis of silver nanoparticles can be by bacteria *Bacillus licheniformis* (including the enzyme nitrate reductase in the nitrogen cycle). Conversion of nitrate  $\text{NO}_3^-$  to nitrite  $\text{NO}_2^-$  as an electron was shifted to the incoming Ag ions depends on the enzyme NADH hydrogenases (Nicotinamide Adenine Dinucleotide) which may transform  $\text{Ag}^+$  to  $\text{Ag}^0$ . This enzyme is a significant factor in the biosynthesis of metal nanoparticles [30] (see Fig.1.6). Moreover, alkaline conditions (pH 10) have been reported to be a better condition for NPs formation. Thus their formation is faster and does not need agitation to get NPs formed in alkaline solution [31].

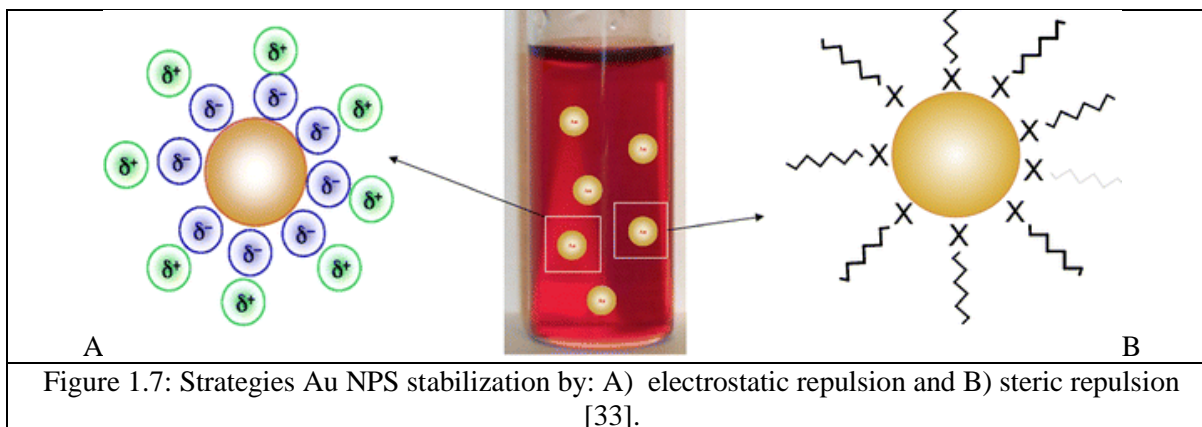




### 1.3.2 Capping agent

Capping or stabilizing agents are added to prevent NPs from aggregating (due to their high surface energy and growing in all directions without a stabilizing agent) [32]. There are many stabilizers that act as ligands (e.g. polymers and surfactants, proteins, biomolecules (DNA and RNA), microorganisms, bacteria and extract of plants [33]).

The capping agent or surfactant surrounds the nucleated NPs. For example, Au NPs are stabilized with soft thiol base groups that bond (Au-S) with the soft acid (Au) due to their higher affinity (coordination and complexation) with the NP surface than the solvent. These reagents should have a functional group or an atom lone electron pair that can react with Au particle. There are two basic modes of stabilization: (i) generation of electrostatic repulsion forces between NPs that repulse each other by forming a charged coating at the NPs surface (Fig. 1.7) and (ii) nonionic bulky agents that generate steric repulsion between particles forming a steric coating around the NPs surface [33].



## 1.4 Properties of gold and silver

Gold and silver are malleable transition metals. They have a high electrical and thermal conductivity. Silver has been known for its antibacterial and antifungal activities and used more to prevent infection due to increase the resistance of bacteria to antibiotics. Ag NPs is used in dressing for injuries (causes by burns) and wounds (caused by surgery) [34].

Table 1.1: The physical properties of gold and silver.

	gold	silver
Group	11	11
period	6	5
block	d	d
Per shell	2,8,18,32,18,1	2, 8, 18, 18, 1
Atomic number	79	47
Relative atomic mass	196.967	107.868
Electron configuration	[Xe] 4f <sup>14</sup> 5d <sup>10</sup> 6s <sup>1</sup>	[Kr] 4d <sup>10</sup> 5s <sup>1</sup>
Oxidation states	5, 4, <b>3</b> , 2, 1, -1	<b>1</b> , 2, 3
Crystal structure	Face centered cubic (fcc)	

When two metallic atoms combine, they form metallic bonds, which are non-directional. Metallic bonds consist of positive charge metal atoms in constant positions, surrounded by sea of delocalized electrons with small excitation energies ( $\Delta E$ ). There is a decrease in  $\Delta E$  as the number of atoms exhibiting increase orbital overlap increases.

### 1.4.1 Surface Plasmon Resonance (SPR)

When materials possess a real negative charge with a small imaginary positive dielectric constant ( $k$ , a quantity measuring the ability of substance to store electrical energy in an electric field) they can support a surface plasmon resonance. “Plasmons are pseudo-particles representing electron gas quantum fluctuations in the conducting material. Resonant excitation of these vibrations by electromagnetic waves in a thin layer of the conducting material, placed between the two media with different refraction index ( $n$ ), is named surface plasmon resonance” [35]. SPR is a coherent oscillation of the surface conduction electrons. This is excited by electromagnetic radiation. Au NPs and Ag NPs have many benefits in biomedical applications owing to their unique localized surface plasmon resonance (LSPR) [36]. The LSPR band depends on the size and shape of NPs. The colour exhibited by Ag NPs and Au NPs is due to the coherent excitation of all free- electrons with the conduction band causing (SPR), an in-phase oscillation (see Fig. 1.8).

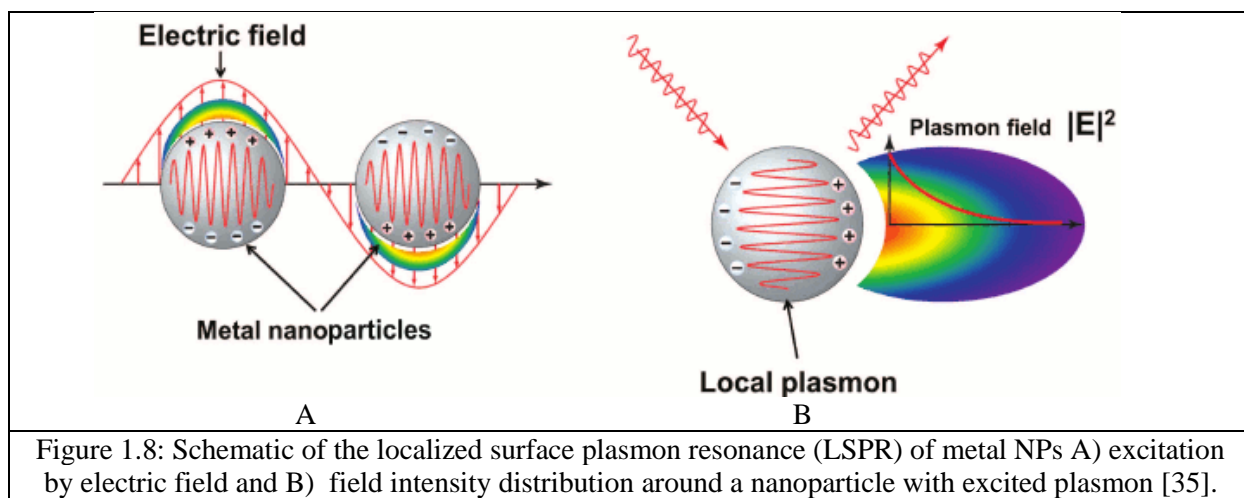
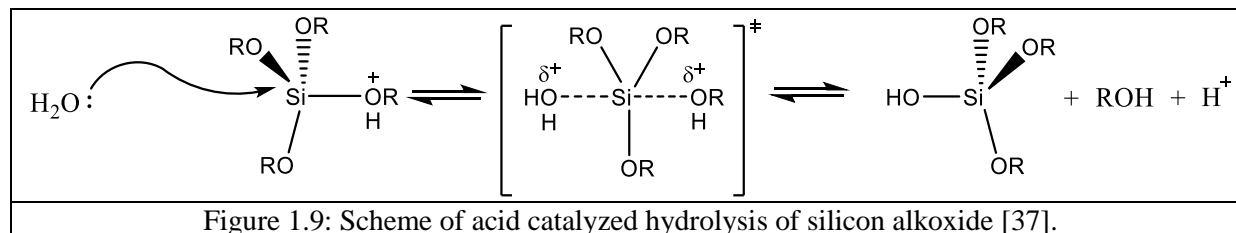


Figure 1.8: Schematic of the localized surface plasmon resonance (LSPR) of metal NPs A) excitation by electric field and B) field intensity distribution around a nanoparticle with excited plasmon [35].

### 1.4.2 Sol-gel method

A sol-gel method (see Fig. 1.9) is one of the most suitable methods to synthesize different metal oxides as NPs due to its low processing temperature, easy of fabrication and control, and its higher reagent purity and homogeneity. It includes the progression transition of a system from a liquid (sol) into solid phase (gel). Usually, it starts with inorganic salts or alkoxides and alcohols. The hydrolysis and condensation (polymerization) reactions are main process in the sol-gel

method to form a colloidal suspension or sol. When sol is cast into a mould, then a gel will form progressively. Sol-gel chemistry can be acid or base catalysed [37].



## 1.5 Antibacterial activity

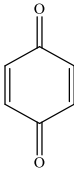
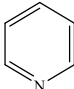
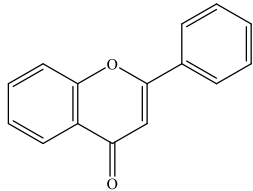
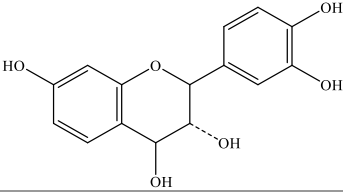
The development of increasingly of resistant strains of bacteria creates a vast challenge for society. Scientists are now attempting to respond to antimicrobial resistance by discovering new therapeutic strategies. This requires the evolution of a new effective bactericide [38]. There are two approaches: (i) to reverse the selective advantage of resistant bacteria competing with their sensitive drugs, and (ii) to drive a resistant bacterial population back toward drug sensitivity. Fighting against antimicrobial resistance (AMR) is necessary to preserve potent antimicrobial drugs for both humans and animals. The rational use of the existing antimicrobials and the combined use of new strategies is a key strategy to solve the problem of AMR. Combining existing antimicrobials with compounds that inhibit their specific resistance mechanisms would be a good choice. There is renewed interest in the investigation of alternative essential cellular processes, including bacterial central metabolic pathways, as the drug targets for the next generation of antimicrobials. Moreover, metallic NPs can both kill bacteria and inhibit biofilm formation. With single-drug therapy, there is always a selective advantage to resistance. Specific combinations of drugs can inhibit bacterial growth while disfavoring resistance to the individual components [39].

### 1.5.1 Plant derived antimicrobial (PDAm)

Plant-derived antimicrobials (PDAm) mostly originate in secondary metabolites. The importance of these plants that is their antibiotic activity has no resistance, because plants have an unlimited

ability to give a range of secondary metabolites (almost all of which are aromatic compounds). These have an ability to treat and control infections. Table 1.2 shows that a phenol derivative in these compounds (glycosides, alkaloids, quinones, flavonoids, steroids and tannins) have an ability to reduce pH and increase the membrane permeability. PDAs are classified as antimicrobials in a dose range 100-1000  $\mu\text{m}/\text{mL}$  for MIC [40].

Table 1.2: Plants derivatives with functional groups and properties [40].

Plant-derived antimicrobial groups	Structure	Chemical properties
Quinones		Conjugation cyclic-dione structure
Alkaloids		Naturally occurring amines having nitrogen in heterocyclic ring
Lectins and polypeptides	-	Lectins are carbohydrate binding proteins (phytoagglutinin) with MW around 17000-400000
Flavones/flavonoids/flavonols		Are ubiquitous in plants 'parts, fruits, seeds, flowers and even honey. Flavones are hydroxylated phenolics containing one carbonyl group.
coumarins	-	Are phenolic substances made of fused benzene and alpha pyrone ring forming toxic compounds found in plants.
Terpenoids and essential oils	-	Isoprene derivatives having a general $\text{C}_{10}\text{H}_{16}$ .
Tannins		Large polyphenolic compound containing sufficient hydroxyls and other suitable groups.

In general, bacteria are classified as Gram-negative and gram-positive. Furthermore, their structural differences lie in the organization of a key component of the membrane (peptidoglycan). Gram-negative bacteria exhibit only a thin peptidoglycan layer (2-3nm) between the cytoplasmic membrane and the outer membrane. In comparison, Gram-positive bacteria lack the outer membrane but have a peptidoglycan layer of around 30 nm thickness [41]. Ag and Au NPs are not toxic to human cells; at the same time, they kill fungi and bacteria. Indeed, they have important biocompatibility. For example, bacteria cannot easily develop a resistance to Ag NPs due to the NPs multiple effects on the bacteria membrane cell [42]. Silver NPs are an effective antimicrobial agent against different pathogenic microorganisms and many microbes reduce metal ions to metals (see Fig. 1.10) [43].

### ***1.5.2 Ag NPs***

Silver exhibits lower toxicity to mammalian cells, while exhibiting higher toxicity to microorganisms, compared with many metals [44], because Ag NPs can be immobilized when coated onto a filter for water purification or coated onto medical devices or in dental resin components to reduce the ratio of infection [45]. Ag NPs allow new strategies in the treatment of multidrug-resistance in bacteria. Firstly, Ag NPs have multi-functionality (e.g. anti-fungal and anti-bacterial). Secondly, Ag NPs can be a control vector in transmitted infection (e.g. that have an important contribution to many diseases). Thirdly, Ag NPs can be employed for wound healing and as part of an anti-vector-born disease strategy [46].

### ***1.5.3 Au NPs***

Au NPs are important materials because they exhibit unique properties (e.g. resistance of surface oxidation, surface-enhanced emission, higher Fermi potential and the chemical inertness and their large surface-to-volume ratio) [47]. Au NPs have a large number of atoms available to attach with the surface of bacteria [21]. Recent studies suggest that biosynthesised Au NPs are a promising candidate for the preparation of drugs and other medical applications (i.e. anti-tumor, labeling, imaging, apoptosis and interactions with DNA) [26]. In medicine, many studies show that Au NPs are worthy of more attention, because they have biocompatibility (which is a key advantage). Thus, Au NPs are compatible with the human body cell and yet have resistance to

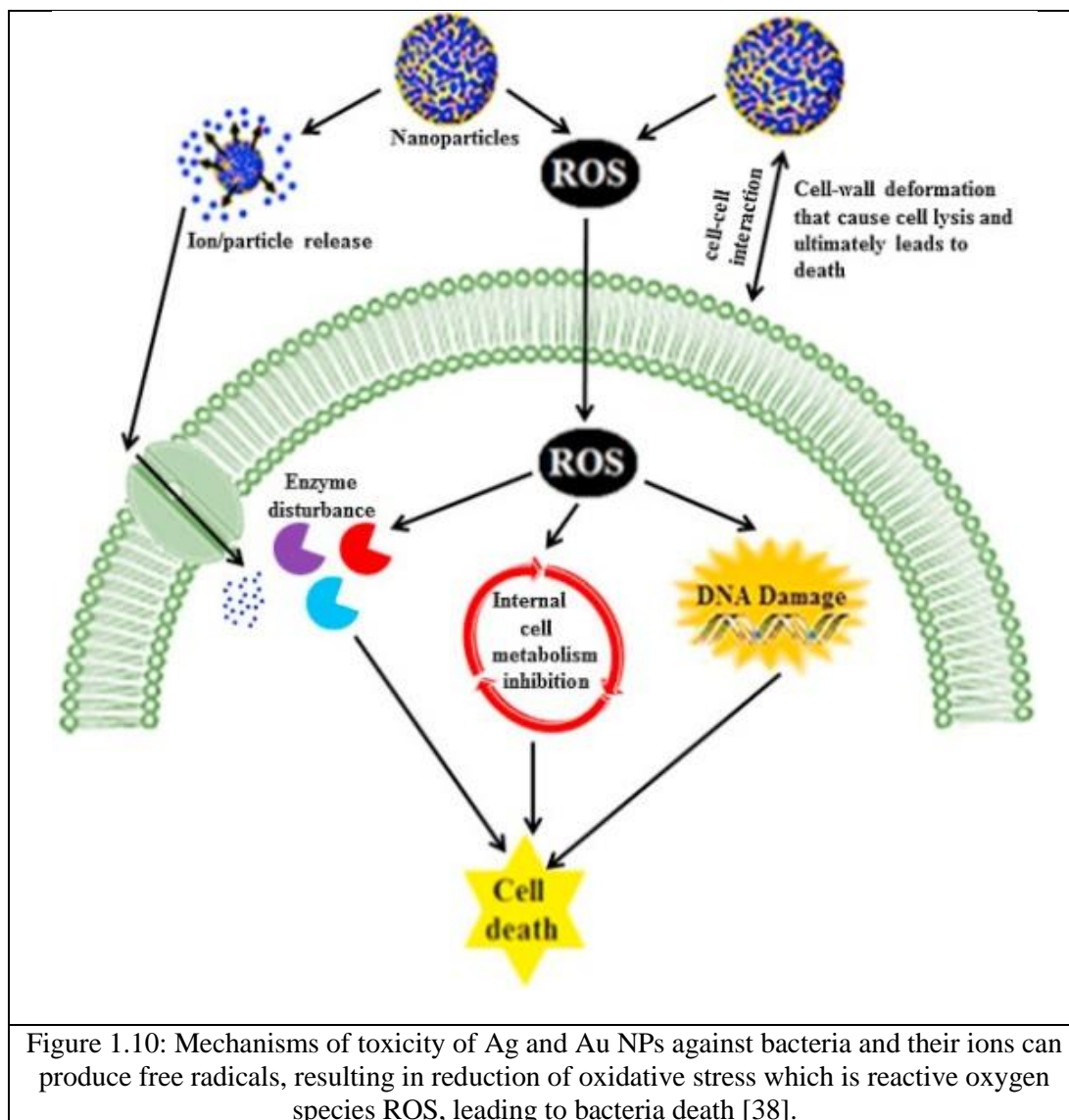
corrosion [27]. Au NPs show a significant anti-bacterial activity depending on their size and shape as well as the type of bacteria [28].

### ***The Antibacterial mechanism of NPs***

Several mechanisms appear to be involved in defining the effect of Ag and Au NPs:

- reaction with biomolecules (like DNA, RNA or enzymes during an electron release mechanism) leading to weaker DNA replication. Ag ions form a complex with DNA [39].
- combination with proteins (causing denaturation and inactivating them by reducing bacterial proteins levels [48]). Ag NPs could lead to the denaturing of protein. For example, Ag ions react with nucleophilic amino acid residues in protein and attach to amino, carboxyl, imidazole, thioyl (R-SH), and phosphate groups of membrane or enzyme proteins, finally leading to cell death [49]. Moreover, it could lead to form Ag complexes [50] with electron donors containing S, O, or N (thiols, carboxylates, phosphate, hydroxyl, amines, imidazoles and indoles) [49].
- Ag NPs attach and anchor to the surface of cells causing a change in the structure and causing damage, significantly disturbing vital cell functions, affecting permeability, causing pits and gaps, depressing the activity of respiratory chain enzyme and leading to cell death [22]. Interaction and attachment to the cell membrane surface and disturbance of respiration and permeability [18]. For example, Ag and Au NPs have strong binding to the bacterial cell wall (via electron donating groups), allowing them to disrupt the bacterial cell membrane, causing leakage of nucleic acids and cytoplasm. [53]. Silver ion could be reduced by the enzyme leading to formation of silver nuclei that inhibit several functions in the cell [50].
- increase in ATP (where ATP generation is a significant part in the respiration chain of bacteria via the  $\text{NAD}^+/\text{NADH}$  reaction) intercellular ATP levels, leading to bacterial death. Induction of photo-mutagenic processes in the presence of the light; (inducing free radical generation, causes damage to DNA and essential proteins). Also, catalyzed oxidation reactions, produce (ROS) that leads to the death of bacteria [26].

- Silver nanoparticles inhibit the multiplication of bacteria and do not need direct contact with the bacteria because they produced ROS that diffuses from fibers or pads to the surrounding environment [26].



Furthermore, it is reported that a Ag NP possesses cytotoxicity and genotoxicity. A Ag NP reduces the ATP content (adenosine triphosphate (ATP) is a nucleotide which performs many essential roles and provides the energy of the cell) of living cells leading to the mitochondrial dysfunction. The formation of ROS (oxygen is metabolized and converted to  $O_2^-$ ) by several



components of the mitochondrial respiratory chain [54]) leads to damage of DNA and chromosomal dysfunction [55].

## **1.6 Photocatalysis**

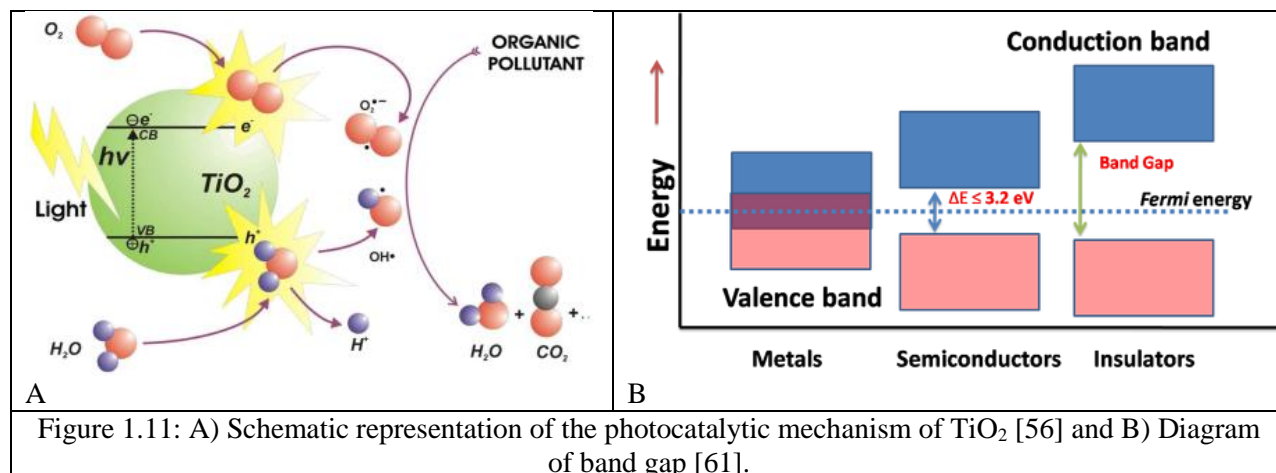
Photo-activated chemical reactions include the interaction of a photon with chemical compounds to generate free radicals. Such free radicals can be produced from  $\text{H}_2\text{O}_2$  or  $\text{O}_3$  as oxidation compounds under UV because of low  $\lambda$  and high energy radiation. Another method to generate free radicals is to use a semiconductor such as  $\text{TiO}_2$  photocatalyst. It has a band gap semiconductor and it generates highly oxidizing species as  $\text{OH}\cdot$  on its surface [56]. Photocatalysis is a photoinduced reaction process which is accelerated by a catalyst. These reactions are activated by the absorption of photons of sufficient energy (greater than the band gap energy of the catalyst). Heterogeneous photocatalysis is a combination of photochemical reaction and catalysis operating together [57]. That means, chemical reactions are carried out using both light and in the presence of a catalyst (homogeneous or heterogeneous) [58].

The main advantages of photocatalysts are that they: (i) can use sunlight as a source of irradiation (especially useful in developing countries) [59], and (ii) lead to complete mineralization and degradation of the organic pollutants to  $\text{CO}_2$  and  $\text{H}_2\text{O}$  in moderate condition. It can be performed at normal pressure and temperature with atmospheric oxygen as an oxidant. Nowadays, many studies have reported on how one can raise the efficiency of existing photocatalytic processes. However, new nano-materials are often required to enhance photocatalytic performance [60] (see Fig. 1.11A).

### **1.6.1 Semiconductor (SC) materials**

SCs are materials having a band gap between the valence band and conduction band that is larger than for metals (e.g. 1.4eV) and less than for insulators (e.g. 9eV) (see Fig. 1.11B). There are two types of semiconductor at a p-n junction: n-type (increasing electrons, with donor atoms and

Fermi level is near to the valence band) and p-type (increasing holes, with acceptor atoms and Fermi level is near to the conduction band) [62].



Photocatalytic processes are initiated by electron excitation from the valence to conduction band when semiconductors absorb photon with energy equal or great than band gap, leaving an electron vacancy known as a hole in valence band. Thus, this hole is assumed to behave as a particle with positive charge and effective mass. The electron-hole recombination must be prevented in order to have a photocatalysis [58]. The valence band holes are considered powerful oxidants and conduction band electrons considered good reductants. The band gap energy is inversely proportional to the size of semiconductor NPs [63]. The minimum wavelength to excite an electron depends on band gap energy of photocatalyst, which is calculated according to Eq (1.1):

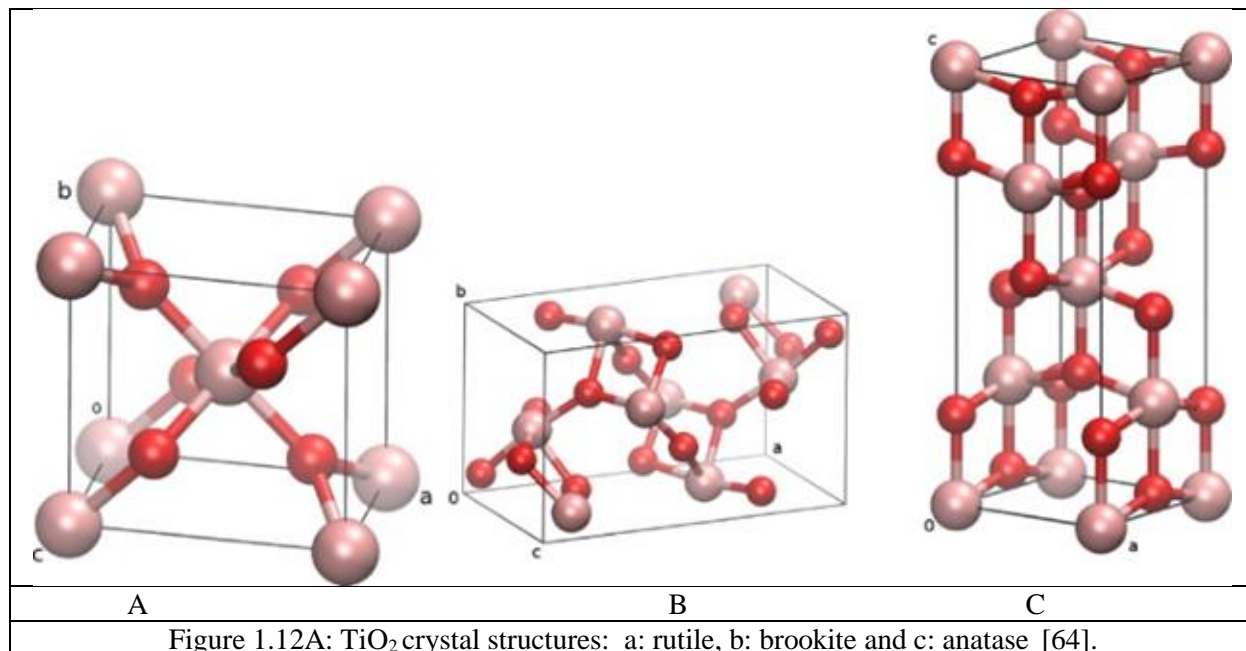
$$\Delta E \text{ (eV)} = 1240 / \lambda_{\text{max}} \text{ nm} \quad \text{--- (1.1)}$$

The defect levels are produced by atom ion vacancies created by oxygen. The defect on the surface of the photocatalyst acts as a temporary surface trap for charge carriers (holes or electrons), leading to non-radiative relaxation. This greatly reduces the quantum yield by

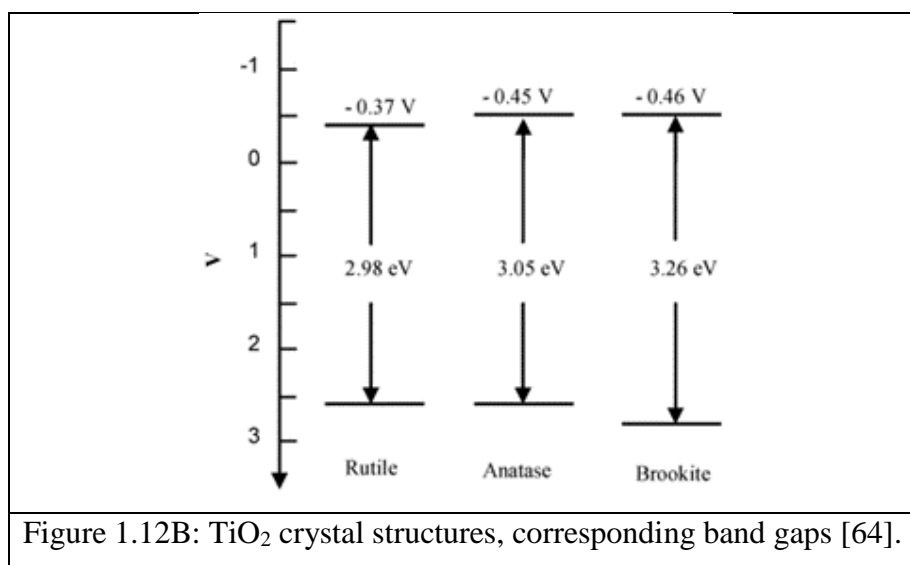
preventing radiation recombination. Along with the NPs revolution, the optical properties of SCs add to their dimensionality, and so a function of size and optical properties become strongly dependent on the size owing to the quantum confinement of holes and electrons [64].

### 1.6.2 $\text{TiO}_2$ NPs

Titanium dioxide ( $\text{TiO}_2$ ) NPs have received much research attention in last decade as photocatalysts [65]; titania is a semiconductor. It exists in three phases: anatase, rutile and brookite (see Fig 1.12A). These phases have high refractive indexes (anatase = 2.488, rutile = 2.609, brookite = 2.583); rutile is the stable phase at higher temperature. Its optical band gap is 3.0eV (corresponding to  $\lambda=415\text{nm}$ ). Anatase is formed at lower temperature (rarest of the naturally occurring forms); it has an optical energy gap of 3.2eV (corresponding to  $\lambda=380\text{nm}$ ). Furthermore, anatase is used a significant photocatalyst because it is thermodynamically less stable than rutile and undergoes transition to rutile phase (at 450-1200°C) [58]. This transformation is dependent on many factors as initial phase and particle size, preparation conditions and temperature.



Moreover, it exhibits a shorter wavelength absorption edge (an absorption discontinuity or a sharp discontinuity in the absorption spectrum). These discontinuities occur at wavelengths where the energy of an absorbed photon corresponds to an electronic transition or ionization potential (see Fig. 1.12B) [60]. Both anatase and rutile have the same symmetry (tetragonal) despite having different structure. Anatase has octahedrons of  $\text{TiO}_2$  that share four edges hence the four-fold axis. Rutile has sharing of two edges of octahedron forming chains. Brookite has an orthorhombic crystalline structure. For all phases, each titanium atom coordinate with 6 oxygen atoms and each oxygen atom coordinate with three titanium atoms [64].  $\text{TiO}_2$  is an intrinsic n-type (similar to ZnO) semiconductor and it has oxygen 2p character in valence band and its conduction band is principally Ti  $3d^2 4s^2$  in character. In the atomic limit, each  $\text{TiO}_2$  unit contributes for 2p orbitals (two filled oxygen) and 2p orbitals (four half-filled oxygen) and four titanium valence electrons. In the pure material, 2p orbitals have the four titanium valence electrons (filling the vacant oxygen level). When an oxygen atom is removed three oxygen, 2p orbitals are removed, but only 4 electrons. The remaining two electrons are forced to reside in Ti 3d orbitals, i.e. the conduction band [66].



$\text{TiO}_2$  can only be activated by UV light due to the anatase (2.9eV) and rutile (3.0eV) band gaps. This translates to a small part of the solar light (around 4-5%) that reaches the Earth [60]. UV

radiation consists of UVA (400-315 nm), UVB (315-290 nm) or UVC (290-200nm) in the near UV. The UVB and UVC regions are filtered out by the ozone layer [67].

During recent years, efforts have been directed at getting nanostructured TiO<sub>2</sub>-based photocatalysts with a large specific surface area [64]. Nanoparticles show very different features than bulk materials because of their high surface area to volume, as they have more active atoms sites at the surface compared to inner atoms. Thus, in this case, the increased surface energy associated with sites of the NPs leads to an increase in the rate of chemical reactions on the surface of NPs [58] because surface-to-volume ratio is very high in NPs [65].

Nanostructured TiO<sub>2</sub> spheres (which are considered zero-dimension nano-materials) usually possess many features: a large specific surface area and a high pore size and volume. Therefore, increasing the accessible surface area is beneficial, provided the rate of mass transfer leads to organic pollutants adsorption is good. Moreover, TiO<sub>2</sub> spheres allow as much light as possible to access inside NPs, thus increasing the light-harvesting capabilities of the TiO<sub>2</sub> [67].

The photocatalytic performance of TiO<sub>2</sub> is predominantly influenced by improving the photo-quantum efficiency law (is observed when the size of the particles is too small to be comparable to the  $\lambda$  of electron) by various parameters (such as concentration, specific surface area per unit volume or contact area, crystalline phase and presence of other phases [59], controlling size and shape of NPs, structure composition, reducing the fast recombination of photo-generated electron and photo-generated hole pair ( $e^-h^+$ ) and extending the absorbance of TiO<sub>2</sub> photoresponse into the visible light) [68],  $\lambda_{\max}$  and initial organic contaminates (OCs) [67].

The important factors affecting the process are: amount of catalyst, presence of ions, agitation to overcome diffusion-limitation, temperature, initial organic contaminant concentration, pH, irradiation time and light  $\lambda$  intensity and flux. There are many advantages to using TiO<sub>2</sub> as photocatalyst: (i) a strong activity for the decomposition of organic pollutants (ii) nontoxicity, (iii) chemical stability, (iv) long durability, (v) low cost (the abundant presence on Earth) (vi) bio-compatibility [67], (vii) physical/optical/electrical properties and transparency to visible light, and (viii) high specific area [64]. TiO<sub>2</sub> has a more negative conduction band edge potential. This means a higher potential energy for photo-generated electrons, that are relatively easy to use and produce, exhibiting higher photo reactivity (photonic efficiency 10%) [59], and a high

tolerance to light-induced corrosion. Furthermore, TiO<sub>2</sub> is recognized as one of the most important semi-conductors, because of this it has been extensively used in many fields: ( e.g. sensors, solar energy conversion devices, photochromes and especially as photocatalysts for water purification and to decompose organic contaminants in air [69]). In bio-medicine, it is used for: (i) photo-dynamic therapy for cancer therapy. (ii) biological sensors (iii) and cell imaging [65]. Moreover, commercially, TiO<sub>2</sub> NPs are used in sun creams that absorb UV [70]. It is also utilized as a pigment (brilliant white) owing to its resistance to discoloration, its brightness and its high refractive index. It can be found in food coloring, in toothpastes, tiles, self-cleaning surface and tents are coated with TiO<sub>2</sub> unique photoinduced super hydrophilicity [59]. TiO<sub>2</sub> has distinctive physicochemical properties as result of their many properties such as: shape and size ( $\Delta E \propto 1/\text{size}$  depending on quantum efficiency law), crystal structure, electronic structure and doping [65].

### ***1.6.3 TiO<sub>2</sub> and hybrid system***

Major challenges have been identified that remain to be solved to enhance TiO<sub>2</sub> photocatalytic activities: reducing its large band gap (3.2eV) causing low efficiency because of its narrow  $\lambda$  range of light operation range and its inability to absorb in the visible region. Moreover, the recombination rate of photo-induced electron-hole pairs is fast. [58]. Three methods are found to control these problems and raise the efficiency of TiO<sub>2</sub>: (i) harvest more visible sunlight, (ii) increase the particle size, and (iii) doping with a metal or nitrogen, sulfur or carbon atoms which could shift it to longer wavelengths (above 400 nm). Recent literature has revealed how the efficiency and selectivity of TiO<sub>2</sub> photocatalytic reactions should rise [60]. Many strategies have been employed involving modified TiO<sub>2</sub> NPs to be more effective owing to different physicochemical properties [71]. Some dopant, metals are NPs that have unique properties such as high surface area to volume ratio [65]. That means novel spectral and optical properties (like Ag and Au NPs). Depositing Ag and Au NPs onto TiO<sub>2</sub> NP surfaces leads to efficient electron transport and maximizes electron-hole separation and the important factor is surface plasmon resonance in Ag and Au NPs. Hence, electrons in the metal surface can transfer to the SCs by UV light reducing recombination of electron-hole pairs and effective separation. Also, significantly preventing metal NPs from erosion in real applications [67]. (see Fig.1.14A).

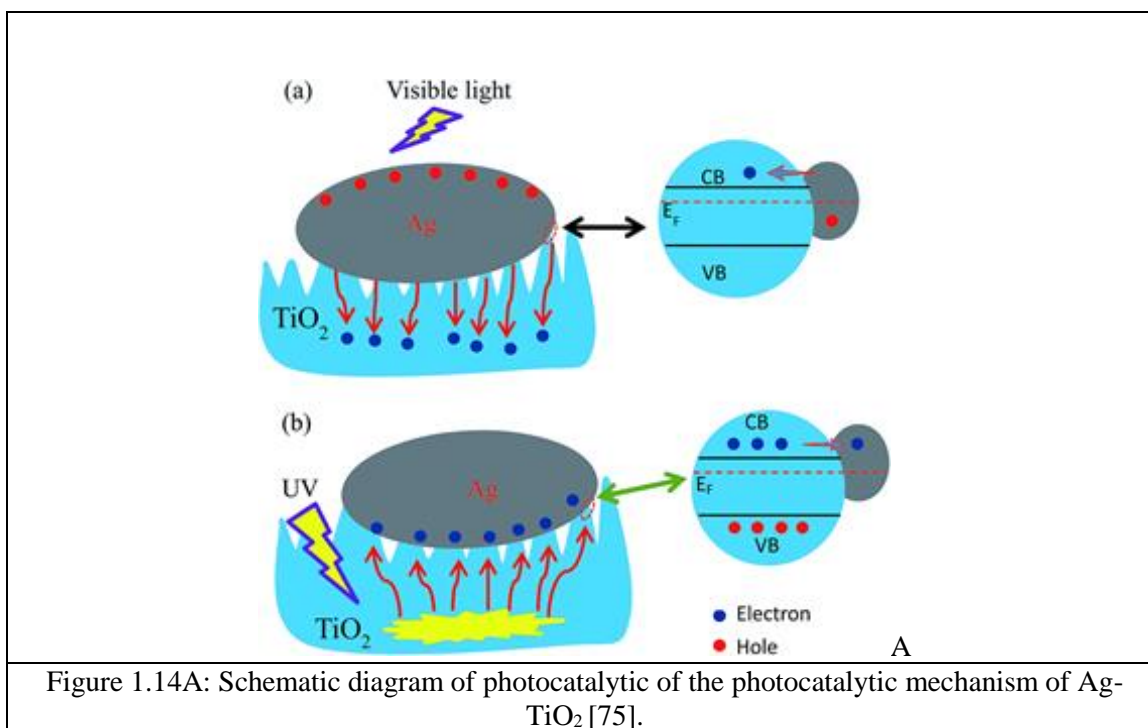
Recently, it has been demonstrated that Ag and Au NPs with TiO<sub>2</sub> (as dopant or core@shell) structure considerably improves photocatalysts because they induce electron transfer to TiO<sub>2</sub>

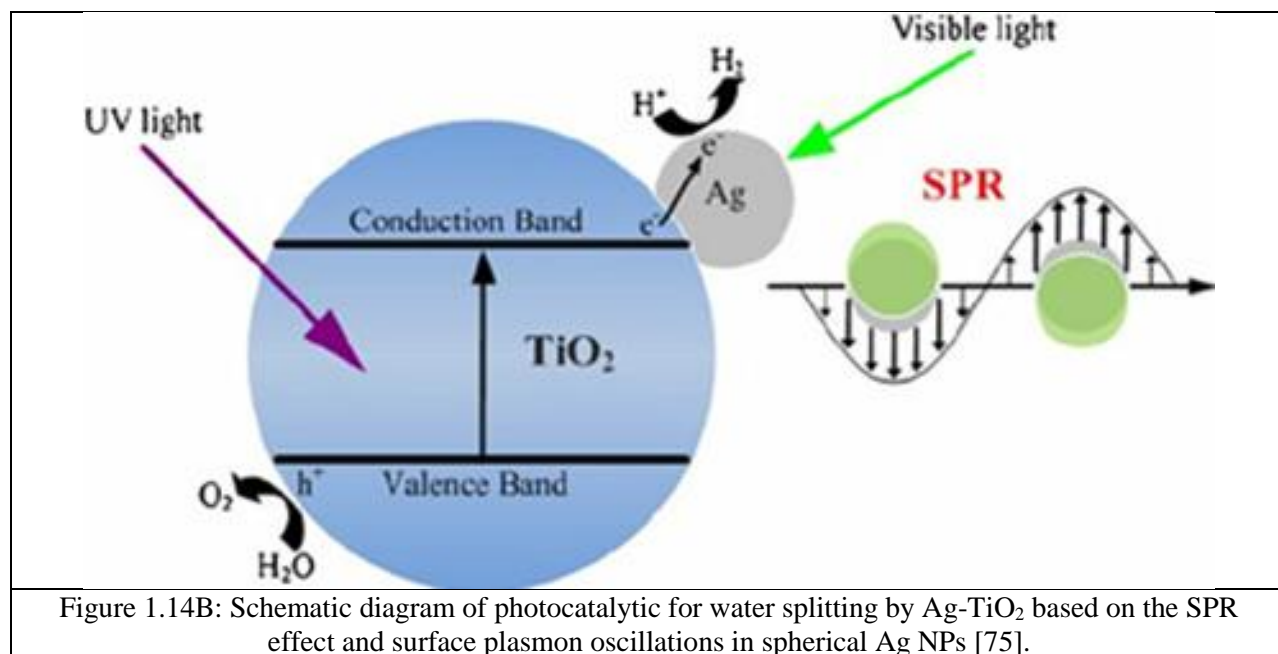
causing charge separation, shifting the band gap to the visible region. Also, TiO<sub>2</sub> NPs doped with metals have significant attention in photocatalysis for water purification because these NPs show superior efficiency to pure TiO<sub>2</sub> [68]. However, TiO<sub>2</sub> doped with metals have some limitations. For example, it is difficult to narrow the band gap because of recombination sites of photo-excited charge carriers [72]. In addition, defect-induced charge trapping with M-TiO<sub>2</sub> has a lot of electron traps. So, this leads to be favourable for the separation of photo-induce electron-hole [68].

#### 1.6.4 Surface plasmon resonance (SPR) and TiO<sub>2</sub> NPs

The surface plasmon resonance absorption by metal NPs is a promising method for the development of visible-light-responsive TiO<sub>2</sub> photocatalysts. Ag and Au NPs [73] have been considerably investigated owing to their unique electron, optical and magnetic properties which are based on surface plasmon resonance (SPR) [17].

The presence of activation metal or ions in TiO<sub>2</sub> introduces new energy level to the transition metal inside the band gap of TiO<sub>2</sub>. Thus, the absorption shift to visible light region comes from metal energy level to the conduction band of TiO<sub>2</sub> [75] (see Fig.1.14).





## 1.7 Green chemistry and photocatalysis

Green chemistry methods of synthesis/processing have come into favour in preference to chemical and physical approaches due to its environmentally-friendly nature. Amongst them, biomimetic methods of preparing TiO<sub>2</sub> with different bio-materials (that show a high absorption of light and a good conductivity) are particularly useful. Moreover, bio-materials were used because the extracts and organisms act both as capping and reducing agents in synthesizing NPs [76]. Active carbon was used for dye removal from waste water from one form to another form. More recently, many studies have reported that different biotemplate structures has received attention to synthesis a number of nanoparticles like proteins, viruses, DNA and yeast [77]. Photocatalysis has attracted great interest in recent years due to its compliance with green chemistry. The main challenge resides in enhancing photocatalytic performance, through higher chemical stability, more efficient electron transfer and larger surface areas [68].



## **1.8 Aims of present research**

In the light of the above literature reviews the aims of the present research were to use Portobello mushroom spores (PMS) as:

- 1- surfaces to synthesize  $\text{TiO}_x$ , Ag, Au to form NPs/PMS and their nanohybrids as  $\text{TiO}_x$ -Ag,  $\text{TiO}_x$ -Au and Ag-Au NPs and in addition immobilized,  $n\text{Ca}^{2+}$ ,  $\text{CaCO}_3$  and nHAp,
- 2- a template for  $\text{TiO}_x(\text{PMS})$  biomimetic photocatalysts for control of water pollution by organic and coloured pollutants,
- 3- a natural microsphere for drug delivery system, and
- 4- a new antimicrobial.

The author believed that this would add new novel information to the scientific literature and might lead to positive nanotechnology outcomes for communities.

## **Chapter 2: PMS and Related Works**

---

An assessment of the literature on the general green synthesis of TiO<sub>2</sub>, Ag and Au NPs, HAp, drug delivery, antibacterial and photocatalysis using plant, bacteria and fungus is presented in this chapter.

### **2.1 Introduction**

At present, much of the relevant literature reports on the use of different types of mushroom extract for the biosynthesis of Ag, Au NPs. The biosynthesis of TiO<sub>x</sub>, Ag and Au NPs using PMS is new and no one has prepared this before. Subsequent sections summarize and discuss literature reports which are available currently.

The importance of PM as a living organism is based on its ability to produce complex materials with interesting structures and morphologies due to different natural-selection functions. These functions have the potential to solve many global problems biologically. Some of these problems are medical issues (as disease therapy and microbial resistance) and others relate to pollutant removal. In biomineralization, often the mineral formation is normally motivated and controlled via organic materials as polysaccharides and collagen. These materials can organize inorganic crystallization at various stages: nucleation, growth, phase, orientation and assembly. Many researchers have reported on the novel properties of biogenic materials [78].

### **2.2 Biosynthesis of NPs**

Despite the success of chemical methods (using reducing agents) and physical methods (e.g. evaporation-condensation and laser ablation) in preparing NPs, there are still some limitations: (i) the release of hazardous by-products, (ii) long time of processing and (iii) purification may be difficult. Therefore, biosynthesis of NPs using biological organisms may be a better alternative method using enzymatic reactions and the photochemical characteristics of bacteria, fungi, plants

and algae. These biological methods have been suggested as possible eco-friendly, easily available, acting as reducing and capping agents. These biomaterials may therefore offer alternative ecofriendly routes to NPs and act as natural NP bio-factories [20].

### **2.2.1 Green synthesis of NPs and antimicrobial resistance (AMR)**

Generally, antimicrobial resistance (AMR) is one of the important global health problems impacting on health and safety [79]. The infections will cause deaths of about 300 million people in the next 35 years if not effectively treated. Hence, this was one focus of the present research.

Recently, one study highlighted that the availability of information technology (e.g. electronic surveillance) about AMR infections will facilitate the prevention and containment of such emerging infectious diseases [80]. Several studies have suggested that the development of new antimicrobial agents could help fight against AMR. This can be a rational and combinational use of existing old antimicrobial drugs and combinational use of anti-resistance [39]. Further, this chapter summarizes 2015 publications relating to antimicrobial resistance in the environment (involving plant in wastewater, agriculture and hospitals) [81].

## **2.3 Toxicology and NPs**

The toxicity of NPs has an important impact on human health and the environment. This can be from their high surface to volume ratio (i.e. their particle size), but also their morphology, degree of aggregation and concentration and because of all these they interact uniquely with the surrounding environments [20]. Often their toxicity increases as particle size decreases, possibly due to their: (i) ease of penetration of cell walls, (ii) high solubility and vapour pressure (Kelvin equation), (iii) higher reactivity with large number of defects and lower number of nearest neighbors (N) and (v) low stability metastable structures.

- **Particle size effect**

Particle size effects have long been known in metal catalysts [82] and can be attributed to the increasing fraction of metal surface atoms as the particle size decreases say from 10nm to 2nm. It

was reported that the greatest inhibition of algal growth was seen with ZnO NPs with weaker inhibition by Fe<sub>2</sub>O<sub>3</sub> NPs. The EC<sub>50</sub> values (the concentration of a drug that gives half-maximal response) were in the order ZnO (2mg/L) > NiO > CuO > TiO<sub>2</sub> > Fe<sub>2</sub>O<sub>3</sub> (76 mg/L) [83]. It ought to relate to particle size effects seen in other spheres of chemistry, e.g. catalysis of structure-sensitive and insensitive reactions over small metal particles notes at Brunel in the 1980s. Some reactions can be structure-sensitive and others structure- insensitive depending on the specific sites most suited to catalysis of a reaction [84]. The toxicity of smaller Pt NPs is of concern, but it is thought this toxicity may be reduce by increasing the particle size [85]. While the bioactivity-toxicity of 8-9nm cerium dioxide (CeO<sub>2</sub>) NPs is also of concern. The disinfection effect of Ag-CeO NP is clearer in *E.Coli* than *S.aureus* [86].

It seems to the author that for metallic and oxide nanoparticles their (i) ease of penetration through cell walls, (ii) metastability, (iii) reactivity-bioactivity-biototoxicity, (iv) structure, (v) solubility and (vi) vapour pressure will all be affected by particle size and morphology.

## **2.4 Related works**

There are many studies of the synthesis of NPs and antimicrobials using plant material (e.g. leaves, seeds and roots) [87]. The next section will describe some of the relevant literature that was published during 2016-2018.

It was reported that ZnO and MgO NPs were active against two pathogenic fungal species at different concentrations. This study confirmed that higher concentrations of NPs were most effective in inhibiting the germination of fungal spores at 12mg/L [88].

### **2.4.1 Ag NPs**

A simple biosynthesis of Ag NPs (14 nm the size) was reported [89] using the aqueous extract of stem bark of *Syzygium cumini* (SC) plant. Ag NPs have antibacterial activity at 3mM dependent on their size and shape. If the size of Ag NPs is less than 10nm, there is an interface with *E.coli*. producing electronic interaction [89].

Phyto-Ag NPs have received research attention using several species of plant extract combination of biomolecules (e.g. proteins, carbohydrates, terpenoids, alkaloids, tannins, phenolic acids and saponins) that can play a vital role in the reduction and stabilization of NPs. Several studies have been reported the biosynthesis of Ag NPs in 1mM of AgNO<sub>3</sub> [23]. The eco-friendly thermal route to the preparation of 70-192nm sized Ag NPs using an *aloe vera* plant extract showed that these have antibacterial activity but no cytotoxicity towards human peripheral blood mononuclear cells [90]. Numerous studies have shown that spherical 14nm Ag NPs were produced using brown algae-seaweed and seagrasses [20]. In another study, phytochemical molecules in *Seabulckthorn* (SBT) leaf extracts were useful as reducing agents to synthesize 10-40nm SBT@Ag NPs. These NPs exhibited antibacterial activity with minimum inhibition concentration at 2µg [91].

Green synthesis of Ag NPs using *Prunus persica* [92], *Citrullus lanatus* fruit [93] and saffron (*Cocus sativus L.*) waste has been reported. 12-20nm Ag NPs exhibited significant antibacterial effect against *Escherichia coli* and other five types of bacteria [94]. A similar study using *Eriobotrya japonica* leaf extract attempted the synthesis of spherical 20nm Ag NPs with antibacterial activity [95]. In another study, an extract of plant *Radix Puerariae* was used to synthesize 10-35nm spherical-oval Ag NPs at pH 9 and for 9h. Also, the results showed shorter reaction times, higher reaction rates, reusability of catalyst and the potential for a variety of desirable products being synthesized [96].

#### 2.4.2 Au NPs

There are many studies reporting the synthesis of Au NPs using plant materials and their extract such as *Menta piperita*, *Cinnamomum zeylanicum*, *Sebania drummondii*, *Breynia rhamnoides* and *Acalypha indica* [97]. The green synthesis of 10-50nm Au NPs used the extract of *Acacia nitotica* twig bark after 10 min at room temperature (RT). These were characterized by XRD, TEM, FTIR and UV-Vis. Au NPs exhibited a high sensitivity and good selectivity for the detection of nitrobenzene [98].

In addition, Au NPs are widely used in biomedical applications, as well as for cell tracers, bio-sensing and bio-diagnostics, because they easily bind with thiol and amine groups enabling surface modification with amino acids and the DNA [99]. It has been reported that 3.5nm Au

NPs capped by lysine are biocompatible and not immunogenic [99]. It has been stated that PMS can be a bio-template in an innovative approach to combine the advantages offered by NPs and devices with medicine and surgery to treat disease and enhance life. Moreover, it can be used to reduce and prepare NPs. These NPs could be used as nano-medicine as Ag and Au NPs as antibacterial and antifungal because NPs enhance these properties [100].

Biogenic synthesis of 50nm spherical Au NPs using extracellular membrane fraction of *E.coli* K12 was investigated at RT and without pH adjustment. It was observed that reduction and stabilization of Au NPs was due to certain membrane-bound peptides of *E.coli* K12, affecting its heterogeneous photo catalytic activity in degradation of 4-nitrophenol [101].

Bioreactor bacteria had the ability to bio-reduce Au ions to Au<sup>0</sup> NPs in an eco-friendly approach after 4h; TEM and XRD confirmed that the average size of the product Au NPs was 9nm [102]. Other green synthesis of Au NPs used the aqueous extra of *Elettaria cardamomum* [103], polysaccharides [104] and *Indian propolis* [105].

Better drug release was reported to be due to nanoconjugates with  $\pi$ -back bonding between Au NPs and the polyesters. The carboxy group in polyester play an important role via  $\pi$ -back bonding to Au NPs-multi block copolyester producing nanoconjugates. This could be used as a prospective drug carrier or drug delivery system [106].

### **2.4.3 TiO<sub>2</sub> NPs**

Recently, some studies reported photocatalytic hydrogen generation using TiO<sub>2</sub> NP/carbon nano tubes (CNTs) under visible light irradiation. They have concentrated on visible light photoinactivation of *E. coli* bacteria by using CNT/TiO<sub>2</sub> and thin films under visible light photoinactivation at various CNT contents [107]; some reports also indicate photoinduced antibacterial activity of TiO<sub>2</sub> by using UV irradiation. Importantly, it has been reported that the toxicity of TiO<sub>2</sub> NPs depends on the crystalline phase present (anatase more active than rutile) as much as the size of such particles. Anatase can interact with DNA double strands and change their secondary structure [54]. TiO<sub>2</sub> NPs and nanohybrids (e.g. TiO<sub>2</sub>-Ag/PMS and TiO<sub>2</sub>-Au NPs/PMS) have been reported to be useful as more active photocatalysts [108].

#### 2.4.4 HAp biotemplate

There are many methods of preparing HAp/biotemplates. It was reported that nano-HAp (nHAp) was produced using natural  $\text{CaCO}_3$ -eggshells as a direct source of calcium precursor by a simple solid-state sintering method. This study revealed that the relative density and grain size played a significant role in governing the properties of the HAp-eggshell samples [109]. Other studies demonstrated that HAp crystals are generally obtained on a nanoscale rather than at a microscale using conventional methods (e.g. in-situ deposition or mineralization within a biomacromolecular matrix), because it is comparatively difficult to synthesize microscale HAp particles. Using  $\text{CaCO}_3$  as a template has allowed the synthesis of carbonated-hydroxyapatite microspheres from the conversion of  $\text{CaCO}_3$  spherulite templates within a collagen matrix under mild conditions [110]. Hollow microspheres of HAp nanosheet/nanorod-assembled hierarchical nanostructures can be prepared with a nanoporous structure by a microwave-assisted hydrothermal method using a disodium salt of biocompatible creatine phosphate [111]. Another study has reported on the importance of plant-derived natural biocomaterials in tissue engineering; the possibility of using mushroom as a designer scaffold was one focus. Mushrooms are often used in biomedical applications and more than 100 species of mushrooms are documented by traditional Chinese medicine for treatment of a wide range of ailments. [112]. Some studies have concentrated on the use of mushroom-derived chitosan (linear polysaccharide; Poly-(D) glucosamine) as a component in calcium-based cements in the development of bone substitutes and other novel biomaterials for tissue regeneration. It is reported that nano-fiber coated mushroom is a novel 3D scaffold for bone generation, without any threat of fungal infection while animal studies prove the efficacy of this biological scaffold. This revelation proves that the botanical scaffold can be used in medical applications for spatially-defined bone regeneration [112]. Moreover, it is revealed that bacterial cellulose was modified by chitosan and citric acid, with HAp deposition after soaking treatment in  $\text{CaCl}_2$  and  $\text{NaHPO}_4$  solutions increased soaking cycles. The absorption capacity was thought to be key to the study of binding of  $\text{Ca}^{2+}$  into modified bacterial cellulose that affected HAp. The Ca/P ratio was of 1.1 for such low crystallinity of HAp [113]. The scientific information on medicinal, reishi mushroom (*G. lucidum*) relates to anti-osteoporotic activity. It acts by improving the minerals (e.g. Fe, Ca and P in the concentrations ranged by (1-5%) affected by daily diets, drinks and food supplementation) content of serum that is related to the bone health [114]. Using a

freeze-drying approach, 3D composite scaffolds have been prepared for bone engineering. This was composed of chitosan, fucoidan and natural nano-HAp. The composite revealed a suitable micro architecture for nutrient supplementation and cell growth [115].

#### **2.4.5 Drug delivery**

There are many studies that have shown that the design of drug delivery systems can be natural, involving biocompatibility, eco-friendly and morphology (surface shape and size). Pollen of *Betula pendula* was used for microcapsule drug delivery when loaded with a cancer therapeutic agent. The results showed that cumulative drug release was 65% for 24h sitting in PBS. However, it was completed within 1h from a control and so it had potential to be used as an oral drug delivery system [116]. Another study [117] showed that pine pollen microcapsules had a morphology compatible with being a drug delivery system after protein removal. The result showed that pollen microcapsules were 3 times better than natural pine pollen [117].

It is said that eco-friendly *Bacillus* spore was an oral carrier [118]. Spores were loaded by curcumin for cancer therapy and it had the ability for inhibiting colon cancer cells [118]. Moreover, two oral drug deliveries of *lycopodium clavatum* spore capsules was investigated. In the first, the outer walls of spores included target objects. In the second, alginate microgranules were studied. The load level of peptide was controlled using molecular mass and the mechanism release from two loadings was suggested [119]. Hollow microcapsules have been prepared for oral drug delivery used with sunflower sporopollenin exine, where the microcapsule was loaded with protein of bovine serum albumin that was released, reaching 100% after 2h in simulated gastric fluid (SGF) and after 8h in simulated intestinal fluid (SIF). The results showed that hollow microcapsules of sunflower are a versatile platform as oral drug delivery [120].

Recently, a redox strategy was used for oral drug delivery using Fe<sup>3+</sup>-crosslinked alginate aerogel that was co-impregnated by AA and ibuprofen. The results showed that a marked acceleration of release ratio of AA was achieved in both phosphate buffer saline (PBS) and HCl solution. AA reduced the crosslinking of Fe<sup>3+</sup> to Fe<sup>2+</sup>. The latter did not react strongly with alginate leading to hydration of the chains. However, ibuprofen released was faster in PBS (pH 7.4) than HCl solution (pH 2) due to the greater degree of swelling of the alginate matrix that caused fast dissolution in PBS [121].



Another alginate matrix ( $\text{Ca}^{2+}$ -crosslinked alginate-maltose composite) has been prepared via the template method. The resulting microneedles were loaded with insulin and applied for transdermal delivery on diabetic rats. A clear effective hypoglycemic effect was noticed with biodegradable microneedles due to better insulin release. It was suggested that  $\text{Ca}^{2+}$  crosslinked alginate-maltose could be used to encapsulate insulin and then utilized in transdermal delivery [122]. Moreover, others used glucose [123] and proteins [124] for transdermal delivery. An eco-friendly method was investigated using *pelargonidin* plant on diabetic rats. Nano capsulation (via emulsion-diffusion-evaporation) was thought to be a method to overcome the limitations of using this free plant. The results showed that poly lactide-co-glycoside NPs were more effective in controlling the diabetogenic effects than free plant. This was due to improved dissolution; the release was slow and had a long-acting effect on the flavonoid present in NPs [125].

Many studies have indicated that insulin can be encapsulated in NPs, peptides, chitosan/alginate [126] and polymeric NPs [127]. It has been reported that acrylamide-crosslinked polymer (and its derivatives as a hydrogel) could be loaded with insulin (50UI) whose release could then be studied. The hydrogels show fast insulin release because of the large channel and pore size of these hydrogels [128]. It indicated that nanocarriers were prepared using insulin-loading poly-lactide-co-glycolide which were modified with chitosan for oral drug delivery [129]. Further, there are many routes to drug delivery of ascorbic acid (AA) (e.g. AA-dissolving microneedle [130], AA-2-glucoside-hyaluronic acid [131]), haemoglobin (e.g. Hb-Au NPs [132] and croton *bonplandianum* leaves extract-Ag NPs-Hb [133]) and insulin (e.g. insulin infusion pump [134] and insulin in treatment [135]). Other various routes include aerogels-hydrogels (e.g. AA- $\text{Fe}^{3+}$ -alginate aerogel [121]) and  $\text{Ca}^{2+}$ -alginate for transdermal delivery of insulin [122], insulin-smart hydrogel [136] and Hb-ternary polymeric [137]), thermogel [138], nanomaterials [139], NPs [140] (e.g. *pelargonidin*-encapsulated NPs [125] and silica NPs [141]), microneedles (e.g. multiplexed transdermal as based sensor [142], polymers [143], PVA [144]), and microneedles (e.g. nanocarriers [145], microcapsules (e.g. bovine serum albumin [120]), spores and pollen (e.g. Cu- *Trichoderma viride* spores [146], spores capsules of *Lycodium clavatum* [119], pollen of *Betula Pendula* [116] and pine pollen [117]) and HAp networks [147].

Encapsulation can involve *Lycopodium* spores-loaded with bovine serum albumin and alginate using vacuum loading [148]. Another study used ibuprofen loaded as a drug in to sporopollenin

exine capsules (SEC). The results show that the SEC has a low drug loading, but is thought to be safer for drug delivery [149].

#### **2.4.6 Cytotoxicity**

The necessary chemical composition used depends on the intended application. In biomedical imaging, Au NPs and iron oxide are used as contrast agents with magnetic properties. For medical devices, Ag NPs can be used for their antibacterial activity [150]. Therefore, different NPs can have different effects on physiological systems. It has been reported that copper and zinc oxide NPs caused cytotoxicity due to DNA damage. However, iron oxide NPs caused only a small cytotoxicity effect. Interestingly, Au NPs are considered safe although their long-term toxic effect is sufficiently characterized. Moreover, 18nm Au NPs do not have cytotoxicity towards cells (human red blood corpuscles (RBCS)) up to 250 $\mu$ M. Au NPs prepared with cysteine glucose surface modifiers were not toxic at concentration up to 25 $\mu$ M [151]. On the other hand, 13nm Au NPs reduced actin (globular proteins) stress fibers leading to a major inverse effect on the cells [99].

#### **2.4.7 NPs and natural photocatalysts**

Recently, air pollution is seen as a major problem in the world, alongside bacterial contamination. Methods intended to solve these problems include adsorption, photodegradation and ultrafiltration etc. Further, there are many eco-friendly methods (using natural products [152] and their extracts [153]) to remove color and contamination. Preparation used fruit peel, (mangos, orange and banana) seeds, leaves (neem and loquat) [154] and leaf extract (*Calotropis gigantean*) [155].

Recent literature has revealed that different biotemplate structures can be used to synthesize nanomaterials, such as dandelion pollen for good TiO<sub>2</sub> photocatalytic activity towards methylene blue. Cai *et al* reported green chemistry provided a route to increase photocatalytic activity using flower-shape TiO<sub>2</sub> nanocrystals through the assembly on graphene oxide sheets. Enhancing the photocatalytic TiO<sub>2</sub> depends on its surface area, size, morphology and crystallinity [77]. Using orange peel can enhance photocatalytic activity possibly because it contains hydroxyl and carboxyl groups which are very active sites for metal sorption (absorption and adsorption) [60].

Kondo *et al.* reported that TiO<sub>2</sub> hollow spheres have a high specific surface area and enable multiple diffractions and reflections of light [67]. Compared with conventional methods, there are many advantages to this approach which show unique features, such as being environmentally friendly, having a higher surface area, more catalytically active sites (hydroxyl and carboxyl groups), significant enhancement of photocatalytic activity, low cost and mild reaction conditions at RT and pressure, providing simplicity for the synthesis route. This route is complete in one or two steps in a reaction time of a few minutes [69]. The use of green biosynthesis is an attempt to remove Mg<sup>2+</sup>/Ca<sup>2+</sup> from water using activated melon (*Citrullus lanatus*). The maximum times required for Ca<sup>2+</sup> (20min) and Mg<sup>2+</sup> (25min) were moderate. Thermodynamic parameters were computed and it showed that the sorption process was spontaneous and exothermic ( $\Delta G^\circ = \Delta H^\circ - T\Delta S^\circ$ ) [156]. Ahmad *et al.* attempted to prepare nanohybrid Ag-TiO<sub>2</sub> using a sol-gel approach. Different characterizing techniques were used as XRD, TEM and SEM. The antibacterial activity exhibited 100% inhibition of Gram-positive and Gram-negative bacteria growth at 0.2-0.1 M of Ag-TiO<sub>2</sub> NPs [157]. Similarly, the hydrothermal technique green method was used to synthesize TiO<sub>2</sub>-Ag NCs. TiO<sub>2</sub>-Ag composite material that promoted photoactivity towards the MB solution under solar light and antimicrobial properties. Ag NPs (5nm) decorated on compact aggregates of TiO<sub>2</sub> were prepared using polyvinylpyrrolidone (PVP) as the stabiliser or reducing agent.

The synergistic relationship between Ag and TiO<sub>2</sub> clearly indicated a synergy. When the size of NPs decreased, it induced better antimicrobial activities against Gram negative (*Escherichia coli*) and Gram positive (*Bacillus subtilis*) [158]. An eco-friendly method was attempted to synthesize SnO<sub>2</sub> NPs using the extract of root bark from *C. spinosa*. The synthesized 47nm SnO<sub>2</sub> NPs were spherical. GC-MS results confirmed that 7-hydroxy-6-methoxy-2H-1benzopyran-2-one had a higher area 67%. Also, it clearly revealed the maximum rate of photodegradation of Congo red dye (industrial effluent) [159]. A new study has evaluated a novel technique where TiO<sub>2</sub>-assisted laser desorption/ionization (LDI) mass spectrometry was utilized for faster metabolites analysis to detect AMR. This study revealed a novel implementation through pathway and network analysis proving the feasibility of metabolomic analysis against *E. coli*. and four other clinical strains. This method is simple with faster preparation analysis than many traditional methods such as liquid chromatography (LC), nuclear magnetic resonance (NMR) spectroscopy and gas chromatography (GC) [160].

## **Chapter 3: Experimental Techniques**

---

This chapter outlines the basic characterisation methods used in this study: scanning electron microscopy (SEM), transmission electron microscopy (TEM), X-ray diffraction (XRD), secondary ion mass spectrometer (SIMS), Fourier transform infrared spectroscopy (FTIR) and micro-FTIR, NanoDrop-UV spectroscopy Electrophoresis and white light interferometry (WLI).

### **3.1 Electron microscopy (EM)**

Electron microscopy is a powerful tool to examine solid samples. In this section, the types of electron microscope will be described in more detail, including the benefits, disadvantages, operating principles and method preparative of each.

EM is a type of microscopy that uses a beam of electrons instead of light to create an image for a sample with higher magnification and resolving power than a light microscope. Here, EM allows viewing of very small objects in finer details. However, the electron beam (which has a high current density) can generate heat and subsequently char non-metallic samples due to the confirmed area. In EM, electromagnetic lenses are used to control the path of electrons. The electron beam passes through the center of solenoids (a coil of wire around the outside of a tube) on its way down the column of the EM towards the specimen. Electrons are very sensitive to magnetic fields and can be controlled by changing the current through the lenses [161].

The resolving power of EM is related to the wavelength of the irradiation used to form images. Therefore, when electrons travel faster their wavelengths are shorter and the resolution increases when the accelerating voltage (quoted in kilo voltage keV) of the electron beam is increased. [162]. According to Abbe's resolution equation, the resolution of EM increases due to reduction in the wavelength (see Eq. 1) [163].

$$keV = 1240/\lambda \quad - - - (3.1)$$

For example, for the accelerating voltage at 10keV an electron beam has a  $\lambda = 0.123\text{nm}$  [163]. EM is used to investigate samples to understand: (i) chemical and biological structures of specimens to enhance our understanding of mechanisms, function, chemistry and physiology, (ii) characterization of surface and surface changes and (iii) metals, ions, NPs crystallinity [164].

### ***Types of Electron microscope (EM)***

There are several types of electron microscopes that include: scanning (SEM) and the transmission (TEM) electron microscopes. Both provide 3D sample structure [165]. To compare these two techniques:

Firstly, an electron emission source (gun) is used in both to produce the electron beam. The gun is usually fitted with a tungsten filament cathode, which is the source of the electron beam. An anode is used to accelerate the electron beam, and electrostatic and electromagnetic lenses help to focus the beam on the sample. When the electron beam passes at the surface (SEM) or through the specimen (TEM), it is scattered and provides an image of the microscopic structure of the specimen, which can be viewed through the objective lens of the microscope. A vacuum system allows the electrons to travel [166].

Secondly, the electron beam is scanned across of the specimen in a raster pattern to induce magnified images or mapping of the sample. In SEM, electrons interact with the surface of the sample. As a result, the images from an SEM can be good representations of the real shape of the specimen. However, in TEM, the electrons in the primary beam are transmitted through the sample and it is capable of building up a bigger and greater depth of view of the image of sample (see Fig. 3.1) provided this is partially electron transparent. Therefore, the resolution (the ability to see two items as separate areas) of TEM tends to be better than that achieved with a SEM.

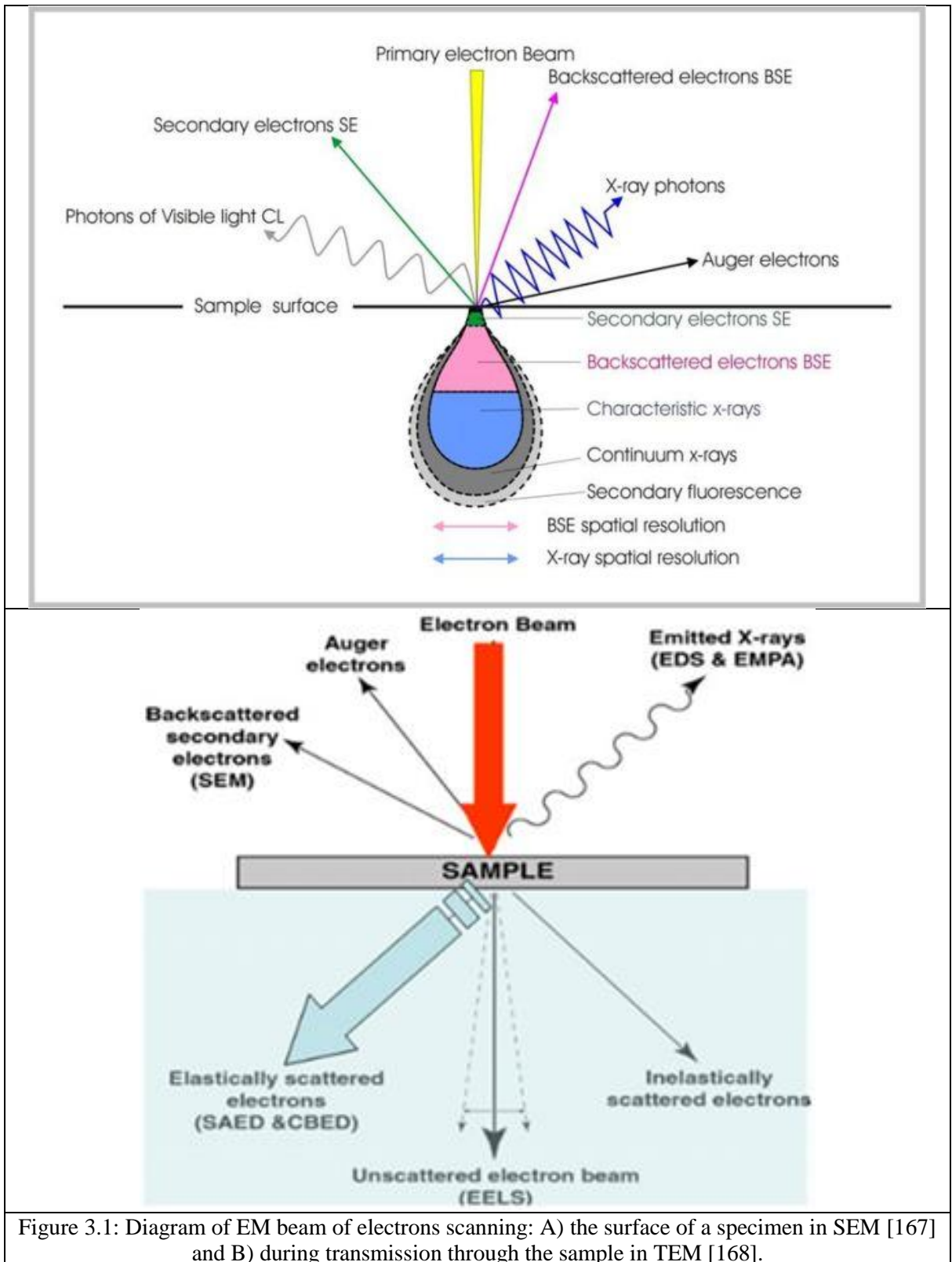


Figure 3.1: Diagram of EM beam of electrons scanning: A) the surface of a specimen in SEM [167] and B) during transmission through the sample in TEM [168].

SEM uses a secondary electron (SE) generated from the interaction at the surface of the sample leading to the use of low accelerating voltages (the difference in electric potential between two points) to prevent the beam scanning the sample. Here, it can use the low range of keV (1-5keV) for biological specimens [169] and can reach 50keV for metals. TEM prevents beam going into the sample and the range of keV reaches to 200keV. TEM resolution can be down to 0.2nm. SEM is able to resolve details of about 2nm.

### 3.1.1 Scanning electron microscopy (SEM)

SEM can be used to reveal morphological details of specimens (chemical and biological) with better resolution than in optical microscopy because the wavelength of the electron beam is less than that of visible light [164]. However, they must be conducting and able to withstand vacuum conditions. Here, SEM uses a beam of electrons to see samples smaller than the wavelength of visible light. For example, a 100keV of TEM electron beam has a wavelength  $(3.88 \text{ pm}) \times 10^4$  smaller than an optical microscope using light at 400 nm related to Eq. 3.1.

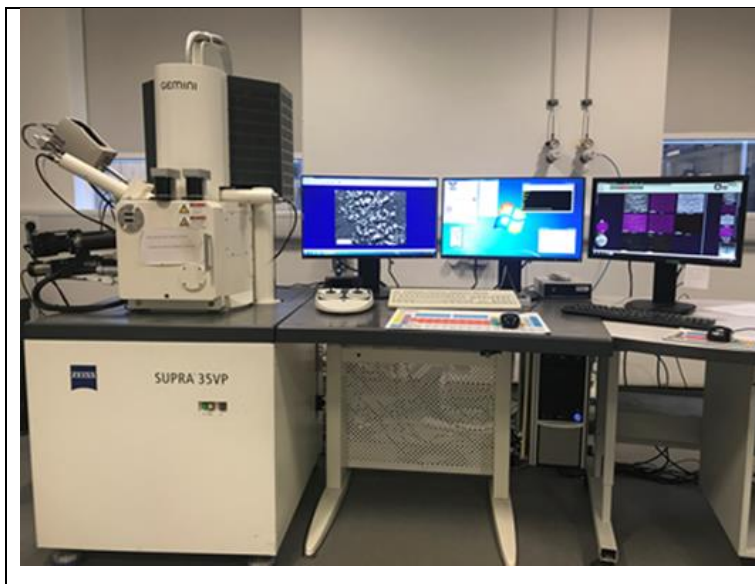


Figure 3.2A: SEM at Brunel University London.

SEM images are typically obtained by scanning a focused beam of electrons across the sample of interest, in an evacuated chamber. This beam is produced using an electron gun, typically employing a tungsten filament. This filament is heated electrically until it emits

electrons, which are focused using magnetic lenses. This loses energy as it passes through [163] and is converted to another type of energy such as (secondary electrons, heat, light and backscattered electrons). The primary electron beam excites and interacts with the specimen surface which emits secondary electrons (SE). Then, the detector (located on the top to record SE) is used to form an image from the SE by scanning across the surface (see Fig 3.2B) to produce an image of 3D structure of sample [161].

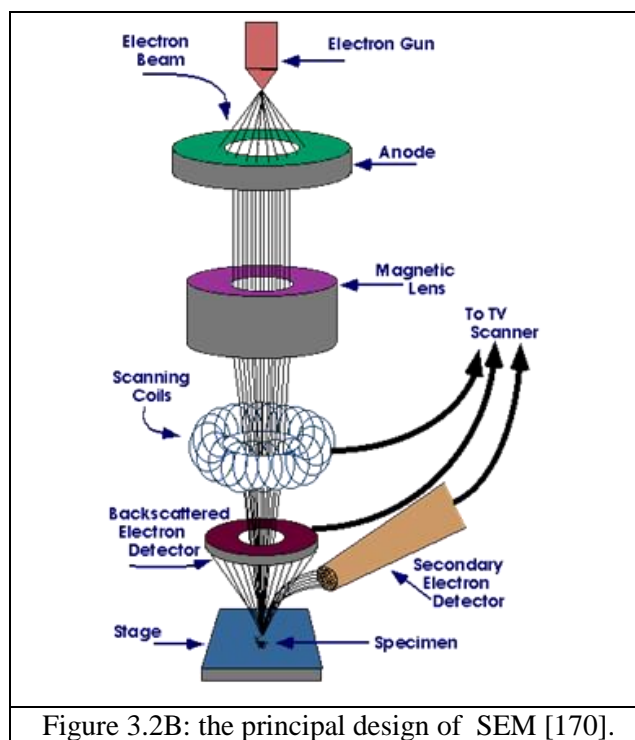


Figure 3.2B: the principal design of SEM [170].

- **Preparation of samples**

In SEM specimens tend to charge when scanned by the electron beam, and especially in the secondary electron imaging mode. This causes scanning faults and other image artifacts. Samples are therefore usually coated with an ultrathin layer of electrically conducting material (graphite or Au), deposited on the sample either by low-vacuum or by high-vacuum evaporation.

Most PMS samples were analyzed by supporting on double carbon tape on aluminum SEM stub using SEM with energy dispersive X-ray (EDX) after one of the following



preparations: For example, one drop of a liquid suspension was placed on the stub surface and left to dry at RT (see Fig.3.3A). The sample on the stub was coated with gold under vacuum using the sputter coater (uses an electric field and argon gas). The rate of gold coating depending on sputtering rate (as a function of current and voltage; see Fig.3.3B). When the sample was placed inside the chamber, the voltages should adjust it. Au /PMS samples were coated with platinum 1keV, using plasma current 10mA and for 45s (3 times). Ag, Ti and all samples were coated with gold 1.5keV, 1.5mA. Then, the sample was put inside the chamber of SEM and the operation of acceleration voltage was 5keV. For EDX analysis, the samples were not coated with gold (as this would have made elemental analysis inaccurate) but the acceleration voltage was dropped to 20keV to minimize charging. Additionally, coating may have increased the signal/noise ratio for samples of low atomic number (Z). As a result, an improvement arises because secondary electron emission for high-Z materials is enhanced.

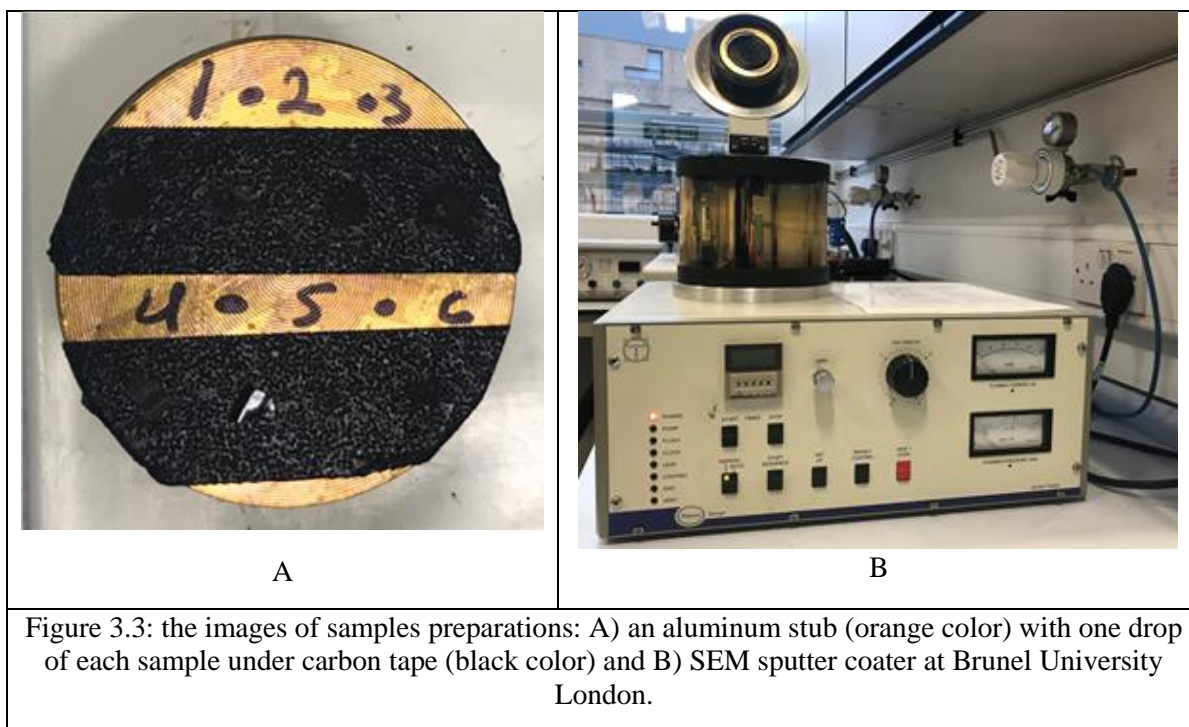


Figure 3.3: the images of samples preparations: A) an aluminum stub (orange color) with one drop of each sample under carbon tape (black color) and B) SEM sputter coater at Brunel University London.

For SEM study of anti-bacterial activity, agar/Petri dish samples a fixation process was necessary to prevent deterioration. The electron beam has a huge current density and it can focus into very tiny areas in a specimen. This area becomes hotter with potential drying.

Therefore, some steps were followed to prepare such biological specimens for SEM: replacing water by ethanol using osmium tetroxide to keep lipid structure and glutaraldehyde (2%) for crosslinking proteins and drying samples at RT and Au coating to prevent the charging of bacteria.

Furthermore, increasing the quantity of SE from the surface area of bacteria, can increase the signal to noise ratio [161] (see Fig. 3.4). For biological samples, there are two problems to get high resolution SEM imaging: (i) enough contrast, (ii) for bacteria, a conducting surface is important to reduce charging at magnifications higher than 1000x [164].

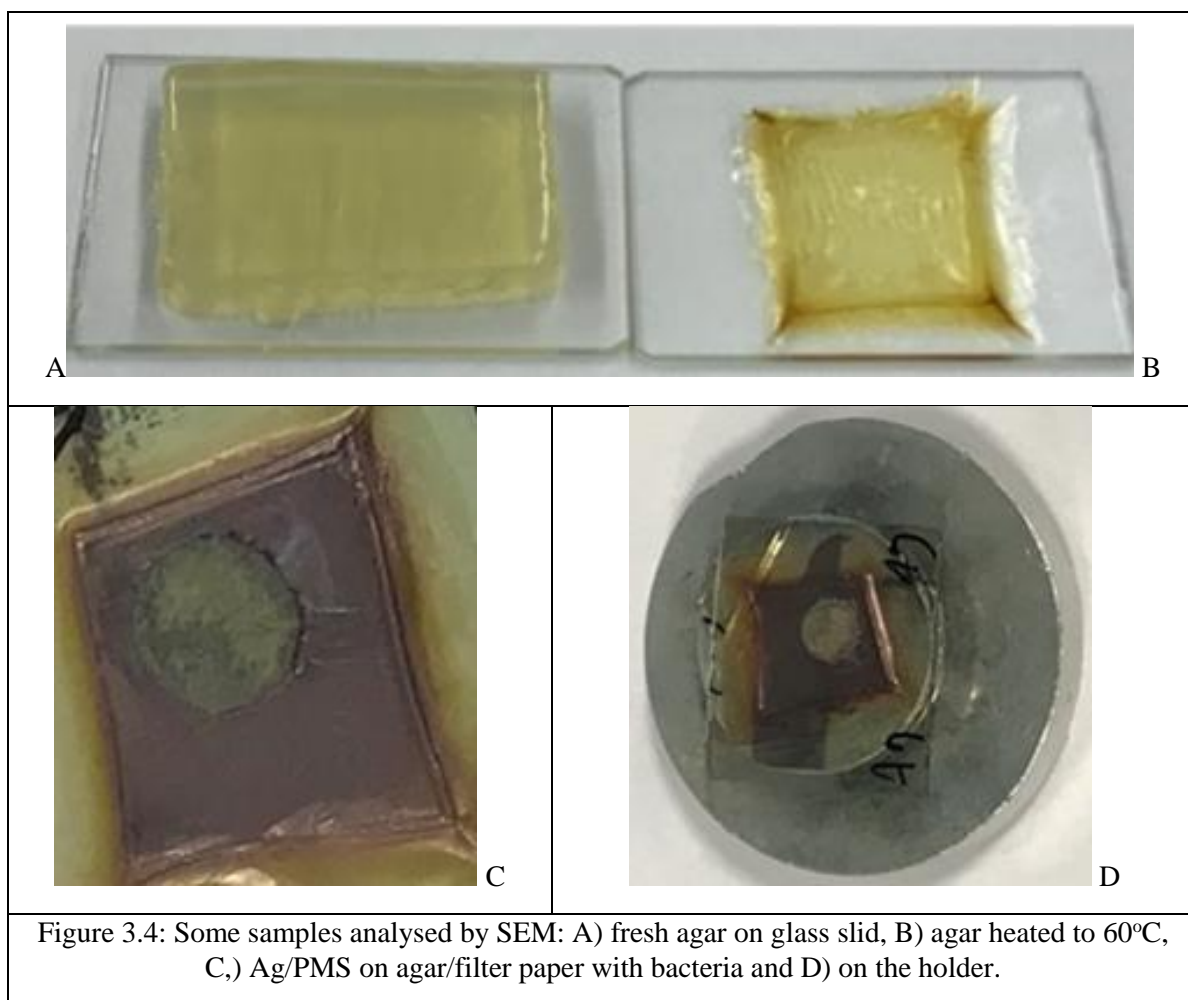


Figure 3.4: Some samples analysed by SEM: A) fresh agar on glass slid, B) agar heated to 60°C, C,) Ag/PMS on agar/filter paper with bacteria and D) on the holder.

Surface morphology and particle size were examined by scanning electron microscopy (SEM, Supra35 VP) with EDX after Pt or Au coating using a sputter coater (Polaron

Range). Energy dispersive X-ray (EDX) analysis was used by EDAX detector (silicon dzijt detector (SDD) type)).

### 3.1.2 *Transmission electron microscope (TEM)*

The transmission electron microscope directs a high voltage electron beam towards the specimen and thereby creates a magnified image of the sample. The most significant limitation of the TEM is the requirement for very thin samples, usually less than 100 nm. As a result, most biological specimens need to be chemically fixed and dehydrated in order to be embedded in a polymer resin so that it can be viewed with a TEM [171] as a stable microtomed section.

- *Preparation of samples*

For preparation of samples/PMS, many steps should be following for the embedding process. This process can be polymerized inside a hardened block for sectioning as slides using microtome.

TEM samples were prepared by two methods: (i) a few mg of chemical solid samples (as Bio-Oss and HAp alone) were dispersed with ethanol by ultrasonic bath (ultrasonic waves made compression produce cavitation bubbles in solution due to rare fraction cycles) for 1min then, adding one drop of the dispersed sample on carbon Cu-grid and left to dry at RT (see Fig. 3.5A). (ii) adding a few mg of the samples/PMS and mixing these with low viscosity resin. These resins offer many advantages: (i) good contrast, (ii) rapid penetration, (iii) stability under the electron beam and (iv) easy sectioning.

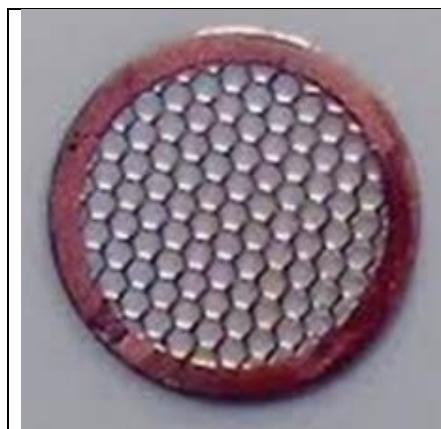
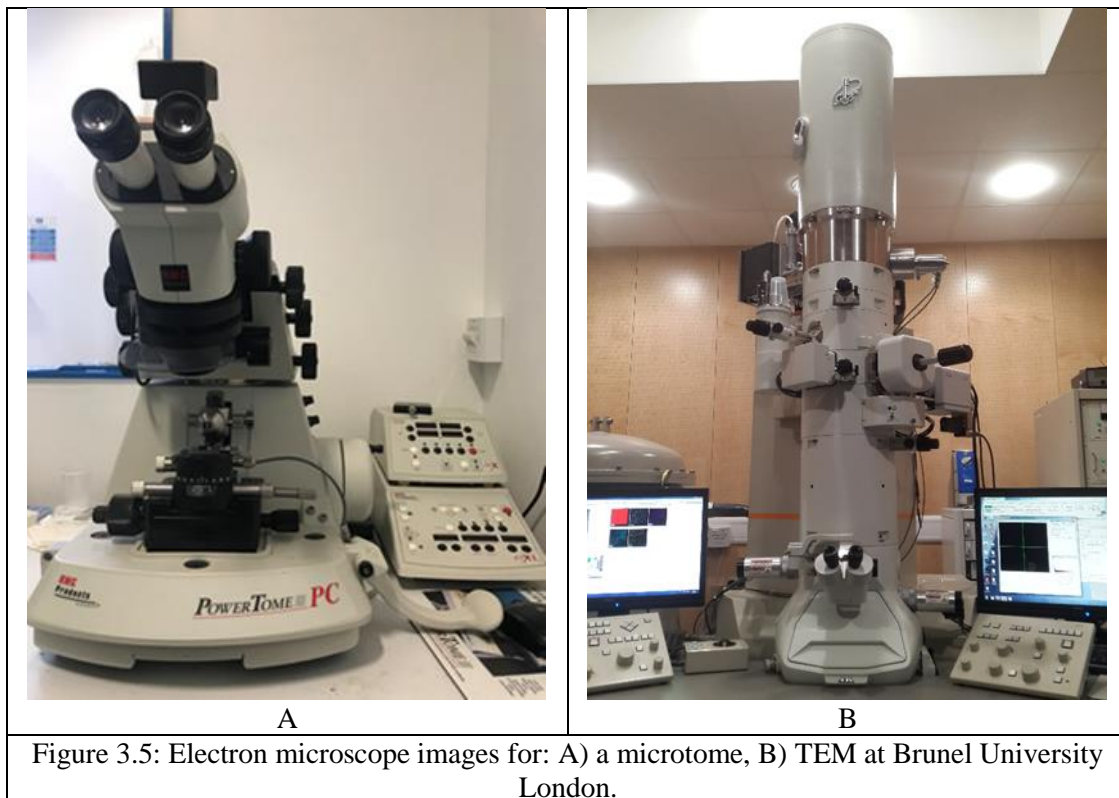


Figure 3.5A: Cu-grid used in TEM.

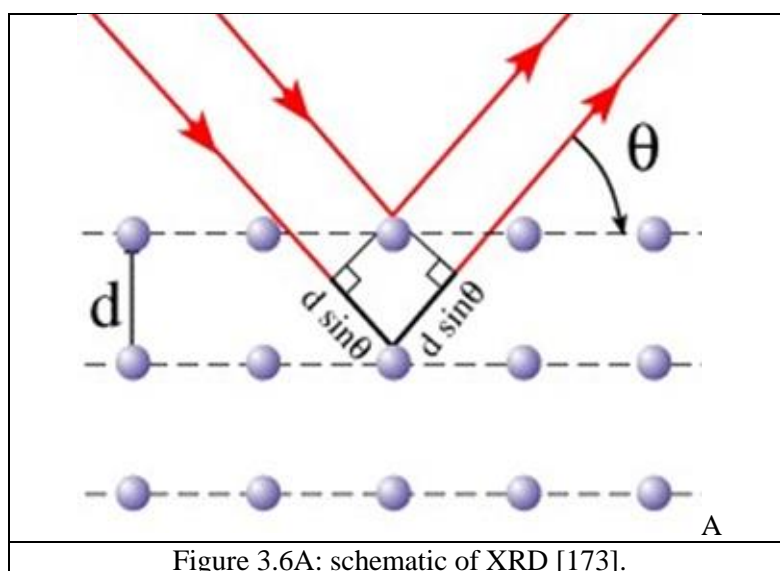


A suitable mixture preparative for a medium hardness block is: 12g of low viscosity resin (Taablv), 4 mg low viscosity VH1 hardener, 9 mg of low viscosity VH2 hardener and 0.65mg LV accelerator. After embedding into the resin block, they were put into a small vial (1mL) and left at 60°C overnight to reduce their viscosity. Then, after setting, a microtome was used to make thin slices of sample. The cut sample was floated on water, in order to eliminate wrinkles and distortion in the sample (a process known as ultramicrotomy). Usually, sections of 50nm thickness are collected onto the TEM grid which was 400 mesh (mesh = 37 $\mu$ m). Sectioning the sample allows one to look at a cross-section of the sample in order to view its internal (ultra) structure [164]. The resin wasn't stable above 80keV beam energy. Transmission electron microscopy (TEM, Jeol 2100f, field emission gun (FEG) was used to assess morphology and particle size using a Gatan camera/imaging software (Gatan microscopy suite, version 3). The TEM operated at 80kV (for images) and 200keV (for fast Fourier Transform FFT).

### 3.2 X-Ray Diffraction (XRD)

X-ray diffraction (XRD) was been carried out on samples using software TOPAD Rietveld analysis with a copper anode (Cu  $K_{\alpha}$ ) radiation ( $\lambda = 1.54056 \text{ \AA}$ ) over the  $2\theta$  range of  $10\text{-}70^{\circ}$ . The XRD peak positions were calibrated with  $\text{Al}_2\text{O}_3$ . The 3D structure of crystalline minerals is defined by regular, repeating planes of atoms to form a crystal lattice. XRD technique can provide detailed information about unit cell lattice parameters of phases (a, b and c) and related cycle of materials. Material properties are highly dependent on their structure [172].

XRD consists of an X-ray source and detector to read the reflected beam when X-ray beam interacts with these planes of atoms in the sample. Part of the beam is transmitted, absorbed by the sample scattered, refracted and diffracted. Diffraction of an X-ray beam by a crystalline solid is analogous to diffraction of light. X-rays are diffracted by each mineral phase differently, depending on the crystal lattice and how these atoms or ions are arranged. When an X-ray beam hits a sample and is diffracted, one can measure the distances between the planes of the atoms that constitute the sample by applying Bragg's Law ( $d$  is the distance between adjacent planes of atoms (the  $d$ -spacing), and  $\theta$  is the angle of incidence of the X-ray beam; (see Fig. 3.6).



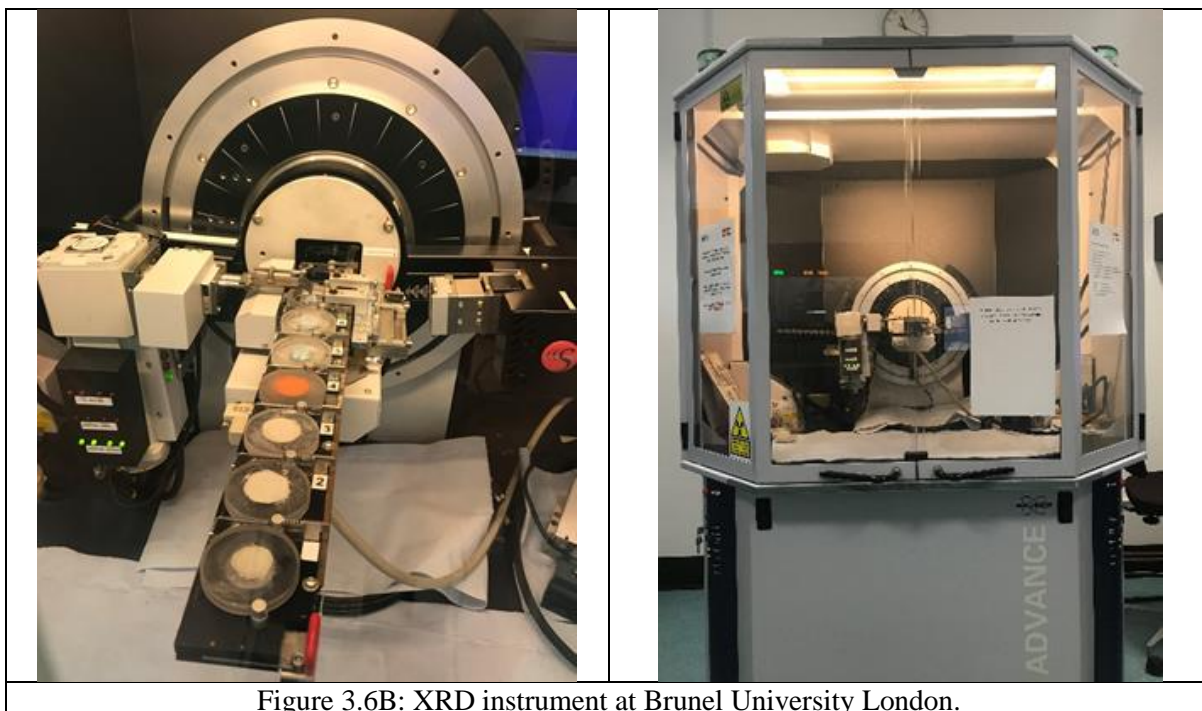


Figure 3.6B: XRD instrument at Brunel University London.

### 3.2.1 Determination of crystal size using the Scherrer Equation

The Scherrer equation can always be used to estimate the size of the crystallite ( $D$ ) based on the width of the diffraction peak at half intensity, FWHM ( $2\theta$ ):

$$D = K\lambda / \beta_{1/2} \cos\theta_{hkl} \quad \text{--- (3.2)}$$

$D$  = the volume weighted crystallite size (nm),

$K$  = the shape factor ( $K= 0.94$ ),

$\lambda$  = the radiation wavelength (0.154060nm for Cu- $K_{\alpha}$ ),

$\beta_{1/2} (hkl)$  = instrumental-corrected integral breadth of the reflection (in radius) = the broadening (band width) of the  $hkl$  diffraction peak at half-height ( $\theta$ ) in radians, and

$\theta_{hkl}$  = the Bragg diffraction peak angle [174].

Generally, crystallite size ( $D$ ) is a measurement of the size coherence diffraction domain and it acts as poly-crystalline aggregates. Crystallite size is not the same as particle size; often, it is smaller [175].

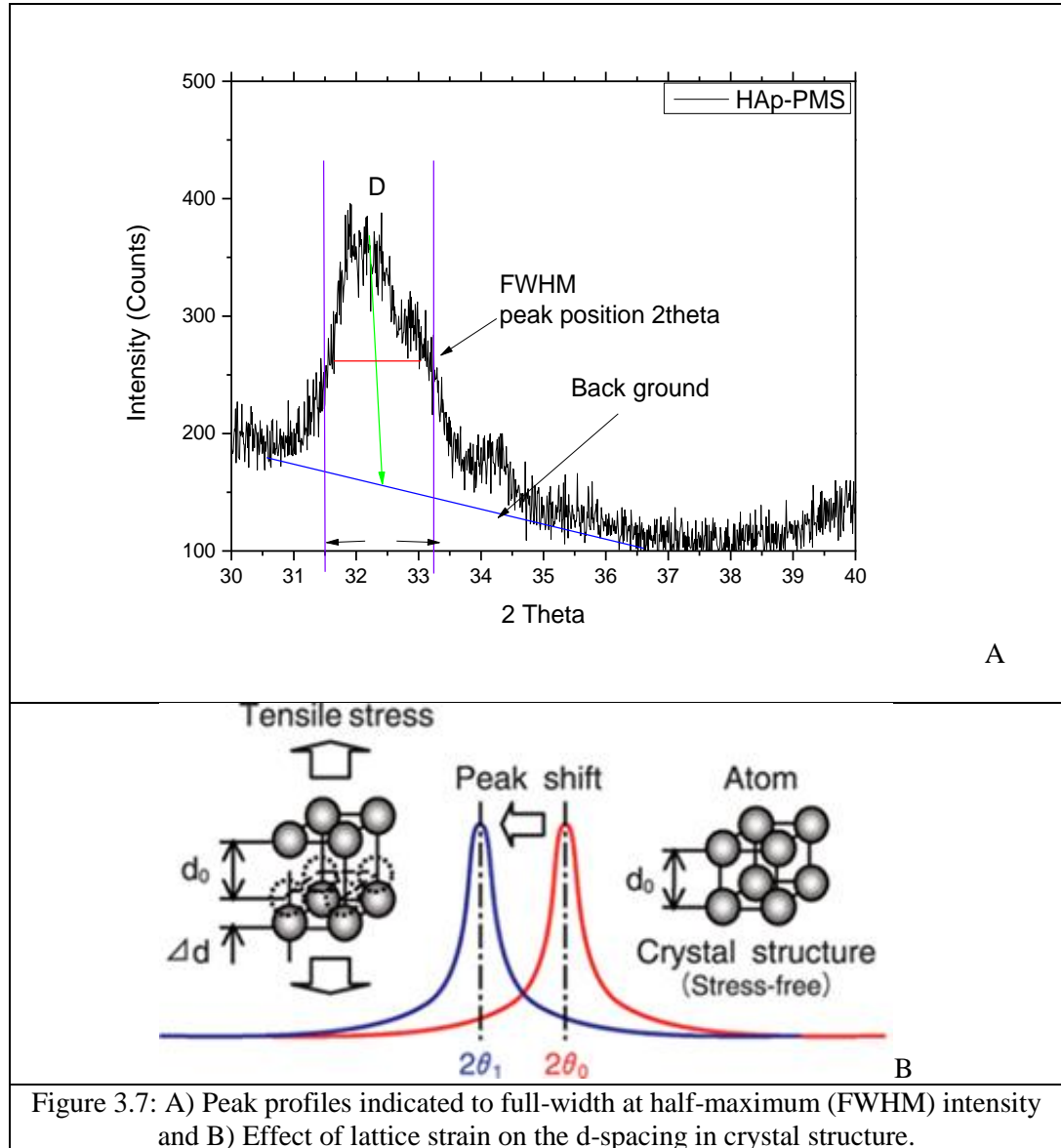


Figure 3.7: A) Peak profiles indicated to full-width at half-maximum (FWHM) intensity and B) Effect of lattice strain on the d-spacing in crystal structure.

There are two factors causing deviation from perfect crystallinity and effectiveness of the Bragg peak; crystallite size ( $D$ ) and lattice strain ( $\epsilon$ ) leading to: (i) increased peak width (broadening), (ii) shift in the position of Bragg angle, (iii) effect of intensity peak [174]. Analysis of XRD peak profiles indicated that full width at half-maximum (FWHM) is sensitive to the variation in nanostructure and stress-strain accumulation in the material

[174]. The main properties extracted from the width of peak analysis are lattice strain ( $\epsilon$ ) (is a measure of distribution of lattice constants arising from crystal imperfections) and crystallite size ( $D$ ) (see Fig. 3.7A). The Scherrer method is known to calculate crystallite size. This equation has not taken account peak broadening reducing from other factors such as instrumental effect and inhomogeneous strain.

$$\beta(hkl) = [(\beta_{hkl})^2_{measured} - (\beta_{hkl})^2_{instrument}]^{1/2} \quad \text{--- (3.3)}$$

X-ray diffraction peak broadening reveals the  $\beta$ ,  $D$ ,  $\epsilon$ , Elastic modulus ( $E_{hkl}$ ) and tensile stress in the materials (see Fig. 3.7B) [174].

### 3.2.2 Determination of crystallite size ( $D$ ) and lattice strain ( $\epsilon$ ) using the Williamson-Hall approach

The Williamson-Hall approach (W-H) equation is a simple approach both crystallite size ( $D$ ) and lattice strain ( $\epsilon$ ) induced broadening are not complex due to considering the peak width as a function of  $2\theta$  [175]. The Williamson-Hall approach (W-H) is given by:

$$\beta_{(hkl)} \cos \theta_{hkl} = k\lambda/D + 4\epsilon \sin \theta_{hkl} \quad \text{--- (3.4)}$$

$$y = z + mX \quad \text{(Linear equation with intercept)}$$

From plot  $\beta_{(hkl)} \cos \theta_{hkl}$  along Y-axis and  $\sin \theta_{hkl}$  along X-axis, lattice strain ( $\epsilon$ ) can be calculated from the slope ( $m$ ) which is equal  $4\epsilon$ . Also, crystallite size ( $D$ ) can be calculated from the intercept ( $Z$ ) of the linear fit made to the plot which is equal to  $K \lambda/D$ . Assuming the lattice strain ( $\epsilon$ ) is uniform in the materials, this indicates the isotropic nature of the crystal [174].

Elastic modulus ( $E_{hkl}$ ) is the constant of proportionality being the modulus of elasticity and it is a Young's modulus in the perpendicular direction to the set of crystal lattice plane ( $hkl$ ) hexagonal crystal phase. Also, it is related to their elastic compliances  $S_{ij}$  and for a hexagonal HAp crystal phase Elastic modulus ( $E_{hkl}$ ) is according to equation (9) [174].



$$E_{hkl} = \frac{[h^2 + \frac{(h+2k)^2}{3} + (\frac{al}{c})^2]^2}{S_{11} \left(h^2 + \frac{(h+2k)^2}{3}\right)^2 + S_{33}(\frac{al}{c})^4 + (2S_{13} + S_{44})(h + \frac{(h+2k)^2}{3})(\frac{al}{c})^2} \quad (3.5)$$

The elastic compliances and their standard handbook values are given:

$$S_{33} = 10.9 \times 10^{-12}$$

$$S_{44} = 15.1 \times 10^{-12}$$

$$S_{13} = -4.0 \times 10^{-12} \text{ [174].}$$

Hook's Law can be used to determine the lattice deformation stress ( $\sigma$ ) by Eq. 3.6

$$\sigma = E_{hkl} * \varepsilon \quad (3.6)$$

When modified Eq. 3.6 is given by:

$$\beta \cos\theta = \frac{K\lambda}{D} + 4 \frac{\sigma \sin\theta}{E_{hkl}} \quad (3.7)$$

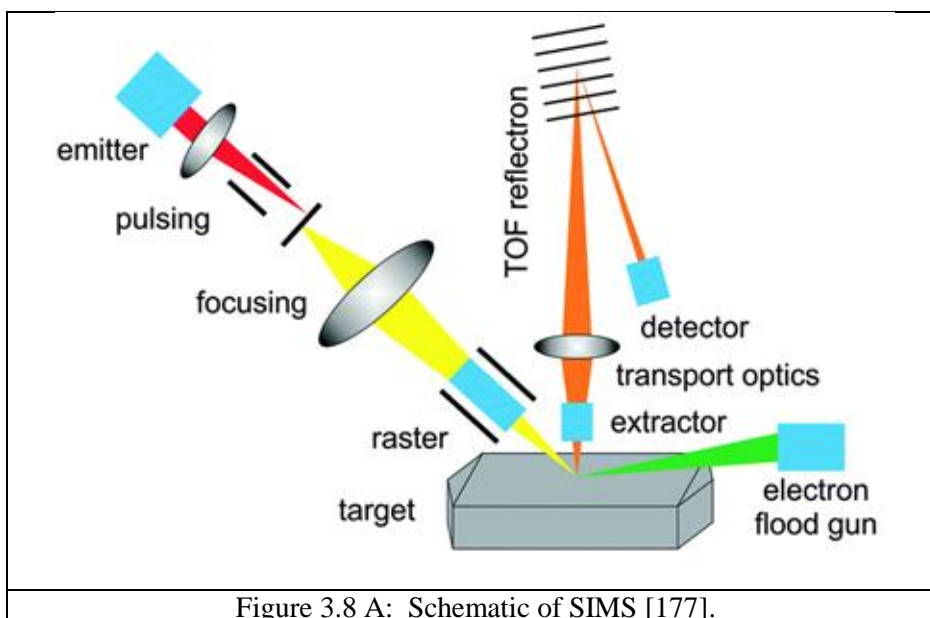
Lattice deformation stress ( $\sigma$ ) can be extracted from the slope and crystallite size (D) from the intercept of linear fit made to the plot.

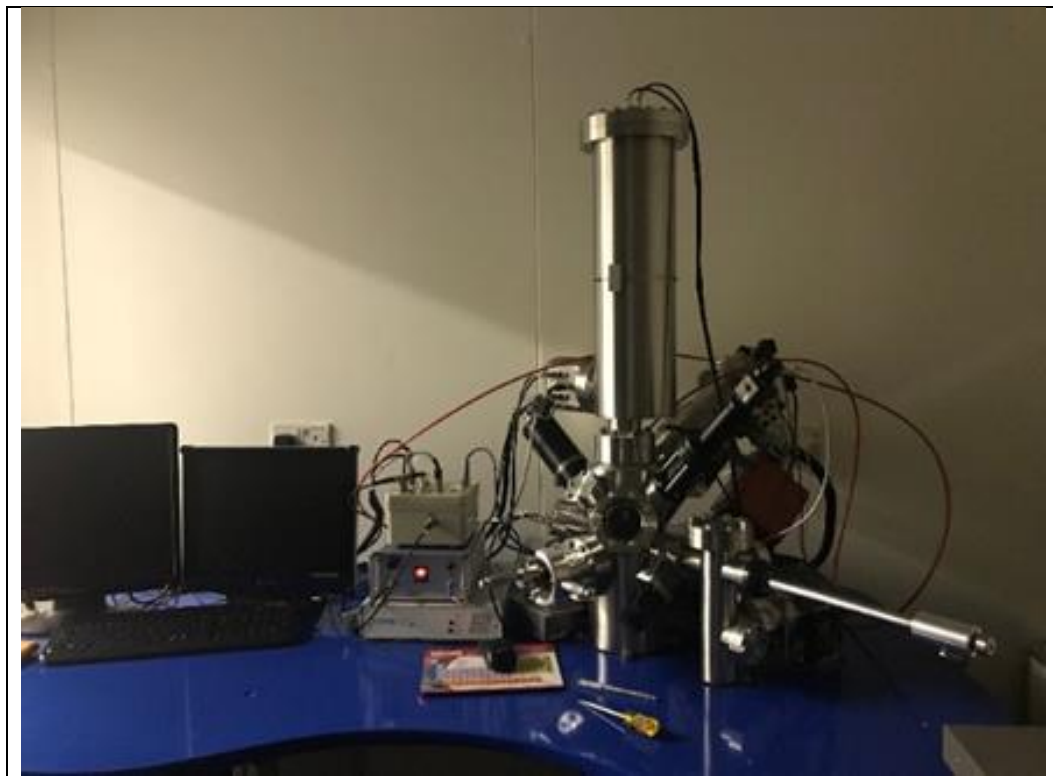
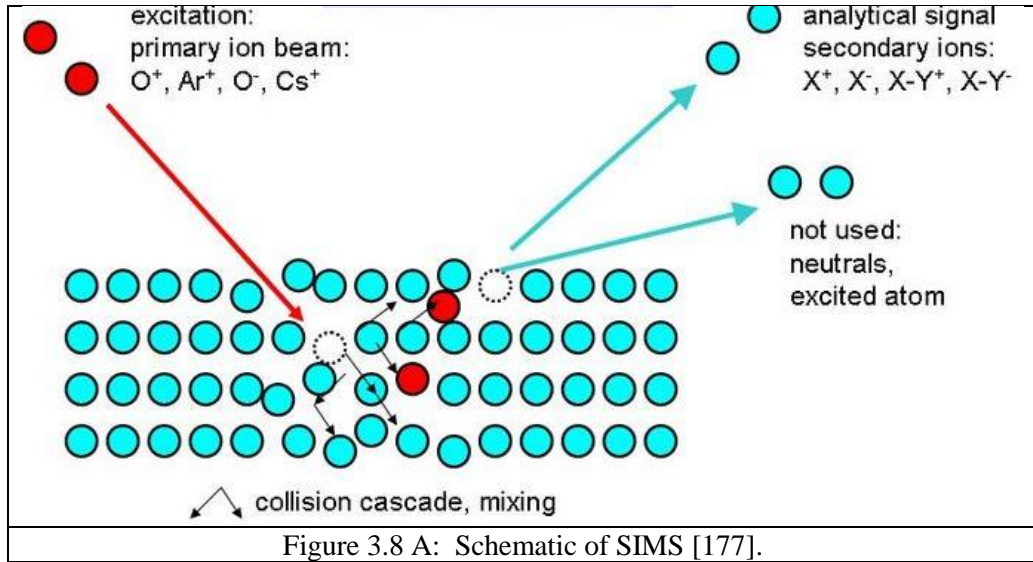
Powder samples were supported on a silica wafer and placed on the diffractometer holder which loaded into the instrument. X-Ray diffractometry used was a Bruker Advance D8 including a Cu-K $\alpha$  ( $\lambda=0.154060\text{nm}$ ) tubes for routine analyses and a Lynx Eye detector. The equipment has two settings for routine phase identification and a  $\frac{1}{4}$  cradle setting for residual stress, multi-layer and polar analyses. The software used in characterization of the crystal structure of present samples was TOPAS.

### 3.3 Secondary ion mass spectrometer (SIMS)

Secondary ion mass spectrometry (SIMS) is used to investigate surface composition through fragment's energy. It is one of the most sensitive techniques available for analysis of the distribution of trace elements in biological specimens [176] when they interact with a primary beam of heavy particles. The principle of SIMS is the interaction of the primary ion beam ((usually  $O^{2+}$ ,  $O^-$ ,  $Cs^+$ ,  $Ar^+$ ,  $Ga^+$  or neutrals) with the sample (under vacuum). These provide sufficient energy to ionize many elements in the sample surface; charged particles (secondary ions) are ejected from a sample surface. Most atoms and molecules removed from the sample surface (referred to as sputtering) are neutral, but a percentage is ionized. If the primary beam is composed of positively charged ions, the resultant ionization favours production of negative ions. If the primary beam is of negative ions, then this favours generation of positive ions. These ions are then accelerated, focused, and analyzed by a mass spectrometer ( see Fig.3.8) [177].

The secondary ion mass spectrometer (SIMS) used was the KORE (Z-7861-M). The sample was prepared by placing one drop on a silicon wafer and leaving it to dry. The software used was Texture and Elemental Analysis Microscopy (TEAM).





### 3.4 Fourier transform infrared spectroscopy (FTIR) and micro-FTIR

FTIR spectroscopy is a type of molecular spectroscopy that is used to identify the functional groups (in materials that have changed in dipole moment in molecules). The infrared light has frequency to interact with the vibrations (stretching and bending) of chemical bonds. Depending on the vibration of each functional group, the molecules will be absorbed at different wavenumber. The software with Fourier transform (FT) algorithm converts the interferogram to FTIR spectrum (T% versus wavenumber ( $400\text{-}4000\text{cm}^{-1}$ )). The FTIR method is simple, rapid and economical, since samples can be measured as found in nature without any chemical pre-treatment [178]. Micro-FTIR ( $\mu\text{-FTIR}$ ) provides simultaneous spatially resolved and chemically-resolved information in the  $\mu\text{m}$  size range. It also reveals the chemical composition and the structure of suitable materials. The intensity scale associated with each image depended on the density scale (Beer-Lambert Law) as a blue and red color area and corresponded to low and high absorption values as given by spectral integration. The main advantages of  $\mu\text{-FTIR}$  are (i) composites and mixtures analyzed to determine where chemical components could be found, (ii) small samples can be tested allowing for particles as small as  $\sim 5\mu\text{m}$  to be examined [179] (see Fig. 3.9A).

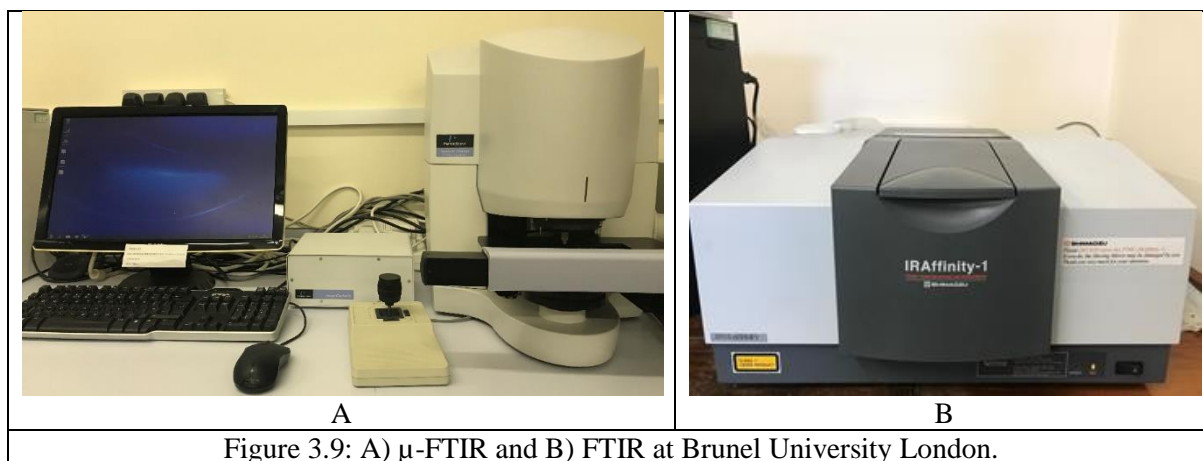


Figure 3.9: A)  $\mu\text{-FTIR}$  and B) FTIR at Brunel University London.

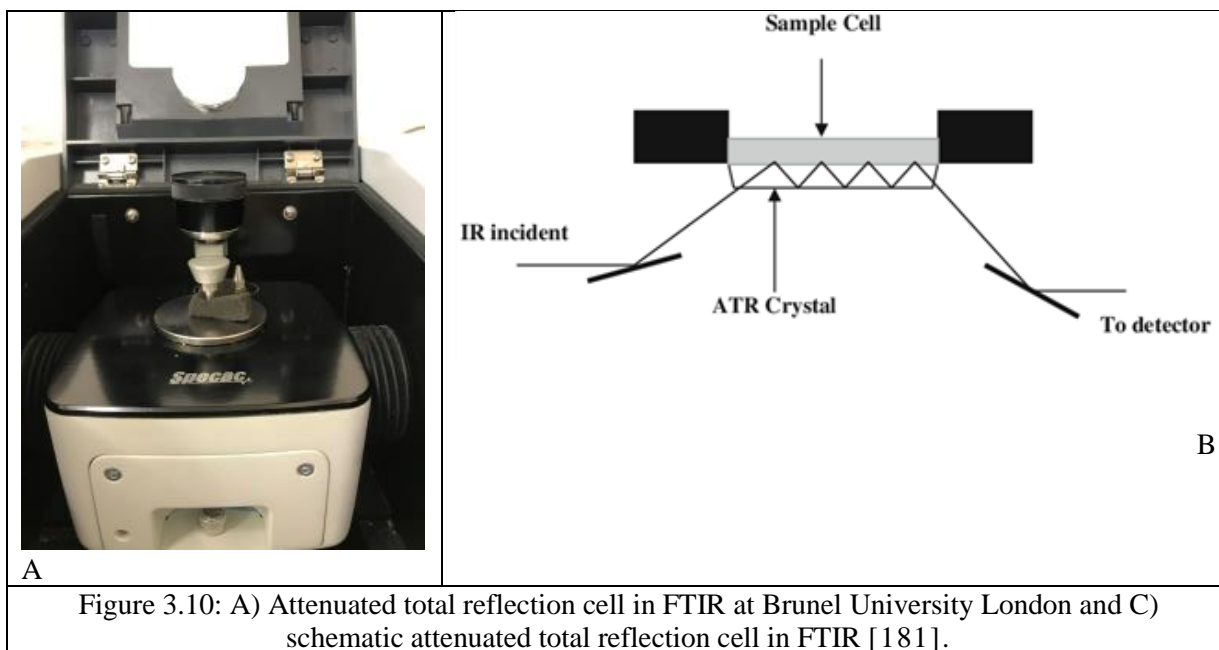


Figure 3.10: A) Attenuated total reflection cell in FTIR at Brunel University London and C) schematic attenuated total reflection cell in FTIR [181].

In addition, IR spectra of a sample always includes interference signals due to nonchemical effects, such as light scattering due to sample morphology and changes in the refractive index. For example, light scattering is directly related to bioparticle morphology, which varies substantially in shape, size, and texture across plant and fungi. In addition, scattering effects are dependent on the refractive index of the bioparticle and refractive index variations within a bioparticle, due to variation in chemical composition [180]. The FTIR sample was placed on the attenuated total reflection (ATR) stage which is an accessory that operates by measuring the changes that occur in an internally reflected IR beam when this comes into contact with a sample. An IR beam is directed onto an optically dense crystal with a high refractive index at a certain angle. This internal reflectance creates an evanescent wave that extends beyond the surface of the crystal into the sample that is held in contact with the crystal. There a drop of sample dispersion was micropipetted or a few milligrams were deposited on a holder for FTIR analysis and stainless steel for  $\mu$ -FTIR.

FTIR spectra of the samples were recorded on a IR-affinity-1 (Shimadzu; FTIR-8400S).  $\mu$ -FTIR micrographs were collected with a rapid scan system consisting of a Bio-Rad spectrometer using a Perkin-Elmer Spotlight equipped with a mercury-cadmium-telluride focal plane array (FPA). FPA consists of 16 gold-wired infrared detector elements. An aperture size of  $6.25\mu\text{m} \times 6.25\mu\text{m}$  was used, meaning that each pixel sampled a  $6.25\mu\text{m} \times$

6.25  $\mu\text{m}$  area on the sample plane, with 32 co-added scans per pixel. The spectral resolution is  $16\text{ cm}^{-1}$ . No transformation or post-processing of the spectra was carried out.

### 3.5 NanoDrop-UV spectroscopy

Spectrophotometer measures  $1\mu\text{L}$  samples with high accuracy and reproducibility. The full spectrum (220-750nm) spectrophotometer utilized a sample retention technology that employs surface tension alone to hold the sample in place which eliminates the need for the containment sample devices (e.g. cuvettes) and allows for clean-up in seconds. In addition, the NanoDrop 1000 Spectrophotometer had the capability to measure highly concentrated samples without dilution (50X higher concentration than the samples measured by a standard cuvette UV-Vis spectroscopy (see Fig. 3. 11).



Figure 3.11: NanoDrop at University of Basrah.

UV/Vis spectrophotometry is simple for samples as small as  $1\mu\text{L}$  using the NanoDrop 1000 spectrophotometer. The small sample requirement and ease of use make the NanoDrop 1000 ideally suited for measuring: (i) nucleic acid concentration and purity of nucleic acid samples up to  $3700\text{ng}/\mu\text{L}$  (dsDNA; ds means double strand) without dilution, (ii) fluorescent dye labeling density of nucleic acid microarray samples, (iii) purified protein analysis ( $A_{280}$ ) up to  $100\text{mg}/\text{mL}$  bovine serum albumin (BSA), (iv) expanded spectrum measurement and quantification of fluorescent dye labeled proteins, conjugates, and

metalloproteins, (v) Pierce Protein 660nm Protein Assay and (vi) cell density measurements [182]. There a 1 $\mu$ L of a sample dispersion micropipetted was on a holder and the result was obtained as the nanogram concentration (ng) of sample.

### 3.5 Electrophoresis

Electrophoresis (EP) is a method for separating molecules from each other on: (i) charge: (molecules with a negative charge (anions) will be attracted to the positively charged node (anode) such as proteins, (ii) size: shorter molecules move faster and easily through the pores of the gel such as DNA (this phenomenon is called sieving) and (iii) shape: configuration.

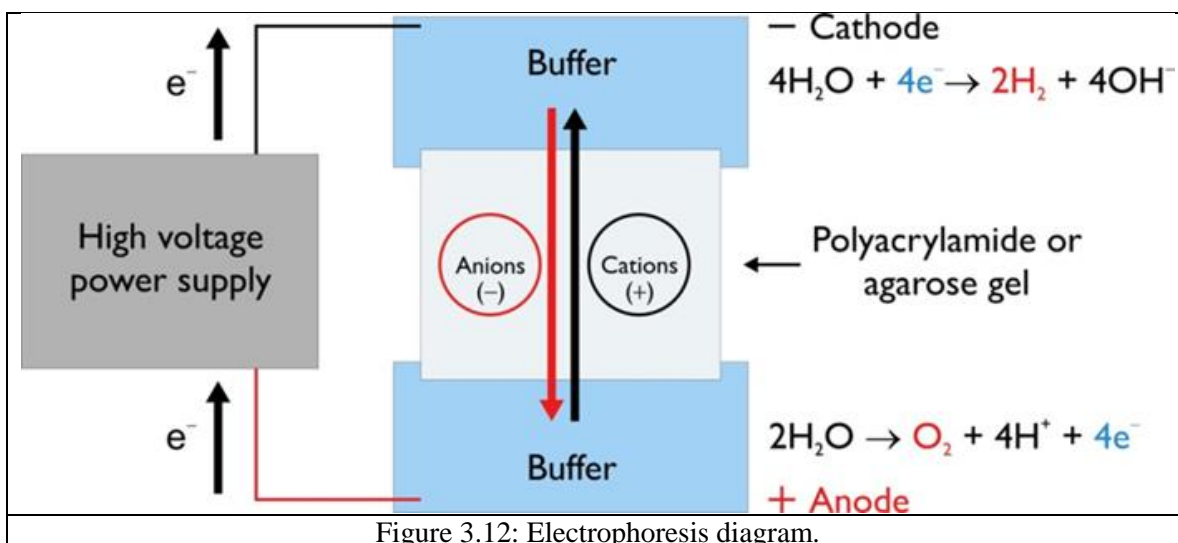


Figure 3.12: Electrophoresis diagram.

The basis of separation depends on how the sample and gel are prepared. Electrical charge employs electromotive force to move molecules through a porous gel. The gel is a cross-linked polymer whose composition and porosity is chosen based on the specific weight and composition of the target to be analyzed [183]. To separate proteins and small nucleic acids (RNA or DNA), the gel normally used is polyacrylamide. In contrast, polyacrylamide is a neurotoxin and must be avoided. When larger nucleic acid (bigger than a few hundred bases) the matrix is purified agarose (a poly saccharide matrix was used as a diagnostic tool

to visualize DNA molecules) composed of long unbranched chains of uncharged carbohydrate without cross-links leading to gel with large pores allowing for the separation.

There are advantages for using agarose: (i) easily cast and handled because agarose setting is a physical rather than chemical change, (ii) the sample is easily recovered, (iii) the gel resulting can be stored in refrigerator and (iv) this gel can be used for the separation of DNA fragments ranging from 50 base pairs (bp) to several millions of bases. The rate of migration depends on many factors (i) composition (ii) percentage of agarose and (iii) ionic strength of buffer solution. The buffer solution used for EP was Tris-acetate-EDTA (TAE) (for acidic) and tris-borate-EDTA (TBE) (for basic). TAE is better than TBE because borate can polymerize or react with cis diols in RNA. Therefore, TAE is the best because it has the lower buffering capacity but provides the best resolution for larger DNA [183]. The negatively charged groups create a flow of water in the opposite direction to the movement of DNA (depend on size) in a process called electroendosmosis (EEO) and can therefore retard the movement of DNA and cause blurring of bands. Ethidium bromide is a fluorescent dye that intercalates between bases of nucleic acids and allows very convenient visual detection of DNA fragments in gel (orange) [183].

- ***Preparation of samples***

The samples were prepared using the following conditions: (i) ethidium bromide-stained agarose gel electrophoresis containing total genomic DNA on of PMS alone, (ii) control which was DNA in TE (buffer solution), (iii) samples in the light at RT and in the dark at 37°C. Here, electrophoresis (Fisher Scientific, USA), Eppendorf tube (Fisher Scientific, USA) and Incubator (Binder, Germany) were used.

### **3.7 White light interferometry (WLI)**

White light interferometry (WLI) is a technique which is used to characterize the surface roughness and texture. Moreover, WLI is used to be a complementary technique in the biotechnology application due to the ability to resolve the texture of large surface area with sub-nm resolution. Furthermore, WLI is used for monitoring the topology of samples like measuring the thickness, surface area and roughness [184].



Many techniques were used but they have many limitations. Comparison of advantages, disadvantages and errors of the various methods used: (i) high resolution limits view field (ii) they normally include destructive or charged preparation of the samples when used with SEM [185] (iii) the samples exposed to high vacuum conditions. Therefore, WLI is a unique technique which combines a large field of view and high resolution [184]. It has many advantages as (i) non- destructive, (ii) non- contact, (iii) high sensitive and (iv) repeatability (see Fig. 3.13) [185].



### 3.3 Conclusions

The selected techniques chosen have advantages and disadvantages. For example, TEM analysis is very effective but only nano gram of samples are probed. One the other hand, XRD requires larger samples, but the structural analysis may therefore be a better average

are must weigh up and appreciate these differences. Other techniques such as Extended x-ray absorption fine structure (EXAFS) were not available in the timescale available. The author returns to consider error and uncertainties in chapter 13.

## Chapter 4: Materials and preparative methods

---

This chapter explains the materials used and preparation methods used in PMS harvesting and their use in preparation of TiO<sub>2</sub>, Ag, Au NPs/PMS and their nanohybrids. Also, the chapter will describe the experimental techniques used to investigate and analyze the nHAp/PMS, AA, Hb and insulin loaded into PMS. In addition, it outlines the antimicrobial and photocatalysis experimental methods.

### 4.1 Materials

Brown fresh Portobello mushrooms spores were purchased from the market (PMS; Sainsbury's; London), The reagents used included: titanium(iv) isopropoxide Ti(OC<sub>3</sub>H<sub>7</sub>)<sub>4</sub> (ACROS organics 98%), ethanol (Sigma Aldrich, 99.9%), 2-propanol (IPA Fluka, 99.9%), tri-sodium citrate dihydrate (C<sub>6</sub>H<sub>5</sub>Na<sub>3</sub>O<sub>7</sub>·2H<sub>2</sub>O) (tri-sodium citrate TSC, Sigma Aldrich, 99%), sodium borohydride (NaBH<sub>4</sub>, BDH, 95%), silver nitrate (AgNO<sub>3</sub>) (Fisher chemical, above 99%), gold (III) chloride hydrate (AuCl<sub>3</sub>·xH<sub>2</sub>O) (Sigma Aldrich 99.9%). ethidium bromide (100%, BDH), TBE 10X (tris- boric acid-EDTA) (100%, bio base) and NaCl. DNA extraction Mini Kit (Geneaid Company) was also used for NPs/PMS biosynthesis. The reagents which were used for HAp/PMS and drug delivery samples preparation were calcium chloride (CaCl<sub>2</sub>·2H<sub>2</sub>O, Sigma, 99%), sodium carbonate (Na<sub>2</sub>CO<sub>3</sub>; Sigma; 99%), sodium dihydrogen phosphate (Na<sub>2</sub>HPO<sub>4</sub>; Fisons; 99.5%), poly (vinyl alcohol) (PVA; BDH; RMM 115000), glutaraldehyde (C<sub>5</sub>H<sub>8</sub>O<sub>2</sub>; Sigma; 25%), calcium chloride (CaCl<sub>2</sub>·2H<sub>2</sub>O; Alfa Aesar; 99%), sodium bicarbonate (Na<sub>2</sub>HCO<sub>3</sub>; Sigma; 99%), potassium chloride (KCl; Sigma; 99%) sodium chloride (NaCl; Fisher; 100%). Bio-Oss (Geistlich) and Nano HAp powder (Sigma; 97%). All were used as received. For drug delivery studies the following were used: ascorbic acid (Sigma; 99%), hemoglobin human (Sigma) and insulin (Actrapid; Novo Nordisk LOimited). For antibacterial activity studies, two bacterial strains (pathogenic) were used during the testing: *Staphylococcus aureus* (Gram positive) and *Escherichia coli* (Gram negative). In addition, *Aspergillus spp.* and *Candida spp.* were

used as fungi from University of Basrah. *Escherichia coli-K12* (MRB-150-300) was bought in the UK from Breck land scientific (lyophilized bacteria as powder to avoid any contamination). For photocatalytic studies, methyl orange (Sigma Aldrich; 85.9%; RMM 327.33; MO) and commercial titania (P25; Sigma Aldrich; 35-65m<sup>2</sup>.g<sup>-1</sup>) were used.

## 4.2 Preparative Methods

### 1. *Portobello Mushroom Spores (PMS)*

The caps of fresh Portobello mushroom (different size) were cut and placed upside down in a glass petri dish (10-14cm size) without shaking the caps for 2-4 days (see Fig. 4.1A). A fine brown deposit of spores was obtained after a few hours. The best harvest method left the mushroom to release their spores for a long time to ensure that almost all spores were released and collected. (see Fig. 4.1B). Portobello mushroom spores (PMS) were stored at RT (see Fig. 4.1C).

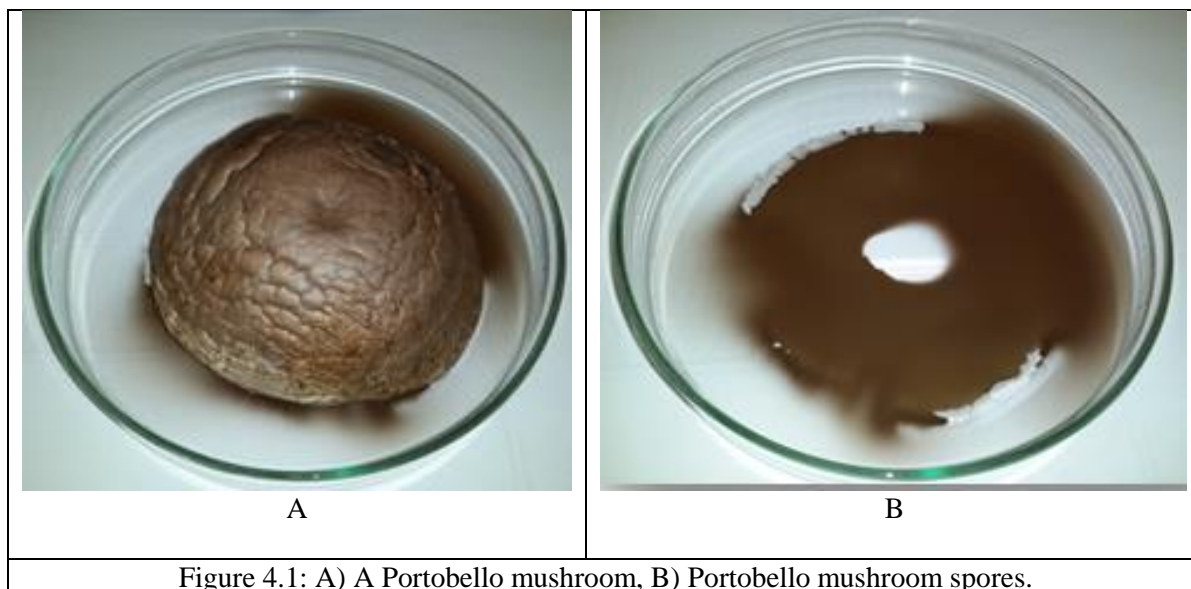


Figure 4.1: A) A Portobello mushroom, B) Portobello mushroom spores.

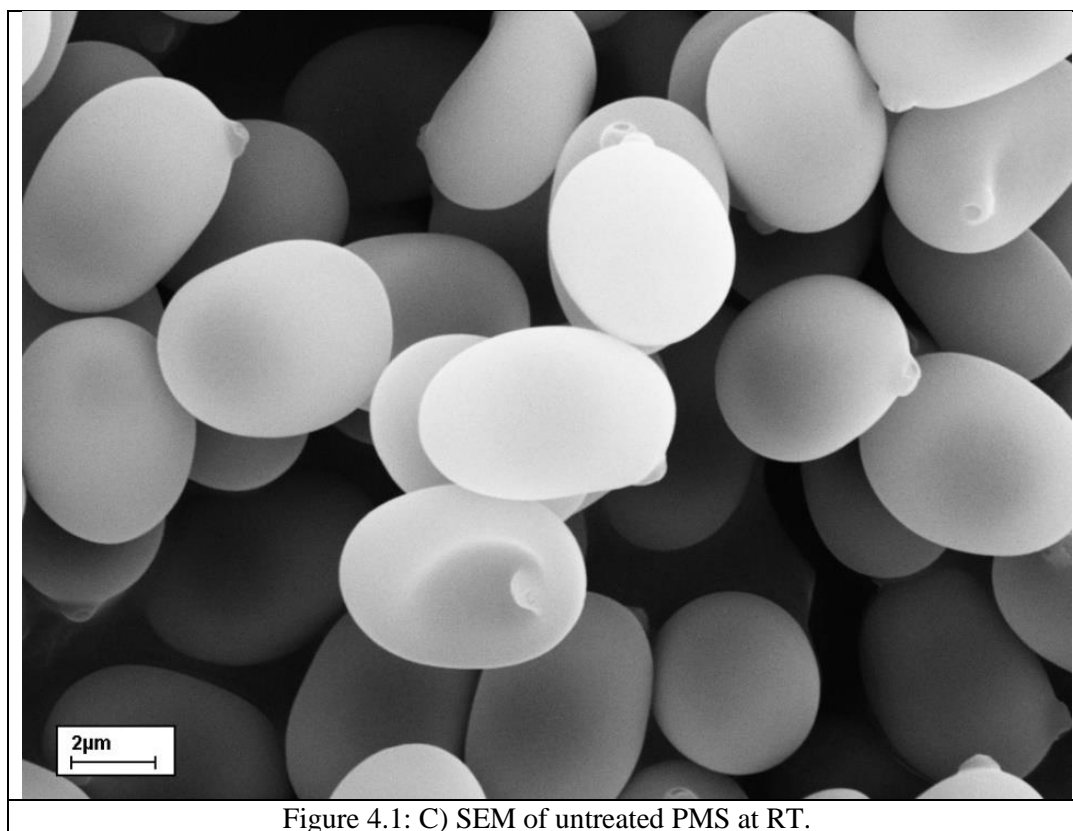


Figure 4.1: C) SEM of untreated PMS at RT.

#### 4.2.1 Preparation of TiO<sub>2</sub> NPs/PMS

4mg of PMS were dispersed in 5mL of IPA with magnetic stirring. 5mL of titanium(IV)isopropoxide (Ti(OC<sub>3</sub>H<sub>7</sub>)<sub>4</sub>) solutions in IPA at different concentrations (0.03, 0.3 and 3mM) were added dropwise, with continued magnetic stirring for 1h at RT [186] separately. The sample was decanted and washed with further IPA and then dried in air at RT. During Ti(OC<sub>3</sub>H<sub>7</sub>)<sub>4</sub> treatment, it was expected that surface-OH groups on PMS would react to give Ti-O-C linkages. After dry in air, hydrolysis with moisture in air would give surface TiO<sub>2</sub> on PMS.

#### 4.2.2 Preparation of Ag NPs/PMS

Four solutions were prepared as follows:

##### (a) Citrate-derived Ag NPs

50mL of AgNO<sub>3</sub> (1mM) was heated to its boiling point and 5mL of 1% sodium citrate dehydrate (C<sub>6</sub>H<sub>5</sub>Na<sub>3</sub>O<sub>7</sub>·2H<sub>2</sub>O) (tri-sodium citrate TSC) was added dropwise as a reducing

agent with magnetic stirrer. The color changed after 30 min to a greenish yellow and the solution was cooled at room temperature. The pH of the solution was adjusted [187] to 10.

**(b) Borohydride-derived Ag NPs**

20mL of NaBH<sub>4</sub> (2mM) was placed in a flask with magnetic stirrer and cooled as reducing agent. 2mL of AgNO<sub>3</sub> (1mM) was added dropwise for 20 min (one drop per second). The color changed to greenish yellow [187]. The pH of the solution was adjusted to 10.3.

**(c) Citrate-Borohydride derived Ag NPs**

20mL of NaBH<sub>4</sub> (2mM) solution was mixed with 1mL of tri-sodium citrate dehydrated (TSC) as reducing agent (2mM) and heated to 60°C with magnetic stirrer for 30 min in the dark to give a reductant solution. Then, 10mL of AgNO<sub>3</sub> (1mM) was added drop by drop increasing the heat to 90°C for 20 min. The pH of the solution was adjusted to 10.5 by adding NaOH (0.1M) and the color completely changed from colorless to greenish yellow after 30 min. The product was cooled at room temperature [188]. Here, these reagents are the reducing agent for aldehyde and ketones groups to alcohol.

**(d) 1mM of AgNO<sub>3</sub>**

This solution was prepared to react directly with PMS without any reducing agents to know how PMS reduces Ag ions to NPs, which is the next step.

**(e) Using Portobello mushroom spores (PMS) and bio-synthesise Ag NPs**

The spores were washed twice with water and acetone. 4mg of PMS was dispersed in 5mL water and 5mL/AgNO<sub>3</sub> (1 and 3mM) was added. Then, the pH of the solutions adjusted under magnetic stirrer for 1h. During these reactions, it was expected that functional groups on the PMS surface support synthesis Ag NPs on/in the PMS surface faster, better and at RT than other three reducing agents above.

### 4.2.3 Preparation of Au NPs/ PMS

4mg of Portobello mushroom spores (PMS) were washed twice with water and acetone respectively. Then, the PMS were dispersed in 5mL water using an ultrasonic bath (30w) for 2 min. At this point, 5mL of AuCl<sub>3</sub> solution (with concentrations of 0.1M, 1mM and 0.2mM) were added to the PMS dispersion under magnetic stirring at room temperature.

The pH of the suspensions was 1.4 and adjusted to around 4, 7, 8, 9 and 10 by adding NaOH (0.1 and 0.01M). These solutions of Au NPs/PMS were left for 1h under magnetic stirring. The color changed for some solutions after 1-2h. Here, it was expected that thiol (SH) groups on PMS surface support synthesis Au NPs on/in PMS surface faster, better and at RT.

#### 4.2.4 Preparation of nanohybrids/PMS

- **Method No.1: TiO<sub>x</sub>-Ag NPs/PMS (mixed TiO<sub>2</sub>-Ag then added to PMS)**

5mg of PMS was dispersed in 5mL in IPA by ultrasound for 2min. Then, 5mL of Ti(OC<sub>3</sub>H<sub>7</sub>)<sub>4</sub> (3mM) in IPA was mixed with 5mL AgNO<sub>3</sub> (1mM) in IPA under magnetic stirring for 30 min. This solution was added to the PMS suspension with magnetic stirring and mixed for 1h. The same steps were used to prepare TiO<sub>x</sub>-Au NPs/PMS in IPA and Ag-Au NPs/PMS in water.

- **Method No.2** (added in same time)

This method will explain which ions (TiO<sub>2</sub> or Ag) will react on the PMS to produce surface held NPs/PMS:

##### *1-TiO<sub>x</sub>-Ag NPs/PMS<sub>IPA</sub>*

4mg of PMS was dispersed in 5mL of IPA with ultrasonic agitation (30w) for 2 min. One drop of KOH/IPA (0.1M) was then added to the above suspension under magnetic stirring. 5mL of Ti(OC<sub>3</sub>H<sub>7</sub>)<sub>4</sub>/IPA (1mM) and 5mL of AgNO<sub>3</sub> in IPA (1mM) were then added to the PMS suspension simultaneously and magnetically stirred for 30 min. The color changed to brown. The same steps were used to prepare TiO<sub>x</sub>-Au NPs/PMS in IPA and Ag-Au NPs/PMS in IPA.

Here, it was expected that nanohybrids of TiO<sub>2</sub>-Ag ions, TiO<sub>2</sub>-Au ions react with PMS surface and then metal ions depended on redox reactions. Core@shell could be formed between Ag and Au NPs on PMS surface possibly involving redox reactions.

**2- Au-Ag NPs/PMS<sub>H2O</sub>**

Ag-Au NPs/PMS was prepared by adding 4mg of the PMS to 4mL water and 1mL of buffer solution (pH 10) under magnetic stirring. To this was added 5mL of (1mM) AuCl<sub>3</sub> in water and 5mL of AgNO<sub>3</sub> (1mM) in water simultaneously for 20 min under magnetic stirring for 30 min. The color changed to pink. The sample was decanted and washed with water.

- **Method No.3**

All samples prepared had a lower wt.% metal suggested by EDX analysis and then another metal was added to it:

**1- Ag-TiO<sub>2</sub> NPs/PMS<sub>IPA</sub>**

4mg of PMS was dispersed in 5mL in IPA ultrasonically for 2 min. Then, one drop of KOH/IPA (0.1M) was added to the above suspension under magnetic stirring. 5mL (1mM) AgNO<sub>3</sub> in IPA were added to the PMS suspension under magnetic stirring for 30min. The sample was decanted and washed with IPA. 5mL of Ti(OC<sub>3</sub>H<sub>7</sub>)<sub>4</sub> (1mM) in IPA was then added to the Ag NPs with PMS under magnetic stirring for 1h. The same steps were used to prepare Au-TiO<sub>2</sub> NPs/PMS<sub>IPA</sub>.

**2-Ag- Au NPs/PMS<sub>H2O</sub>**

4mg of PMS was dispersed in (4mL water and 1mL of buffer solution), pH 10 under magnetic stirring. 5mL of AgNO<sub>3</sub>/water (1mM) was added to the PMS suspension with magnetic stirring for 30 min. The sample was decanted and washed with water and 5mL AuCl<sub>3</sub> in water (1mM) were added to Ag NPs with PMS suspension under magnetic stirring for 30 min. The colour changed to light pink. The NPs/PMS were decanted and washed with water. It was expected that nanohybrids of TiO<sub>2</sub> with Ag ions, or Ag ions react with PMS surface and then Au ions depended on redox reactions.



### 4.2.5 nHAp/PMS

#### 1. Preparation of ions/PMS ( $\text{Ca}^{2+}$ /PMS, $\text{CO}_3^{2-}$ /PMS and $\text{PO}_4^{3-}$ /PMS)

A sample of (4-4.1mg) PMS was washed twice with water and acetone respectively and then dispersed in 5 mL water (ultrasonic bath 15 min) and then  $\text{CaCl}_2$  solution (5 mL; 5.5mM) was added dropwise. Then, the solution was left for 1h under gentle magnetic stirring  $37\text{C}^\circ$  and left overnight, filtered and dried to get  $\text{Ca}^{2+}$ /PMS.

$\text{CO}_3^{2-}$ /PMS were prepared in a similar way using  $\text{Na}_2\text{CO}_3$  (5 mL; 5.5mM).

$\text{HPO}_4^{3-}$ /PMS was prepared in a similar way using (5mL; 1.3mM  $\text{Na}_2\text{HPO}_4$ ) (see Table 4.1).

#### 2. Preparation of nano- $\text{CaCO}_3$ /PMS

A  $\text{Na}_2\text{CO}_3$  solution (5mL, 5.5mM) was quickly added into the suspension of PMS with magnetic stirring  $37\text{C}^\circ$  [189] for 1h and then dried.  $\text{CaCl}_2$  solution (5mL, 5.5mM) was added to  $\text{CO}_3^{2-}$ /PMS. [110].

#### 3. Preparation of nano-HAp/PMS

$\text{Na}_2\text{HPO}_4$  solution (5mL, 1.3mM) was added drop-wise to two suspensions of  $\text{CaCO}_3$ /PMS separately with magnetic stirring  $37\text{C}^\circ$  for 1h and then left 3 days and dried [110] (see Table 4.1).

Table 4.1: The steps to preparations nHAp/PMS.

Solutions	Conc. (mM)	V (mL)	Suspensions
$\text{CaCl}_2$	5.5	5	$\text{Ca}^{2+}$ /PMS
$\text{Na}_2\text{CO}_3$	5.5	5	$\text{CO}_3^{2-}$ /PMS + $\text{CaCl}_2 = \text{CaCO}_3$ /PMS + $\text{Na}_2\text{HPO}_4 =$ nHAp/PMS
$\text{Na}_2\text{HPO}_4$	1.3	5	$\text{PO}_4^{3-}$ /PMS

#### 4. Preparation of nHAp/PMS in poly (vinyl alcohol) PVA

A sample (6mg) of PMS was mixed with 7.5mL 5% PVA, cross-linked (0.269mL, 3% glutaraldehyde (1mol % for the monomer unit of PVA), 0.112 mL 0.1M HCl and 1.5mL water mixed for 2h at RT. The sample was then dried for 2 days. The formation of nHAp/PMS on PVA cross-linked was prepared via 3 steps: step 1: the dimensions of PMS/PVA crosslinked polymer (27.9 mg; the diameter is 2x1.8 cm) was immersed in 15

mL (5.5mM) Na<sub>2</sub>CO<sub>3</sub> solution for 1 hour at 24°C and dried using filter paper. Step 2: the sample was immersed in (5.5mM) CaCl<sub>2</sub> solution for 1h. Then, the samples were washed and dried on filter paper. Finally, the sample was immersed in 1.3mM Na<sub>2</sub>HPO<sub>4</sub> for 1h. This procedure was repeated for 8 reaction cycles [190]. Lastly, the sample was held at 37°C for 3 days [110].

#### 4.2.6 Bioactivity studies

Study of bioactivity has been widely used for clinical applications because of the ability to enhance bone-tissue formation on the sample's surface. The samples could also be bonded with the living tissue. Now the samples (described in section 4.2.5) were immersed in biological simulated body fluid (SBF) at 37°C for 14 days and the solution was changed every 2 days. The SBF solution changed leading to more reliable, accurate and perfect simulation of the bioactivity. Evaluation of weight % was calculated using the wt.% after 14 days of immersion in SBF according the % equation (4.1) [191].

$$\% = \frac{(w_2 - w_1)}{w_1} \times 100 \quad \text{--- (4.1)}$$

where W<sub>1</sub> and W<sub>2</sub> are the weight of sample before and after immersed in SBF.

##### 1. *In vitro* bioactivity evaluation

Simulated body fluid (SBF) is purposed to (i) predict bioactivity of the samples by the apatite formation and (ii) prepare HAp surface coatings on samples [192]. SBF was prepared to be similar to human blood plasma using the Kokubo method/reagents in double distilled-water and explained in Table 4.2 [193].

Bioactivity was evaluated by immersing the Bio-Oss, Nano HAp, nHAp/PMS and nHAp/PMS- PVA hydrogel samples in standard simulated body fluid (SBF) whose pH of SBF was adjusted to 7.4. The temperature was kept at 37°C. Every sample (1mg/mL) was immersed in SBF for 14days. The solution was renewed every 3 days in order to encourage apatite deposition [194]. After incubation for 14 days, the samples were removed, washed gently with deionized water and dried at RT for 2 days in a fume hood. Finally, the

formation and growth of HAp layers was investigated by measuring the solution concentration of Ca and phosphate ions, pH and wt.% HAp developed [194].

Table 4.2: The compositions of reagents used to prepare the SBF.

Reagent	g/L	Reagent	g/L	Reagents	g/L
NaCl	7.996	CaCl <sub>2</sub>	0.278	1M HCl	40mL
NaHCO <sub>3</sub>	0.350	Na <sub>2</sub> SO <sub>4</sub>	0.071	MgCl <sub>2</sub> 6H <sub>2</sub> O	0.305
KCl	0.224	(CH <sub>2</sub> OH) <sub>3</sub> CNH <sub>2</sub>	6.057	K <sub>2</sub> HPO <sub>4</sub> 3H <sub>2</sub> O	0.228

## 2. *In vitro* dissolution evaluation

Naturally, HAp associated with collagen/extracellular matrix proteins in the human body leads to superior mechanical properties of bone. This HAp has a slow rate of formation and a slow rate dissolution [195]. nHAp/PMS are ideal to combine HAp with biomolecules to take advantage of their material properties. The present dissolution studies were undertaken in a phosphate buffer saline (PBS) with the following samples: Bio-Oss, Nano HAp, nHAp/PMS and nHAp/PMS- PVA hydrogel at pH 7.4 during incubation at 37°C for 30 days with agitated 50rpm. The concentration of samples was (1mg/mL). The concentrations of Ca ions and pH were monitored every 2-3 days [194]. Finally, the samples were removed, washed gently with deionized water and dried at RT for 2 days in a fume hood. The *in vitro* dissolution was determined by changes in Ca ions, pH and surface morphologies of samples.

### 4.2.7 Methods of Assessing the Uptake and Release of AA, Hb Protein and

#### Insulin

10mL of 0.1mM of AA solution in water (pH 6.8) was added to 3mg of PMS mixed for 5 min and left to adsorb at RT for 5h. AA has an absorbance maximum and was measured at 265nm. This was measured to assess AA solution concentrations. A similar method was used for nHAp/PMS and PMS/PVA hydrogel (10%) and a similar method was also used for 2mg Hb in 10mL which had an absorbance maximum at 404nm and 400μL insulin (40IU) in 10mL H<sub>2</sub>O) which had an absorbance maximum at 270nm. This gave a maximum loading ratio:

$$\text{Loading ratio} = \left( C_2 / C_1 \right) \times 100 \quad \text{---} \quad (4.2)$$

and a swelling ratio (Q):

$$Q = ( W_s - W_d / W_d ) \times 100 \quad \text{---} \quad (4.3)$$

where  $W_s$  and  $W_d$  the weight of swollen and dried PVA hydrogel.

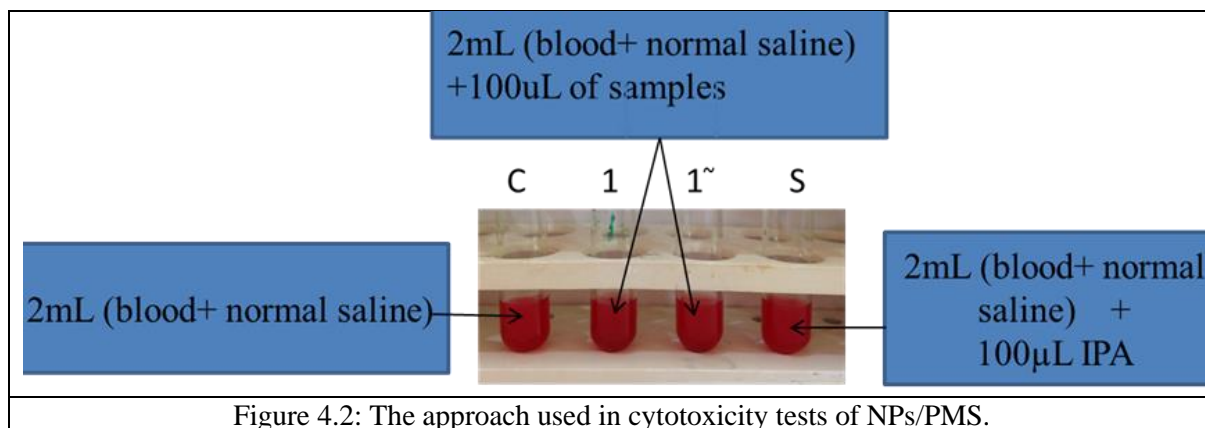
To investigate AA release from pre-loaded PMS, 3mg of AA-loaded PMS was immersed in 10mL of phosphate buffer saline (PBS; pH 7.4), mixed for 5 min and left to desorb AA at 37°C for 24h in an incubator. As in AA uptake experiments, the absorbance was measured at 265nm. A similar method was used for HAp/PMS and PMS/PVA hydrogel and HAp/PVA microsphere. PVA microspheres were prepared as the literature [196]). A similar method was used for Hb and insulin uptake ( $\lambda_{\text{max}} = 404\text{nm}$  and  $270\text{nm}$ ) in distilled water and simulated intestinal fluid (SIF) and simulated gastric fluid (SGF) ( $\lambda_{\text{max}} = 272\text{nm}$ ).

Each sample was immersed in water (pH 6.8) as a control for AA, Hb and insulin. The % drug release was thereby studied as a function of time. Samples pre-loaded with insulin were immersed separately in 10mL simulated intestinal fluid (SIF; pH 7.4), simulated gastric fluid (SGF; pH 1.2) and distilled water (pH 6.8).

#### 4.2.8 Cytotoxicity test

Cytotoxicity tests of NPs/PMS were undertaken against fresh human red blood corpuscles (RBCs) [197] using a suspension of NPs/PMS (100 $\mu$ L same antibacterial activity concentration). IPA was the standard and blood was a control: 2mL of human blood was mixed with 40mL of a normal saline solution (NaCl pH 7.4). The solution was divided into 4 test tubes, each one containing 2mL of mixed (human blood and normal saline solution). At this point, every test tube (1 and 1) contained 100 $\mu$ L of PMS sample and were left at RT in duplicate. The standard test tube contained 100 $\mu$ L IPA (solvent) that was mixed with human blood and normal saline solution. The control test tube contained 100 $\mu$ L mixed of

human blood and normal saline solution). Finally, turbidity of the mixture was examined after 15, 30, and 60 min before the blood cells were hemolyzed completely (see Fig. 4.2).



#### 4.2.9 Study of the effects of NPs/PMS on DNA

##### 1. Samples collection DNA extraction

From volunteers, 3mL of venous blood was collected in an EDTA tube and was then used freshly to extract the human genomic DNA. Human genomic DNA was extracted from all fresh blood samples using the DNA extraction Mini Kit, according to the kit protocol. DNA quantity and quality were assessed by Nanodrop (Nanodrop/optizen system) at 260nm respectively. DNA with PMS and NPs/PMS was visualized by 0.8% agarose gel electrophoresis which was stained with ethidium bromide and using the reagent 1X- Tris borate EDTA (TBE) buffer solution [198]. Study of the effects of NPs/PMS on DNA were performed by preparation of 1.5mg of PMS dispersed with 1mL of tris- 0.1M HCl and 0.01M EDTA solution (TE buffer). The purpose of the TE buffer was to solubilize DNA while protecting it from degradation. Then, 10µL of DNA in TE was mixed with 10µL of PMS suspension. The mixture was divided into 4 vials: 2 vials were left in the dark at 37°C and another 2 vials were left under light (neon 50Hz) at RT for 1h. The PMS- DNA mixture was electrophoresed for 15 min at 60eV on a (0.8%) agarose gel in 1X TBE buffer. The gel was stained with ethidium bromide and photographed under UV light. The same steps were used with DNA- TiO<sub>2</sub>, Ag and Au NPs/PMS.

## **2. Detection of DNA by agarose gel electrophoresis**

DNA was visualized by agarose gel electrophoresis according to Sambrook and Russel using the reagents: preparation of (0.8%) agarose gel 1X- TBE buffer (25mL) was mixed with 0.2g agarose. The solution was boiled until completely dissolved. The gel was left to cool down to about 50-60°C. Then 2 $\mu$ L of ethidium bromide was added to the gel [183]. The comb was put in one of the cast endings and the agarose solution was poured in the cast after the endings were blocked to avoid leakage and left to cool to RT. Then the cast was put in the electrophoresis cavity after lifting the comb which were fixed [183].

## **3. Migration of DNA on agarose gel and NPs/PMS**

The electrophoresis tank was filled with 1X-TBE buffer about 3mm above the gel. 9 $\mu$ L of extracting DNA was added to 3 $\mu$ L of bromophenol blue, and then loaded in the walls of agarose gel. Electrodes of electrophoresis apparatus was linked to the power supply system at (60V and 120 mA), so that the black electrodes in the electrophoresis apparatus would be linked to black electrodes in the power supply system and the same thing was undertaken for the red electrodes. The loaded dye was left for 30 min to migrate from the walls to the other side.

## **4. Visualizing DNA on a UV transilluminator**

The gel was tested with a UV light and a digital photograph of the fluorescent ethidium bromide-stained DNA separation pattern was taken.

## **5. The effect of prepared NPs/PMS on human genomic DNA**

The effect of the prepared NPs/PMS on DNA was studied by mixing 10 $\mu$ L of DNA with 10 $\mu$ L of NPs/PMS solutions, then the mixture incubated at 37°C for 1hour in the dark and another 1h under light at RT [183]. To study the effect of/on PMS-based samples on genomic human DNA, 10 $\mu$ L of each sample was mixed with 10 $\mu$ L of human genomic DNA. The mixture incubated at 37°C for 1h; then the absorbance of mixture was measured at 260nm [199] and the DNA concentration was thereby assessed.

#### 4.2.10 Determination of Median Lethal Dose (LD<sub>50</sub>)

- **Animal and experimental design**

All the animal experiments reported here were carried out in compliance with the national regulation governing animal experiments. The mice were obtained from central animal facility (Veterinary Medicine College, University of Basra). Animals were acclimatized to standard laboratory conditions of light-dark (14-10h) and temperature (22±3°C) for 3 days prior to experiments. The mice were fed water and standard laboratory diet. All the mice were housed in polyacrylic cages (3 mice per cage). Total number of mice was 60 healthy male and female albino mice (one of the two white-coloured varieties of the domesticated house mouse). Albino mice were then divided into the following studies (weight about 35±5): 10 groups, each group contained 6 mice (3 male and 3 female) [200].

- **Dose preparation and administration**

Albino mice were fasted for 18h prior to dosing. TiO<sub>2</sub>, Ag and Au NPs/PMS were dispersed in distillate water and administered once orally by using a stomach tube with different doses in the range 50,100 and 200µg/kg [197]. The group C was given 0.5mL normal saline only to represent a control group. The mice were observed for 2, 24, 48 and 72h for any toxic signs and symptoms [200].

#### 4.2.11 Antimicrobial Measurements

Antibacterial activity was determined in duplicate using Mueller Hinton agar. PMS and NP/PMS samples were dispersed in (and diluted with) IPA or H<sub>2</sub>O. The antibacterial activity of NPs/PMS was assessed against two pathogenic bacteria species: *Staphylococcus aureus* (Gram positive) and *Escherichia coli* (Gram negative) in the agar well diffusion method. Overnight cultures were used. After 24h of incubation, bacterial suspension (inoculum) was diluted with sterile physiological solution, for the diffusion test, to 10<sup>8</sup> CFU/mL (colon forming unit) (turbidity = McFarland barium sulfate standard 0.5) [201]. The control sets (IPA and H<sub>2</sub>O) were maintained under the same conditions. The bacterial inoculums were uniformly spread using a sterile cotton swab on a sterile Petri dish containing agar. 50µL of the PMS or NP/PMS samples were added to each well (6 mm

diameter holes cut in the agar gel, 20mm apart from one another). The plates were incubated for 24 h at 37°C, under aerobic conditions. After incubation, confluent bacterial growth was observed. The diameter of the zone of inhibition was measured directly in mm [201].

In the agar diffusion disc-variant measurements, NP/PMS were dispersed in (and diluted with) IPA and were used to impregnate 6 mm filter paper discs (Whatman no. 2) to a loading of 10µL or mg.m<sup>-2</sup>. The discs were maintained at 25°C until evaporation was complete and were then kept under refrigeration until the test, when they were placed onto the surface of the agar and incubated overnight at 37°C, at which point the zones of bacterial inhibition were recorded. These measurements were in duplicate [202]. In anti-fungal activity measurements, the NP/PMS samples were assessed against two pathogenic fungi species: *Aspergellis.spp.* and *Candida.spp.* using an agar diffusion disc method. Here the plates were incubated for 72h at 37°C under aerobic conditions. After incubation, confluent fungi growth was observed. The radius of the regions of inhibition of the fungal growth were again measured (mm); again tests were performed in duplicate [100].

#### **4.2.12 Biotemplate TiO<sub>x</sub> overcoating and addition of Au/Ag NPs**

A 3mM Ti(OC<sub>3</sub>H<sub>7</sub>)<sub>4</sub> solution was made up in 5mL 2-propanol and filtered (0.22µm). 4-5 mg Portobello mushroom spores (PMS) were washed twice with water and acetone respectively and were then dispersed in 5 mL IPA with magnetic stirring for 1-2h.

PMS (4-5mg) was dispersed in 5 mL IPA (ultrasonic bath for 15 min). At this point, 5 mL of alcoholic (IPA) AuCl<sub>3</sub> solution (3mM) was added with magnetic stirring at room temperature. The pH of the suspensions was 1.4. Solutions were left for 3h under magnetic stirring. The colour of the solution changed after 1-3h. The same steps were used to prepare Ag NPs/PMS using 3mM of AgNO<sub>3</sub>. These were considered green methods of synthesis of the Ag and Au NPs using the PMS cell wall.

Ag-TiO<sub>x</sub>/PMS was prepared by ultrasonically dispersing 4-5 mg of PMS in 5mL IPA for 15 min. Then, 5mL of alcoholic (IPA) AgNO<sub>3</sub> solution (3mM) was added to the PMS dispersion with magnetic stirring at room temperature for 3h. The Ag/PMS was left overnight. Then to 5mL of Ag NPs/PMS was added Ti(OC<sub>3</sub>H<sub>7</sub>)<sub>4</sub> (3mM) in IPA with magnetic stirring for 3h. The same steps were used to prepare Au-TiO<sub>2</sub>/PMS in IPA.



#### 4.2.13 Biotemplate TiO<sub>2</sub> replica formation

Overcoated biotemplate samples (TiO<sub>x</sub>/PMS, Ag/PMS, Au/PMS, Ag-TiO<sub>x</sub>/PMS and Au-TiO<sub>x</sub>/PMS) were calcined at 500°C in air for 3h to remove the organic substrate, giving TiO<sub>2</sub> replicas (TiO<sub>2</sub> (PMS), Ag-TiO<sub>2</sub> (PMS) and Au-TiO<sub>2</sub> (PMS)) [108].

#### 4.2.14. Photocatalytic activity

The experiments were carried out, at RT, in quartzes cuvette. The light source was at 254nm and 365nm, 15 walls (two tube each wavelength) and overhead white light.

Milligrams of samples (TiO<sub>2</sub> NPs/PMS, Ag-TiO<sub>2</sub> NPs/PMS and Au-TiO<sub>2</sub> NPs/PMS) were tested at RT and calcined at 500°C in air for 3h to remove the organic substrate. Then, they were reacted with 0.1mM MO (at maximum absorbance 464nm) for 1h in dark under magnetic stirring to reach the adsorption/desorption equilibrium. These samples were characterized by UV-Vis spectroscopy over 10h. A commercial photocatalyst powder called P25 was used as standard.

##### ➤ The adsorption ability

The measurement of adsorption ability of photocatalysts was carried out by measuring the adsorption percentage of MO in an aqueous solution at RT. Mg of photocatalyst were added to 10mL of 0.1mM or 0.01mM of MO aqueous with stirring in the dark. Then, photocatalyst samples were left for 1h to precipitate the photocatalysts and the UV-Vis adsorption spectra were measured at  $\lambda_{\max}$  464nm. All the measurements were repeated two times.

$$Q_t = (C_o - C_t)V/W \quad \text{----- (4.4)}$$

$Q_t$ : adsorption amount of MO (mmol/mg) onto the photocatalyst,

$C_o$ : the initial concentration of MO (mmol/mL),

$C_t$ : the concentration of MO at the time (mmol/mL),

$V$ : the volume of MO (mL),  $W$ : the mass of NPs/PMS (mg).

## **Chapter 5: Characterization results for Portobello mushroom spores (PMS)**

---

In this chapter, the characterization of PMS using SEM, TEM, SIMS, FTIR and TGA is explained. The aim here was to study if an edible Portobello mushroom spore (PMS) could be used as a template and reducing agent to prepare novel biocompatible materials for: (i) drug delivery, (ii) assembly of replacement bone with no toxicity or environmental issues, (iii) photocatalyst and (iv) antimicrobial treatments. It is shown that PMS can be used as vectors on which to fabricate submicron and nano-sized particles (NPs) for these different applications.

### **5.1 Introduction**

Edible mushrooms are useful foods and also their spores have a significant role in the human body due to medical properties, as a food and to resist disease [203]. They are rich in protein, fibres and high in essential amino acid content, producing specific alkaloids, while fortunately being poor in fats. They supply a nutritionally important range of vitamins (B1, B2, B12, C, D and E) and antioxidants (not normally destroyed and deactivated by cooking). Edible mushrooms may also be a source of many different nutraceuticals (e.g. unsaturated fatty acids, phenolic compounds and ascorbic acid) [204]. Furthermore, it was reported that they contain trace amounts of some heavy metals (e.g. cobalt, iron, chromium, copper, zinc and manganese) [205]. The mushroom is rich in N-acetyl glucosamine, and other components (e.g. sodium, potassium, phosphorus, conjugated linoleic acid, traces of calcium and 143 amino acids) that make it congenial for bone regeneration [206]. Moreover, mushroom is used as anti-ageing agent (reducing fine line and pigmentation). As a result, it can be used directly in diets to promote human health. The chemical compositions and nutrition value of edible mushrooms define their medicinal value [207] and their activity against hyper-cholesterolemic disease, hypertension, infections, cancer and diabetes [208]. On the negative side, spores may cause respiratory diseases such as asthma due to the inhalation of mushroom spores [180].

### 5.1.1 Mushroom spores

The mushroom spores are the products of asexual reproduction in normal conditions. These save the genetic material of microbial life. Spores and pollens (pollen are carriers of the plant's genetic material needed for pollination) are on the market as natural remedies [209]. The chemical structure of spores contains tyrosine and glycoside [210], sulfonic acid and organosulfur compounds (R-sulfonyl hydroxide) [211]. The total fatty acid in spores can be defined as free acid and methyl ester and can be extracted using many techniques (e.g. GC-MS [212], HPLC, Raman spectroscopy [211] and microwave-assisted extraction) [213].

### 5.1.2 Comparison between spores, pollen and seeds

Both spores and pollen are reproductive products that are generally single cells. The fungi, algae and plants produce spores, but only seed-bearing plants produce pollen. Often microscopic in size, durable and easily transported, pollen and spores can be found in many different environments and have a long fossil record. However, because many different plants and fungi produce similar-looking spores or pollen, it is sometimes difficult to identify them in the fossil record [214]. The spore/pollen walls have multiple layers and components. Sporopollenin contain a polymer of carotenoid esters and polyhydroxylated unbranched aliphatic units with small quantities of oxygenated aromatic rings and phenylpropanoids. Sporopollenin is highly resistant to physical, chemical and biological degradation. All pollen are spores, but not all spores are pollen [215] (see Fig.5.1A). The spore (fungi) differs from seed (plant) in many ways: structures, sizes, and types (see Table 5.1 and Fig. 5.1) [216].

Table 5.1: The main differences between spores and seeds [216].

	Spores (fungi)	Seeds (plant)
Structure	Simple and unicellular (single cell)	Complex (advance) and multicellular
Size	Small size (around 5µm, needing an optical or electronic microscope to see it) and lighter	Bigger than spore (can be seen)
Type	Homo (uniform size) Hetero (small (male) and big (female))	Diploid (two paired) and haploid (one paired)
	Have very small stored food resources (air pocket)	Does not have

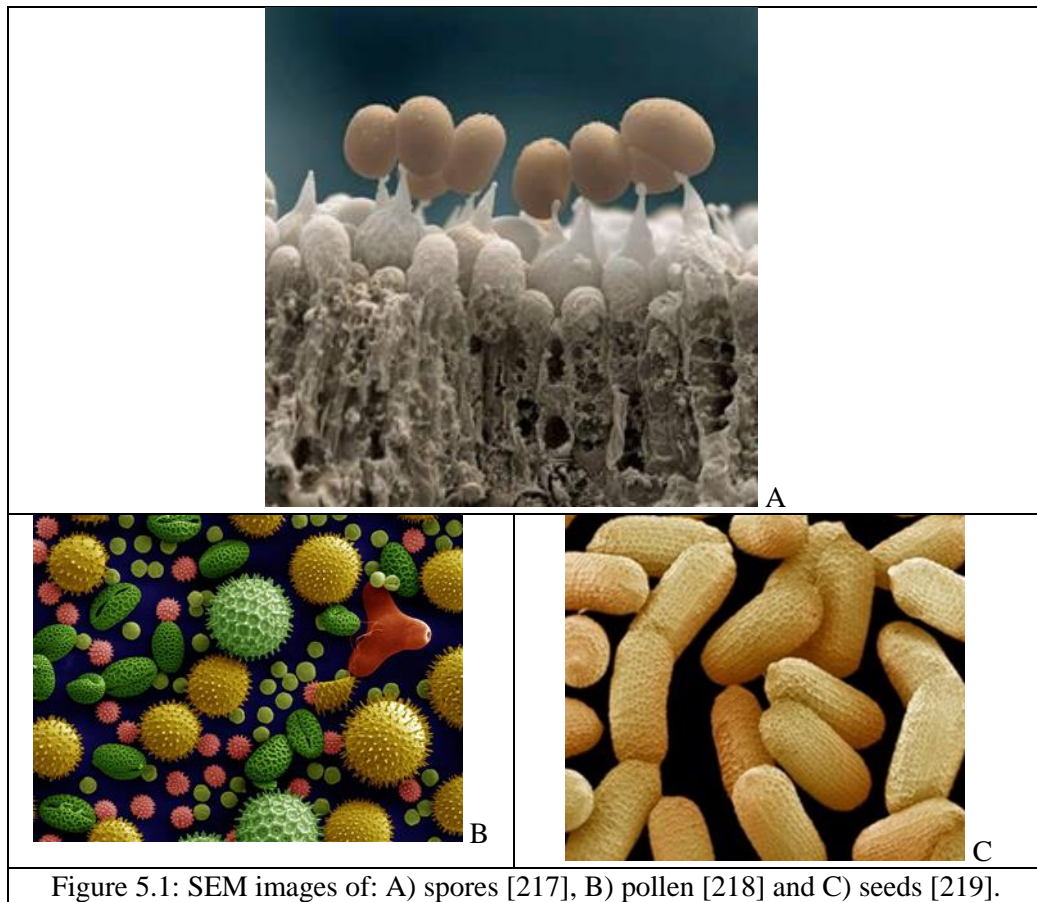


Figure 5.1: SEM images of: A) spores [217], B) pollen [218] and C) seeds [219].

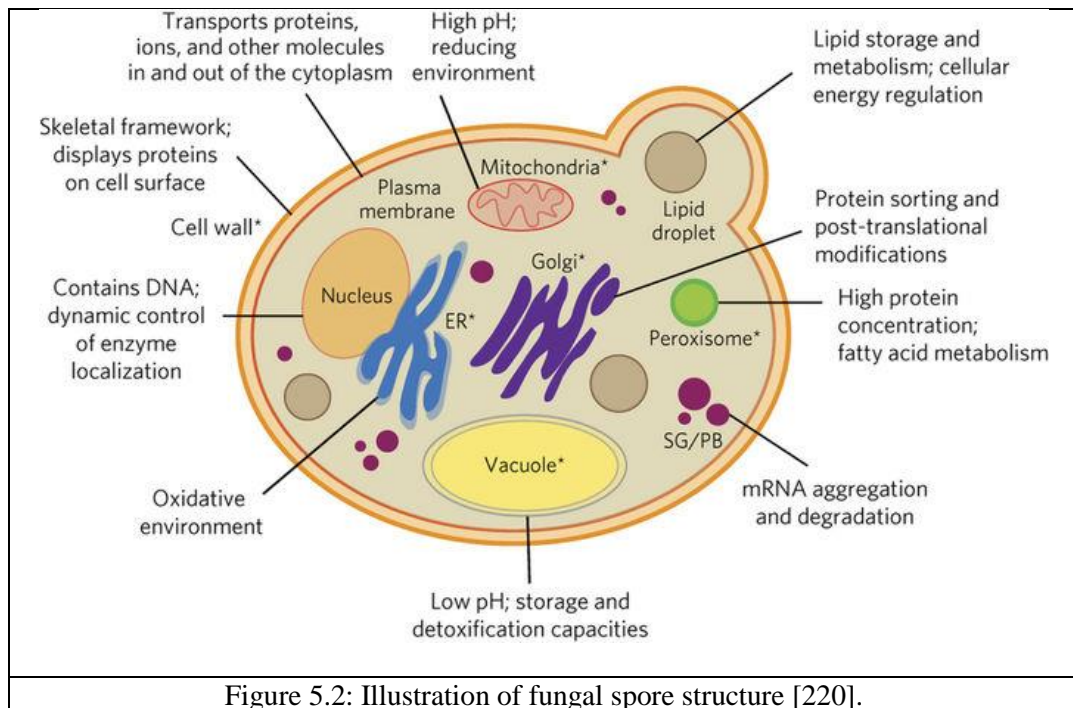


Figure 5.2: Illustration of fungal spore structure [220].

### 5.1.3 Sporopollenin

Sporopollenin is the outer shell and major component of exine (exine is the outer of the two major layers forming the walls) of spores and pollen. It is resistant to non-oxidative chemicals, enzymes and strong chemical reagents [210]. It was reported that sporopollenin has been reacted with ammonia using  $\text{LiAlH}_4$  as a catalyst to convert to a primary amine form. Notably, the carboxylic acid in the organic polymer (of the external shell) reacts to form amide groups leading to a new material with solid-phase applications [221].

### 5.1.4 Cell Walls Structure of Spores

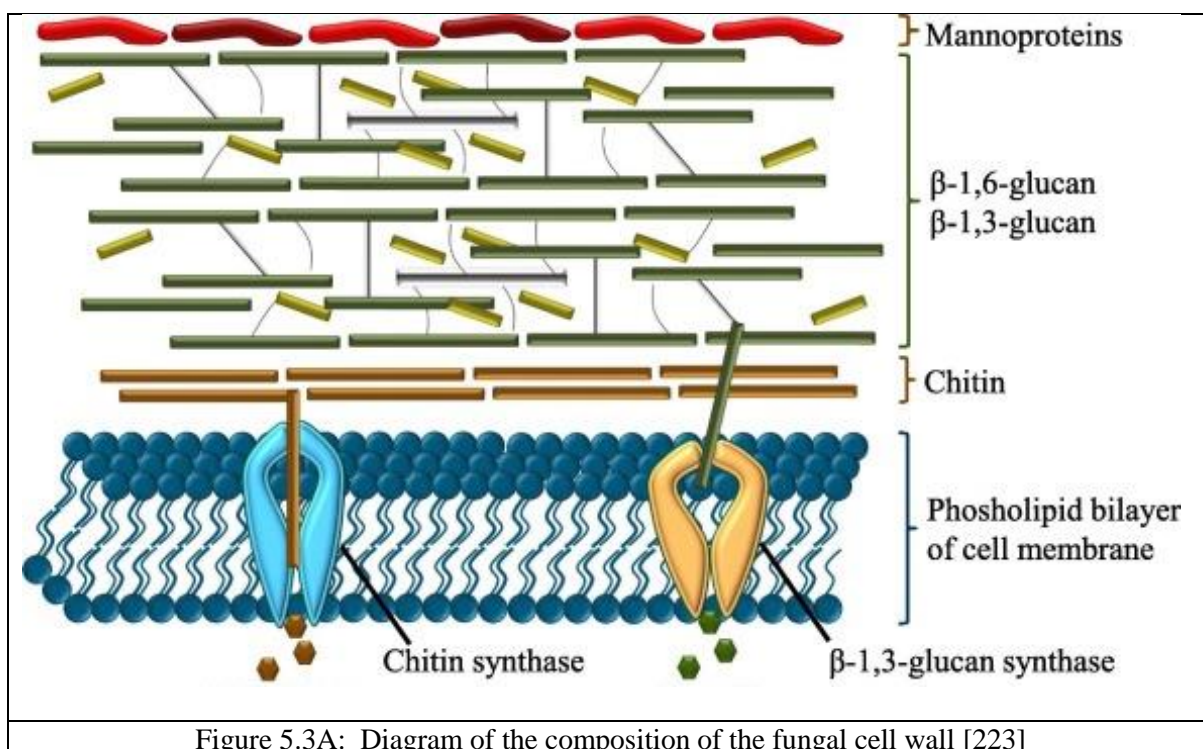
The cell walls of spores are normally made up of a three-dimensional complex network giving it resistance to environmental stress and mechanical strength. The components of fungi cell wall pathogens are not represented in plant and human cells. Therefore, the immune system of plants and humans have evolved to recognize the elements in cell wall of fungi [210]. There are many properties of a cell wall: UV protectant, elastic properties, antioxidant, chemical and physical resistance [209]. The chemical structure of a cell wall contains:

- (i) polysaccharide glucan (polymer of glucose which is mainly sugar, xylose and mannose),
- (ii) chitin complex (polymer of sugar) is found in the cell wall due to rigid layers and fillable fungal cell walls,
- (iii) melanin is a black pigment which helps to prevent UV damage and it acts to make the cell wall tougher, and
- (iv) proteins [222] and remodeling enzyme like chitinase and glucanase [210].

The cell wall has a high total concentration of solute due to the pressing of the cell membrane onto the wall and osmotic uptake of water. Like plant, the cell wall is detected by receptors in the cell. The core of the cell wall contains polysaccharide as  $\beta$ -(1-3) glucan with 4% inter-chain form hydrogen bond and chitin like scaffold around the cell.  $\beta$ -(1-3) glucan plays an important role in wall organization. Glucan and chitin (as polysaccharides) are synthesized in the plasma membrane by transmembrane enzymatic complexes [210]. Figure 5.3A shows that the outermost part of the cell wall consists of:

- (i) chitin which has different levels dependent on fungi [223] (brown line) located near to the cell membrane,
- (ii)  $\beta$ -1,3- and  $\beta$ -1,6-glucan (green line) close to the chitin fibres, and

- (iii) mannoproteins (red curve). The transferring N-acetylglucosamine residues are used to synthesize chitin from uridine diphosphate-N-acetylglucosamine (UDPGlcNAc which is brown hexagon) to a growing fibre that is shuttled through the cell membrane by the transmembrane chitin synthase (light blue). Further,  $\alpha$ ,  $\beta$ -1,3-glucan synthase (yellow) is used to synthesize  $\beta$ -1,3-glucan by the use of uridine diphosphate-N-glucose (UDPGlc which is a green hexagon) as a donor to transfer glucose to the extruded  $\beta$ -1,3-glucan fibre [223].



Furthermore, the physical properties indicate that the porosity (with pores around 200-300nm depending on type of spores) in the spore's shell helps to transfer the genetic content, water, and nutrients across the wall. These pores are nano-diameter channels in size. These nano channels (micro-rather-than-nano) can be used to (i) load a drug for delivery and (ii) to empty the shell using chemical or physical methods (see Fig. 5.3B) [209].

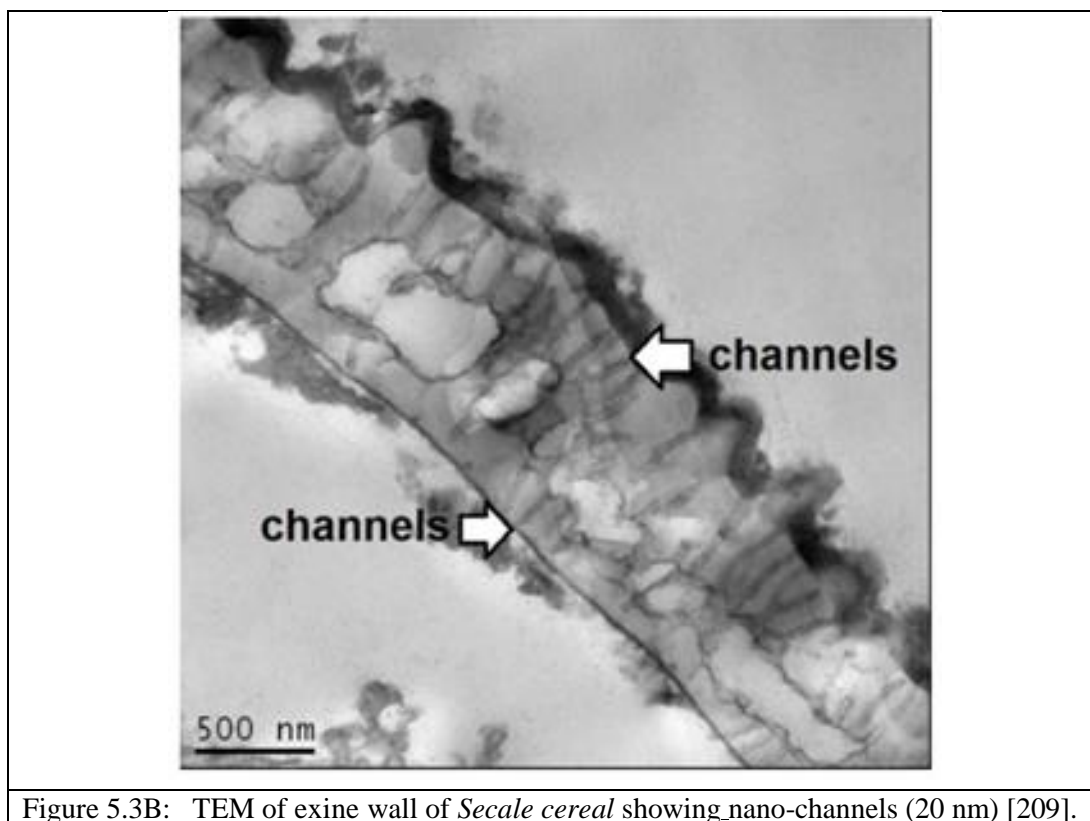


Figure 5.3B: TEM of exine wall of *Secale cereal* showing nano-channels (20 nm) [209].

Melanin (high RMM component of phenolic and indolic compounds) is a pigment that is a negatively charged hydrophobic. Some studies reported that the rigidity of the cell wall increases due to the melanin structure in human fungal pathogens [210].

### 5.1.5 Portobello Mushroom

Portobello mushroom (PM) (*Agaricus bisporus*, brown cap) is a type of fungi which is a eukaryote (chromosome in nucleus with a membrane) like a human cell, because a fungal cell contains a membrane-bound nucleus. Furthermore, PM (as fungal cell) has ribosomes, mitochondria, Golgi bodies and a cell membrane. This membrane is a lipid bilayer which allows phospholipid and ion molecules to move freely. Like animals, fungi use sources of carbon from complex organic compounds rather than fix CO<sub>2</sub> from air. Unlike plants, PM (fungi) do not have chloroplasts and they display colors from other cellular pigments from red, green to black [210]. It was reported that fungi are an important source of thermally-adapted hydrolytic enzymes. It is useful for industrial processes that are related to fungal biomass deconstruction. These organisms are receiving increasing interest because their enzymes enable saccharification at higher temperatures (assuming at a basic level that the



reaction rate approximately doubles for every 10°C rise in temperature) and avoids contamination [224]. Harvesting PMS was reported to be a simple methodology to collect spores involving funnel trapping [225]. There is a relationship between spore abundance, gravity and humidity using plastic lids of petri-dishes. When the cap of a mushroom is at the top the spores can be removed by the gravity and electrostatic forces out of the mushroom and deposited on a filter paper [226].

The recent trend in tissue engineering research is based on seeding cells into porous biodegradable polymer matrices. The ideal biomaterial should be biodegradable, non-toxic and porous aiding the migration of host cells into the matrix permitting growth into complete tissue analogs *in vivo* [112]. Mushroom and derivatives were used in antitumor, anti-diabetic, wound healing, antibacterial, anti-parasitic, antiviral, preventing dental plaque, immunomodulatory, cardiovascular [114] drug delivery system, and as a biomaterial for tissue engineering [111].

Here, PMS was characterized using many techniques that are described in chapter 3. The harvesting method was described in section 4.2.1.

## 5.2. Results and discussion

Mushroom spore was previously characterized in many studies [227]. The average weight of the PMS used in this study was calculated. PMS was characterized using many techniques. The spores were collected on two separate occasions when they fell out of mushroom caps due to gravity after 2 days and 2 weeks. Already the spores, have charge and they are attracted and attached to a petri-dish. Further, the mushroom humidity helped PMS discharge at short times; the spore transfer of spores depended on an active spores discharge mechanism [226]. Spores were released from the gills (located under the cup of mushroom). The results show that the PM has water content around 73% (see Table 5.2). After two days 103.933mg of Portobello mushroom were harvested to get 12mg of spores. Table 5.3 shows that the averages of 84.6mg of Portobello mushroom (PM) over two weeks produced 8.6mg of harvested Portobello mushroom spores (PMS). PM appeared to have water content around 67%.

Table 5.2: Portobello mushroom spores (PMS) harvested in two days.

No.	W <sub>1</sub> of PM sample (mg)	W <sub>2</sub> of PM sample (mg) after 2 days	W <sub>3</sub> of harvested spores (mg)
1	109.620	66.016	16
2	130.230	78.840	12
3	109.540	64.193	8
4	74.225	38.325	15
5	96.052	51.897	9
Average	103.933	59.854	12

Table 5.3: Portobello mushroom spores (PMS) harvested in two weeks.

	W <sub>1</sub> of PM sample (mg)	W <sub>2</sub> of PM sample (mg) after 2 weeks	W <sub>3</sub> of harvested spores (mg)
1	93.270	63.26	6
2	90.432	57.89	4
3	90.156	66.59	16
4	75.140	50.46	12
5	74.105	45.90	5
Average	84.620	56.82	8.6

### 5.2.1 SEM and TEM analysis

The size, the shape and the surface morphology of PMS could be measured by both SEM and TEM. The micrographs of PMS (dried on an aluminium stub) were analyzed to determine the variation in/on PMS morphology and shape at different temperatures (RT and 500°C) using SEM. Figure 5.4A shows the SEM images of PMS at RT. This revealed smooth, brown and oval shapes with average length around 5µm, looking like a red blood cell [203]. The PMS appeared aggregated and hollow (presumably it collapses partially due to the SEM vacuum); some can be seen as swollen and dented or concave. The surface view on one side is thick and on others is thin. Moreover, the PMS shape is not changed by heating at 100°C apart from some change in concave/convex shape on fluid loss, because spores have rigid cell walls due to their containing chitin (complex polysaccharide which is an essential structural component and provides rigidity to the fungal cell wall to resist chemical and physical challenges) [223]. It can be noticed that some damage to the cell wall is present (thickness is around 252nm).

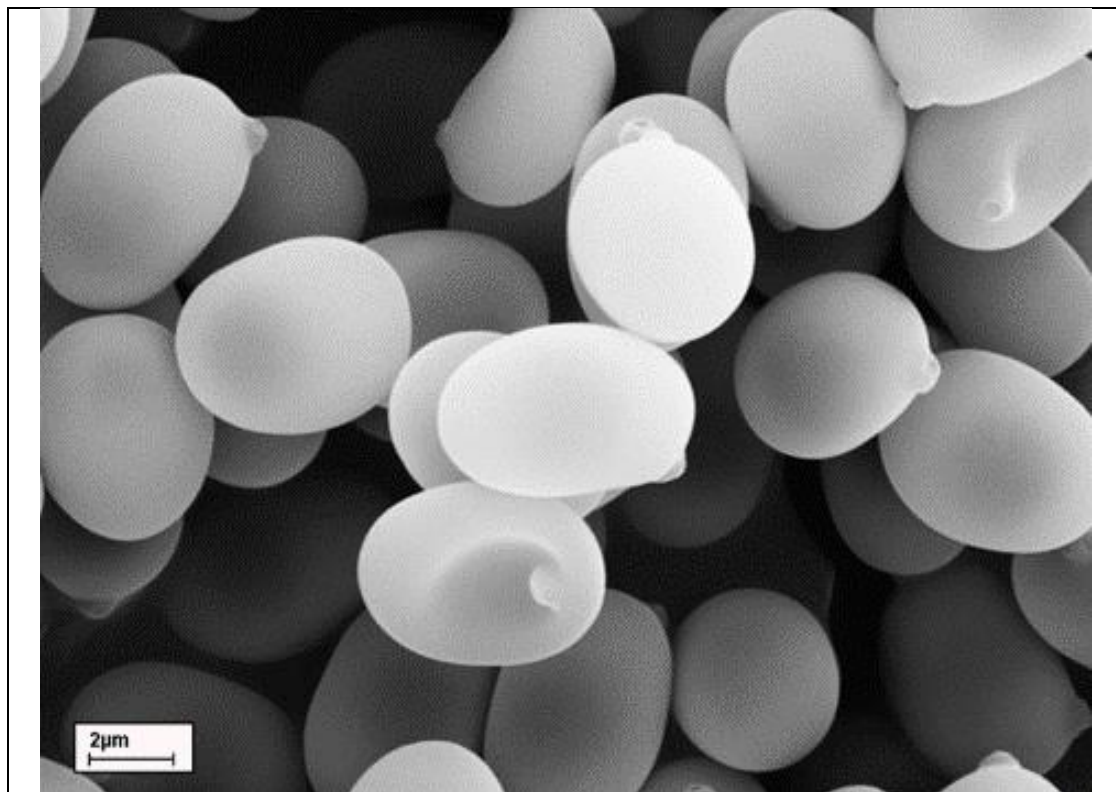
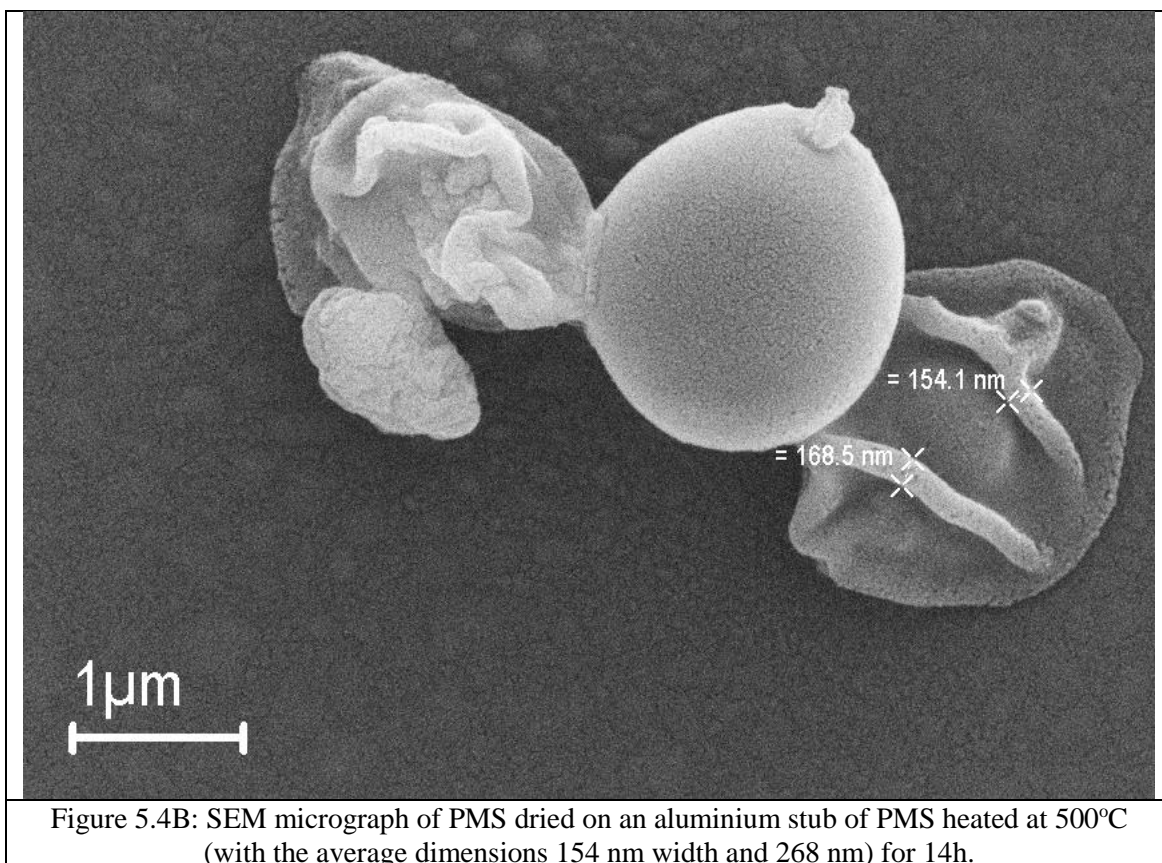


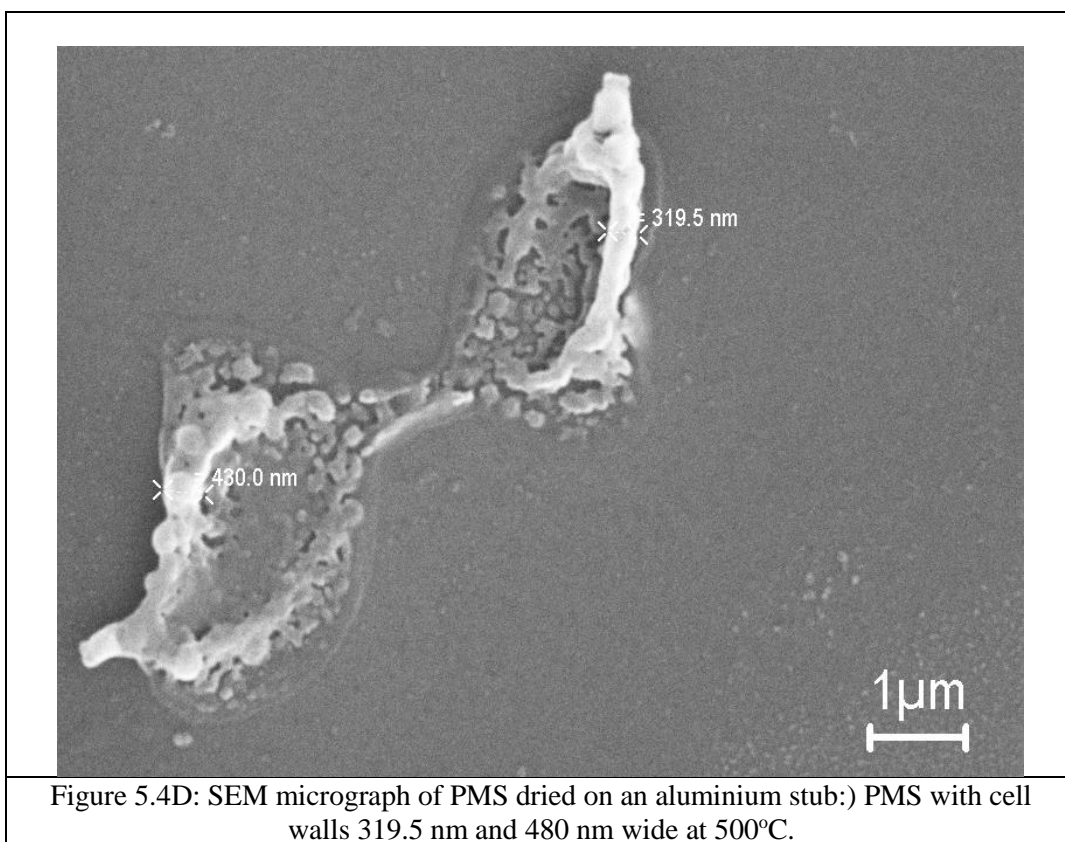
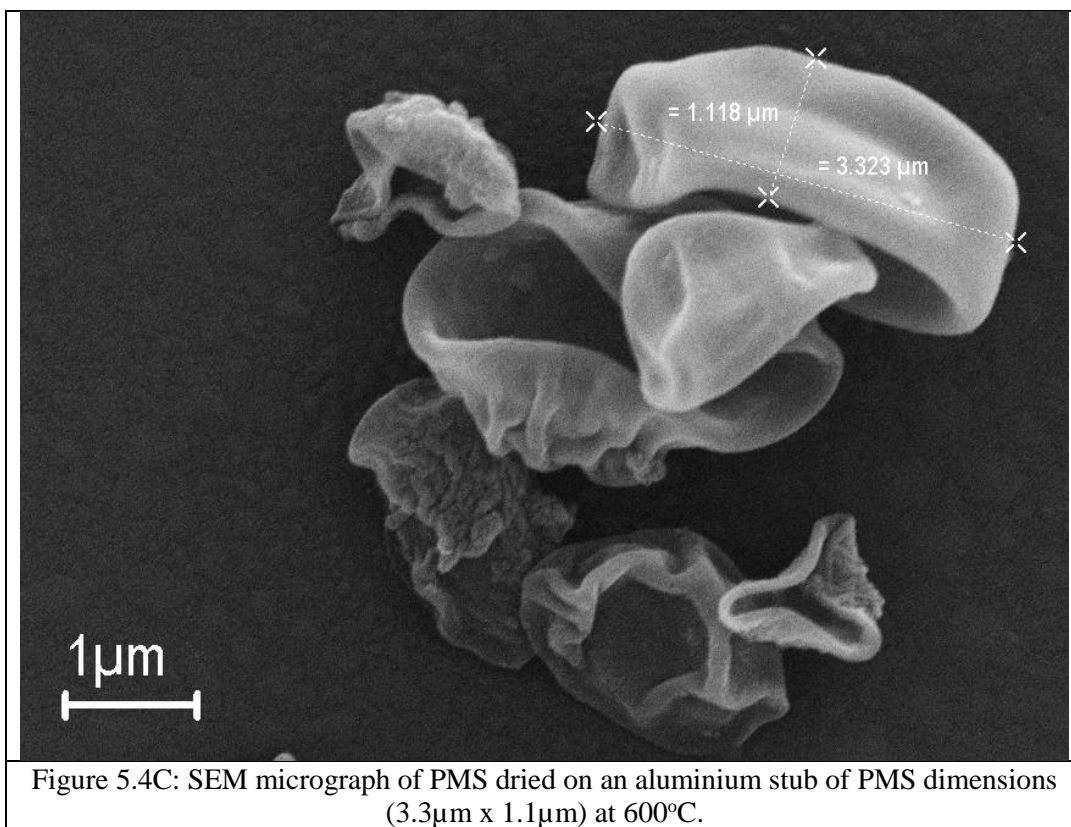
Figure 5.4A: SEM micrograph of PMS dried on an aluminium stub at RT (scale bar = 2 $\mu$ m).

PMS was heated to 500°C for 14h under air in normal atmosphere (see Fig. 5.4B, C and D) on a cover glass (containing SiO<sub>2</sub> (80%), B<sub>2</sub>O<sub>3</sub> (12%), Na<sub>2</sub>O (4.2%), Al<sub>2</sub>O<sub>3</sub> (2.2%), PbO and MgO). Figure 5.4D shows that the PMS shrank in size from around 5 $\mu$ m to significantly smaller sizes with collapsed morphologies due to the decomposition of the PMS organic matrix in terms of degradation of hydrocarbons. The cell wall is 319.5nm and 480nm wide. Approximately, PMS wall is around 500nm and PMS length is around 6  $\mu$ m (optical microscope results). That means, the PMS wall is 18-20% of spores. Moreover, the residue of chitin is one of the most insoluble compounds in nature [223]. Clearly, the average of dimensions of PMS are 3.3 $\mu$ m x 1.2 $\mu$ m in vacuum conditions.



The cell contains a chitin-binding motif to protect the fungal cell wall against hydrolysis during condition changes [223]. Therefore, only the structure residue can be seen even after heating at 500°C.

EDX-SEM analysis for PMS samples that were heated to 500°C in air was characterized by point analysis for 4 locations for many different spores. This analysis reveals that PMS residues have different elemental compositions. Table 5.4 shows that PMS have a highest percentage 58% for oxygen. Markedly, only 0.01% N is seen from amino acid residue because it has evaporated. The retia of elements is represented in short chain, chitin oligomers (as a signal molecule leading to nuclear  $\text{Ca}^{2+}$  spiking and activation), glucan and proteins in the fungal cell wall [223]. Here, some of different elements' percentage increases after heating and the higher detection levels of the cell wall is Na 5.8% and K 3.4%. Also, when cells were heated a significant increase in Ca 0.17% levels was obtained (see Table 5.4).



A TEM micrograph of PMS (a thin slice of resin/PMS on carbon copper grid) at RT was analysed to determine the surface morphology and dimensions of the cell wall in PMS. Figure 5.5 gives TEM evidence of the smooth spore's oval shapes. Figures 5.6 and 7 show that the average dimensions of spores are 253nm width of cell wall of PMS and 5.017  $\mu\text{m}$  length. These results were confirmed by SEM and optical microscopy. EDX analysis using TEM for PMS samples at RT was characterized by point analysis for 7 locations for many different spores. This analysis reveals that PMS residues have carbon and oxygen elemental compositions only. Figure 5.8 shows that PMS have a highest percentage: 74% for carbon than oxygen 31%. Remarkably, no N or other elements are seen here due to its weak emission. Generally, the TEM results are in agreement with the SEM observations.

Table 5.4: EDX of elemental analysis of PMS for RT and after heating to 500°C in air.

Elements	O	Na	K	C	P	Ca	N
At. % at RT	14.3	0	0.2	74.17	0.2	0.05	10.25
At. % at 773K	58.11	5.84	3.45	6.85	1.48	0.17	0.01

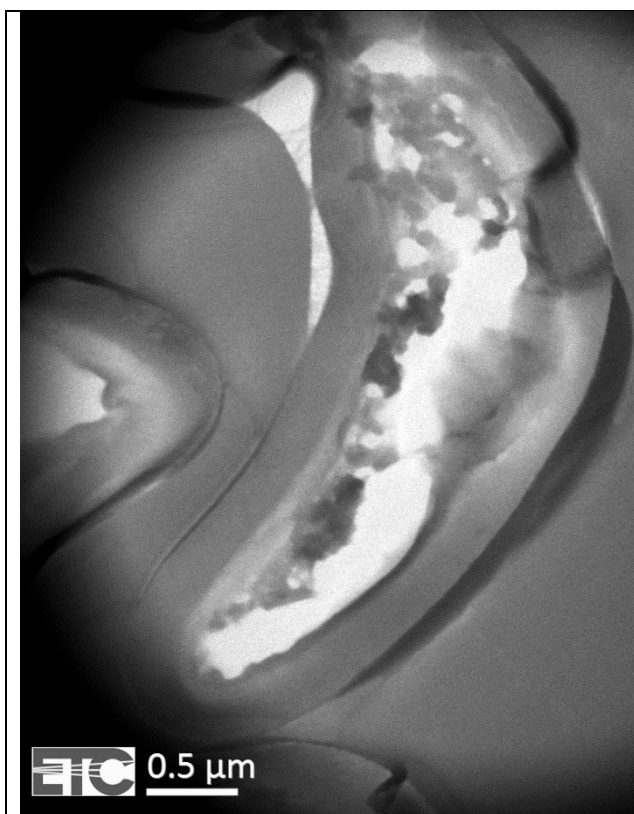
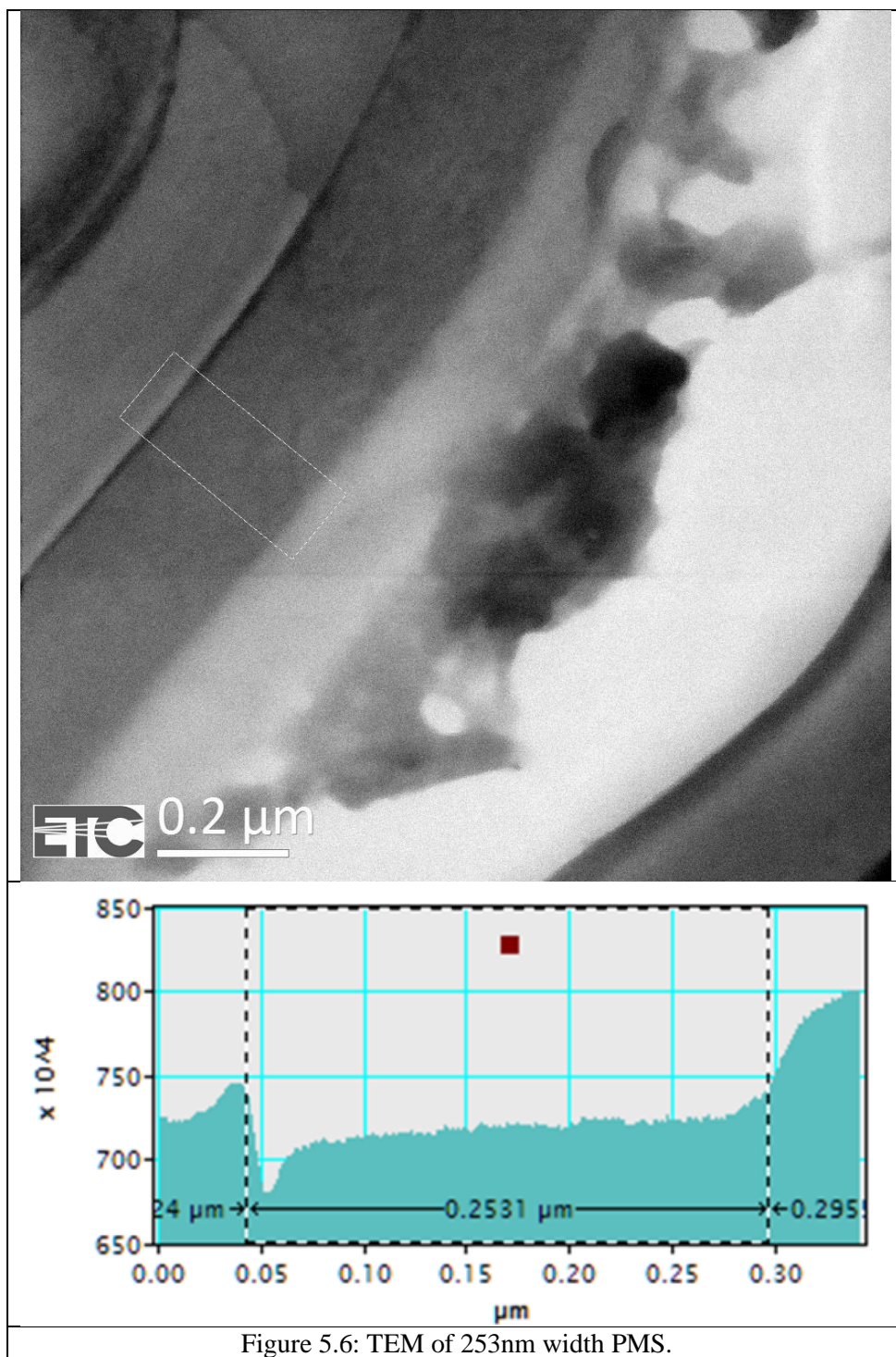


Figure 5.5: TEM micrograph of fresh PMS (a thin slice of resin/PMS on carbon copper grid at RT (the scale bar 0.5  $\mu\text{m}$ ).



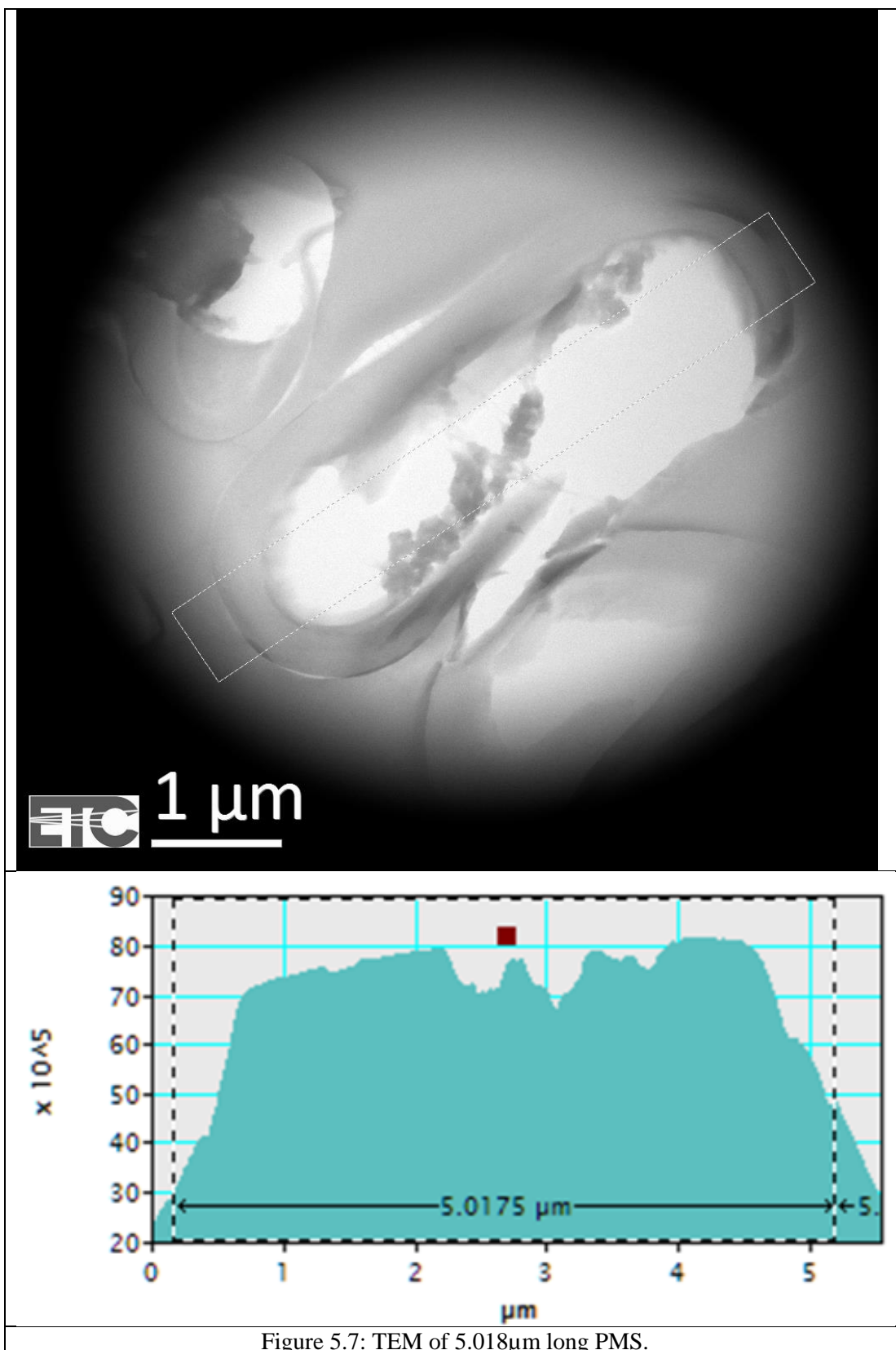
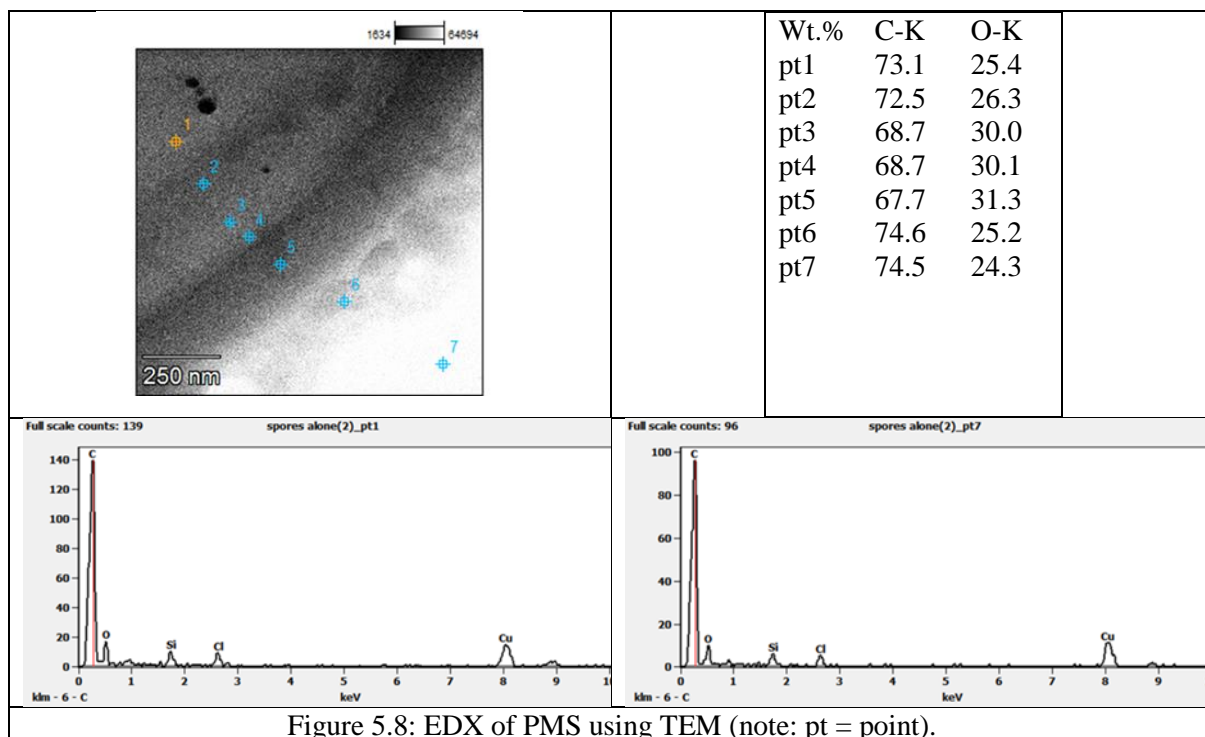


Figure 5.7: TEM of 5.018μm long PMS.



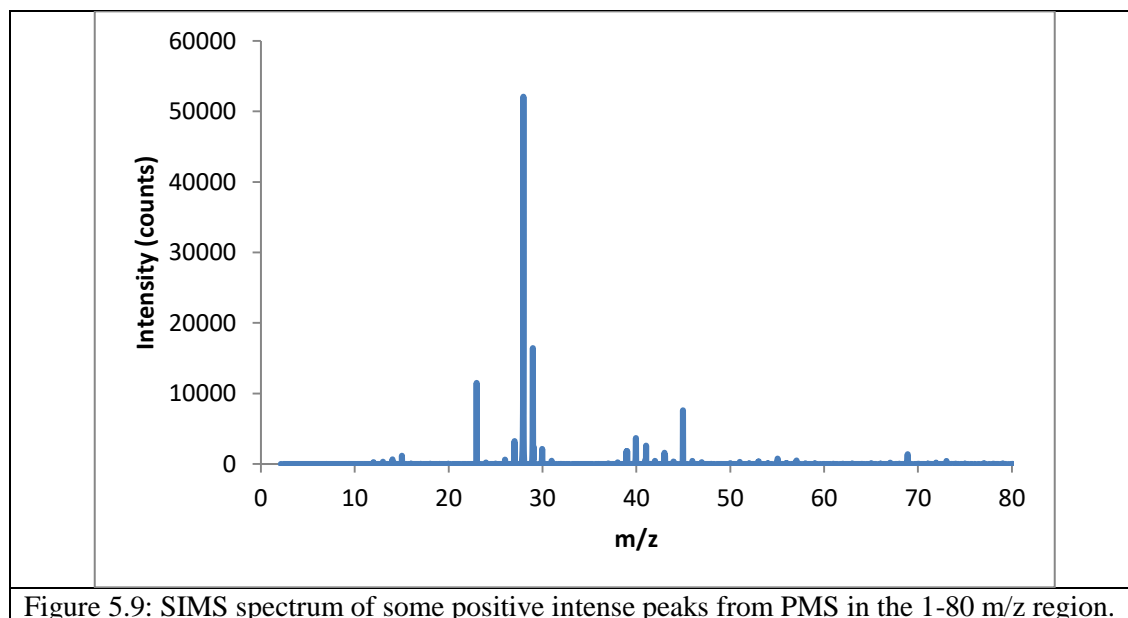


### 5.2.2 SIMS

SIMS was used to investigate surface composition of PMS. Identification of the molecular peak within the sample spectrum was done in order to determine the surface composition. The molecular peak for the positive spectrum was shown in Table 5.5 and Figure 5.9 and 10. The positive SIMS for PMS produced some intense peaks. The proteins and amino acid [228] peaks from  $m/z$  15–68 with raw intensities above 50000 counts were shown, including peaks from the mica substrate. PMS peaks at 28 $m/z$  have a high intensity compared with peaks at 45 and 68 $m/z$  related to carbonyl compound respectively.

Table 5.5: Comparison of the intensities of some positive SIMS peaks for PMS.

$m/z$ peak	SIMS intensity for PMS	Chemical assignment	$m/z$ peak	SIMS intensity for PMS	Chemical assignment
15	1200	$C-H_3^+$	40	4000	$Ca^{2+}$
23	10000	$Na^+$	45	7500	$C_2 H_5 O^+$
28	50000	$C_2-H_x^+$	68	1400	$C_x H_y O^+$
29	15000	$K^+$	-	-	-



### 5.2.3 FTIR and $\mu$ -FTIR

FTIR can provide chemical characterization via identifiable spectral features. Here, vibrational spectra of spores can be used for simple and rapid identification through straightforward correlation between spectra and biochemical composition [180]. It cannot be used with Raman spectroscopy for dark-coloured spores due to the strong fluorescence background and laser-induced degradation. Therefore, evidently FTIR has more potential for general studies of such bioparticles; biochemical analysis of fungal spores by FTIR could provide economical, reliable, simple and timely information [180]. Study of the bands in the FTIR of PMS (see Fig. 5.10) confirmed that proteins, amino acids, polysaccharides and phosphates were present.

Important FTIR regions for spores:

- 1- Broad peak at  $3270\text{ cm}^{-1}$  relates to O-H and N-H stretching (attributed to amino acids).
- 2- Two peaks at  $2924\text{-}2850\text{ cm}^{-1}$  refer to C-H stretching (related to carbohydrates).
- 3- Absorption at  $1700\text{-}1500\text{ cm}^{-1}$  related to chitin and proteins compound in the cell wall; the two peaks at  $1741$  and  $1369\text{ cm}^{-1}$  can be attributed to free fatty acids (C=O stretch in carboxylic acids and C–O–H bending, respectively); in addition, it has

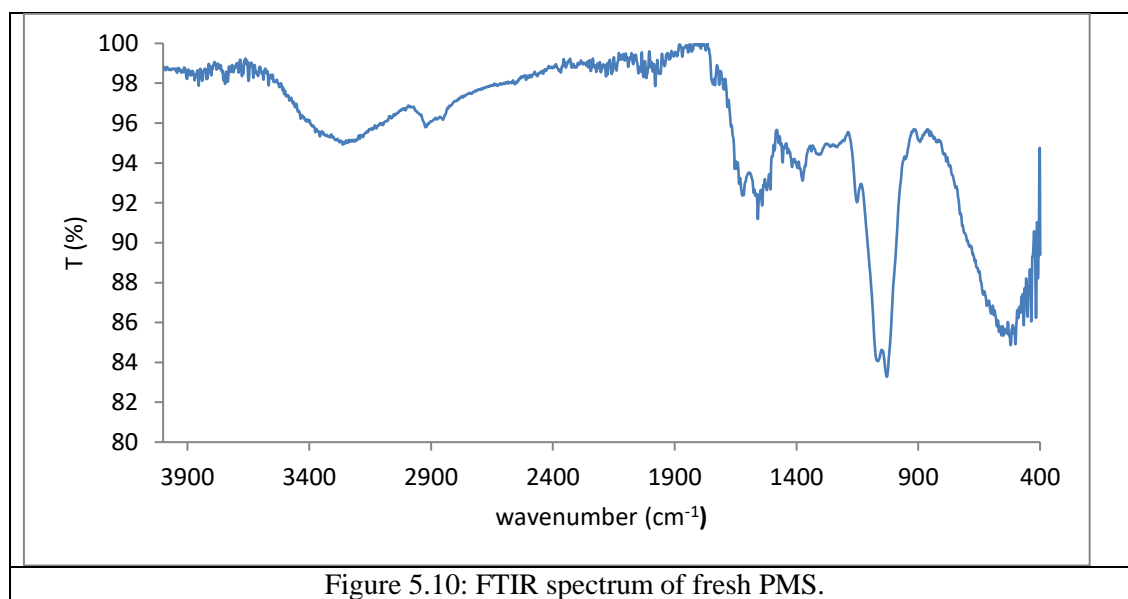
strong peaks at 1622 and 1024  $\text{cm}^{-1}$  that can be attributed to phospholipids (C=O stretch in esters and P–O– stretch, respectively).

- 4- Absorption at 1200-900  $\text{cm}^{-1}$  may refer to carbohydrate bands C-O-C [180].
- 5- 1064  $\text{cm}^{-1}$  band may be C-N in PMS (see Table 5.6).

Table 5.6: Important functional groups seen in FTIR of PMS.

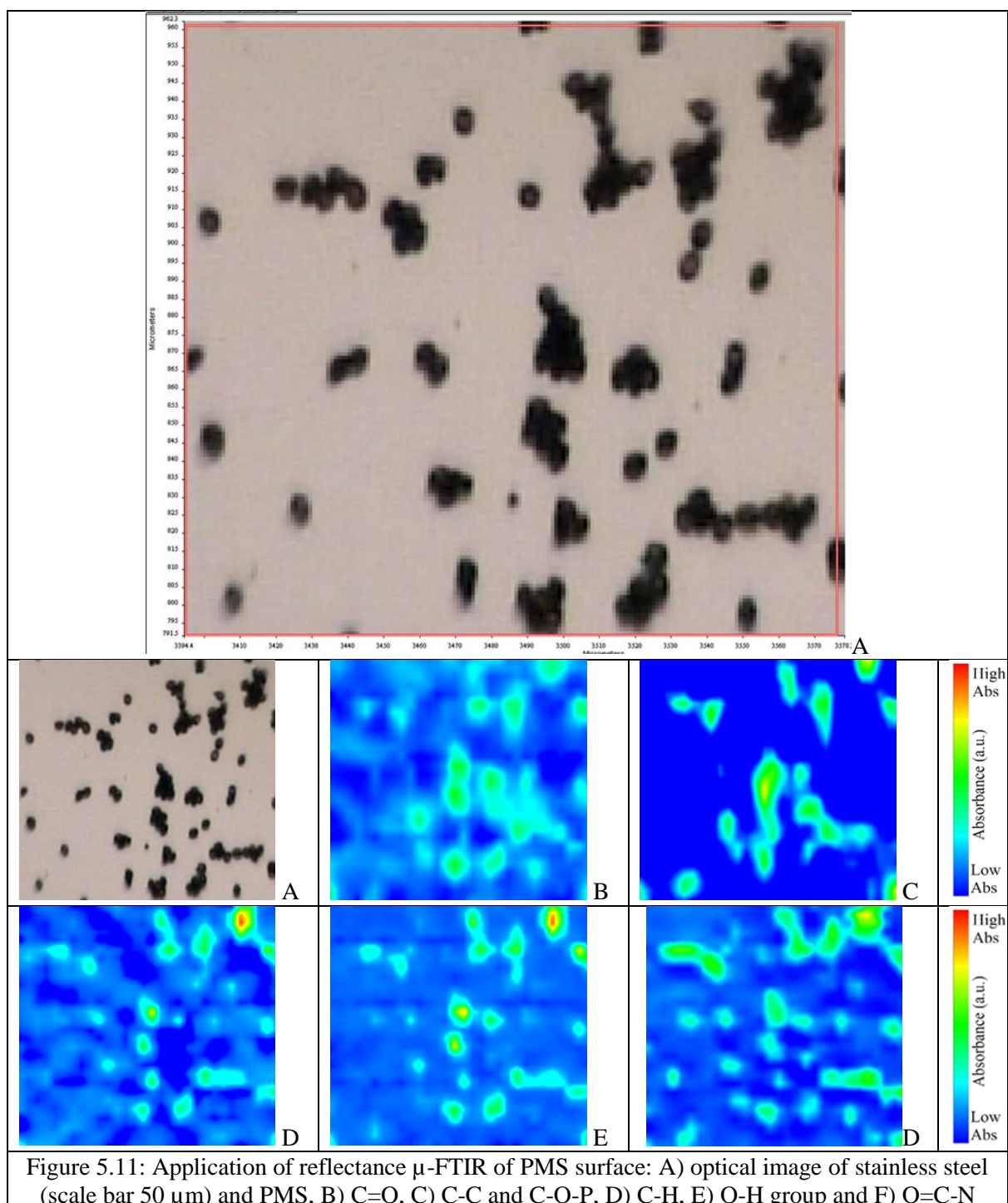
Functional group	O-H	N-H	C-H	C=O	C-O	C-N	P-O
Wave number ( $\text{cm}^{-1}$ )	3270	3270	2924 -2850	1741, 1622	1369	1064	1024

An infrared spectrum of a bioparticle can be divided into specific regions containing signatures of lipids, proteins, carbohydrates, and grain wall biopolymers such as chitin. The corresponding spectral signals of these chemicals are highly specific, and thus FTIR spectroscopy is an excellent tool for biochemical analysis of fungi spores.



Like FTIR,  $\mu$ -FTIR is a powerful analytical tool that gives a spectrum of infrared energy absorbed by the samples. The full range is 4000 to 750  $\text{cm}^{-1}$  and false-colour image of the samples (0 to 0.725 absorbance) scanned using  $\mu$ -FTIR. An aperture size of 6.25  $\mu\text{m}$  x 6.25  $\mu\text{m}$  was used, meaning that each pixel of image was a 6.25  $\mu\text{m}$  x 6.25  $\mu\text{m}$  area on the sample plane, with 32 co-added scans per pixel. The spectral resolution was of 16  $\text{cm}^{-1}$ .

Figure 5.11 shows different infrared absorbing organic molecules in PMS. The red areas show absorbance of infrared of carbonyl and hydroxyl groups which are associated with proteins and polysaccharides. Further, the presence of phosphorylated group as phospholipid associated with nucleic acid.



### 5.2.4 Optical Microscopy

For accurate measurement PMS diameters without vacuum-induced distortion optical microscopy was undertaken. Measurements were taken with an appropriate objective for the size of the material being investigated to ensure accurate and reliable measurements PMS diameters. Optical microscopy, being non-vacuum and without electron beam charging gives accurate images allowing ready measurement of PMS diameters. Figure 5.12 shows that PMS have a similar oval shape and dimension in H<sub>2</sub>O and pH 4, 7 and 10. The dimensions of PMS are around 7.14 x 4.76µm in all solutions. Hence, the pH value does not affect the PMS morphology, but it affects the PMS surface.

PMS self-assembles in pH 10 solution and might do so even more effectively at interfaces. It can be seen that there is some PMS aggregation, meaning that OH<sup>-</sup> ions cause PMS attraction. On the other hand, untreated PMS had an air pocket within it that could be filled in the production of materials. For example, metal cations could be inserted into spores or it could be used as a drug delivery system. It might also allow heating of PMS without spore rupture. Figure 5.13 and 14 show that the highest percentage of 30 PMS diameters 83% is around 7 µm in solution pH 10. This is slightly longer than the average PMS diameters seen in SEM around 6µm suggesting vacuum treatment causes 63% reduction in PMS size. Such SEM effects on biological samples are sometimes seen.

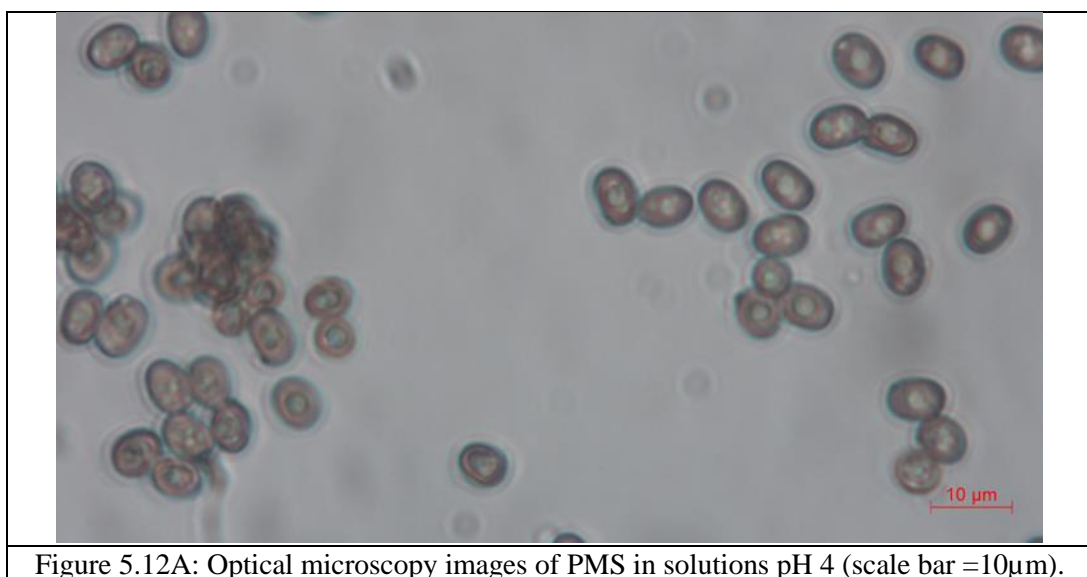


Figure 5.12A: Optical microscopy images of PMS in solutions pH 4 (scale bar =10µm).

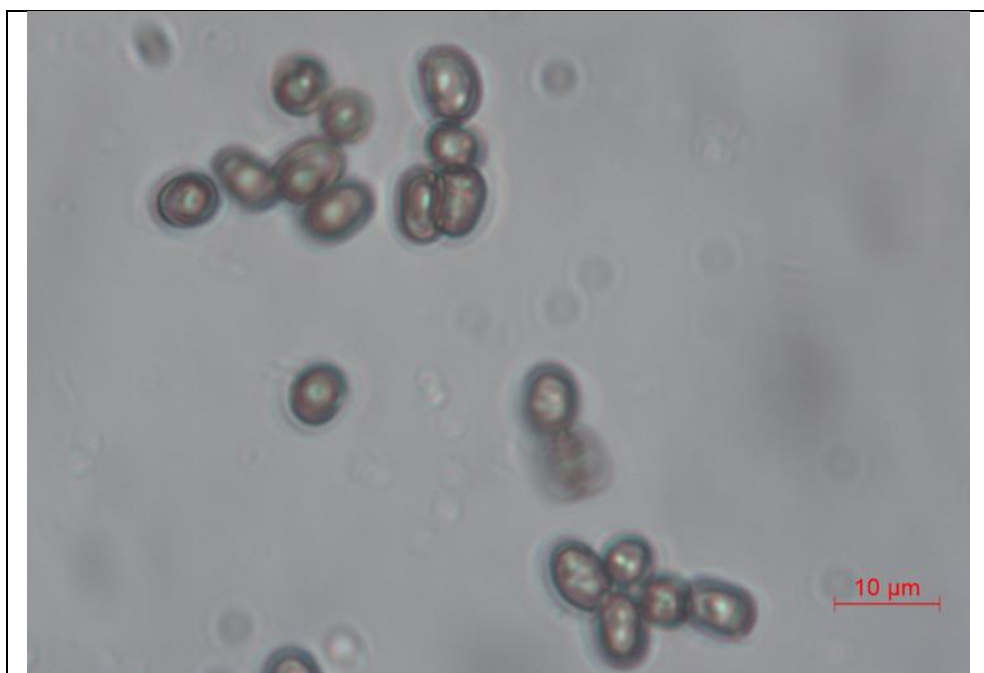


Figure 5.12B: Optical microscopy images of PMS in solutions in pH 7 (scale bars in red 10 $\mu$ m).

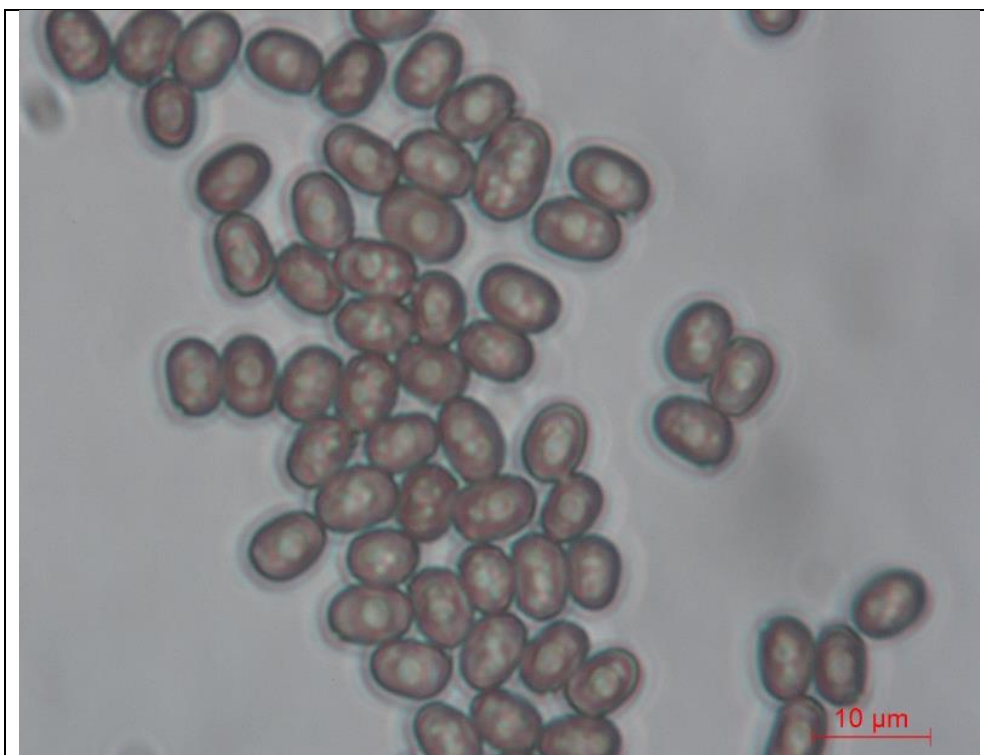
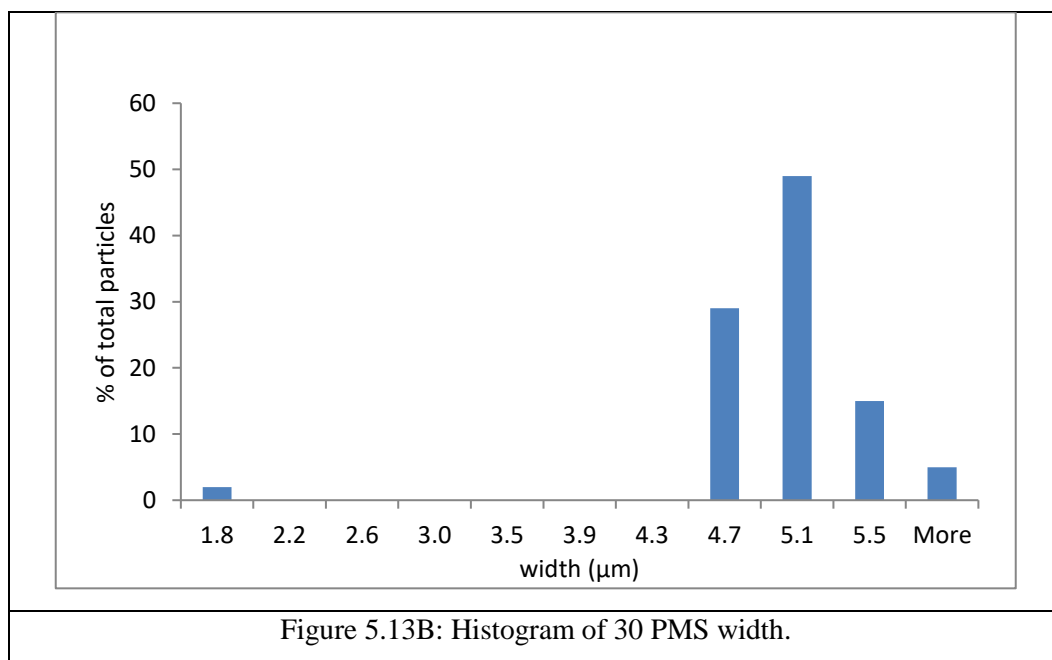
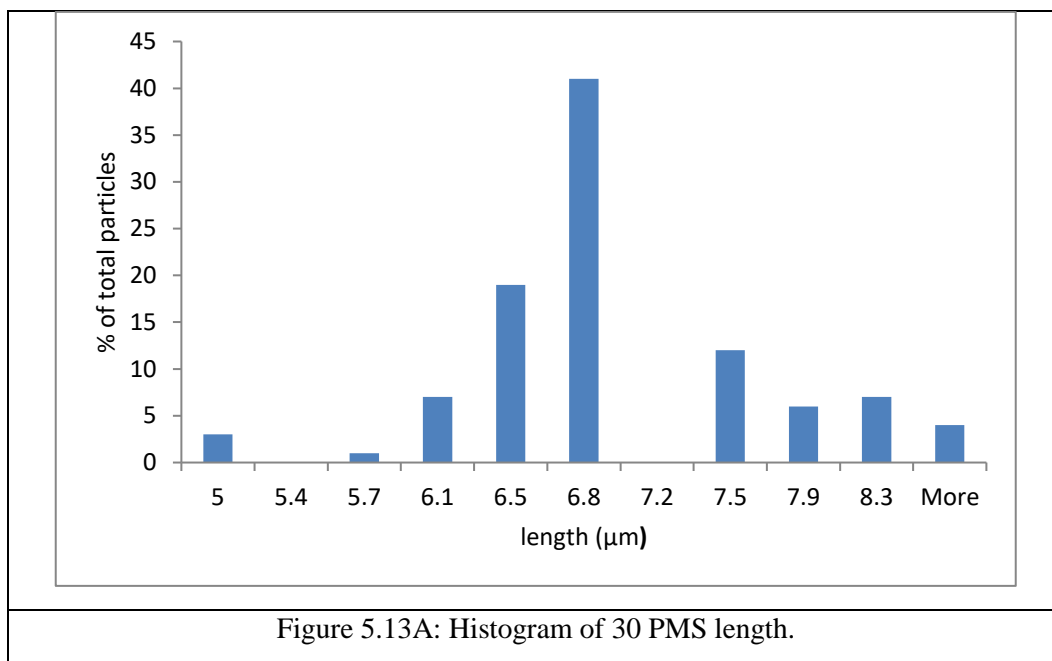
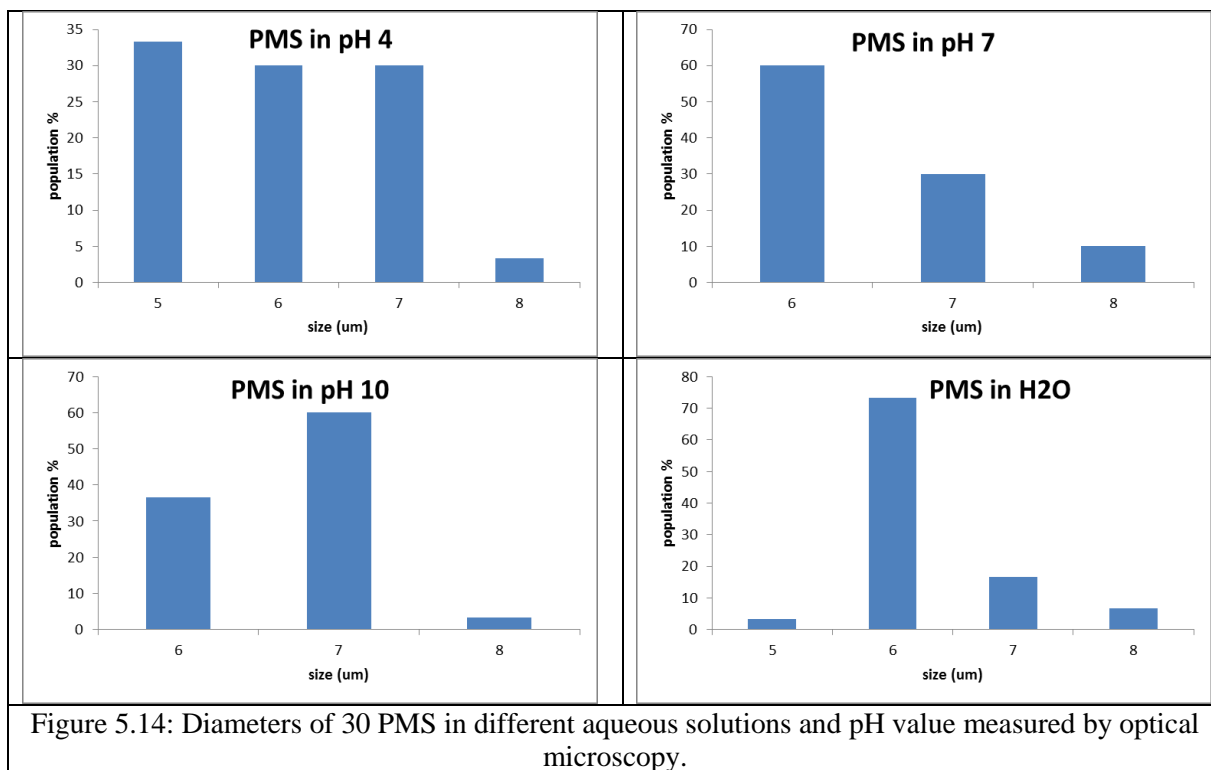


Figure 5.12C: Optical microscopy images of PMS in solutions pH 10 solution (scale bars in red 10 $\mu$ m).



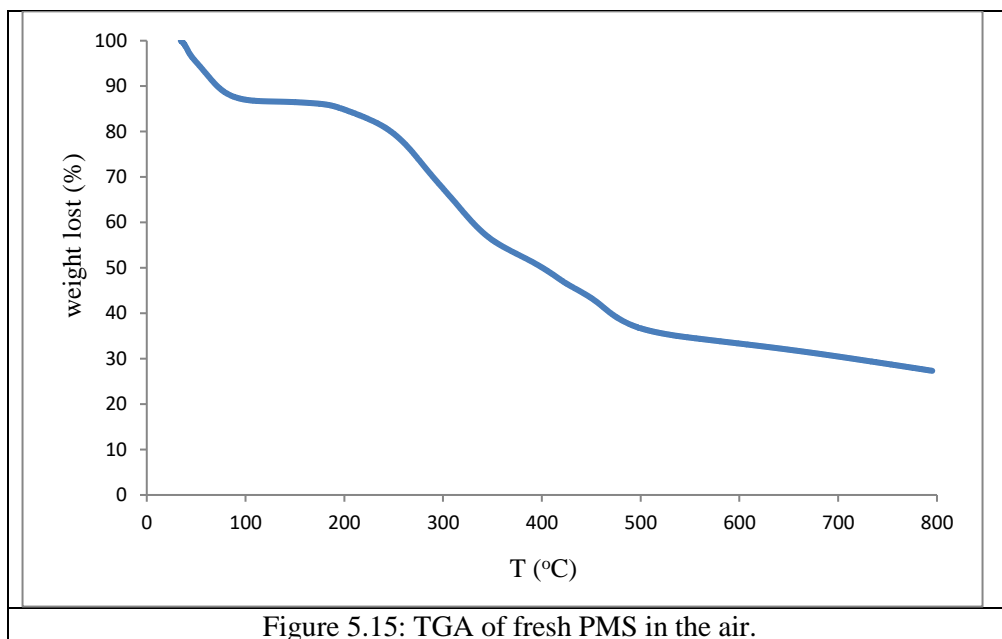


### 5.2.5 Thermal gravity analysis (TGA)

Using TGA, the thermal stability of PMS was assessed. The thermal stability of fresh PMS was studied with normal heating rate performed between 20°C and a maximum of 950°C at rate of 10°C min<sup>-1</sup> in air. Figure 5.15 shows TGA evidence that the PMS exhibited a loss of water around 13% when held at 104°C that was associated with physically-bound water because PM has a large amount of water. The weight loss, 32% at 361°C is due to the decomposition of the PMS organic matrix in terms of degradation of hydrocarbons and loss of hydroxyl groups. At 794°C the weight loss was 73% and the residue was 27% (2.5mg, down from 9.2mg).

Overall TEM-SEM indicated spores' homogeneity in shape (oval), size (6 mm), resilience in both acid and base (pH 6.8) using optical microscopy and thermal stability up to 200°C which is confirmed by TGA.





### 5.3 Conclusions

In this study, the PMS was characterized by SEM, EDX, TEM, TGA, FTIR, UV-Vis and SIMS. It is apparent that PMS has advantages of homogeneity of shape (oval), size (6  $\mu\text{m}$ ), resilience in both acid and base (pH 6.8) and stability up to 200°C. Here, it is suggested that PMS may be loaded with a therapeutic drug. Moreover, it has many surface functional groups that help PMS use as a template and reducing agents for preparation of NPs. The adsorption and uptake of some biomolecules and ions (e.g. ascorbic acid to protect skin, insulin for drug delivery for diabetes and HAp for bone replacement) will in later chapters be explored. It is hoped that PMS can be coated NPs to help with new nanomedical applications.

## **Chapter 6: Green biosynthesis of TiO<sub>2</sub>, Ag, Au NPs and nanohybrids using the spores of edible Portobello mushroom as biotemplates**

---

This chapter describes a green chemical approach to the synthesis of TiO<sub>2</sub>, Ag and Au NPs using PMS as a template and reducing agents and then nanohybrids. In this chapter, the PMS reducing agent is compared with chemical reagents (NaBH<sub>4</sub> and citrate). The factors affecting nanohybrid formation with PMS that were investigated included: solvent (H<sub>2</sub>O and IPA), pH and temperature described in section 4.2.1-4.2.4). The product samples were characterized by SEM, TEM, EDX, TGA, FTIR, UV-Vis, DLS and SIMS (that are described in section 3.1-4).

The aim of this chapter is to demonstrate that PMS might be a novel, useful and reductive bio-template, allowing the advantageous generation of NPs in devices with medicine/surgery to treat disease and enhance human life. It was thought that PMS could be used to prepare to use surface-held NPs (e.g. Ag and Au) that could be used as nanomedicine with enhanced antimicrobial properties.

### **6.1 Introduction**

#### **6.1.1 Metal nanoparticles**

The past decade has seen the rapid development of nanotechnology within biomedical and engineering disciplines, but one needs to be sure of their biocompatibility, safety, speed and cost effectiveness. At present, nanotechnology has paved the way for some therapies [229], catalytic, bio-sensing, nano-drug delivery, microelectronic [227] and air water purification applications. Metal nanoparticles (NPs) have unique properties, making them distinct from the equivalent bulk material of the same composition because of their high surface area and volume ratio [230]. Metal nanoparticles can be produced on a nanoscale using several different methods: including chemical vapor deposition (CVD), irradiation and chemical reduction of metal salts, but most of these processes give rise to harmful by-products [231]. Currently researchers are interested in developing methods of nanomaterials synthesis that are more environmentally-friendly; the focus for this is now shifted from physical and chemical processes towards greener chemistry and biosynthesis [232] using PMS.

### 6.1.2 Nanohybrids

This term describes two or more components of nano-dimensions that combine into a novel hybrid structure of nm dimensions (see Fig.6.1) creating new properties, which differ from conventional components. Furthermore, the hybrid nanostructure can induce synergies as a result of intimate biotemplate/particle interactions [233]. There are two possible processes by which nanohybrids can nucleate and grow: (i) heterogeneous and (ii) homogeneous. The former must be achieved while the latter should be avoided [233].

The relevant lattice parameters (the physical dimensions of the unit cells in a crystal lattice) and relative ease of electron transfer are important factors in forming a dumb-bell shape intermediate (when the components have a similar lattice parameter and crystal structure) and a core@shell shape (when there is a large lattice incompatibility) composite [233]. A significant approach currently is to produce non-homogenous core-shell nanohybrids, where the core and surface are different. For example, shell Au or Ag NPs combined with TiO<sub>2</sub> core (or vice versa) act as an electron trap promoting interfacial charge transfer processes [57]. Nanohybrids have been produced with an Ag or Au NP core surrounded by a TiO<sub>2</sub> shell thereby forming a core@shell [232] e.g. Ag@TiO<sub>2</sub>. This approach has numerous advantages, including:

- (i) enhanced core stability because of the encapsulation inside the TiO<sub>2</sub> shell, and
- (ii) changed surface plasmon resonance (SPR) [234] (the resonant oscillation of conduction electrons at the interface between a negative and positive permittivity material stimulated by incident light peaks) [235].

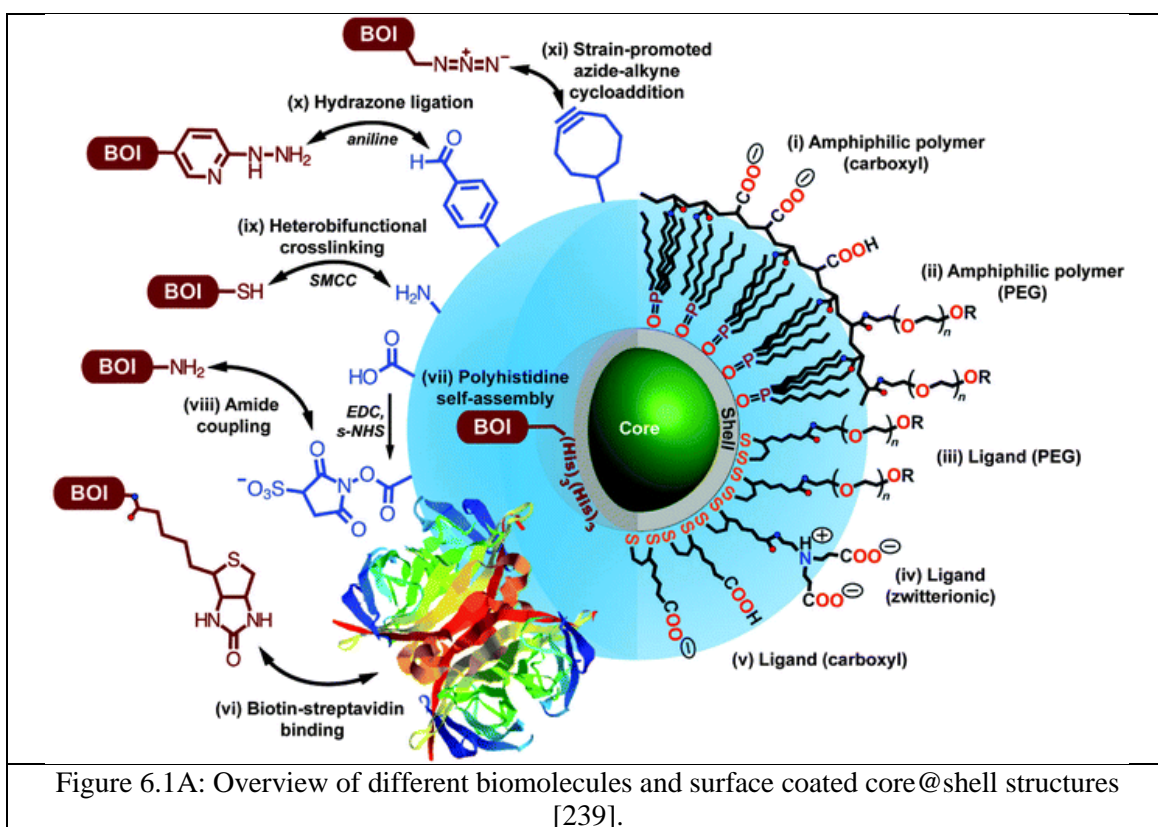
Applications for nanohybrids include bioimaging, solar energy conversion, cancer, catalysis and drug delivery [233]. Novel physicochemical properties can be produced through change in the interaction (i.e. the surface structure, chemical composition and size [236]). Such properties are important for applications such as wound healing. Hence, materials as TiO<sub>2</sub>-Au NPs and Ag@TiO<sub>2</sub> NPs could be produced with improved bonding between an implant and existing bone as a scaffold [237]. Core@shell Au@Ag has advantages including:

- (i) a unique interaction in which electrons are readily transferred from the NP layer to the core internal NPs layer [238], which can be manipulated to

create NP probes (that are highly active and more stable against oxidation) for sensing and diagnostics, and

- (ii) Au and Ag NP enhanced optical/electronic properties, where Au NPs possess a very high resistance to oxidation and have a high molar extinction coefficient ( $\epsilon$ ) (i.e. a measurement of how strongly a chemical species attenuates light at a given wavelength), while, Ag NPs possess the highest molar extinction coefficient of any metal [238].

Of course, biomolecules can conjugate onto the hybrid particles (e.g. the large molecules of DNA, enzymes, hormones, and carbohydrates, and the smaller molecules of sugar, vitamins, lipids and peptide); both large and small molecules have strong bioactivity at the supramolecular level. These properties could be used in smart drug delivery applications [233].



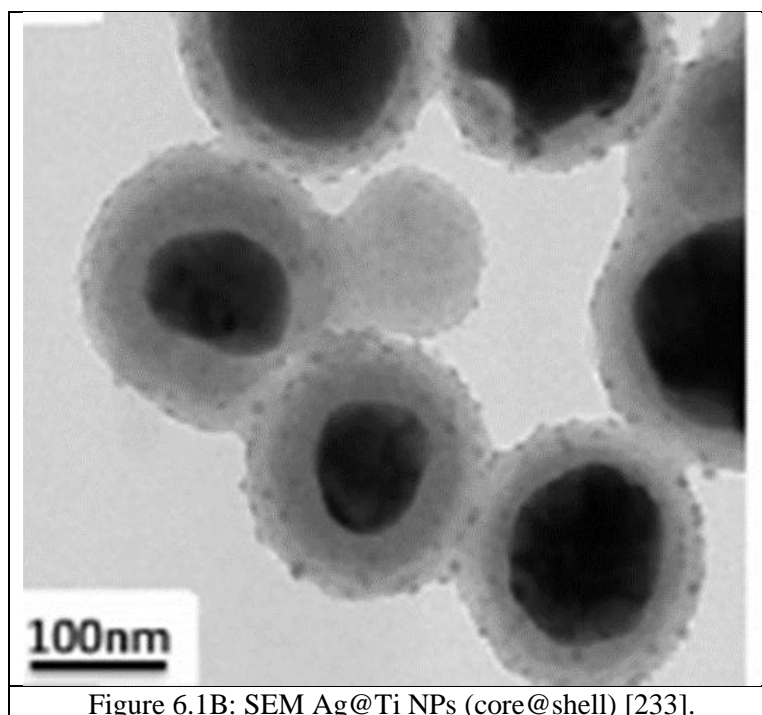


Figure 6.1B: SEM Ag@Ti NPs (core@shell) [233].

## 6.2 NPs and biological properties

### 6.2.1 TiO<sub>2</sub> NPs

Semiconductor TiO<sub>2</sub> has emerged in recent years as a contender material in biomedical, photocatalytic, biofuel cell, sensor, electronic [240] and also pigmentary applications [241]. TiO<sub>2</sub> NPs have different properties compared to larger TiO<sub>2</sub> particles, due to their strongly oxidizing properties (e.g. complete oxidation of organic substrates to CO<sub>2</sub>).

Furthermore, TiO<sub>2</sub> NPs possess strong catalytic properties: they can absorb UV radiation effectively, due to their small size and large surface area per unit mass. Therefore, TiO<sub>2</sub> has novel bioactivity properties and can play a role in meeting challenges in energy conversion and human health with TiO<sub>2</sub>. Photocatalysis can be activated only under UV irradiation: e.g. for  $\lambda < 380$  nm, which comprises only 5% of sunlight) generating reactive oxygen species (ROS) from oxygen molecules which produced by-products during the mitochondrial electron transfer; it can kill bacterial and fungal cells in water [54]. On the other hand, TiO<sub>2</sub> NP can represent a hazard to human health, because their large surface area creating enhanced reactivity with other molecules [242]. In addition, this high surface area leads to production of even more toxic ROS. Also, depending on their size [243], these NPs can pass through the membrane of a living cell and damage the biological system exacerbating the toxicity or allowing greater penetration and mobility through the human body [242].

### 6.2.2 Ag NPs

The biosynthesis of silver NPs has attracted attention because they have eco-friendly and compatibility benefits [244]. The strong toxicity of silver towards a vast range of microorganisms is well known (possibly as a result of Ag NPs binding to proteins or lipo-poly-saccharides in the cell membrane leading to collapse). Therefore, Ag NPs have been used as anti-microbials and anti-fungal in clothes, electronics, pharmaceuticals and food containers [245]. Ag NPs exhibit unique properties (high surface area and volume ratio) which differ from their bulk equivalents, due to their small size and the in high surface/volume ratio [246] (the ratio of surface/ volume on Ag NPs increases [247] exponentially with a decreasing particle size [248]). For example, small particles with a large metallic surface are favoured biocidal [249]. There are two methods for the preparation of nano-silver. Firstly, the “top-down” approach, (whereby bulk silver metal is reduced down to the nano form low cost and with no solvents present) and secondly, the “bottom-up” approach (whereby nano-Ag forms or self-assembly as from dissolved silver salts in a given solvent, reducing to  $\text{Ag}^0$  and then forming the Ag NPs by nucleation/growth [250]).

### 6.2.3 Au NPs

Gold NPs also exhibit unusual properties, leading to their application in biotechnology, catalysis, electronics and optics [251]. Again the properties and applications of Au NPs depend on their size and shape [252]. In general, Au NPs provide a non-toxic route to gene delivery systems and medicines because they are bio-compatible. So, Au NPs are able to deliver large biomolecules (nucleic acid (DNA and RNA), peptides and proteins)) and can be used to increase the biorecognition of anticancer drugs, which can easily assemble on the AuNPs surface [251].

Numerous studies have investigated Au NPs with a partial positive charge (stabilized by back donation with a carbonyl group and the formation of  $\pi$ -back donation between d orbital of  $\text{Au}^0$  (filled and high electronic density) with antibonding orbital ( $\pi^*$  empty) of the carbonyl group [106]).

Most of the methods for the synthesis of Au NPs utilize chemical agents/reductants. For example, tri-sodium citrate, N-N dimethyl formamide and sodium borohydride ( $\text{NaBH}_4$ ) [24]. These chemicals have potential environmental risks. More recently, green chemistry syntheses have been used with bio-organisms and biomolecules to

produce nanoparticles because the reductants are renewable/non-toxic environmentally benign [24]. Au NPs and Ag NPs have many benefits in biomedical applications owing to their unique properties: chemical stability, magnetic, nonlinear optical behavior, catalytic activity, high electrical/thermal conductivity and localized surface plasmon resonance (LSPR) [36]. PMS and PMS-derived NPs were described in chapter 4; methods used in assessment of PMS-derived materials were described in section 4.2.2.

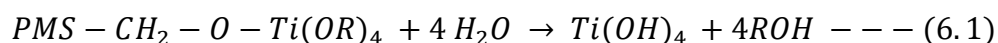
### 6.3 Characterization Results

TiO<sub>2</sub> NPs/PMS and nanohybrids using PMS as templates and reducing agents were characterized by SIMS, FTIR and residual gas analysis (RGA). Firstly, many attempts (from 10mg to 2mg) were made to characterise of PMS in the 4-5mg amount available before drying and after reaction with metal salts producing NPs. Samples (4-5)mg has many sites to interact with metals to produce NPs. 3-0.03mM in IPA solution of Ti isopropoxide produced TiO<sub>2</sub> over layers on PMS surface. These characterisation results are now described.

#### 6.3.1 NPs/PMS

##### 1- TiO<sub>x</sub>/PMS

TiO<sub>x</sub> NPs/PNS were prepared using a simple sol-gel method. Titanium (iv) isopropoxide in IPA was added dropwise to PMS suspension in water with the stirring. The preparation of TiO<sub>x</sub> NPs includes two steps: hydrolysis and condensation reactions to form Ti hydroxide as shown in Eq. 6.1 and 2 [253]:

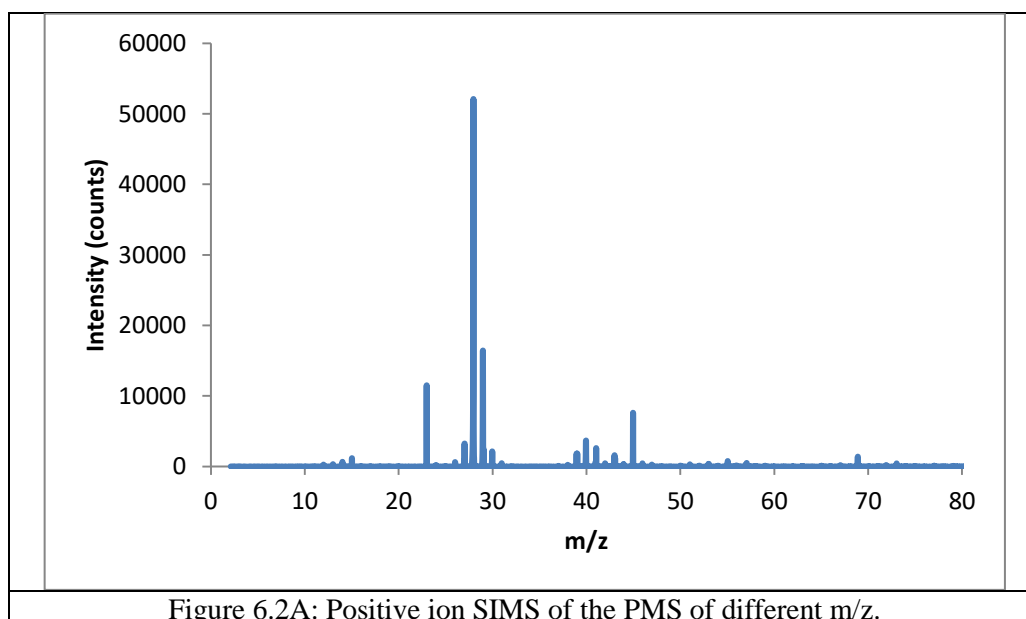


Secondary ion mass spectrometry (SIMS) was used to investigate the surface composition for PMS and TiO<sub>x</sub> NPs/PMS. The positive SIMS for PMS and TiO<sub>x</sub>/PMS showed some intense peaks [254]. Table 6.1 and Fig. 6.2 illustrates that PMS peaks at

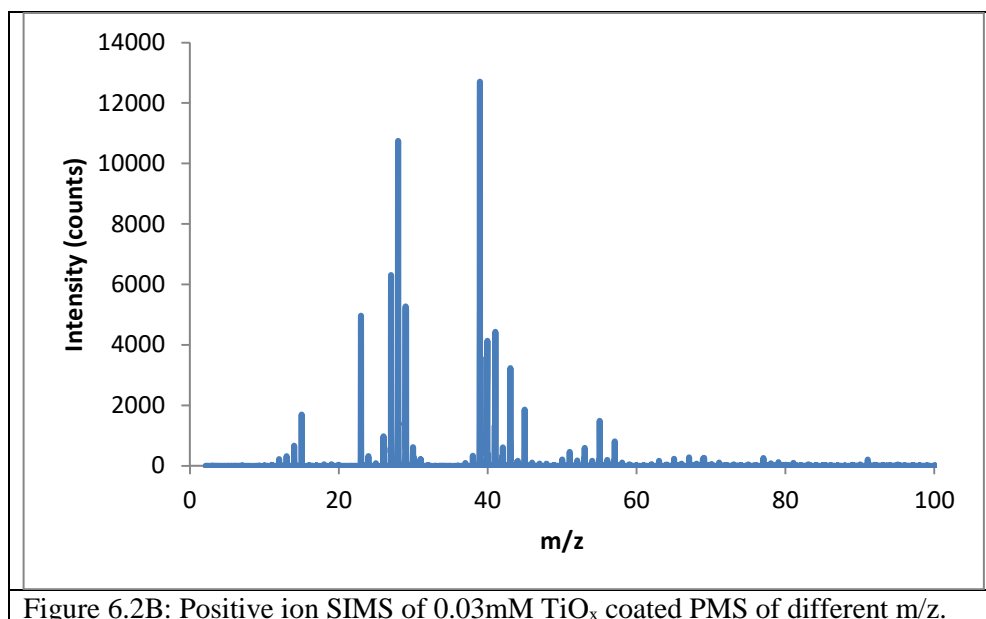
28, 45 and 68m/z are decreased in intensity as a result of  $\text{TiO}_x$  coating, while peaks at 63 and 64 m/z related to  $\text{TiO}^+$  and  $\text{TiOH}^+$  respectively appeared [255]. That means  $\text{TiO}_2$  reacts with functional groups on the PMS surface as  $\text{OH}^-$  and  $\text{COO}^-$  leading to the disappearance of some PMS peaks and new peaks of  $\text{TiO}_x$  appeared. The PMS ion fragments need to be related to surface functional groups seen in FTIR. Figure 6.3 shows FTIR spectra of  $\text{TiO}_x$ -coated PMS in different concentrations (0.03, 0.3 and 3mM) from IPA solution and then dried in air at RT. Proteins and polysaccharides play an important role in any reaction with metal ions, because of the  $\text{COO}^-$  and O-H groups which have a strong ability to chelate/react with Ti ions [256].

Table 6. 1: Comparison of the intensities of some positive SIMS peaks for the PMS and  $\text{TiO}_x/\text{PMS}$ .

m/z peak	SIMS intensity for PMS	SIMS intensity $\text{TiO}_x/\text{PMS}$ produced from 0.03mM alkoxide solution	Chemical assignment
15	1200	---	$\text{C-H}_3^+$
23	10000	---	$\text{Na}^+$
28	50000	14000	$\text{C}_2\text{-H}_x^+$
29	15000	---	$\text{K}^+$
40	4000	---	$\text{Ca}^{+2}$
45	7500	2000	$\text{C}_2\text{H}_5\text{O}^+$
63	---	175	$\text{TiO}^+$
65	---	240	$\text{TiOH}$
68	1400	75	$\text{C}_x\text{H}_y\text{O}^+$







The important FTIR absorption bands seen are those at  $1056\text{ cm}^{-1}$  recognized as C-O-Ti. Another peak at  $408\text{ cm}^{-1}$  refers to Ti-O-Ti bonds. There is a shift and an intensity decrease of bands that are obtained when  $\text{TiO}_x$  reacts with PMS. The two bands at  $1618\text{ cm}^{-1}$  and  $1554\text{ cm}^{-1}$  are observed and refer to primary and secondary amides that arise due to carbonyl stretch and -N-H stretch vibrations in the amide linkages of the protein. So, the carbonyl group of peptides of proteins and amino acid has a strong ability to bind Ti ion [256].

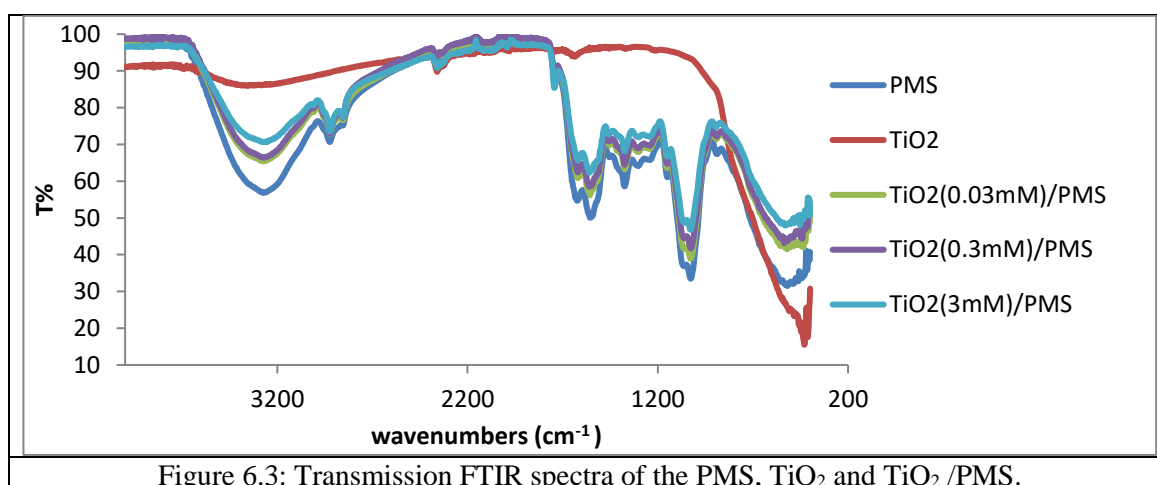
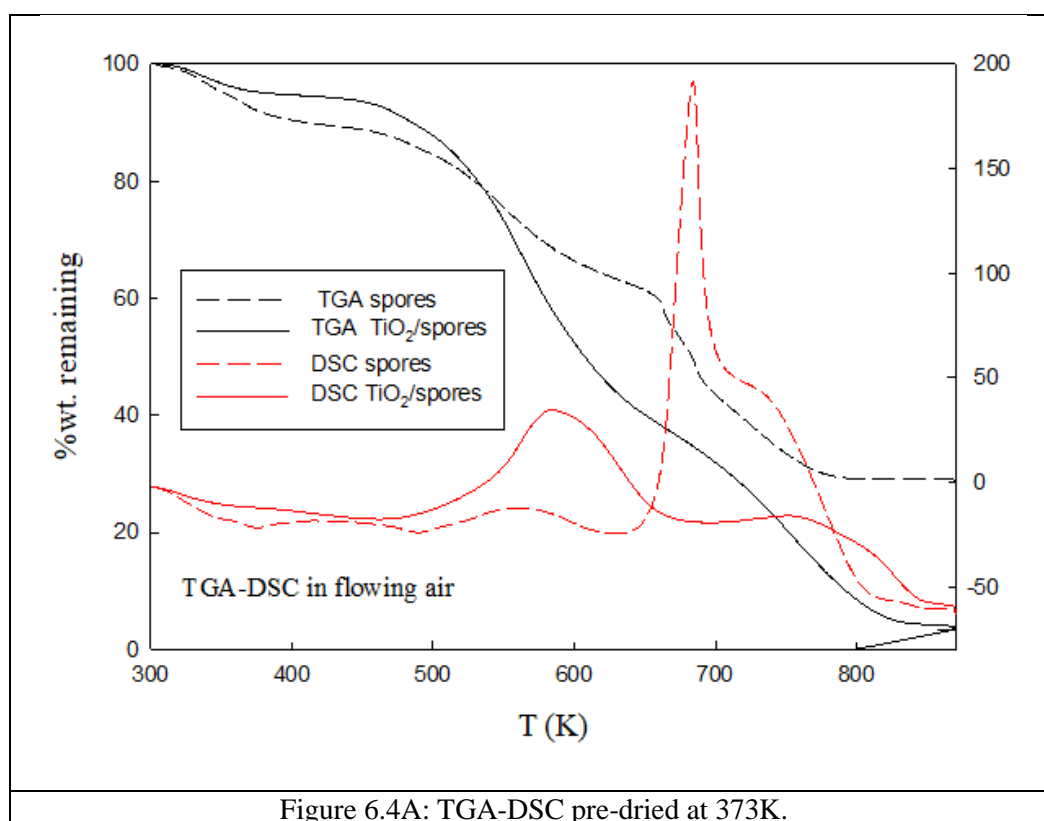
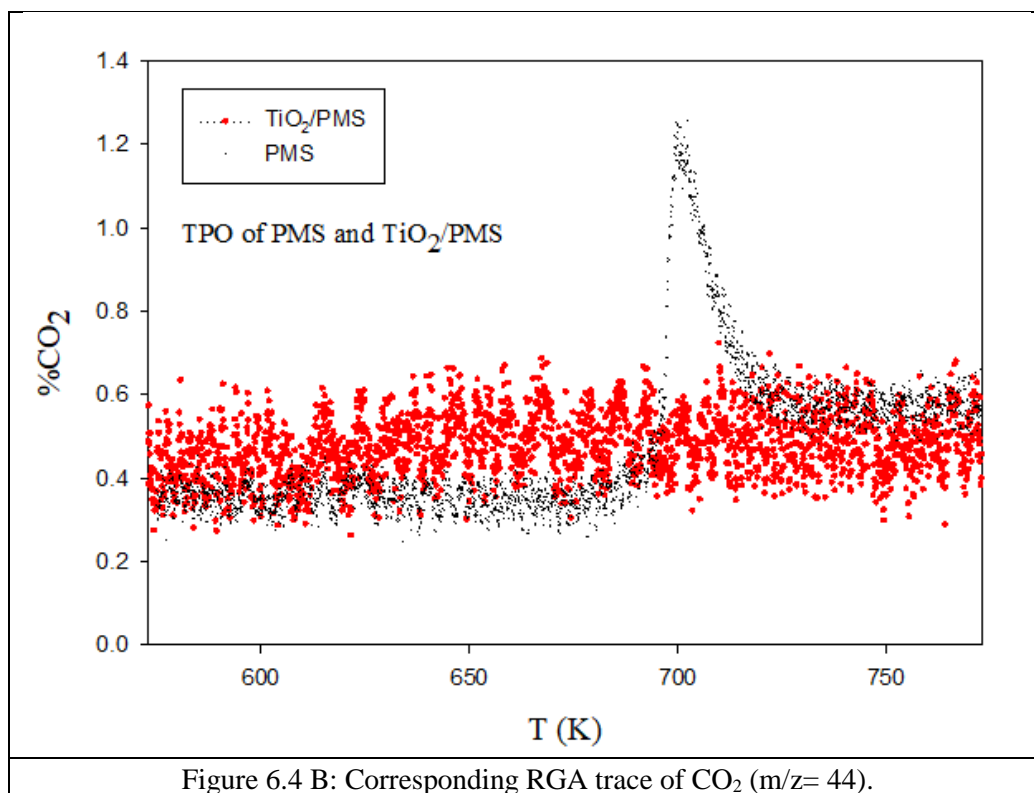


Table 6.2: FTIR detected functional groups seen for TiO<sub>2</sub> NPs coated PMS.

Functional group	O-H	N-H	C=O	C-O	C-N	C-O-Ti	Ti-O-Ti	C-Cl	O-P
wavenumber (cm <sup>-1</sup> )	3300	3294	1618, 1554	1373	1149	1056	408	690	1030

Residual gas analysis (RGA) confirmed that TiO<sub>2</sub> interacts with PMS surface. Figure 6.4A shows the TGA-DSC trace of untreated PMS and TiO<sub>x</sub>/PMS pre-dried at 373 K during heating in flowing air; TiO<sub>x</sub> modifies the weight-loss profile of PMS (retarding wt loss at low temperature and then accelerating it at 550-750K). The RGA trace in Figure 6.4B shows PMS released CO<sub>2</sub> at around 700K, but TiO<sub>x</sub>-coated PMS did not, suggesting that the TiO<sub>2</sub> is retarding bio-template oxidation and heating CO<sub>2</sub> release; this is a reflection of the strength of the TiO<sub>x</sub>-PMS interaction.





### 3. Ag and Au NPs coated PMS

Different concentrations (1-3mM) for Ag and Au salts were used to react with the PMS surface to produce surface-bound NPs, held there by electrostatic interactions, thereby avoiding aggregation. The Ag, Au and NP hybrids were characterized by SEM, TEM, EDX, DLS, FTIR, UV-Vis and TGA. Ag and Au NPs have high electronic density and filled d-orbital that interact with carbonyl group as  $\pi$ - back donation due to the vacant p-orbital which accepts electronic density from Ag and Au NPs [106]. This leads to strong binding between Ag and Au NPs with the carbonyl group on the PMS surface (see Fig. 6.5).

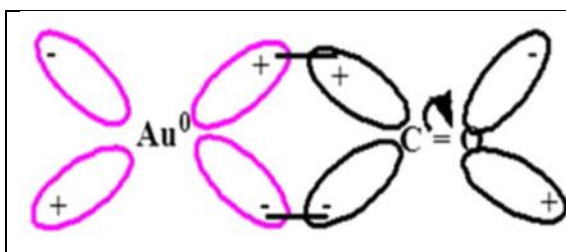
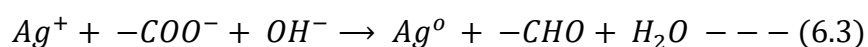


Figure 6.5: Back donation between an atom in Au NP and a carbonyl group [106].

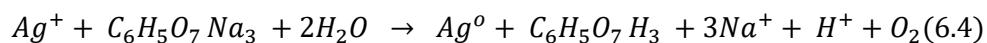
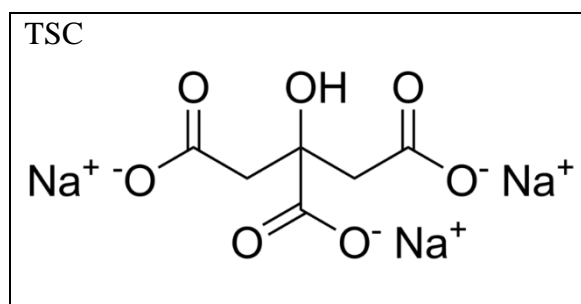
- **Ag NPs/PMS**

Silver NPs were prepared using  $\text{AgNO}_3$ , tri-sodium citrate (TSC),  $\text{NaBH}_4$  and a mixture of TSC- $\text{NaBH}_4$  as reducing agents. The prevailing pH value has an important impact on product properties.

- (i) The PMS surface contains many functional groups: e.g. polysaccharides have a carbonyl group which is highly polar ( $\text{C}^+-\text{O}^-$ ) and namely an aldehyde. This structure is flat (trigonal) and hydroxyl ions can attack the carbonyl group. The mechanism of reaction in an alkaline environment ( $\text{pH} \geq 10$ ) occurs according to the following equations (6.3) [257]:

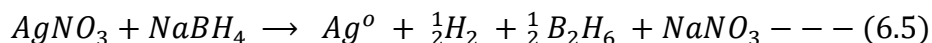


- (ii) Ag NPs were prepared using TSC as a reducing agent near its boiling point. The reaction can be expressed as follows [187]:



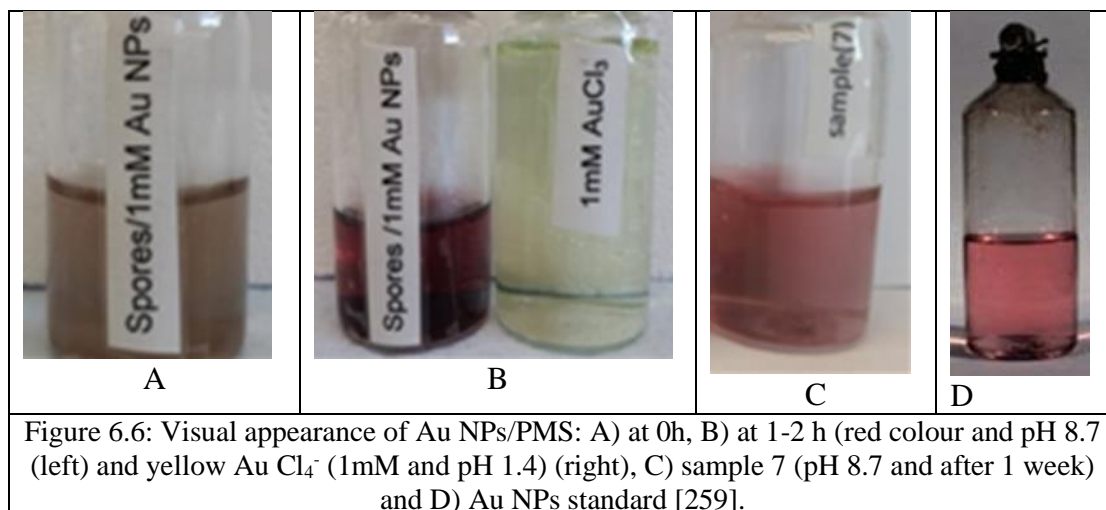
The reduction of  $\text{Ag}^+$  ions to  $\text{Ag}^0$  nanoparticles (NPs) took place only at high pH, implying that the carboxylic group of the acetate group is responsible for the electron transfer from acetate to the silver ion (leads to the formation of free radical ( $\text{CH}_3\cdot$ ) accompanied to form Ag NPs [258]. The reaction of Ag ions with TSC and  $\text{NaBH}_4$  includes a two-stage thermal treatment. Initial reduction was performed by  $\text{NaBH}_4$  at  $60^\circ\text{C}$ , which generated Ag nuclei (instant nucleation). The second stage was performed (favourably) at  $90^\circ\text{C}$ , where TSC reduces the remaining Ag ions [188].

- (iii) Ag NPs were prepared using a strong reducing agent (i.e. sodium borohydride) and the reaction [187]:

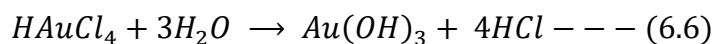


- **Au NPs coated PMS**

Figure 6.6 demonstrates the appearance of different colours (deep and light pink, yellow, blue and colourless) for samples in water. This is evidence of the synthesis of Au NPs in the presence of PMS and a clear indication of PMS reduction of  $Au^{3+}$  to  $Au^0$ .



Chloroauric acid ( $HAuCl_4 \cdot 3H_2O$ ) has acidic properties, because hydronium ion ( $H_3O^+$ ) can separate from the molecules giving water and proton ions ( $H^+$ ). Also, chloroauric acid is a strong monoprotic conjugate acid and is unstable in aqueous solution. Therefore, it is hydrolyzed to auric acid and hydrochloric acid.



The aqueous chloroaurate ions ( $AuCl_4^-$ ) were reduced during interaction with the PMS cell walls. Many functional groups were found on the surface of these cells ( e.g. aldehyde, carboxylic, sulfhydryl (R-SH), riboflavins, proteins and amino acids [251]).

These functional groups have a negative charge, depending on the pH of the solution. They strongly bind gold ions and they are responsible for the reduction of  $\text{Au}^{3+}$  to  $\text{Au}^0$  [256]. Further, rich carboxyl group on PMS surface has strong interaction with Au NPs makes PMS an excellent stabilizer and  $\text{OH}^-$  can be used as reducing agents [260]. Here, AuNPs lose their charge and the ions in the acidic or basic solution will be in equilibrium with  $\text{H}^+$  and  $\text{OH}^-$ . For example,  $\text{COO}^-$  will be the pH-dependent equilibrium with  $\text{H}^+$  to form  $-\text{COOH}$ . This situation makes the NPs aggregate due to losing their colloidal stability [261].

Further, in an acidic chloroauric acid ( $\text{HAuCl}_4 \cdot 3\text{H}_2\text{O}$ ) solution, one could have cleavage of glycosidic (a molecule in which a sugar is bound to another functional group via a glycosidic bond) linkages (C-O-C) of the chain in polysaccharide, which is already in the PMS. Gold ions were present in the reaction medium and could be trapped/adsorbed on the surface of the PMS cell wall or held there by an electrostatic interaction between  $\text{Au}^{3+}$  and the PMS negatively-charged functional groups; the enzyme which is present on the surface in the cell wall reduces  $\text{Au}^{3+}_{(\text{aq.})}$  to gold ( $\text{Au}^0$ ) [24].

In a basic solution, the Au NPs is saturated with negative charge leading to colloidal stable [261]. The adsorption of chloroaurate ions ( $\text{AuCl}_4^-$ ) on the surface would be accompanied by a change in pH value. Bio-reduction from NADH (nicotinamide adenine dinucleotide) by NADH-dependent reductase involves an electron carrier ( $\text{NAD}^{++} + e^-$ ). In addition,  $\text{Au}^{3+}$  electron is reduced to  $\text{Au}^0$  [251]. In general, edible mushroom extracts can be used as a reducing and protective agent for the synthesis of nanoparticles in one step. [232].

### 6.3.2 SEM and TEM of Ag and Au NPs/PMS

Figure 6.9A illustrates the hollowed oval-shaped morphology of  $5\mu\text{m}$  sized PMS that in many ways were similar to red-blood cells that has been maintained from the untreated state (see Fig. 5.4 in section 5.2.1) even after silver or gold reduction. Clearly the Ag and Au zero-valent surface structures were biosynthesised by the functional groups in the PMS cell wall. However, one now sees on the PMS surface in Fig. 6.7 some aggregation of Ag or Au NPs., but the reader sees in a moment that this aggregation only relates to a small fraction of surface-held species.

Interestingly, the PMS shape was not changed even on heating in air to 100°C but there was an increase in PMS convexity/concavity presumably as a result of fluid loss from the PMS. EDX-analysis was undertaken after biotemplates PMS removal in air at 500°C, at which point the PMS has collapsed leaving a residual structure that has shrunk to around 1.33µm in size (see Fig. 6.9). EDX analysis confirmed (see Table 6.3/ Fig. 6.8) that 61wt% Ag and 48wt% Au remained in the residue. With chemical reductants present the residue contained less Ag. The citrate/Ag NPs/PMS is (1.7 wt.% Ag) and BH/Ag NPs/PMS is (wt.%Ag). This emphasises the value of the PMS biosynthesis.

Table 6.3: EDX-derived elemental compositions of Au NPs/PMS (from HAuCl<sub>4</sub>), 1mM and pH 10) at RT and 500°C in air.

Elements	Wt.% at RT	Atom. % at RT	Wt.% at 500°C	Atom. % at 500°C
O	17.26	18.76	3.4	16.5
Na	----	---	0.84	2.9
K	1.08	0.52	0.60	1.3
C	49.84	73.49	3.20	21.2
P	0.18	0.11	0.6	1.4
Ca	0.14	0.07	1.26	2.2
N	12.15	15.04	0.3	1.4

One should remember TEM on microtome sections of PMS alone was reported in section 4.2.1. TEM was now undertaken on microtome sections of NP-containing PMS to deduce the primary particle size and distribution of Ag NPs (see Fig. 6.10 and 6.11), Au NPs (see Fig. 6.12) and Au-TiO<sub>x</sub> NPs (see Fig. 6.13) within the PMS cell walls.

First it is clear that discrete spherical 12nm Ag NPs exist throughout the PMS cell wall. If in Figure 6.10C one sees that the cells walls are 252nm thick, then one could distribute up to 50 such NPs as one proceeded through the cell wall from one side to the other. TEM of Ag NPs/PMS provided similar results to those of SEM with Ag NPs directly in the cell wall of the spores (see Fig.6.11). TEM of PMS alone is described in section 5.2.1

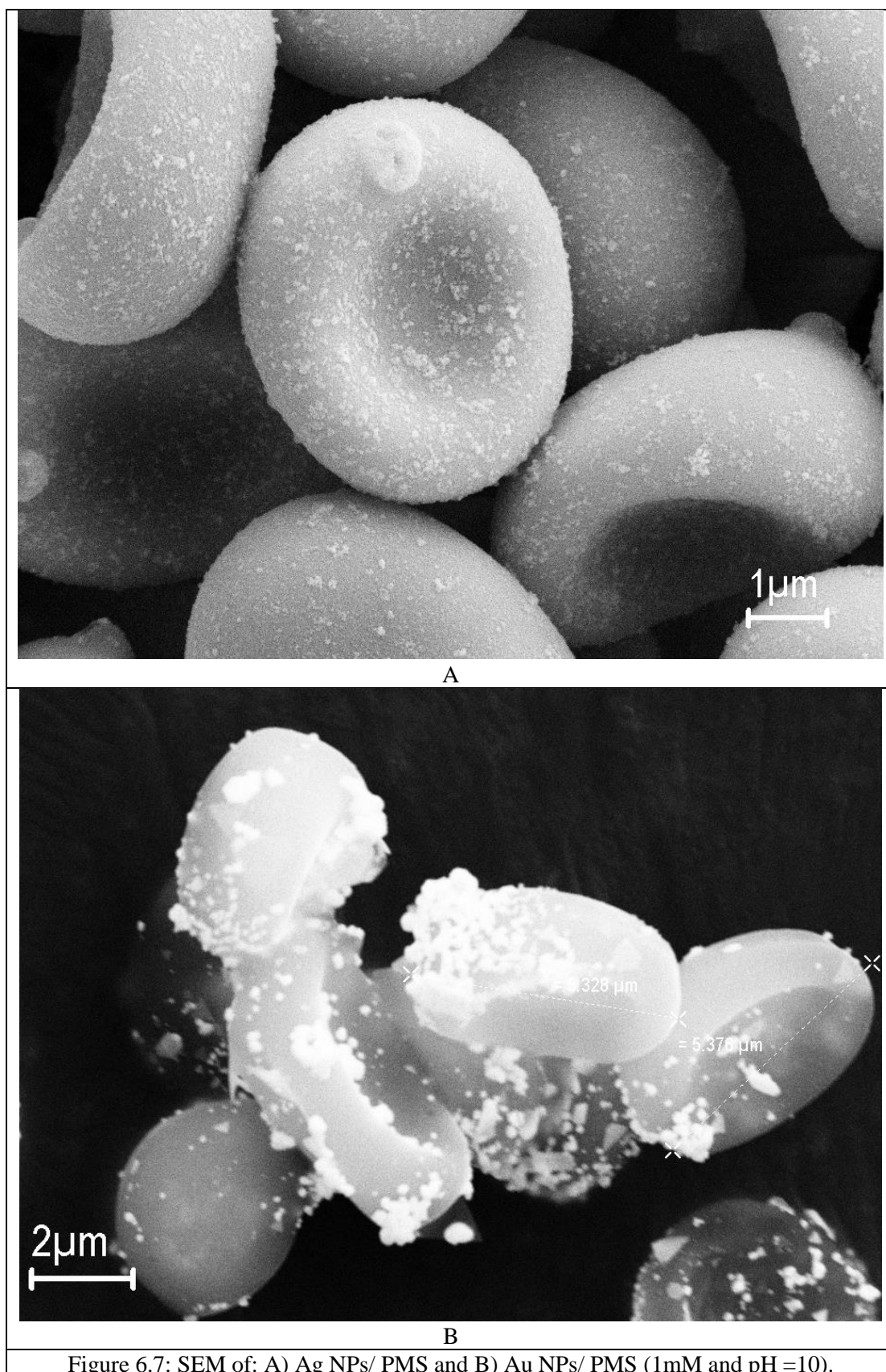
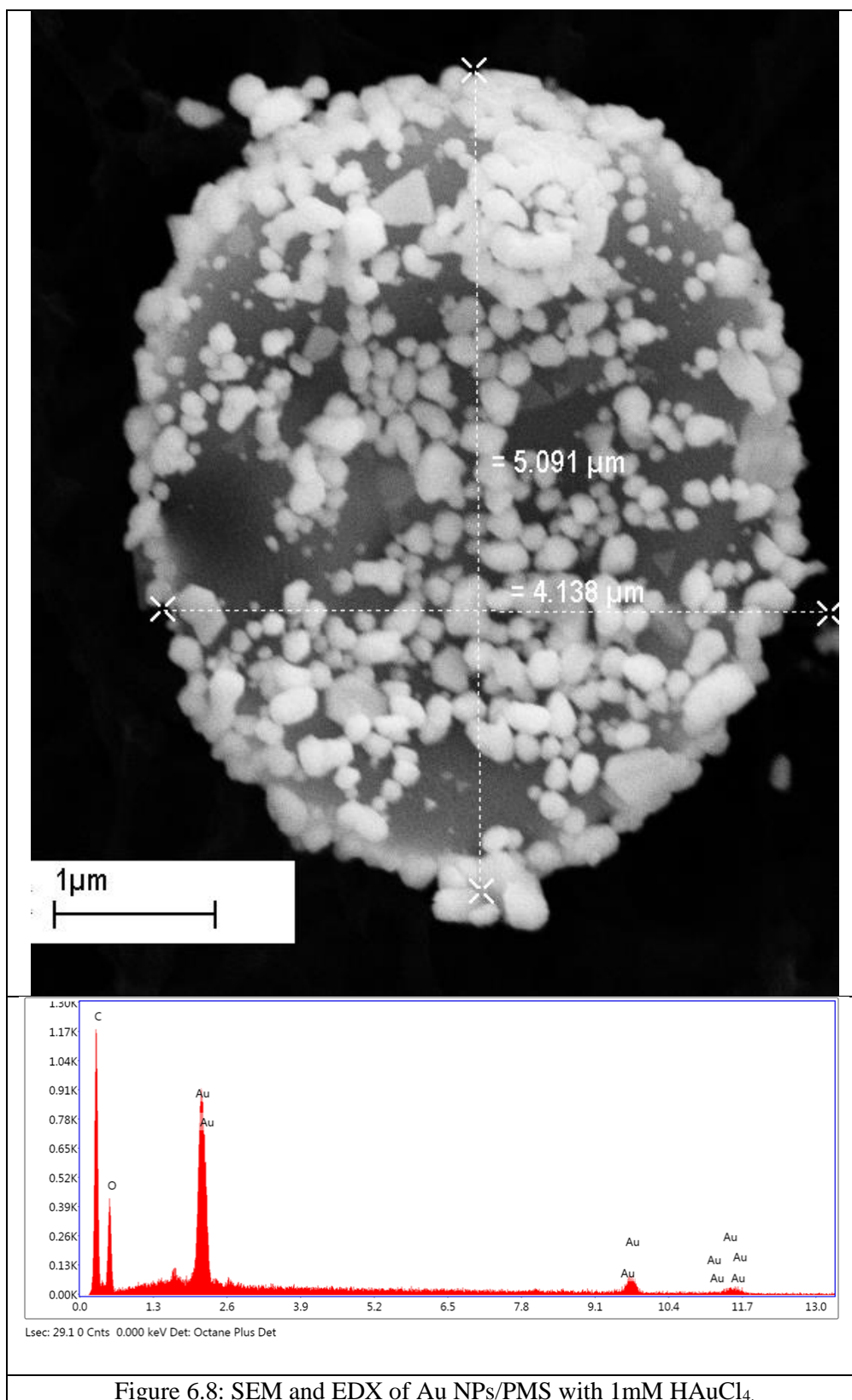


Figure 6.7: SEM of: A) Ag NPs/ PMS and B) Au NPs/ PMS (1mM and pH =10).





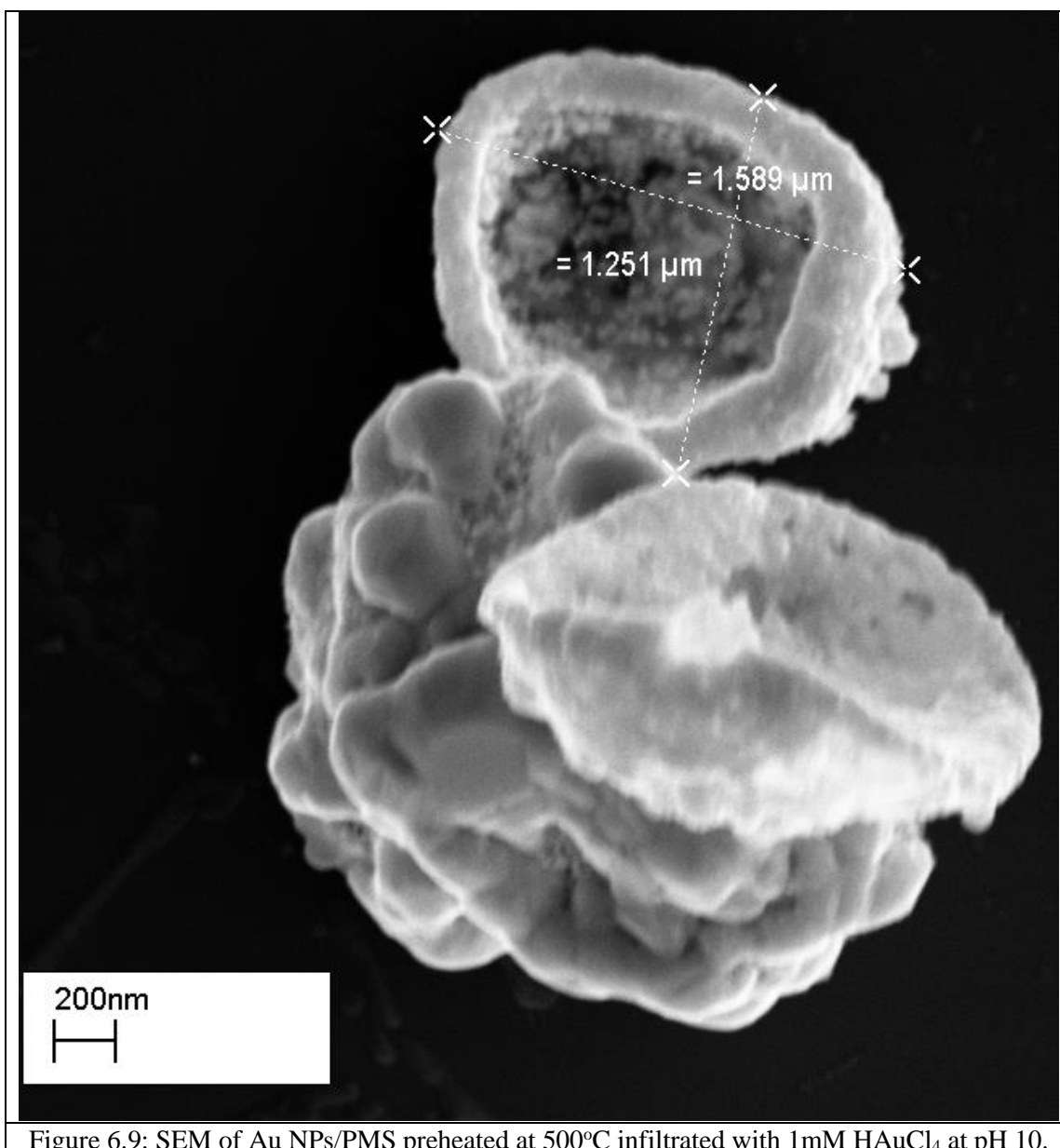


Figure 6.9: SEM of Au NPs/PMS preheated at 500°C infiltrated with 1mM HAuCl<sub>4</sub> at pH 10.

Second, the Au NPs in the PMS cell wall were on average 5-10nm in size (see Fig. 6.12C) and were slightly distorted to a hexagonal morphology. It would have been interesting to do electron diffraction on such NPs within the PMS cell wall, but this proved difficult.

Third, Figure 6.13 suggests that chromatographic separation of Au and TiO<sub>x</sub> species has occurred as fluid moves into the PMS cell wall with Au NPs going further into the cell wall (but continuing to be nm in size), while the TiO<sub>x</sub> is held-up at as surface-held TiO<sub>x</sub> species.

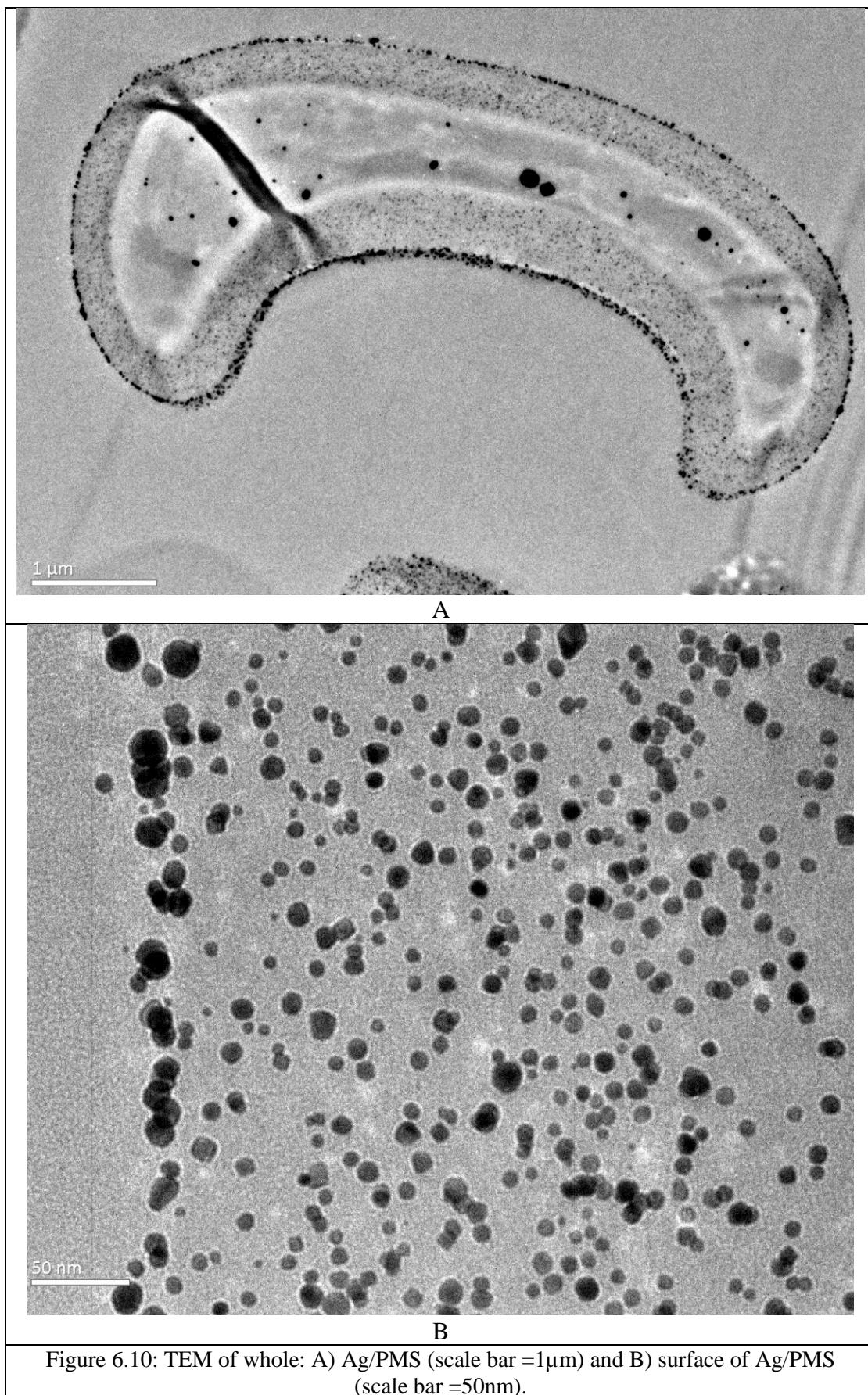


Figure 6.10: TEM of whole: A) Ag/PMS (scale bar =1μm) and B) surface of Ag/PMS (scale bar =50nm).

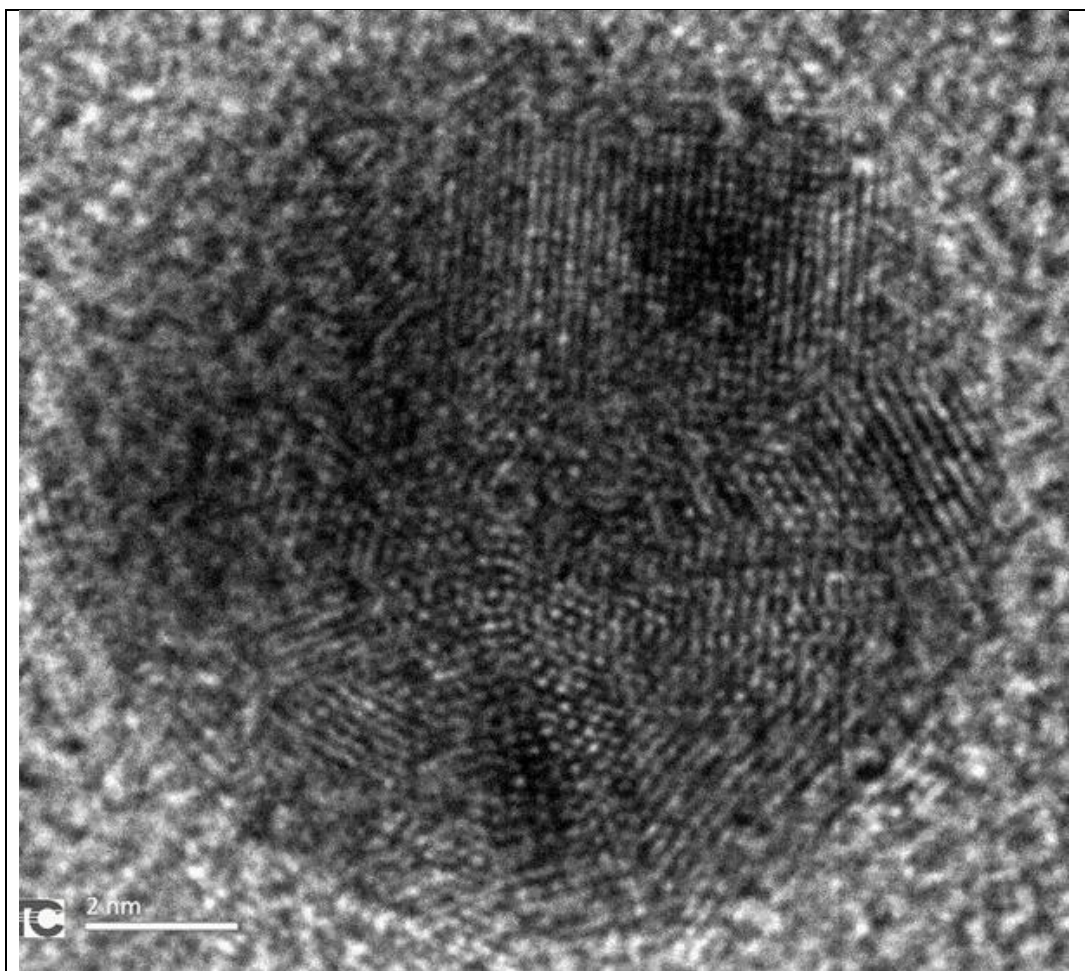


Figure 6.11: TEM of one Ag NP within the cell wall of Ag/PMS (scale bar = 2nm).

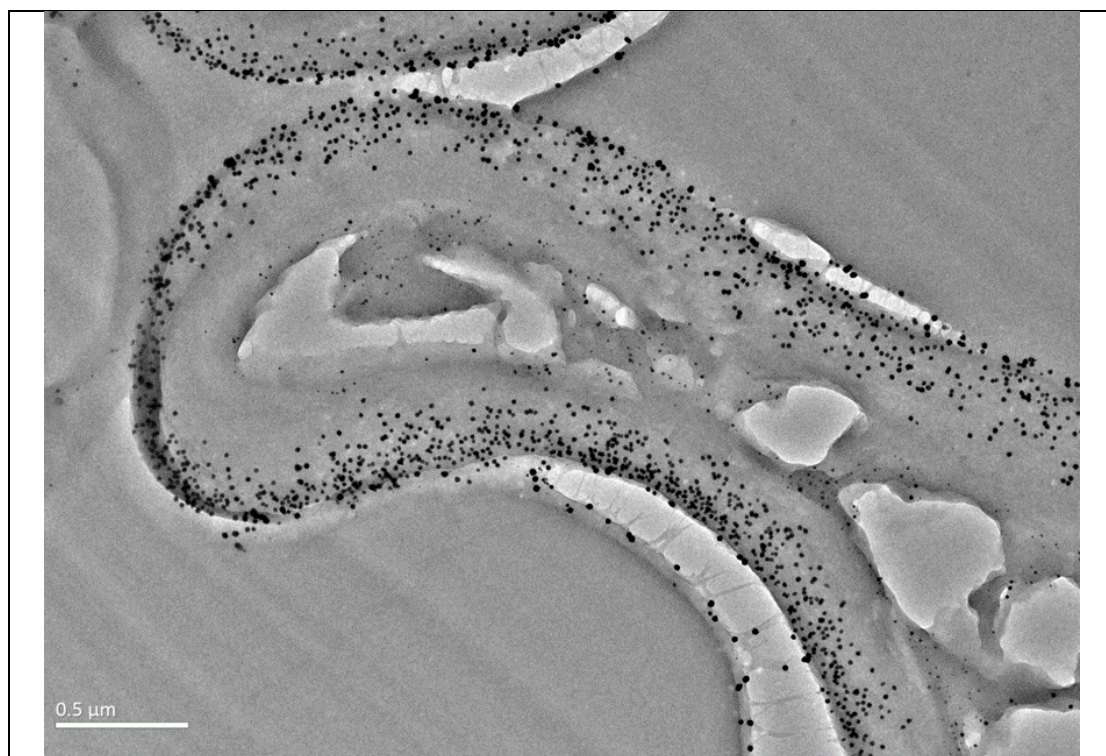


Figure 6.12A: TEM of whole Au/PMS (scale bar = 0.5μm).

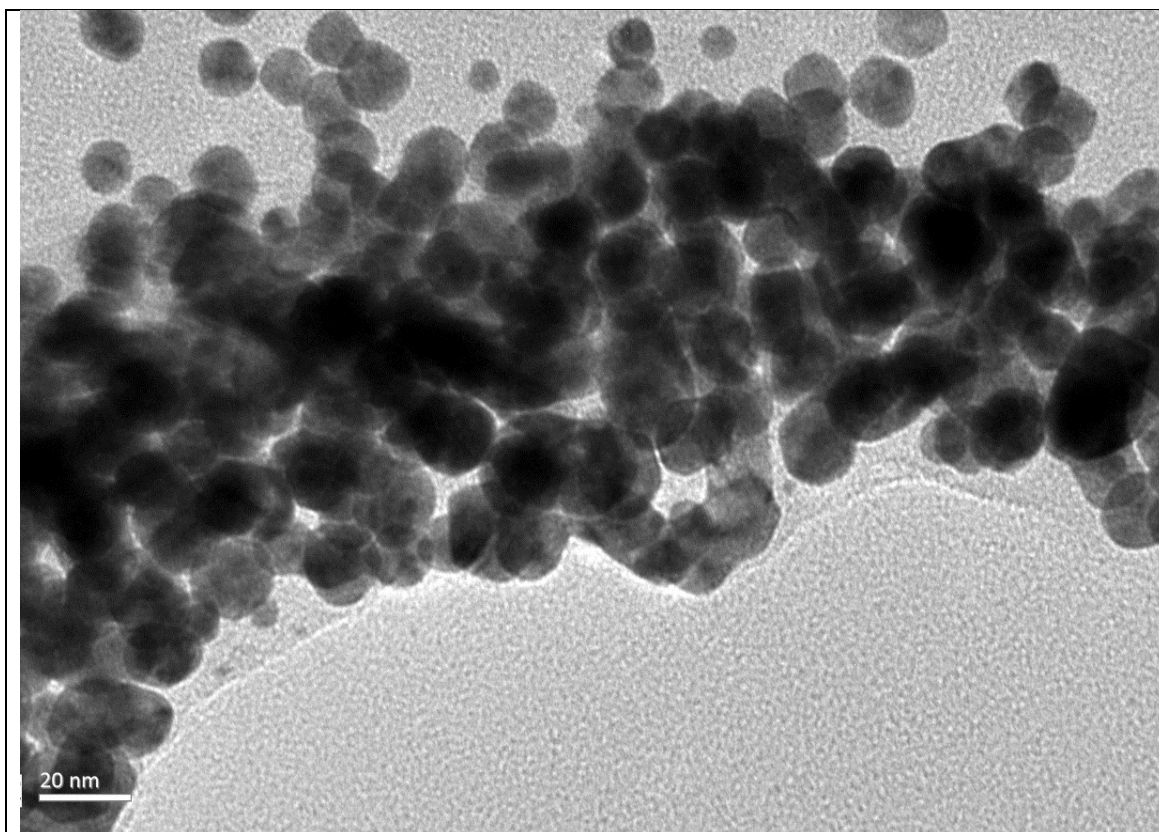


Figure 6.12B: TEM of surface of Au/PMS (scale bar =20nm).

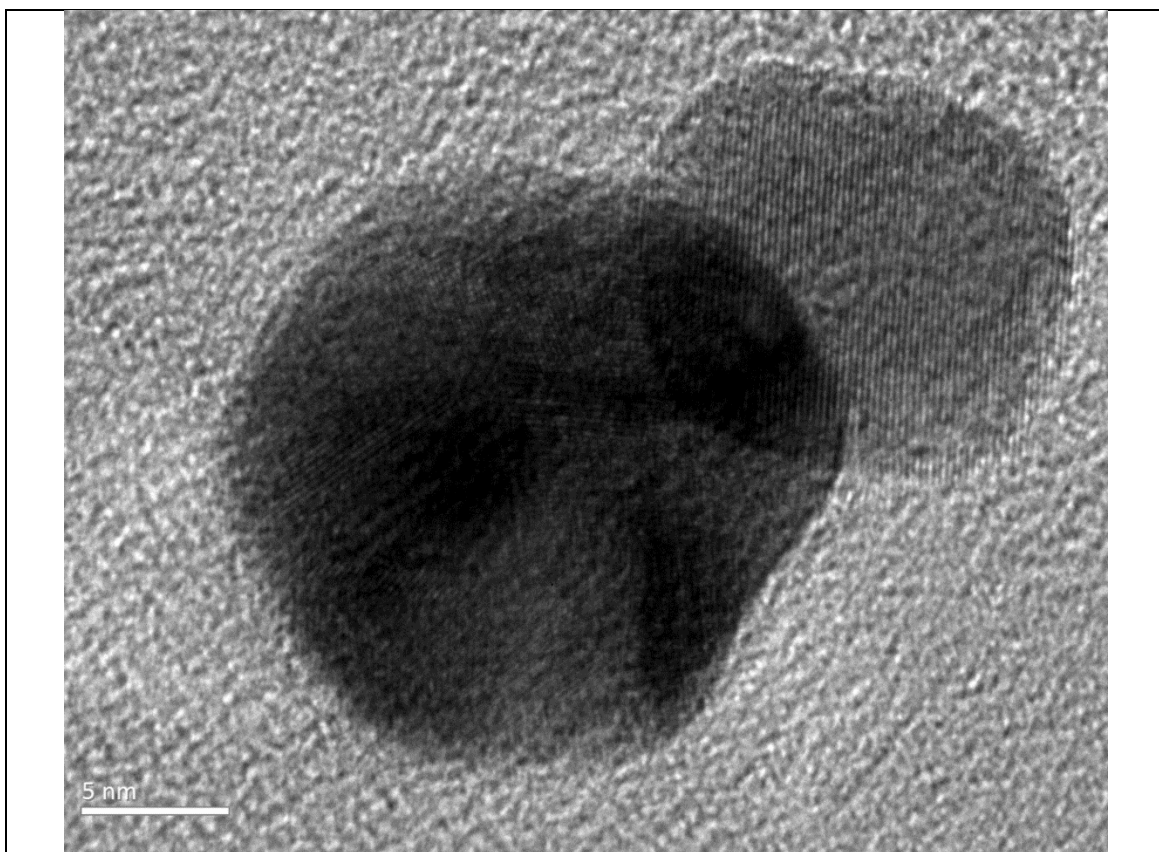


Figure 6.12C: TEM of Au NP within the cell wall of Au/PMS (scale bar =5nm).

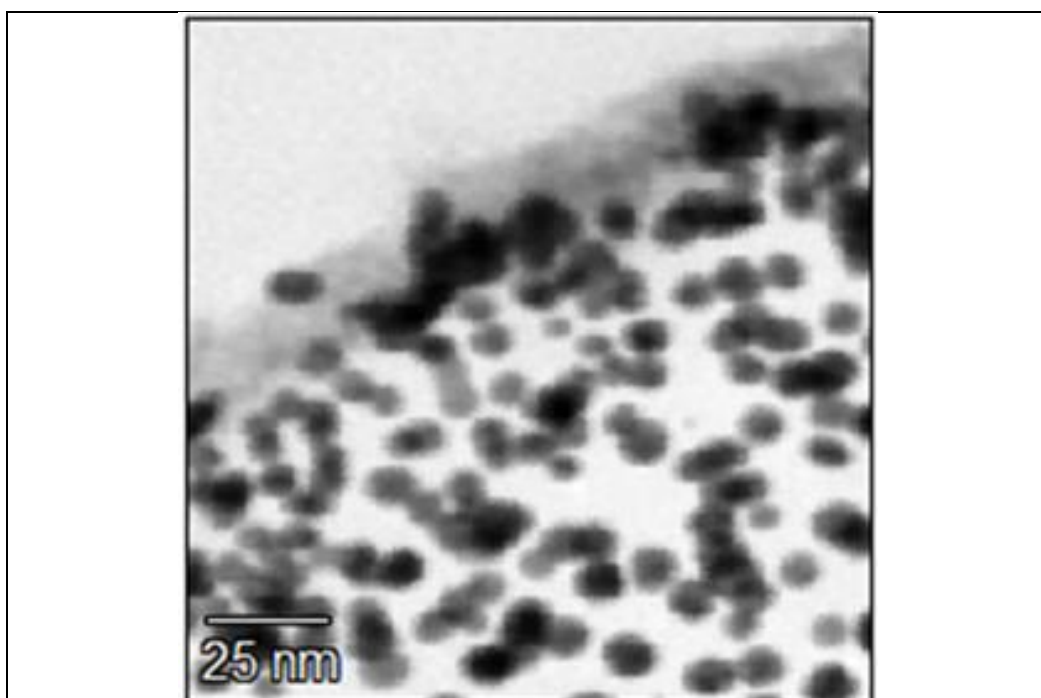


Figure 6.13A: TEM of Au NPs and  $\text{TiO}_x$  layers in the cell walls of  $\text{Au-TiO}_x/\text{PMS}_{\text{IPA}}$ .

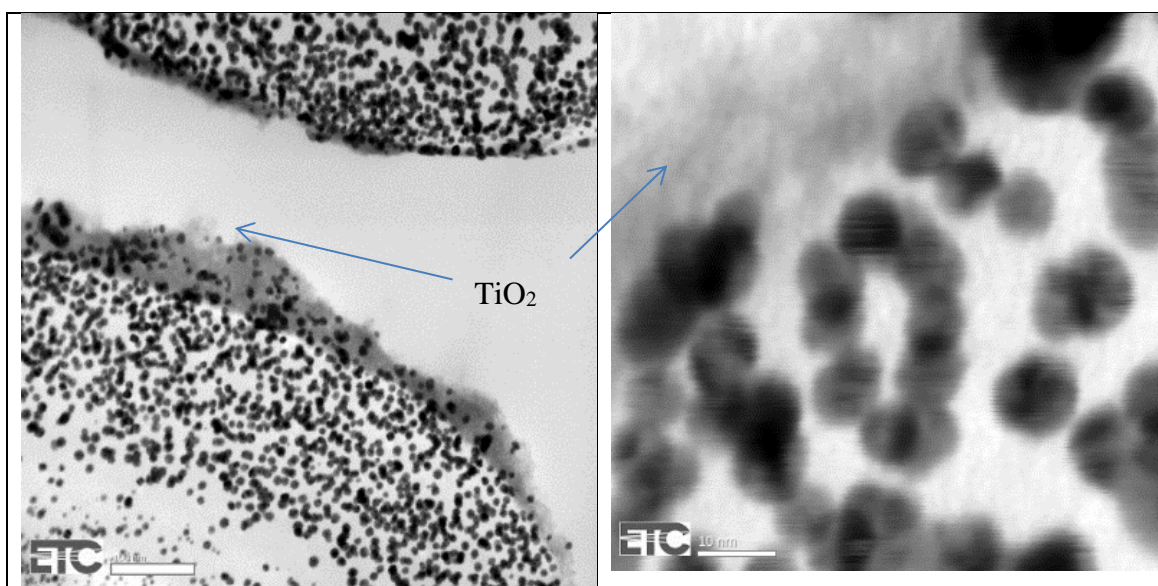
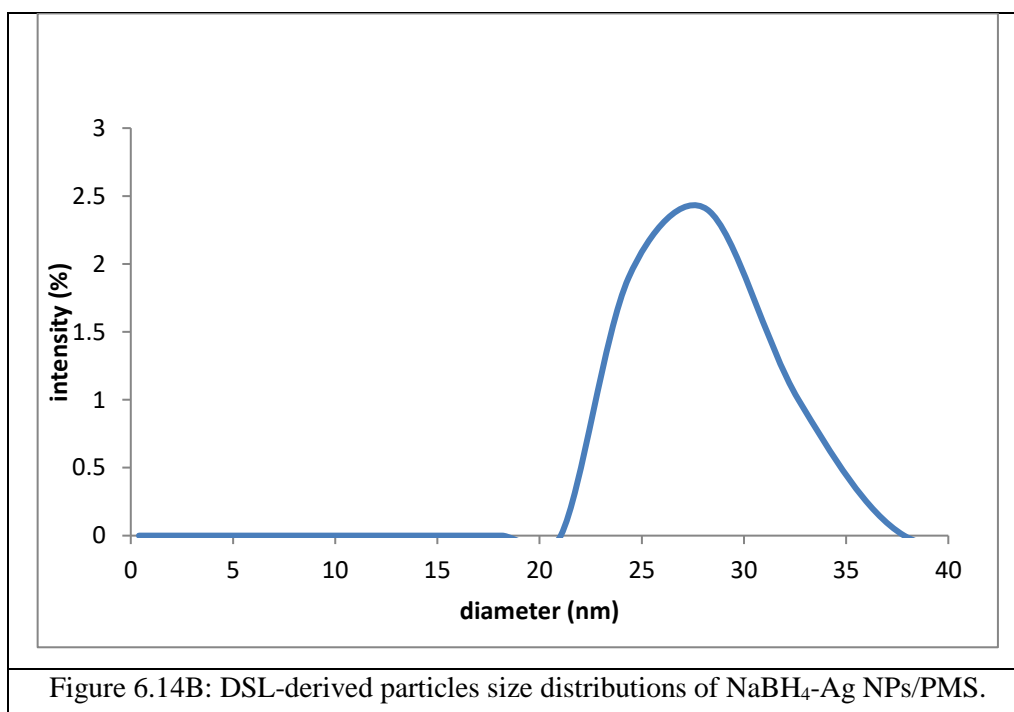
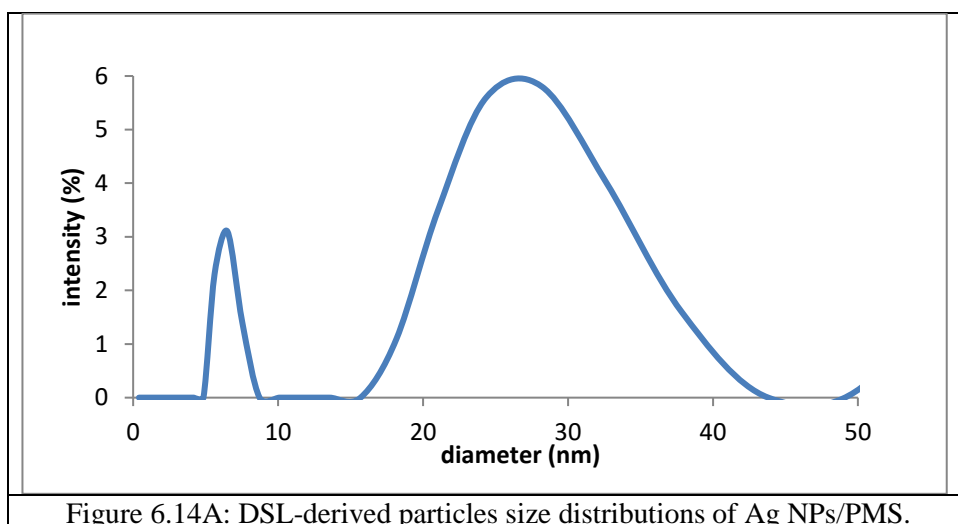


Figure 6.13B: TEM of Au NPs and  $\text{TiO}_x$  layers in the cell walls of  $\text{Au-TiO}_x/\text{PMS}_{\text{IPA}}$  (scale bar = 10nm).

### 6.3.3 DLS analysis of Ag NPs

The particle size distribution of  $\text{PMS}/\text{Ag}$  NPs was obtained from Dynamic Light Scattering (DLS). Fig. 6.14 and 6.15 show the size of particles observed in the 6-50 nm

diameter range. Clearly, PMS is too large to be seen in DLS because the poly dispersity index (it is a number calculated from a simple two parameters fit to the correlation data) is more than 0.7 indicated that the PMS has a very broad size distribution. That means, PMS is probably not suitable for DLS. The results in Fig. 6.14 and 15 must be showing NPs not bound to PMS that remain in suspension.



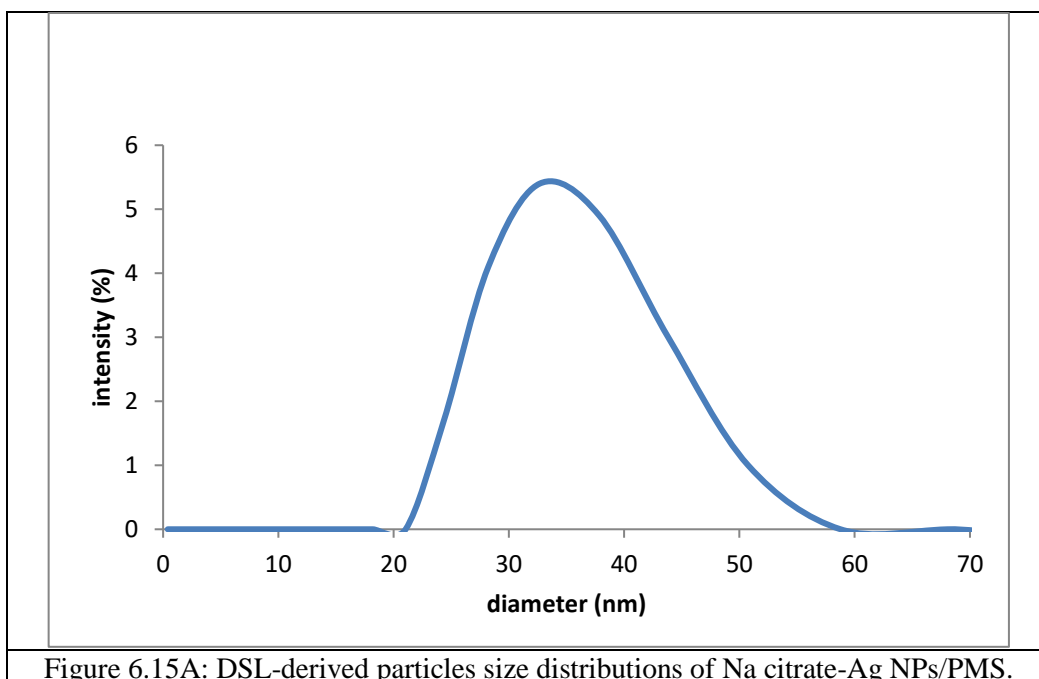


Figure 6.15A: DSL-derived particles size distributions of Na citrate-Ag NPs/PMS.

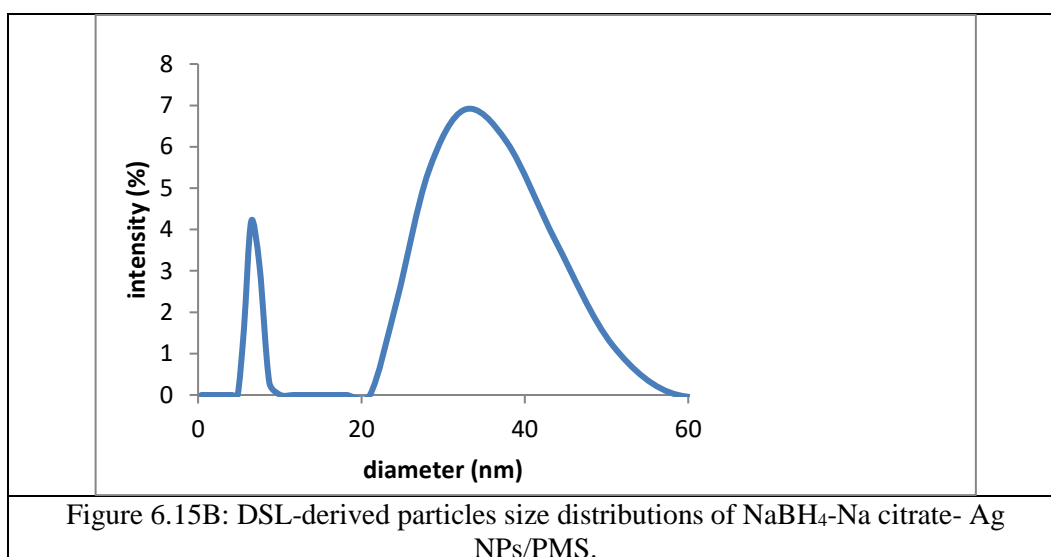


Figure 6.15B: DSL-derived particles size distributions of NaBH<sub>4</sub>-Na citrate- Ag NPs/PMS.

### 6.3.4 FTIR

FTIR measurements have confirmed an interaction between Ag and PMS, where the PMS is thought to be responsible for the synthesis and stabilization of silver nanoparticles. FTIR evidence suggests that all Ag NPs/PMS have the same FTIR spectrum (see in Fig.6.16). Ag NPs/PMS absorb strongly at 1620 and 3310  $\text{cm}^{-1}$  and show a shift in band width after synthesis. Table 6.4 shows the important functional groups which react with silver ions compared with PMS alone.

It is known that edible mushrooms consist of 75% proteins. In FTIR of Ag NPs on PMS, it was evident that there were variations in the absorption band, densities and



small shift of hydroxyl, carbonyl and amino groups [257] in the PMS. This means, the carbonyl group in amino acids, peptides of proteins, enzymes and polysaccharides of PMS might have bound strongly to silver and play a role in its reduction ( $\text{Ag}^{+1}$  to  $\text{Ag}^0$ ) by the oxidation of aldehyde group to carboxylic acid [262]. So, possibly the proteins could have formed a layer on the Ag NPs which prevents agglomeration of NPs [245]. Therefore, Ag NPs are stabilized in the nano composite [229].

Table 6.4: FTIR-detected functional groups seen for Ag NPs/PMS.

Functional group	O-H	N-H	C=O
Wavenumber ( $\text{cm}^{-1}$ ) for Ag NPs/PMS	3300	3294	1618
Wavenumber ( $\text{cm}^{-1}$ ) for PMS alone	3270	3270	1741-1622

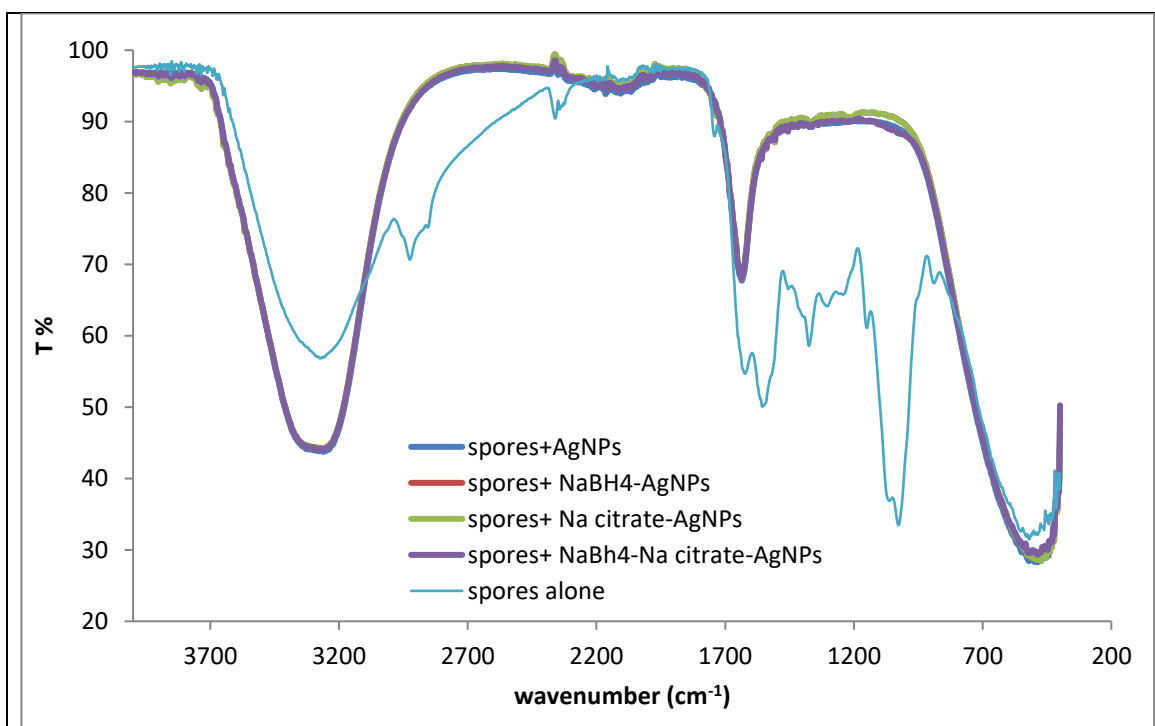


Figure 6.16: Transmission FTIR spectra of different Ag NPs/PMS samples.

### 6.3.5 UV-Vis

The optical properties of Ag NPs/PMS were studied with UV-Vis. A colour change during Ag NPs synthesis was clearly observed. The generation of a greenish-yellow colour is a clear indication of the formation of Ag NPs. This colour appears because silver has a surface plasmon resonance absorption band [263]. It is explained that the shape and position of  $\lambda_{\text{max}}$  for Ag NPs gives evidence about particle size [264].

Figure 6.17 shows the UV-Vis spectra of Ag NPs. In general, Ag NPs absorb in the visible region of the electromagnetic spectrum [231] at 380-450nm. Differences in the position of the peak maximum and intensity were seen. Ag nanoparticles are characterized by a peak with maximum between 400-420nm. The absorbance intensity was thought to be proportional to their concentration (and absorbance value was approximately 3.5 because the product concentration may be high).

Table 6.5: UV-Vis characterization of Ag NPs in the present PMS.

Ag NPs	$\lambda_{\max}$	color	pH
Citrate	420	Greenish -yellow	10.5
Borohydride	410	Brown-yellow	10
Citrate-borohydride	400	Green-yellow	10.5

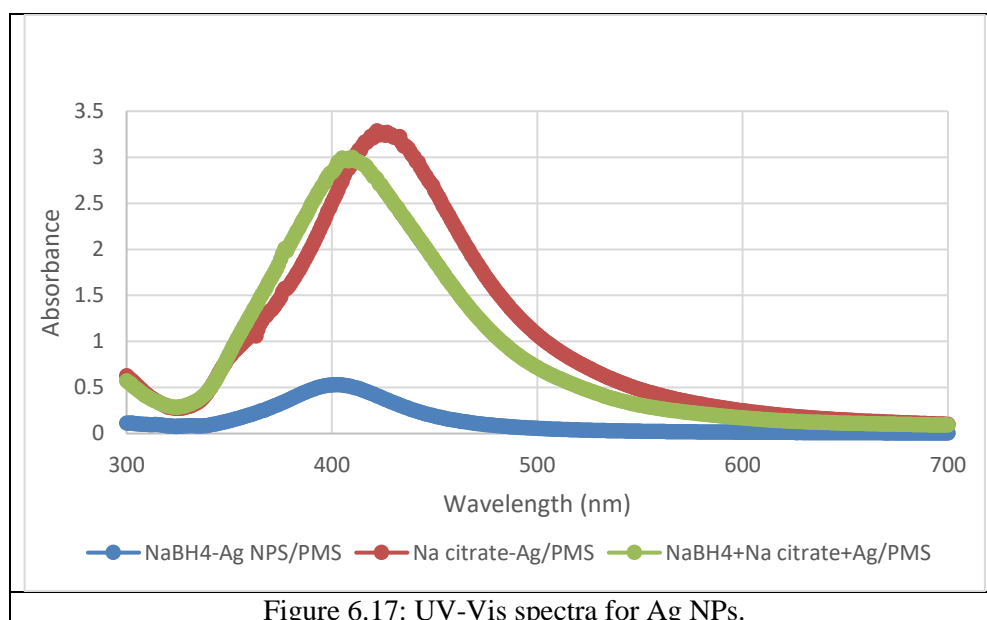
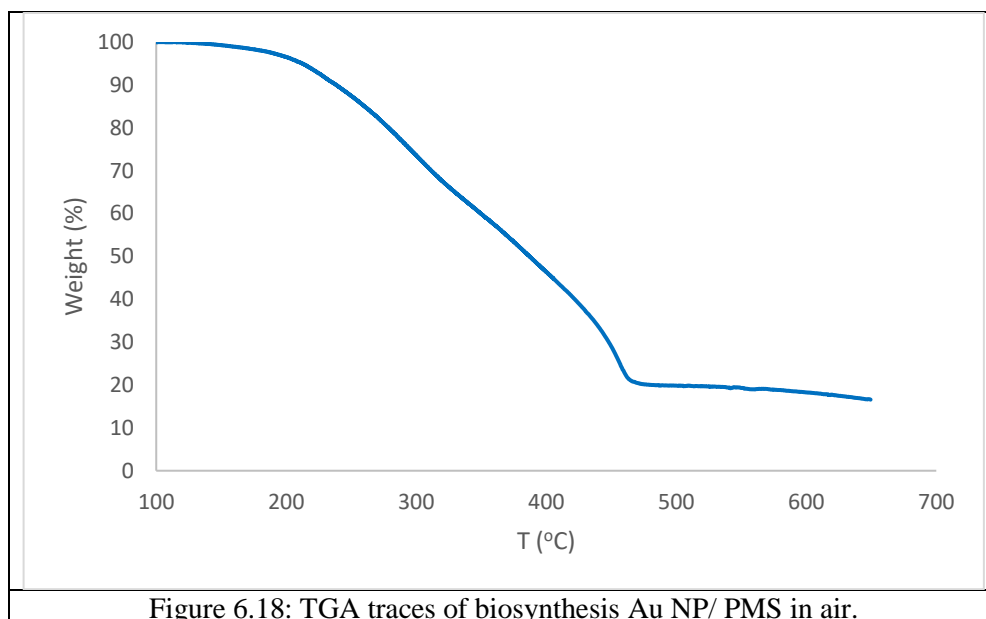


Figure 6.17: UV-Vis spectra for Ag NPs.

### 6.3.6 TGA

Thermogravimetric analysis (TGA) was used to investigate the effect of coated Au NPs on the thermal stability of PMS in air. Figures 6.18 shows the thermal stability of Au NPs/PMS 88%wt in air. TGA temperature was initially ramped to 100°C (10°C/min) for 30mins to dry the sample; it was subsequently ramped 650°C for thermal analysis. It can be seen from this figure that Au NPs coated onto the PMS exhibited a loss of weight mostly likely due to hydrocarbons and other organic molecules from PMS. The residue weight was around 16% at 450°C.



### 6.3.7 Au and Ag nanohybrids with PMS

The next samples were prepared using PMS as a template and a reducing agent by three methods and have two components in different ratios. The reduction-oxidation (redox) reactions produced Au and Ag NPs directly onto the PMS surface. Hydrolysis with  $\text{AuCl}_4^-$  and Ti alkoxides leading to  $\text{TiO}_2$  are likely to be pH dependent. The extent of hydrolysis increases with pH; hydrolysis was complete above pH 8.  $\text{Au}(\text{OH})_3 \cdot \text{H}_2\text{O}$  is chiefly found as a neutral species [236].

- **Method No.1** (described in section 4.2.4)

Initially all samples were prepared in 2-propanol (IPA) solvent, as this allowed Ti isopropoxide use. The levels of Ag, Au and  $\text{TiO}_2$  introduced onto PMS (as detected by EDX) are shown in Table 6.6. SEM on these samples was not undertaken and so no comments can be made about NP or PMS morphology. There is almost 5x (29x) times more  $\text{TiO}_x$  taken up by PMS than Ag (Au). However, the levels of Ag-Au were similar in the final sample. One explanation for the high  $\text{TiO}_x$  incorporation is that the alkoxide-PMS surface interaction is strong. Alternatively, it may be that IPA is not the most effective solvent for maximising Ag-PMS or Au-PMS interactions. There may thus be a conflict between the requirements of non-aqueous interfacial sol-gel chemistry and cation uptake from aqueous solutions.

Table 6.6. EDX-derived compositions of samples on PMS (prepared in IPA solvent by method No.1)

NPs on PMS	At% Ti	At% Ag	At% Au	Atomic ratio	Colour
Ti-Ag	5.23	1.17	-	4.47	colourless
Ti-Au	3.50	-	0.12	29.17	light yellow
Au-Ag	-	0.16	0.10	1.6	light purple

- **Method 2.** (described in section 4.2.4)

Here the Ti alkoxide concentration in IPA was decreased from 3mM to 1mM in the hope that this would minimise any TiO<sub>x</sub> overloading of the PMS surface. Table 6.7 shows that the Ti (although so too are the levels of Ag and Au) are lowered significantly, but that when Ag-Au are introduced without TiO<sub>x</sub>, the uptake is similar and higher than in the method 1 case (see Table 6.6) whether IPA or H<sub>2</sub>O is the solvent. These results suggest that Au and Ag species react equally strongly with the PMS surface to produce a 'sombbrero' of NPS around the PMS.

Table 6.7. EDX-derived compositions of samples on PMS (prepared in two solvents by method No.2) under basic conditions

NPs on PMS	At% Ti	At% Ag	At% Au	Atomic ratio	Colour
Ti-Ag	0.08	0.08	-	1.00	brown
Ti-Au	0.06	-	0.01	6.00	colourless
Au-Ag (IPA)	-	0.25	0.29	0.86	light pink
Au-Ag (H <sub>2</sub> O)	-	0.48	0.39	1.23	pink

Figure 6.19 shows SEM evidence that the TiO<sub>2</sub>-Ag, TiO<sub>2</sub>-Au and Ag-Au NPs deposited in method 2 using IPA solvent did not affect the PMS morphology and are well-dispersed on the PMS surface. Figure 6.20 shows when Ag-Au was deposited on PMS from water, it was badly agglomerated and poorly dispersed. Hence better defined samples are prepared from IPA solvent. In contrast, some Au-Ag NPs show on the PMS surface (from IPA and H<sub>2</sub>O). Clearly, Au-Ag NPs in water appeared to be regular particles (see Fig.6.8). Au NPs can effectively nucleate on a preformed Ag NP surface, leading to a Ag@Au morphology. One would expect Ag NP cores and Au nano-shells if AgNO<sub>3</sub> was added first.

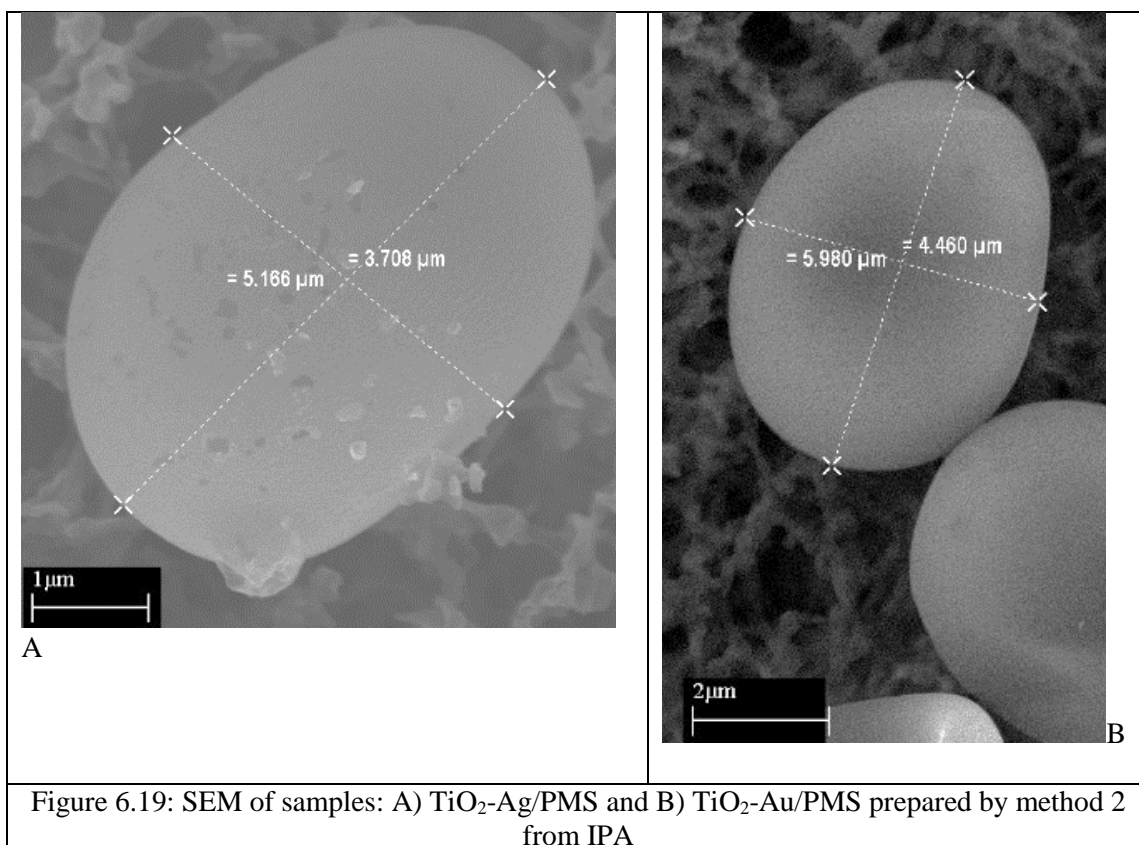


Figure 6.19: SEM of samples: A)  $\text{TiO}_2\text{-Ag/PMS}$  and B)  $\text{TiO}_2\text{-Au/PMS}$  prepared by method 2 from IPA

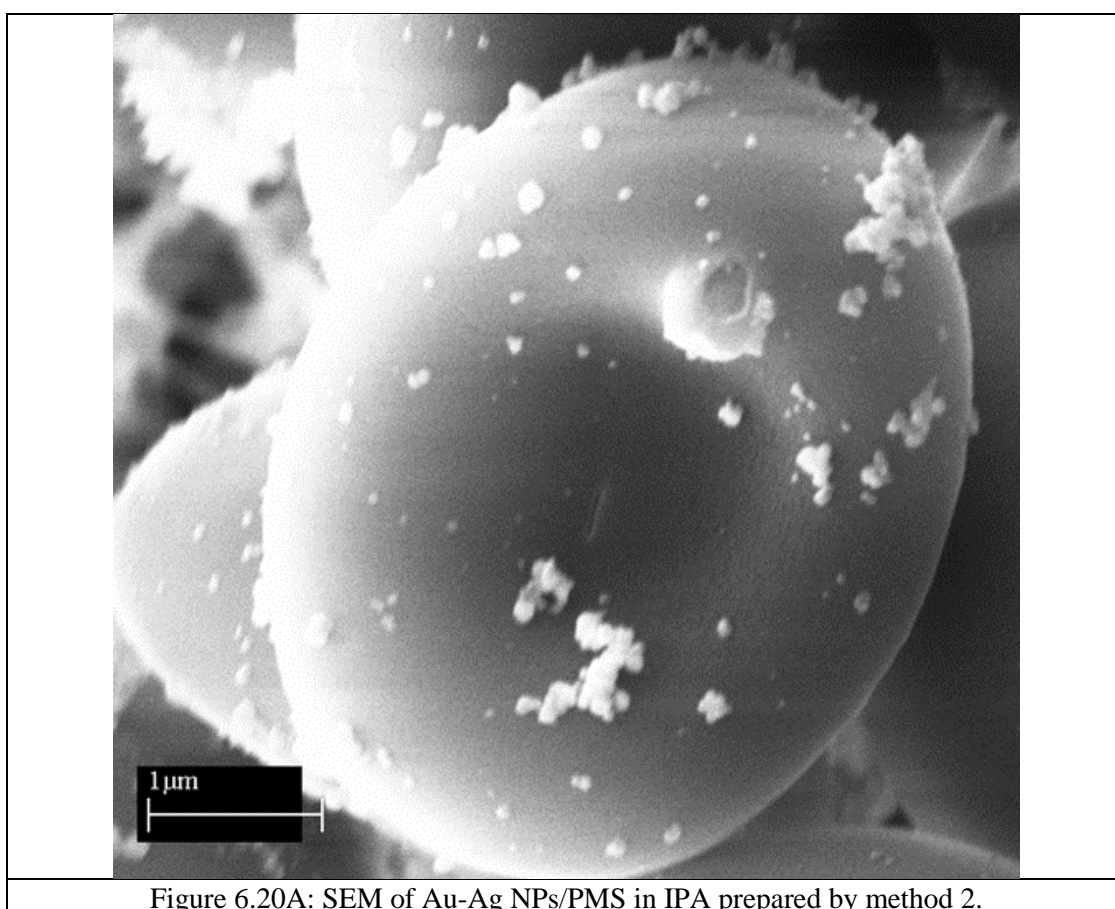


Figure 6.20A: SEM of  $\text{Au-Ag NPs/PMS}$  in IPA prepared by method 2.

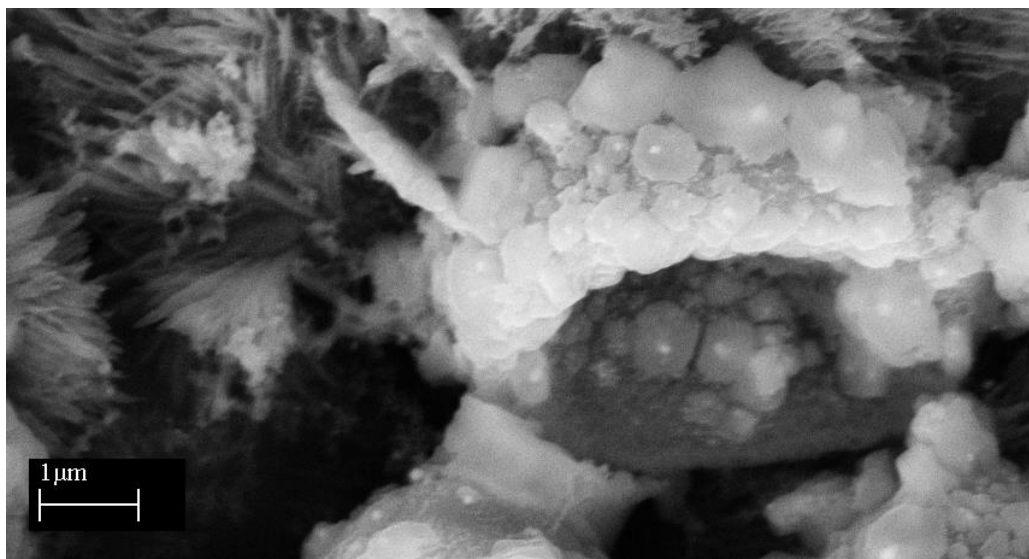


Figure 6.20B: SEM of Au-Ag NPs/PMS in H<sub>2</sub>O (filtrate) prepared by method 2; scale bar is 1 μm.

The EDX-derived distributions of Ag and Au loadings in Ag-Au/PMS produced by method 2 from water are considered in Table 6.8. This was the sample with the poorly dispersed Ag-Au seen by SEM in Figure 6.20. Clearly the total loading of Ag (51 wt.%) is higher than for Au (27 wt.%), but the loadings vary from location to location and even for the background are non-zero. This raises questions of accuracy in the author's mind.

TEM and the associated selected area electron diffraction (SAED) pattern with bright circular spots was now used to analyse samples (see Fig. 6.21-23 for the Au-TiO<sub>x</sub>/PMS and Ag-TiO<sub>x</sub>/PMS which prepared by method No.2). This showed the 10nm Au and Ag NPs on the PMS wall surrounded by TiO<sub>x</sub>. Their nanocrystalline nature was confirmed by the selected area electron diffraction (SAED) pattern with bright circular spots. The lattice fringe for Au-TiO<sub>2</sub> NPs had spacings of 0.23nm and 0.27nm corresponding to (111). Further, the (200), (220), (222) and (311) planes of the face centred cubic (FCC) lattice of Au NPs confirm that Au NPs are nanocrystalline. EDX suggested that Au-TiO<sub>x</sub>/PMS contained 7.7 at %Ti and 92.3 at %Au. In the future this ratio will need to be changed to raise the TiO<sub>x</sub> content for some applications.

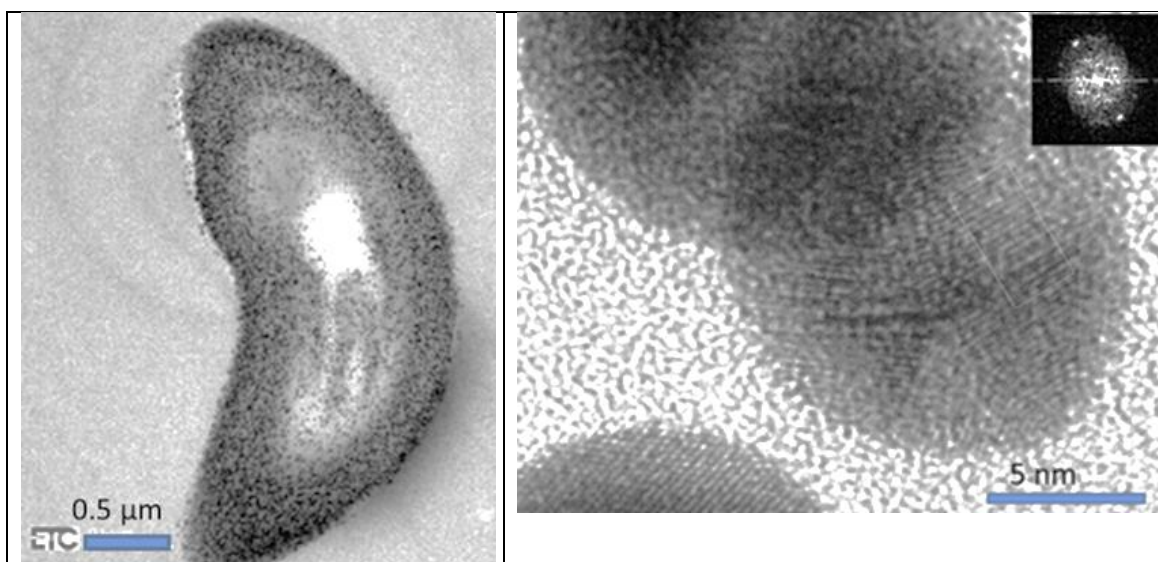


Figure 6.21: TEM images, selected area electron diffraction with bright circular spots of Au-TiO<sub>x</sub>/PMS.

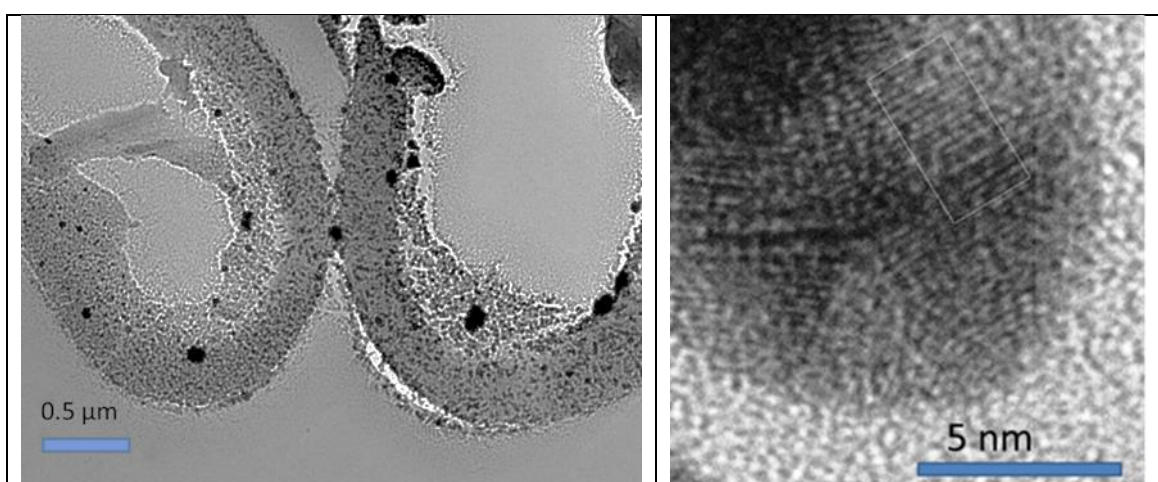


Figure 6.22: TEM images and selected area electron diffraction for Ag-TiO<sub>x</sub>/PMS.

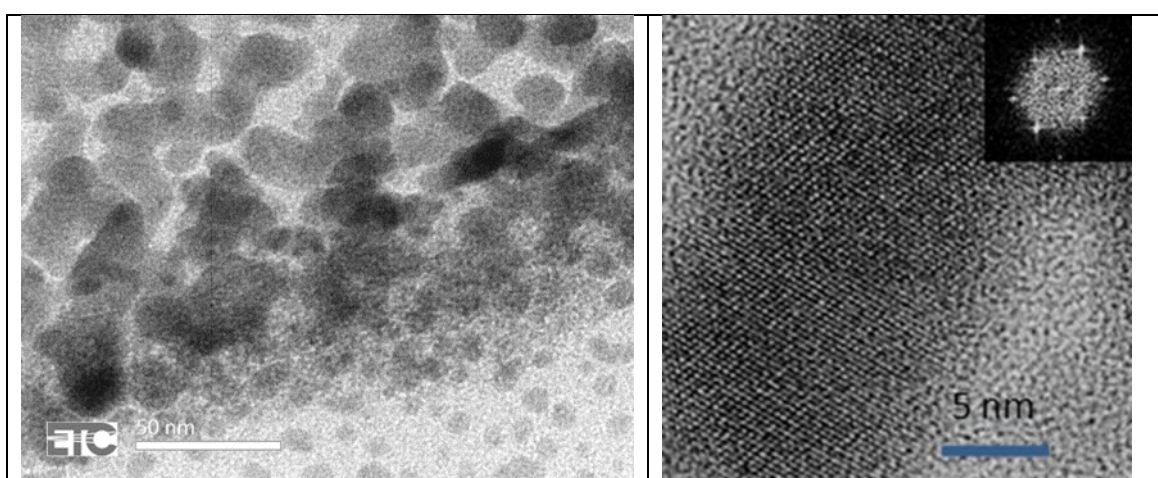


Figure 6.23: TEM images and selected area electron diffraction with bright circular spots Ag-TiO<sub>x</sub>/PMS<sub>IPA/H<sub>2</sub>O</sub>; (scale bar =50nm and 5nm)

### Calculation of weight of Au-Ag NPs/PMS

Table 6.8: EDX-derived elemental compositions of Au-Ag NPs/PMS derived from water and their background (prepared by method No.2).

	Wt.% Au NP	Wt.% Ag NP
(i)Au-Ag NPs with PMS	5.32	3.57
(ii)Background	1.93	2.10
(iii)Au-Ag NPs (white aggregate) on PMS	5.97	34.90
(iv)Au-Ag NPs with PMS (filtrate)	10.63	2.36
(v)Background (filtrate)	1.82	0.27
(vi)Au-Ag NPs aggregate out of PMS (filtrate)	1.85	8.14
Total	27.52 %	51.34 %

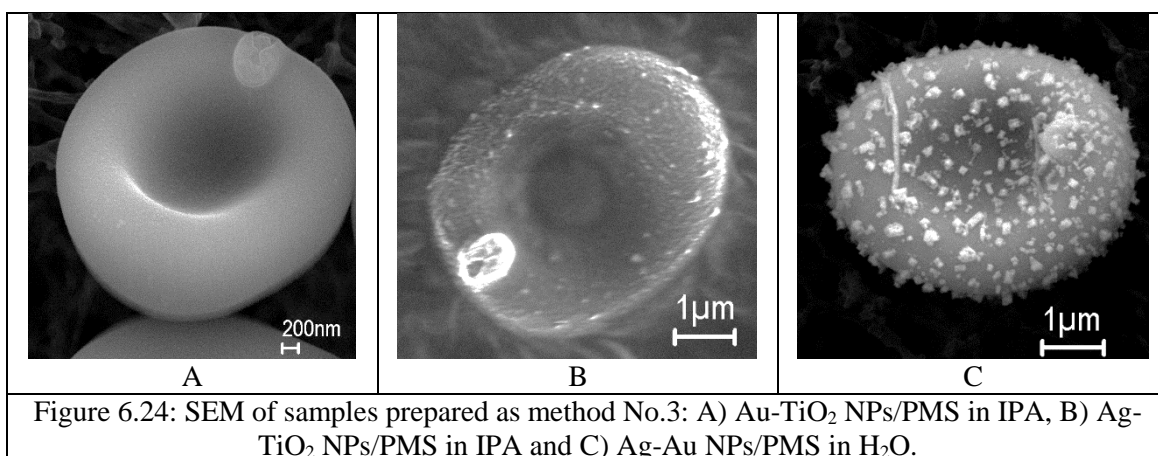
- **Method No.3 (described in section 4.2.4)**

Clearly, again  $TiO_x$  supports Ag and Au deposition in all samples, giving approximately the same at % and yet a significant difference was seen due to the change in the concentration of  $TiO_2$  (1mM).

Table 6.9: EDX-derived compositions of samples with PMS (prepared by method No.3).

	At. % Ti	At. % Ag	At. % Au	colour	pH
Ti-Ag NPs in IPA	0.04	0.13	---	colourless	basic
Ti-Au NPs in IPA	0.15	----	0.04	colourless	basic
Au-Ag NPs in $H_2O$	---	5.08	2.36	light pink	10

Figure 6.24 indicates that the morphology of PMS is unchanged by NP deposition and the Ag- $TiO_2$  and Ag-Au seen on the PMS surface was clear. Ti-Ag appeared as more nanoparticles on the PMS surface (Fig. 6.24B). Au-Ag NPs appeared in different morphologies and sizes (Fig. 6.24C).





➤ **Micro-FTIR ( $\mu$ FTIR) and FTIR**

Figure 6.25-29 show optical images,  $\mu$ -FTIR chem-maps and FTIR NPs of Ag/PMS, Au/PMS, Au-Ag/PMS, Au-TiO<sub>x</sub>/PMS and Ag-TiO<sub>x</sub>/PMS.  $\mu$ FTIR allows mapping of chemical functional groups in PMS (existing the red colour). The intensity scale associated with each image is such that blue and red extremes respectively correspond to low and high absorption values as given by spectral integration; this is directly related to a density scale (Beer–Lambert Law). Figures 6.25b-29b show some heterogeneity in the total absorbance of samples (4000-700 cm<sup>-1</sup>). Figures 6-25C show variations in the absorption bands of hydroxyl, carbonyl and amino groups in FTIR spectra of these samples at 1369 cm<sup>-1</sup> (C-O) and 1064 cm<sup>-1</sup> (C-N). These may be responsible for the reduction of the chloroaurate ions (AuCl<sub>4</sub><sup>-</sup>) and silver ions, along with saccharides, thereby biosynthesizing NPs [265].

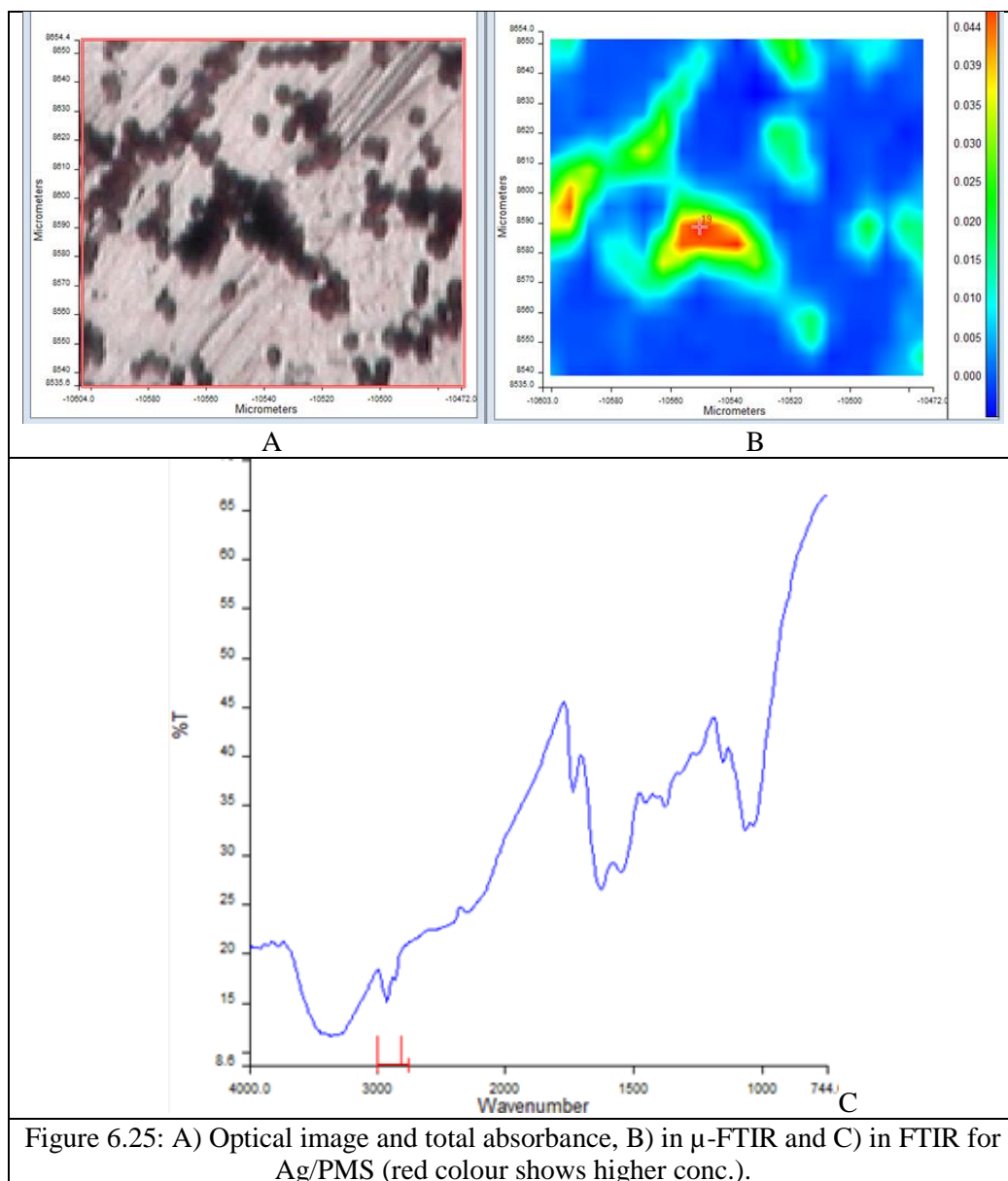


Figure 6.25: A) Optical image and total absorbance, B) in  $\mu$ -FTIR and C) in FTIR for Ag/PMS (red colour shows higher conc.).

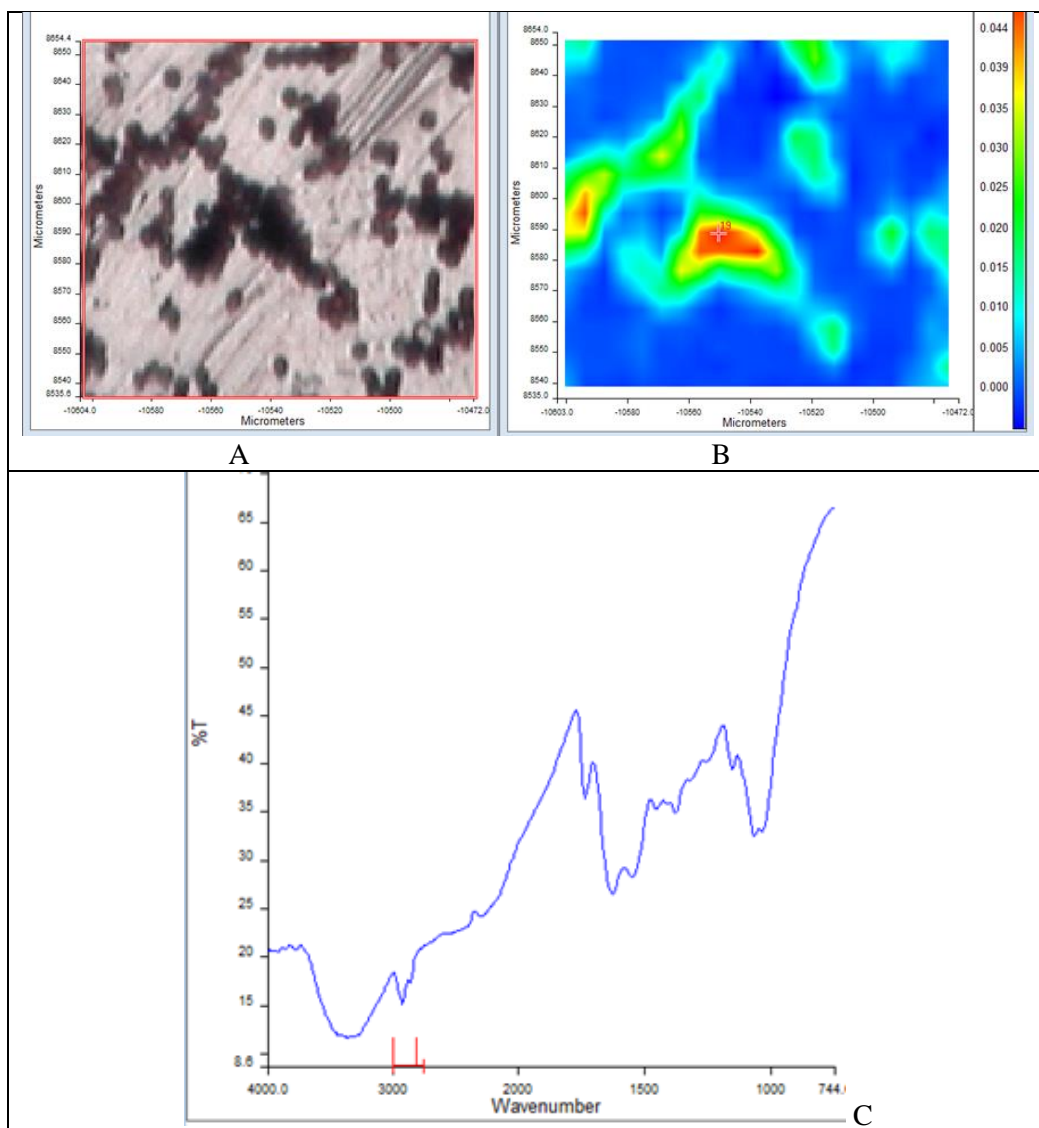


Figure 6.26: A) Optical image and total absorbance, B) in  $\mu$ -FTIR and C) in FTIR for Au/PMS (red colour shows higher conc.).

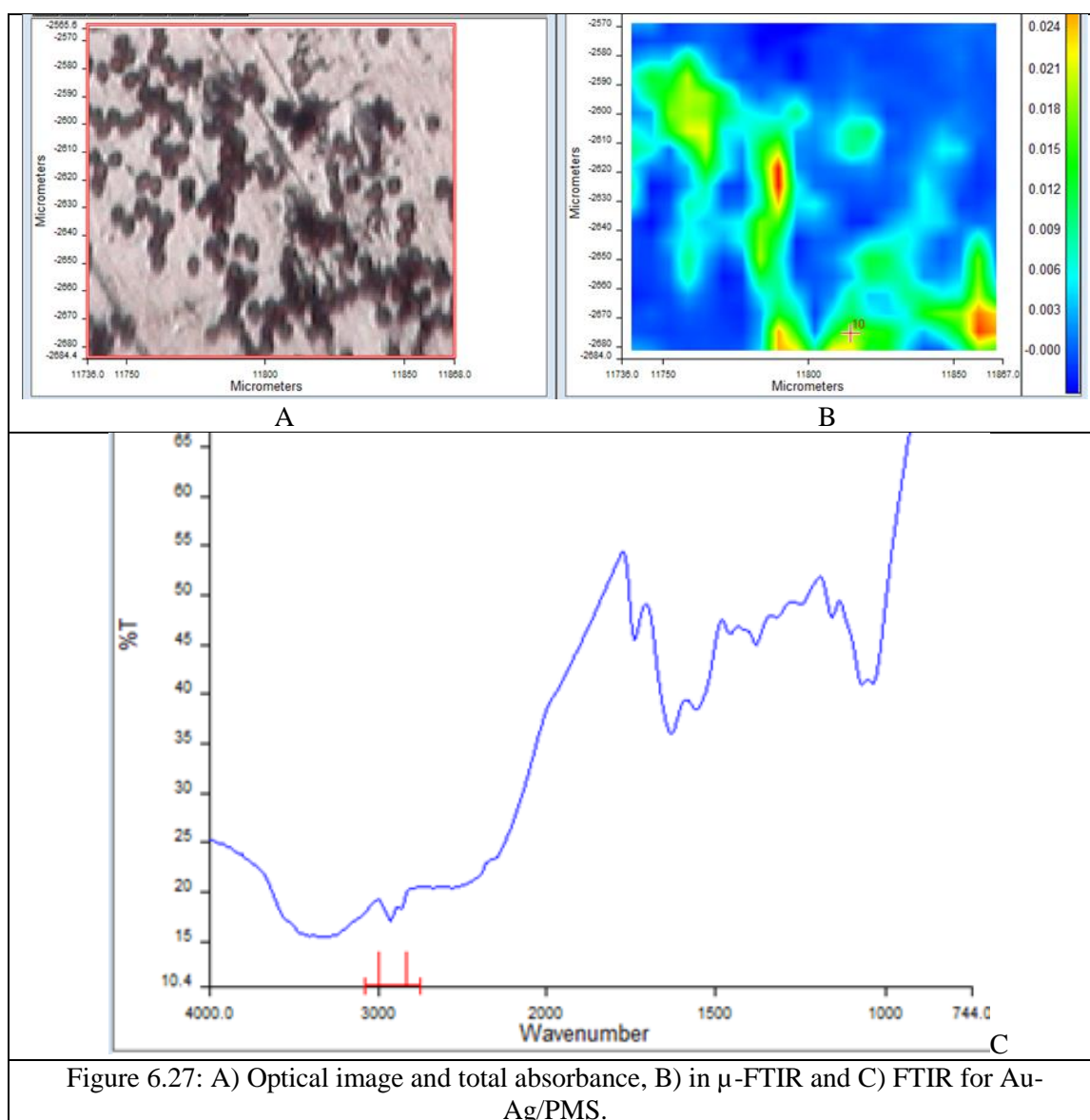


Figure 6.27: A) Optical image and total absorbance, B) in  $\mu$ -FTIR and C) FTIR for Au-Ag/PMS.

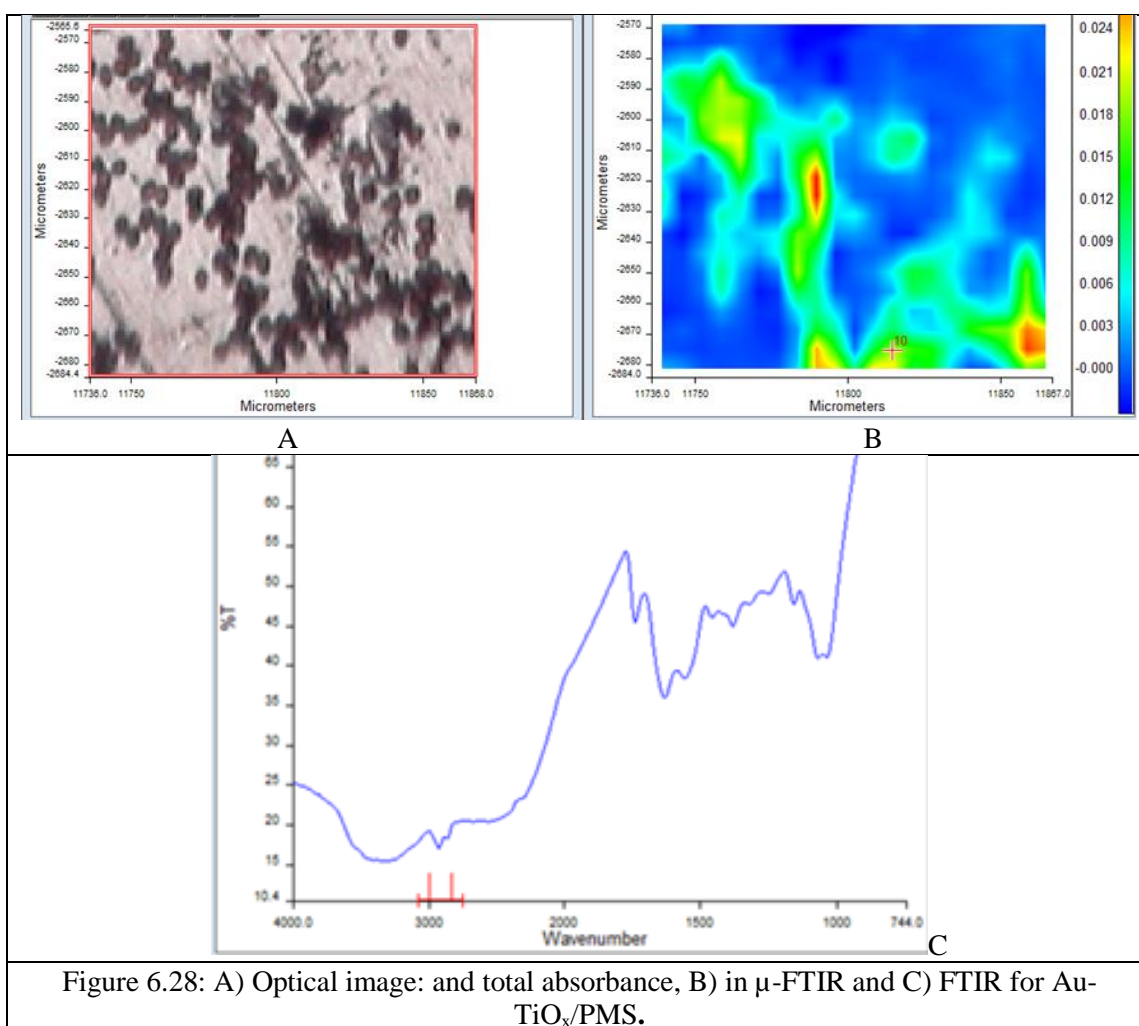
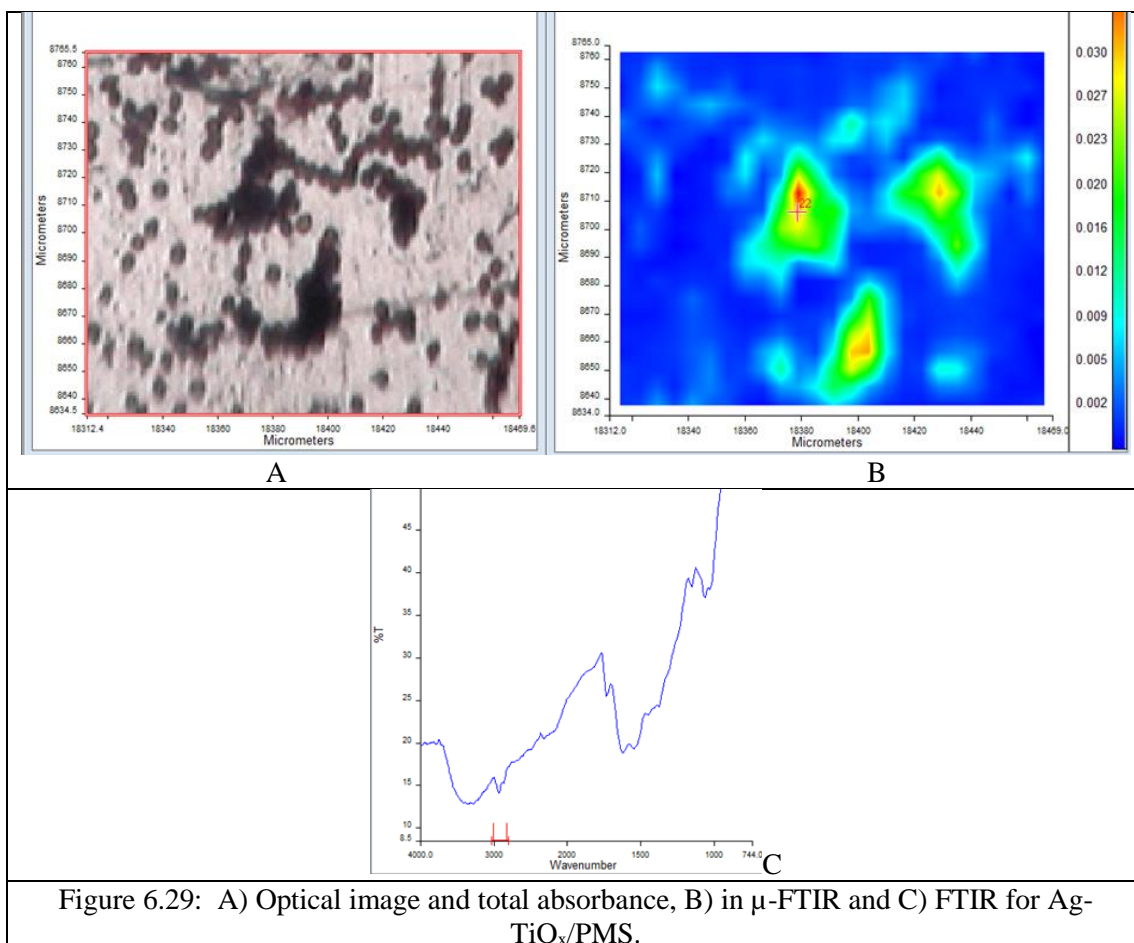


Figure 6.28: A) Optical image: and total absorbance, B) in  $\mu$ -FTIR and C) FTIR for Au-TiO<sub>x</sub>/PMS.



### ➤ Factors affecting nanohybrids formation with PMS using SEM

Many factors were studied in the preparation of PMS nanohybrids produced with different additions of various salts of Ag, Au and Ti alkoxide (as explained below). During the biosynthesis process of samples, the solvent, amount of the salt concentration, time and basic environment were changed in a way that allowed for studying the effect of factors on synthesizing NPs

#### 1- *Effect of solvent effect*

In all samples, it appeared that water is a better solvent compared to IPA. Firstly, in the same method (No. 2) with the same salts, Au-Ag NPs were found as large aggregates on the PMS when using IPA as a solvent. However, their distribution was much better when water was the solvent. Of course, Au and Ag salts dissolve well in water, which is a better solvent than IPA for the preparation of Ag-Au NPs (by methods No.1 and 2) because the ratio % increase in Ag NPs (2% in IPA to 4% in H<sub>2</sub>O) and Au NPs (2% in IPA to 5% in H<sub>2</sub>O). Secondly, with method No. 3, Figure 6.30 illustrates that Au-Ag

NPs/PMS are clearly coated in water as solvent, but less well for TiO<sub>2</sub>-Ag NPs using a IPA solvent.

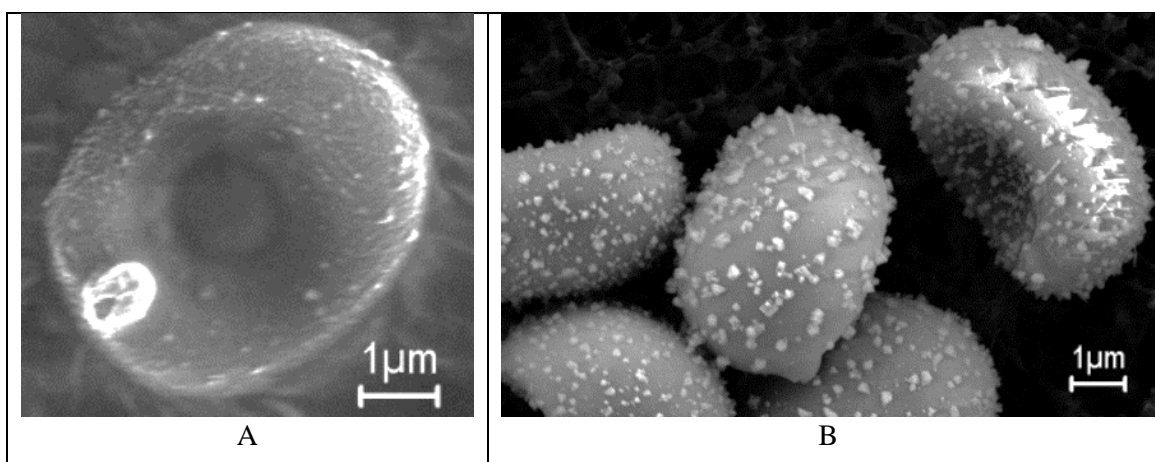


Figure 6.30: SEM of samples prepared with PMS by method No.3 with different solvents: A) TiO<sub>2</sub>-Ag NPs/PMS in IPA and B) Au-Ag NPs/PMS in H<sub>2</sub>O.

## 2- Effect of time

The effect of the time for nanohybrid PMS was now explored. Au-Ag NPs/PMS was prepared in the same concentration (1mM), by method No.3 and with the same solvent (water). The precipitate was filtrated after one day. Then, after 7 days, the samples were prepared for SEM analysis. Figure 6.31 illustrates that time is a pivotal factor, because the precipitate of Au-Ag NPs/PMS (see Fig.6.31A) clearly shows nanoparticles.

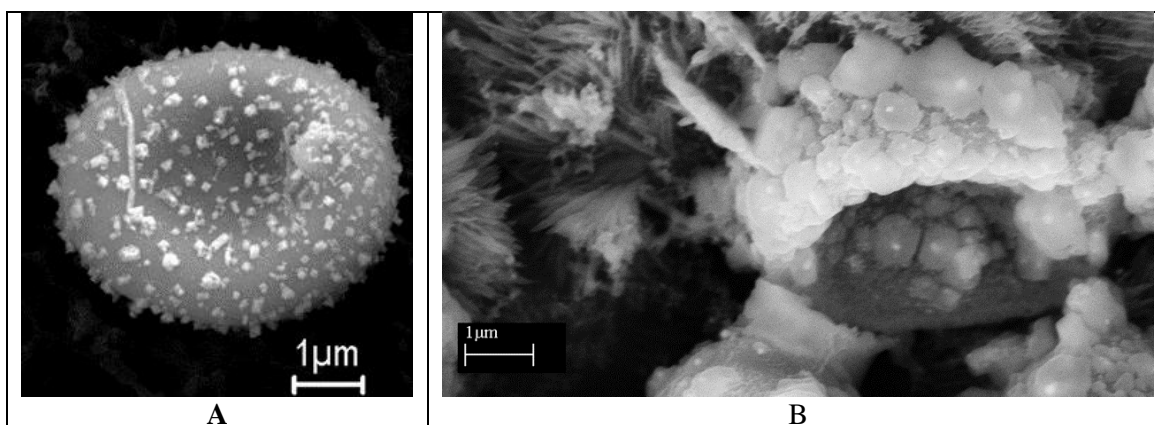


Figure 6.31: SEM of samples prepared with PMS from the same solvent, by the same method and at the same concentration (1mM) but where time was longer: A) Au-Ag NPs /PMS from H<sub>2</sub>O and B) Au@Ag NPs/PMS (filtrate) in H<sub>2</sub>O after 1 week; (scale bar=1μm).

However, the filtrate solution contained some Au-Ag NPs/PMS where they took around 7 days to nucleate and aggregate as nanoparticles. Ag@Au nanohybrids can be clearly seen in Figure 6.31B that shows that more Au NPs can grow around Ag NP, forming larger shell thicknesses.

### 3- *Effect of pH*

The two samples, which were prepared by method No.3, at the same concentration (1mM), but with different solvents and pH, have different weight ratio and structures. TiO<sub>x</sub>-Ag NPs were prepared in basic solution (1 drop of 0.1M KOH in IPA) and left to react with PMS (see Fig. 6.30A). It can be said that the IPA does not facilitate stabilization or enable pH measurement that may be >> 7. However, when Au-Ag NPs were prepared, a buffer solution (pH=10) was added to the solution. Figure 6.31B shows that the pH factor is very clear in the reaction of nanoparticles with the PMS. Many functional groups were found on the surface of PMS (e.g. aldehyde, carboxylic, sulfhydryl (R-SH), riboflavin and amino acids). These functional groups have a negative charge, depending on the pH of solution. They have a strong ability to bind with gold and silver ions. It seems that they are responsible for the reduction of Au and Ag ions to zero-valent/nano-scales.

## 6.4. Conclusions

Present results show that nanoparticles (NPs) can be biosynthesized at room temperature on the reductive/chelating surfaces of Portobello mushroom spores (PMS). Using this green approach surface-held TiO<sub>x</sub>, Ag, Au, Ag-TiO<sub>x</sub> and Au-TiO<sub>x</sub> NPs have been prepared. Such surface NPs were characterized by SEM, EDX, TGA, FTIR, UV-Vis, DLS and SIMS. Different preparative conditions were studied: chemical reducing agents (e.g. NaBH<sub>4</sub>, TSC and their mixtures), pH, time and concentration with and without PMS as a biotemplate-reducing agent. The results suggest that the NP coating is achieved with Au NPs on PMS in a water-free solvent condition. In contrast, TiO<sub>2</sub> NPs do not coat to a high weight loading using IPA as a water-free solvent. A pH of 10 helps to activate the PMS surface (containing as it does many functional groups such as COO<sup>-</sup> and OH<sup>-</sup>). PMS is a useful biotemplate and reductive-chelator; its use is better than simple chemical reagents in solution.



## Chapter 7: Biosynthesis of nHAp/PMS microspheres for medical applications

---

In this chapter, ions ( $\text{Ca}^{2+}$ ,  $\text{CO}_3^{2-}$ ,  $\text{HPO}_4^{2-}$  and  $\text{Ag}^+$ ) were incorporated onto/into PMS and thereby nHAp/PMS nanohybrids were prepared to use in bone replacement as a scaffold. This research characterized all these samples using SEM, TEM, XRD, EDX,  $\mu$ -FTIR, UV and TGA which are described in chapter 3.

### 7.1 Introduction

Over the last decades, many biomimetic materials synthetic studies have attempted to imitate natural material growth. There has been an increased demand to produce biomaterials (e.g. for bone regeneration that mimic the properties of real bone) [266]. Bone tissue engineering (providing scaffolds) is a significant part of biotechnology and regenerative medicine (that develops functional materials for orthopedic reconstruction delivers biomolecules to cells [115]). Thus, scientists have paid special attention to synthesize hydroxyapatite (HAp) and especially nano-size hydroxyapatite (nHAp) due to its:

- (i) excellent biocompatibility [267],
- (ii) fast stabilization with tissues,
- (iii) slow biodegradation [266] and
- (iv) good biomedical applications, (like artificial and bone repair, bone filler bioactive coatings [268], gene and drug delivery, proteins chromatographic packing, scaffold [192] and bone for tissue engineering ) [269].

HAp has a chemical similarity to the crystal calcium phosphate mineral present in biological hard tissue ( e.g. teeth and bones which are the inorganic constituent of biological hard tissue) [189]. Remarkably, HAp has potential to be an interface between a metal implant with the tissues of human body *in vivo* [270], because of its high osteoconductive properties. This is partly because the unit cell of HAp and natural bone are the same. This is the main reason why HAp has been proposed as an implant material. Natural bone contains carbonate ions, and some reports show that carbonated

hydroxyapatites are biologically reactive than pure HAp [271] (i.e. HAp alone has weak load-bearing properties and a tendency to migrate from implant sites [267]). In addition, HAp has good thermal stability [272] and no constituent toxicity [111].

HAp exists in tendons, bone and teeth; giving stability, hardness and functionality. It is largely used in orthopaedics or in dental implants due to the formation of a strong bond with other adjacent hard tissue. HAp integrated into bone does not cause inflammation or any immune reaction during implantation as a bone filler [273]. As a result of these properties, HAp is effective in such applications using biocompatible materials; both its purity and morphology can be modified [274].

### 7.1.1 Bone structure

The main composition of human bone tissue is a naturally occurring organic/inorganic hybrid mainly consisting of 65-70% HAp with  $K^+$ ,  $Mg^{2+}$ ,  $Cl^-$ ,  $Na^+$  and  $F^-$  [275] (see Table 7.1), with 10 % water and organics (collagen, etc.) in small amounts [273].

Table 7.1: Composition of inorganic mineral content of some adult human tissues [273].

Elements	(wt.%)			Elements	(wt.%)		
	enamel	dentin	bone		enamel	dentin	bone
Ca	36.5	35.1	34.8	Mg	0.44	1.23	0.72
P	17.7	16.9	15.2	K	0.08	0.05	0.03
Ca/P ratio	1.63	1.61	1.71	F	0.01	0.06	0.72
Na	0.5	0.6	0.9	Cl	0.30	0.01	0.13

The primary organic phase of the bone matrix is collagen, which is secreted by osteoblast cells. The collagen forms into self-assembled bundles of fibers, which mostly orientate themselves parallel to the load-bearing axis of the bone [276]. Moreover, the HAp/collagen combination contributes to the mechanical properties of bone and slow rate of dissolution. Here, it was envisaged that the combination of HAp with a polymer matrix or organic biomolecule could take advantage of the material's properties and would be easily optimized. The apatitic calcium phosphate bone mineral consists of small amounts of carbonate, a small amount of sodium, magnesium and other trace elements [195]. Pure HAp alone does not contain any carbonate; it is very different from the biological apatites (see Fig. 7.1) that contain carbonate and are calcium-deficient [266].

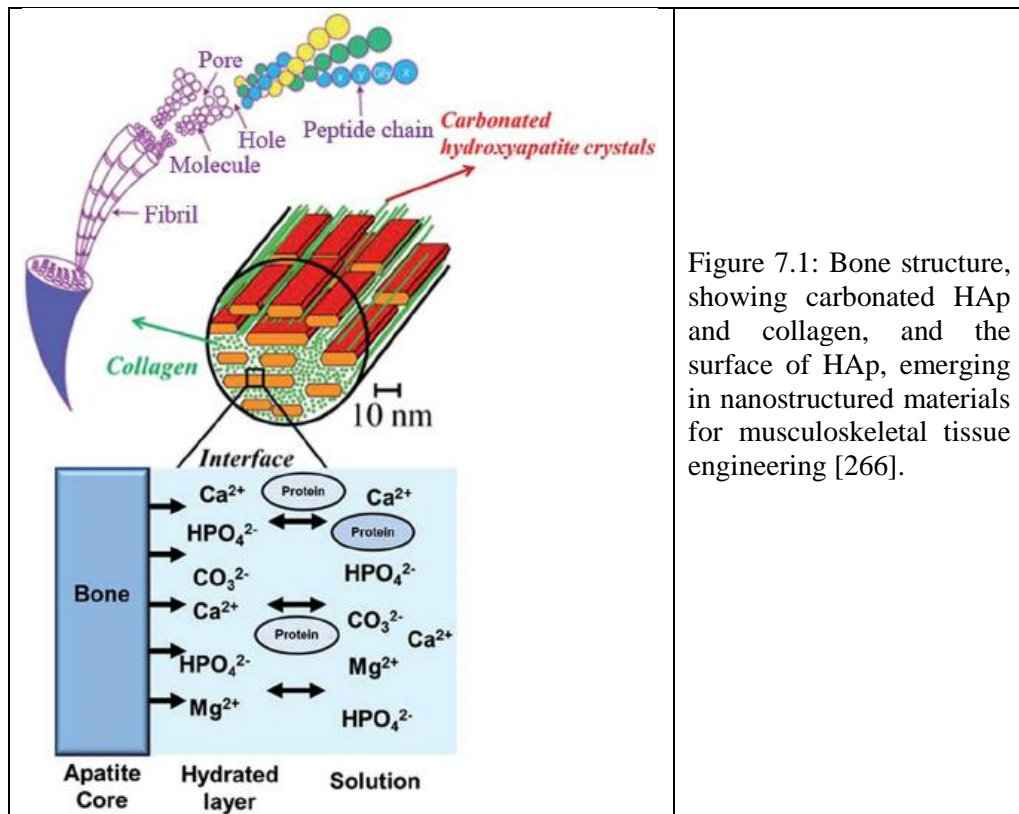


Figure 7.1: Bone structure, showing carbonated HAp and collagen, and the surface of HAp, emerging in nanostructured materials for musculoskeletal tissue engineering [266].

The solubility of solid ceramics can be modified by changing their composition (i.e. substituents or impurities), and physical form (i.e. particle size, density or porosity). Crystallinity, particle size, morphology and defects play a significant role in the extent of such ceramic solubility. For example, the average particle size is one of the factors affecting solubility through the Kelvin equation (see eq. 7.1) [277]:

$$\log S/S_0 = 2\gamma v_m / 2.303 RT r \quad \text{----- (7.1)}$$

where, S: the solubility of infinitely large particles,

$S_0$ : the solubility of nanoparticles,

$V_m$ : the molar volume,

$\gamma$  : surface tension of the solid,

r: the radius of the nanoparticles,

R: gas constant (8.3 J/K mol) and

T: isothermal temperature (K).

According to the Kelvin equation, the solubility of a nanoparticle increases as the radius or diameter of the nanoparticle decreases. That means, a nanoparticle is more soluble than a micro particle. Further the surface tension of NPs may differ from bulk materials. Here, small bone chips that used to be harvested in operations were interesting because of their potential to fill a large bone gap, and this was taken up. Into the bone gap are placed such small fragments of bone clipped from an adjacent callus. Interestingly, circulation is allowed to return and the gap becomes filled with blood around the fragments of chipped bone [278].

Bone particle shape can be (i) a needle-like (with 5-20nm as a width and 60nm lengths, which are responsible for the strength and rigidity of bones) or (ii) plate-like (typically 50nm long, around 25nm wide and on average 3nm thick) [276].

### 7.1.2 The crystalline structures

A single unit cell of HAp consists of 44 ions, which include 10  $\text{Ca}^{2+}$ , 6 tetrahedral ( $\text{PO}_4^{3-}$ ), and 2  $\text{OH}^-$  groups along the c-axis, leading to balance of charge; these are all organized into a hexagonal structure [279]. The lattice parameters are  $a = b = 9.4225 \text{ \AA}$  and  $c = 6.8850 \text{ \AA}$ . Submicroscopic crystals of calcium phosphates in bone resemble the crystal structure of synthetic HAp [273]. HAp is reported as having two crystalline structures: hexagonal and monoclinic [280]. The more important structure is the hexagonal one that is elongated in the c-axis, owing to the symmetry of the unit cell. The HAp structure includes unconnected tetrahedral phosphate groups [268] with calcium ions in the spaces, and  $\text{OH}^-$  ions along the c-axis balance the charge [281]. The c-plane is terminate with phosphate ions and acquires negative charge. This means that the c-plane HAp surface can be more hydrophilic (negatively charge) than the a-plane HAp surface (positively charge). Bones consist of HAp nanocrystals arranged on collagen belts. It is known that the shapes of bones are controlled by crystallinity, grain size and the aspect ratio (AR) of areas between the end (c-plane) and side (a-plane) faces of HAp nanocrystals (see Fig. 7.2) [282].

Commercial samples of HAp include Bio-Oss, Nano and  $\beta$ -TCP; these are used in clinical applications. They have with high crystallinity [266]. Pure HAp [ $\text{Ca}_{10}(\text{PO}_4)_6(\text{OH})_2$ ] has a stoichiometric apatite phase with a molar ratio of Ca/P of 1.67 [268]. For biomedical applications, HAp (Ca/P = 1.67),  $\beta$ -TCP (Ca/P=1.5) and biphasic calcium phosphate (which mainly consists of a HAp and  $\beta$ -TCP mixture in various ratios) are mainly used. In living systems the Ca/P is found in the form of crystalline HAp and

amorphous calcium phosphate (ACP) [273]. Methods of HAp synthesis and their technological parameters can significantly impact the physicochemical properties and the stoichiometry of the synthesized product, its crystallinity average, particle size, phase, composition, thermal stability, microstructure and mechanical properties [273]. These can be well-controlled by the precise conditions of the chemical precipitation route [274].

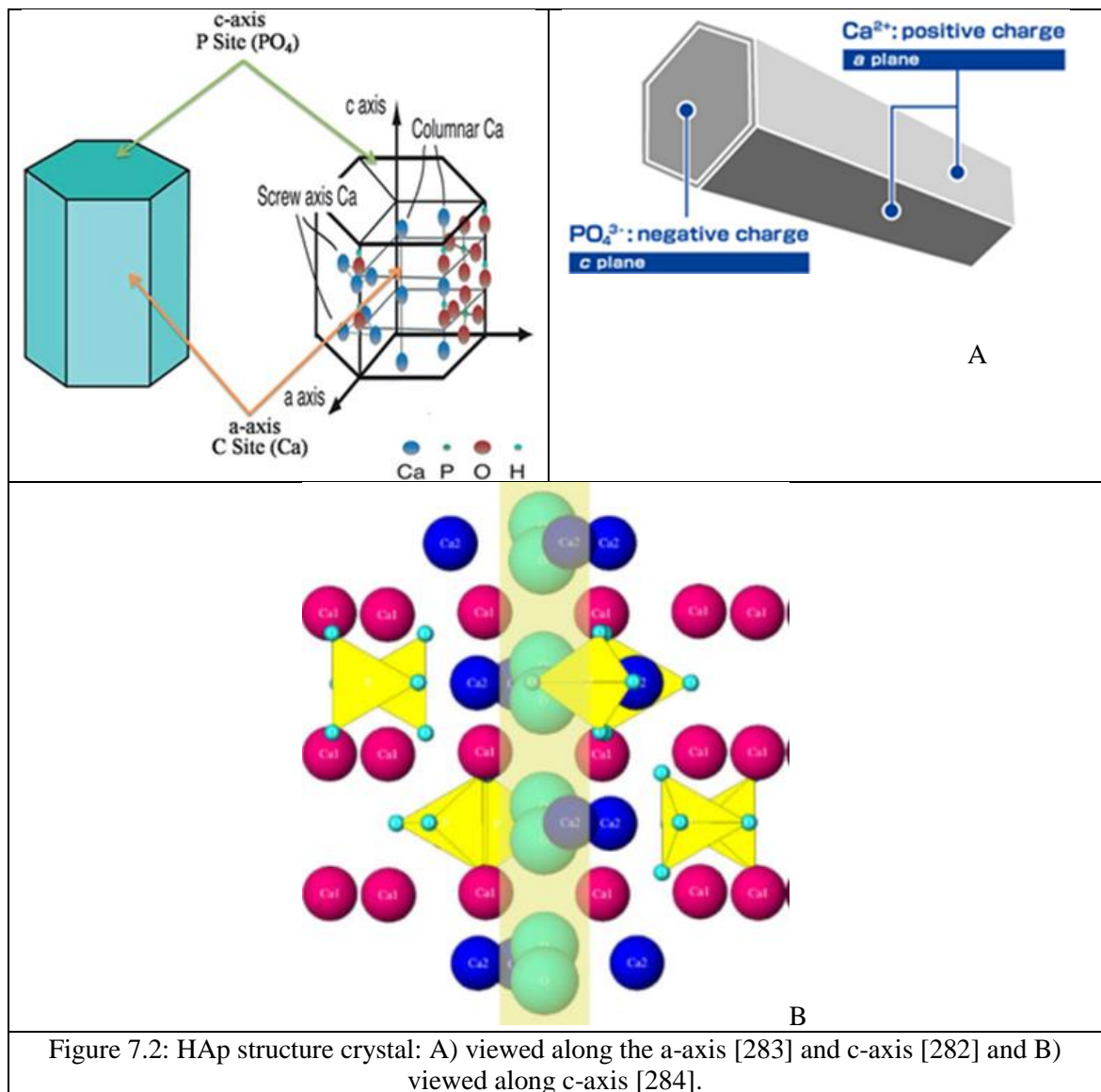
### 7.1.3 Nano and hollow spheres of HAp

The average crystallite size is important to the understanding and defining the properties of all nanoscale materials. nHAp exhibits different interesting properties (e.g. surface reactivity, optical, magnetic and other physical properties) that depend on its average particle size [174], that also defines biocompatibility and adsorption (removing heavy metal and separation of biomolecules) properties [285].

In medical applications, nHAp crystal is better positioned to serve as a HAp substitute of bones than larger micro-HAp and so it plays an important role in defining its biological activity and cytophilicity (a generic term referring to substance that is attracted to cells as cytophilic antibody) during bio-mineralization [276] because of its:

- (i) high surface area energy (leading to the enhancement of the mechanical properties),
- (ii) physical properties (different from those of bulk particles),
- (iii) novel growth process (where the size of 20 nm of particles is shown to be the best inhibitor of cell growth [276]), and
- (iv) desirable cell multiplication (so as to optimize biological functionality), a property which is highly dependent on particle size.

Porous hollow HAp microspheres are even more useful for biomedical applications (due to their high capacity for the loading of drugs and their specific surface area). Many methods have therefore been developed for the preparation of HAp hollow spheres (e.g. DNA-templated hydrothermal methods, biopolymer (polyaspartic acid)-assisted assembly from HAp nanorods, solvothermal methods and others [111]).



## 7.2 Methods of Analysis

### 7.2.1 General approach

Using PMS as biotemplates can be affected via their surface which contains suitable sites for the nucleation and growth of nHAp crystals. For example, proteins, lipids, glycoproteins and polysaccharides can control the nucleation of Ca and  $\text{PO}_4^{3-}$  phase by stereochemical recognition. Moreover, carboxyl or hydroxyl groups can act as synthetic mimics of a natural template and these function groups can react with Ca and  $\text{CO}_3$  ions leading to a change in their concentration and act as nucleation sites able to orient growth of nHAp/PMS crystals [286].

There are many factors that impact on  $\text{CaCO}_3$  crystallization by  $\text{CO}_2$  bubbling into  $\text{CaCO}_3$  solution as:

- (i) pH effect on the morphology of crystals because when the pH value increased, the precipitation of time decreased,
- (ii) the concentration of  $\text{CaCl}_2$  influences the morphology of crystal because it determines the factor which is supersaturation (S) (a dimensionless ratio of the concentration of salt to equilibrium molecular solubility product  $K_{sp}$ ). The relationship is ( $S = C / K_{sp}$ ) and
- (iii) temperature and stirring speed show a little influence on the morphology of crystal [287].

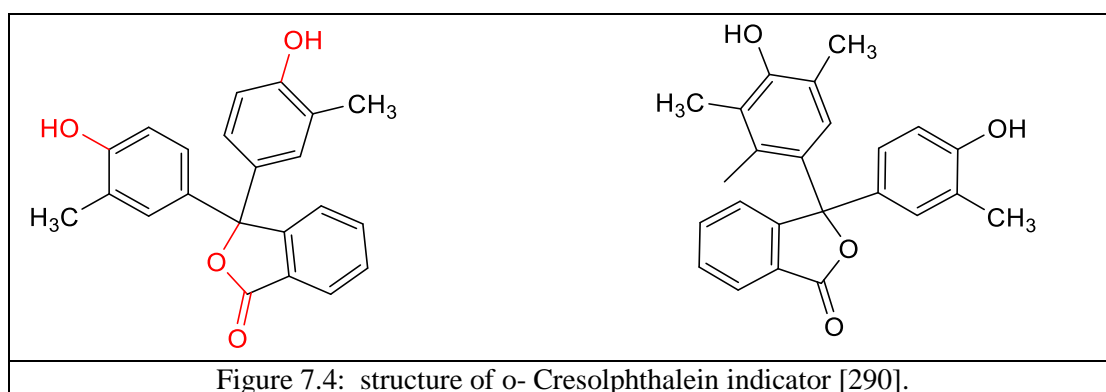
$\text{CaCO}_3$  particles has been introduced into an aqueous solution under  $37^\circ\text{C}$  to obtain  $\text{CaCO}_3/\text{PMS}$  and  $\text{CaCO}_3$  microspheres. Traditional methods for fabricating HAp microspheres mainly rely on the approaches involving organic solvents and surfactants that are hazardous to human health and the environment. A hydrothermal chemical reaction always includes harsh conditions such as high temperature and high pressure that will undoubtedly damage the bioactivity of the bio-macromolecules. Here, the preparation of nano-HAp (nHAp) was rapid, surfactant-free, and environmentally-friendly. It is important to note that here one presents a method in which nHAp/PMS is that prepared contained carbonate; some reports show that carbonated hydroxyapatites are biologically more reactive than pure HAp [271]. The Ca/P ratio in the inorganic component on the PMS (mainly carbonate-substituted apatite) is thought to more closely resemble biologically-inspired HAp, such as bone mineral and the nano-apatite-derived from  $\text{CaCO}_3$  templates and shows a typical nano-rod shape. Because natural bone contains carbonate, some reports show that carbonated hydroxyapatites are biologically more reactive than pure HAp [271] ( HAp alone has no strong load bearing properties and a tendency to migrate from implant sites [267]). In contrast, HAp Bio-Oss phase is not clear and has a rod shape. Such carbonated apatite with poorly crystallized features is significant for reabsorption and remodeling processes in tissues. A colorimetric analysis method is used to determine the concentration of phosphate and  $\text{Ca}^{2+}$  ions using spectrophotometry. At first, to determine the concentration of phosphate ions, an adaptation of the ascorbic acid method is used. The analysis of orthophosphate  $\text{PO}_4^{3-}$  ions is based on the reaction of a phosphor-molybdate blue complex using ascorbic acid as acidic solution reductant. The mechanism of the reaction occurs in two stages:

- (i) the reaction phosphate ions with (molybdenum dioxide) for formation of a structure heteropoly acid complex  $[\text{PMO}_{12}\text{O}_{40}]^{n-}$  [288] and





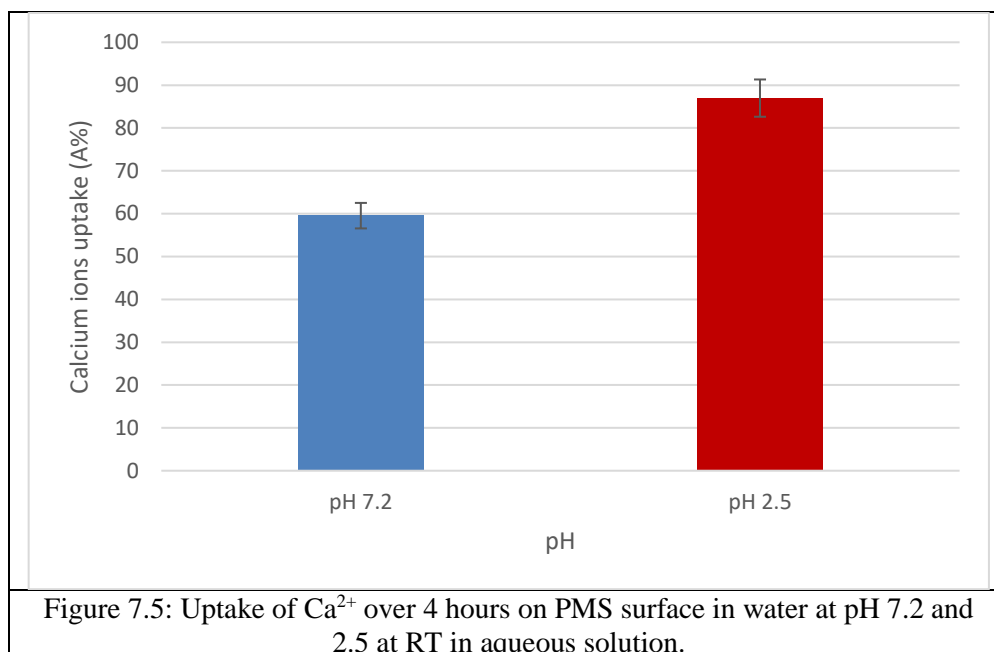
An alternative approach to the analysis of  $\text{Ca}^{2+}$  and  $\text{PO}_4^{3-}$  concentrations uses O-cresolphthalein as a chelating agent and a pH indicator used in titrations (see Fig. 7.4). It is soluble in ethanol, not in water. It is colourless below pH 8.2, and purple above pH 9.8. At first, ortho-cresolphthalein is mixed with 8-hydroxyquinone in acid medium to avoid  $\text{Mg}^{2+}$  interference (i.e. removal of  $\text{Mg}^{2+}$  ions). Then, this solution is reacted with  $\text{Ca}^{2+}$  ions in alkaline medium (pH 10.7) using 2-amino-2-methyl-1-propanol (AMP). At last, a red colour appears depending on  $\text{Ca}^{2+}$  ions concentration. The mechanism of the reaction depends on concentration of Ca ions. At low  $\text{Ca}^{2+}$  ions concentration, one-to-one complex forms while two moles of  $\text{Ca}^{2+}$  ions react with one mole of O-cresolphthalein at high  $\text{Ca}^{2+}$  concentrations [290].



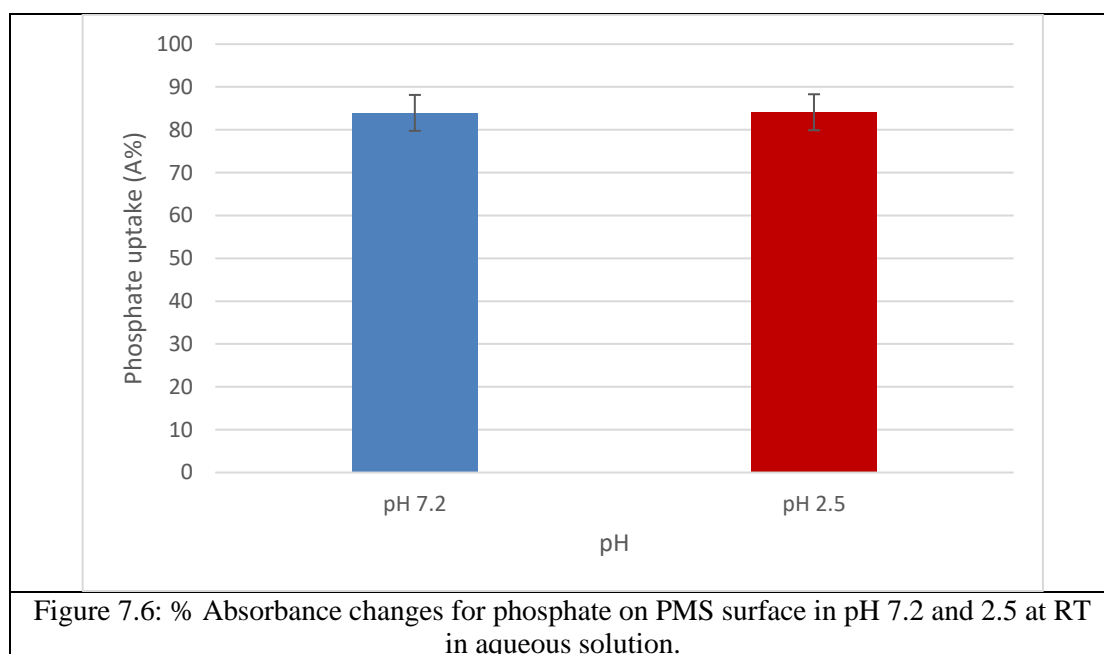
## 7.3 Results and Discussion

### 7.3.1 Uptake of Ca and phosphate ions on PMS surfaces

The uptake of  $\text{Ca}^{2+}$  and phosphate ions by PMS in  $\text{H}_2\text{O}$  at RT was measured over 4h as showed in Figure 7.5 and 7.6. At pH 2.5, the uptake of (Ca/PMS) was higher than phosphate/PMS at the same time, because the main charge of the PMS surface is negative (with many hydrophilic (negatively charge) groups) are able to interact with the small  $\text{Ca}^{2+}$  ions [291]. For example, the negative charge of carboxylic groups on the surface of PMS can bind with  $\text{Ca}^{2+}$  electrostatically with the formation of a  $-(\text{COO})_2\text{Ca}$  complex [113].

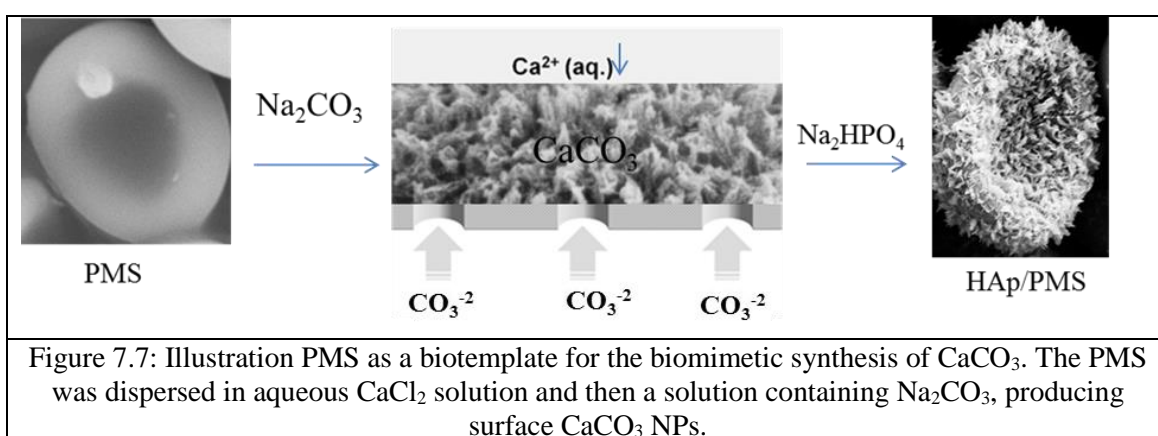


Decreasing the pH value appears to increase  $\text{Ca}^{2+}$ /uptake (Fig. 7.5), but leaves phosphate ion uptake unchanged (Fig. 7.6). Thus, at pH 2.5,  $\text{Ca}^{2+}$  showed a higher concentration on the PMS surface reaching to up 90%, suggesting that Ca ions (positive charge) reacts with carboxyl group (negative charge) electrostatically on PMS surface more than at pH 7.2 (when it was around 60%). In contrast, phosphate ions/uptake (around 80%) is unchanged by pH.



### 7.3.2 nHAp/PMS

The method has just three steps:  $\text{Ca}^{2+}$  adsorption,  $\text{CO}_3^{2-}$  adsorption and  $\text{PO}_4^{3-}$  adsorption on PMS with the formation of nHAp on the PMS a biotemplate (Fig. 7.7). The phosphate was introduced into the PMS suspension immediately after the synthesis of the  $\text{CaCO}_3$  NPs, and then the active sites on the cell wall of PMS are triggered to construct a composite upon elevation of the system to physiological temperature [110]. Thus, the conversion of the  $\text{CaCO}_3$  particles and the self-assembly of nHAp/PMS occurred at the same time. The author believes that PMS provides many suitable sites for nucleation and growth of nHAp crystals.



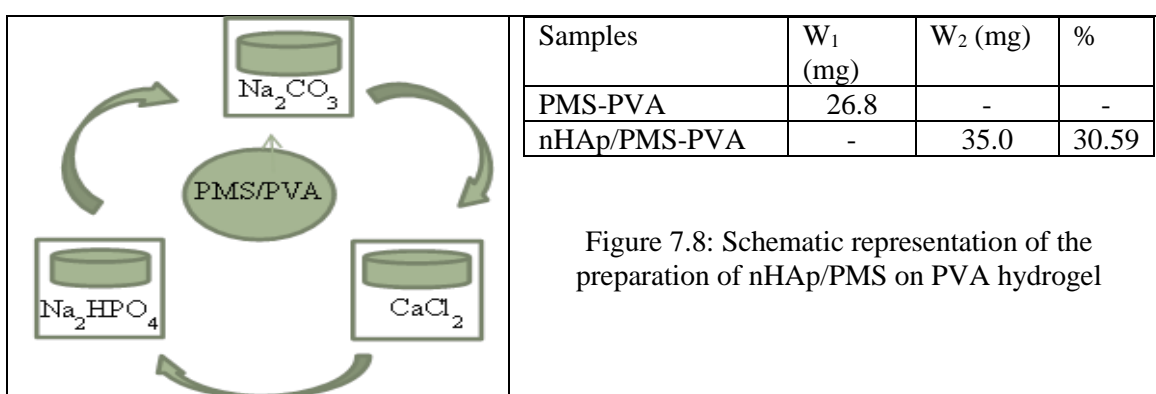
Here, PMS was used as novel platform for biomimetic mineralization for  $\text{CaCO}_3$ , which is then in contact with a phosphate solution according to Eq.(7.4) [286]:



The chemical nature of the PMS is important, since a cooperative effect between PMS-bearing  $\text{COOH}$  and  $\text{OH}$  groups has been recognized as the key factor. The growth of  $\text{CO}_3^{2-}$  crystals was facilitated by sodium carbonate introduction and diffusion through the macropores of the support and across the PMS surface, yielding biomimetic calcium carbonate mineralization. Then, HAp nano-rods form through a crystal-growth process at  $37^\circ\text{C}$  over 3 days owing to the electrostatic adsorption of phosphate onto the PMS surface. Then, these nHAp nanocrystals start to self-assemble to form nanostructures on the PMS surface. In addition, PMS has phosphorus in the cell wall structure (as phospholipids); this helps to produce more phosphate ions [286]. PMS produce  $\text{OH}^-$  and  $\text{COO}^-$  on its surface, which react with  $\text{Ca}^{2+}$ , then this will incorporate phosphate ions to form the nuclei from a reaction between  $\text{PO}_4^{3-}$  and  $\text{Ca}^{2+}$  ions in aqueous solution.

### 7.3.3 nHAp/PMS-PVA hydrogel film

Figure 7.8 shows nHAp/PMS formation in PVA hydrogel film by sequentially immersing this in three solutions for 8 reaction cycles. PVA hydrogel is used as a model matrix, with hydrogel-based scaffolds widely used for building suitable microenvironments [110] for compositions and structures similar to natural tissues. nHAp crystals are formed using conventional methods with bio-microtemplate PMS and combined with a PVA hydrogel matrix. The weight increase (30.59%) was calculated after 8 reaction/immersion cycles.



### 7.3.4 SEM and TEM

#### 1. nHAp/PMS

The morphologies of the nHAp/PMS were observed by SEM, as shown in Figure 7.9A and B. SEM micrograph of nHAp/PMS reveals rod shapes for surface nHAp crystals that are in high concentrations. The size is around 10-50nm, which agrees with TEM and XRD data. The elemental analysis of nHAp/PMS by EDX confirmed P, Ca and O levels and a Ca/P atom ratio to 1.7-1.8 (see Fig. 7.9C).

When calcined at 800°C for 3h, nHAp/PMS revealed a residual hollow microsphere structures (see Fig. 7.10) which suggests that nHAp/PMS might (like PMS) be used as a drug delivery system due to their ability to circulate in the blood and deliver a therapeutic drug payload to tissue and cells [192].

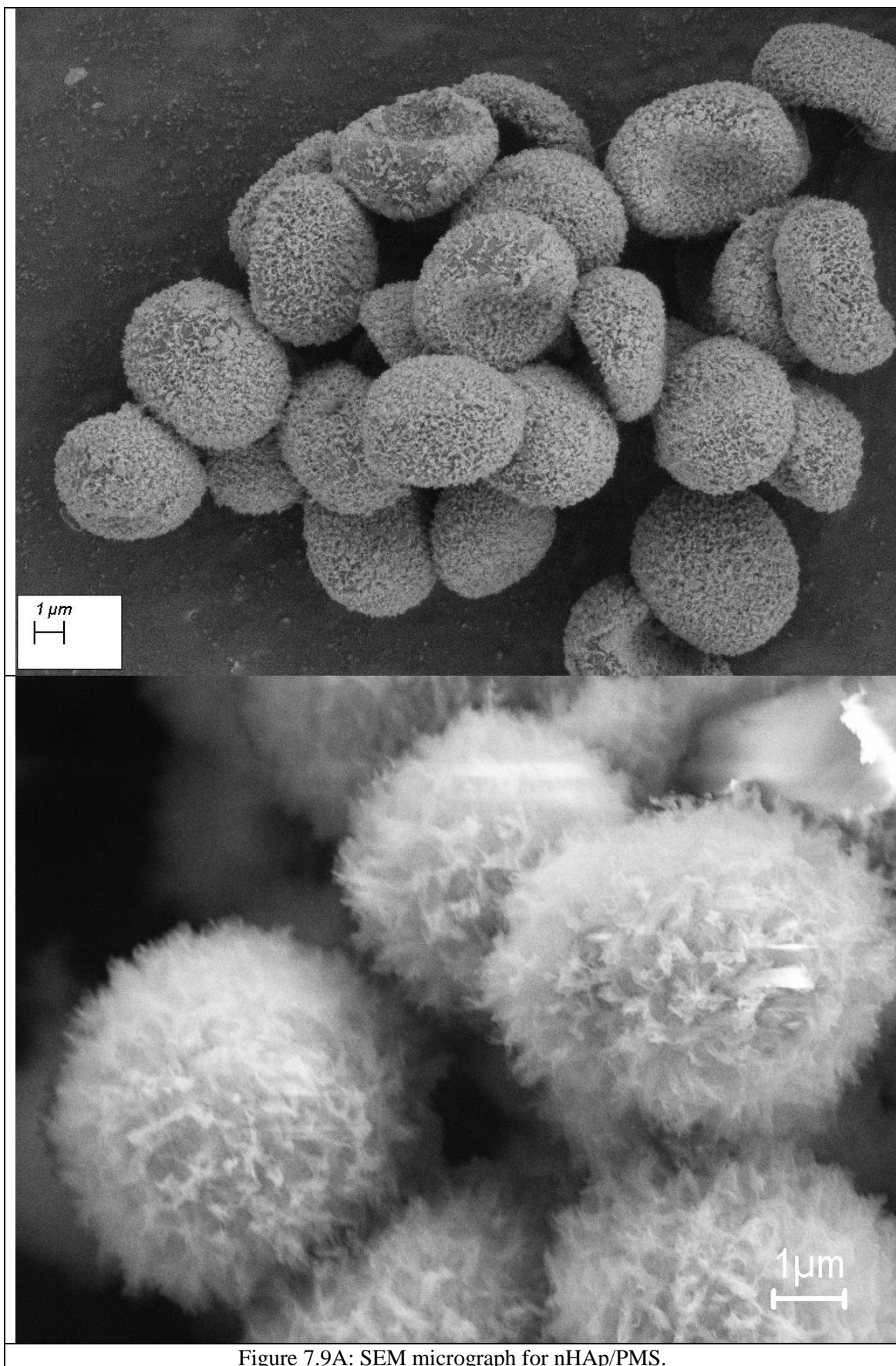


Figure 7.9A: SEM micrograph for nHAp/PMS.

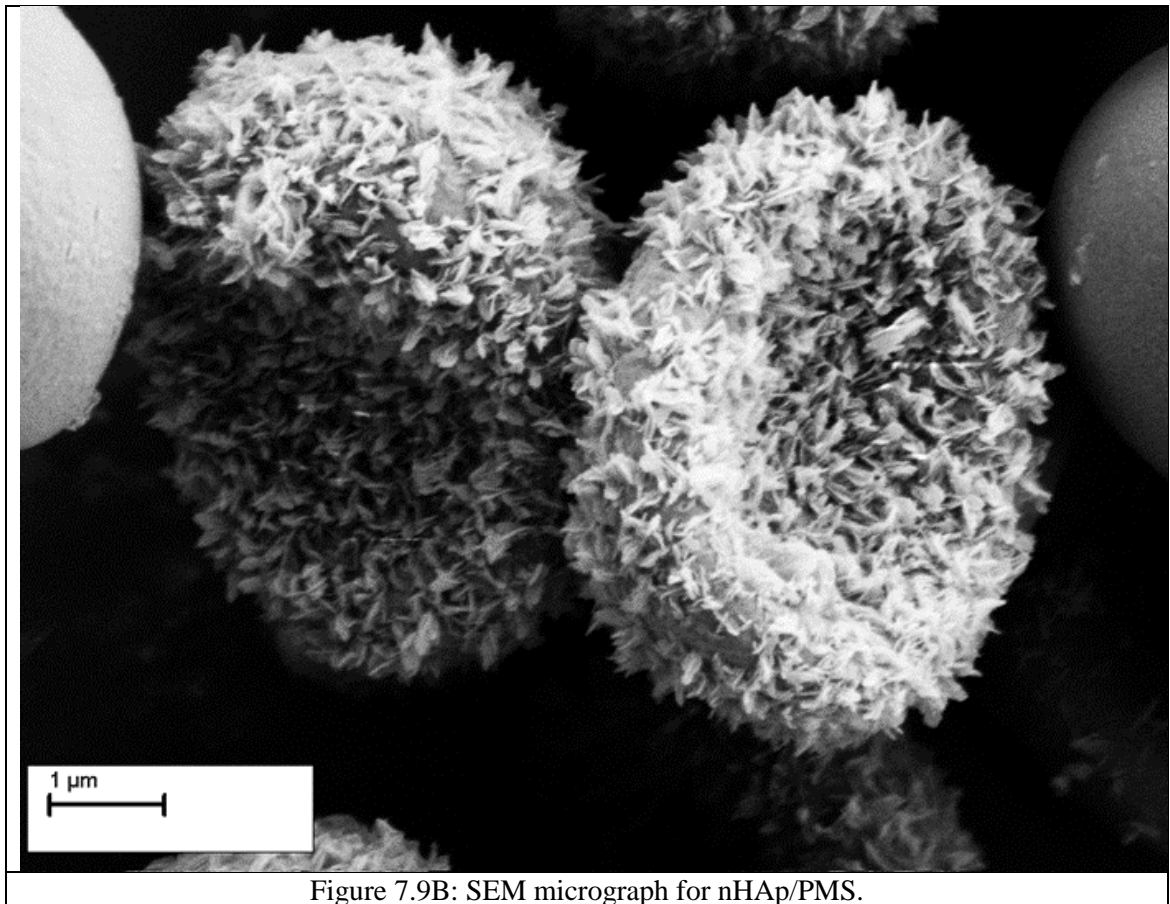


Figure 7.9B: SEM micrograph for nHAp/PMS.

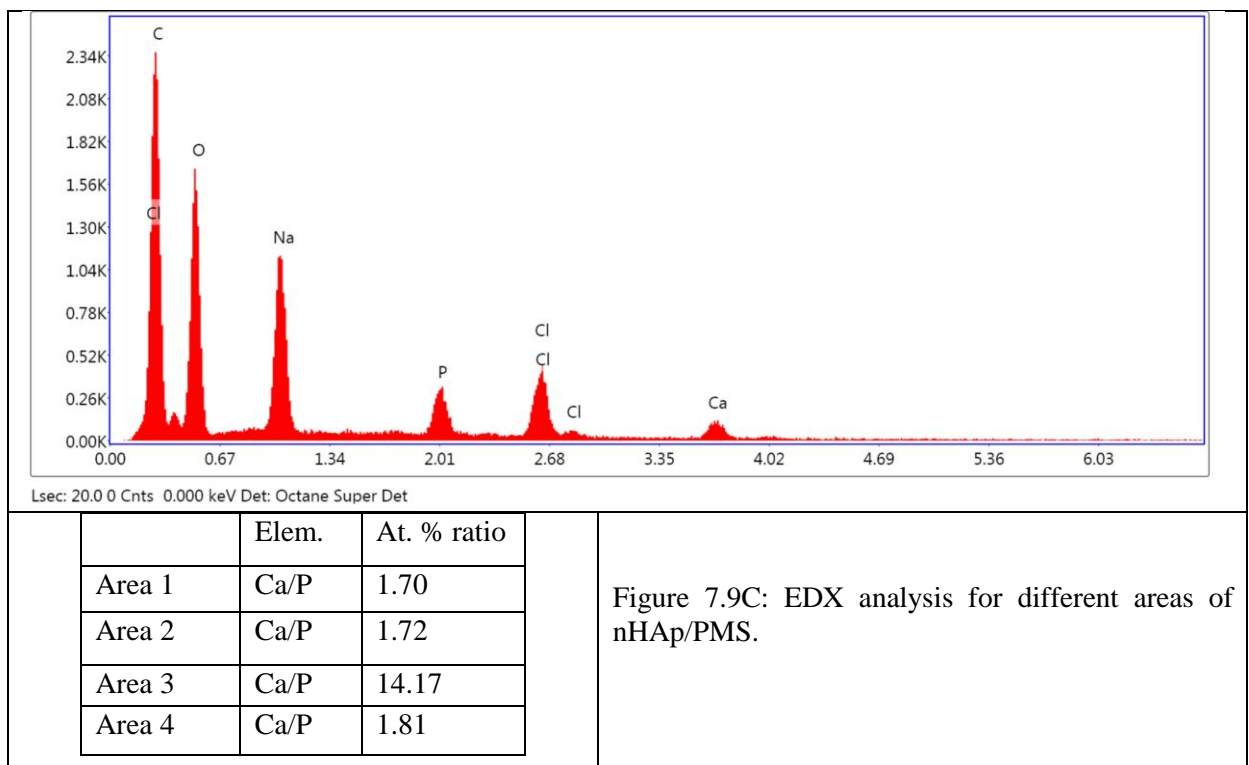


Figure 7.9C: EDX analysis for different areas of nHAp/PMS.

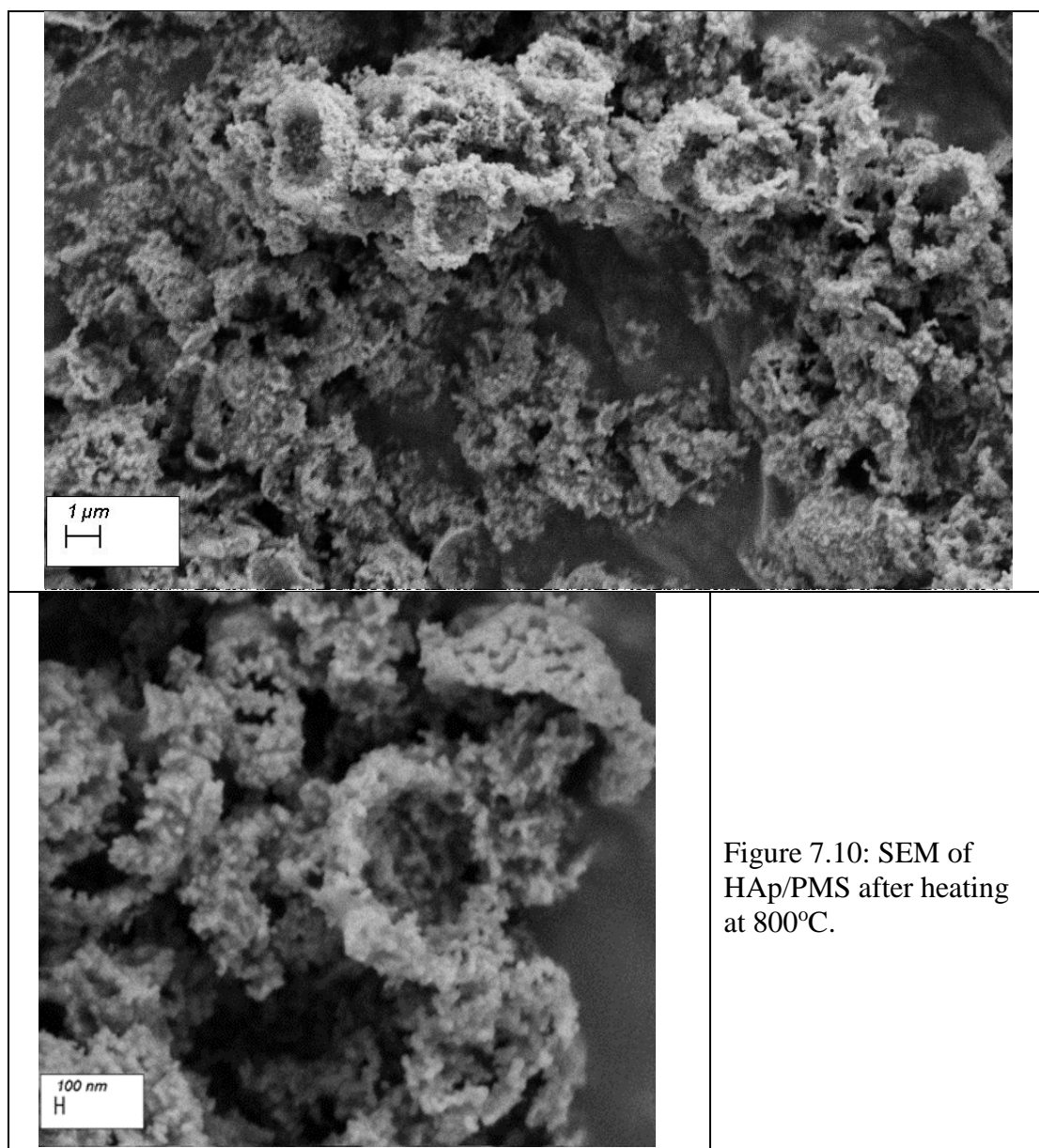


Figure 7.10: SEM of HAp/PMS after heating at 800°C.

The nHAp/PMS structure was confirmed by the high resolution TEM (200keV) and selected area electron diffraction (SAED) pattern with bright circular spots. Figure 7.11 indicates that the morphology of nHAp is rod-shaped on the PMS surface with some aggregation of NPs [292]. The average length of nHAp/PMS was around 30-50nm, while the average width is around 5-7nm. These results were confirmed by SEM and XRD data. In general, the ratio of average length to width is significant in the determination of the absorbability of HAp. Therefore, the nano-rod structure of nHAp/PMS can be adsorbed on the tooth more than a sheet shape [292].

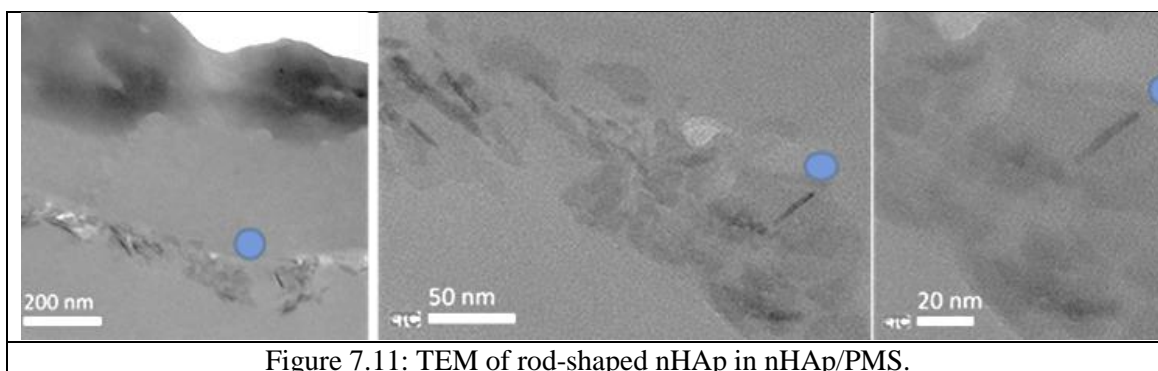


Figure 7.11: TEM of rod-shaped nHAp in nHAp/PMS.

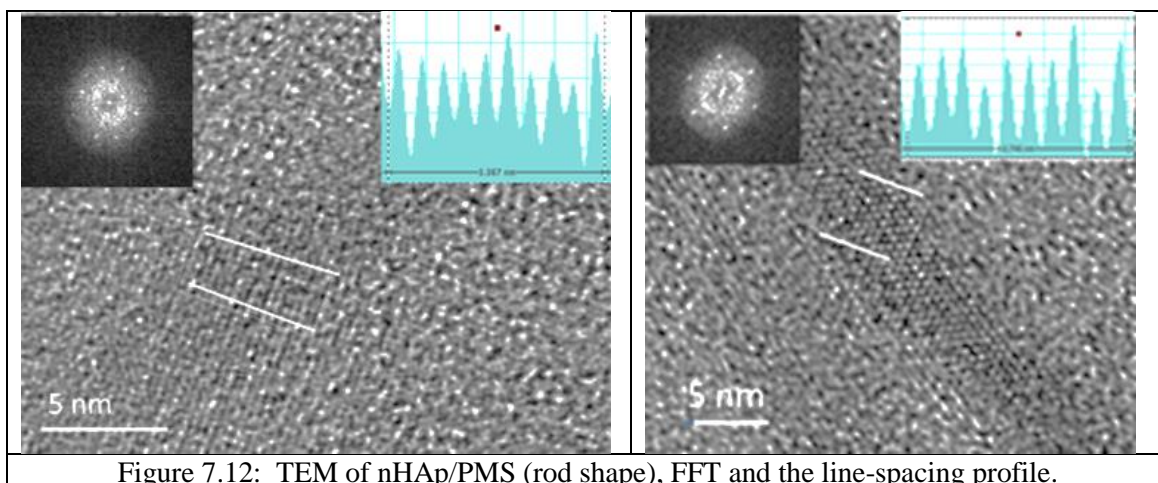


Figure 7.12: TEM of nHAp/PMS (rod shape), FFT and the line-spacing profile.

The lattice fringe spacing noted for nHAp on PMS had a d-spacing = 2.71 nm ( $\theta = 32.9$ ) and the lattice spacing is (300) (see Fig. 7.12 and Table 7.2).

Table 7.2: TEM resulted of nHAp/PMS from the lattice fringe spacing.

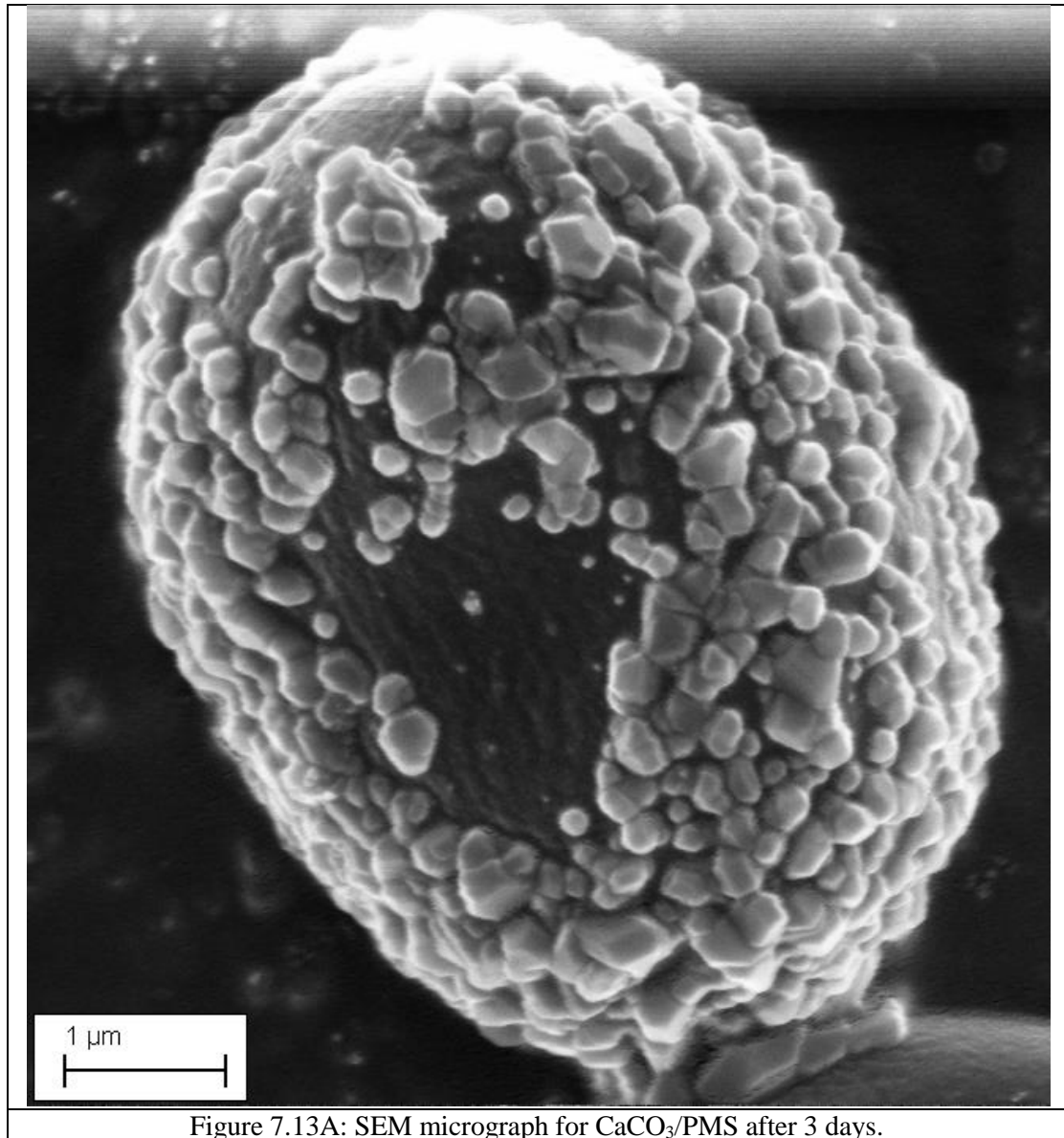
Samples	d-spacing (nm)	$2\theta$	Dominant (hkl)
nHAp/PMS	3.367, 2.71	26.45, 32.9	012, 300
Bio-Oss	2.717-2.719	32.9	300

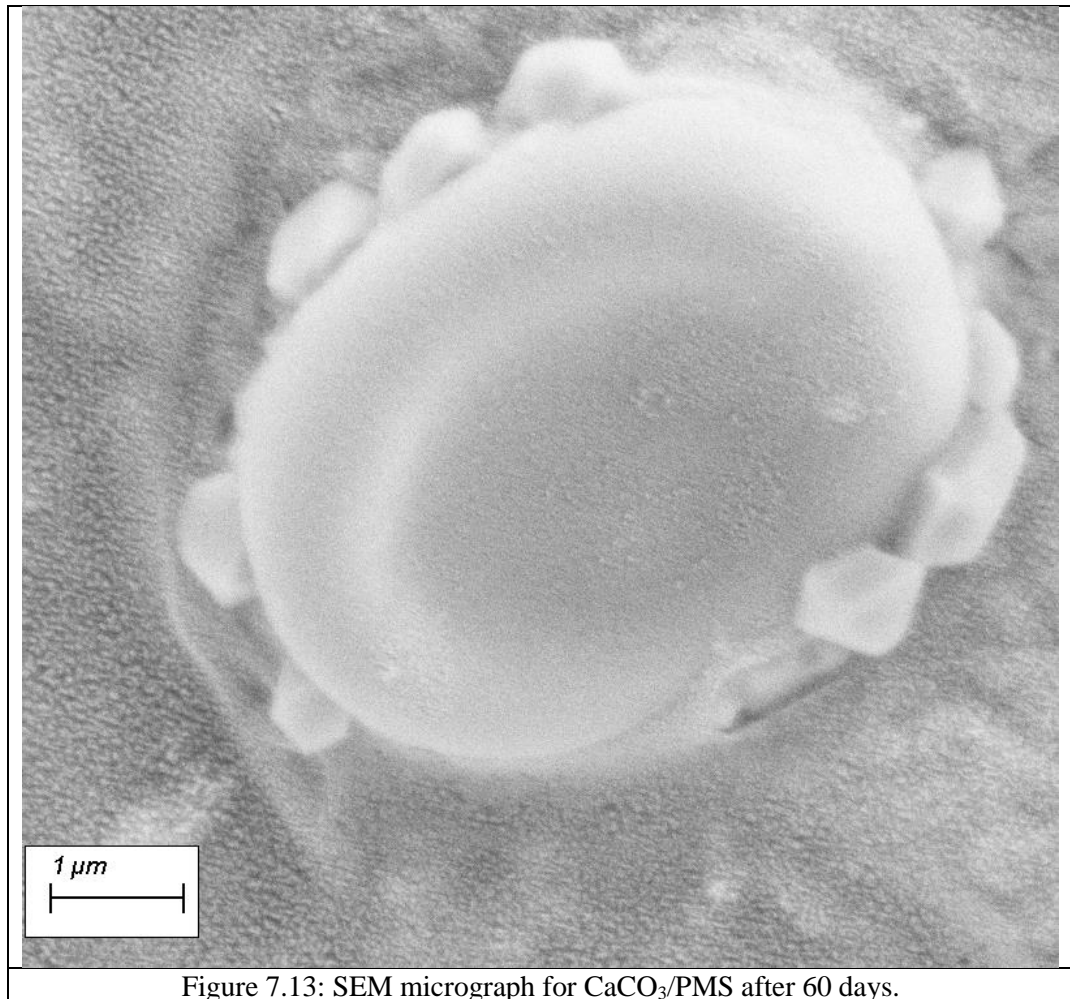
The nucleation and growth of nHAp nano-rods could be attributed to the specific surface energies associated via the different planes of HAp crystal. These planes will determine the  $\text{OH}^-$  concentration available to interact with hydroxyl groups on PMS surface. Each plane has a different average  $\text{OH}^-$  concentration, which will determine the morphology and growth rate. Here,  $\text{OH}^-$  on the bio-template PMS could help the HAp nucleation happen, where free  $\text{Ca}^{2+}$  and  $\text{PO}_4^{3-}$  react with  $\text{OH}^-$  in uniaxial directions (plane with less hydroxyl concentration) [292].



## 2. CaCO<sub>3</sub>/PMS

Figure 7.13 shows CaCO<sub>3</sub> particles on the PMS surface in high concentrations, the structure is hexagonal on the PMS surface after 2 months, when particles on the surface may have coalesced.





### 3. nCa/PO<sub>4</sub><sup>3-</sup>-Ag/PMS

SEM of unfractured and fractured PMS/Ag-Ca<sub>3</sub>(PO<sub>4</sub>)<sub>2</sub> after 3 days (Fig. 7.14) showed that fractured the spores are empty. The dimensions of the cell wall of PMS after 1 day of coated with Ag NPs and Ca<sub>3</sub>(PO<sub>4</sub>)<sub>2</sub> are 312 nm and 429 nm. The NPs were found inside and on the surface of cell wall of PMS. Moreover, EDX elemental profiles suggest that Ca ratio > (Ag and phosphate) (see Fig. 7.15). Possibly this particle PMS fractured before being coated with Ag-Ca<sub>3</sub>(PO<sub>4</sub>)<sub>2</sub>.

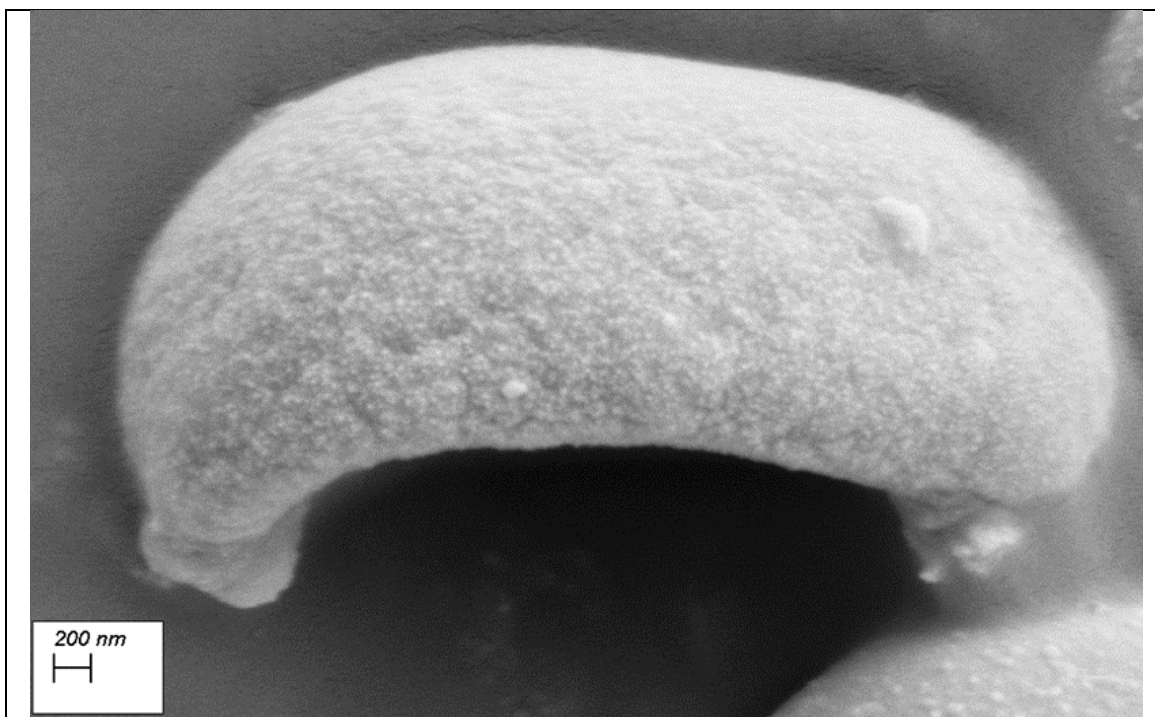


Figure 7.14A: SEM of PMS/Ag-Ca<sub>3</sub>(PO<sub>4</sub>)<sub>2</sub>. A) after 3 days and B) fractured PMS.

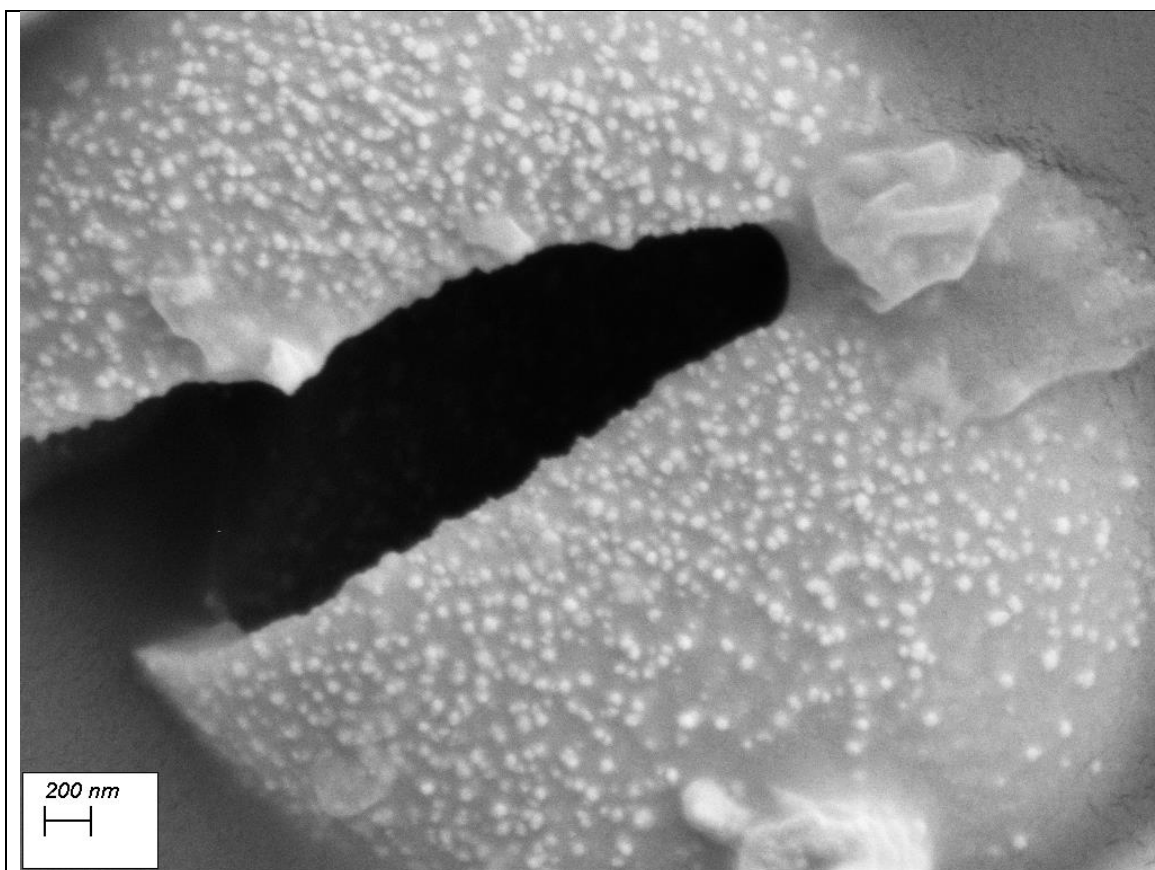


Figure 7.14B: SEM of PMS/Ag-Ca<sub>3</sub>(PO<sub>4</sub>)<sub>2</sub>. A) after 3 days and B) fractured PMS.

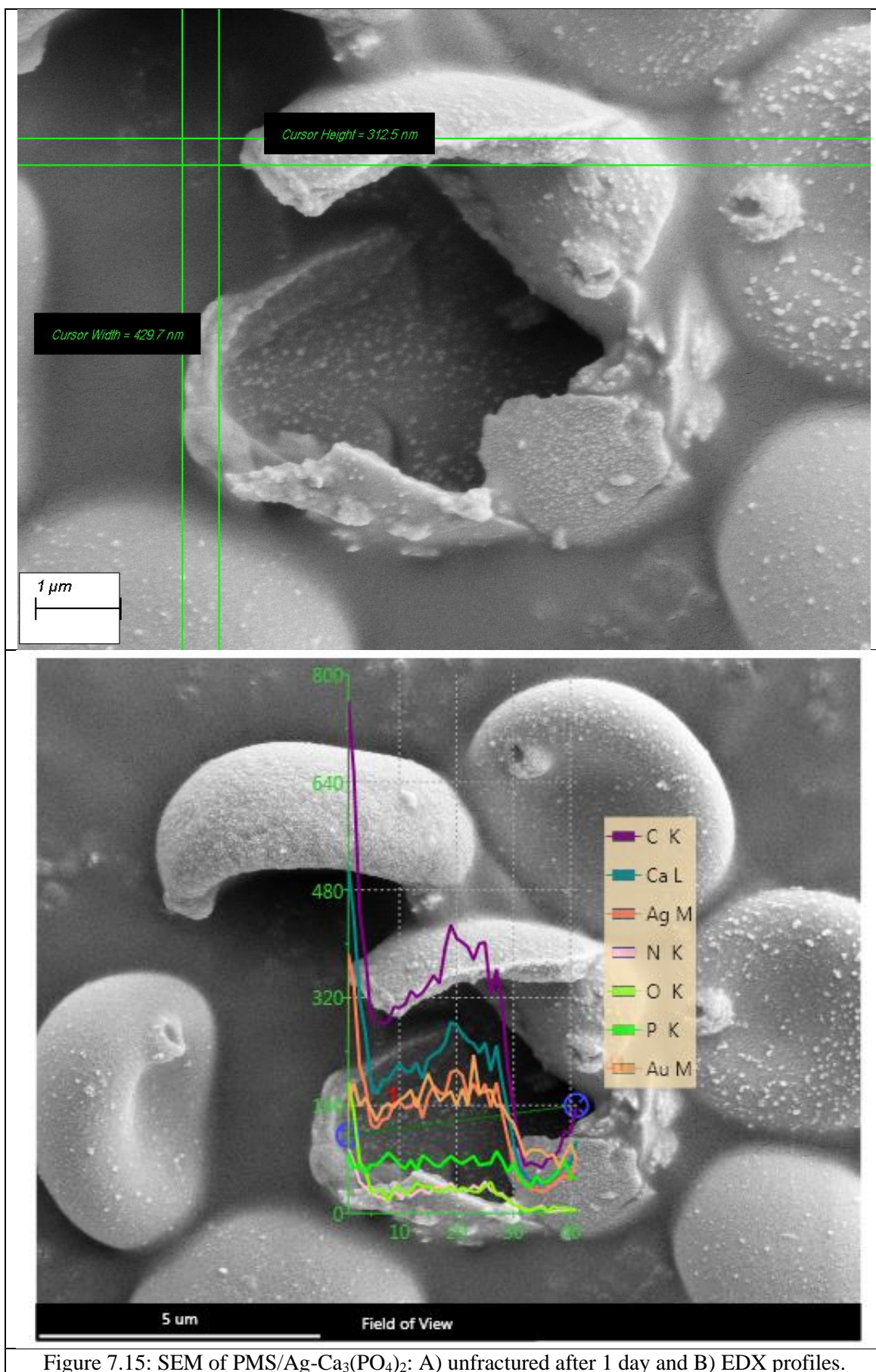


Figure 7.15: SEM of PMS/Ag-Ca<sub>3</sub>(PO<sub>4</sub>)<sub>2</sub>: A) unfractured after 1 day and B) EDX profiles.

#### 4. Bio-Oss

Bio-Oss (commercial HAp) particles and aggregates was observed by TEM and SEM (Fig. 7.16 and 17); the particles were of large dimensions. The Ca/P molar ratio was 2.61 (which is higher than standard HAp). Often commercial HAp does not have well-defined properties and qualities defined by the manufacturer. Frequently, the manufacturer's information about the offered product is not accurate/complete, which is troubling in terms of usage of raw HAp material for development of implants [273].

TEM of HAp Bio-Oss images demonstrate that the commercial HAp powder has a different and random-shaped particles with Ca/P atom ratio of 2.50-2.73 (see Fig. 7.16). Their crystalline nature was confirmed by selected area electron diffraction (SAED) pattern with bright circular spots and the lattice fringe spacing; here d-spacing = 2.717nm (which corresponds to (300) [293]). These results were confirmed by XRD data.

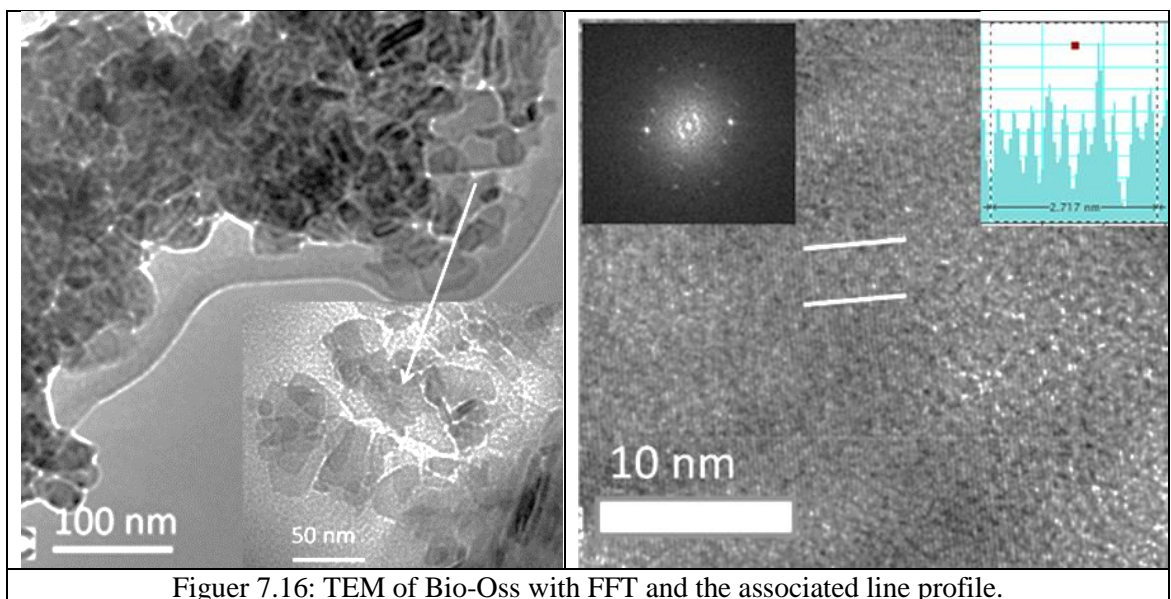
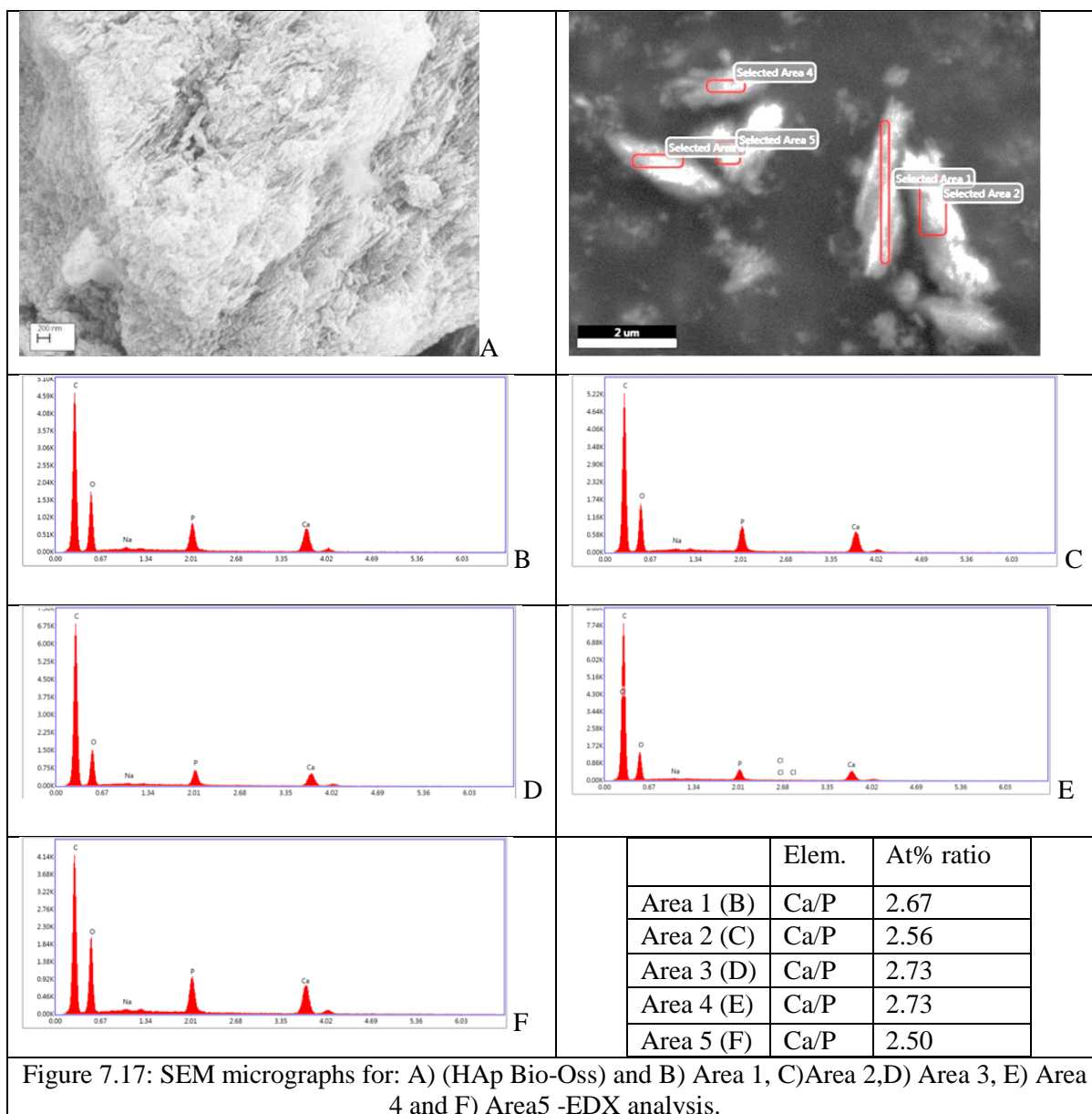


Figure 7.16: TEM of Bio-Oss with FFT and the associated line profile.



### 7.3.5 X-ray diffraction (XRD)

XRD can provide detailed information about lattice parameters of phases, unit cell dimensions (a, b and c), crystallinity and particle size of materials. The XRD pattern of nHAP/PMS is shown in Figures 7.18 and 19. The synthetic sample was in good agreement with the reference pattern of pure hydroxyapatite [174], but some characteristic peaks were broad and related to a weakly crystalline phase of the HAp sample. Poorly crystalline biological apatites complicate characterization by XRD [189]. The nHAp/PMS exhibits line-broadening peaks due to the presence of HAp NPs, and it can be indexed as hexagonal HAp. However, Bio-Oss has higher crystallinity evidenced by its sharp diffraction peaks.

The contributions of each phase are convoluted causing an additional apparent broadening of the diffraction peaks. The average crystallite size ( $D$ ) of nHAp/PMS measured using the Scherrer equation is found to be 17nm (see Table 7. 3) compared with Bio-Oss which has 19.6nm crystallites on average. These results were confirmed in TEM analysis and SEM (the calculations of crystallite size and strain were described in section 3.2). XRD results show in Table 7.3 that the lattice parameter of nHAp/PMS are  $a$  9.3932Å and  $c$  6.8725Å that are close to Bio-Oss. A lower  $a/c$  lattice parameter ratio means a reduction in  $a$  lattice parameter and a simultaneous increase in the  $c$  lattice parameter and may suggest rod-like particles. The increased  $a/c$  ratio contributes to reduced crystallinity. Here, nHAp/PMS has an  $a/c$  ratio of 1.366, that is less than that for Bio-Oss (1.370) because the  $a$ -lattice parameter has decreased and the  $c$  parameter is constant (here) or increasing [276]. The peaks width (FWHM) in Bio-Oss are sharp due to the peak width varying inversely as the crystallite size gets bigger [279].

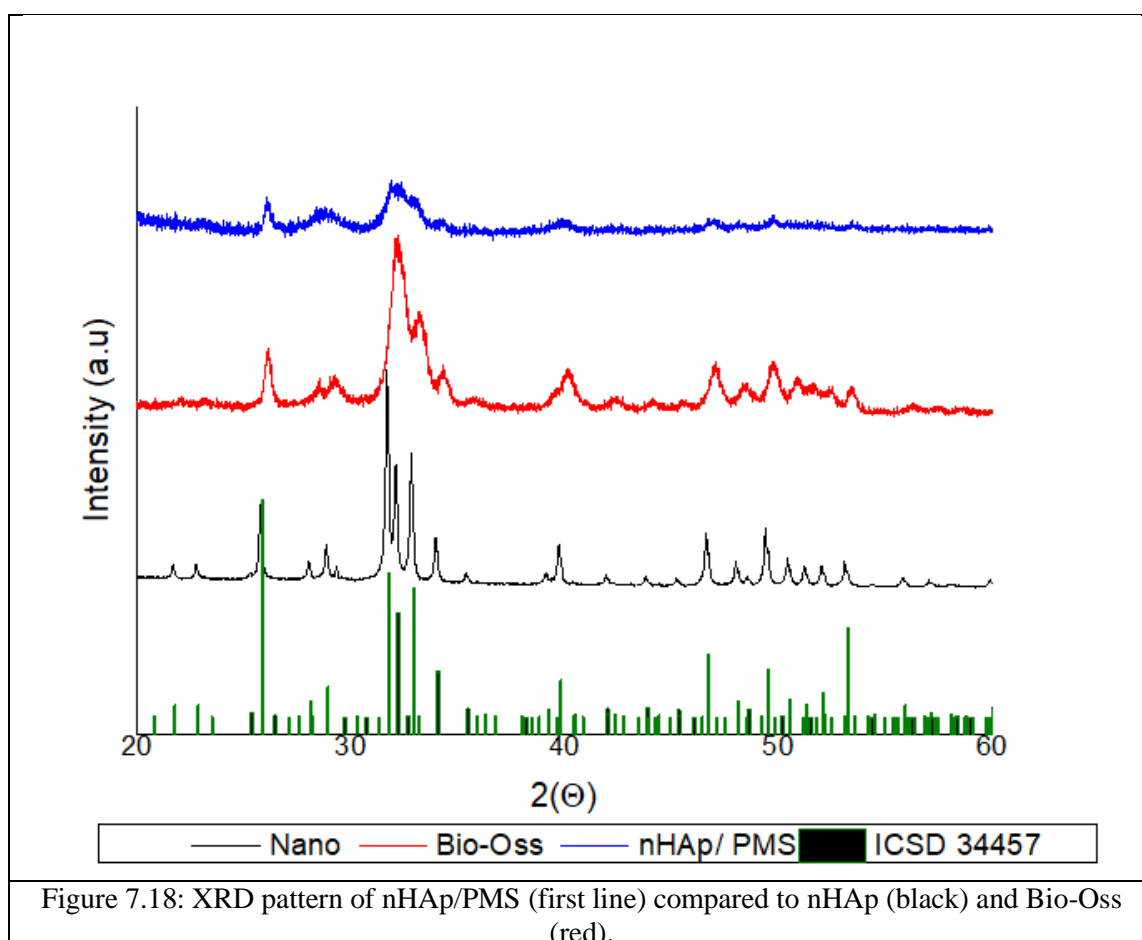
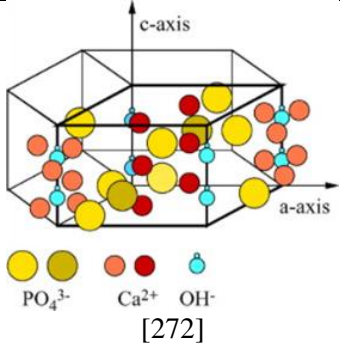


Figure 7.18: XRD pattern of nHAp/PMS (first line) compared to nHAp (black) and Bio-Oss (red).

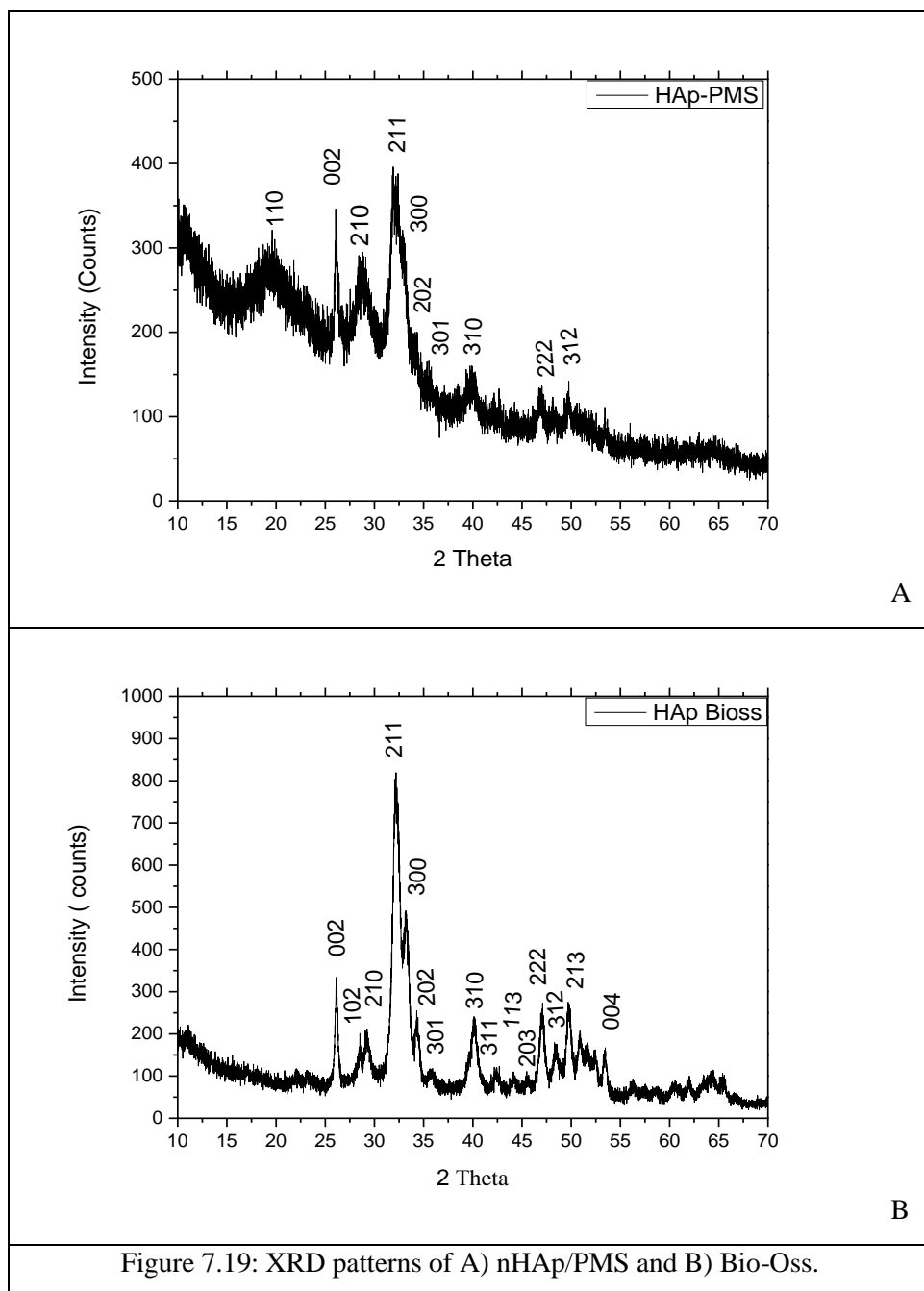
Table 7.3: Lattice parameters and average crystallite size (D) of nHAp/PMS compared with standard HAp (using topaz software).

Sample	a (Å)	c (Å)	a/c	D (nm)
nHAp/PMS	9.3932	6.8725	1.366	17.3
Bio-Oss	9.4401	6.8874	1.370	19.6
Nano	9.4193	6.8841	1.368	216
HAp [293]	6.881	16.318	0.421	-



PO<sub>4</sub><sup>3-</sup>    Ca<sup>2+</sup>    OH<sup>-</sup>

[272]





Significantly, it has been observed that the crystallinity of nHAP/PMS is affected and its peak gets broader. The diffractograms of nHAP/PMS are relatively broad; ions are more prevalent than in the Bio-Oss. These results reveal markedly reduced crystallinity [280]. The crystallite size broadening is most pronounced at large angles of  $2\theta$ . The height of the major peak for the nHAp/PMS decreased by 50%, and the half-width increased by 60% relative to the major peak for the nHAp/PMS compared with Bio-Oss [294].

The crystal size (D) of nHAp/PMS (17.3nm) in Table 7.3. In addition, the crystal size (D) for Nano is big because the sample is relatively poor. The Scherrer method can be used to calculate the average crystallite size (as described in section 3.2). This equation has not taken account of peak broadening reducing from other factors such as instrumental effect or strain.

#### ***Determination of crystallite size (D) and lattice strain ( $\epsilon$ ) using Williamson-Hall approach***

The Williamson-Hall approach (W-H) equation is a simple approach that allows both the average crystallite size (D) and the lattice strain ( $\epsilon$ )-induced broadening to be deduced to considering the peak width as a function of  $2\theta$  [175]. The Williamson-Hall approach (W-H) is given by:

$$\beta(hkl) \cos \theta_{hkl} = \frac{K\lambda}{D} + 4\epsilon \sin \theta_{hkl} \quad \text{--- (7.5)}$$

$$y = z + mX \quad \text{(linear equation with intercept)}$$

From a plot of  $\beta(hkl) \cos \theta_{hkl}$  (Y-axis) against  $\sin \theta_{hkl}$  (X-axis), lattice strain ( $\epsilon$ ) can be calculated from the slope ( $m$ ) =  $4\epsilon$  and average crystallite size (D) from the intercept (Z) =  $K\lambda/D$ . One assumes the lattice strain ( $\epsilon$ ) is uniform or isotropic in the materials, [174]. The Young's elastic modulus ( $E_{hkl}$ ) is proportional to the modulus of elasticity in the perpendicular direction to the set of crystal lattice plane (hkl). It is also related to the elastic compliances  $S_{ij}$ . For a hexagonal HAp crystal phase. Elastic modulus ( $E_{hkl}$ ) is given by equation (7.6) [174].

$$E_{hkl} = \frac{[h^2 + \frac{(h+2k)^2}{3} + (\frac{al}{c})^2]^2}{S_{11} \left(h^2 + \frac{(h+2k)^2}{3}\right)^2 + S_{33}(\frac{al}{c})^4 + (2S_{13} + S_{44})(h + \frac{(h+2k)^2}{3})(\frac{al}{c})^2} \quad (7.6)$$

The elastic compliances and their standard handbook values are given:

$$S_{33} = 10.9 \times 10^{-12}$$

$$S_{44} = 15.1 \times 10^{-12}$$

$$S_{13} = -4.0 \times 10^{-12} [174].$$

Hook's Law can be used to determine the lattice deformation stress ( $\sigma$ ) by Eq. 7.7:

$$\sigma = E_{hkl} * \varepsilon \quad (7.7)$$

Hence:

$$\beta \cos\theta = \frac{K\lambda}{D} + 4 \frac{\sigma \sin\theta}{E_{hkl}} \quad (7.8)$$

where the lattice deformation stress ( $\sigma$ ) can be extracted from the slope while the crystallite size ( $D$ ) is deduced from the intercept of a linear fit plot.

Table 7.4: D-spacing and elastic modulus ( $E_{hkl}$ ) calculation of nHAp/PMS.

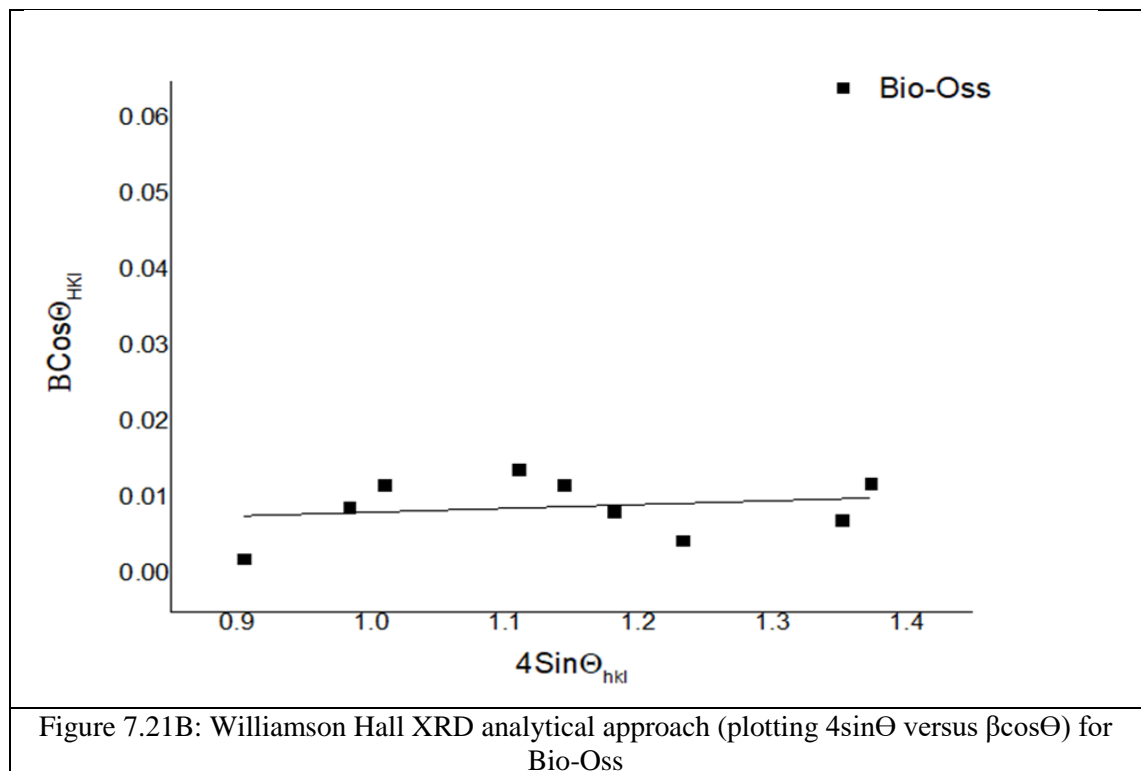
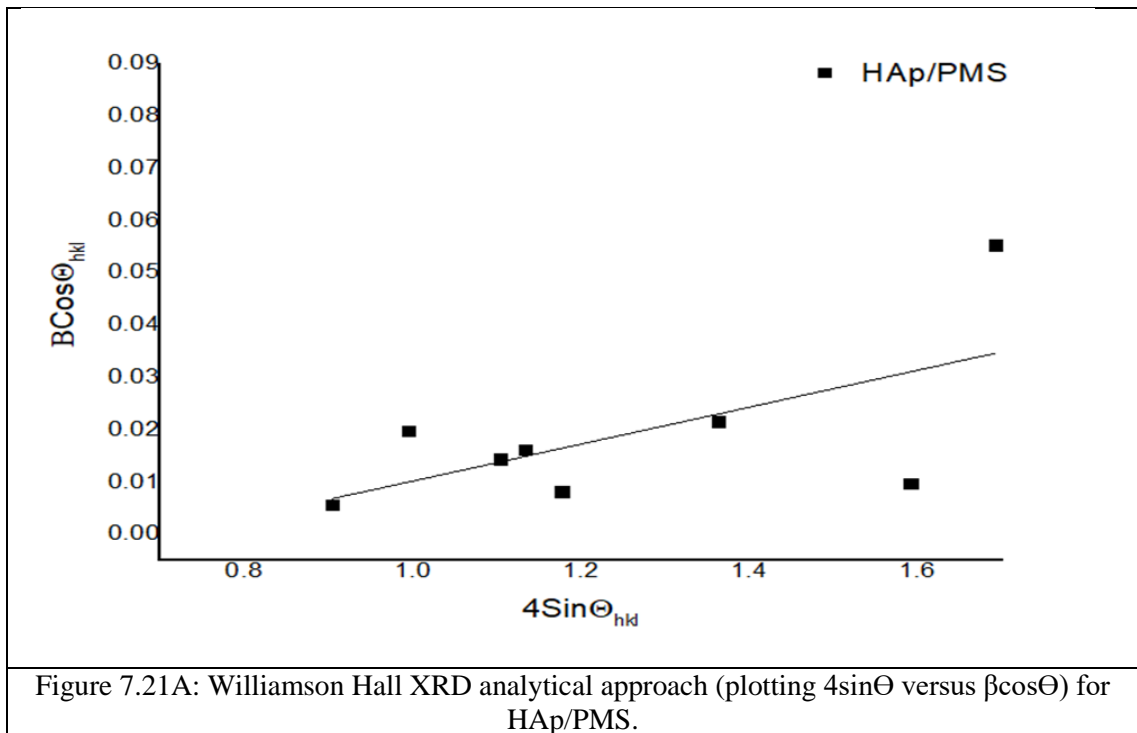
d-spacing (Å)	hkl	$E_{hkl}$	$\theta^\circ$
0.4521	111	$7.59 \times 10^{10}$	9.8188
0.34125	002	$2.04 \times 10^{14}$	13.057
0.3101	220	$1.34 \times 10^{11}$	14.395
0.2793	-142	$3.63 \times 10^{13}$	16.019
0.2263	-420	$1.34 \times 10^{11}$	19.913
0.1937	171	$6.09 \times 10^{11}$	23.444
0.1822	-551	$1.68 \times 10^{12}$	25.025
0.4521	111	$4.03 \times 10^{13}$	9.818
0.2620	042	$2.72 \times 10^{13}$	17.110
0.2721	300	$1.34 \times 10^{11}$	16.459
0.1714	014	$1.99 \times 10^{14}$	26.723

For HAp intended for biological samples,  $\sigma$  reaches around 120 GPa. Many factors can reduce  $\sigma$  and the intrinsic mechanical properties (e.g. purity, porosity and chemical composition). Thus, the modulus of HAp in bone is lowered to around 80 GPa [295].

XRDLB and the Williamson-Hall approach (W-H) revealed nHAp in nHAp/PMS had larger  $\epsilon$  strain than Bio-Oss and Nano (see Fig. 7.20). Figure 7.21 shows how the WH approach allows deconvolution of broadening associated with crystallite size ( $D$ ) and strain ( $\epsilon \propto 1/E_{hkl}$ ) depending on Eq. 7.7. The nHAp/PMS has a small degree of scatter of experimental data points (close to the linear fit) than Bio-Oss. Here, it is thought that the stress is a reasonable approximation for HAp/PMS and Bio-Oss, but the data for Nano is less with too different gradients at different  $\theta$ .

Parameters	nano-HAp	Bio-Oss	HAp/PMS
a (Å°)	9.42	9.44	9.39
b (Å°)	18.83	18.75	19.01
c (Å°)	6.88	6.88	6.87
$d_{xrd}$ (nm)	74.7	45.9	5.8
Strain $\epsilon \times 10^3$ (unitless)	0.60	10	40
$E_{hkl}$ (300,002) (GPa) $\times 10^{-10}$	1.03	1.03	1.02
Deformation stress (MPa) $\times 10^{-10}$	1.06	0.311	3.316

Figure 7.20: Deduced average crystallite size ( $D$ ), strain parameter,  $E_{hkl}$ , and the stress of Nano, Bio-Oss and nHAp/PMS ( $d$  in the table = crystal size; using topaz software).



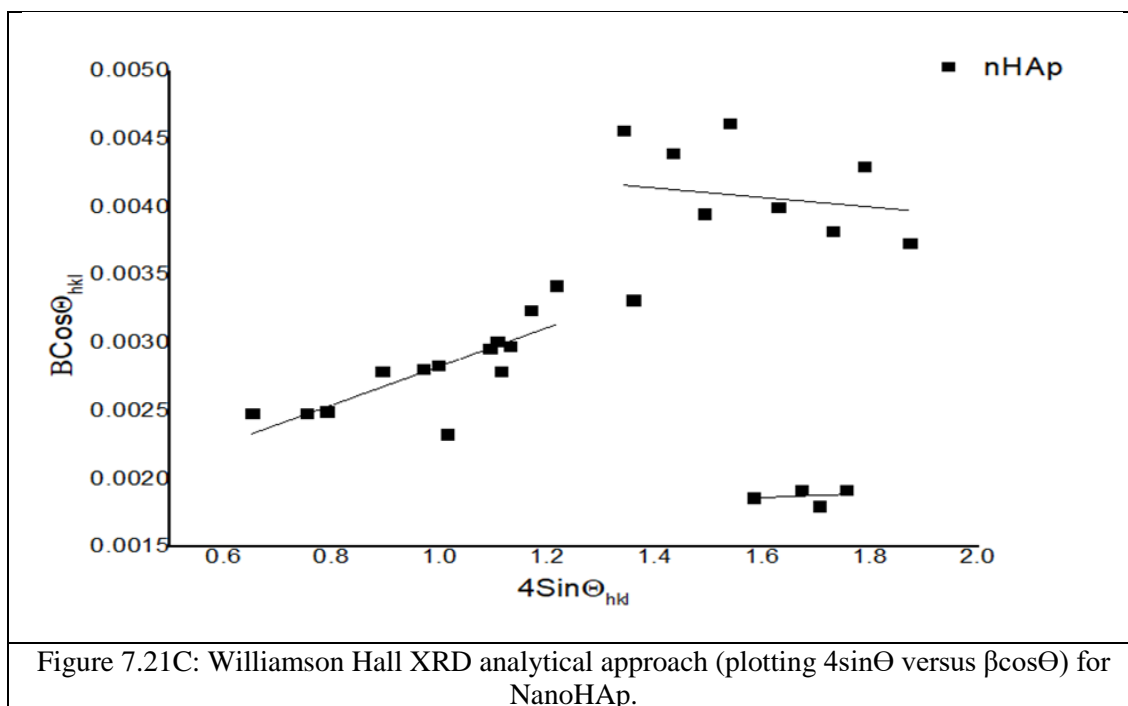


Figure 7.21C: Williamson Hall XRD analytical approach (plotting  $4\sin\Theta$  versus  $\beta\cos\Theta$ ) for NanoHAp.

### 7.3.6 FTIR

The FTIR spectra show the apatite peaks in Bio-Oss and nHAp/PMS (see Fig. 7.22). The P-O absorption bands are strong and sharp peaks ( $1026-983\text{ cm}^{-1}$ ) in all samples, even in PMS alone. That means, the PMS already has phosphate group: the peak at  $873\text{ cm}^{-1}$  refers to the vibration stretching mode of P-O bond and the peaks at  $559$  and  $433\text{ cm}^{-1}$  attributed to the vibration bending mode of O-P-O bands in the  $\text{PO}_4^{3-}$  apatite groups in nHAp/PMS. The carbonate group forms weak peaks at  $1394$ ,  $1388$  and  $1394\text{ cm}^{-1}$  [273] in nHAp/PMS. In PMS, the peak at  $1369\text{ cm}^{-1}$  indicates proteins and the peak was shifted to  $1394\text{ cm}^{-1}$  due to the reaction of HAp with proteins in the PMS on the cell surface (see Table 7.5).

Table 7.5: Frequency of FTIR functional groups in HAp samples.

	$\nu$ (O-H)	$\nu$ (N-H)	$\nu$ (C-H)	$\nu$ (C-O)	$\nu$ (P-O)	$\nu$ ( $\text{PO}_4^{3-}$ )
nHAp/PMS	3628	3184-br.	2758 -2864 w.	1394 w.	1026 v.s and sh.	873, 559, 433
PMS	3672	3331-br.	2970- 2821 w.	1369 w.	1016-983 w.	464 br.
Bio-Oss	-	-	-	1388 w and sh.	989 m.	655, 553 m. and sh.

s = strong, m = medium, w = weak, b = broad, sh. = sharp

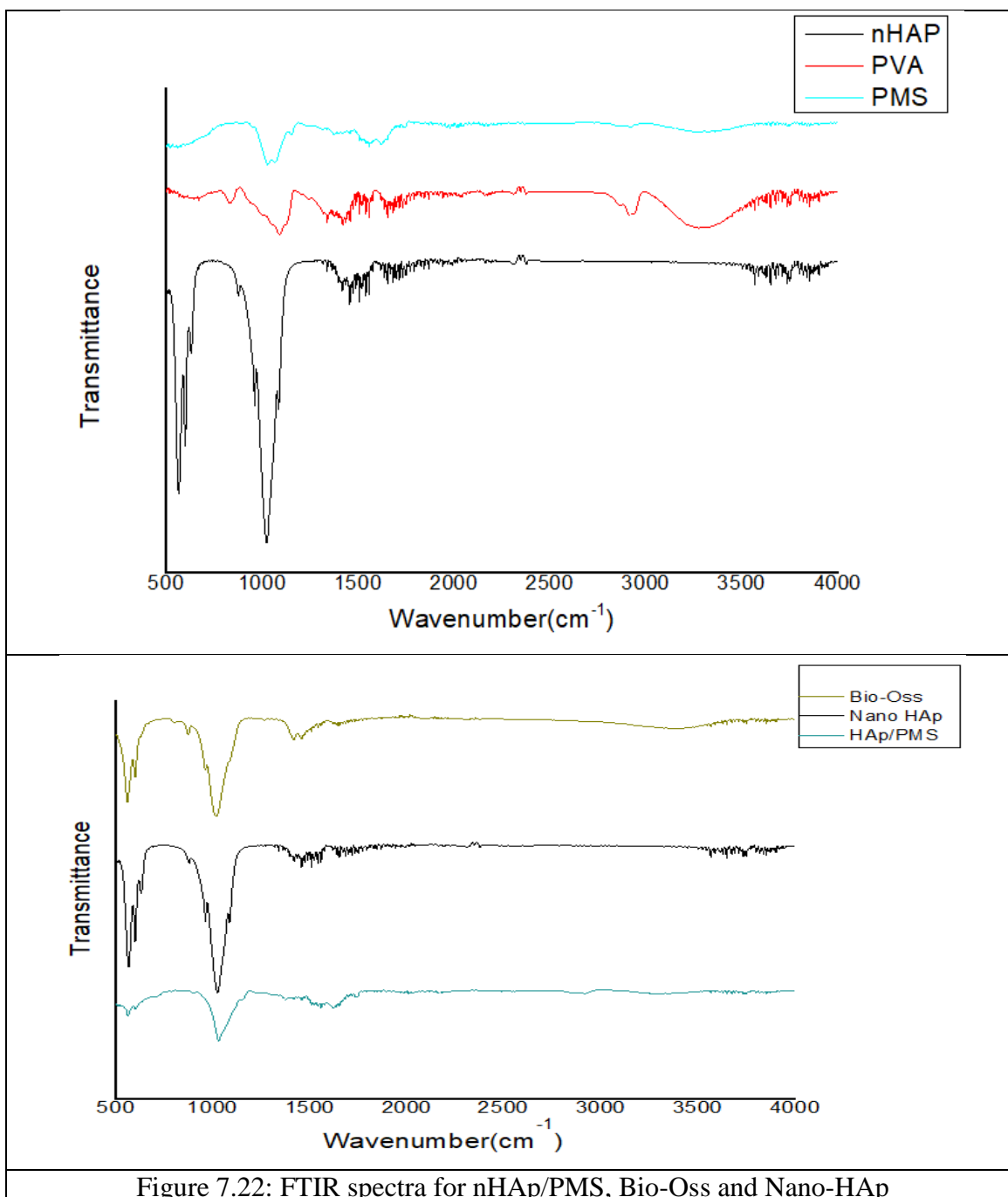
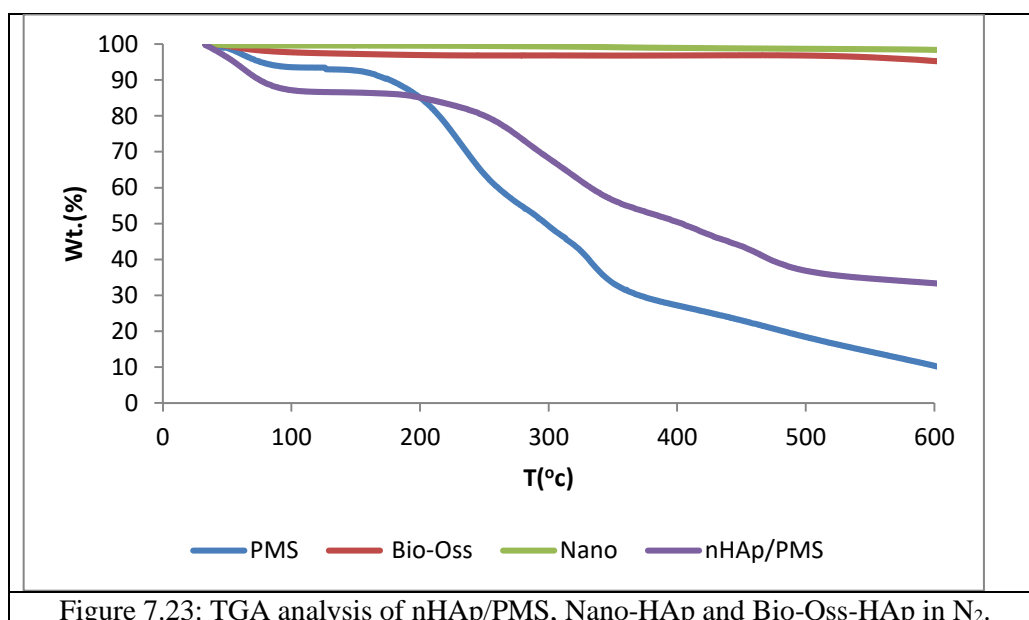


Figure 7.22: FTIR spectra for nHAp/PMS, Bio-Oss and Nano-HAp

The absorption band at  $3628\text{ cm}^{-1}$  due to overlapping with the broad band of adsorbed water arises by the stretching mode of hydroxyl groups in the HAp structure [273]. Meanwhile, the broad band at  $3350\text{ cm}^{-1}$  corresponds to strongly bound  $\text{H}_2\text{O}$ . Also, the  $1687\text{ cm}^{-1}$  band observed in the nHAp/PMS can be attributed to the  $\nu_2$  bending mode of adsorbed  $\text{H}_2\text{O}$  (see Fig. 7.22) [109]. A weak band was detected for  $\text{CO}_3^{2-}$  around  $1460\text{ cm}^{-1}$  because the small number of  $\text{PO}_4^{3-}$  ions in nHAp structure was replaced by  $\text{CO}_3^{2-}$  ions. Carbonate ion is a part of bone structure [195].

### 7.3.7 TGA

The thermal stability of nHAp/PMS and other samples was determined using TGA in N<sub>2</sub> (see Fig. 7.23). A weight loss of approximately 6.5% was seen for nHAp/PMS from RT to 134°C, arising from evaporation of water and then a weight loss of about 74% up 598°C associated to the loss of carbohydrates because PMS degradation. In contrast, Bio-Oss and nano HAp (nHAp) lost a weight only around 3.3% at 681.5°C related to loss of water from the lattice. The total weight loss around 880°C is 90% for HAp replica (PMS loss will leave a HAp replica) compared with HAp Bio-Oss only 94.9% and 10% and 95% residue, respectively.



### 7.3.8 The mechanism of nucleated nHAp-PMS

PMS is an organic biotemplate. Organic macromolecules include proteins, lipids and polysaccharides. COO<sup>-</sup> groups and electron pairs for two oxygen atoms of a carboxyl group act as a claw to react with Ca<sup>2+</sup> on the surface of PMS. Also, hydroxyl groups on the PMS surface determine the HAp growth rate on PMS. HAp growth is along direction [002] planes revealing an increase in the concentration of OH<sup>-</sup> groups [292]. Self-assembly leads to surface of HAp nuclei and then nHAp/PMS [296]. After that, more calcium ions help HAp crystals to grow along the c-axis with oriented mineralization induced; HAp crystals were arranged parallel to each other [296]. Here, PMS has a good surface chemistry accelerating growth nanorods HAp.

The inorganic component of the Ca/P-phase on the PMS surface mainly consisted of carbonate-substituted apatite, which is thought to more closely resemble biologically-inspired HAp (such as bone mineral whose mineral content has been identified as HAp with low crystallinity). It has been reported that bones contain a large quantity of carbonate ions around (5% - 8%). Certainly, apatite present in bones contains few OH<sup>-</sup> ions. Also, only the apatite present in teeth enamel contains a high OH<sup>-</sup> (and low CO<sub>3</sub><sup>2-</sup>) content. Furthermore, the adsorption of atmospheric CO<sub>2</sub> yield CO<sub>3</sub><sup>2-</sup> that could become embedded into the crystalline lattice of nHAp/PMS. CO<sub>3</sub><sup>2-</sup> could cause deformation in the crystal lattice of the stoichiometric nHAp/PMS and change the crystallographic nature of the structure of biological apatite [276].

#### 7.4 Conclusions

A novel method of preparing templated nano-hydroxyapatite (nHAp) microspheres from the conversion of CaCO<sub>3</sub> replicas on bio-macromolecular Portobello mushroom spore (PMS) templates under mild conditions has been optimized and described. They have been characterized and investigated using TEM, SEM, TGA, XRD, UV-Vis and FTIR. The aim of this study was to attempt to mimic bone mineralization behavior, altering scaffold nano collagen. This approach can the author hopes in the future be used for designing smarter scaffolds for tissue engineering, artificial bones and regenerative medicine. XRD revealed that nHAp/PMS has low HAp crystallinity compared with commercial HAp (Bio-Oss). Clearly, PMS surfaces contain hydrophilic (polar) groups which can provide suitable sites in which HAp can nucleate and then grow. Moreover, PMS has many functional groups which are necessary for the formation of chemical bonds with bone (by adsorptive and electrostatic interactions with reagent's species). In particular, surface hydroxyl and carboxyl groups act as nucleation sites able to direct the orientation of growth of the surface nHAp crystals. The results of the present study suggested that the nHAp/PMS and nHAp/PMS-loaded PVA hydrogel film may be used to regenerate bone and/or deliver any transdermal drug painlessly and harmlessly when placed on the human skin.



## Chapter 8: The bioactivity studies of nHAp/PMS

---

In this chapter, the biomedical bioactivity and dissolution applications were investigated for ions/PMS (Ca, PO<sub>4</sub> and Ag) and nHAp/PMS (preparations described in chapter 4) and compared with commercial HAp (Bio-Oss and Nano HAp). The characterisation of all these samples was undertaken using SEM, EDX and UV which are described in chapter 3.

### 8.1 Introduction

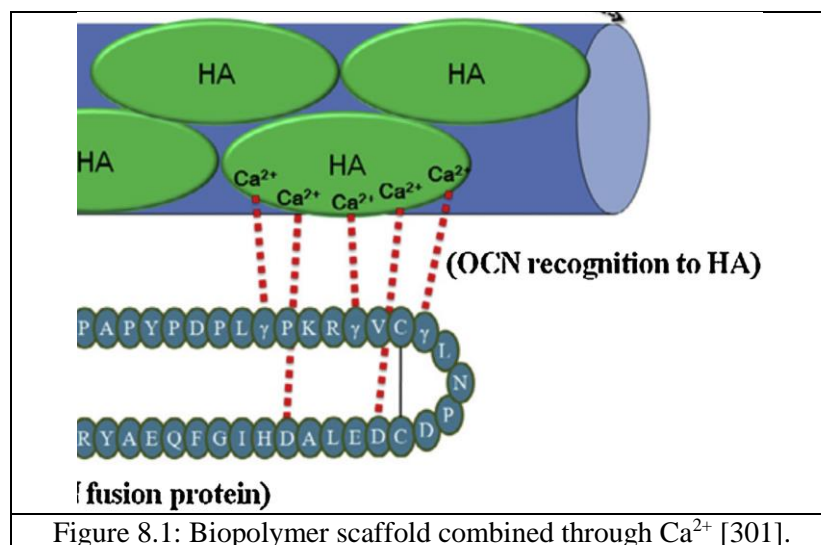
A scaffold is a 3D substrate for a human cell in the body tissue. Its main aim is to serve as a template for tissue regeneration (bone acts like a scaffold to give structure, shape and strength to the frame of the human body) [297]. It provides a supporting matrix of bone cells and an essential environment for bone cells to migrate and multiply [298] (leading to direct chemical bonding with natural bone [299]). The properties (biological, chemical and bio-physical properties) of an ideal scaffold will control and benefit the processes at the tissue and at the cellular level [300].

The scaffold must be biocompatible, have an interconnectivity and yet be a porous network allowing cell movement. It must be non-immunogenic and allow transfer of nutrients waste products and oxygen [194]. There are many biological elements providing essential roles in biological processes (e.g. Ag, Mn, Zn, Cu and Co (see Fig. 8.1A)). One might want, these elements to be incorporated into the scaffold and then offer the opportunity for their release therapeutically [298].

There are different scaffolds for tissue regeneration depending on the materials on which scaffolds are based:

- (i) natural material (like coral and material formed from cell as peptides, collagen and heparin),
- (ii) synthetic materials (like polymers to improve mechanical properties: strength, compressive and toughness), many bioactive polymers have been used for bone tissue replacement (e.g. poly-lactic acid (PLA) and poly-vinyl alcohol (PVA) [267], and

hybrid scaffolds (e.g. HAp/polyamide and HAp/poly (lactic-co-glycolic acid) (PLGA). Their synthesis (see Fig. 8.1B) has importance in that they are biologically recognized by respective organs but cannot be purified from an immunology point of view. Such hybrid scaffolds /HAp crystalline or amorphous calcium phosphate are preferred because they have properties that can be controlled and optimized for roughness, porosity and a dissolution rate [301].



### 8.1.1 Types of methods

Biom mineralization is the process by which the matrix of a living organism produces mineral micro-crystals. A living organism provides a physical and chemical environment that controls the nucleation and growth of a unique mineral phase. Moreover, these phases exhibit a structural hierarchical order, owing to superior physical properties not found in either their inorganic counterparts or in synthetic materials. The combination of inorganic compounds, (e.g. salts) into biomolecules often gives the structures hardness/rigidity. For example, carbonate is found in diatoms, silicate exists in algae [272] and phosphate in Portobello mushroom.

HAp can be prepared by different routes such as:

- (i) combustion synthesis,
- (ii) wet chemistry techniques or precipitation (based solvent is aqueous) [195],
- (iii) sol–gel route (based on solvent is organic) [266],
- (iv) hydrothermal synthesis, and
- (v) solid-state sintering [109] and plasma [274] etc.

The properties of the synthesised calcium phosphate products are defined by temperature, pH, concentration and reagents (type, purity and quality). All of the above mentioned preparation routes can modify the HAp products and its impact on the tissue response of these bioceramic implants [273].

The methods of assessment of bioactivity used in this study are described in section 4.4.

## 8.2. Results

### 8.2.1 bioactivity study

It can be observed from Table 8.1 that nHAp/PMS has a higher percentage of phosphate ions absorbed on/in nHAp/PMS surface, which is 60% more than Bio-Oss 37% and Nano 42% after 336 immersion hours (14 days). That means, more HAp could nucleate and grow on nHAp/PMS because there are more active sites on the PMS surface that attract more Ca and phosphate ions in SBF to react on the PMS surface leading to deposition from SBF. Furthermore, the nanoparticles of nHAp/PMS catalysed more HAp deposition until all the surface is covered because they have a high surface area for nHAp formation. Therefore, the weight increasing indicates that nHAp/PMS does not dissolve in the SBF over 14 days. Rather, the Ca and phosphate ions from SBF deposit on nHAp/PMS due to many active sites on the surface of PMS. Moreover, the carbonate in the nHAp/PMS layer formed helps to bond in living bone [194]. Nano (commercial HAp) exhibited a deposition process of Ca and phosphate ions from SBF more than Bio-Oss. This demonstrates that in terms of a deposition process Nano-HAp is more active (with little dissolution) due to its volume and high surface area [301]. HAp/PMS-PVA as a hydrogel has 473% that is a highest % compared with other samples.

Table 8.1: Weight increasing of HAp samples immersed in SBF after 14 days.

Samples	W <sub>1</sub> (mg)	W <sub>2</sub> (mg)	%
Bio-Oss	19.0	26.2	37.89
Nano	19.0	27.1	42.63
nHAp/PMS	19.0	30.5	60.52
HAp/PMS-PVA	13.5	77.4	473.3

SEM analysis, (Fig. 8.2-3) of deposits of Ca/phosphate ions on PMS after 1h confirmed that deposition was inside and outside spores (although it is unclear if some PMS was fractured before Ca<sup>2+</sup>/phosphate deposition). At first, the Ca<sup>2+</sup> ions adsorb on PMS

surface and insert in the membrane cell (Ca/P-PMS inside spores (deep 659 nm) with a spherical shape). The dimensions of the cell wall of Ca/P- modified PMS are 310.4 and 219.5 nm. SEM suggested that the PMS diameter becomes larger and more rigid with crystal NPs found at all PMS sites. This process may sometimes lead to breaking or cracking some of the spores (see Fig. 8.3).

The morphology of HAp crystals formed may depend on the prevailing pH, the concentration of  $\text{Ca}^{2+}$  and phosphate ions and temperature [192]. Here, the pHs for samples which were immersed in SBF for 14 days are shown in Figure 8.4. In the first 1h, Bio-Oss and Nano (commercial samples) immersed in SBF tend to have a strong tendency to reach pH 11-10 (from an initial pH for SBF of (7.4) possibly due to the dissolution of HAp in SBF).

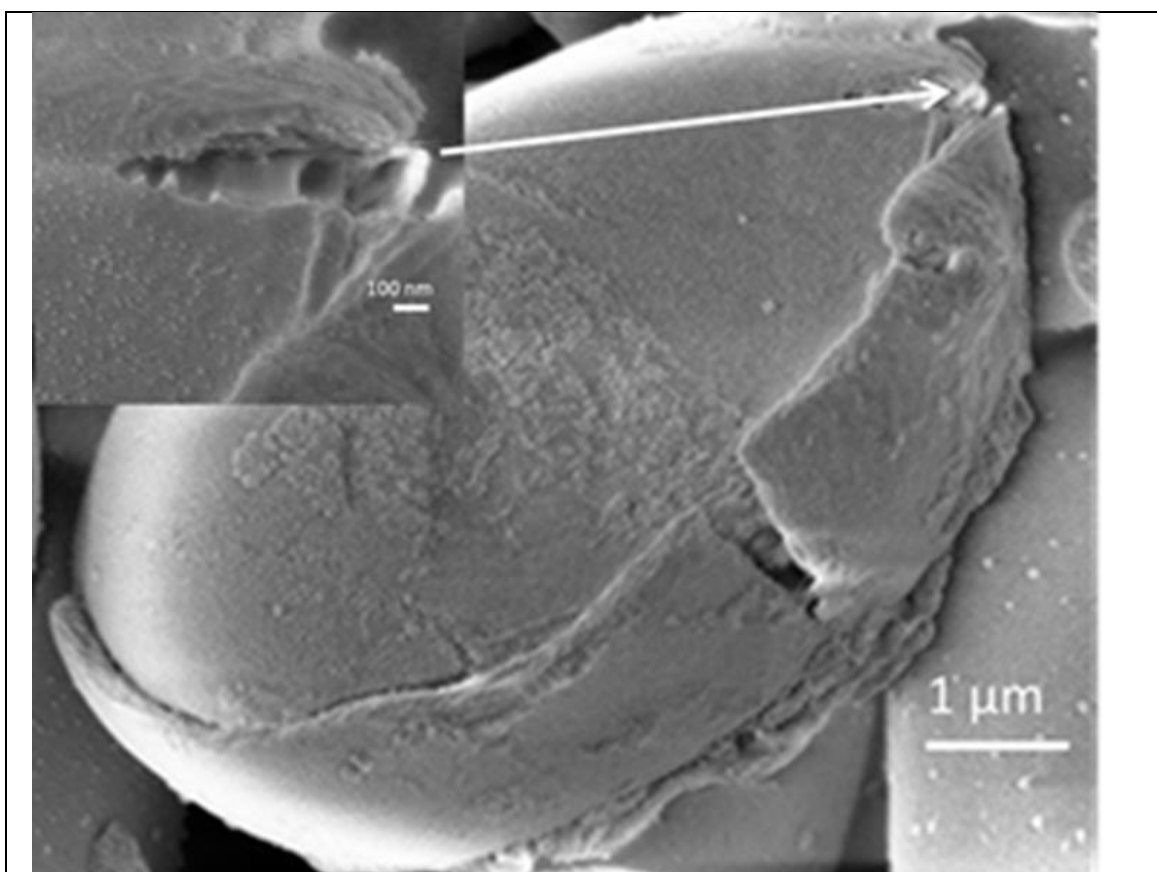
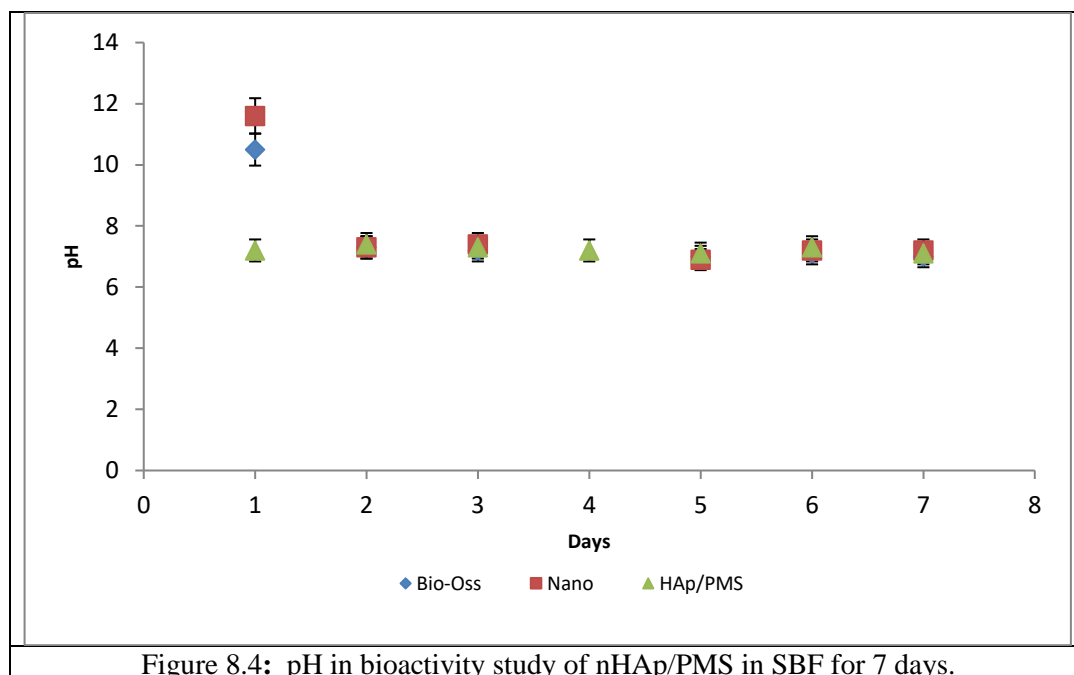


Figure 8.2A: SEM of  $\text{Ca}^{2+}$ /phosphate ions modified in/on PMS (broken) external appearance membrane cell of PMS after 1h.





Furthermore, Figure 8.4 indicates that both Bio-Oss and Nano scaffolds lose phosphate ions from SBF after 4 days (because of the deposition on these scaffolds). It is suggested that  $\text{Ca}^{2+}$  and phosphate ions penetrate the porous Bio-Oss and nHAp/PMS and gradually nucleate as HAp and then crystallize. After that, the pH remained around 7 over the time studied. The Bio-Oss and Nano porosity may help bone deposition bioactivity [193]. In contrast, in the case of nHAp/PMS scaffold, there was no significant change in pH (7.4 to 7.2). Here, the Ca and phosphate ions react on the PMS surface and the material bioactivity increases; compare results obtained from the percentage of HAp/PMS which is high (60% higher than with Bio-Oss 37.89% and Nano 42.63%). Furthermore, comparing the material evolution in SBF, pH values showed a similar trend after 2h. It appears that the nHAp/PMS scaffold is more soluble than Bio-Oss and Nano, due to the constancy of the solution pH in the nHAp/PMS scaffold case [302].

nHAp/PMS scaffold reveals (Fig. 8.5) lower Ca ion concentrations in solution than other samples due to  $\text{Ca}^{2+}$ /phosphate deposition on nHAp/PMS. Interestingly, after 36-48h, nHAp/PMS has a lower concentration of Ca ions in SBF solution than Bio-Oss and Nano (due to depositions on the nHAp/PMS scaffold) suggesting that this is the perfect time for bioactivity and bone formation. After 76h, the concentration of ions remains constant, suggesting that the dissolution/deposition processes are balanced and take place at the same time as the bone formation [301]. Increasing the period of immersion

in SBF, causes more layers of ions to form increasing the thickness of apatite formation on the PMS surface leading to saturated active sites on nHAp/PMS. Therefore, Ca ion levels increased in the solution of SBF (after 84h). Figure 8.6 shows phosphate ions concentrations in SBF solution over various samples were broadly similar.

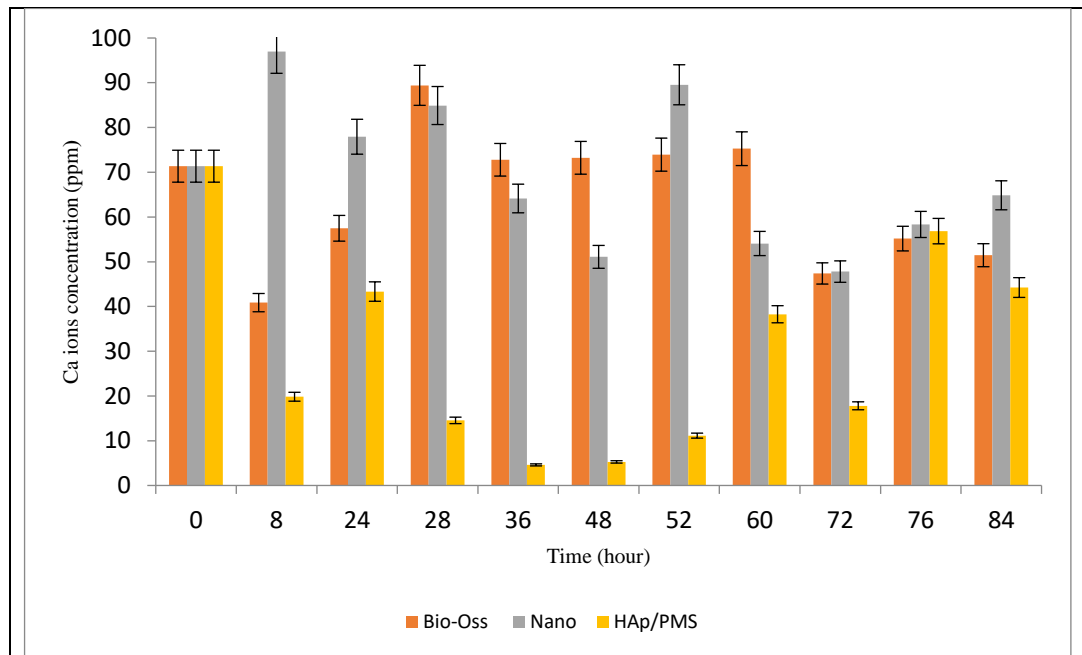


Figure 8.5: Bioactivity and concentration  $\text{Ca}^{2+}$  ions in SBF solution containing nHAp/PMS, Bio-Oss and Nano-HAp.

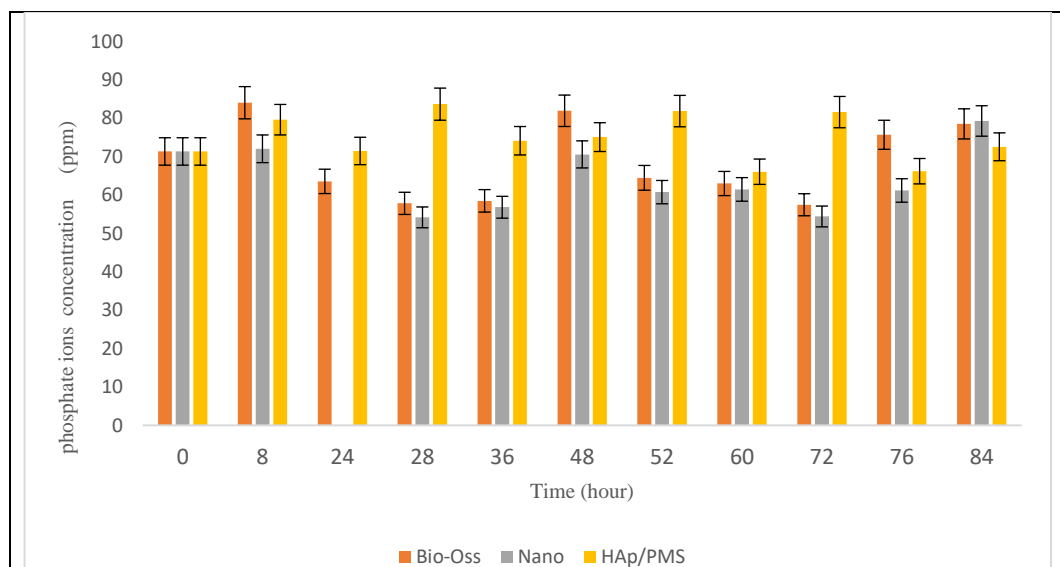


Figure 8.6: Bioactivity and concentration of  $\text{PO}_4^{3-}$  ions in SBF solution containing nHAp/PMS, Bio-Oss and Nano-HAp.

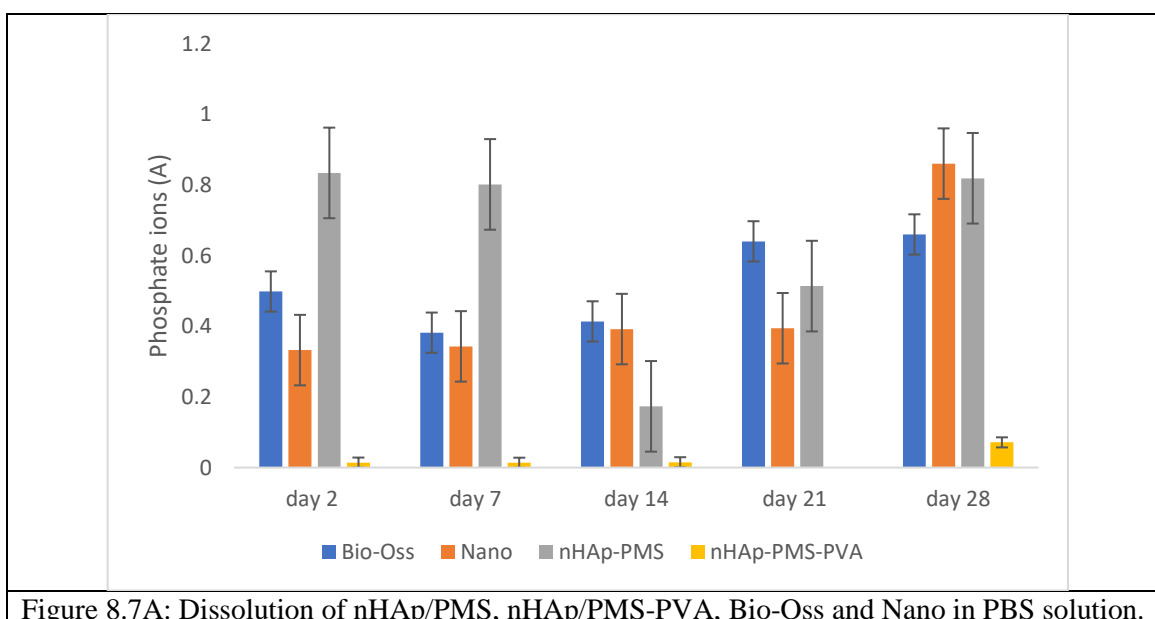
### 8.2.2 Dissolution studies

It was observed that nHAp/PMS swelled in some parts and lost its adhesion to the substrate. Table 8.2 shows that nHAp/PMS has a highest percentage of weight gain (108%) on sitting in PBS for 30 days, because of its high surface area, larger number of active sites and surface hydrophilic (polar) interactions with ions in PBS leading to rapid ion adsorption. Possibly in HAp/PMS-PVA the polymer hinders uptake [285].

Table 8.2: Weight gain of samples in PBS for 30 days.

Samples	W <sub>2</sub> of (mg)	W <sub>1</sub> of (mg)	%
Bio-Oss	20.2	19.0	6.31
Nano	20.3	19.0	6.84
nHAp/PMS	39.6	19.0	108.42
nHAp/PMS-PVA	21.2	19.0	11.57

The dissolution study showed (Fig.8.7) that nHAp/PMS provides a suitable surface for bone-like apatite because PMS has more functional groups (as OH<sup>-</sup> and COO<sup>-</sup>) that attract positive ions in PBS (as K<sup>+</sup> ions). Similarly, nHAp attracts negative charged (PO<sub>4</sub><sup>3-</sup>) leading to increased phosphate concentration. Therefore, nHAp/PMS has a lower concentration of phosphate ions in solution and higher concentration of phosphate ions on nHAp/PMS due to attracting more NPs and causing aggregation on their surface after 14 days. Here, nHAp/PMS shows a low rate of degradation in SBF. As a result, this can help the cell adhesion with bone cells and it can be used by these samples as a scaffold. However, Bio-Oss and Nano started to degrade after 21 days due to dissolution in SBF.





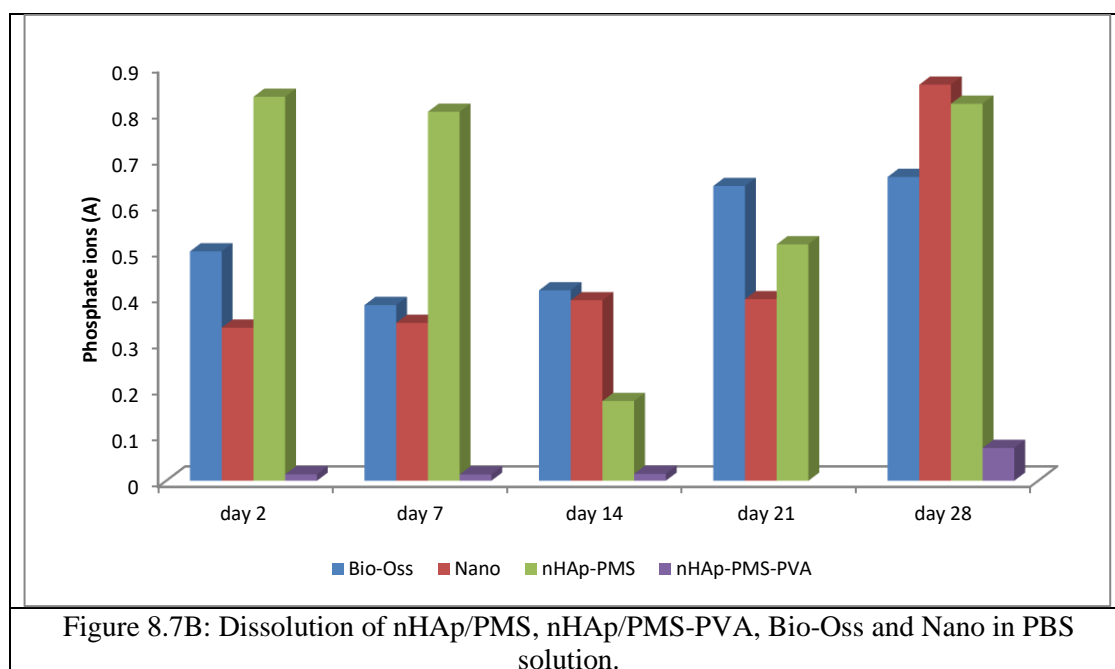


Figure 8.8-8.9 show SEM evidence of the state of nHAp/PMS, nHAp/PMS-PVA, Bio-Oss and Nano after a 14 day bioactivity test in SBF. The finest (20-50nm) and least-dense HAp phase has been laid down by nHAp/PMS. The author believes that this is the case because deposition on PMS involves steps:

- (i) incubation: where the PMS surface becomes more negatively charged and where PMS surface-held functional groups ( $\text{OH}^-$ ,  $\text{COO}^-$  and  $\text{PO}_4^{3-}$ ) electrostatically-attract  $\text{Ca}^{2+}$ ,
- (ii) nucleation: where  $\text{NH}_4^+$  attracts HAp-held  $\text{OH}^-$  and  $\text{PO}_4^{3-}$  [301] and
- (iii) growth: where  $\text{Ca}^{2+}$ -rich phase accumulates  $\text{PO}_4^{3-}$  leading to bone-like apatite growth [193] with its surface covered in phosphate ions[192].

Figure 8.9 shows that the morphology of Bio-Oss and Nano surface is less dense HAp layer formation on nHAp/PMS. Moreover, the nHAp/PMS can be observed after incubation for 2 days SBF (see Fig. 8.10A). Here, it exhibited a pore structure that provides a suitable surface topography for cell adhesion. In fact, the open porous structure of space is able to absorb tissue ingrowth. Further, the pore size is important for cellular adaptation, sufficient nutrient permeation and new bone formation [194]. The results reveal that the PMS surface chemistry (with its ion-binding potential) is viable up to 14 days of culturing in SBF [303], all the time accumulating HAp. On more

nHAp/PMS in SBF this leads to the enhancement of mineralization and supports its osteoblast activity [297]. Also, EDX results reveal that the Ca, P and O elements found on the PMS surface confirmed the growth of a calcium phosphate layer on nHAp/PMS (see Fig. 8.11).

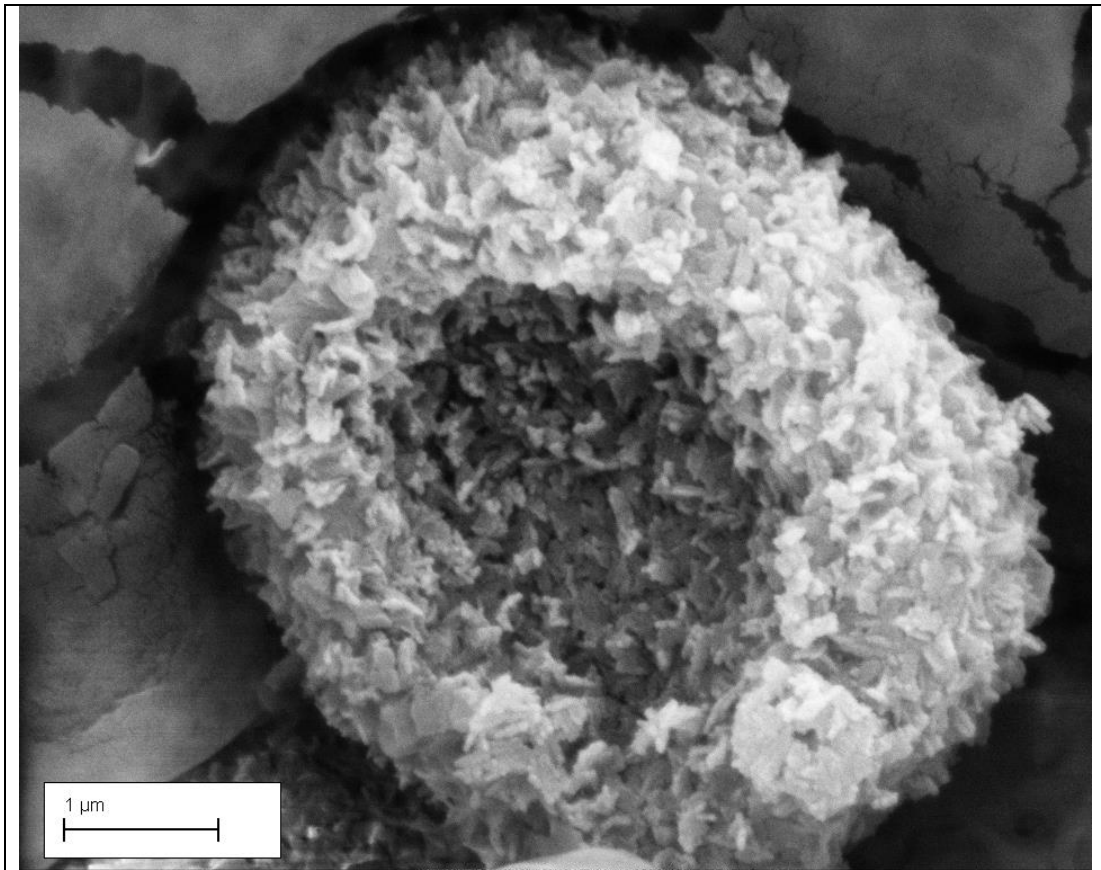


Figure 8.8: SEM of PMS after the bioactivity study in SBF over 14 days for nHAp/PMS (scale bar =1μm).

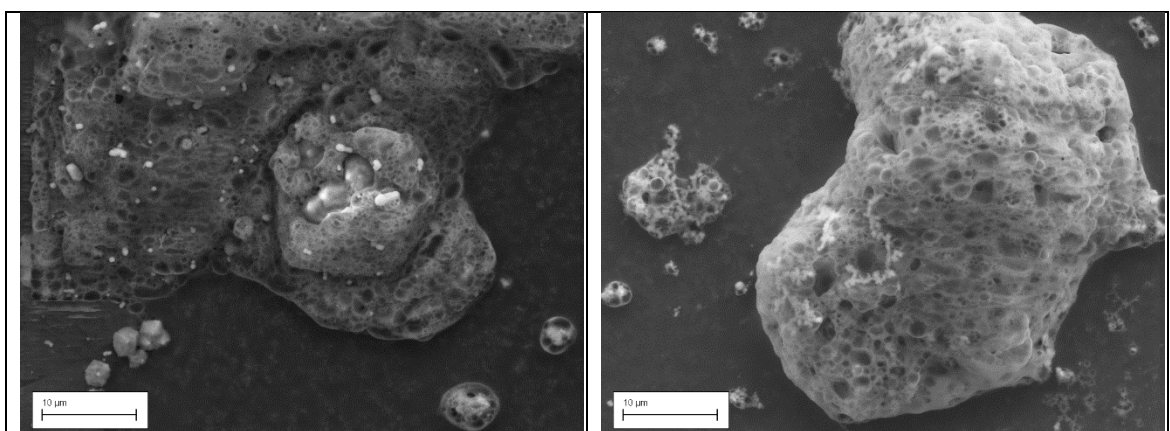


Figure 8.9: SEM of two samples after the bioactivity study in SBF for 14 days: A) Bio-Oss and B) Nano (scale bar =10μm).

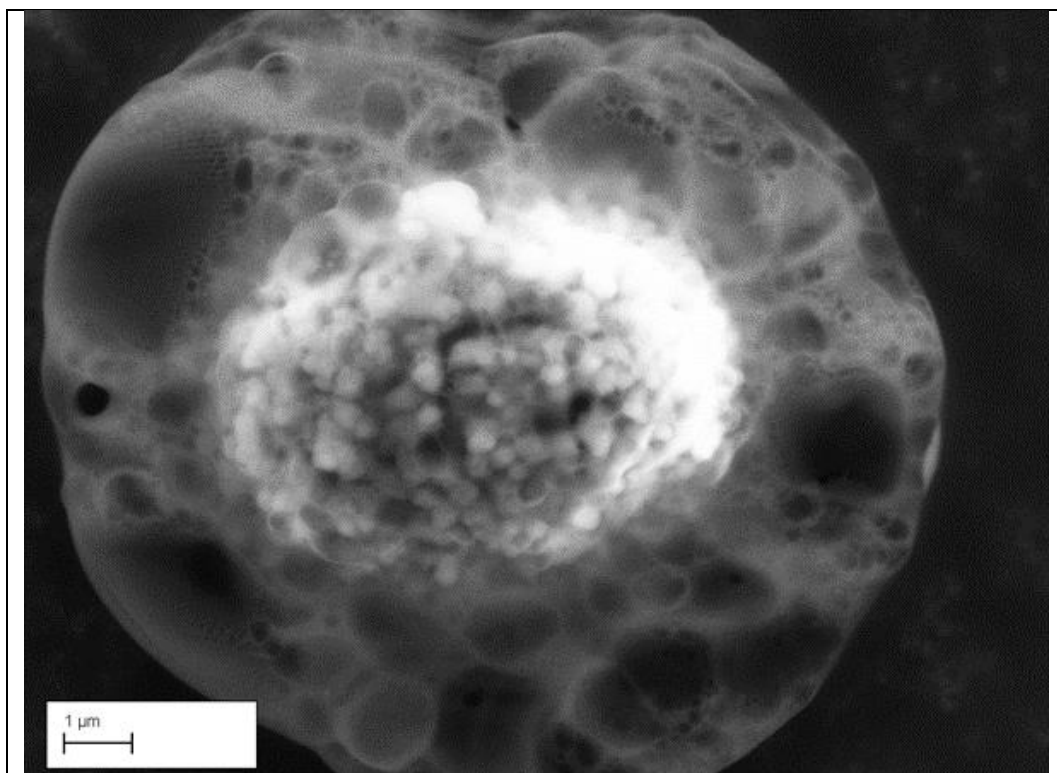


Figure 8.10A: SEM of nHAp/PMS in a bioactivity study of in SBF after 2 days.

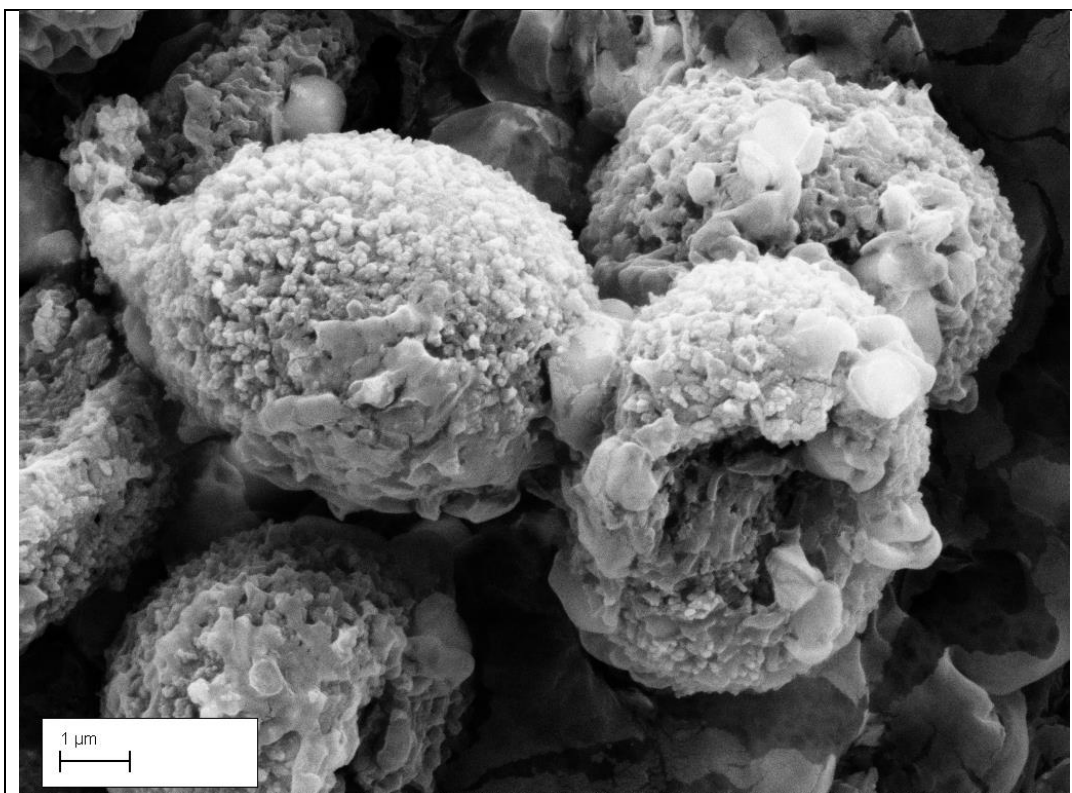


Figure 8.10B: SEM of nHAp/PMS in a bioactivity study of in SBF after 14 days.

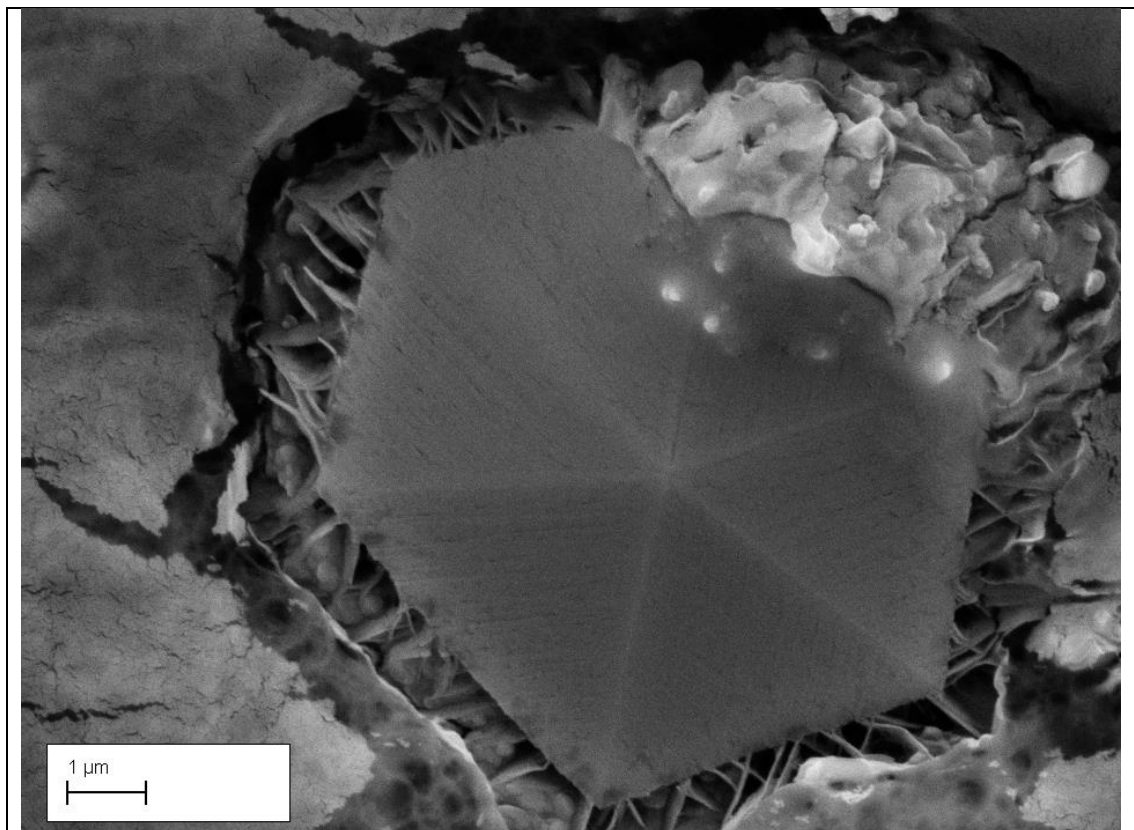


Figure 8.11A: SEM of the bioactivity study in SBF after 7 days for nHAp/PMS (scale bar =1 $\mu$ m).

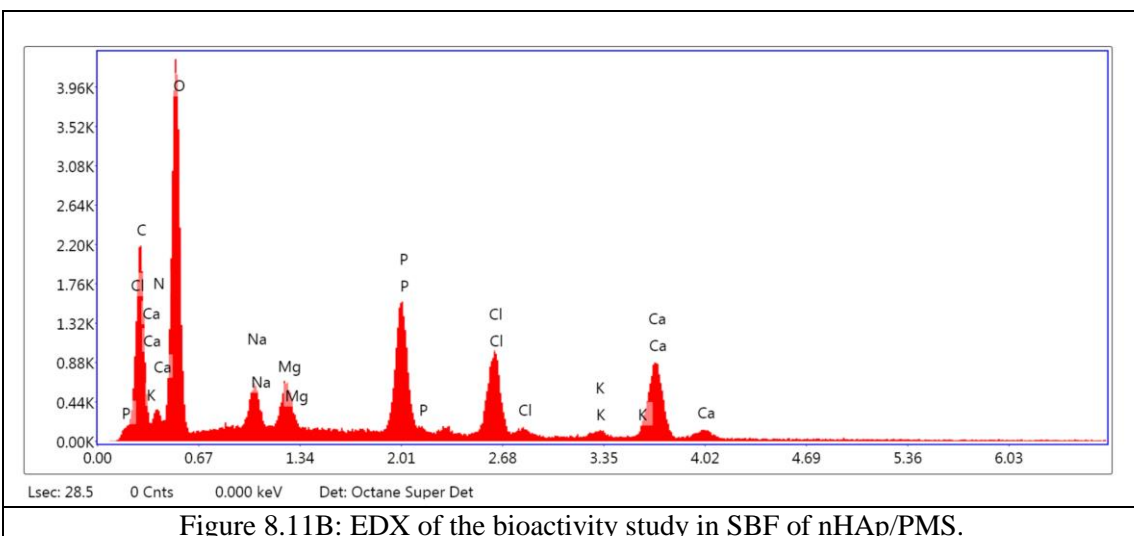


Figure 8.11B: EDX of the bioactivity study in SBF of nHAp/PMS.

However, Figure 8.12 shows that the morphology of the samples changed after dissolution in PBS for 30 days, with more pores seen on the surface of the nHAp/PMS sample possibly due to biodegradation (see Fig. 8.12). During dissolution, after 7 days, the dissolution of Bio-Oss and Nano was more than nHAp/PMS and nHAp/PMS-PVA

leading to a low rate of dissolution. These samples and their aggregates could create pores of similar dimension to them and their aggregates (see Fig. 8.13) [194].

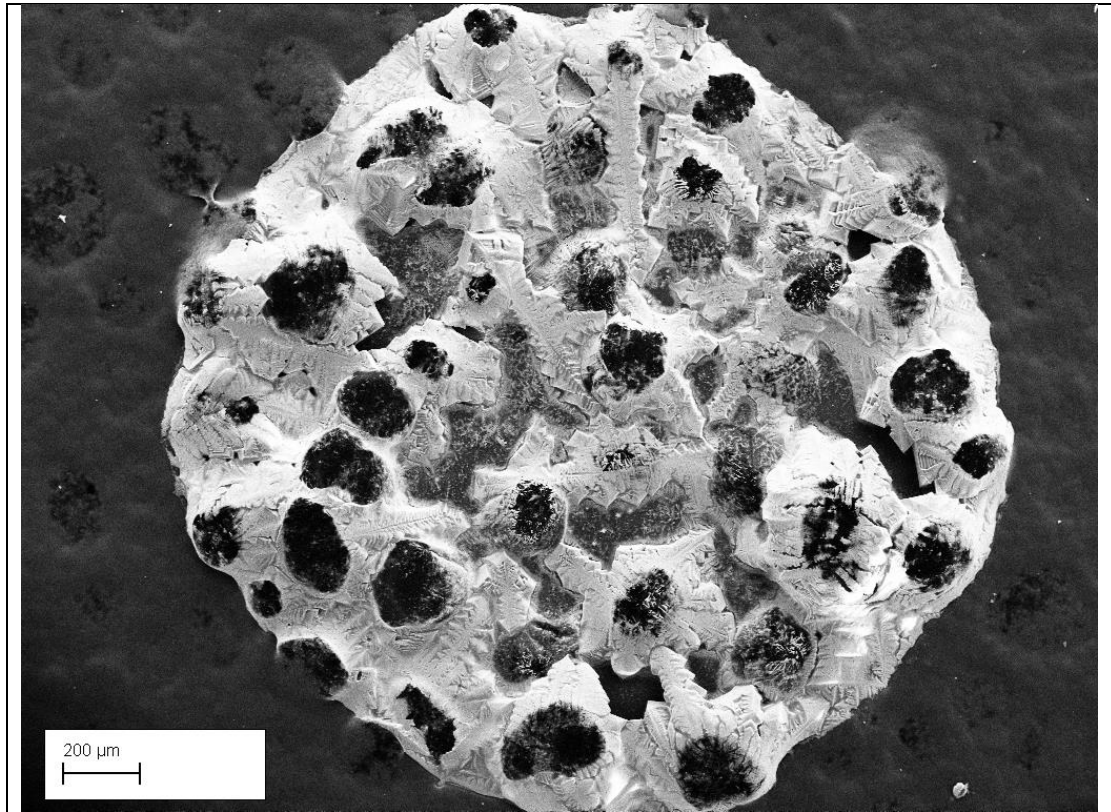


Figure 8.12: SEM of nHAp/PMS in PBS for 30 days.

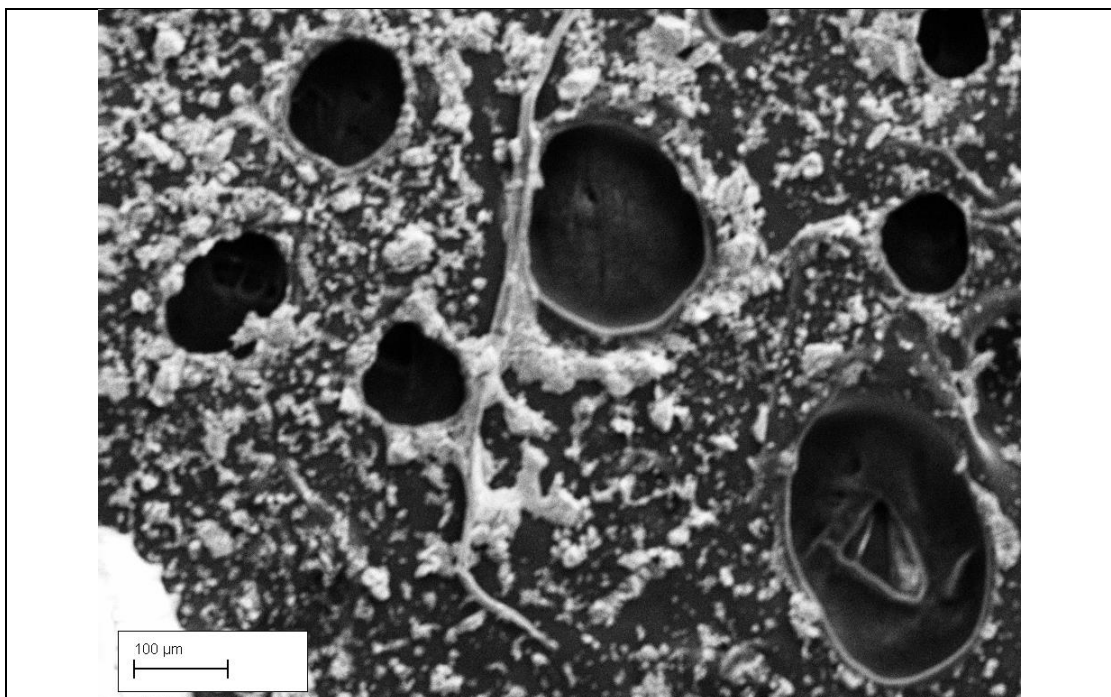
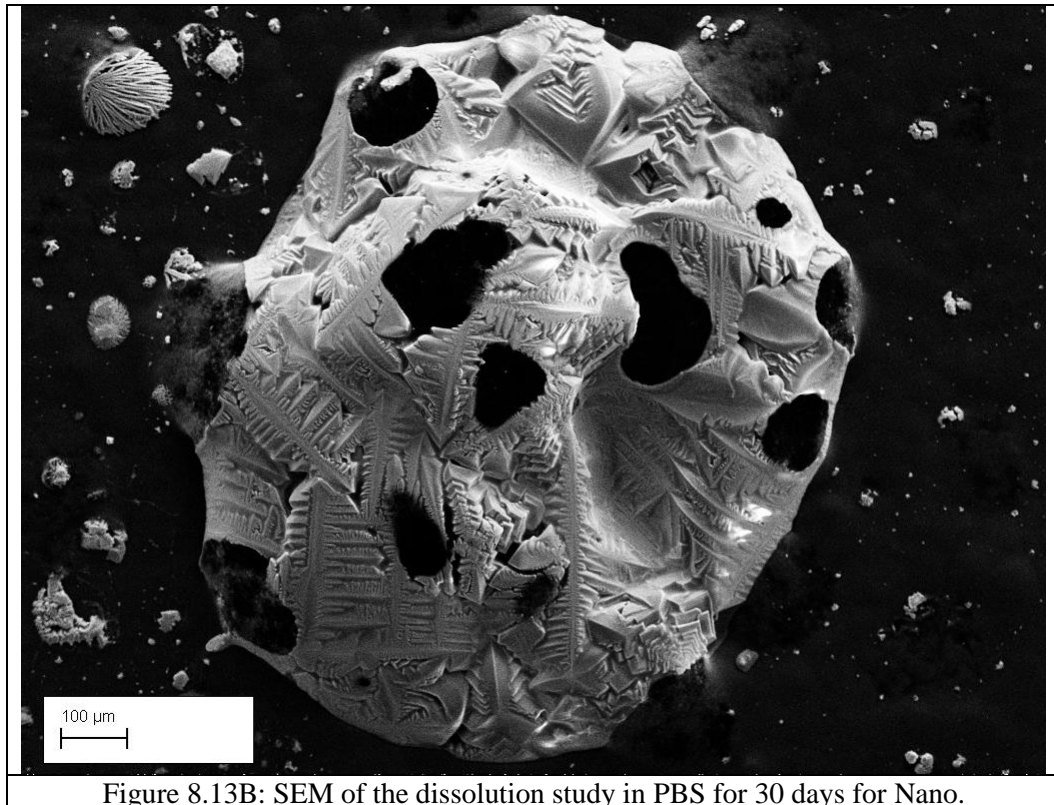


Figure 8.13A: SEM of the dissolution study in PBS for 30 days for Bio-Oss and B) Nano.



### 8.3 Conclusions

*In vitro* bioactivity and the dissolution of HAp and HAp/PMS samples were evaluated using SBF and PBS environments, respectively. The bioactivity study showed rapid formation of bone-like HAp on the nHAp/PMS surface by SEM and UV. Here, PMS acts as a chelating reagent to accelerate the mineralization process. The apatite layer increased in extent with time in SBF. *In vitro* dissolution of nHAp/PMS and after 30 days, it was less than Bio-Oss and Nano leading to a low rate of dissolution. Because of the morphology of the samples changed after dissolution in PBS for 30 days and more pores seen on the surface of the nHAp/PMS sample due to biodegradation Here, nHAp/PMS could create pores of similar dimension to them and their aggregates.

## **Chapter 9: The drug delivery and protein adsorption by hollow microsphere by Portobello mushroom spores (PMS) using ascorbic acid (AA) hemoglobin (Hb) and insulin as model therapeutic agents.**

---

In this chapter, the adsorption or uptake of PMS/biomolecules has been investigated to explore the potential of a mode of drug delivery. AA/PMS could well, it was thought, be used for skin protection. Hb/PMS, insulin/PMS, nHAp/PMS might well be used for a drug delivery system and PMS suspension as a food supplement. The PMS samples were compared with PVA hydrogel as model synthetic microspheres. Bioactivity and dissolution were studied using simulated body fluid (SBF). The samples were characterized by SEM,  $\mu$ -FTIR and UV (described in chapter 3).

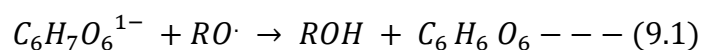
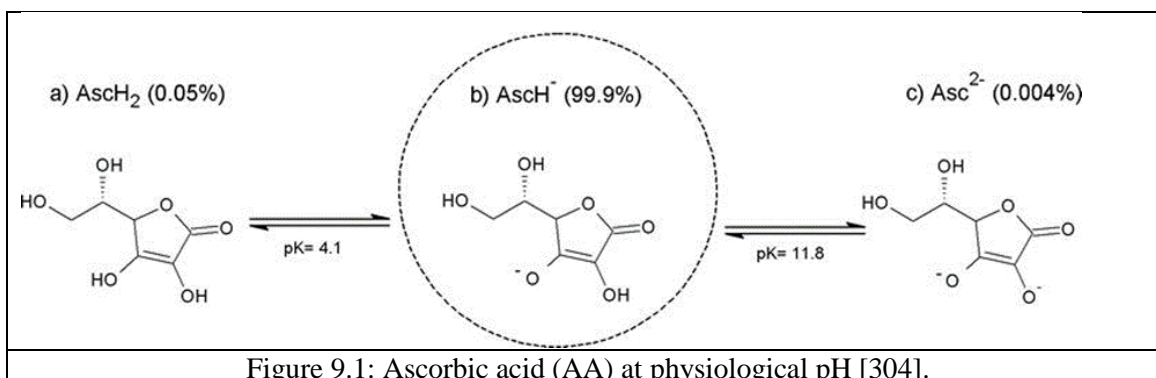
### **9.1 Introduction**

Recent research trend in tissue engineering has been based on seeding cells into porous matrices of biodegradable polymers. The ideal biomaterial should be biodegradable, non-toxic and porous (aiding the migration of host cells into the matrix permitting growth into complete tissue analogs *in vivo*) [112]. Mushrooms and their derivatives have been used in antitumor, anti-diabetic, wound healing, antibacterial, anti-parasitic, antiviral, preventing dental plaque, immunomodulatory, cardiovascular, hepato protective, [114] drug delivery systems and have been used as bio-materials for tissue engineering [111].

#### **9.1.1 Ascorbic Acid**

Ascorbic acid (AA;  $C_6H_8O_6$ ; Mwt. 176.12 g/mol) is vitamin C (L-hexuronic acid; water-soluble) and is essential for metabolic processes. It can be present in all body fluids. At physiological pH (7.2), Figure 9.1 indicates that the ascorbate anion ( $HAs^{1-}$ ) is more acidic because it is stabilized (in the form Fig. 9.1B) via electron delocalization and is found at around 99% of AA. It affects more than 0.05% of  $H_2As$  and 0.004% of ascorbate ions  $Asc^{2-}$  [304]. The ascorbate ions ( $HAs^{1-}$ ) is a reducing agent and an antioxidant that inhibits the risk of cancer via neutralizing free-radicals that damage

DNA [305] (see the equation below). AA is known as a reductant of metals generating NPs (e.g. Au NPs which reducing/capping agents [306]).



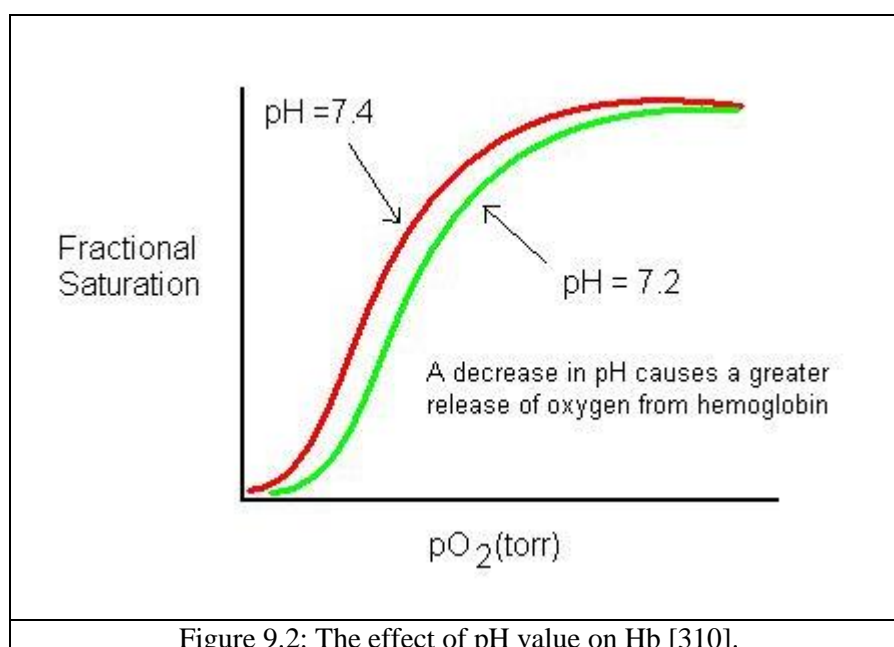
Several studies indicated that AA can be deposited on the skin and is able to act as a sunscreen for the skin [307]. Others, use cross-linked chitosan microspheres to encapsulate AA for drug delivery via spray drying [305]. AA can also be intercalated in a Ca/Al layered double hydroxide drug delivery system [308].

Collagen is important for the strength and function of the skin and is an important factor in skin rejuvenation and affects wrinkle reversal. The amount of collagen in the skin tends to decline with age; therefore, it is widely used as a moisturizer in cosmetic creams and products. Vitamin C (L-ascorbic acid) has been widely used in cosmetic and dermatological products because of its photoprotective effect and the ability to scavenge free radicals and destroy oxidizing agents. It can also induce collagen synthesis and suppress the pigmentation of the skin, while reducing signs of photoaging. Moreover, it is used to treat and prevent cancer via many mechanisms: (i) antioxidant (because it has many phenol groups to inhibit the free radicals and reduce toxicity of chemotherapeutic agents), (ii) stimulation of collagen formation, which is necessary for stopping tumour growth and (iii) correction of AA level and (iv) enhancement of the immune system in the human body [305].



### 9.1.2 Hemoglobin

Hemoglobin (Hb) is a globular protein with quaternary structure (RMM 64450 g/mol; soluble in water) which is a tetramer consisting of (two dimers that bind to oxygen) two  $\alpha$ -chains and two  $\beta$ -chains (four globin chains), each associated with a heme group (4 heme with 4 polypeptide chain  $2\alpha$  and  $2\beta$  gives 1 hemoglobin molecule). Hb has a negative charge and it is found in all vertebrates and it is the major oxygen-transport protein found in the red blood cells [309]. The Bohr effect describes the increase in affinity of Hb when the pH is high. Here, Hb loses  $H^+$  from amino acid leading to a change in its structure and increasing the ability of oxygen bonding (see Fig. 9.2). In constant, the oxygen affinity of Hb decreases when pH is low because Hb picks up  $H^+$ .



Some researchers have reported that nHAp hollow microspheres can be used in the delivery of adsorbed hemoglobin using inorganic phosphorus. The amount of adsorbed Hb increased on the HAp porous hollow/microsphere in proportion to their specific area. Furthermore, the Hb released in phosphate buffer saline (PBS) solution in pH 7.4 was higher than at pH 6 [111]. Previous study has indicated that nHAp porous/hollow microspheres using a DNA-templated had a high drug loading capacity and a better ability to release Hb in different concentrations [269].

### 9.1.3 Drug Delivery and Nanomaterials

Ingestion/oral routes are significant and convenient types of drug delivery. Exposure of the drug to pH values of the stomach can result in pH-induced oxidation-hydrolysis-denaturation of protein therapeutics, leading to loss of the activity of the release drug [311]. Enzymatic degradation is caused by proteases, nucleases and lipases present in the full GI tract, resulting in digestion of biological molecules prior to their absorption. Such problems need to be overcome [127]. In addition, the vehicle of the drug delivery should be biocompatible [126]. Drug release depends on the specific properties of the drug [312], pH changes, temperature and solubility in the prevailing solvent [209]. The mechanisms of drug release can be explained in terms of host swelling, diffusion and degradation [313].

Hydrogels can be thought of as possible 3D that can be used for drug delivery systems due to their soft and hydrophilic surface interfaces to react with the tissue in the human body. Factors such as the nature of the drug, degree of the hydrogel crosslinking and hydrogel pore size are important. [314]. For example, polyvinyl alcohol (PVA), and pullulan (polysaccharide)-PVA interpenetrating polymeric network (IPN) microspheres have been used as drug delivery systems [315]. Furthermore, developing polymeric NPs has historically been limited by their low bio-availabilities [127].

Several studies have shown that bioactive ceramics [316] and polymeric microspheres [312] might be used in drug delivery to improve bone regeneration, growth of bone tissue and controlling bone infection (releasing antibiotics) [317]. Their advantages can be suggested to be high surface area and porosity, large pore volume and reduced toxicity [318].

#### 1. Insulin

Human insulin consists of two chains polypeptide ( $\alpha$ -chain 21 amino acid and  $\beta$ -chain 30 amino acid) ( $C_{257}H_{383}N_{65}O_{77}S_6$ ; RMM.5808) which are produced from  $\beta$ -cells in the pancreas in the human body. It has a negative charge and low solubility at pH 7.2 (2 mg/mL of insulin at pH 2–3). Insulin is considered a hormone (destroyed in the stomach if taken orally, due to the prevailing acidity) that regulates the metabolism of fats and carbohydrates via promoting glucose absorption from blood (see Fig. 9.3) [319]. The electrostatic interactions (attractive or repulsive) are an important factor in insulin adsorption at pH 7.4. When the membrane of sample has no charge groups or almost neutral charge, hydrophobic interaction between the membrane of sample and insulin

can contribute to the extraction of insulin adsorption, which was less dependent on pH and was mainly due to hydrophobic interaction. A pH about 5.4 causes insulin aggregation [320].

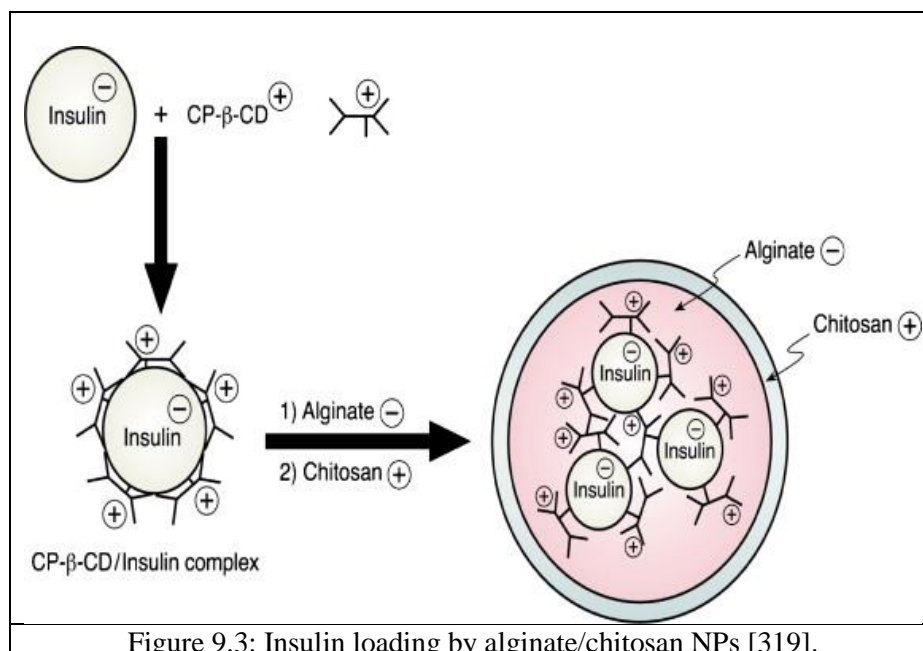


Figure 9.3: Insulin loading by alginate/chitosan NPs [319].

## 2. Oral Delivery of Insulin (In)

Insulin (In) has been used as a model protein, because it is a well-known therapeutic protein and standard treatment for diabetes. Usually, insulin is associated with multi-daily injections. Therefore, there has been significant interest in the development of oral non-invasive delivery systems. Since unfortunately, injections are often painful, especially for children, leading to low patient compliance. Oral delivery is an improved method of protein delivery and can be much easier than dealing with injections and can improved patient compliance [321]. Insulin has been used in many methods but with some limitations. Doses of insulin are sometimes not enough to generate a hypoglycaemic (decreasing blood sugar below the normal levels) response. Natural encapsulation using spores for drug delivery is thought to have many benefits: (i) uniform size, (ii) unique properties, (iii) internal cavity that can be used to accept-release range of drugs and (iv) no toxic organic solvents.

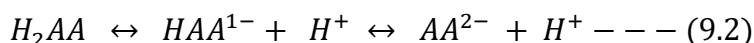
The methods used in the assessment of the uptake and release of AA, Hb and insulin are described in section 4.5.

## 9.2 Results and discussion

### 9.2.1 Uptake Studies

#### 1. Ascorbic Acid

Ascorbic acid ( $\lambda_{\max} = 245\text{nm}$ ) is water soluble and dissociated in water depending on the solution acidity as monovalent ascorbate anion ( $\lambda_{\max} = 265\text{nm}$ ) and then dissociated to divalent ascorbate anion ( $\lambda_{\max} = 297\text{nm}$ ) according to the following equation [322]:



Here, AA is dissociated to the monovalent ascorbate anion ( $\lambda_{\max} = 265\text{nm}$ ). Table 9.1 and Fig. 9.4 indicate that PMS alone has a high extent of AA adsorption (99.8%) at a relatively low concentration (0.149mM) compared with other samples. The adsorption is slower with nHAp/PMS (0.143mM) and PMS/PVA (0.141mM) because PMS has a smooth surface and so is able to ad/absorb AA directly.

Table 9.1: The AA loading of the samples using different concentrations for 24h at RT.  $[AA]_1$  is the initial concentration of the loading solution;  $[AA]_2$  is absorbed 0.15mM on PMS (3mg/10mL; after the initial  $[AA]_1$  was subtracted from final  $[AA]$  solution after 1 day) in  $H_2O$

Samples	$[AA]_1$ (mmol) at $t=0$	$[AA]_2$ absorbed on PMS (mmol)	Loading uptake/adsorption (%)
PMS alone	26.418	26.370	99.82
nHAp/PMS	26.418	25.31	95.80
PMS/PVA hydrogel	26.418	24.961	94.48

Figure 9.5 shows that there is an electrostatic interaction between the PMS surface (with its many functional groups which have -OH, -COO and -NH) and AA: i.e. there is a broad OH peak at  $3400\text{ cm}^{-1}$  and the sharp C=O peak at  $1750\text{ cm}^{-1}$  (group) after PMS surface interaction. The FTIR spectra show important peaks of pure AA (i.e.  $3400$  (hydroxyl; broad),  $1750$  and  $1640$  (carboxyl; sharp) and  $1020\text{ cm}^{-1}$  (C-O; sharp)). After uptake on/in the PMS surface, the broad peak of pure AA is decreased in intensity as hydrogen bonding for AA molecules decreased and interacted with the PMS surface. Here, the evidence confirms the stability of AA and that AA was chemically unchanged by PMS. With increasing AA concentration by a factor of 3 the average % ad/absorption decreased to half 49.6% but the absolute extent of uptake; essentially it is assumed that the active sites as  $OH^-$  and  $COO^-$  on spore's surface are no saturated with AA molecules residual. Observations of nHAp/PMS and PVA hydrogel show a similar

trend and good extent of ad/absorption at 0.15mM AA solution concentration (95-94%) with less AA taken up than for the PMS alone.

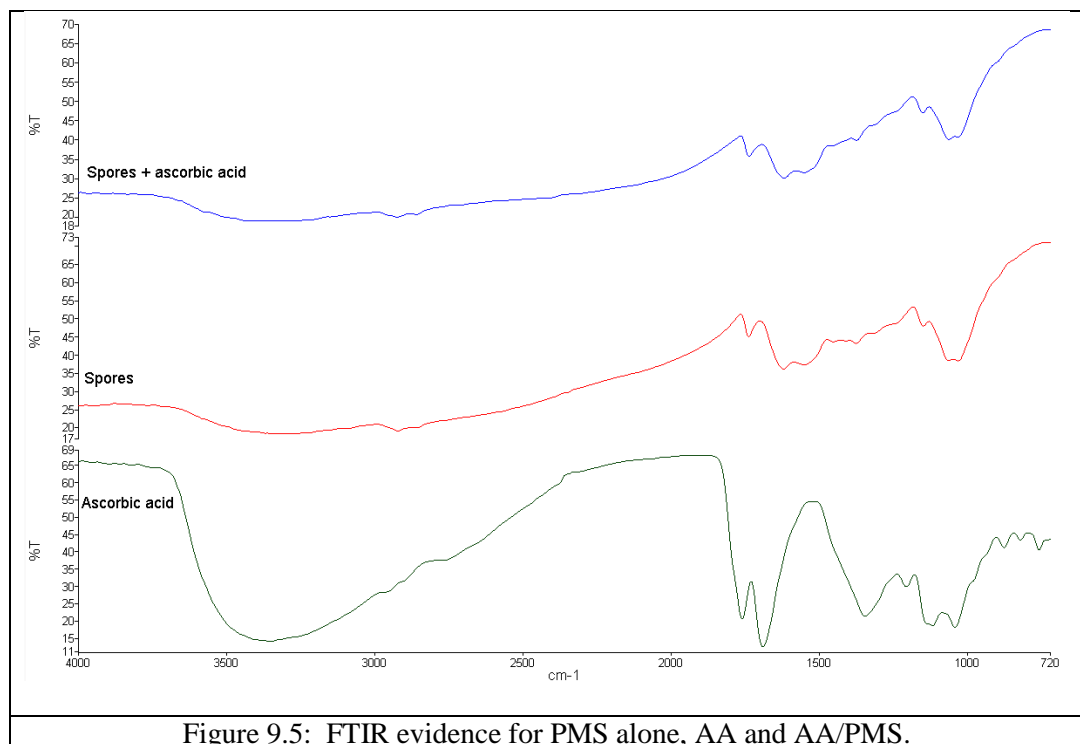
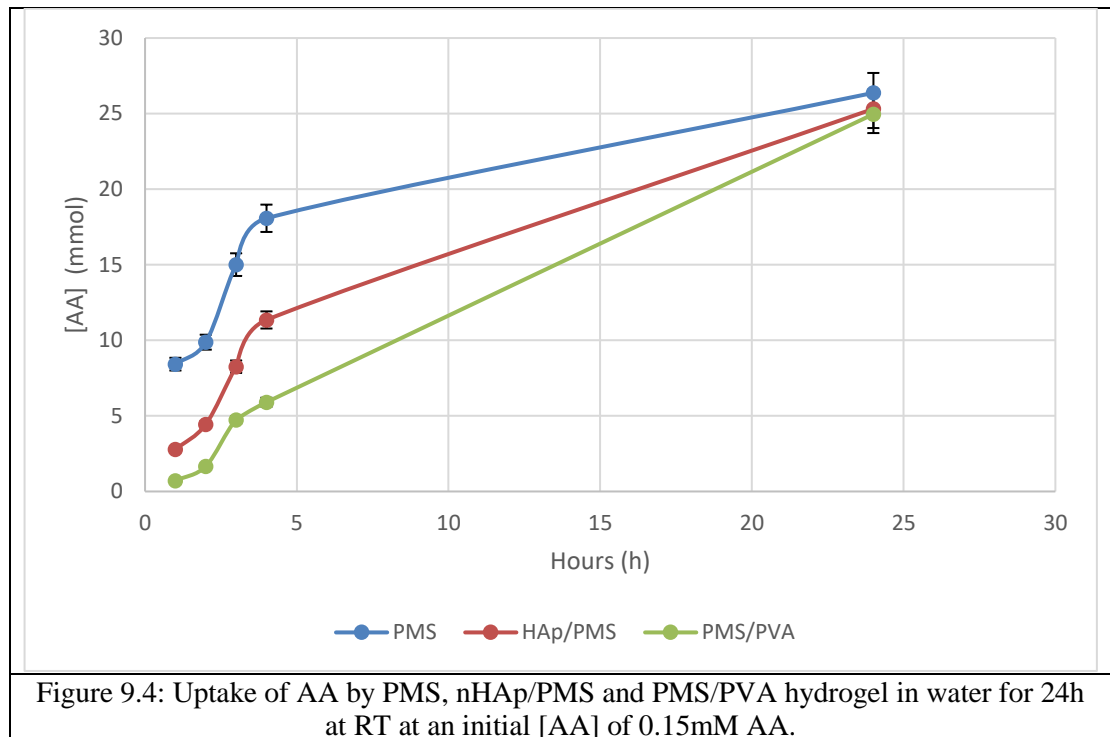
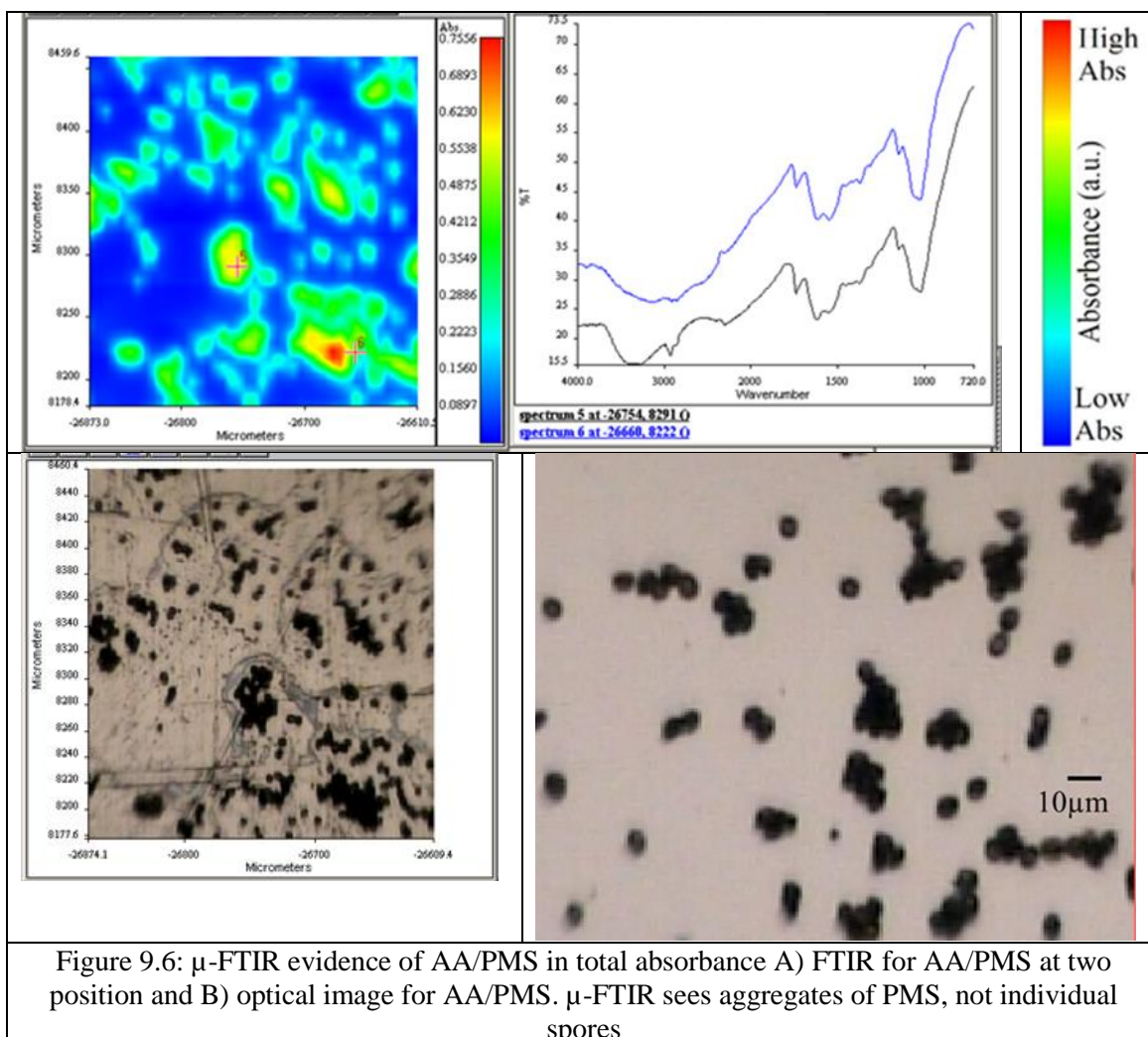
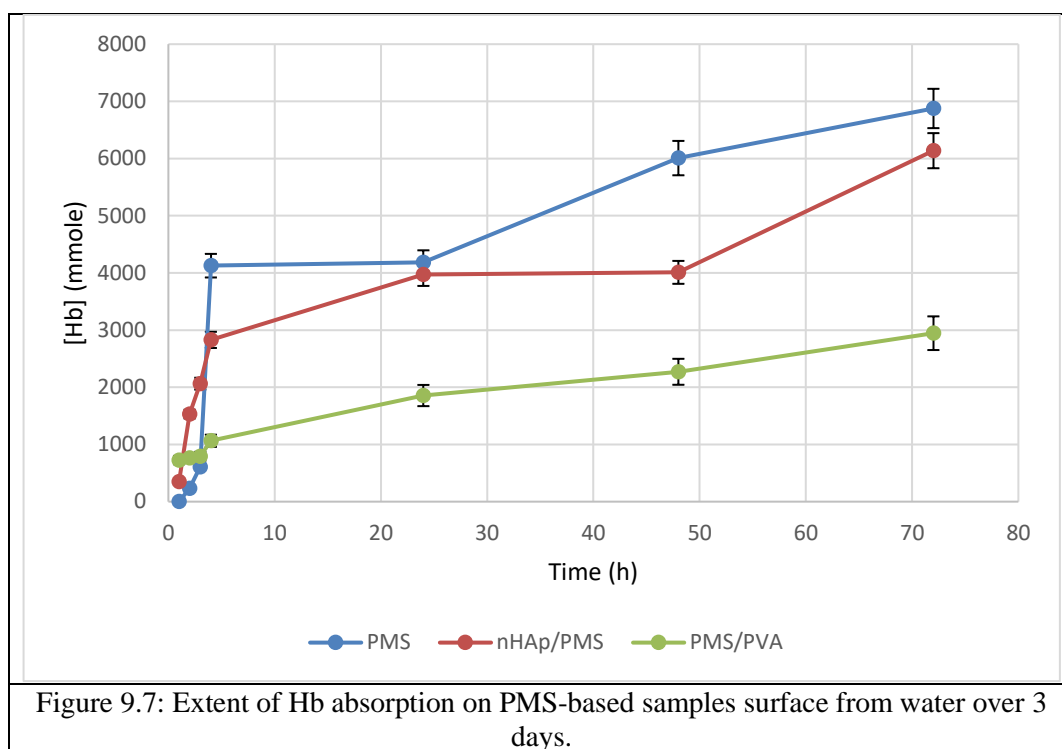


Figure 9.6 is a chemical map of AA/PMS derived from micro-FTIR. This shows that the strong interaction (red to yellow area) in AA/PMS sample indicated to adsorb ascorbic acid on/in the PMS surface.



## 2. Hemoglobin (Hb) Adsorbed on PMS Surface

Hb is a model of protein. Its adsorption/release was also investigated with PMS alone, nHAp/PMS and PMS/PVA hydrogel at a constant concentration (0.2 mg/mL;  $3 \times 10^{-4}$  mM) with agitation at 24h and 37°C. Figure 9.7 and Table 9.2 show that the extent of adsorption Hb on three samples. This PMS-based samples continued to broadly increase with time up to 80h. The uptake of Hb by nHAp/PMS is broadly the same as with PMS, with is experimental error. Possibly, one should deduce that the HAp on PMS is not blocking entry of Hb to PMS (see Table 9.2). After 1day, it can be observed that nHAp/PMS and PMS have the same level of Hb adsorption (around 6 mmol).



The large Hb protein must interact with the PMS surface functional groups. Protein sorption presumably will be due hydrogen bonding, van der Waals, hydrophobic and electrostatic interaction). All these are possible on the PMS surface in parallel solvent water probably also enters the PMS causing swelling PMS and leading to an increase in its surface area. In contrast, nHAp/PMS and PMS/PVA hydrogel reached a saturated state after 3 days on Hb loading of 31% and 15% respectively.

Table 9.2: Hb loading of these PMS-based samples for 3 days at RT.  $[Hb]_1$  is the initial concentration of the loading solution;  $[Hb]_2$  is the adsorbed amount on PMS (3mg/10mL; after the initial  $[Hb]_1$  was subtracted from final  $[Hb]$  solution after 3 day)

Samples	$[Hb]_1$ (mmol)	$[Hb]_2$ adsorb (mmol)	Loading (%)
PMS	19.33	6.87	36
nHAp/PMS	19.33	6.13	32
PMS/PVA hydrogel	19.33	2.94	15

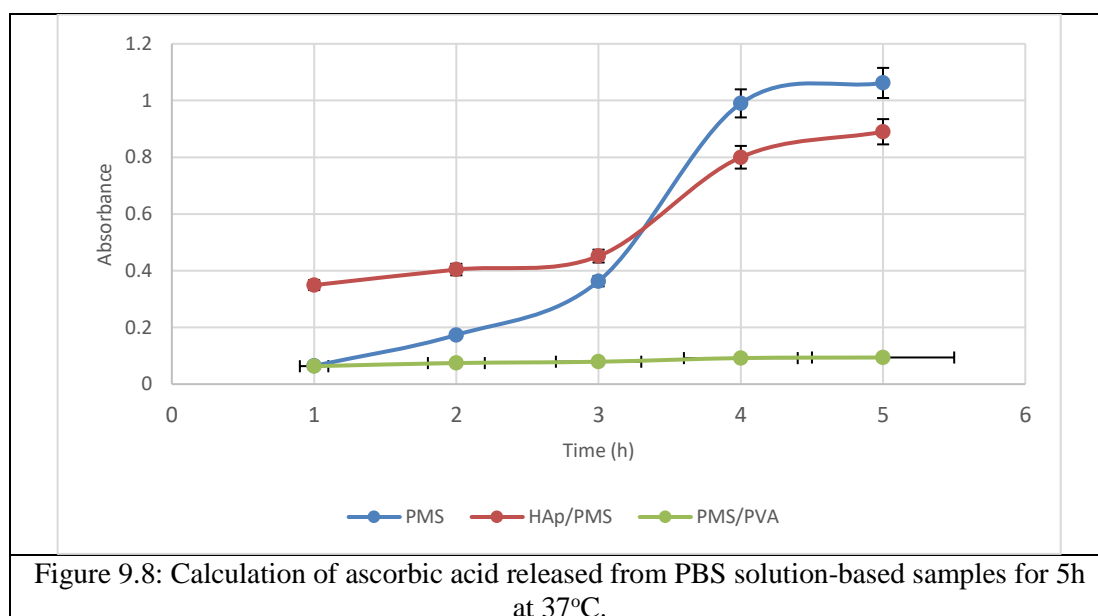
### 9.2.2 AA, Hb and In Drug release

*In vitro*, the release studies of ascorbic acid (AA a model vitamin) and hemoglobin (Hb a model protein) hollow PMS, nHAp/PMS, HAp-PVA hydrogel microspheres and PMS-PVA-hydrogel has been measured in phosphate buffer saline (PBS) at pH 7.4 at

37°C over periods of 5h. The amounts of reagent release were estimated using UV (where  $\lambda_{\max}$  varies with the analytic).

### 1. Ascorbic Acid

The results show that AA release from nHAp/PMS had a higher initial rate of AA release than PMS in the first two hours but by 3-5h this is reversed. At all times AA release from PMS and nHAp/PMS was greater than when PVA was present. PMS-based samples are shown in Figure 9.8 Here the rough surface morphology of nHAp/PMS (due to nHAp which has a rod structure) does not significantly block the release of AA.

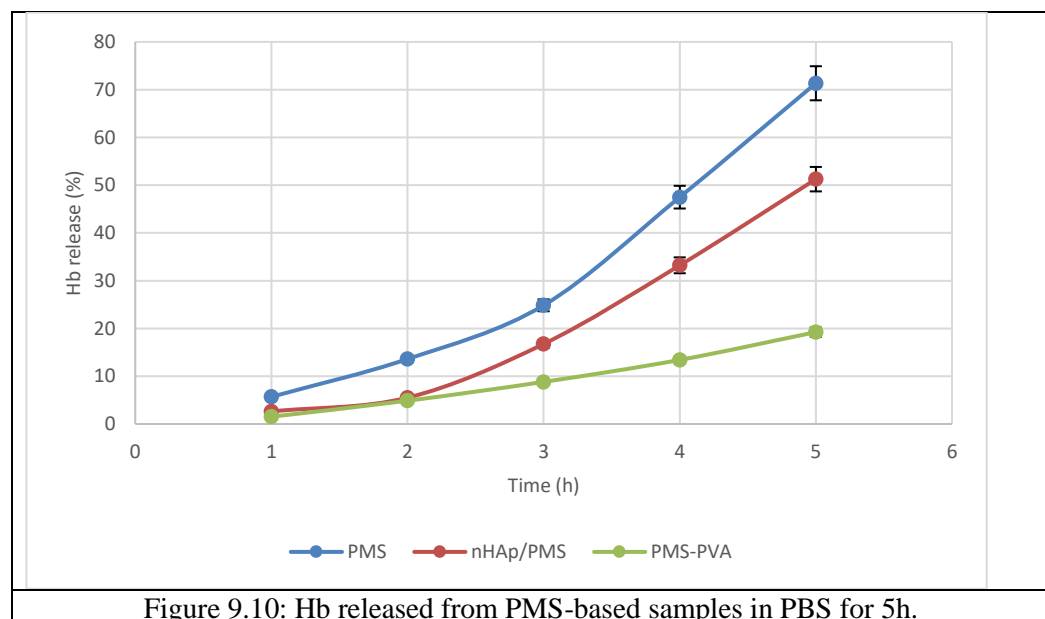
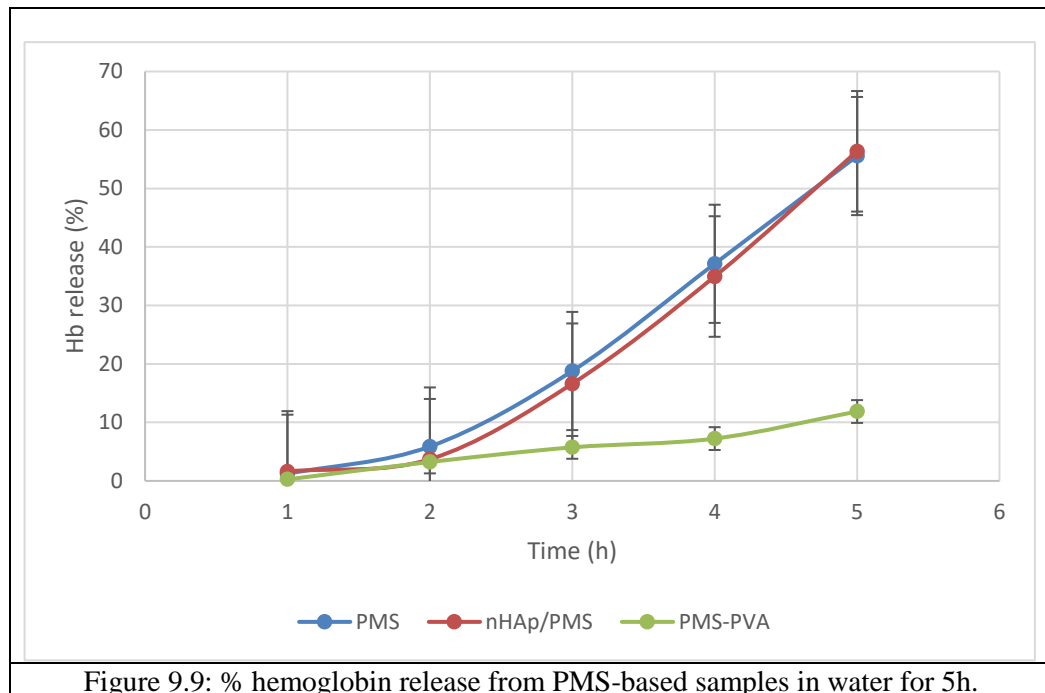


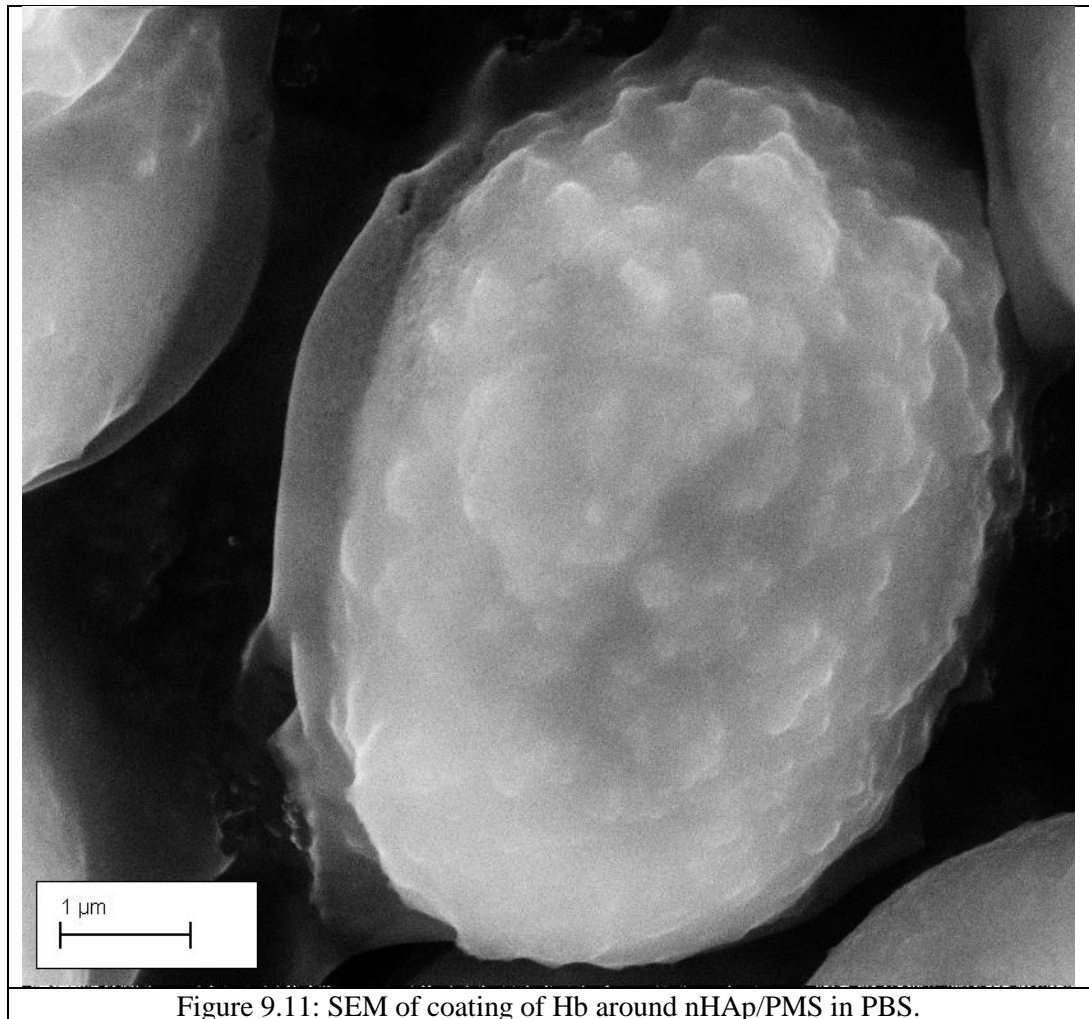
### 2. Hemoglobin

Hb release from the PMS-based samples was studied in water (as a control and PBS solution (pH 7.4) over 4h and at 37°C. Figure 9.9 shows no significant change for %Hb release with nHAp/PMS and PMS in water for 5h at 37°C. Again, Hb release was similar for PMS and nHAp/PMS; in other words, nHAp does not hinder Hb release, unlike PVA. Figure 9.10 shows that with the PMS-based samples Hb release into PBS solution. This was higher for PMS than into water (see Fig. 9.9) and increased with time. SEM (see Fig. 9.11) shows a slight variation in the morphology of Hb/PMS release in PBS. First, there appears to be a thin layer around the PMS surface that glues together PMS aggregates, it may be that HB is the glue between PMS. Furthermore, there was no denaturation or damage of the spores as a result of take up and release.



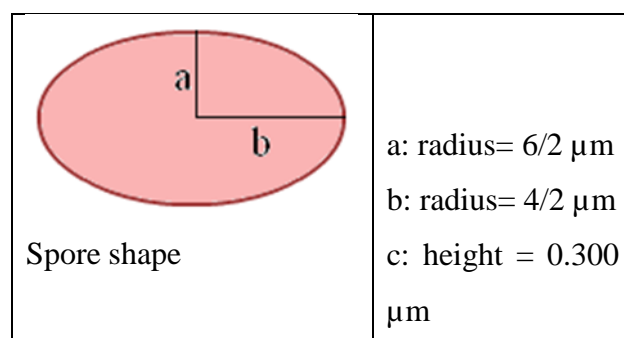
Clearly, nHAp/PMS exhibited a rough surface with its thick layer of nHAp on the PMS surface which presumably attracted more drug molecules onto the PMS surface. Consider for a moment whether this uptake/release is only a surface phenomenon (adsorption/desorption).





- **Surface Area (SA) of PMS**

The overall shape of PMS is oval ( $a = 3\mu\text{m}$  and  $b = 2\mu\text{m}$  in the schematic below and height average  $0.300\mu\text{m}$ ) confirmed by SEM and TEM). Therefore, the volume and surface area of PMS can be calculated as the follows:



(i) **PMS Volume**

$$\begin{aligned}
 1- \text{ Volume of PMS (oval)} &= \frac{4}{3} \pi a.b.c \\
 &= \frac{4}{3} \times 3.14 \times 3 \times 2 \times 0.3 = 7.536 \mu\text{m}^3 \\
 &= 7.5 \times 10^{-18} \text{m}^3
 \end{aligned}$$

$$\text{volume of PMS in 3mg} = 22.5 \times 10^{18} \text{nm}^3$$

$$\begin{aligned}
 2- \text{ Weight of PMS if predominantly H}_2\text{O (water-filled, } \rho_{\text{H}_2\text{O}} &= 10^6 \text{ g/m}^3) \\
 &= \rho_{\text{H}_2\text{O}} \times \text{vol}_{\text{PMS}} \\
 &= (10^6 \text{ g/m}^3) \times (7.5 \times 10^{-18} \text{ m}^3) \\
 &= 7.5 \times 10^{-12} \text{g PMS}
 \end{aligned}$$

$$1 \text{ pico (pg)} = 10^{-12} \text{g} = 7.5 \text{pg}$$

**(ii) Number of PMS per g, mg and 3mg**

$$\text{No. of PMS per g} = 1 / 7.5 \times 10^{-12} = 10^{12} / 7.5$$

$$\text{No. of PMS per 1mg} = 10^9 / 7.5 = 133 \times 10^6 = 133 \text{ million per mg.}$$

$$\begin{aligned}
 \text{No. of PMS per 3mg} &= 132 \times 10^6 \times 3 \text{ mg} = 400 \text{ million in 3mg} \\
 &\approx 4 \times 10^8 \text{ in 3mg}
 \end{aligned}$$

**(iii) Surface area (SA) of PMS**

$$\begin{aligned}
 \text{SA (oval)} &= \pi a.b = 3.14 \times (3 \mu\text{m}) \times (2 \mu\text{m}) \\
 &= 18.84 \mu\text{m}^2
 \end{aligned}$$

$$\begin{aligned}
 \text{SA for PMS per 3mg} &= \text{SA} \times \text{no. PMS per 3mg} \\
 &= 18.84 \mu\text{m}^2 \times (10^6 \text{ nm}^2) \times (400 \times 10^6 \text{ nm}^2 \text{ per 3mg PMS}) \\
 &= 7520 \times 10^{12} \text{ nm}^2 \text{ per 3mg PMS}
 \end{aligned}$$

**• AA molecules sorbed of 3mg PMS**

**(i) Number of molecules for 0.1mM AA in 10mL H<sub>2</sub>O**

$$\text{No. of AA molecules in 10mL} = 6 \times 10^{23} \times 0.15 \text{mM} / 1000 \times 10 \text{mL} / 1000 = 6 \times 10^{17} \text{ molecules}$$

**(ii) % of AA taken up**

surface area of PMS in 3mg =  $7520 \times 10^{12} \text{ nm}^2$

number of AA molecules in 10mL of 0.15mM =  $6 \times 10^{17}$

**(iii) AA molecules absorbed**

= (loading %) x (No. AA molecules)

For: PMS =  $0.99 \times (6 \times 10^{17}) = 5.9 \times 10^{17}$  molecules

nHAp/PMS =  $0.95 \times (6 \times 10^{17}) = 5.7 \times 10^{17}$  molecules

PMS/PVA =  $0.94 \times (6 \times 10^{17}) = 5.6 \times 10^{17}$  molecules

**(iv) Number of molecules for 0.1mM AA in 10mL H<sub>2</sub>O sorbed of 3mg**

= AA molecules absorbed / No. of PMS per 3mg

For PMS =  $5.9 \times 10^{17} / 4 \times 10^8 = 1.48 \times 10^9$  molecules

nHAp/PMS =  $5.7 \times 10^{17} / 4 \times 10^8 = 1.43 \times 10^9$  molecules

PMS/PVA =  $5.6 \times 10^{17} / 4 \times 10^8 = 1.40 \times 10^9$  molecules

**(v) Area of AA adsorbed (molecules) per 3mg PMS (nm<sup>2</sup>)**

= AA molecules absorbed of 3mg PMS / Surface area (SA) of PMS

For PMS =  $(1.48 \times 10^9) / 7520 \times 10^{12} = 2 \times 10^{-7} \text{ nm}^2 = 2.2 \text{ pm}^2$

nHAp/PMS =  $(1.43 \times 10^9) / 7520 \times 10^{12} = 19 \times 10^{-7} \text{ nm}^2 = 1.9 \text{ pm}^2$

PMS/PVA =  $(1.40 \times 10^9) / 7520 \times 10^{12} = 19 \times 10^{-7} \text{ nm}^2 = 1.8 \text{ pm}^2$

Table 9.3: AA molecules adsorbed per nm<sup>2</sup> surface area of PMS.

	AA molecules adsorbed	AA molecules adsorbed of 3mg PMS	Area of AA absorbed (molecules) on PMS
PMS	$5.9 \times 10^{17}$	$1.48 \times 10^9$	$2.1 \text{ pm}^2$
nHAp/PMS	$5.7 \times 10^{17}$	$1.43 \times 10^9$	$2 \text{ pm}^2$
PMS/PVA	$5.6 \times 10^{17}$	$1.40 \times 10^9$	$1.9 \text{ pm}^2$

This is very small for each AA and so the author calculates that AA must logically also be absorbed into PMS and PMS/PVA samples. Now consider Hb.

### ***Number of molecules for 0.2mg Hb in 10mL H<sub>2</sub>O***

$$(i) \quad M = (\text{wt./ RMM}) \times (1000/ \text{vmL}) = (0.2/ 64458) \times (1000/10\text{mL}) \\ = 31 \times 10^{-4} = 0.31\text{mM}$$

No. of molecules for 0.31 mM Hb in 10 mL H<sub>2</sub>O:

$$= 6 \times 10^{23} \times (0.31\text{mM} \times 10^{-3}) \times (10\text{mL}/1000) \\ = 1.86 \times 10^{18} \text{ molecules.}$$

### **(ii) Maximum concentration of internally-held (adsorbed) Hb**

Hb molecules absorbed = (Loading ratio%) x (No. Hb molecules)

For:	PMS	= 0.35 x (1.8 x 10 <sup>18</sup> )	= 65 x 10 <sup>16</sup>
	nHAp/PMS	= 0.31 x (1.8 x 10 <sup>18</sup> )	= 57.6 x 10 <sup>16</sup>
	PMS/PVA	= 0.15 x (1.8 x 10 <sup>18</sup> )	= 28 x 10 <sup>16</sup>

### **(iii) Hb molecules sorbed of 3mg PMS**

$$= \text{Hb molecules absorbed/ No. of PMS per 3mg} (4 \times 10^8)$$

For:	PMS	= (65 x 10 <sup>16</sup> ) / (4 x 10 <sup>8</sup> )	= 16.2 x 10 <sup>8</sup>
	nHAp/PMS	= (57.6 x 10 <sup>16</sup> ) / (4 x 10 <sup>8</sup> )	= 14.4 x 10 <sup>8</sup>
	PMS/PVA	= (28 x 10 <sup>16</sup> ) / (4 x 10 <sup>8</sup> )	= 7 x 10 <sup>8</sup>

### **(v) Area of Hb adsorbed in PMS (nm<sup>2</sup>)**

$$= \text{Hb molecules absorbed of 3mg PMS / Surface area (SA) of PMS}$$

For:	PMS	= (16.2 x 10 <sup>8</sup> ) / (7520 x 10 <sup>12</sup> )	= 22 x 10 <sup>-7</sup> nm <sup>2</sup> = 2.2pm <sup>2</sup>
	nHAp/PMS	= (14.4 x 10 <sup>8</sup> ) / (7520 x 10 <sup>12</sup> )	= 19 x 10 <sup>-7</sup> nm <sup>2</sup> = 1.91pm <sup>2</sup>
	PMS/PVA	= (7 x 10 <sup>8</sup> ) / (7520 x 10 <sup>12</sup> )	= 9 x 10 <sup>-7</sup> nm <sup>2</sup> = 0.9pm <sup>2</sup>

Again, this is not likely.

Table 9.4: Hb molecules adsorbed per nm<sup>2</sup> surface area of PMS.

	Molecules Hb adsorbed	Molecules of Hb adsorbed on 3mg PMS	Area of adsorbed Hb (molecules)/ on PMS
PMS	$0.63 \times 10^{16}$	$63 \times 10^6$	$2.2 \text{ pm}^2$
nHAp/PMS	$0.55 \times 10^{16}$	$55 \times 10^6$	$1.91 \text{ pm}^2$
PMS/PVA	$0.027 \times 10^{16}$	$0.027 \times 10^6$	$0.9 \text{ pm}^2$

Table 9.4 and 9.5 compare the extents of adsorption and the area occupied by each AA and Hb on PMS, nHAp/PMS and PMS/PVA. The number of AA molecules adsorbed on the PMS surface is higher than these of Hb molecules (compared with other samples) and these results related to the surface area of PMS. The % adsorption of AA (99%) is higher than that for Hb (35%). The area occupied by each AA molecules adsorbed ( $2.1 \text{ pm}^2$ ) is lower than that for Hb ( $2.2 \text{ pm}^2$ ); AA and Hb are taken up by samples are adsorbed but each AA and Hb would occupy too small. Hence the authors suggest that the AA and Hb are internally held or adsorbed not adsorption.

One must remember that proteins have a high tendency to spontaneously and irreversibly adsorb at most aqueous-solid interface [323] and that Hb is a globular protein with a molecular mass of 66.5 k Da, composed of two  $\beta$  and two  $\alpha$  subunits, which are structurally similar, each binding one heme group.

Others find AA occupies a larger area of a surface than Hb. For example

- (i) 5-10m<sup>2</sup>/g SiO<sub>2</sub> adsorbs 0.97mg AA (176.12g/mol) which suggested each AA occupies 3000 pm<sup>2</sup> of the surface [324].
- (ii) 1.3-8.2pmol of Hb (65458g/mol) on 1cm<sup>2</sup> which suggests each Hb occupies 500 pm<sup>2</sup> of the surface [325].

Similarly, here on PMS a similar ratio of adsorbate cross-sectional area is seen, but the absolute numbers are much smaller: (i) each AA occupies  $2.1 \text{ pm}^2$  and (ii) each Hb occupies  $2.2 \text{ pm}^2$ .

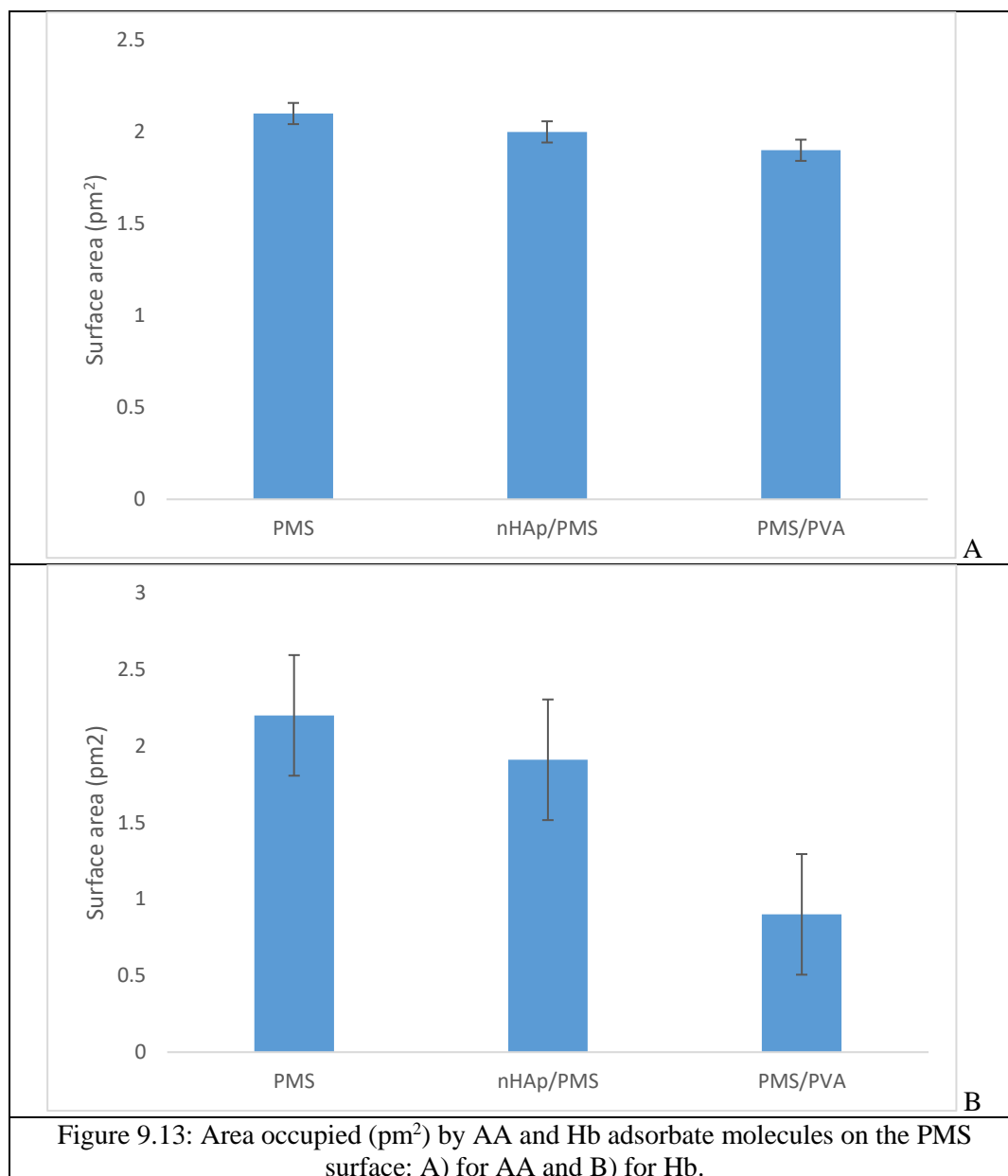


Figure 9.13: Area occupied (pm<sup>2</sup>) by AA and Hb adsorbate molecules on the PMS surface: A) for AA and B) for Hb.

It is possible that the chemistry and hollow shape, structure and size of PMS makes an attractive adsorbing surface area. Clearly, in all samples, the number of AA molecules per PMS are lower than Hb (see Fig.9.13). These results suggested that because of the smaller size of AA molecules. This way allows more AA molecules to insert inside PMS compared with Hb molecules which are large. Furthermore, Hb is a globular protein with quaternary structure (different interactions as hydrogen bond, ionic bond, hydrophobic and Van der Waals interactions): this structure makes Hb absorption difficult on the PMS surface.

### 3. Insulin Swelling Study

Swelling ratio of PMS/PVA was measured on a pure sample without any insulin loading at different pHs for 24h at 37°C. The results (see Table 9.5) show that in SIF at pH 7.2, the swelling ratio increased (161%) due to the presence of PMS inside PVA leading to lower crosslinking density in the PVA hydrogel. Similarly, in aqueous solution, the swelling ratio (145%) increases the uptake of water at a high solution ionic strength. This increases hydrogen bonding between PMS-PVA hydrogel and water; the swelling ratio increases up to a thousand times more than their dry weight [326]. The hydrophilic PVA hydrogel allows it to absorb biological fluids water via hydrogen bonding [327]. The swelling of PMS alone could not be tested because it is difficult to control the wt. of PMS dispersed in the solutions.

Table 9.5: The swelling ratio (Q) of PMS/PVA hydrogel after 24h in different pH solutions at 37°C.

	H <sub>2</sub> O (pH 6.8)	SIF (pH 7.2)	SGF (pH 1.2)
W <sub>1</sub> (mg)	3.7	3.6	3.5
W <sub>2</sub> (mg)	9.1	9.4	6.2
% Q	145	161	77

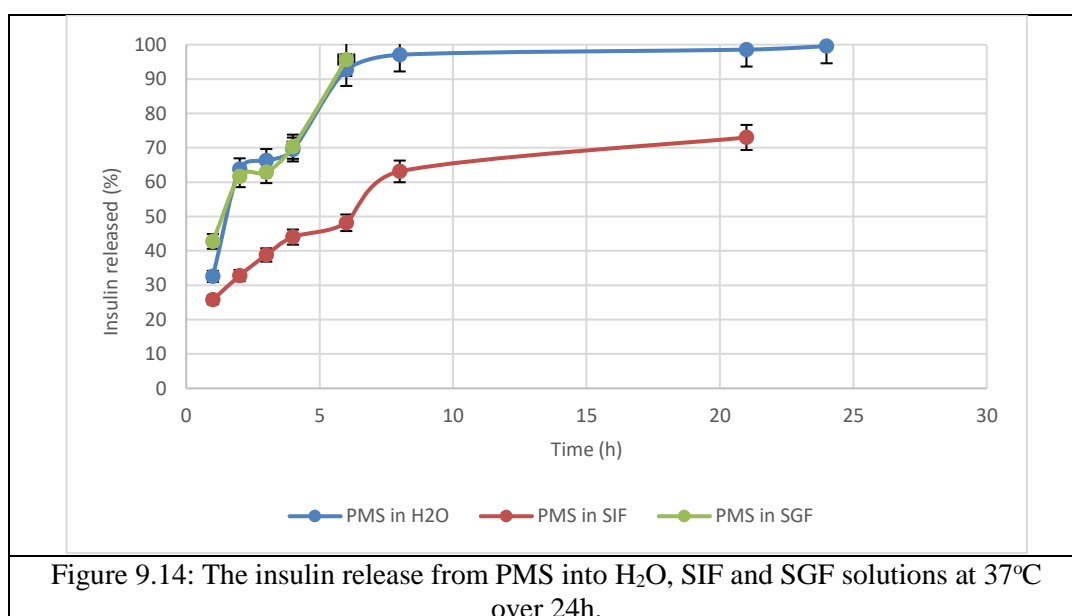


Figure 9.14: The insulin release from PMS into H<sub>2</sub>O, SIF and SGF solutions at 37°C over 24h.

*In vitro*, release study of insulin release at an insulin loading of (400 $\mu$ L (40IU)/10mL H<sub>2</sub>O) was undertaken at ( $\lambda_{\max} = 270\text{nm}$ ) into H<sub>2</sub>O, SIF and SGF for PMS alone, PVA hydrogel, PMS/PVA hydrogel and nHAp/PVA microsphere was undertaken for 24h. Here, 0.0347mg of insulin is equivalent to one international unit (IU) of insulin and



1mL insulin contains 100IU (3.5mg insulin) [328]. Figures 9.14 and 15 indicate that PMS alone exhibited a faster and more extensive insulin release in different pH solutions (SIF (pH 8.2), SGF (pH 1.2) and water) over 24h than PVA. Thus, PVA hydrogel forms hydrogen bonds with insulin, leading to a decrease in drug release rate. Therefore, the insulin release takes longer with PVA than PMS [329]. Some dissolution may occur with insulin/PMS alone at pH 1.2 after 6h; insulin is a protein and is damaged in acidic solutions.

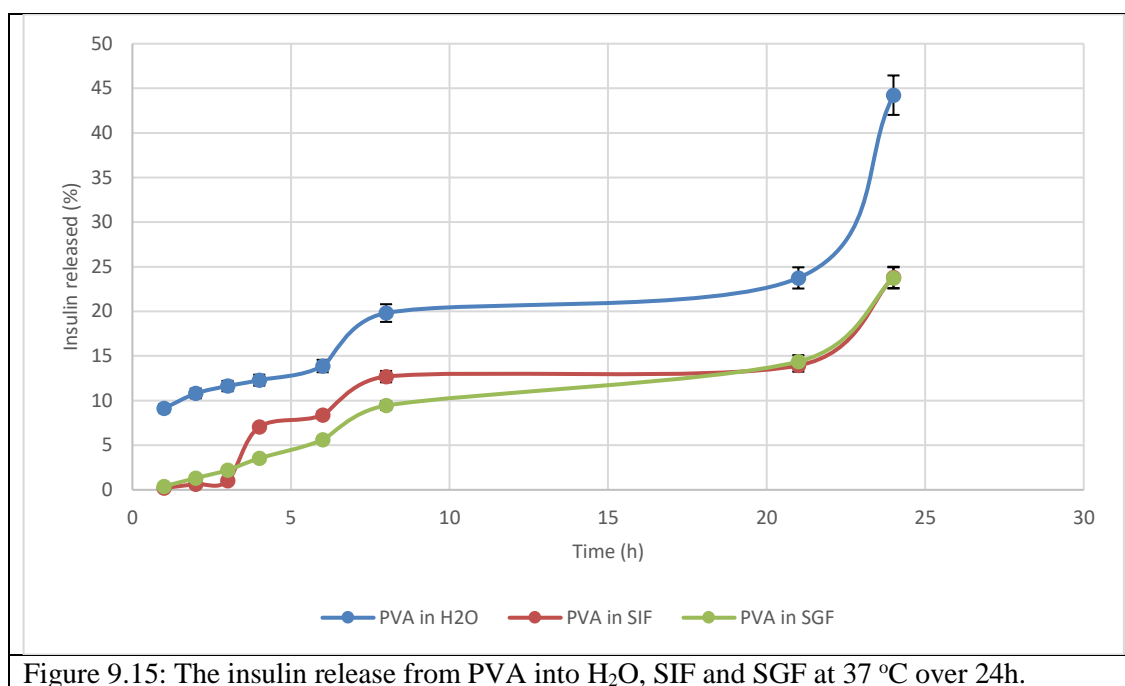


Figure 9.15: The insulin release from PVA into H<sub>2</sub>O, SIF and SGF at 37 °C over 24h.

PMS/PVA hydrogel sample (Fig. 9.16) and the nHAp/PVA microsphere sample had rather slow insulin release (about 30% over 24h) in different aqueous environments in agreement with earlier data [128]. The amount released relates to the quantity of insulin sorbet in the samples and then diffusion (except where insulin-nHAp/PVA microspheres were degraded [327] in SGF (pH 1.2) after 6h). Figures 9.17-18 show that PMS exhibits the highest release rate for insulin in water and SIF compared with other samples. The PMS/PVA hydrogel is similar to PVA hydrogel in terms of its insulin release rate (depending on the pH of solutions). nHAp/PVA microspheres exhibit a good release rate because of the non-restrictive surface covering of nHAp and porous hollow structure in water and SIF only [330].

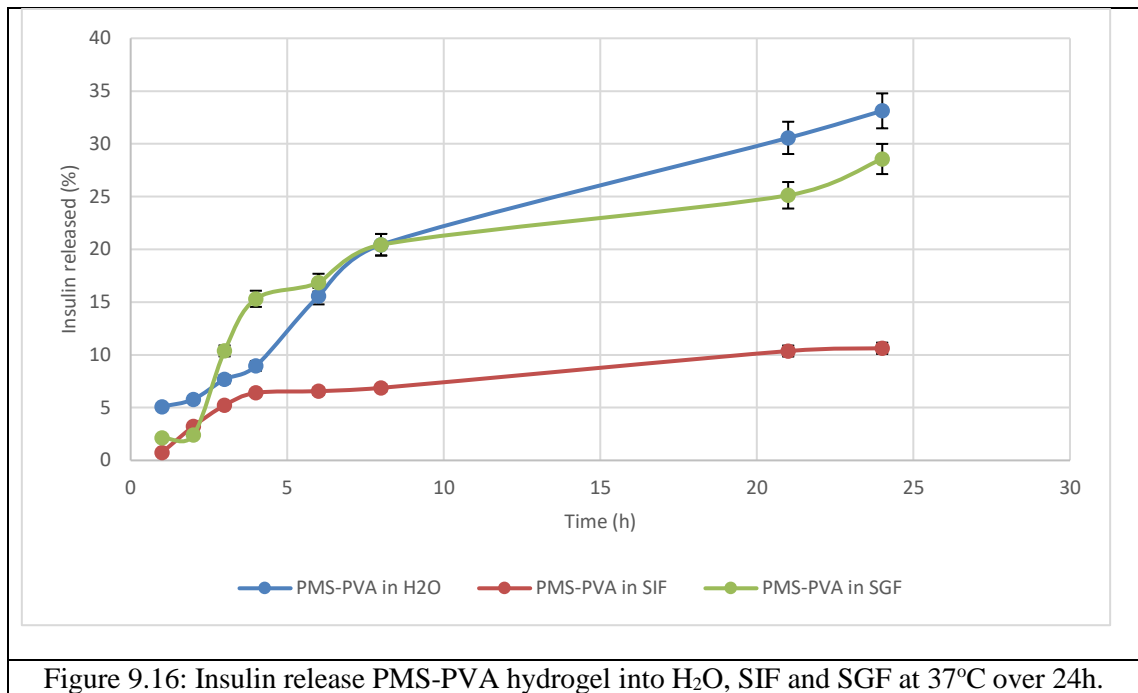


Figure 9.16: Insulin release PMS-PVA hydrogel into H<sub>2</sub>O, SIF and SGF at 37°C over 24h.

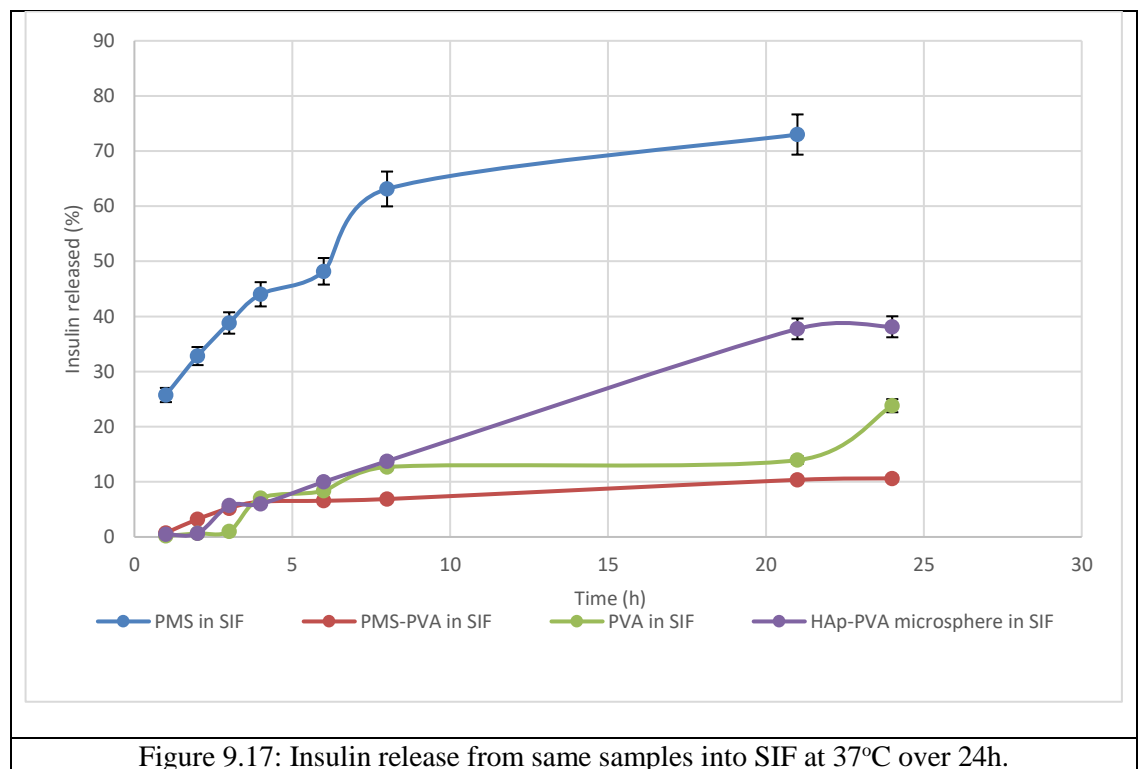


Figure 9.17: Insulin release from same samples into SIF at 37°C over 24h.

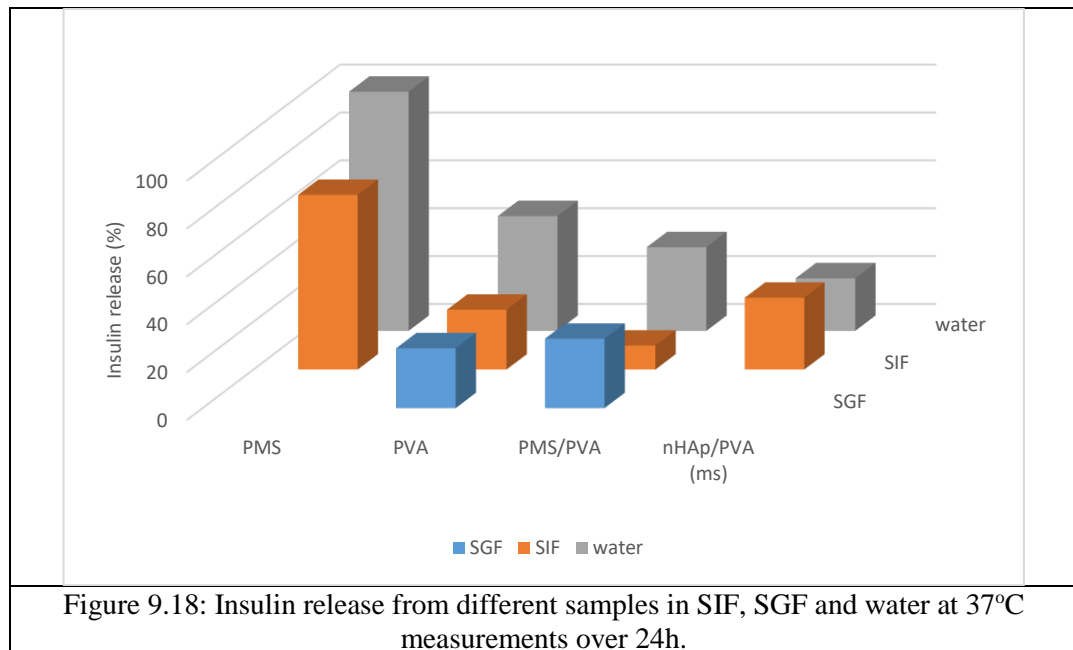


Figure 9.19 shows that some samples have had a better linearity (obeying the Higuchi equation (see Eq. 9.3) [305] based on Fick on diffusion of insulin):

$$Q = k_H \cdot t^{1/2} \quad \text{--- (9.3)}$$

where  $Q$ : the amount of insulin release at time ( $t$ )

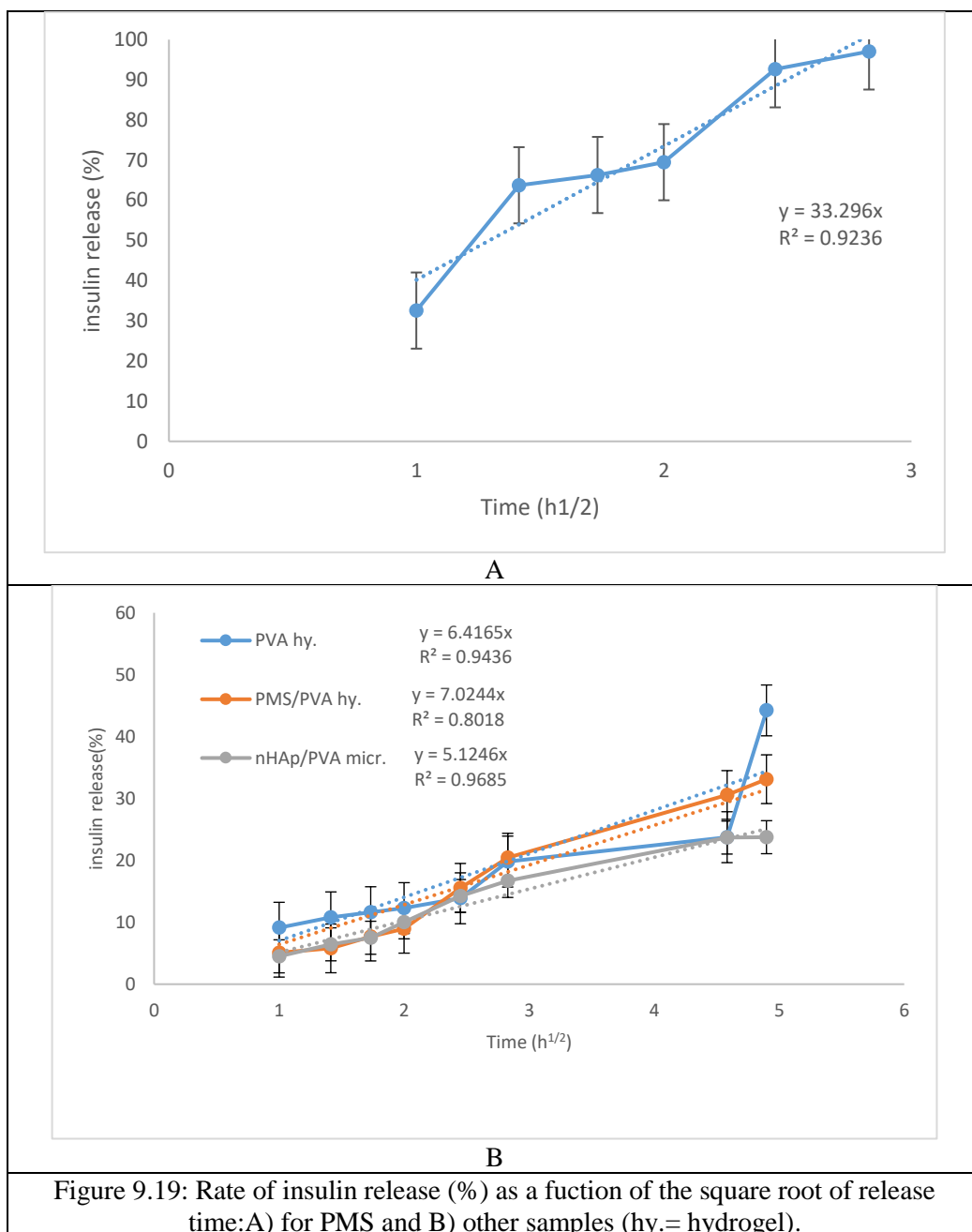
$k_H$ : the Higuchi rate constant ( $h^{-1}$ ) and

$t^{1/2}$ : the square root of time [111].

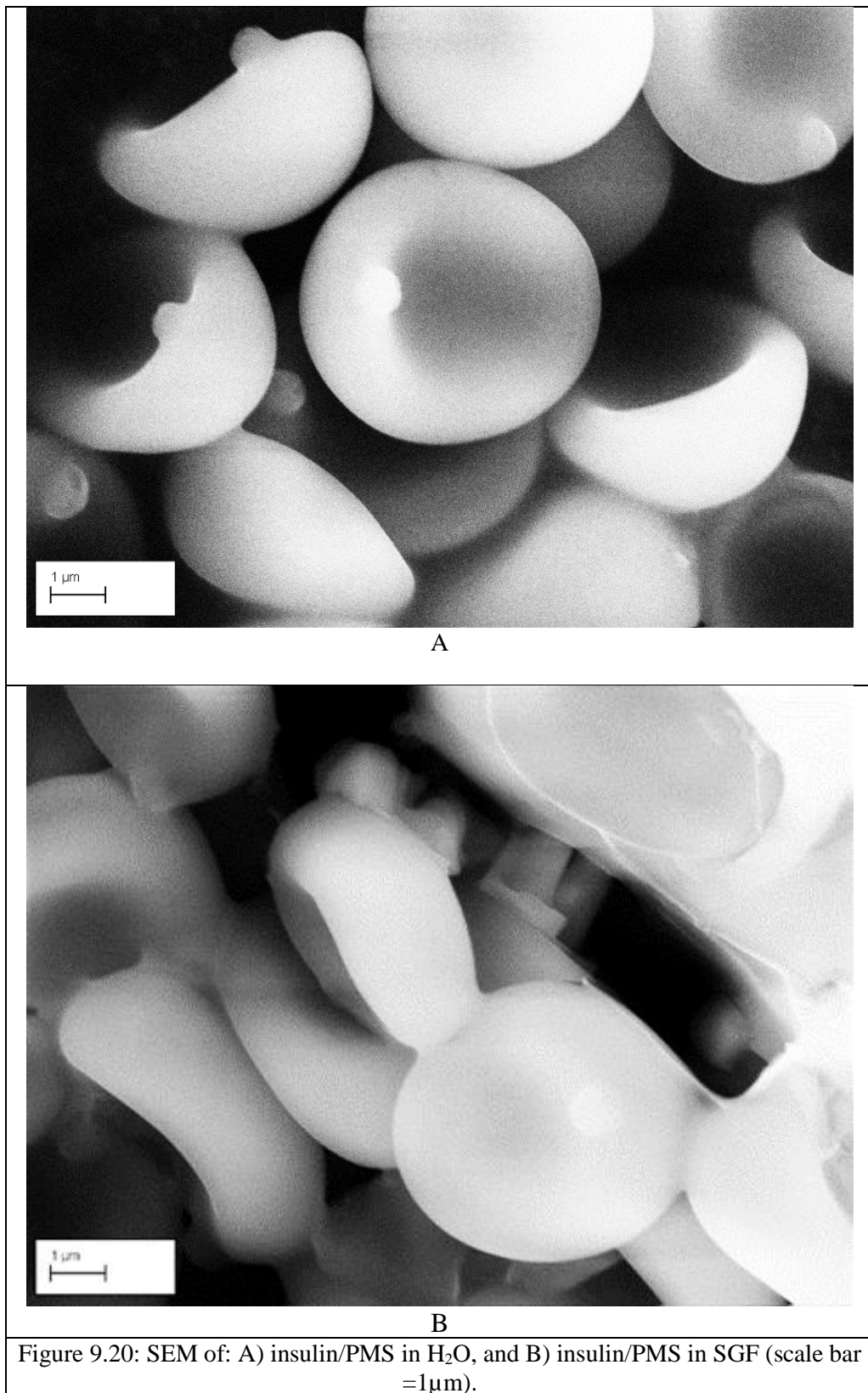
The rate constant for insulin release was deduced from the gradients in Figure 9.19. The correlation coefficient ( $R^2$ ) was found to be 0.96-0.80. However, the correlation was worst for PMS and the controlling step may have changed with time. Probably, mechanism of insulin release from samples followed Fick's first law of diffusion [269]. This was less true for PMS (nonlinear).

Table 9.6: the release kinetics of samples and rate constant.

	$R_2$	$k_H$ rate constant ( $h^{-1}$ )
PMS	0.9236	33.29
PVA	0.9436	6.416
PMS/PVA	0.8018	7.024
nHAp/PVA	0.9685	0.968



SEM of *in vitro* release results show that the morphology of insulin-loaded/PMS surface exhibited no variation in PMS size or aggregation as a result of a thin insulin layer. Possibly, nano channels (200-300nm) as the porous PMS shell wall helped the insulin movement into and out of PMS. In future this may allow design of drug delivery [209].



Here, then it is shown that a morphology of PMS (size, hollow, oval shape and cell wall structure) can be used as an oral drug delivery system (because it is already used as non-allergenic food). Normally, PMS has a consistent

- (iv) size ( $\sim 6 \mu\text{m}$ ),
- (v) hollow shape (allowing a high loading of a drug) and
- (vi) cell wall allowing inflow and outflow of insulin

giving controlled insulin release (due to its cell wall having good properties enabling drug transport through porosity of PMS (nano-channel), chemical and physical resistance). Moreover, PMS can be coated with nHAp to control the insulin loading and release rate.

### 9.3 Conclusions

A novel method has been devised in which ascorbic acid (AA, a model vitamin), hemoglobin (Hb) (as a model protein) and insulin (as a hormone) have been introduced into hollow PMS, HAp/PMS, HAp-PVA hydrogel microspheres and PMS-PVA hydrogels. Further work is in hand to determine whether therapeutic agents can be introduced into such micro-capsules and then released beneficially together. These are ascorbic acid and antibiotic gentamicin. Here, these nano composite have been tested as oral drug delivery systems. The samples were characterized using UV and SEM. The effect of pH on the swelling ratio was studied. *In vitro* studies suggested that PMS has the ability to accept and release ascorbic acid, hemoglobin and insulin, depending on pH (in SIF and SGF) and temperature ( $37^\circ\text{C}$ ). It is believed that PMS has many advantages as a drug delivery system: homogeneity of shape (oval), size ( $6\mu\text{m}$ ), resilience in both acid and base (pH 6.8) and stability up to  $200^\circ\text{C}$ . In addition, AA-loaded/PMS is much better than AA from supplements only. That means, one could use PMS with vitamins as supplements. Furthermore, the insulin/PMS loaded/PVA hydrogel film may be able to deliver insulin in a transdermal manner in drug delivery that is painlessly and harmless as a result of being placed on human skin; it promises sustained-release insulin for the treatment of diabetes without daily painful injections.

## **Chapter 10 : Nanoengineering the antibacterial activity of biosynthesized nanoparticles of TiO<sub>2</sub>, Ag and Au and their nanohybrids with Portobello mushroom spores (PMS) (TiO<sub>x</sub>/PMS, Ag/PMS and Au/PMS) making them optically self-indicating**

---

In this chapter: (i) new methods of measuring antibacterial activity were assessed, and (ii) novel TiO<sub>x</sub>/PMS, Ag-TiO<sub>x</sub>/PMS, Au-TiO<sub>x</sub>/PMS and Ag/PMS and their nanohybrids have been assessed for antibacterial activity against *Eschericia coli* and *Staphylococcus aureus* and for antifungal activity against *Asperillus.spp* and *Candide.spp*. Thus, the aim was to use PMS as a template to reduce and prepare TiO<sub>x</sub>/PMS, Ag-TiO<sub>x</sub>/PMS, Au-TiO<sub>x</sub>/PMS and Ag/PMS NPs that could be used as antimicrobials in nanomedicine. These were tested for antimicrobial activity. These could be enhanced new antibacterial and fungal agents.

### **10.1 Introduction**

Nanomaterials are used in bone/tissue engineering [331] and in the control of infections [332] associated with MRSA, antibiotic-resistant bacteria [333] and multi-drug resistant *Staphylococcus aureus* [334]. Microbial infections have become a global health problem, with antibiotic-resistant genes (ARG) and antibiotic-resistant bacteria (ARB) emerging. It is well established that antimicrobials include 5-40nm Ag nanoparticles (NPs) [334] that may be biosynthesized by green routes using: (i) *Chlorella vulgaris* microalgae cells [335], (ii) *Centella asiatica* extract [336], (iii) *Arnicae anthodium* extract [337] or (iv) *Phlomis bracteosa* plants [338]. In the last case, FTIR showed that the polyphenols were mainly responsible for reduction and capping of synthesized Ag NPs with their characteristic surface plasmon resonance (SPR) peak at 453 nm. Biomimetic Ag-oxide nanomaterials [339], nanopatterned surfaces [340] and bio-NP composites [341] are also interesting in an antimicrobial sense, as are bioactive Ti-oxide surfaces [342]. It therefore seemed appropriate to investigate PMS-derived Ag NPs, Au NPs and TiO<sub>x</sub>/PMS, Ag/PMS and Au/PMS.

It also seemed suitable to test these nanomaterials against Gram-positive *Staphylococcus aureus* [335] and Gram-negative *Escherichia coli* [343]; here we wished to measure the diameters of zones of inhibition (mm) on agar plates as previously [338], while also using new methods of assessment and characterizing where the NPs were in relation to the PMS cell wall using SEM [334].

### 10.1.1. Antimicrobial Mechanisms

Bacteria can be classified depending on the structure/functional components of their cell walls into:

- (i) Gram-positive bacteria (e.g. *Staphylococcus aureus* (*S.aureus*)) whose cell walls contain a thick surrounding layer (20-50nm) of peptidoglycan (PG) which is attached to specific acids [53] and,
- (ii) Gram-negative bacteria (e.g. *Escherichia coli* (*E.coli* )) which is more chemically-structurally complex; here the PG layer is thin and the cell wall tends to be negatively charged [42], with the outer membrane containing lipopolysaccharides [51].

Anti-bacterial agents can be (a) bactericidal (killing bacteria) and (b) bacteriostatic (slowing bacterial growth [53]). The mechanism of antibiotic resistance may be innate or may involve prevention of the antibiotic from penetrating the bacterial cell wall [344] or hydrolysis/modification/degradation/inactivation of the antibiotic [345]. Most anti-microbial agents exhibit inhibition, affect DNA/RNA synthesis, affect the cell membrane or damage the proteins in the cell [46]. With the development of biomedical nanomaterials, safer and alternative anti-microbial agents have started to emerge; these may be unique or may increase the activity of the conventional anti-microbial agents [345]. Treatment strategies include: (i) photo-disinfection with  $\text{OH}\cdot$  [344], (ii) UV-disinfection at say 264 nm [344], (iii) photo-catalytic disinfection when reactive oxygen species (ROS) ( $\text{O}_2\cdot^-$ ,  $\cdot\text{OH}$  or  $\text{O}_2^-$ ) are generated [344] (e.g. with  $\text{TiO}_2/\text{H}_2\text{O}$ ) [344] and (iv) nanoparticle disinfection. Nanomaterials can be expected to become more important, due to their unique chemical [346], mechanical [347], catalytic [348], electrical, magnetic, optical and biological properties [349]. Such properties make NPs powerful tools for vast and diverse applications (e.g. anti-microbial, diagnosis, imaging and thereby drug delivery (because NPs provide unprecedented opportunities to molecular process and interrogate cellular clinical application [350])). NPs have recently emerged as unique anti-microbial agents due to their shape, size and high surface area to volume



ratio; NPs are of the same dimensions as proteins, nucleic acid, membrane of receptors, antibodies and other biomolecules [351]. Antimicrobial NPs [352] operate by mechanisms that are similar (but slightly different due to their different chemical properties, and their size, surface area, shape, crystallinity, charge, surface energy, chemical composition and aggregation [45]). Such NP properties govern their interaction with/in living cells and the way in which they (i) damage or disrupt the integrity of bacterial membrane, (ii) change the microbial cell wall and nucleic acid pathway, (iii) block the enzyme pathway and (iv) destruct the cell membrane [46]. Conversely, the cytoplasm of Gram-negative bacteria is a strong reducing environment that can affect the oxidation state for metal NPs [352]. Relevant antimicrobial NPs include (i)  $\text{TiO}_2$  that has weak mutagenic potential, but is lethal to *S.aureus* and *E.coli* under UVC (100-280nm) in 60 min [352], (ii) plasmonic Ag and Au that are chemically stable, non-toxic to human cells, biocompatible [42] and exhibit localized surface plasmon resonance (LSPR) [36] and colour (due to the coherent excitation of all free-electrons with the conduction band causing (SPR) an in-phase oscillation) [52].

Ag NPs when coated onto a filter for water purification or coated onto medical devices or in dental resin components to reduce infection [45]. Also, it can be employed in wound healing and can control vector transmitted infection [46]. Ag NPs react with biomolecules (like DNA, RNA or enzymes during an electron- release mechanism) weakening DNA replication, combine with proteins (causing denaturation and inactivating them by reducing bacterial proteins levels [48]). Further, they interact with P- or S- containing compounds (like DNA leading to damage of the cell wall) [51] and may attach to the cell membrane surface and disturb respiration and permeability [52].

Au NPs have a large number of atoms available to attach [353] to the surface of bacteria [354]. Biosynthesized Au NPs are promising for many medical applications, such as anti-tumor, labeling, imaging, apoptosis and interaction with DNA [355] (see section 11.1.1). They also show good biocompatibility, being compatible with human body cells and being resistant to corrosion [43]. Au NPs show a significant anti-bacterial activity depending on their size and shape and also the type of bacteria [350]. They strongly bind to the bacterial cell wall, allowing them to disrupt the bacterial cell membrane. Then, they cause leakage of nucleic acids and cytoplasm [345], induce photo-mutagenic processes causing damage to DNA and essential proteins [53]. The increase in ATP (where ATP generation is a significant part in the respiration chain of bacteria via the  $\text{NAD}^+/\text{NADH}$  reaction) intercellular ATP levels, leading to bacterial

death and catalyze oxidation reactions, producing ROS that lead to the death of bacteria [356].

Ag-TiO<sub>x</sub> and Au-TiO<sub>x</sub> nanohybrids show strong anti-microbial activity due to their multi-functionality, e.g. Ag-TiO<sub>2</sub> and Au-TiO<sub>2</sub> NPs exhibit excellent anti-microbial action [357]. Recently, green bio routes have been used to synthesis NPs (fungi, bacteria, and plants) [355] that may have interesting anti-microbial activity. Nanoparticles have been recognized and applied in medical fields as a coating of medical devices, health-care products, and drugs in recent years. Ag and Au NPs are more powerful in medicine especially Ag NPs as antibacterial materials. New NPs should be safer because many NPs had raised serious arguments: the toxic effects in cell cycle and causing oxidative damage due to some NPs releasing ions from their surface. These ions may be controlled possibly by particle size, oxygen availability and shape [358].

The PMS-derived NPs are described in section 4.2.1-2 and the antibacterial and methods of fungal activity measurement are described in section 4.9.

## 10.2 Anti-microbial and Anti-Fungal Activity Results

Tables 10.1 and 2 show that IPA, Au<sup>3+</sup><sub>(aq)</sub> and Ag<sup>+</sup><sub>(aq)</sub> are active in inhibiting both Gram-positive (*Staphylococcus aureus*) and Gram-negative (*Escherichia coli*) bacteria, but not water or PMS alone. The IPA result relates to alcohol washing of hands and is presumably an effect of dehydrolysis of the cells by the alcohol. At the same time TiO<sub>x</sub>/PMS, Ag-TiO<sub>x</sub>/PMS, Au-TiO<sub>x</sub>/PMS and Ag/PMS in water are active in bacterial inhibition. In contrast, Au/PMS is not at all active because there is a strong Au-PMS interaction arising from ready reduction of Au<sup>3+</sup><sub>(aq)</sub> by the PMS surface. Conversely it can be no free Au<sup>3+</sup><sub>(aq)</sub> after the interaction with dispersed PMS. Table 10.3 shows the antibacterial and antifungal activity of five samples produced from a H<sub>2</sub>O suspension. Again Au/PMS was inactive. Interestingly, Au-TiO<sub>x</sub>/PMS was active in inhibiting *E.coli* and *S.aureus*, but not at all active in inhibiting *Asperillus.spp* and *Candide.spp*. TiO<sub>x</sub>/PMS, Ag/PMS and Ag-TiO<sub>x</sub>/PMS on the other hand were broadly equally active in an antibacterial and an antifungal sense.

Table 10.1: Visual assessment of diameter (mm) of zone of inhibition activity against *E.coli* and *S.aureus* by samples (9mm diameter)

	controls			NPs/PMS in IPA			NPs/PMS in H <sub>2</sub> O		
	H <sub>2</sub> O	IPA	PMS	TiO <sub>x</sub> /PMS	Ag - TiO <sub>x</sub> /PMS	Au - TiO <sub>x</sub> /PMS	Au <sup>0</sup> /PMS	Ag <sup>0</sup> /PMS	Au <sup>0</sup> -Ag <sup>0</sup> /PMS
<i>E.coli</i>	0	15	0	15	16	20	0	13	11
<i>S.aureus</i>	0	13	0	18	17	17	0	15	12
NP or PMS (mg/100μL)	-	-	4	0.016	0.01/0.007	0.01/0.01	0.039	0.021	-

Table 10.2: Visual assessment of diameter (mm) of zone of inhibition activity of precursor salts and ions Au against *E.coli* and *S.aureus* (9mm diameter)

	salts in IPA			salts in H <sub>2</sub> O	
	Au <sup>3+</sup>	Ti <sup>4+</sup>	Ag <sup>+</sup>	Ag <sup>+</sup>	Au <sup>3+</sup>
<i>E.coli</i>	19	19	24	14	15
<i>S.aureus</i>	28	22	24.	16	17
Salt or ion (mg/100μL)	3.05	2.55	0.05	0.05	3.05

Table 10.3: Visual assessment of diameter (mm) of zone of inhibition activity (6mm diameter) of samples dispersed in H<sub>2</sub>O

	TiO <sub>x</sub> /PMS 8μg/50μL	AgTiO <sub>x</sub> /PMS 13-21μg/50μL	AuTiO <sub>x</sub> /PMS 42-130 μg/50μL	Au/PMS 25 μg/50μL	Ag/PMS 13 μg/50 μL
<i>E.coli</i>	9-7	10-9	8-9	0.00	9-11
<i>S.aureus</i>	20	8-10	7-7	0.00	9-8
<i>Aspergillus.spp.</i>	7	8	0.00	0.00	7-9
<i>Candid.spp.</i>	11	9-7	0.00	0.00	11-12

At Brunel University London, Table 10.4 shows the antibacterial activity seen for Ag NPs/PMS, water and air using Mueller Hinton agar. This is reassuringly similar to that seen in Basrah. Here, in the agar diffusion disc-variant measurements, the samples were dispersed in H<sub>2</sub>O and then, these samples were used to impregnate 6mm filter paper discs (Whatman no. 2) to a loading of 50μL. These results were compared with University of Basrah results.

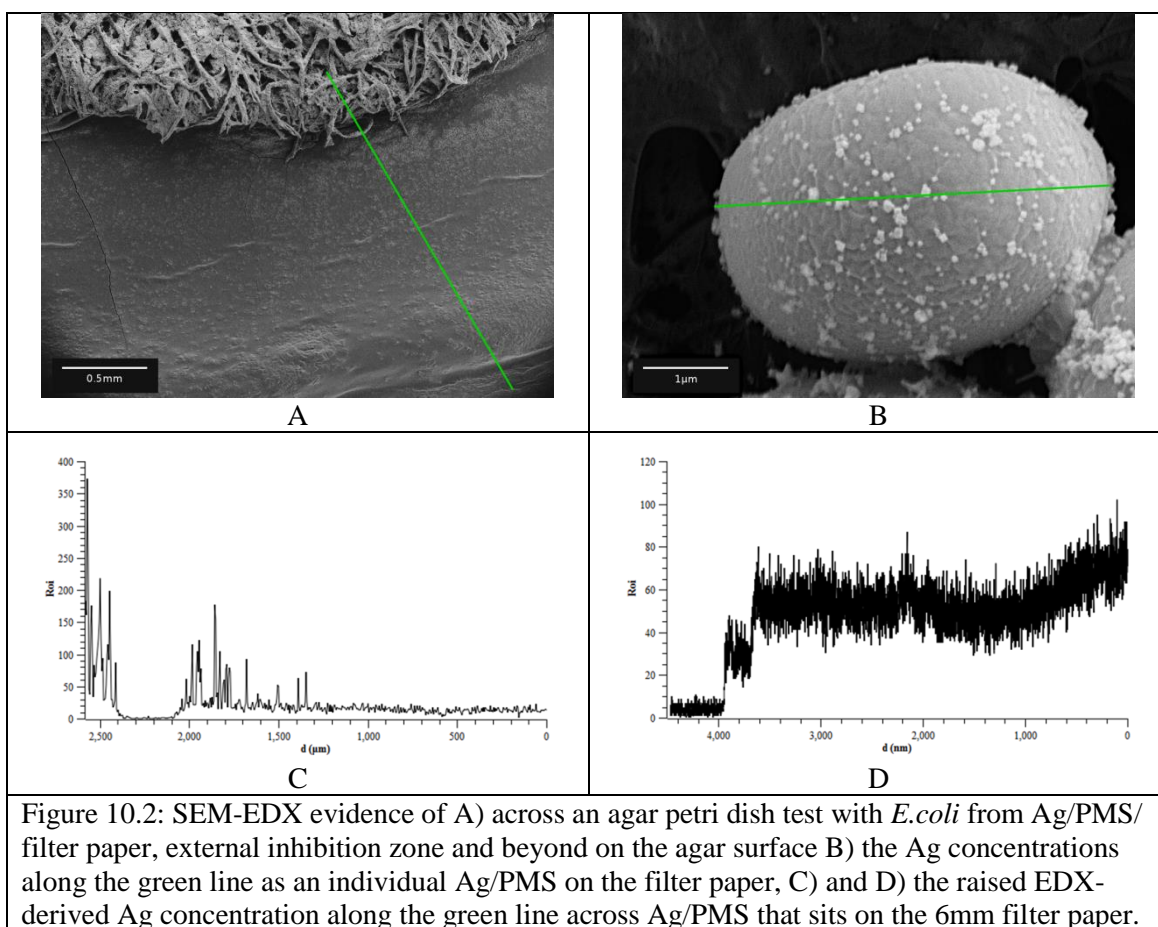
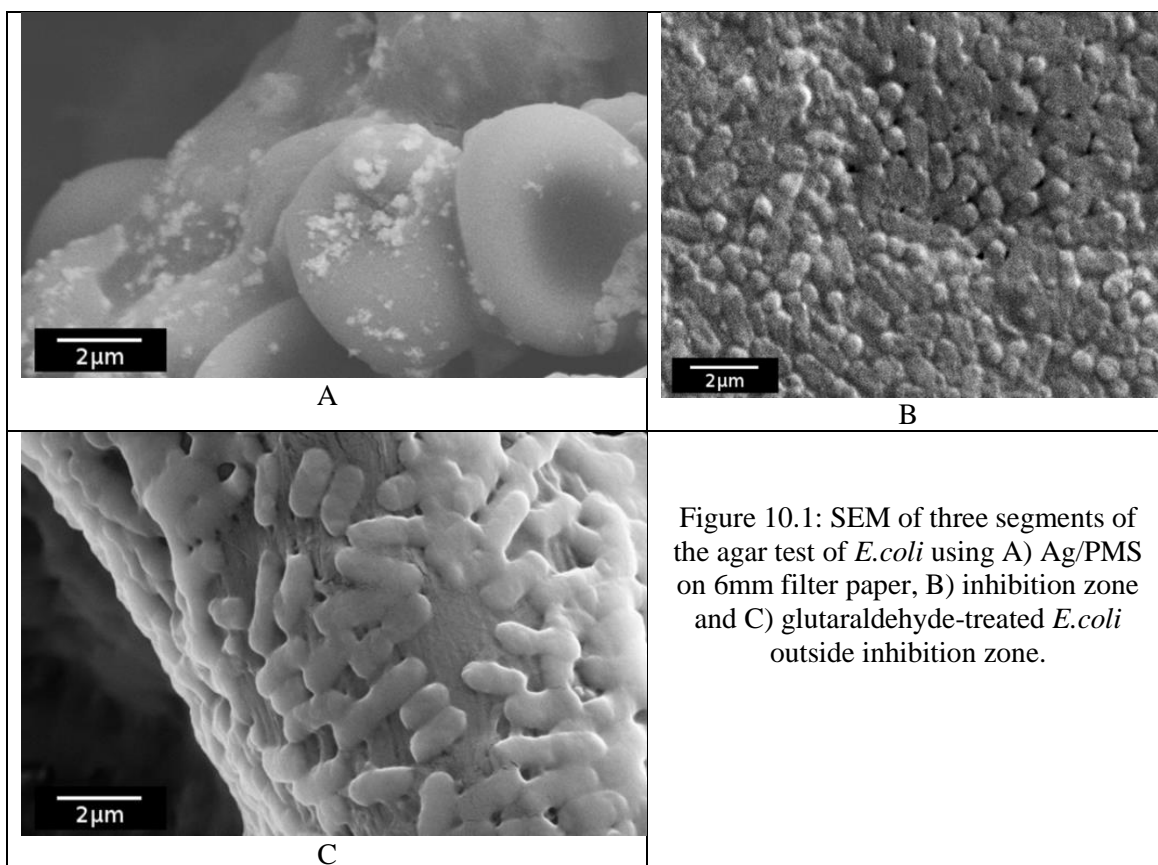
Table 10.4: Diameter (mm) of inhibition activity against *E.col. K12* in Brunel University compared with University of Basrah.

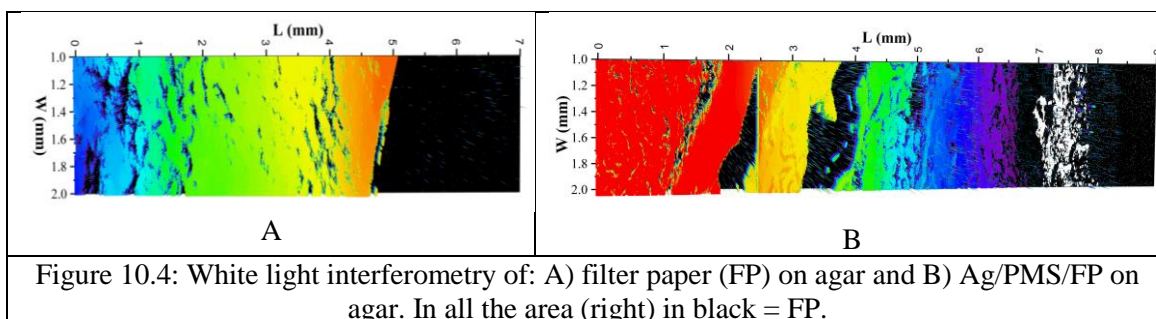
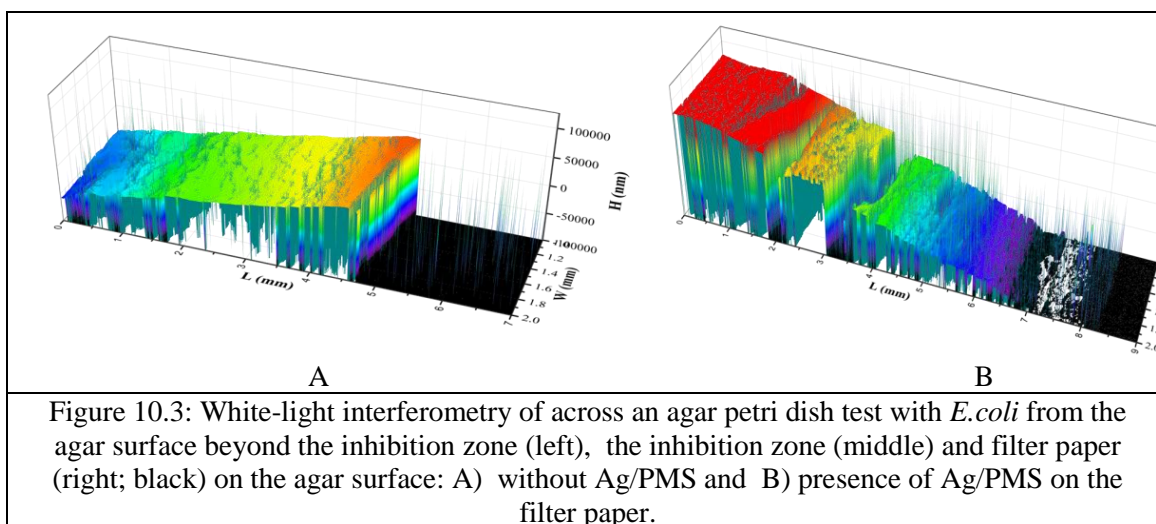
	V (μL) of samples	H <sub>2</sub> O	Ag/PMS
Brunel (6mm)	50	0	13
Basrah (9mm)	100	0	13
Basrah (6mm)	50	0	11

### 10.2.1 Novel SEM- EDX and White-light interferometry analysis

Here, the author wished to determine whether SEM-EDX could provide evidence of Ag migration in inhibition zone testing. Scanning electron microscopy (SEM) is still a significant technique which can be used to reveal morphological details of biological specimens and diagnosis [164]. SEM is a microscope which uses a beam of electrons (instead of light) to create specimen's images. The operation of SEM is that it focuses a beam of electrons on the surface of specimen rather than transmission. The primary electrons beam excites and interact with the specimen surface and this surface emits secondary electrons (SE). Then, the detector is used to form an image from the SE by scanning across the surface. In this case, it is able to produce an image of 3D structure of bacteria [161] in principle. However, the electron beam has a huge current density and it can focus into a very tiny area in a specimen. This area becomes hotter and then chars the bacteria. But here agar and water are present keeping and Au overcoating (normally used to avoid charging) was not possible. Hence there are several problems with getting high resolution SEM imaging in these samples [164]. Nevertheless, imaging of Ag/PMS on the filter paper and *E.coli* in the inhibition zone and on the agar surface was possible (see Fig. 10.1).

Interestingly, Figure 10.2A shows that the Ag/PMS is not seen in the inhibition zone, but EDX detects Ag on the surface of PMS and at a distance out from the filter paper (FP). This is presumably because  $\text{Ag}^{\text{x}+} - \text{Ag}^{\text{o}}$  diffuses out from the Ag/PMS in-on the FP. White-light interferometry (WLI) across an agar petri dish test with *E.coli* is shown in Fig.10.3. Evidence is seen with the different colours of the agar surface beyond the inhibition zone (Fig. 10.3A; left of image), through the inhibition zone (middle) to the low reflectance 6mm filter paper (right of image; black) on the agar surface. Here, absence of Ag/PMS where the surface is rather smooth and presence of Ag/PMS on the filter paper where there are chemical crevices is noted. In the future this may be useful in defining diffusion-inhibition zone.





### 10.2.2 The antimicrobial mechanism for NPs/PMS

Ag-TiO<sub>x</sub>/PMS is an active antimicrobial and antifungal agent, but Au-TiO<sub>x</sub>/PMS is only active against bacteria. This again may reflect the strength of the Au-PMS interaction. One would expect that NPs (zero-valent and charged) would bind to PMS through several functional groups in the microbial cell [350] and would thereby be immobilized (avoiding the free NPs that worried the Royal Society [13]).

#### 1. Cell wall of microbial

The properties of the bacteria cell wall can play a crucial role in different NPs/PMS because the wall is designed to provide rigidity, shape and strength to protect the cell from osmotic rupture. Gram positive bacteria were found to be more susceptible to the NPs/PMS than Gram negative bacteria because of the difference in their cell wall structure. Gram negative bacteria are considered to be more resistant due to their outer membrane acting as a barrier to many environmental substances including antibiotics [53]. In addition, the charge on the membrane of *E.coli* is negative because of the

excess number of carboxyl groups, which upon dissociation makes the cell surface negative. The opposite charges of bacteria and nanoparticles are attributed to their bioactivity due to electrostatic forces leading to electrical interaction between the *E.coli* and NPs/PMS increasing the possibility of collisions and decreasing the bacteria growth [51].

## 2. Effect of NPs/PMS

The increasing surface area/decreasing the particle size, could be helping to improve NP anti-microbial activity [350]. NPs have a large surface area available for interaction, which enhances the bactericidal effect more than the large sized particles; hence they impart cytotoxicity to the microorganisms. However, the aggregation of NPs leads to decreasing the property of the interaction of NPs with bacteria cells [51]. The size of NPs can give rise to electronic effects which promote their surface reactivity and prevent the aggregation of NPs. For example, NPs with a diameter less than 10 nm have anti-microbial activity, but NPs with diameter 30-50nm did not have good anti-microbial activity until NPs reached 20 $\mu$ g/mL [350]. NPs/PMS with diameter 5-30nm have a good antimicrobial activity.

## 3. Free radicals

TiO<sub>x</sub> NPs/PMS and nanohybrid have good anti-bacterial activity against *E.coli*. When the cell of bacteria absorbs the NPs significant oxidative stress happens due to the generation of free radicals like  $\cdot$ OH, O<sub>2</sub><sup>-</sup> and H<sub>2</sub>O<sub>2</sub> by oxidation of poly-unsaturated phospholipids. Hence, these lipids started to submit a peroxidation reaction subsequently leading to: (i) glutathione (GSH) depletion, (ii) stress or eventual disruption in the morphology of cell membrane and (iii) the electron transfer leading to cellular death [43].

## 4. Type of NPs

Ag NPs/PMS and monohybrid have excellent anti-bacterial activity against both *E.coli* and *S.aureus* due to the generation of ROS following the administration of NPs. Our results show that Ag NPs/PMS have anti-bacterial activity in lower concentration than other NPs. High activity of silver NPs is attributed to species difference as they dissolve

to release  $\text{Ag}^0$ ,  $\text{Au}^0$ ,  $\text{Ag}^+$ ,  $\text{Au}^+$  clusters. Several mechanisms have been suggested leading to the inhibition of bacteria growth:

- Ag NPs bind with proteins or lipo-poly-saccharide in the cell membrane leading to collapse [53],
- Ag NPs induce phosphate and interaction with atoms which have a high electron density like S, O and N. These are essential biological molecules as a thiol group because Ag NPs have an extreme chemical affinity for a sulfur group. The interaction with thiol or cysteine in protein leads to denaturation effects, loss of the subsequent enzyme and changing cytoplasmic components [43],
- NPs attack the respiratory chain and inhibition of the respiratory enzymes with the division of cells and causing death [51] and
- NPs start to act on dehydrogenases of electron transport and reduction of cellular adenosine triphosphate (ATP) level.

Interestingly, Au NPs/PMS do not have any bacterial activity. It is likely that Au NPs:

- self-assemble in 4-5 $\mu\text{m}$  long PMS indicating a strong NP-PMS interaction [45],
- cause aggregation with a decreased inhibitory effect; increasing surface area generates further biophysical interactions [51], and
- on PMS may be absorbed only on the cell of bacteria but cannot penetrate inside bacteria cells [350].

The ability of biomolecules (like nucleic acid and proteins) to chelate [43] and adsorb [356] Au NPs may direct the NPs to specific sites [43] or change their biological effects [356]. Nevertheless, Au NPs are particularly attractive for target direction diagnostics and therapeutics in the human body [43]. The potent anti-fungal property of  $\text{TiO}_x/\text{PMS}$  is the most effective catalyst for chemical transformation [356]. Present data suggests that Ag/PMS has a potential as a biocide against *Aspergillus.spp.* and *Candide.spp.* Indeed, the disrupting of the structure cell membrane and inhibiting the normal budding process is due to the damage of the membrane integrity [36]).

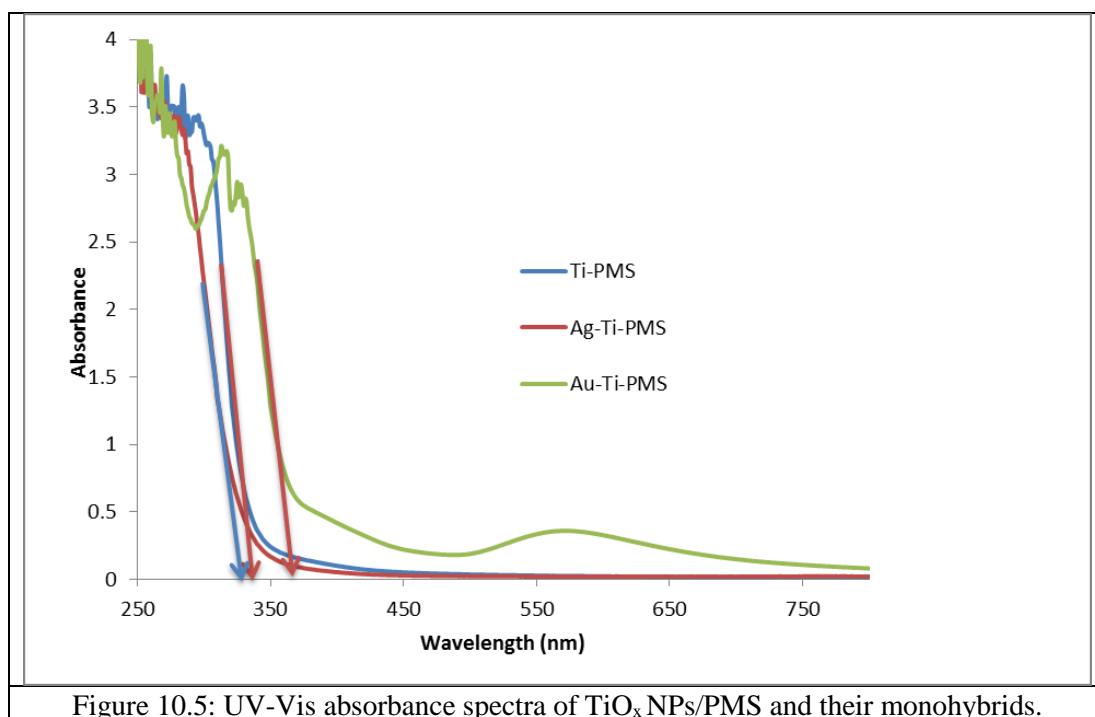
The results of the present study support the suggestion that plant-derived NPs have antibacterial properties that can be utilized as antibacterial agents in new drugs for the therapy of infectious disease caused by pathogens [229].

## 5. Optical properties

Optical amplifiers (e.g. liquid crystals) have been reported [359] to be useful for detection of Gram-positive and Gram -negative bacteria. The authors are considering



whether their Au-Ag/TiO<sub>x</sub> bionanomaterials also have useful optical properties. Conversely, UV promotes antibacterial effects in TiO<sub>2</sub> nanocomposites even after cessation of UV irradiation [360]. Figure 10.5 shows that Au-TiO<sub>x</sub>/PMS shows a surface plasmon resonance (SPR) with a maximum at 518 nm, confirming the presence of Au NPs seen in TEM (see chapter 6), and this might be used to follow its antibacterial activity, making this nanomaterial self-indicating.



### 10.3. Conclusions

Using a green approach TiO<sub>x</sub>, Ag, Au, Ag-TiO<sub>x</sub> and Au-TiO<sub>x</sub> NPs have been prepared using PMS to study the microbial activity. The present results show that Ag/PMS were active in bacterial inhibition towards *Escherichia coli* and *Staphylococcus aureus*, but Au/PMS was not active (suggesting a strong Au-PMS interaction). TiO<sub>x</sub>/PMS, Ag/PMS and Ag-TiO<sub>x</sub>/PMS were equally active in an antibacterial and an antifungal sense when tested against *Asperillus.spp.* and *Candide.spp.* Here the author reports on the process of fine-tuning these antibacterial properties, progress on making these nanomaterials optically self-indicating and movement towards optical control of their antibacterial activity. Au-TiO<sub>x</sub>/PMS shows a surface plasmon resonance (SPR) with a maximum at 518nm that might be useful in following its anti-bacterial properties (i.e. making the bionanomaterial self-indicating). The future of such green bio-nanomaterials is strong.

## Chapter 11: Nanocytotoxicity and genotoxicity of TiO<sub>x</sub>, Ag and Au NPs/PMS in human blood and nucleic acid for future medical applications

---

In this chapter, the nanomedicine TiO<sub>x</sub>/PMS, Ag/PMS, Au/PMS, Ag-TiO<sub>x</sub>/PMS, Au-TiO<sub>x</sub>/PMS will be described for nanocytotoxicity, genotoxicity and LD50 in human blood using electrophoresis and Nano Drop (explained in chapter 3).

### 11.1 Introduction

#### 11.1.1 Cytotoxicity

Nanoparticles have received much attention because they are used in many fields especially in bio-applications. TiO<sub>2</sub>, Ag and Au NPs have been the subject of different studies relevant to antimicrobial agents, therapeutics, fluorescent labels, drug delivery, medical imaging and transfection vectors. In the past ten years, there has been evidence about the growing of ecotoxicological effects (the effects of toxic chemicals on biological organisms) of NPs [55].

A few studies have been reported concerning the interaction of NPs with living cells because of the main effects of NPs in the human body, such as:

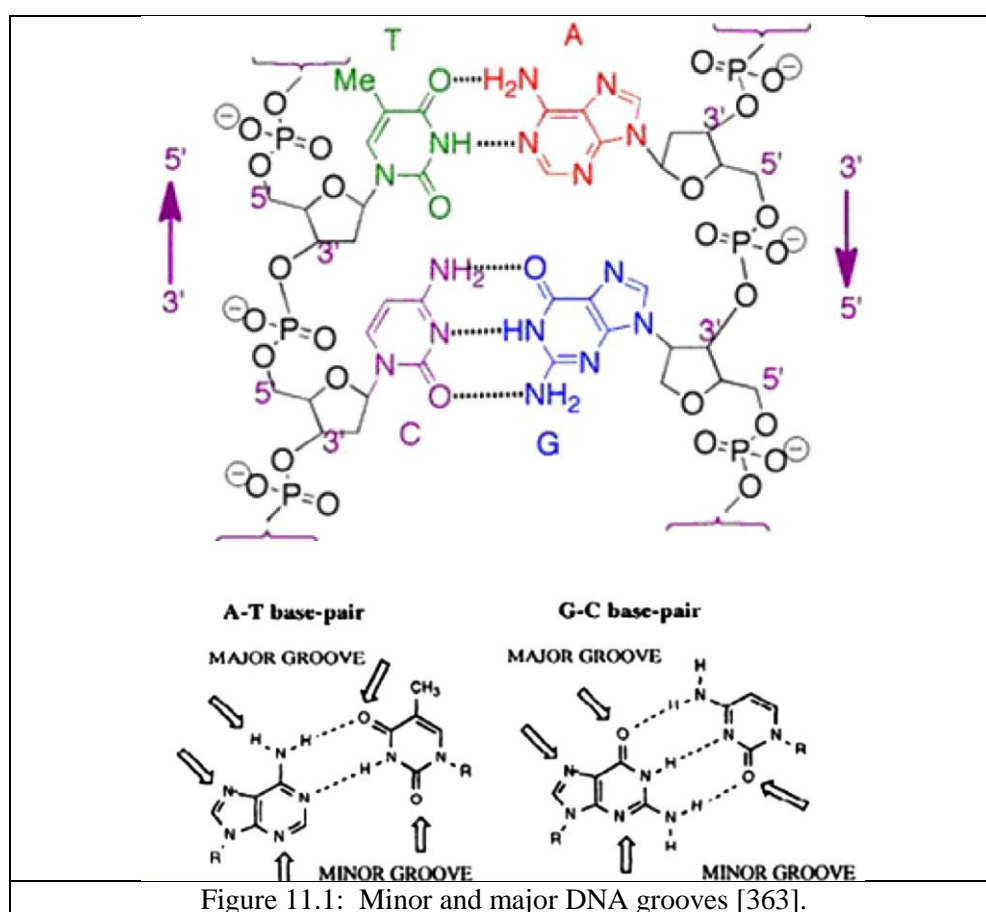
- (i) NPs inducing oxidative stress inflammation, and indirect DNA damage in a cell body, and
- (ii) NPs causing size/shape-dependent cellular damage in living systems; these NPs have similar sizes to many cellular components like DNA, RNA and proteins [242],

where the physico-chemical properties of the NPs modulate their dynamic interaction with biomolecules and cellular organelles [361], and, possibly their toxicity [362].

Here, the author assumes that NPs may by-pass the cell membrane and lead to harm in living cell and [99] cause inverse effects in living cells [54]. When DNA is exposed to UV light, excited levels are created in DNA leading to mutagenic photoproducts. This is where, single-stranded DNA can transfer an electron between stacked bases. The ability to observe and study photoinduced DNA offers exciting opportunities to explain the fundamental principles that govern energy and charge migration in multi-chromophoric systems made of organic building blocks. Systems play a central role in biological and

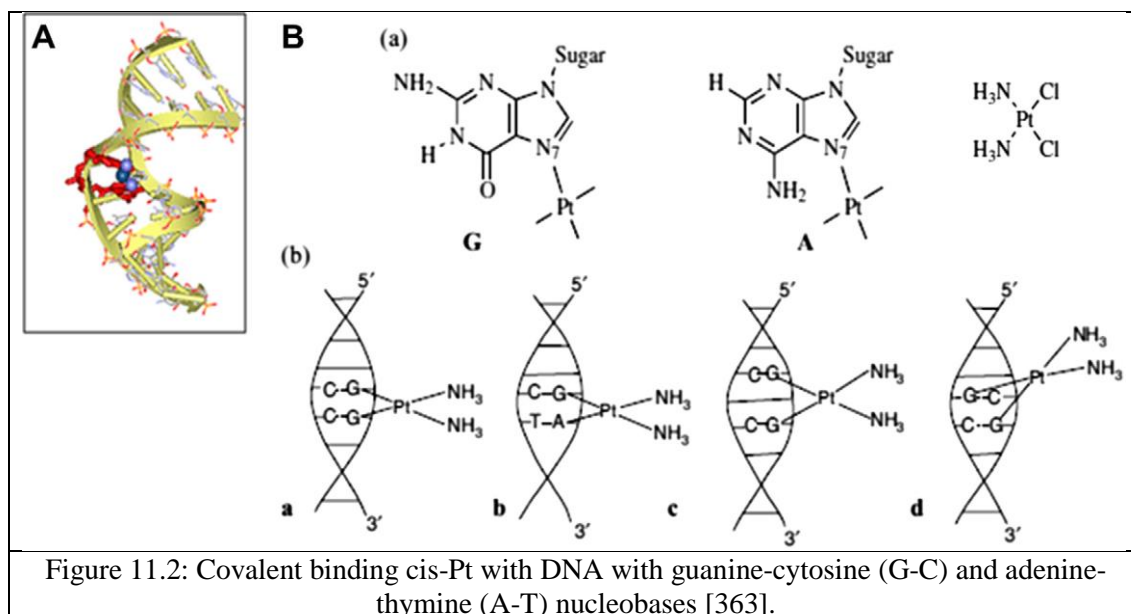
biomimetic energy harvesting and photocatalysis [243]. There are three ways for drugs to interact with DNA:

- (i) drugs interact with protein which binds to the DNA,
- (ii) drugs interact during RNA binding to DNA to form RNA hybridization,
- (iii) small molecules electrostatically interact with DNA via intercalation between base pairs in DNA and the minor DNA grooves (where the two DNA strands are near (deep-narrow) to each other) and the major DNA grooves (where the two DNA strands are far (shallow-wide) from each other) ( see Fig. 11.1) [363].



- **Types of drug-DNA interaction**

Firstly, covalent binding is invariable (and irreversible causing the inhibition of DNA processes completely). Then, it subsequently leads to cell death, see cis-Pt for example (Fig. 11.2). This type of inhibition involves an alkylating agent because it attaches an alkyl group to guanine in DNA. It is considered to be relatively toxic [363].



Secondly, non-covalent binding is reversible (fixed). Hence, it is sometimes preferred over covalent adduct formation and involves lower toxicity. The significant effects of non-covalent binding involve the DNA conformation, related structure perturbation and interaction with normal DNA protein-like topoisomerase due to affect the function of mitochondrial DNA and DNA strand breaks [363].

### Classification of non-covalent binding

- (i) **Intercalation:** this is when a molecule stacks perpendicular to the DNA backbone without forming covalent interaction or it cleaves the hydrogen bond between the two base pairs in DNA. Depending on the intercalator, the DNA must open the space between two base pairs dynamically by a varying degree of unwinding. For example, the ethidium cation (used in gel electrophoresis) that unwinds DNA, this is about 26°. There are many forces that sustain the stability of DNA-intercalator complex (hydrogen bonding, Van der Waal's forces, charge transfer forces and hydrophobic interactions). This mode is preferred by the presence of an extended fused aromatic ligand. Thus, the complex is stabilized by  $\pi$ - $\pi^*$  stacking interaction and it is less sensitive to ionic strength [363]. When the aromatic system is less extended, the intercalation is generally prevented during the clashing of the additional ligands with phosphodiester backbone. The intercalation of a planar ligand of the Co and Cu

complexes in the DNA base pairs stack forming a covalent interaction or cleaves the hydrogen bond [363].

- (ii) **Groove Binding:** Small ligands bind to the minor groove of the DNA by hydrogen bonding with bases (usually to O No.2 of thymine and N No.3 of adenine) and Van der Waal's forces. This binding is usually specific to adenine-thymine (AT) rich sequences because:
- (a) AT regions are close and narrower than (GC) groove regions,
  - (b) The stereochemistry that is presented by the C-atom No.2 amino group of the guanine base. This priority, in addition to the designed tendency for the electro-negative pockets of (AT) sequences, is due to a better Van der Waal's interaction between groove walls and the ligand in this place. Unlike the intercalator, groove binding drugs induce no structural rearrangement of DNA helix like Ni and Zn complexes, consider intercalation of Ni and Zn complexes into the DNA base pairs as adenine-thymine (AT) which is close and narrower than (GC) groove regions [363].
- (iii) **External Binding:** The ligands interact with DNA phosphate backbone where the ligand self-associates to form higher-order aggregates (it is electronic in nature). Here, the ligand stack on the anionic DNA backbone reduces charge-charge repulsion between the ligands. Mg and Ru complexes, which have divalent positive charge, bind with phosphate sugar back-bone in the DNA (negatively charged) dependent on ionic strength [363].

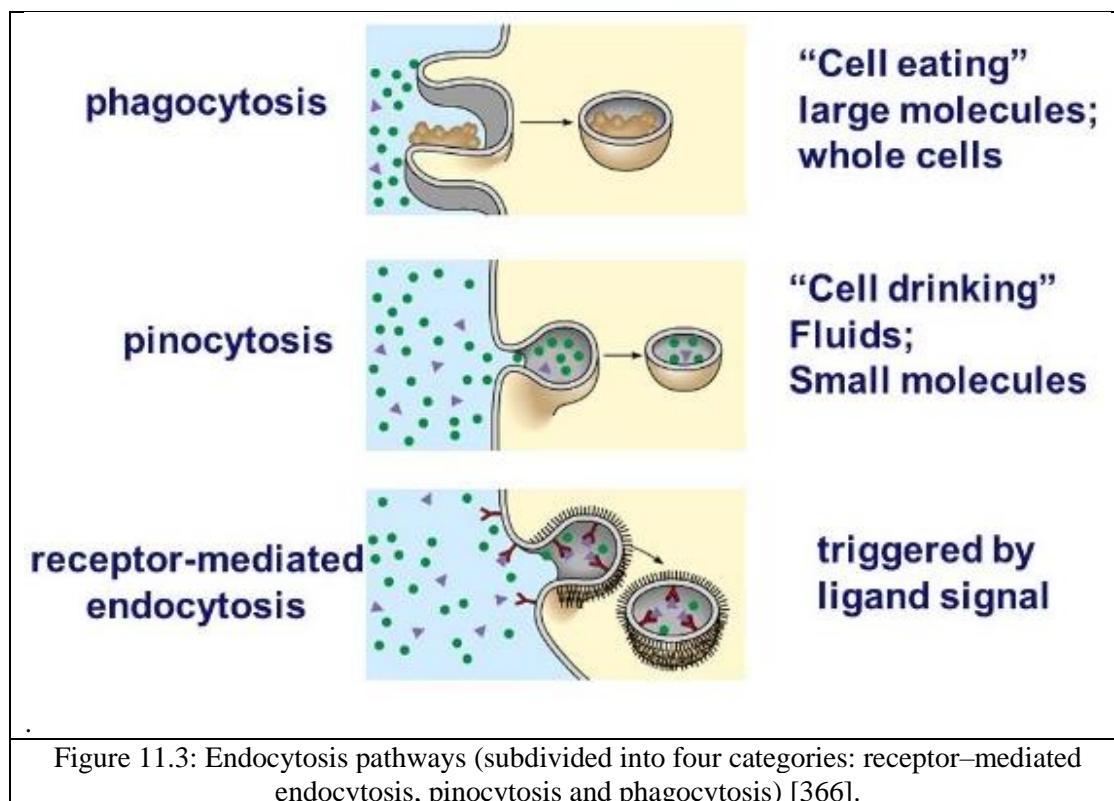
Hung et al. reported that Au NPs have higher cytotoxicity compared to Ag NPs because the charged Au NPs may adsorb serum proteins and enter cells by the more complicated endocytosis pathway [99].

- **Endocytosis and exocytosis and effect nanoparticles physicochemical properties on biological system**

The understanding of the endocytosis and exocytosis mechanism of NPs is significant to reducing the toxicity of NPs. Thus, one can design NPs to be safer, and control their efficient entry into/exit from cell of human and tissues [364].

Endocytosis of NPs is the uptake of small proteins or ions into the cell where special transport channels enable their translocation across the cell membrane.

When macro molecules and proteins are too large to enter through the plasma membrane, the cell has a different mechanism for their uptake from media. These uptake mechanisms refer to endocytosis (see Fig. 11.3) [365] and this mechanisms depends on: (i) changing the size of the transport vesicle, (ii) internalization machinery (tool), (iii) properties of the cargo (load) [366].



There are four types of pathway where NPs can enter the human cell, these include:

- (i) phagocytosis that engulfs (swallows) with particles of bigger than  $0.5 \mu\text{m}$ ,
- (ii) pincytosis where the cell absorbs particles ( $\sim 100 \text{ nm}$ ) from extracellular fluids (and small membrane-bound vesicles are formed which encapsulate the ingested species [8]),
- (iii) clathrin/caveolar-mediated endocytosis, where energy-dependent process by cells internalize biomolecules, and
- (iv) micropinocytosis, which is an endocytic process by which the cells internalize particles and fluids together, and vesicles (length  $0.2\text{-}5\mu\text{m}$ ) are formed.

At the first step of endocytosis the cargo (load) for internalization is engulfed (swallow) by pit formation or invagination (make cover) of the plasma membrane [365]. NPs are

coated with the serum proteins and then pass through the plasma membrane of cells. Here, the plasma membrane of cells could select the endocytosis pathways of NPs depending on their surface chemistry, specific cell type [365], size and shape [364]. Therefore, there are many factors can explain nanotoxicity of NPs and effect nanoparticles physicochemical properties on biological system:

- (i) surface chemistry can be determined by the chemical composition on the NP's surface and charge. The surface charge of NPs can influence their pathway of cellular uptake and efficiency because biomolecules in a biological system have various charges. Different surface charges are important as they influence uptakes by macrophages. For example, positively charged NPs exhibited a higher phagocytic uptake than neutrally or negatively charged NPs [364].
- (ii) Size is an important factor that affects the interaction of NPs with cell in the same composition. It is critical *in vivo* functions of NPs which are dependent on size such as internalization, targeting and clearance [213]. Generally, Au NP's cellular maximum uptake was observed with size 50nm and this size makes Au NPs nontoxic. Further, Au NPs with 5 -15nm inhibited colony formation in mouse fibroblast cells above 50 $\mu$ M [214]. It was reported that the intercellular uptake of Au NPs depends on size, shape, surface coating, concentration and aggregation. Also Au NPs at 50nm diameter showed the highest efficient cellular uptake compared with other sizes [365]. On the other hand, Au NPs of size 4nm showed the highest uptake in the macrophages depending on the number of NPs taken up per cell comparing with 11, 19, 35 and 45nm. Moreover, Au NPs with size less than 100nm were phagocytosed through scavenger receptor mediated phagocytosis [364].
- (iii) Shape: Rod-shape nanoparticles exhibit the highest uptake in human cancer cell followed by spheres, cylinders and cubes. Studies reveal that the uptake of the rod-shaped NPs by macrophages were more efficient than with spherical NPs. However, the spherical NPs were taken up by cancer cells more efficiently than were rod-shaped NPs [364].

Exocytosis of NPs is responsible for their systemic elimination and toxicity. The cellular uptake may be considered because of completion between the receptor diffusion kinetics and thermodynamic driving forces wrapping. The size effect on exocytosis can be explained. The size 50nm of Au NPs showed the fastest wrapping

time, because the receptor–ligand interaction could produce sufficient free energy leading to drive the NPs into cells. However, smaller NPs had slower wrapping times and so exhibited a faster rate of exocytosis. It was noted that 14nm Au NPs have an exocytosis rate faster than the 74nm [364]. In addition, the fraction of the rod-shaped NPs which exit out of the cell was normally higher than the spherical NPs, although the work demonstrated that the exocytosis of NPs was also dependent on the proteins in the surrounded medium. These proteins were carried into the cell along with NPs and interacted with biological molecules in the cells [364].

### **11.1.2 Median lethal dose**

Median lethal dose (LD<sub>50</sub>) is the dose by which 50% of the species under study in standard laboratory conditions were killed. The value of LD<sub>50</sub> indicates the toxicity of materials (low LD<sub>50</sub> means low toxicity) [367].

## **11.2. The results**

The electrophoresis approach used here is described in section 3.5.

### **11.2.1 Molecular results**

Study of the effects of NPs/PMS on DNA is described in section 4.2.9. and median lethal dose (LD<sub>50</sub>) is described in section 4.2.10. Figure 11.4 and 5 show the 0.8% agarose gel electrophoresis of the extracted DNA, the bands of total genomic DNA/PMS observed as purified compact bands under UV light. Electrophoresis in a sample of DNA-NPs/PMS, has also been examined. The migration of DNA on agarose gel was done under the influence of electrical field by which the DNA molecule moved faster than the DNA-NPs/PMS, that appear as a retarded band when binding with double strand DNA. Usually smaller DNA molecules move faster than larger ones. Then, the molecules are separated by size. Therefore, the absorbance of DNA nucleotides decreased with TiO<sub>2</sub> NPs/PMS more than Au-TiO<sub>2</sub> NPs/PMS and Ag-TiO<sub>2</sub> NPs/PMS. Table 11.1 suggests TiO<sub>2</sub> NPs/PMS samples had an ability to bind with DNA nucleotides in the light and dark.



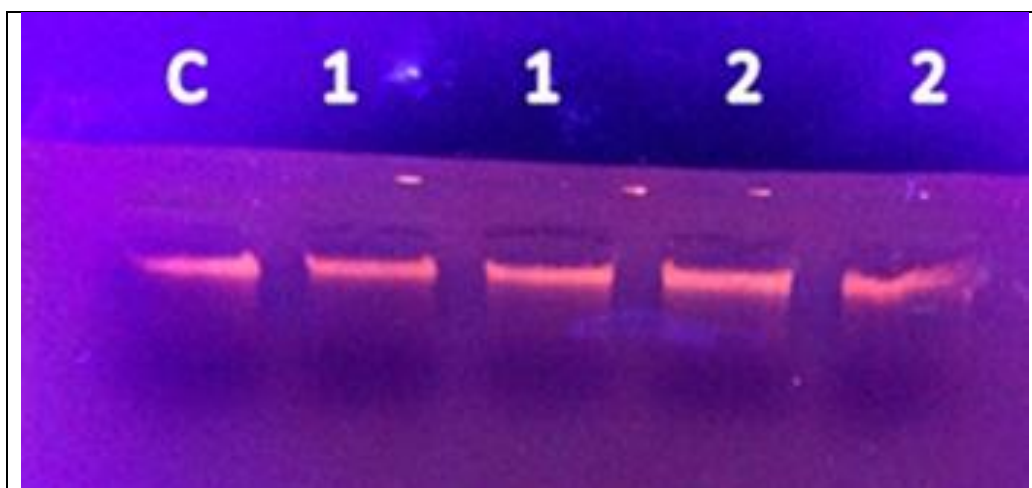


Figure 11.4: Ethidium bromide–stained agarose gel electrophoresis containing total genomic DNA on of PMS alone. Control (C): DNA in TE, (buffer solution) 1: PMS sample under light at RT, 2: PMS sample in the dark at 37 °C.



Figure 11.5: Ethidium bromide–stained agarose gel electrophoresis containing total genomic DNA on of NPs/PMS. C: Control (DNA + TE (buffer solution)), 1: TiO<sub>2</sub>/PMS sample in the dark at 37 °C, 1: TiO<sub>2</sub> /PMS sample in the light at RT, 2: TiO<sub>2</sub> -Ag NPs/PMS (same), 3: TiO<sub>2</sub> -Au NPs/PMS (same)

Table 11.1: DNA conc. entreated (ng/μL) which interacts with NPs/PMS using electrophoresis.

Samples of mixture of NPs	Control DNA (Conc.ng/μL)	Conc. ng/μL of DNA with NPs	
		Light	dark
TiO <sub>2</sub> /PMS	4.05	29.65	51.75
Ag-TiO <sub>2</sub> /PMS	16.5	29.5	62.7
Au-TiO <sub>2</sub> /PMS	2.5	12.06	25.1

Table 11.2 shows that the binding value of TiO<sub>2</sub>/PMS is higher than Ag-TiO<sub>2</sub>/PMS and Au-TiO<sub>2</sub> NPs/PMS using Eq. (11.1).

$$A_{bonding} = \frac{(A_{DNA/NPs} - A_{DNA})}{A_{DNA}} \quad \text{--- (11.1)}$$

$A_{\text{bonding}}$  = the absorbance of the binding nucleotide with the sample.

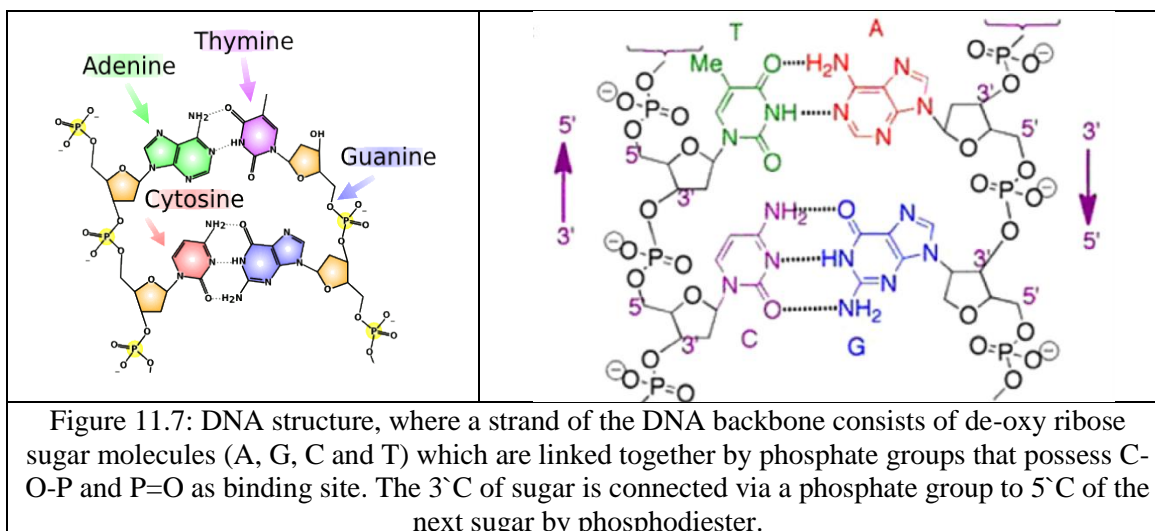
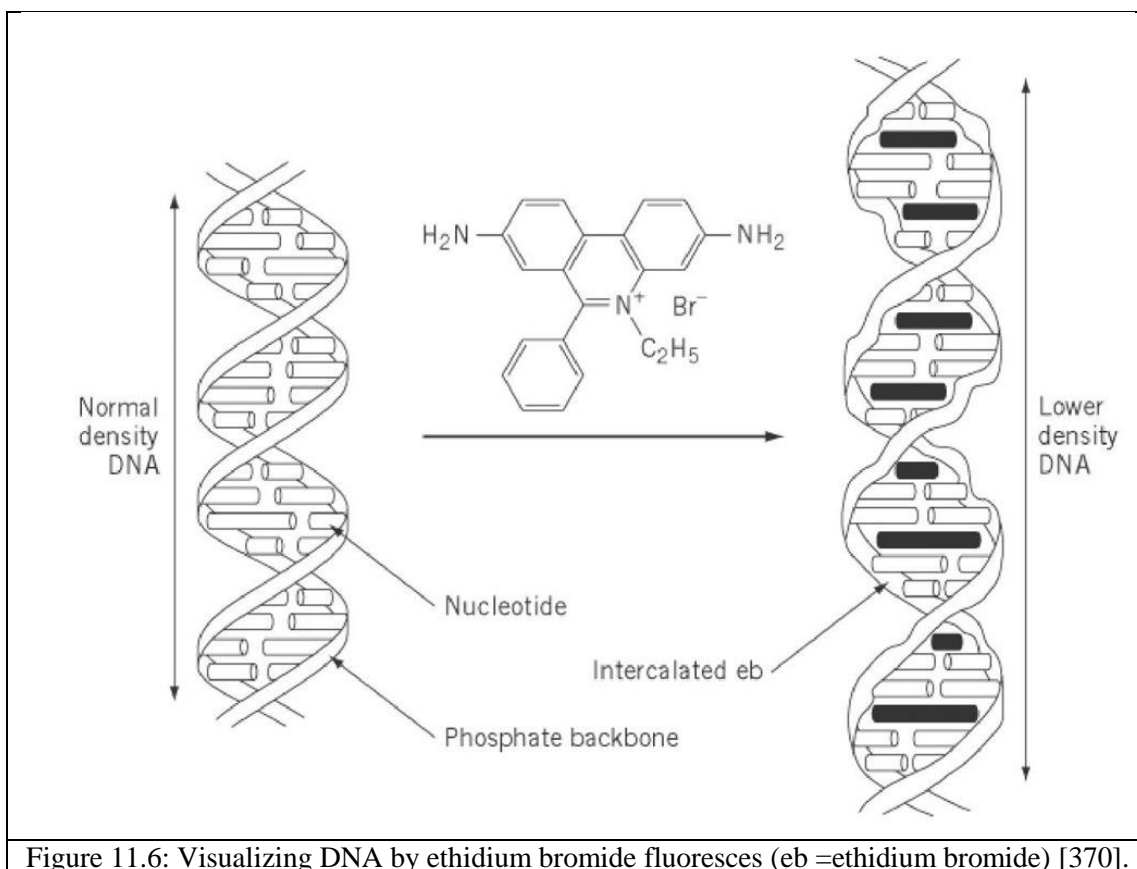
$A_{\text{DNA}}$  = the absorbance of the whole nucleotide in DNA alone.

$A_{\text{DNA/NPs}}$  = the absorbance of the DNA with the sample [368].

Table 11.2: The absorbance (A) of the interaction of NPs/PMS with DNA and  $A_{\text{bonding}}$  using electrophoresis.

Samples of mixture of NPs	A of Control DNA	A of DNA with NPs		$A_{\text{bonding}}$	
		Light	dark	Light	dark
TiO <sub>2</sub> /PMS	0.081	0.593	1.35	6.320	15.66
Ag-TiO <sub>2</sub> /PMS	0.33	0.59	1.254	0.787	2.8
Au-TiO <sub>2</sub> /PMS	0.05	0.240	0.502	3.8	0.402

The retarding behaviour of the DNA migration in agarose gel electrophoresis suggests that the binding between DNA (negative charged) and NPs/PMS (positive charged) occurs mainly through electrostatic interactions among the samples. On the other hand, the NPs can interact between two nucleic bases in DNA [369]. It is evident that there is interaction between DNA and NPs/PMS compared with control. When ethidium bromide (mutagen) intercalated into the major groove of DNA and the running DNA through an EtBr-treated gel and visualizing it with UV, any band containing more than 20ng DNA becomes distinctly visible (see Fig. 11.6). Here, the samples interact with DNA instead of Et Br [370]. In this case, the bands do not appear like the control band. Table 11.2 shows how five PMS-based samples interacted with human blood DNA at 37°C in light and dark conditions after samples had been separated into a PMS-sediment and a supernatant liquid. Data are shown as the % of the absorbance (260nm;  $A_{260\text{nm}}$ ) of the added DNA. In almost all supernatant liquid samples and PMS sediment samples (in light and dark conditions),  $A_{260\text{nm}}$  increased greatly beyond the level of the DNA added initially. The only samples that did not show this effect in the supernatant liquid were Ag-TiO<sub>x</sub>/PMS and Au-TiO<sub>x</sub>/PMS, but even then, the PMS sediment did show an elevated  $A_{260\text{nm}}$ . Figure 11.7 illustrates the structure of DNA.



### ***The mechanism of DNA-NPs/PMS***

PMS-based nanomaterials clearly interact with DNA. The base pairs of DNA possess strong absorbance at 260nm [371]; if the DNA helix is denatured, base stacking is destroyed and UV absorbance goes up. The effect of PMS and most NP/PMS samples was to increase absorbance at 260nm above that for the DNA introduced (both in light

and dark conditions and in the supernatant and PMS sediment). The only exception was for the supernatant liquid of Ag-TiO<sub>x</sub>/PMS<sub>(H<sub>2</sub>O, IPA)</sub> and Au-TiO<sub>x</sub>/PMS<sub>(H<sub>2</sub>O, IPA)</sub>. One assumes that all other samples lower base stacking, block of DNA replication and cause DNA damage [30]. Figure 11.8 shows that the absorbance changes in the form of hyperchromism and hypochromism. For example, the bases absorb UV radiation. If strands are allowed to anneal, base stacking reduces UV absorbance: hypochromism. If helix is denatured, base stacking is destroyed, UV absorbance goes up (hyperchromism).

The present results appear to show that hyperchromism occurs suggesting breakage of the DNA structure. That means interaction between TiO<sub>x</sub> NPs/PMS and nanohybrid with DNA.

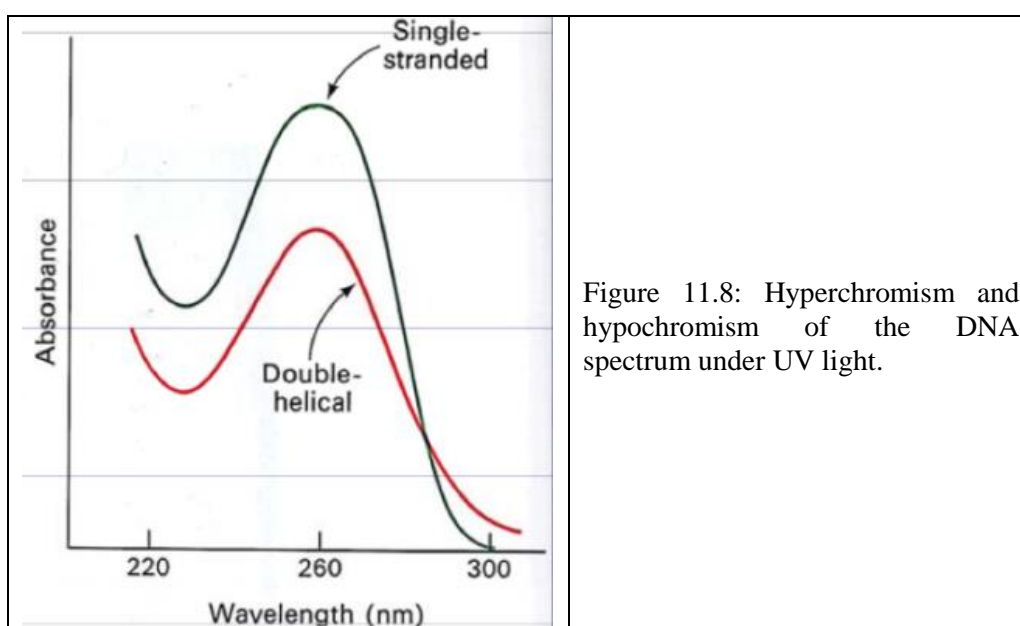


Figure 11.8: Hyperchromism and hypochromism of the DNA spectrum under UV light.

Electrostatic interactions can change the conformation/structure of DNA. For example, H-bonds, hydrophobic effect and stacking interactions between complementary bases hold the two strands of DNA together. When NPs/PMS were added, the base-base interaction was reduced in the DNA structure, owing to many bases becoming free form and H-bond breakage leading to an increase absorbance [371]. Furthermore, the presence of a single stranded DNA will be higher than double stranded DNA in the same concentration. The mechanism of reaction can occur by the phosphate group of DNA which has a negative charge. The positive charge of metals can bind to P=O to form P-O-M via an electrostatic reaction [372]. From the results one can see that there are future applications for using these materials as anticancer drugs by destroying the nuclear materials for the tumour cells.

Ag NPs appear to enter the cell and intercalate between the purine and pyrimidine base pairs disrupting the hydrogen bonding between the two anti-parallel strands and denaturing the DNA molecule [373]. In general, all samples can analyze DNA in dark and light. NPs/PMS in mixture and precipitate have an excellent effect which reaches 60ng/ $\mu$ L. In contrast, NPs/PMS monohybrid supernatant show some decrease in absorbance due to lower NPs/PMS concentration [354]. The interaction between  $\text{TiO}_x$  NPs/PMS and monohybrid with human DNA under UV can be explained via the covalent interaction and non-covalent interaction. First, NP/PMS hybrids can bind to alkylation or intra and inter strand crosslinking of DNA as a covalent interaction. Secondly, the non-covalent interaction leads to DNA strands breakage, changing DNA conformation or torsional tension [363]. Additionally, non-covalent interaction involves the following:

- $\text{TiO}_x$ /PMS and hybrids could be interacting between base pairs,
- they bind to a sugar phosphate group's backbone or the major or minor groove and,
- the electrostatic interaction of these NPs includes binding to the exterior of the helix by non-covalent interaction [371].

Several hypotheses can be suggested to explain the increase in absorbance at 260nm:

- (i) exposure of the bases' purine and pyrimidine of DNA when NPs interact with DNA leading to a slight change in the human DNA conformation and
- (ii) NPs release ROS causing DNA damage [54].

### 11.2.2 Effect of NPs/PMS nanohybrids on nanocytotoxicity

The NPs/PMS ( $\text{TiO}_2$ , Ag and Au NPs/PMS), and their nanohybrid (Au- $\text{TiO}_2$ /PMS and Ag- $\text{TiO}_2$ /PMS) were used in order to determine their effect on nanotoxicity against RBCs (human blood). The nanocytotoxicity was evaluated using standard which contained (blood with normal saline (NaCl, pH 7.4) +IPA) and the control (blood with normal saline) at 100  $\mu$ L for all solutions for 1h. Here, IPA (as a solvent) was used as a control to confirm that IPA had no nanocytotoxic effects because any impact in blood cells can instead be attributed to samples of PMS. Normal saline used to keep the blood from clotting. According to Figure 11.9 and Table 11.3, the results illustrate that the NPs/PMS had no cytotoxicity against the human red blood cells for 1h because no turbidity was observed. All the samples remained clear solutions compared with control.

That means, all samples are safer for 1h independent of their composition, size and shape.

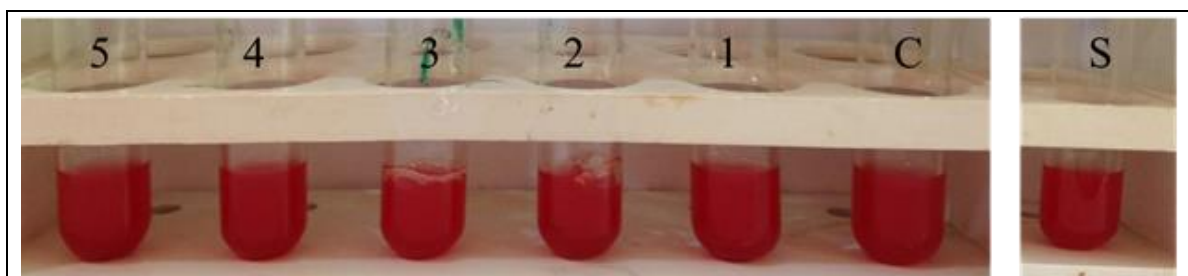


Figure 11.9: Cytotoxicity of NPs/PMS against RBCs. S= standard (blood + normal saline +IPA), C= control (blood + normal saline (NaCl, pH 7.4)), 1= TiO<sub>2</sub>/PMS, 2= Ag NPs/PMS, 3= Au NPs/PMS, 4= Au-TiO<sub>2</sub>/PMS, 5= Ag-TiO<sub>2</sub>/PMS.

Table 11.3: The nanocytotoxicity of supernatant NPs/PMS against RBCs.

No.	NPs/PMS	Conc. ng/ $\mu$ L	Toxicity against RBCs
1	TiO <sub>2</sub> /PMS	16	NT
2	Ag NPs/PMS	26	NT
3	Au NPs/PMS	5	NT
4	Au-TiO <sub>2</sub> /PMS	84-26	NT
5	Ag-TiO <sub>2</sub> /PMS	42- 26	NT

Note: NT means nothing observed.

### 11.2.3 Median Lethal Dose (LD<sub>50</sub>)

In experiments albino mice were administrated orally with different doses of TiO<sub>2</sub>, Ag and Au NPs/PMS for 72h. Here, the study of median lethal dose (LD<sub>50</sub>) and toxicity is an important factor for the evaluation of new NPs/PMS to avoid acute toxicity by developing a biomimetic approach.

The results show that Ag and Au NPs/PMS do not have any toxicity from 50, 100 and 250 $\mu$ g/kg after 72h. However, TiO<sub>2</sub>/PMS exhibited (66.6% male and 33.3% female) of mortality at 250 $\mu$ g/kg after 72h [367]. As a result, the LD<sub>50</sub> of TiO<sub>2</sub>/PMS is 100% after oral intubation in Swiss albino mice (see Table 11.4).

There is relationship between LD<sub>50</sub> and toxicity. The value of LD<sub>50</sub> increase means the toxicity of NPS increased. Here TiO<sub>2</sub>/PMS has more toxicity than Ag and Au NPs/PMS. The structural differences could play an important role in the toxicity results [358]. Here, TiO<sub>2</sub>/PMS is less stable than Ag and Au NPs/PMS. This may release positive ions and oxide metals which react with DNA or proteins leading to death of the mice.

Table 11.4: Median Lethal Dose (LD<sub>50</sub>) of TiO<sub>2</sub>/PMS for 6 mice.

Dose (μg/kg)	No. of death mice					
	24h		48h		72h	
	male	female	male	female	male	female
50	0	0	0	0	0	0
100	0	0	0	0	0	0
200	0	0	0	0	2	1
Control (0.5 mL) normal saline	0	0	0	0	0	0

The mechanism whereby Ag and Au NPs/PMS are far were less toxic maybe due to their surface that hardly reduces its intracellular release of toxic ions (e.g. Au<sup>1+</sup>, Au<sup>3+</sup> and Ag<sup>+</sup>, see Fig. 11.10) in the cytoplasm trigger by the acidic lysosome. [361]. Here, the design NPs/PMS have stable surface coatings that are resistant to the acidic pH of lysosomes and limit metal ions leakage [361].

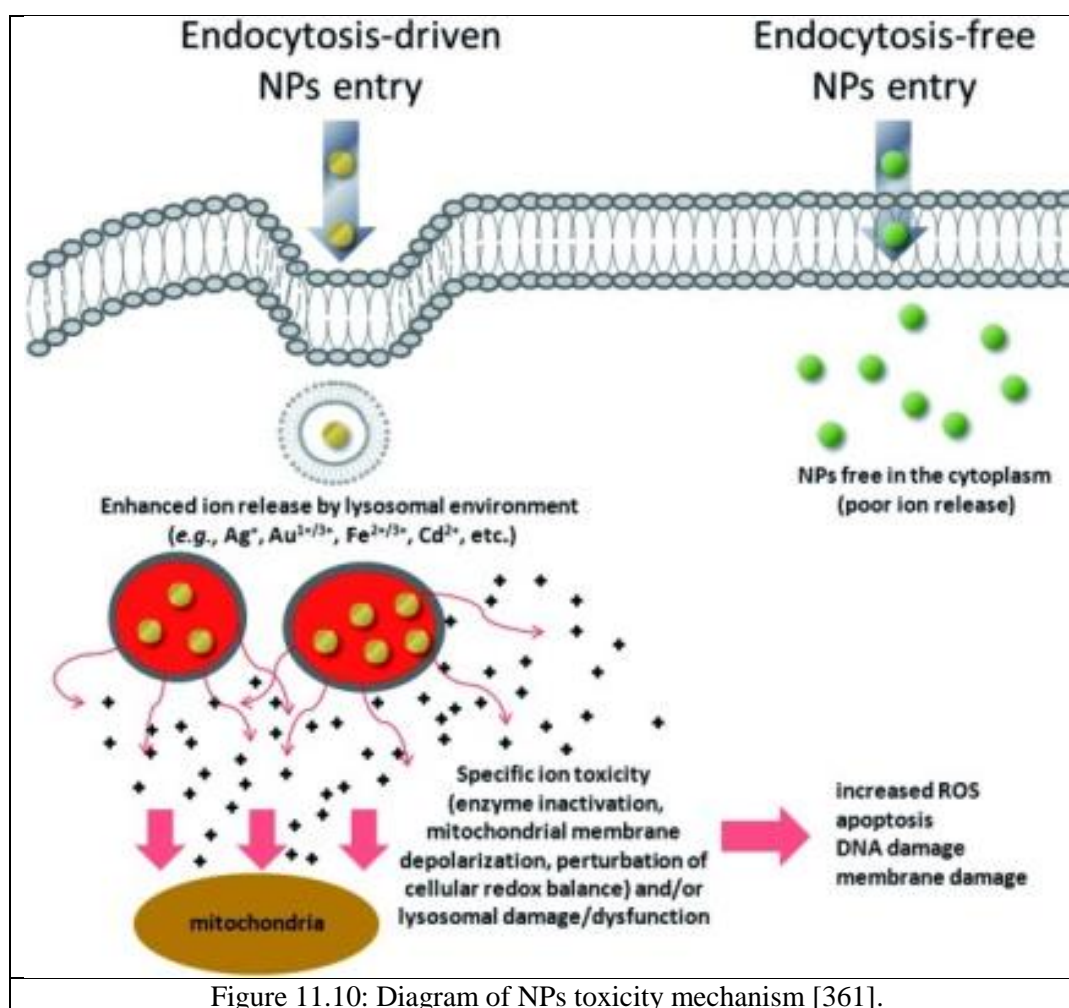


Figure 11.10: Diagram of NPs toxicity mechanism [361].

### 11.3 Conclusions

The increasing use of TiO<sub>2</sub>, Ag and Au nanoparticles leads to human and environmental risk when exposed to NPs. In terms of the cytotoxicity of NPs/PMS and the interaction with human blood, DNA has been investigated *in vitro*. The DNA damage has been examined by measuring UV nano-Drop spectroscopy and agarose gel electrophoresis. The results show no cytotoxicity for these NPs/PMS at 100μL level in human blood and all the other samples do not have any turbidity over 1h using NPs/PMS as a bio-nanoparticle; instead they have been shown to have biocompatibility and natural cell binding ability. All samples (except Ag-TiO<sub>x</sub>/PMS and Au-TiO<sub>x</sub>/PMS) showed an interesting interaction with DNA. Here, there is an interaction between NP/PMS and human DNA. Creating a new drug would dramatically reduce disease as anticancer and other medical applications. As for the LD<sub>50</sub>, results confirm that Ag and Au NPs/PMS do not have any toxicity in concentrations from 50 to 250mg/kg after 72h.



## Chapter 12: Biomimetic TiO<sub>2</sub> formation from interfacial sol-gel chemistry leading to new photocatalysts

---

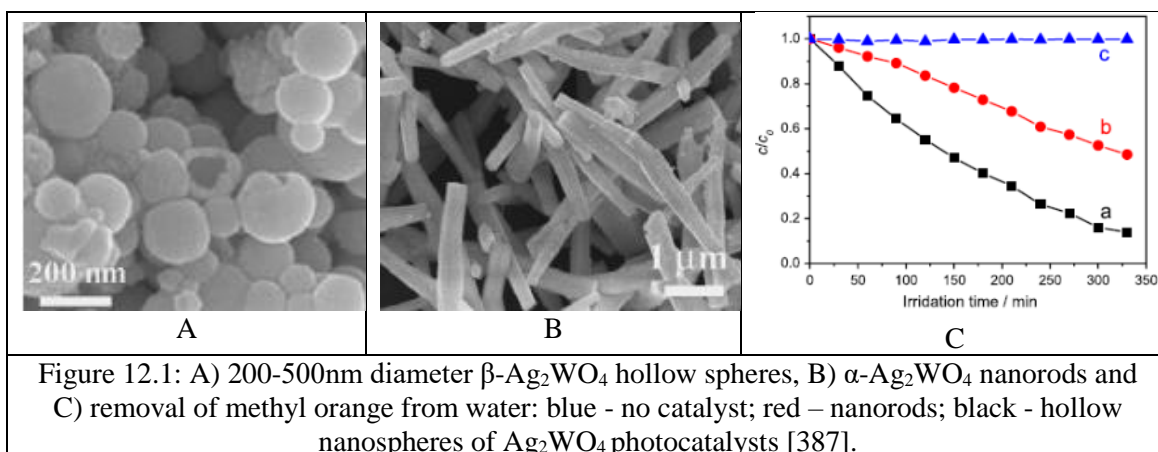
This chapter will describe TiO<sub>2</sub>/PMS and monohybrids/PMS (PMS, TiO<sub>x</sub>/PMS, Ag/PMS, Au/PMS, Ag-TiO<sub>x</sub>/PMS and Au-TiO<sub>x</sub>/PMS, TiO<sub>2</sub> (PMS), Ag-TiO<sub>2</sub> (PMS) and Au-TiO<sub>2</sub> (PMS)) as photocatalysts with methyl orange (MO) as a pollutant using UV-Vis. These samples were compared with P25 anatase-rutile as a reference. The aim was that these nanomaterial samples may be used to target organic water pollutants.

### 12.1 Introduction

In the industrial era, environmental problems (such as air and water pollution) have become more complex to solve [374]. Industry waste toxic agents released into the air and rivers are leading to pollution-related diseases, abnormal climatic changes and global warming [59]. For instance, it is estimated that 15% of all dyes is lost during the dying process and released into waterways. Large quantities of azo compounds are used as dyes [58].

Alternative technologies for control of water pollution by organics include: adsorption on carbon or treatment with O<sub>3</sub> [375], ultrasound/cavitation [376] and TiO<sub>2</sub> [377] or biosynthesised functional CdS, CdTe and AgS photocatalysts [378]. Bio-inspired [379] and biomimetic [380] photocatalysts are promising [381] for removal of organic pollutants in water. Here bio-inspired photocatalysts based on TiO<sub>2</sub> were most appropriate. Bioinspired [382] and biomimetic photocatalysts include TiO<sub>2</sub>/graphene oxide with molecular recognition [383] and TiO<sub>2</sub> nanofibers [384]. The latter was tested with a 300W lamp when 60 mg catalyst was suspended in 100mL of an aqueous solution of 0.18mM methyl orange with magnetic agitation (60 rpm). Leaves have been used to provide a structural inheritance for ZnO photocatalysts [385] that will be used in our on-going research. There are two broad experimental approaches available: process illumination at say 300W [386] and solar/environmental illumination at say 15W [387].

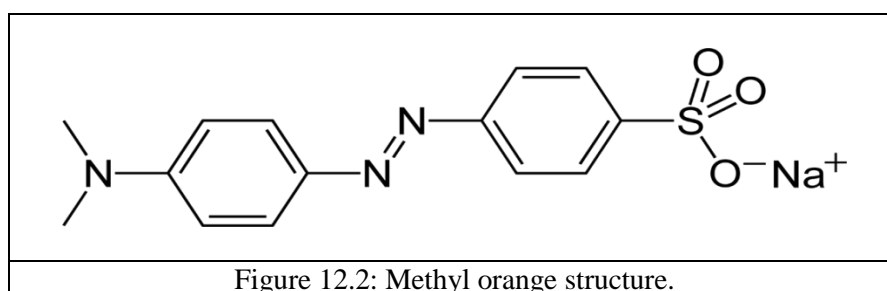
It is also especially relevant that others have seen an effect of macroscopic structure on photocatalytic activity [387]. UV-absorbance suggested that 50mg metastable  $\beta$ - $\text{Ag}_2\text{WO}_4$  was more active in the photodegradation of 0.06mM methyl orange aqueous solution (10mL) at room temperature when irradiated by a 15W lamp at 365nm without agitation when in the form of hollow spheres (200-500nm diameter; 20nm wall thickness;  $165.5\text{m}^2\cdot\text{g}^{-1}$  BET area; see Figure 12.1A) than as solid  $\alpha$ - $\text{Ag}_2\text{WO}_4$  nanorods (Figure 12.1B). The hollow nanospheres had a band gap energy of 2.88eV that was lower than for the nanorods (3.05eV). The author was interested to know whether the photoactivity was structurally dependent or band-gap dependent. She preferred not to use  $\alpha/\beta$ - $\text{Ag}_2\text{WO}_4$ , but rather  $\text{TiO}_2$ , that she knew could produce hollow structures on biotemplates [388]. One problem with  $\alpha/\beta$ - $\text{Ag}_2\text{WO}_4$  was that the thermodynamically favourable  $\alpha/\beta$  phase transition had to be inhibited. Of course with  $\text{TiO}_2$  one has to recognise the potential transformation of anatase to rutile and the effect of any biotemplate-derived impurities [387].



It is interesting that  $\text{TiO}_2$ /graphite can be produced from cellulose on  $1300^\circ\text{C}$  thermal treatment [384], since the authors are also working on  $\text{TiO}_2/\text{C}$  produced from  $\text{TiO}_2$ /biotemplates.

### 12.1.1 Adsorption and photocatalytic activity towards methyl orange (MO)

The dye of methyl orange (MO; see Fig. 12.2) was selected as model pollutants for two reasons (i) MO is a common contaminant in industrial waste water, and (ii) it cannot be photodegraded in the absence of a photocatalyst when exposed to light irradiation [75].

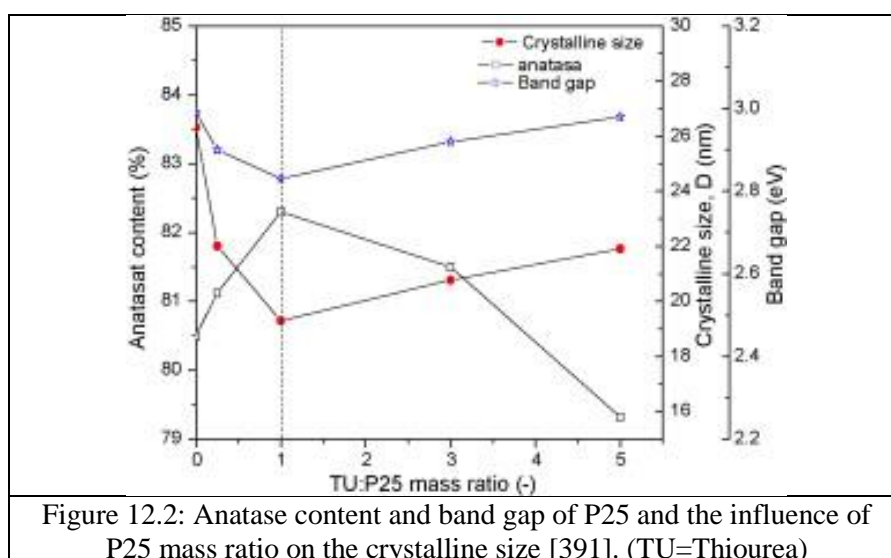


MO possesses an azo group (N=N) conjugated to two phenyl groups leading to a peak in absorbance in the visible region ( $\lambda_{\max} = 464\text{nm}$ ). X-ray diffraction peaks of anatase and rutile  $\text{TiO}_2$  phase in commercial Evonik P25 (that is manufactured by subjecting  $\text{TiCl}_4$  to hydrolysis in the vapour phase at an elevated temperature) showed that it consisted of anatase (A; 85nm crystallites) and rutile (R; 25nm crystallites) in a ratio of 3:1 [389] or 80% 17.9-26.3nm A and 20% 61.8nm R. P25 is known to have a band gap of 3.37eV and an absorption edge at 367.95 nm [390] or 387.50-414.72 nm (2.99-3.2eV) [391]. P25 was used as a point of comparison with biomimetic  $\text{TiO}_2/\text{PMS}$ . Here, we used  $\text{TiO}_x/\text{PMS}$  and  $\text{TiO}_2(\text{PMS})$ , P25, PMS, Ag/PMS, Au/PMS, Ag- $\text{TiO}_x/\text{PMS}$  and Au- $\text{TiO}_x/\text{PMS}$ , Ag- $\text{TiO}_2(\text{PMS})$  and Au- $\text{TiO}_2(\text{PMS})$  (where  $X_{\text{PMS}}$  means template removed) and they were evaluated after template removal prepared in duplicate with magnetic stirring at 60 rpm at 25°C for their (i) rate and extent of adsorption of MO from an aqueous 0.1mM solution over a period of 1h in the dark and (ii) photocatalytic activity over 10h at 25°C by UV-Vis spectroscopy under 254 nm, 365 nm and white light (15W) in air. This analysis does not indicate the nature of the products of decolouration, but it is close to solar/environmental levels of UV illumination [387]. Dividing the photocatalytic rate (mmol MO/mg catalyst/s) by the extent of MO adsorption (mmol MO/mg) gave the turnover frequency (TOF) in  $\text{s}^{-1}$  [392]. Some use the turnover rate for photocatalytic reactions [393]. The absorption edge of the biomimetic photocatalysts and replicas was compared to that of rutile (3.0eV; 415nm) and anatase (3.2eV; 380nm). Methods of characterization of these samples were analysed using (i) transmission electron microscopy (explained in chapter 3) for morphology and particle size for  $\text{TiO}_2$  with Ag and Au (explained in chapter 6) and (ii) UV for the absorption edge.

## 12.2 Characterization Results

### 12.2.1 Absorbance edges and extents of methyl orange adsorption

The P25 revealed an absorption edge at  $\lambda = 410\text{nm}$ , which was consistent with that reported by others [391]. However, unlike the unmodified  $\text{TiO}_2$ , all three photocatalysts (CN-, C-, and N- $\text{TiO}_2$ ) showed a shift of the absorbance spectrum towards the visible light region (400-800) nm.



P25 is a standard material because (i) it exhibits high photocatalytic activities, (ii) it has a large surface area and (iii) it consists of anatase and rutile phases in a ratio of about 3:1. Figure 12.3 depicts the absorption thresholds ( $\lambda_g$ ) as 363, 333 and 373nm for present biomimetic  $\text{TiO}_2$  samples; the corresponding band gap energies ( $E_g$ ) which are calculated by using the Eq: ( $\Delta E = 1240 / \lambda_g \text{ nm}$ ) for  $\text{TiO}_2/\text{PMS}$ ,  $\text{Ag-TiO}_2/\text{PMS}$  and  $\text{Au-TiO}_2/\text{PMS}$  respectively [394] are given in Table 12.1. These results confirm that Au NPs can effectively reduce the apparent band gap of  $\text{TiO}_2/\text{PMS}$  nanohybrid. It has been reported that metal doping introduces an additional impurity level into the band gap of titania. Electronic transitions of  $\text{Au-TiO}_2/\text{PMS}$  from the valence band to the impurity level or from the impurity level to the conductive band can effectively reduce the apparent band gap and red shift ( $\lambda_{\text{max}}$  from 464nm to 490nm) band edge adsorption threshold. That means,  $\text{Au-TiO}_2/\text{PMS}$  has the potential to improve the photocatalytic activity under visible light irradiation.

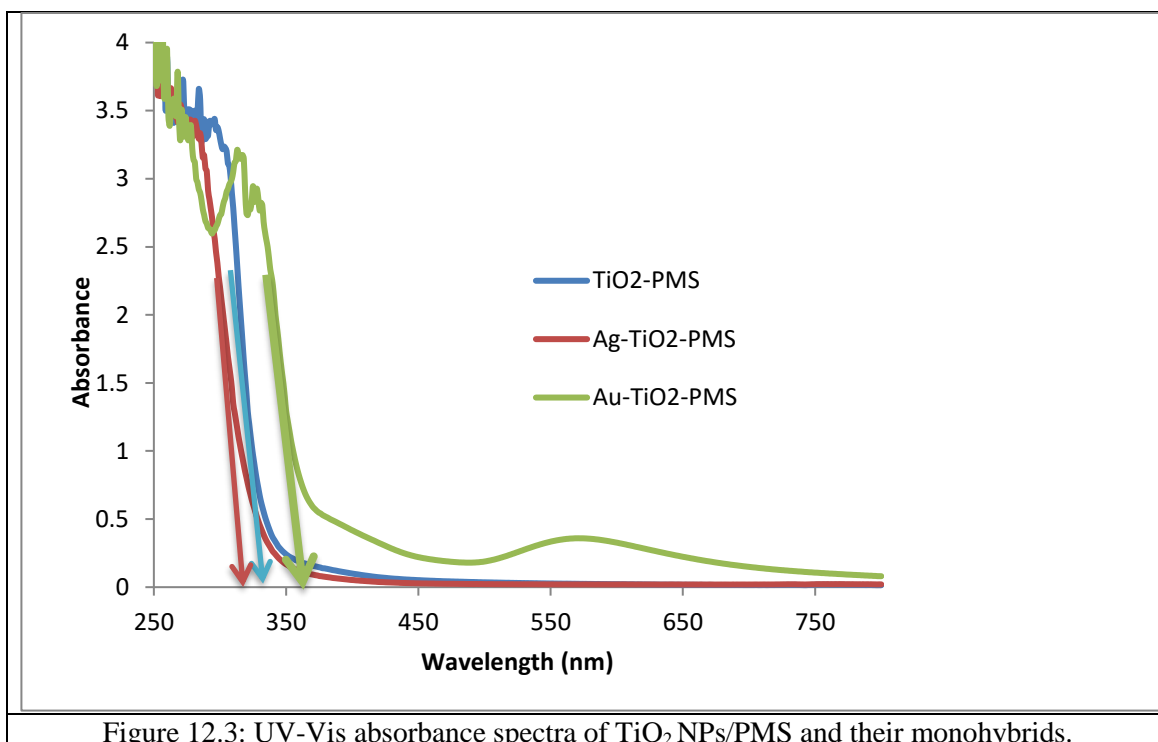


Figure 12.3: UV-Vis absorbance spectra of TiO<sub>2</sub> NPs/PMS and their monohybrids.

In section 6.3.1 one saw that Au NPs/PMS showed a pink colour in water to indicate the formation of Au NPs/PMS. This change in the colour of the reaction mixture is because of the excitation of surface plasmon resonance (SPR) in the Au NPs. Figure 12.3 illustrates the band corresponding to SPR occurs (at 518nm) which indicates the formation of Au NPs (see Table 12.1). Au-TiO<sub>2</sub> NPs/PMS on the other hand exhibits a blue shift of absorption at 373nm corresponding to an absorption edge at 3.3 eV. Previous studies have reported that doped metals in TiO<sub>2</sub> (absorption edge is 3.6) does not change the position of the valence band edge of TiO<sub>2</sub>. Alternatively, it maybe that it introduces new energy levels of Au NPs into the band gap of TiO<sub>2</sub>. Thus, the absorption edge shifts to longer wave lengths [75]. Ag NPs/PMS (416nm) absorption is due to the SPR of silver NPs. The new features with Ag-TiO<sub>2</sub> NPs/PMS that can be noted are the absorbance edge is 3.7eV and it shifts to a lower wavelength (333nm). The band at 333 nm is weakened in intensity when Ag NPs were reacting with TiO<sub>2</sub>. This is different from the case of NPs of Ag with PMS [68]. Table 12.1 shows that absorption edges ( $\Delta E_g$ ) of Ag/PMS and Au/PMS move to a higher wavelength (i.e. towards the visible) compared to P25, but not when TiO<sub>x</sub> is present. This is beneficial in a solar-environmental sense (i.e. photocatalytic activity under visible light irradiation might be enhanced).

Table 12.1: Absorption edges ( $\lambda_{\max}$  (nm)) and MO adsorption capacities (n; molecules MO x  $10^{14}$ /mg)

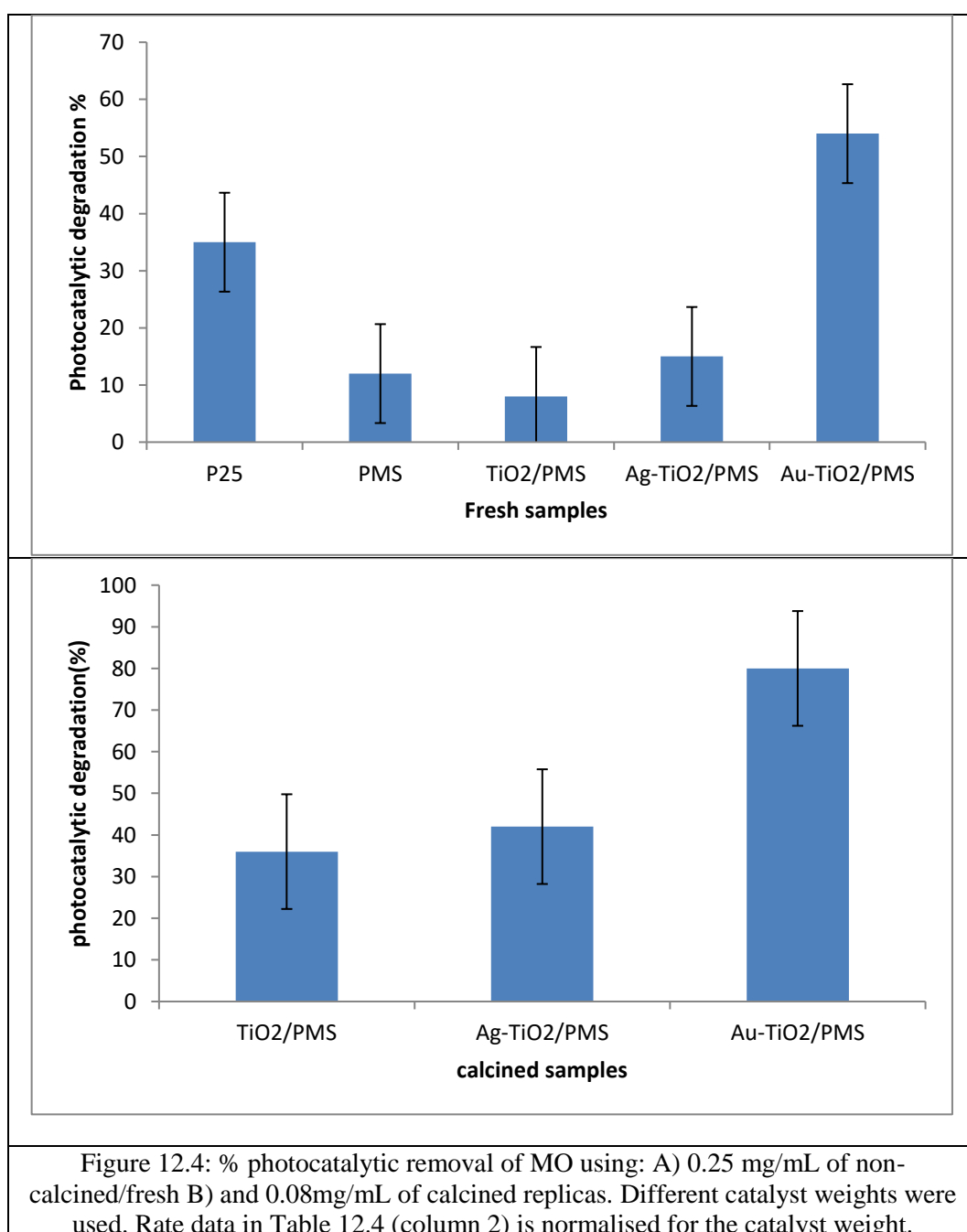
	TiO <sub>x</sub> /PMS	Ag/PMS	Ag-TiO <sub>x</sub> /PMS	Au/PMS	Au-TiO <sub>x</sub> /PMS	P25
$\lambda_{\max}$ (nm)	336	416	333	518	373	410 [391]
n	89.33		72.00		96.00	0.29 [395]
$\Delta E_g$ (eV)	3.6	2.9	3.7	2.3	3.3	

Some have seen a clear correlation between extents of adsorption and rates of photocatalysis on TiO<sub>2</sub>/carbon [396]. Others [397] have looked at the adsorption of MO on P25 and biosorbents; of course here the biotemplate is the biosorbent. A correlation exists between extents of MO adsorption and rates of its photodegradation [395]. P25 adsorbs 16% of MO (when 10mg MO/L and 1g P25/L are used). The adsorption of MO took 1-2h to reach equilibrium; extents of adsorption (n) here are also shown in Table 12.1. Here then it appears that overcoats raised the MO adsorption capacity of PMS by ~300x over that for P25 (4.9 $\mu$ mol/g) [395].

### 12.2.2 Photocatalytic and temperature effect

At high temperature, the samples exhibited superior photocatalytic activity due to their high crystalline form and specific surface area. Using PMS as a template and reducing agents play a significant role to form of hollow structure leading to high specific surface area and enables multiple reflections and diffractions of light. The results show increasing the photocatalytic performed due to the photocatalytic reactions which are based on chemical reactions on the surface. Figure 12.4 shows that the % photocatalytic removal from aqueous solution is higher for Au-TiO<sub>x</sub>/PMS and the Au-TiO<sub>2</sub> (PMS) replica than P25; however, the weight of catalyst used varies. Table 12.2 compares the rates of MO removal from a 0.1mM solution when one corrects per mg of catalyst as measured using MO absorbance (464nm) changes. Rates of MO removal are all greater with present biomimetic PMS-based photocatalysts. One expected to see plasmonic Ag and Au NPs in combination with semiconductors TiO<sub>2</sub>/PMS offering a new generation of the photocatalysts, but the evidence of this is presently equivocal. It may be that the chemical communication between the NPs and the TiO<sub>x</sub> is poor, or that TiO<sub>2</sub> has yet to be formed by calcination. On this point, it is clear that pre-calcination to produce TiO<sub>2</sub>

replicas gave superior photocatalytic activity. Presumably this is due to their nanocrystalline structure and their hierarchical structure left by the PMS biotemplate/reducing agent. It is possible that the product hollow structure has good specific surface area and probably facilitates multiple reflections of incident light. In addition, one sees photocatalytic activity decreasing in the order (but rate constants increasing)  $\text{Au-TiO}_2 \text{ (PMS)} > \text{Ag-TiO}_2 \text{ (PMS)} > \text{TiO}_2 \text{ (PMS)}$ . All rates are greater than commercial P25.

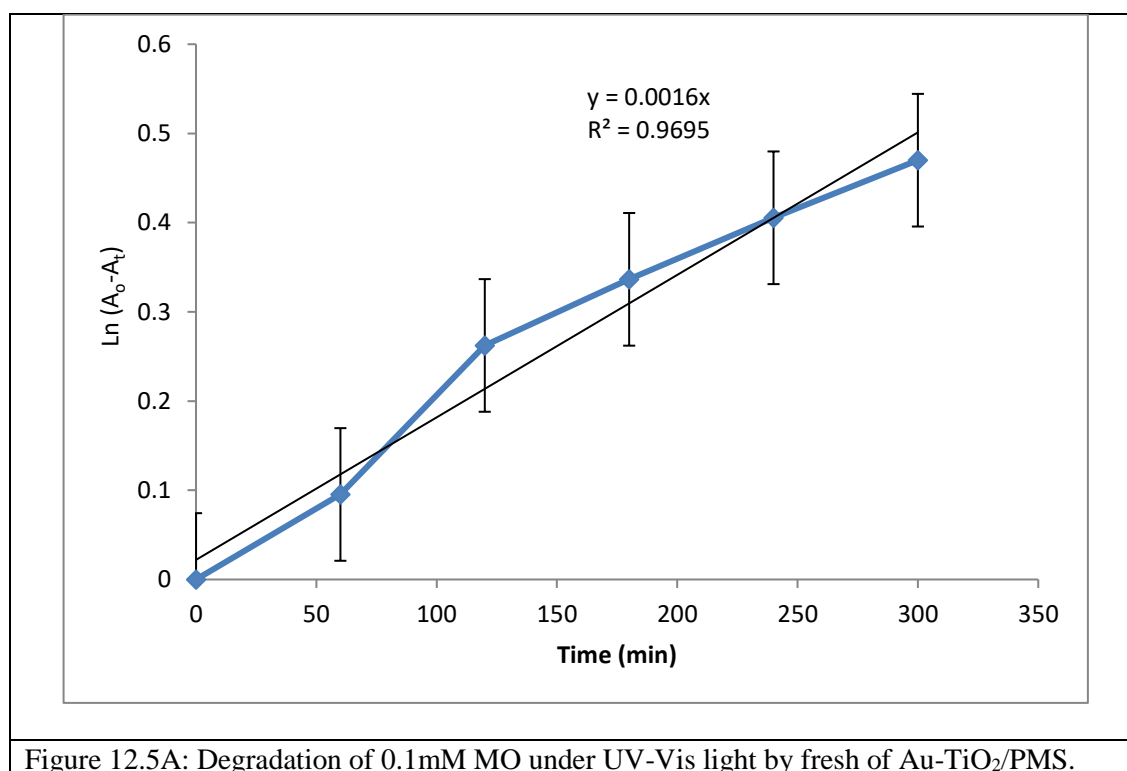


Samples that had been pre-calcined at 600°C exhibited superior photocatalytic activity due to their highly crystalline form and specific surface area. Using PMS as a template and reducing agent plays an important role in forming a hollow structure leading to a high specific surface area and enables multiple reflections and diffractions of light. The results shows that increasing the photocatalytic performance due to the photocatalytic reactions are based on chemical reaction on the surface [67].

Figure 12.5 shows that a linear transform can be used to determine if MO removal is first order,

$$t = \ln(A_0 - A_t) + y \text{ --- (12.1)}$$

where  $A_0$  is the MO absorbance at  $\lambda_{\max}$  at 0 min and  $A_t$  is the  $\lambda_{\max}$  at  $t$  min. This seems to be the case (in that when the  $\ln(A_0 - A_t)$  column is plotted against time the result is a linear plot and this indicates that it is a first-order process, and so,  $k_1$ , the first order ratio constant was being deduced) and column 3 in Table 12.2 gives first-order rate constants. However here the rate and the TOF were considered to be of more importance in the real world.





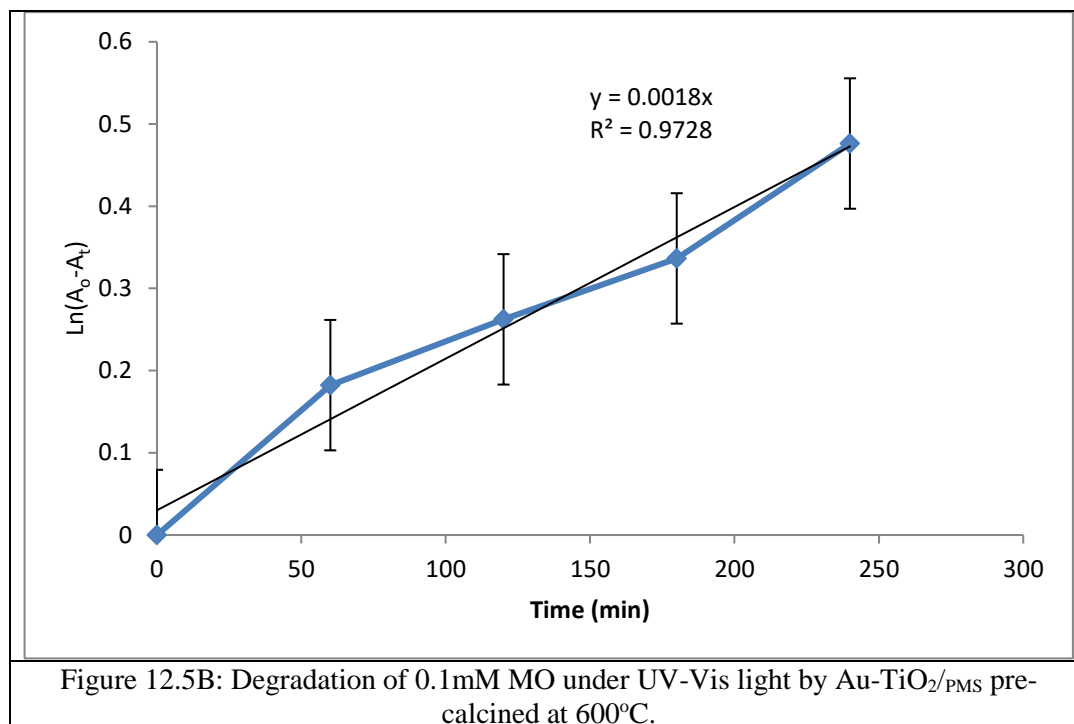


Table 12.2: Rates and first-order rate constants of MO removal from 0.1mM aqueous solutions and derived TOFs.

Sample	Molecules MO x 10 <sup>9</sup> /mg/s	k <sub>1</sub> (min <sup>-1</sup> ) x 10 <sup>3</sup>	TOF x 10 <sup>5</sup> (s <sup>-1</sup> )
P25	132	157.7	455.00
PMS	3205	92.7	
TiO <sub>x</sub> /PMS	1748	211.4	19.57
Ag-TiO <sub>x</sub> /PMS	1370	142.8	19.03
Au-TiO <sub>x</sub> /PMS	6090	51.2	63.44
TiO <sub>2</sub> (PMS)	6700	471.2	
Ag-TiO <sub>2</sub> (PMS)	13889	436.1	
Au-TiO <sub>2</sub> (PMS)	11111	355.6	

### 12.2.3 Turnover Frequency (TOF)

The % MO photocatalytic removal is higher for Au-TiO<sub>x</sub>/PMS and Au/TiO<sub>2</sub> (PMS) replicas than for P25, but then measurements are at different catalyst concentrations. Dividing the rate of photocatalytic removal of MO (molecules x 10<sup>9</sup>/mg/s) from water in Table 12.2 by the extent of MO adsorption (n) from Table 12.1 (molecules MO x 10<sup>14</sup>/mg) allowed the TOF [392] to be calculated. Clearly the TOFs in Table 12.2 column 4 are modest, but the biomimetic replicas have TOFs that decrease in the order Au-TiO<sub>2</sub> (PMS) > TiO<sub>2</sub> (PMS) > Ag-TiO<sub>2</sub> (PMS) and at their highest are just a factor of x7 lower

than for P25 anatase-rutile. Such biomimetic photocatalysts may be used to target organic water pollutants (e.g. via molecular recognition). Target pollutants include alkylphenol ethoxylates (e.g. TX100) that are endocrine disrupters in fish. In 1998, Brunel has a strong record in investigating these oestrogen-mimicking pollutants (Toxicology Letters, 102-103(1998), 337-342). It would be best if these were activated by solar radiation or sunlight, which means designing their absorption adages to higher wavelengths (by Au NPs being added to surfaces, etc.).

### 12.3 Conclusions

The surfaces of Portobello mushroom spores (PMS) have been (i) used to produce Au and Ag nanoparticles, which are held thereon and (ii) overcoated with  $\text{TiO}_x$ . These adsorbed more methyl orange (MO) pollutant from water than commercial P25.  $\text{TiO}_2$  are activated at longer wavelength. After calcination they form biomimetic  $\text{TiO}_2$  (PMS) on removal of the biotemplate; they catalysed faster rates of MO from water (molecules/mg/s) than P25 anatase-rutile. Other biotemplates are now anticipated that will yield biomimetic photocatalysts with higher turnover number  $\text{s}^{-1}$  removal of endocrine disrupters from water.

## **Chapter 13: Discussion on importance and novelty of research and future work**

---

In this chapter, a brief explanation of the aims and the novelty of the research achievements and outcomes are presented. Finally, future work is proposed.

### **13.1 The aims**

Section 1.8 indicated that the aims of the present research were to use PMS:

- (i) surfaces to synthesise Ag, Au,  $\text{TiO}_x$  NPs to form NPs/PMS nanohybrids with antimicrobial properties.
- (ii) as a biotemplate for  $\text{TiO}_{x(\text{PMS})}$  biomimetic photocatalysts for control of water pollution by organic and coloured pollutants.
- (iii) interiors/exterior to incorporate  $\text{Ca}^{2+}$ ,  $\text{CO}_3^{2-}$  and  $\text{HPO}_4^{2-}$  sequentially for formation of nHAp/PMS and
- (iv) interiors and exterior to incorporate model therapeutic drugs (i.e. AA, Hb and insulin).

### **13.2 Extent of Achieving the above Goals**

The author believes that these goals were broadly achieved. For example:

- (i) NPs (Ag, Au and  $\text{TiO}_x$ ) were synthesised on PMS surfaces to produce NPs/PMS that exhibited antimicrobial properties (which are nevertheless non-toxic to mammalian cells [398]).
- (ii)  $\text{TiO}_x$  produced on the PMS biotemplate surface was an effective biomimetic photocatalysts for removal of organic and coloured pollutants. These photocatalyst exhibited good and effective photodegradation of methyl orange.
- (iii) HAp was produced sequentially on PMS, which can be thought of as a smart scaffold to build bone, engineered tissue and nanocarriers; this may be useful in

regenerative medicine. At the same time the author was able to mimic bone mineralization behaviour, altering scaffold and nano collagen.

- (iv) AA, Hb and insulin were loaded onto and released by PMS as an oral or transdermal drug delivery system. This is a novel system that can be used to solve many medical problems (e.g. diabetes). The nHAp/PMS and nHAp/PMS-loaded /PVA hydrogel film may be used to regenerate bone or deliver any drug in a painless and harmless manner.

### **13.2.1 Achievements and novelty**

The present work has shown that PMS can be used in many different medical fields: it can be used with NPs/PMS as antibacterial and fungal agents due to the increase in the resistance of bacteria and fungi to antibiotic these days. The novelty of PMS as a template and reducing agents to synthesise NPs is because:

- 1- PMS has a novel shape that looks like red blood cell; this character makes it more compatible and convenient to use in human body.
- 2- PMS has a unique size (about 6  $\mu\text{m}$ ) and surface chemistry that makes it excellent to act as a nanocarrier. PMS provided more reactive sites/surface functionality/chemical functions (-OH, -COO, -NH and -SH) on the PMS wall cell surface. These functional groups act as reducing, capping and stabilizing agents to produce  $\text{TiO}_x$ , Ag and Au NPs comparable with most plant sources.
- 3- PMS is thermally stable until 200°C and it does not degrade in different physiological solutions.

Many studies have shown a method for encapsulation of iron NPs ( 8.56 mM) into red blood cells using a real-time imaging technique [399].

Further, the use of PMS as a drug delivery system is new, with no previous study in this field. It is a green method, eco-friendly, easy and simple. The drug release will inevitably vary depending on the pH etc. Here, the novelty of PMS is seen as:

- 1- a red blood cell-like appearance which is used to carry tethered drugs [400], desiccation resistance, thermal stability and protein activity on the cell wall of PMS; all these make PMS suitable to be a drug delivery system.
- 2- uniquely advantageous surfaces with multi-functional groups around a hollow space giving good loading properties as a drug delivery system. Moreover, it is already an

acceptable food that means it is suitable for drug loading, since it has no solubility or stability problems in gastric fluids. PMS/drug delivery/release was fast compared with a nanogel microsphere over several days.

- 3- a micro-size that delivers drugs into cells by a non-endocytosis mechanism [401].
- 4- an oval, natural and uniform shape with interacting cell wall/surface chemical properties.
- 5- hydrophilic (polar) groups  $n\text{Ca}^{+2}$  and  $\text{HPO}_4^{2-}$  accepting which can provide suitable sites in which HAp can nucleate and then grow, XRD showed low crystallinity compared with commercial HAp (Bio-Oss). This advantage brings  $n\text{Ca}^{2+}$  into nanomedicine [402] and nHAP/PMS more compatible as source artificial bone after PMS removal.

It has been reported that nHAp-coated hydroxyethyl cellulose/PVA can be prepared as nano-fibrous scaffolds for medical applications ( e.g. as bone tissue engineering [401]). The importance of PMS is that the natural hydroxyl and carboxyl groups (available without chemical usage) on their cell wall surface act as nucleation sites able to direct the orientation of growth of nHAp the surface. *In vitro*, bioactivity showed rapid formation of bone-like HAp on the nHAp/PMS surface (that acts as a chelating reagent to accelerate the mineralization process). The apatite layer increased in extent with time in simulated body fluid (SBF). PMS must, it is assumed, have many functional groups which are necessary for the formation of chemical bonds adsorptive and electrostatic interactions with reagent species. Green synthesise of Ag NPs/PMS was shown to inhibit the growth of bacteria and fungi (but not Au NPs/PMS due to strong bonding with PMS cell wall surface). Ag NPs/PMS and nanohybrid  $\text{TiO}_x/\text{PMS}$ , Ag- $\text{TiO}_x/\text{PMS}$  appear to have excellent anti-bacterial activity against both *E.coli* and *S.aureus* due to the generation of ROS (following the administration of NPs). Ag NPs/PMS have anti-bacterial activity in lower concentration than other NPs. The high activity of silver NPs is attributed to different species dissolving and releasing  $\text{Ag}^0$  and  $\text{Ag}^+$  clusters. The rate of photodegradation of methyl orange (MO) pollutant by  $\text{TiO}_2$  replicas ( $\text{TiO}_2$  (PMS), Ag- $\text{TiO}_2$  (PMS) and Au- $\text{TiO}_2$  (PMS)) was studied. The best rate of MO removal from water (in molecules/mg/s) was seen for Au- $\text{TiO}_2$  PMS rather than P25 anatase-rutile. These results were due to novel product hollow structure of PMS (size and shape), volume ratio to specific surface area for NPs and probably facilitates multiple reflections of incident light.

### 13.3 Future work

There are topics on the horizon that the author/supervisor have outlined in day-to-day research discussions but were not in the end attempted in the time available. PMS could be the starting point of an artificial blood, but research never ends and it is hoped that this will be explored in future collaborative work:

- (i) Hb/PMS could be a novel artificial red blood cell (RBC). Artificial RBCs is one-fiftieth the size of a normal RBCs that is made from purified human hemoglobin. This protein was coated with a synthetic polymer. Recent studies point to design and synthesis RBC: “according to a presentation at the annual meeting of the American Society of Hematology, an artificial red blood cell has been created that can effectively pick up oxygen in the lungs and deliver it to tissues throughout the body” [403], by synthesis nanoliposomes [404], spherical colloidal particle using emulsion polymerization [398] and polystyrene [405]. PMS looks like RBC, is a natural microstructure of the same size and shape, and it has the same internal capacity. All these, could lead to a synthetic RBC in which PMS is loaded with Hb to produce a great artificial RBC. Artificial RBC might be exciting artificial oxygen carriers [406, 407].
- (ii) Au NP hydrogels have been prepared as switchable on/off drug delivery systems [408]. NPs/PMS can be developed to swell, sensitively with optical and thermal switching properties in SIF and SGF.
- (iii) cell surface chemistry or display systems are used to express a protein or peptide on the cellular surface of bacteria, yeast, insect and mammalian cells. These systems have been used because they are simple in operation and easy to analyse. They are free, accessible and stable for binding to the target. These systems might be new biotechnologies that make them a suitable cell factory for producing cellulosic ethanol. There are many different biotechnical and biomedical applications, proving their effectiveness in protein engineering studies, such as vaccine development, bio-absorbents, biocatalysts and biosensors [409].

Using yeast cell surface chemistry was reported using fluorescent labelling technique [410], moreover, a recent study shows that the yeast cell surface can be used as a cell factory to produce fuels and chemicals, because biofuel is an alternative energy to reduce carbon emissions in the world [411]. Similarly, PMS already has proteins and phospholipids in their surface that can lead to selective enzymic activity.

### **13.4 Errors, uncertainties and Novel Analytical Approaches**

The largest errors in the present work were in uptake and release study of PMS samples ( $\text{Ca}^{2+}$ ,  $\text{PO}_4^{3-}$ , AA, Hb and insulin). For example, Figure 9.19 says  $k_H$  for PMS/PVA is 7.02 but at  $1\text{-}2\text{h}^{0.5}$  the gradient corresponds to 4.00 and at  $2\text{-}3\text{h}^{0.5}$  corresponds to 13.88. Hence  $k_H$  is  $9\pm 5$ . These uncertainties could have been minimised with more duplicate experiments, but there were difficulties with PMS harvesting. Many techniques could have been used but were not available in the timescale of the project. Extended x-Ray Absorption Fine Structure (EXAFS) and X-Ray Photoelectron Spectroscopy (XPS) could have revealed the structure around metal centres and chiral AA could have been used.

In another PhD it is hope that such ideas will be pursued.

## References

---

- [1] J. M. Benyus, *Biomimicry Innovation Inspired by Nature*. Harper Perennia, 1997.
- [2] J. M. Benyus, *Biomimicry: Innovation Inspired by Nature*. William Morrow Paperbacks, 2002.
- [3] J. F. V. Vincent, “Biomimetics - A review,” *Proc. Inst. Mech. Eng. Part H J. Eng. Med.*, vol. 223, pp. 919–939, 2009.
- [4] J. F. V. Vincent, O. A. Bogatyreva, N. R. Bogatyrev, A. Bowyer, and A.-K. Pahl, “Biomimetics: its practice and theory,” *J. R. Soc. Interface*, vol. 3, pp. 471–482, 2006.
- [5] B. Bhushan, *Handbook of Nanotechnology*. Springer-Verlag Berlin Heidelberg, Germany, 2004.
- [6] M. T. Klem, M. Young and T. Douglas, “Biomimetic synthesis of  $\beta$ -TiO<sub>2</sub> inside a viral capsid,” *J. Mater. Chem.*, vol. 18, pp. 3821–3823, 2008.
- [7] H. Cölfen and S. Mann, “Higher-order organization by mesoscale self-assembly and transformation of hybrid nanostructures,” *Angew. Chemie. Internat. Edn.*, vol. 42, pp. 2350–2365, 2003.
- [8] G. D. Bixler and B. Bhushan, “Rice- and butterfly-wing effect inspired self-cleaning and low drag micro/nanopatterned surfaces in water, oil and air flow,” *Nanoscale*, vol. 6, pp. 76–96, 2014.
- [9] K. E. Drexler, “Molecular engineering: An approach to the development of general capabilities for molecular manipulation,” *Proc. Natl. Acad. Sci.*, vol. 78, pp. 5275–5278, 1981.
- [10] J. Schulte, *Nanotechnology: Global Strategies, Industry Trends and Applications*. John Wiley & Sons, Limited, 2005.



- [11] K. Subramani and W. Ahmed, *Emerging nanotechnologies in dentistry*. MPS, 2017.
- [12] L. Cheng, *Progress in Microscale and Nanoscale, thermal and Fluid Sciences*. Nova Science, Inc. New York, 2015.
- [13] “Nanoscience and nanotechnologies : opportunities and uncertainties,” *Royal Society/Royal Society of Engineering*, vol. 46, 2004.
- [14] F. Patolsky, G. Zheng and C. M. Lieber, “Nanowire sensors for medicine and the life sciences,” *Nanomedicine*, vol. 1, pp. 51–65, 2006.
- [15] R. Nair, S. H. Varghese, B. G. Nair, T. Maekawa, Y. Yoshida and D. S. Kumar, “Nanoparticulate material delivery to plants,” *J. Plant Sci.*, vol. 179, pp. 154–163, 2010.
- [16] G. Timp, *Nanotechnology*. Springer-Verlag New York, 1999.
- [17] F. Vert, M. Doi, Y. Hellwich, K. Hess, M. Hodge, P. Kubisa, P. Rinaudo and M. Schue, “Terminology for biorelated polymers and applications (IUPAC Recommendations 2012),” *Pure Appl. Chem.*, vol. 84, pp. 377–410, 2012.
- [18] C. P. Poole and F. J. Owens, *Introduction to nanotechnology*. John Wiley & Sons, Inc, Canda, 2003.
- [19] M. A. Shah and T. Ahmad, *Principles of nanoscience and nanotechnology*. Alpha Science International, 2010.
- [20] F. Derek, J. V. Jennifer, M. Shah, B. S. Shashi and E. J. P. G errard, “A Review of current research into the biogenic synthesis of metal and metal oxide nanoparticles via marine algae and seagrasses,” *J. Nanosci.*, vol.1, p. 15, 2017.
- [21] S. Sinha, I. Pan, P. Chanda and S. K. Sen, “Nanoparticles fabrication using ambient biological resources,” *J Appl Biosci*, vol. 19, pp. 1113–1130, 2009.
- [22] N. H. Malsch, *Biomedical nanotechnology*. Taylor and Francis Group, LLC, 2005.
- [23] M. Bilal, T. Rasheed, H. M. N. Iqbal, H. Hu and X. Zhang, “Silver nanoparticles:

- Biosynthesis and antimicrobial potentialities,” *Int. J. Pharmacol.*, vol. 13, pp. 832–845, 2017.
- [24] I. K. Sen, K. Maity and S. S. Islam, “Green synthesis of gold nanoparticles using a glucan of an edible mushroom and study of catalytic activity,” *Carbohydr. Polym.*, vol. 91, pp. 518–528, 2013.
- [25] M. Ovais *et al.*, “Current state and prospects of the phytosynthesized colloidal gold nanoparticles and their applications in cancer theranostics,” *Appl. Microbiol. Biotechnol.*, vol. 101, pp. 3551–3565, 2017.
- [26] Y. Tauran, A. Brioude, A. W. Coleman, M. Rhimi and B. Kim, “Molecular recognition by gold, silver and copper nanoparticles,” *World J. Biol. Chem.*, vol. 4, pp. 35–64, 2013.
- [27] K. Kerstin, B. Bharat and B. Wilhelm, “Multifunctional Plant Surfaces and Smart Materials,” Springer, Berlin, Heidelberg, 2010, pp. 1399–1436.
- [28] R. W. Kelsall, I. W. Hamley and M. Geoghegan, *Nanoscale Science and technology*. John Wiley & Sons, Ltd, England, 2005.
- [29] M. Wilson, K. Kannangara, G. Smith, M. Simmons and B. Raguse, *Nanotechnology basic science and emerging technologies*. University of New South Wales Press Ltd. Australia, 2002.
- [30] Z. Sadowski, *Biosynthesis and Application of silver and Gold Nanoparticles, Silver Nanoparticles*. INTECH, 2010.
- [31] R. Sanghi and P. Verma, “Biomimetic synthesis and characterisation of protein capped silver nanoparticles,” *Bioresour. Technol.*, vol. 100, pp. 501–504, 2009.
- [32] B. Sharma and M. K. Rabinal, “Biologically active l-cysteine as a reducing/capping agent for controlled tuning of gold nanoparticles,” *J. Alloys Compd.*, vol. 649, pp. 11–18, 2015.
- [33] F. Dumur, A. Guerlin, E. Dumas, D. Bertin, D. Gimes and C. R. Mayer,

- “Controlled spontaneous generation of gold nanoparticles assisted by dual reducing and capping agents,” *J. Gold Bull.*, vol. 44, pp. 119–137, 2011.
- [34] N. N. Greenwood, A. Earnshaw, *Chemistry of the Elements*. Elsevier Ltd, 2003.
- [35] D. V Sotnikov, A. V Zherdev and B. B. Dzantiev, “Detection of intermolecular interactions based on surface plasmon resonance registration,” *Biochemistry-Moscow*, vol. 80, pp. 1820–1832, 2015.
- [36] Q. H. Tran, V. Q. Nguyen and A.T. Le, “Silver nanoparticles: synthesis, properties, toxicology, applications and perspectives,” *Adv. Nat. Sci. Nanosci. Nanotechnol.*, vol. 4, p. 033001, 2013.
- [37] A. E. Danks, S. R. Hall and Z. Schnepf, “The evolution of ‘sol–gel’ chemistry as a technique for materials synthesis,” *Mater. Horiz.*, vol. 3, pp. 91–112, 2016.
- [38] M. Bilal, T. Rasheed, H. M. N. Iqbal, H. Hu, W. Wang and X. Zhang, “Macromolecular agents with antimicrobial potentialities: A drive to combat antimicrobial resistance,” *Int. J. Biol. Macromol.*, vol. 103, pp. 554–574, 2017.
- [39] G. Cheng, M. Dai, S. Ahmed, H. Hao, X. Wang and Z. Yuan, “Antimicrobial drugs in fighting against antimicrobial resistance,” *Front. Microbiol.*, vol. 7, pp. 1–11, 2016.
- [40] J. Srivastava, H. Chandra, A. R. Nautiyal and S. J. S. Kalra, “Antimicrobial resistance (AMR) and plant-derived antimicrobials (PDAMs) as an alternative drug line to control infections,” *Biotech*, vol. 4, pp. 451–460, 2014.
- [41] D. Sarvamangala, K. Kondala, N. Sivakumar, M. S. Babu and S. Manga, “Synthesis, characterization and antimicrobial studies of AgNP’S using probiotics,” *Int. Res. J. Pharm.*, vol. 4, pp. 240–243, 2013.
- [42] K. Bankura *et al.*, “Antibacterial activity of Ag-Au alloy NPs and chemical sensor property of Au NPs synthesized by dextran,” *Carbohydr. Polym.*, vol. 107, no. 1, pp. 151–157, 2014.

- [43] F. Regan, J. Chapman and T. Sullivan, *Nanoparticles in Anti-Microbial Materials: Use and Characterisation*. RSC, 2012.
- [44] N. S. Shaligram *et al.*, “Biosynthesis of silver nanoparticles using aqueous extract from the compactin producing fungal strain,” *J. Process Biochem.*, vol. 44, pp. 939–943, 2009.
- [45] Y. Zhou, Y. Kong, S. Kundu, J. D. Cirillo and H. Liang, “Antibacterial activities of gold and silver nanoparticles against *Escherichia coli* and *bacillus Calmette-Guérin.*,” *J. Nanobiotechnology*, vol. 10, p. 19, 2012.
- [46] C. S. Yah and G. S. Simate, “Nanoparticles as potential new generation broad spectrum antimicrobial agents,” *J. Fac. Pharmacy, Tehran Univ. Med. Sci.*, vol. 23, p. 43, 2015.
- [47] M.C. Daniel and D. Astruc, “Gold nanoparticles: assembly, supramolecular chemistry, quantum-size-related properties, and applications toward biology, catalysis, and nanotechnology,” *J. Chemical Rev.*, vol. 104, pp. 293–346, 2004.
- [48] M. Guzman, J. Dille and S. Godet, “Synthesis and antibacterial activity of silver nanoparticles against gram-positive and gram-negative bacteria,” *J. Nanomedicine Nanotechnology, Biol. Med.*, vol. 8, pp. 37–45, 2012.
- [49] D. M. Whitacre, *Reviews of environmental contamination and toxicology*. Springer, 2015.
- [50] M. J. Sweet and I. Singleton, *Silver Nanoparticles: A Microbial Perspective*. Elsevier Inc, 2013.
- [51] S. F. Chen *et al.*, “Large scale photochemical synthesis of M@TiO<sub>2</sub> nanocomposites (M = Ag, Pd, Au, Pt) and their optical properties, CO oxidation performance, and antibacterial effect,” *Nano Res.*, pp. 1–12, 2010.
- [52] V. K. Sharma, R. A. Yngard and Y. Lin, “Silver nanoparticles: Green synthesis and their antimicrobial activities,” *J. Adv. Colloid Interface Sci.*, vol. 145, pp. 83–96, 2009.

- [53] M. J. Hajipour *et al.*, “Antibacterial properties of nanoparticles.,” *Trends Biotechnol.*, vol. 30, pp. 499–511, Oct. 2012.
- [54] K. El-Said, E. Ali, K. Kanehira, and A. Taniguchi, “Molecular mechanism of DNA damage induced by titanium dioxide nanoparticles in toll-like receptor 3 or 4 expressing human hepatocarcinoma cell lines,” *J. Nanobiotechnology*, vol. 12, p. 10, 2014.
- [55] P. V Asharani, G. Low, K. Mun, M. P. Hande and S. Valiyaveetil, “Cytotoxicity and genotoxicity of silver nanopatticles in human cell,” *ACS Nano*, vol. 3, pp. 279–290, 2009.
- [56] A. Ibhadon and P. Fitzpatrick, “Heterogeneous photocatalysis: Recent advances and applications,” *J. Catal.*, vol. 3, pp. 189–218, 2013.
- [57] X. H. Yang, H. T. Fu, K. Wong, X. C. Jiang and A. B. Yu, “Hybrid Ag@TiO<sub>2</sub> core-shell nanostructures with highly enhanced photocatalytic performance,” *J. Nanotechnol.*, vol. 24, p. 10, 2013.
- [58] D. P. Macwan and S. Dave and P. N. Chaturvedi, “A review on nano-TiO<sub>2</sub> sol–gel type syntheses and its applications,” *J. Mater. Sci.*, vol. 46, pp. 3669–3686, 2011.
- [59] J. Schneider *et al.*, “Understanding TiO<sub>2</sub> photocatalysis : Mechanisms and materials,” *J. Chem. Rev*, vol. 114, p. 9919–9986, 2014.
- [60] P. Pattanaik and M. K. Sahoo, “TiO<sub>2</sub> photocatalysis : progress from fundamentals to modification technology,” *Desalin. Water Treat.*, vol. 52, pp. 6567–6590, 2014.
- [61] “<https://nirajchawake.wordpress.com/2014/10/20/semiconductors-why-%E2%88%86e%E2%89%A43-2-ev/>,” 2018. .
- [62] M. Grundmann, *The Physics of Semiconductors: An Introduction Including Nanophysics and Applications*. Springer, 2006.
- [63] J. Mirzaei, M. Reznikov and T. Hegmann, “Quantum dots as liquid crystal dopants,” *J. Mater. Chem.*, vol. 22, p. 22350, 2012.

- [64] S. Mathew, "UV-Visible photoluminescence of TiO<sub>2</sub> nanoparticles prepared by hydrothermal," *J. Fluoresc.*, vol. 22, pp. 1563–1569, 2012.
- [65] S. Ghosh and A. P. Das, "Modified titanium oxide ( TiO<sub>2</sub> ) nanocomposites and its array of applications : a review," *Toxicol. Environ. Chem.*, vol. 97, pp. 491–514, 2015.
- [66] K. Sohlberg, X. Nie, S. Zhuo and G. Maeng, "Doping of TiO<sub>2</sub> polymorphs for altered optical and photocatalytic properties," *Int. J. Photoenergy*, vol. 2009, p. 22, 2009.
- [67] K. Nakata and A. Fujishima, "Reviews TiO<sub>2</sub> photocatalysis : Design and applications," *J. Photochem. Photobiol. C Photochem.*, vol. 13, pp. 169–189, 2012.
- [68] X. H. Yang, H. Fu, X. K. Wong, C. Jiang and B. Yu, A., "Hybrid Ag@TiO<sub>2</sub> core–shell nanostructures with highly enhanced photocatalytic performance," *J. Nanotechnol.*, vol. 24, p. 415601 (10pp), 2013.
- [69] C. Cai, M. Xu, S. Bao, C.-C. Ji, Z.J. Lu and D.Z. Jia, "A green and facile route for constructing flower-shaped TiO<sub>2</sub> nanocrystals assembled on graphene oxide sheets for enhanced photocatalytic activity," *J. Nanotechnology*, vol. 24, p. 275602, 2013.
- [70] G. J. Nohynek and M. S. Roberts, "Grey Goo on the Skin ? Nanotechnology , Cosmetic and Sunscreen Safety J urgen," *Inf. Healthc.*, pp. 251–277, 2007.
- [71] K. Zhang, C. Liu, F. Huang, C. Zheng and W. Wang, "Study of the electronic structure and photocatalytic activity of the BiOCl photocatalyst," *J. Appl. Catal. B Environ.*, vol. 68, pp. 125–129, 2006.
- [72] A. Becheri, M. Durr, P. Lo Nostro and P. Baglioni, "Synthesis and characterization of zinc oxide nanoparticles: application to textiles as UV-absorbers," *Journal of Nanoparticle Research*, vol. 10, pp. 679–689, 2008.
- [73] E. Yasun *et al.*, "Cancer cell sensing and therapy using affinity tag-conjugated gold nanorods.," *J. Interface Focus*, vol. 3, p. 20130006, 2013.

- [74] L. M. Liz-marza, “Tailoring Surface Plasmons through the Morphology and Assembly of Metal Nanoparticles Luis,” *Invit. Featur. Artic.*, vol. 22, pp. 32–41, 2006.
- [75] T. Tong, J. Zhang, B. Tian, F. Chen, and D. He, “Preparation of Fe<sup>3+</sup>-doped TiO<sub>2</sub> catalysts by controlled hydrolysis of titanium alkoxide and study on their photocatalytic activity for methyl orange degradation,” *J. Hazard. Mater.*, vol. 155, pp. 572–579, 2008.
- [76] G. P. Bhat, R. Sharanabasava, V.G. Deshpande , R. Shetti , U. Sanjeev and A. Venkataraman, “Photo-bio-synthesis of irregular shaped functionalized gold nanoparticles using edible mushroom *Pleurotus florida* and its anticancer evaluation,” *J.Photochemistry Photobiol. B Biol.*, vol. 125, pp. 63–69, 2013.
- [77] S.J. Bao, “Environment-friendly biomimetic synthesis of TiO<sub>2</sub> nanomaterials for photocatalytic application,” *Nanotechnology*, vol. 23, p. 205601, 2012.
- [78] Z. Liu, X. Xu and R. Tang, “Improvement of biological organisms using functional material shells,” *J. Adv. Funct. Mater.*, vol. 26, pp. 1862–1880, 2016.
- [79] M. Qiao, G. G. Ying, A. C. Singer and Y. G. Zhu, “Review of antibiotic resistance in China and its environment,” *Environ. Int.*, vol. 110, pp. 160–172, 2018.
- [80] P. Rattanaumpawan, A. Boonyasiri, S. Vong and V. Thamlikitkul, “Systematic review of electronic surveillance of infectious diseases with emphasis on antimicrobial resistance surveillance in resource-limited settings,” *Am. J. Infect. Control*, vol. 46, pp. 139–146, 2018.
- [81] P. L. Keen and M. H. M. M. Montforts, “Antimicrobial Resistance in the Environment,” *Antimicrob. Resist. Environ.*, vol. 88, pp. 1951–1967, 2011.
- [82] G. C. Bond, *Metal-Catalysed Reactions of Hydrocarbons*. Springer Science & Business Media, 2006.
- [83] K.-S. Ko, D.-C. Koh and I. Kong, “Toxicity evaluation of individual and mixtures of nanoparticles based on algal chlorophyll content and cell Count,” *Materials (Basel)*.,

vol. 11, p. 121, 2018.

- [84] G. C. Bond, “The origins of particle size effects in heterogeneous catalysis,” *Surf. Sci.*, vol. 156, pp. 966–981, 1985.
- [85] Y. Yamagishi *et al.*, “Acute and chronic nephrotoxicity of platinum nanoparticles in mice,” *Nanoscale Res. Lett.*, vol. 8, pp. 1–7, 2013.
- [86] D. S. Tsai, T. Sen Yang, Y. S. Huang, P. W. Peng and K. L. Ou, “Disinfection effects of undoped and silver-doped ceria powders of nanometer crystallite size,” *Int. J. Nanomedicine*, vol. 11, pp. 2531–2542, 2016.
- [87] V. V. Makarov *et al.*, “Green nanotechnologies: Synthesis of metal nanoparticles using plants,” *Acta Naturae*, vol. 6, pp. 35–44, 2014.
- [88] S. Y. Ramy and F. A. Osama, “*In vitro* study of the antifungal efficacy of zinc oxide nanoparticles against *Fusarium oxysporum* and *Penicillium expansum*,” *African J. Microbiol. Res.*, vol. 7, pp. 1917–1923, 2013.
- [89] E. C. Sekhar, K. S. V. K. Rao, K. M. S. Rao and S. B. Alisha, “A simple biosynthesis of silver nanoparticles from *Syzygium cumini* stem bark aqueous extract and their spectrochemical and antimicrobial studies,” *J. Appl. Pharm. Sci.*, vol. 8, pp. 073–079, 2018.
- [90] P. Tippayawat, N. Phromviyo, P. Boueroy and A. Chompoosor, “Green synthesis of silver nanoparticles in aloe vera plant extract prepared by a hydrothermal method and their synergistic antibacterial activity,” *Peer J*, vol. 4, p. e2589, 2016.
- [91] T. Kalaiyaran, V. K. Bharti and O. P. Chaurasia, “One pot green preparation of Seabuckthorn silver nanoparticles (SBT@AgNPs) featuring high stability and longevity, antibacterial, antioxidant potential: a nano disinfectant future perspective,” *RSC Adv.*, vol. 7, pp. 51130–51141, 2017.
- [92] R. Kumar, G. Ghoshal, A. Jain and M. Goyal, “Rapid Green Synthesis of Silver Nanoparticles (AgNPs) Using (*Prunus persica*) Plants extract: Exploring its Antimicrobial and Catalytic Activities,” *J. Nanomed. Nanotechnol.*, no. 04, 2017.



- [93] M. Ndikau, N. M. Noah, D. M. Andala and E. Masika, "Green Synthesis and Characterization of Silver Nanoparticles Using Citrullus lanatus Fruit Rind Extract," *Inter. J. Anal. Chem.*, vol. 2017, 2017.
- [94] G. Bagherzade, M. M. Tavakoli and M. H. Namaei, "Green synthesis of silver nanoparticles using aqueous extract of saffron (*Crocus sativus* L.) wastages and its antibacterial activity against six bacteria," *Asian Pac. J. Trop. Biomed.*, vol. 7, pp. 227–233, 2017.
- [95] B. Rao and R.C. Tang, "Green synthesis of silver nanoparticles with antibacterial activities using aqueous *Eriobotrya japonica* leaf extract," *Adv. Nat. Sci. Nanosci. Nanotechnol.*, vol. 8, p. 015014, 2017.
- [96] S. G. Balwe, V. V. Shinde, A. A. Rokade, S. S. Park and Y. T. Jeong, "Green synthesis and characterization of silver nanoparticles (Ag NPs) from extract of plant *Radix Puerariae*: An efficient and recyclable catalyst for the construction of pyrimido[1,2-b]indazole derivatives under solvent-free conditions," *Catal. Commun.*, vol. 99, pp. 121–126, 2017.
- [97] J. R. Peralta-Videa *et al.*, "Plant-based green synthesis of metallic nanoparticles: scientific curiosity or a realistic alternative to chemical synthesis?," *J. Nanotechnol. Environ. Eng.*, vol. 1, p. 4, 2016.
- [98] R. Emmanuel, C. Karuppiah, S. M. Chen, S. Palanisamy, S. Padmavathy and P. Prakash, "Green synthesis of gold nanoparticles for trace level detection of a hazardous pollutant (nitrobenzene) causing Methemoglobinaemia," *J. Hazard. Mater.*, vol. 279, pp. 117–124, 2014.
- [99] H. Yen, S. Hsu and C. Tsai, "Cytotoxicity and immunological response of gold and silver nanoparticles of different sizes," *J. Cytotox. Immunol. Response Nanoparticles*, vol. 5, pp. 1553–1561, 2009.
- [100] I. A. Jaffer Al-Timimi, P. A. Sermon, A. A. Burghal, A. A. Salih and I. M. N. Alrubaya, "Nanoengineering the antibacterial activity of biosynthesized nanoparticles of TiO<sub>2</sub>, Ag, and Au and their nanohybrids with Portobello mushroom

spore (PMS) (TiO<sub>x</sub>/PMS, Ag/PMS and Au/PMS) and making them optically self-indicating,” *SPIE*, vol. 9930, p. 99300B, 2016.

- [101] Sk. Srivastava, R. Yamada, C. Ogino and A. Kondo, “Biogenic synthesis and characterization of gold nanoparticles by *Escherichia coli* K12 and its heterogeneous catalysis in degradation of 4-nitrophenol,” *Nano Res. Lett.*, vol. 8, pp. 1–9, 2013.
- [102] L. M. Rösken *et al.*, “Time-dependent growth of crystalline Au<sup>0</sup>-nanoparticles in cyanobacteria as self-reproducing bioreactors: *Anabaena* sp.,” *J. Nanoparticle Res.*, vol. 16, p. 14, 2014.
- [103] M. Pattanayak, T. Muralikrishnan and P. L. Nayak, “Green synthesis of gold nanoparticles using *elettaria cardamomum* ( ELAICHI ) aqueous extract,” *World J. Nano Sci. Technol.*, vol. 2, no. 2, pp. 52–58, 2013.
- [104] S. Pandey, G. K. Goswami and K. Nanda, “Green synthesis of polysaccharide/gold nanoparticle nanocomposite: An efficient ammonia sensor,” *J. Carbohydrate Polym.*, vol. 94, pp. 229–234, 2013.
- [105] N. Roy, S. Mondal, R. A. Laskar, S. Basu, D. Mandal and N. A. Begum, “Biogenic synthesis of Au and Ag nanoparticles by Indian propolis and its constituents,” *Colloids Surfaces B Biointerfaces*, vol. 76, pp. 317–325, 2010.
- [106] M. Gajendiran, P. Balashanmugam, P. T. Kalaichelvan and S. Balasubramanian, “Multi-drug delivery of tuberculosis drugs by back bonded gold nanoparticles with multiblock copolyesters,” *J. Materials Res. Express*, vol. 3, p. 6, 2016.
- [107] O. Akhavan, R. Azimirad, S. Safa and M. M. Larijani, “Visible light photo-induced antibacterial activity of CNT-doped TiO<sub>2</sub> thin films with various CNT contents,” *J. Mater. Chem.*, vol. 20, pp. 7386–7392, 2010.
- [108] I. A. Jaffer Al-Timimi, U. K. Onwukwe, M. P. Worsley and P. A. Sermon, “Biomimetic TiO<sub>2</sub> formation from interfacial sol-gel chemistry leading to new photocatalysts,” *SPIE*, vol. 9928, p. 99280E, 2016.
- [109] S. Ramesh, A. N. Natasha, C. Y. Tan, L. T. Bang, S. Ramesh and C. Y. Ching,

“Direct conversion of eggshell to hydroxyapatite ceramic by a sintering method,”  
*J.Ceramics Int.*, vol. 42, pp. 7824–7829, 2016.

- [110] S. Liao *et al.*, “Novel synthesis strategy for composite hydrogel of collagen/hydroxyapatite- microsphere originating from conversion of CaCO<sub>3</sub> templates,” *J.Nanotechnology*, vol. 26, p. 8pp, 5015.
- [111] C. Qi, Y. Zhu, B. Lu, X. Zhao, J. Zhao and F. Chen, “Hydroxyapatite hierarchically nanostructured porous hollow microspheres : Rapid , sustainable microwave-H hydrothermal synthesis by using creatine phosphate as an organic phosphorus source and application in drug delivery and protein adsorption,” *J.Chem Pub Soc Eur.*, vol. 19, pp. 5332–5341, 2013.
- [112] R. Balasundari, D. K. Bishi, S. Mathapati, S. B. Naser, K. M. Cherian and S. Guhathakurta, “Nanocoated botanical scaffold in salvage for human tissue regeneration,” *J.Biomater. Tissue Eng.*, vol. 2, pp. 330–335, 2012.
- [113] F. Nurlidar, E. Budianto and D. Darwis, “Hydroxyapatite deposition on modified bacterial cellulose matrix,” *J. Macromol. Symp.*, vol. 353, pp. 128–132, 2015.
- [114] Y. A. Elhassaneen, S. S. Ragab and M. S. Salman, “The Potential Effects of Reishi Mushroom ( *Ganoderma lucidum* ) Consumption on Bone Health Indices and Serum Minerals Profile Disorders Induced by CCl<sub>4</sub> on Rats,” *J.Med. Pla. Res.*, vol. 2, pp. 1–7, 2016.
- [115] B. Lowe, J. Venkatesan, S. Anil, M. Suk and S. Kim, “Preparation and characterization of chitosan-natural nano hydroxyapatite-fucoidan nanocomposites for bone tissue engineering,” *Int. J. Biol. Macromol.*, vol. 93, pp. 1479–1487, 2016.
- [116] I. Sargin *et al.*, “Controlled release and anti-proliferative effect of imatinib mesylate loaded sporopollenin microcapsules extracted from pollens of *Betula pendula*,” *Int. J. Biol. Macromol.*, vol. 105, pp. 749–756, 2017.
- [117] A. K. Prabhakar *et al.*, “Chemical processing strategies to obtain sporopollenin exine capsules from multi-compartmental pine pollen,” *J. Ind. Eng. Chem.*, vol. 53, pp. 375–385, 2017.

- [118] L. Yin *et al.*, “*Bacillus* spore-based oral carriers loading curcumin for the therapy of colon cancer,” *J. Control. Release*, vol. 271, pp. 31–44, 2018.
- [119] N. Sudareva *et al.*, “Two-level delivery systems for oral administration of peptides and proteins based on spore capsules of *Lycopodium clavatum*,” *J. Mater. Chem. B*, vol. 5, pp. 7711–7720, 2017.
- [120] M. G. Potroz *et al.*, “Plant-based hollow microcapsules for oral delivery applications: Toward optimized loading and controlled release,” *Adv. Funct. Mater.*, vol. 27, p. 12, 2017.
- [121] P. Veres *et al.*, “A redox strategy to tailor the release properties of Fe(III)-alginate aerogels for oral drug delivery,” *Carbohydr. Polym.*, vol. 188, pp. 159–167, 2018.
- [122] Y. Zhang, G. Jiang, W. Yu, D. Liu and B. Xu, “Microneedles fabricated from alginate and maltose for transdermal delivery of insulin on diabetic rats,” *Mater. Sci. Eng. C*, vol. 85, pp. 18–26, 2018.
- [123] D. Xia *et al.*, “Ultrafast glucose-responsive, high loading capacity erythrocyte to self-regulate the release of insulin,” *Acta Biomater.*, vol. 69, pp. 301–312, 2018.
- [124] Y. Wang *et al.*, “A Versatile method to prepare protein nanoclusters for drug delivery,” *Macromol. Biosci.*, vol. 18, p. 9, 2018.
- [125] M. Roy, R. Pal, Abhay and S. Chakraborti, “Pelargonidin-PLGA nanoparticles: Fabrication, characterization, and their effect on streptozotocin induced diabetic rats,” *Indian J. Exp. Biol.*, vol. 55, pp. 819–830, 2017.
- [126] P. Mukhopadhyay, R. Mishra, D. Rana and P. P. Kundu, “Strategies for effective oral insulin delivery with modified chitosan nanoparticles: A review,” *J. Progress Polym. Sci.*, vol. 37, pp. 1457–1475, 2012.
- [127] E. Pridgen, F. Alexis and O. Farokhzad, “Polymeric nanoparticle drug delivery technologies for oral delivery applications,” *J. Expert Opin Drug Deliv*, vol. 12, pp. 1459–1473, 2015.

- [128] E. A. Al-Tamemi, A. A. Al-Wattar, A. S. Al-Sawad, I. J. Al-Asadi and A. M. Haddad, “*In vitro* release studies of insulin in hydrogels polymers as oral drug delivery systems,” *Iraqi J. Polym.*, vol. 17, pp. 50–65, 2014.
- [129] C. Liu *et al.*, “A novel ligand conjugated nanoparticles for oral insulin delivery,” *J. Drug Deliv.*, vol. 23, pp. 2015–2025, 2016.
- [130] I. Huh, S. Kim, H. Yang, M. Jang, G. Kang and H. Jung, “Effects of two droplet-based dissolving microneedle manufacturing methods on the activity of encapsulated epidermal growth factor and ascorbic acid,” *Eur. J. Pharm. Sci.*, vol. 114, pp. 285–292, 2018.
- [131] S. Kim *et al.*, “Physicochemical study of ascorbic acid 2-glucoside loaded hyaluronic acid dissolving microneedles irradiated by electron beam and gamma ray,” *Carbohydr. Polym.*, vol. 180, pp. 297–303, 2018.
- [132] M. Chakraborty *et al.*, “To reveal the nature of interactions of human hemoglobin with gold nanoparticles having two different morphologies (sphere and star-shaped) by using various spectroscopic techniques,” *J. Photochem. Photobiol. B Biol.*, vol. 178, pp. 355–366, 2018.
- [133] M. Beg, A. Maji, A. K. Mandal, S. Das, P. K. Jha and M. Hossain, “Spectroscopic investigation on interaction of biogenic, *Croton bonplandianum* leaves extract mediated potential bactericidal silver nanoparticles with human hemoglobin and human serum albumin,” *J. Biomol. Struct. Dyn.*, vol. 36, pp. 711–723, 2018.
- [134] D. Farrar, D. J. Tuffnell and J. West, “Continuous subcutaneous insulin infusion versus multiple daily injections of insulin for pregnant women with diabetes,” in *Cochrane Database of Systematic Reviews*, The Cochrane Collaboration. Published by John Wiley & Sons, Ltd., 2007, p. 37.
- [135] A. Z. Feldman and F. M. Brown, “Management of Type 1 Diabetes in Pregnancy,” *Current Diabetes Reports*, 2016.
- [136] S. Brahim, D. Narinesingh and A. Guiseppi-Elie, “Bio-smart hydrogels: Co-joined molecular recognition and signal transduction in biosensor fabrication and drug

- delivery,” *Biosens. Bioelectron.*, vol. 17, pp. 973–981, 2002.
- [137] A. K. Bajpai and S. Bhanu, “*In vitro* release modulation of hemoglobin from a ternary polymeric delivery vehicle,” *J. Appl. Polym. Sci.*, vol. 85, pp. 104–113, 2002.
- [138] L. Yu *et al.*, “*In vitro* and *in vivo* evaluation of a once-weekly formulation of an antidiabetic peptide drug exenatide in an injectable thermogel,” *J. Pharm. Sci.*, vol. 102, pp. 4140–4149, 2013.
- [139] T. E. Lin *et al.*, “Soft electrochemical probes for mapping the distribution of biomarkers and injected nanomaterials in animal and human tissues,” *Angew. Chemie - Int. Ed.*, vol. 56, pp. 16498–16502, 2017.
- [140] V. N. Bharadwaj, D. T. Nguyen, V. D. Kodibagkar and S. E. Stabenfeldt, “Nanoparticle-Based Therapeutics for Brain Injury,” *Adv. Healthc. Mater.*, vol. 7, p. 16, 2018.
- [141] P.K. Huang *et al.*, “Encapsulation of 16-Hydroxycyclero-3,13-Dine-16,15-Olide in Mesoporous Silica Nanoparticles as a Natural Dipeptidyl Peptidase-4 Inhibitor Potentiated Hypoglycemia in Diabetic Mice,” *Nanomaterials*, vol. 7, p. 112, 2017.
- [142] P. R. Miller *et al.*, “Hollow microneedle-based sensor for multiplexed transdermal electrochemical sensing,” *J. Vis. Exp.*, vol. 3, pp. 1–6, 2012.
- [143] J. W. Lee, M. R. Han and J. H. Park, “Polymer microneedles for transdermal drug delivery,” *J. Drug Target.*, vol. 21, pp. 211–223, 2013.
- [144] S. Yang *et al.*, “Phase-transition microneedle patches for efficient and accurate transdermal delivery of insulin,” *Adv. Funct. Mater.*, vol. 25, pp. 4633–4641, 2015.
- [145] H. Choudhury, B. Gorain, R. K. Tekade, M. Pandey, S. Karmakar and T. K. Pal, “Safety against nephrotoxicity in paclitaxel treatment: Oral nanocarrier as an effective tool in preclinical evaluation with marked *in vivo* antitumor activity,” *Regul. Toxicol. Pharmacol.*, vol. 91, pp. 179–189, 2017.

- [146] M. Vinceković, S. Jurić, E. Đermić and S. Topolovec-Pintarić, “Kinetics and Mechanisms of Chemical and Biological Agents Release from Biopolymeric Microcapsules,” *J. Agric. Food Chem.*, vol. 65, pp. 9608–9617, 2017.
- [147] Y. G. Zhang, Y. J. Zhu, F. Chen and B. Q. Lu, “Dopamine-modified highly porous hydroxyapatite microtube networks with efficient near-infrared photothermal effect, enhanced protein adsorption and mineralization performance,” *Colloids Surfaces B Biointerfaces*, vol. 159, pp. 337–348, 2017.
- [148] R. Mundargi, M. Potroz, S. Park and J. Park, “*Lycopodium* spores: a naturally manufactured, superrobust biomaterial for drug delivery,” *J. Adv. Funct. Mater.*, vol. 26, pp. 487–497, 2016.
- [149] A. Diego-Taboada *et al.*, “Protein free microcapsules obtained from plant spores as a model for drug delivery: Ibuprofen encapsulation, release and taste masking,” *J. Mater. Chem. B*, vol. 1, pp. 707–713, 2013.
- [150] T. Kalaiyaran, V. K. Bharti and O. P. Chaurasia, “One pot green preparation of Seabuckthorn silver nanoparticles (SBT@AgNPs) featuring high stability and longevity, antibacterial, antioxidant potential: a nano disinfectant future perspective,” *RSC Adv.*, vol. 7, no. 81, pp. 51130–51141, 2017.
- [151] I. Fratoddi, I. Venditti, C. Cametti and M. V Russo, “Gold nanoparticles and gold nanoparticle-conjugates for delivery of therapeutic molecules. Progress and challenges,” *J. Mater. Chem.*, vol. B, pp. 4204–4220, 2014.
- [152] N. Gm and A. Jimtaisong, “Natural Products as photoprotection,” *J. Nat. Prod.*, vol. 75, pp. 311–335, 2012.
- [153] M. R. Serafini, A. G. Guimarães, J. S. Quintans, A. A. Araújo, P. S. Nunes and L. J. Quintans-Júnior, “Natural compounds for solar photoprotection: a patent review,” *Expert Opin. Ther. Pat.*, vol. 25, pp. 467–478, 2015.
- [154] Z. Chaidir, R. Zein, D. T. Sagita and E. Munaf, “Bioremoval of methyl orange dye using durian fruit (*Durio zibethinus*) Murr seeds as biosorbent,” *J. Chem. Pharm. Res.*, vol. 7, pp. 589–599, 2015.

- [155] D. Ayodhya and G. Veerabhadram, "One-pot green synthesis, characterization, photocatalytic, sensing and antimicrobial studies of *Calotropis gigantea* leaf extract capped CdS NPs," *Mater. Sci. Eng. B Solid-State Mater. Adv. Technol.*, vol. 225, pp. 33–44, 2017.
- [156] S. Mustapha, M. M. Ndamitso, U. M. Mohammed, N. O. Adeosun and M. Idris, "Study on activated from melon (*citrullus lanatus*) husk as natural adsorbent for removal of hardness in water," *Adv. Anal. Chem.*, vol. 6, pp. 1–9, 2016.
- [157] N. H. Ahmad Barudin, S. Sreekantan, M. T. Ong and C. W. Lai, "Synthesis, characterization and comparative study of nano-Ag-TiO<sub>2</sub> against Gram-positive and Gram-negative bacteria under fluorescent light," *J. Food Control*, vol. 46, pp. 480–487, 2014.
- [158] S. Muniandy, S. Tana, N. H. M. Kausb, S. Sasidharanc and H. L. Leea, "One-step green synthesis of TiO<sub>2</sub>-Ag nanocomposites and their performance towards photocatalytic activities and antimicrobial properties," *Malaysian J. Catal.*, vol. 2, pp. 28–34, 2017.
- [159] E. Haritha, S. M. Roopan, G. Madhavi, G. Elango, N. A. Al-Dhabi and M. V. Arasu, "Green chemical approach towards the synthesis of SnO<sub>2</sub>NPs in argument with photocatalytic degradation of diazo dye and its kinetic studies," *J. Photochem. Photobiol. B Biol.*, vol. 162, pp. 441–447, 2016.
- [160] L. Q. R. Zhang, Q. Qin and B. Liu, "TiO<sub>2</sub>-assisted Laser desorption/ionization mass spectrometry for rapid profiling of candidate metabolite biomarkers from antimicrobial-resistant bacteria," *J. Anal. Chem.*, vol. 60, pp. 3863–3870, 2018.
- [161] P. Echlin, *Handbook of sample preparation for scanning electron microscopy and X-ray microanalysis*. Springer, 2016.
- [162] G. Dehm, J. M. Howe and J. Zweck, "*In-situ* Electron Microscopy: Applications in Physics, Chemistry and Materials Science," John Wiley & Sons, 2012.
- [163] ETC Brunel university, "Introduction to Scanning Electron Microscopy," *IOP*. pp. 1–89, 2014.



- [164] C. G. Golding, L. L. Lamboo, D. R. Beniac and T. F. Booth, “The scanning electron microscope in microbiology and diagnosis of infectious disease,” *J. Nat. Publ. Gr.*, vol. 6, p. 8, 2016.
- [165] G. H. Michler, *Electron Microscopy of Polymers*. Springer, 2008.
- [166] N. Taniguchi, *Nanotechnology Integrated Processing systems for ultra-precision and ultra-fine products*. Oxford university Press Inc., New York, 1996.
- [167] H. Pravinbhai and M. No, “Sample preparation using carbon layer deposition for protection against beam damage Sample preparation using Carbon layer deposition for protection against beam Internship Report,” 2017.
- [168] “<http://www.ammrf.org.au/myscope.>,” 2018. .
- [169] C. Miquel Guennoc, C. Rose, F. Guinnet, I. Miquel, J. Labbé and A. Deveau, “A new method for qualitative multi-scale analysis of bacterial biofilms on filamentous fungal colonies using confocal and electron microscopy,” *J. Vis. Exp.*, vol. 119, pp. 1–9, 2017.
- [170] “<http://www.pi-usa.us/blog/electron-microscopy-nonmagnonmagnetic-vacuum-compatible-and-high-precision-drives-and-positioning-systems-for-electron-microscopesnetic-drives-stages-for-vacuum/>,” 2018. .
- [171] D. H. Anjum, “Characterization of nanomaterials with transmission electron microscopy,” *IOP Conf. Ser. Mater. Sci. Eng.*, vol. 146, p. 10, 2016.
- [172] “[https://www.researchgate.net/publication/260659249\\_X-ray\\_Diffraction\\_Analysis\\_Principle\\_Instrument\\_and\\_Applications](https://www.researchgate.net/publication/260659249_X-ray_Diffraction_Analysis_Principle_Instrument_and_Applications),” 2018. .
- [173] “<https://www.matematicamente.it/forum/viewtopic.php>,” 2018. .
- [174] K. Venkateswarlu, A. C. Bose and N. Rameshbabu, “X-ray peak broadening studies of nanocrystalline hydroxyapatite by Williamson–Hall analysis,” *J. Phys. B*, vol. 405, pp. 4256–4261, 2010.
- [175] R. Yogamalar, R. Srinivasan, A. Vinu and K. Ariga, “X-ray peak broadening

- analysis in ZnO nanoparticles,” *J.Solid State Commun.*, vol. 149, pp. 1919–1923, 2009.
- [176] S. Burns, J. Gardella., “Quantitative ToF-SIMS studies of protein drug release from biodegradable polymer drug delivery membranes,” *Appl. Surf. Sci.*, vol. 31, pp. 1713–1723, 2013.
- [177] P. Mueller and J. Vervoort, “Secondary Ion Mass Spectrometer (SIMS),” University of Edinburgh, 2018.
- [178] C. S. Brian, *Fundamentals of Fourier Transform Infrared spectroscopy*. CRC press, 2011.
- [179] J. J. Ojeda and M. Dittrich, *Fourier Transform Infrared Spectroscopy for Molecular Analysis of Microbial Cells*. Springer Science & Business Media., 2012.
- [180] B. Zimmermann, Z. Tkal, A. Me and A. Kohler, “Characterizing aeroallergens by infrared spectroscopy of fungal spores and pollen,” *J.Pone*, vol. 1, pp. 1–22, 2015.
- [181] “FTIR Spectroscopy Attenuated Total Reflectance (ATR),” 2005.
- [182] “NanoDrop 1000 spectrophotometer V3.7 user’s manual,” *Thermo Sci*.
- [183] D. K. Arora, S. Das, and M. Sukumar, *Analyzing Microbes: Manual of Molecular Biology Techniques Front Cover*. Springer Berlin Heidelberg, 2013.
- [184] C. Larimer, M. Brann, J. D. Suter, G. Bonheyo and R. S. Addleman, “Are those bugs reflective ? Non-destructive biofilm imaging with white light interferometry How a biofilm forms,” 2017.
- [185] S. E. Cross *et al.*, “Evaluation of bacteria-induced enamel demineralization using optical profilometry,” *Dent. Mater.*, vol. 25, pp. 1517–1526, 2009.
- [186] N. Bright, K. Foster and P. Sermon, “Composite Biomimetic Nanomaterials,” *J. ICCE*, vol. 18, 2010.
- [187] P. Van Dong, C. H. Ha, L. T. Binh and J. Kasbohm, “Chemical synthesis and antibacterial activity of novel-shaped silver nanoparticles,” *J.International Nano*

*Lett.*, vol. 2, pp. 2–9, 2012.

- [188] S. Agnihotri, S. Mukherji and S. Mukherji, “Size-controlled silver nanoparticles synthesized over the range 5–100 nm using the same protocol and their antibacterial efficacy,” *RSC Adv.*, vol. 4, pp. 3974–3983, 2014.
- [189] N. Rangavittal, A. . Landa-Canovas and J. M. Gonza, “Structural study and stability of hydroxyapatite and tricalcium  $\beta$ -phosphate : Two important bioceramics,” *John Wiley Sons, Inc.*, pp. 660–669, 2000.
- [190] T. Taguchi, A. Kishidi and M. Akashi, “Hydroxyapatite formation on/in poly(vinyl alcohol) hydrogel matrices using a novel alternate soaking process,” *Chem. Letters*, pp. 711–712, 1998.
- [191] E. Vasilescu, J. Maria, C. Moreno, C. Vasilescu and F. Grigore, “Interactions of some new scaffolds with simulated body fluids,” *J. Rev.Chim.*, vol. 2, pp. 2–5, 2011.
- [192] T. Kobayashi, S. Ono, S. Hirakura, Y. Oaki and H. Imai, “Morphological variation of hydroxyapatite grown in aqueous solution based on simulated body fluid,” *CrystEngComm*, vol. 14, pp. 1143–1149, 2012.
- [193] P. N. Chavan, M. M. Bahir, R. U. Mene, M. P. Mahabole and R. S. Khairnar, “Study of nanobiomaterial hydroxyapatite in simulated body fluid : Formation and growth of apatite,” *J.Mater. Sci. Eng. B*, vol. 168, pp. 224–230, 2010.
- [194] M. H. Fathi, V. Mortazavi, S. B. Mousavi and S. M. Razavi, “Novel nanocomposite coating for dental implant applications *in vitro* and *in vivo* evaluation,” *J. Mater Sci Mater. Med.*, vol. 23, pp. 485–495, 2012.
- [195] H. Alobeedallah, J. L. Ellis, R. Rohanizadeh, H. Coster and F. Dehghani, “Preparation of nanostructured hydroxyapatite in organic solvents for clinical applications,” *J.Biomaterials*, vol. 25, pp. 12–19, 2011.
- [196] D. Buzas, W. Song, X. Jin, T. Shi, D. Markel and W. Ren, “Preparation of polyvinyl alcohol (PVA) microspheres using freeze-thaw cycling methods,” *J.Soc.Bio.Mat.*, vol. 33, p. 655, 2011.

- [197] A. R. Pijtnam, J. E. Kijler, J. R. Miuer, J. D. Meinhart and D. G. Lynn, "Faeriefungin: a new broad-spectrum antibiotic from *Streptomyces griseus* var. autotrophicus.," *J Nat Prod.*, vol. 52, pp. 797–809, 1988.
- [198] J. Sambrook and D. W. Russell, *Commonly Used Techniques in Molecular Cloning*. Cold spring harbor, NY, USA, 2001.
- [199] T. S. J. and F. E.F. and Maniatis, *Molecular Cloning: A Laboratory Manual*. Cold Spring Harbor Laboratory Press, 1989.
- [200] P. N. Saxena and B. Bhushan, "Estimation of median lethal dose of commercial formulations of some type II pyrethroids," vol. 10, pp. 193–197, 2017.
- [201] A. Smania, Jr., F. D. Monache, E. de F. A. Smania and R. S. Cuneo, "Antibacterial activity of steroidal compounds isolated from *ganoderma applanatum* (Pers.) Pat. (Aphyllophoromycetidae) fruit body," *Int. J. Med. Mushrooms*, vol. 1, pp. 325–330, 1999.
- [202] D. A. Vanden Berghe and A. J. Vlietinck, "Screening methods for antibacterial and antiviral agents from higher plants," vol. 6, pp. 47–69, Jan. 1991.
- [203] L. V Graf, R. J. G. Schadeck, L. Donatti, D. F. Buchi, D. D. B. Celular and U. Federal, "Morphological and cytochemical characterization of spores and gills of *lepista sordida* (Fungi: Basidiomycota)," *J. Microbiol.*, vol. 39, pp. 599–601, 2008.
- [204] F. S. Reis, L. Barros, A. Martins and I. C. F. R. Ferreira, "Chemical composition and nutritional value of the most widely appreciated cultivated mushrooms : An inter-species comparative study," *J. Food Chem. Toxicol.*, vol. 50, pp. 191–197, 2012.
- [205] S. E. Mallikarjuna, A. Ranjini, D. J. Haware and M. R. Vijayalakshmi, "Mineral Composition of Four Edible Mushrooms Mineral Composition of Four Edible Mushrooms," *J. Chemistry*, vol. 3, p. 5, 2013.
- [206] M. A. Khan, M. Tania, S. M. R. Amin, N. Alam, M. Uddin and Nazim, "An investigation on the nutritional composition of mushroom (*Pleurotus florida*) cultivated on different substrates," *J. Mushroom*, vol. 2, pp. 17–23, 2008.

- [207] B. Ma, W. Ren, Y. Zhou, J. Ma, Y. Ruan and C. N. Wen, “Triterpenoids from the spores of *ganoderma lucidum*,” *N. Am. J. Med. Sci.*, vol. 3, pp. 495–498, 2011.
- [208] Y. Liu *et al.*, “Chemical composition of five wild edible mushrooms collected from Southwest China and their antihyperglycemic and antioxidant activity,” *J. Food Chem. Toxicol.*, vol. 50, pp. 1238–1244, 2012.
- [209] A. Diego-Taboada, S. T. Beckett, S. L. Atkin and G. Mackenzie, “Hollow pollen shells to enhance drug delivery,” *J. Pharmaceutics*, vol. 6, pp. 80–96, 2014.
- [210] N. A. R. Gow, J. Latge and C. A. Munro, “The fungal cell wall : Structure , biosynthesis and function,” *J. Microbiol Spectr.*, vol. 5, pp. 1–25, 2017.
- [211] C. Of, A. Bisporus, L. Imbach and A. Spores, “Applications of Raman spectroscopy for chemical characterization and protein conformation of *agaricus bisporus* ( *Lange* ) *Imbach (Agaricomycetidae)* spores,” *J. Int. Bioassays*, vol. 3, pp. 3318–3323, 2014.
- [212] I. Brondz, K. Høiland and D. Ekeberg, “Multivariate analysis of fatty acids in spores of higher basidiomycetes: A new method for chemotaxonomical classification of fungi,” *J. Chromatogr. B Anal. Technol. Biomed. Life Sci.*, vol. 800, pp. 303–307, 2004.
- [213] J. C. Young, “Microwave-assisted extraction of the fungal metabolites ergosterol and total fatty acids,” *J. Agric. Food Chem.*, vol. 43, pp. 2904–2910, 1995.
- [214] S. Wallace, A. Fleming, C. H. Wellman and D. J. Beerling, “Evolutionary development of the plant spore and pollen wall,” *AoB Plants*, vol. 11, p. 18, 2011.
- [215] A. Tryon and B. Lugardon, *Spores of the Pteridophyta: surface, wall structure, and diversity based on electron microscope studies*. Springer Science & Business Media., 2012.
- [216] R. Michael, M. Ginnis and K. Tyring., *Medical Microbiology*, 4th ed. ISBN, 2002.
- [217] *Mushroom spores magnified*. Sciencephoto.com, 2018.
- [218] N. Wolchover “Why Are Pollen Allergies So Common?,” livesciencephoto

2012.

- [219] “<https://www.cafepress.com/+parts-structure-seeds-of-the-castor-oil-plant+yard-signs>,” 2018. .
- [220] S. K. Hammer and J. L. Avalos, “Harnessing yeast organelles for metabolic engineering,” *Nat. Chem. Biol.*, vol. 13, pp. 823–832, 2017.
- [221] S. Barrier *et al.*, “Access to a primary aminosporepollenin solid support from plant spores,” *J. Green Chem.*, vol. 12, pp. 234–240, 2010.
- [222] H. Noothalapati *et al.*, “Label-free chemical imaging of fungal spore walls by Raman microscopy and multivariate curve resolution analysis,” *Sci. Rep.*, vol. 6, pp. 1–10, 2016.
- [223] P. H. Fesel and A. Zuccaro, “ $\beta$ -glucan: Crucial component of the fungal cell wall and elusive MAMP in plants,” *J. Fungal Genet. Biol.*, vol. 90, pp. 53–60, 2016.
- [224] G. Guerriero, J. F. Hausman, J. Strauss, H. Ertan and K. S. Siddiqui, “Deconstructing plant biomass: Focus on fungal and extremophilic cell wall hydrolases,” *J. Plant Sci.*, vol. 234, pp. 180–193, 2015.
- [225] C. Castaño *et al.*, “Mushroom emergence detected by combining spore trapping with molecular techniques,” *J. Appl. Environ. Microbiol.*, vol. 83, p. 14, 2017.
- [226] K. Lakkireddy and U. Kües, “Bulk isolation of basidiospores from wild mushrooms by electrostatic attraction with low risk of microbial contaminations,” *J. AMB Express*, vol. 7, p. 28, 2017.
- [227] R. Bhat, R. Deshpande, S. V. Ganachari, D. S. Huh and A. Venkataraman, “Photo-irradiated biosynthesis of silver nanoparticles using edible mushroom *Pleurotus florida* and their antibacterial activity studies,” *J. Bioinorganic Chem. Appl.*, vol. 2011, p. 7, 2011.
- [228] S. Muramoto, D. J. Graham, M. S. Wagne, T. G. Lee, D. W. Moon, and D. G. Castner, “ToF-SIMS Analysis of Adsorbed Proteins: Principal Component Analysis of the Primary Ion Species Effect on the Protein Fragmentation Patterns,” *J. Phys.*

*Chem. C*, vol. 49, pp. 24247–24255, 2011.

- [229] K. Anthony, M. Murugan, M. Jeyaraj, N. K. Rathinam and G. Sangiliyandi, “Synthesis of silver nanoparticles using pine mushroom extract: A potential antimicrobial agent against *E. coli* and *B. subtilis*,” *J. Ind. Eng. Chem.*, vol. 20, pp. 2325–2331, 2014.
- [230] S. Mirunalini, V. Arulmozhi and M. Krishnaveni, “Intracellular biosynthesis and antibacterial activity of silver nanoparticles using edible mushrooms,” *J. Nat.Sci. Biol.*, vol. 4, pp. 55–61, 2012.
- [231] S. Sujatha, S. Tamilselvi, K. Subha and A. Panneerselvam, “Studies on biosynthesis of silver nanoparticles using mushroom and its antibacterial activities,” *Int. J. Curr. Microbiol. Appl. Sci.*, vol. 2, pp. 605–614, 2013.
- [232] D. Philip, “Biosynthesis of Au, Ag and Au-Ag nanoparticles using edible mushroom extract,” *J. Spectrochim. Acta - Part A Mol. Biomol. Spectrosc.*, vol. 73, pp. 374–381, 2009.
- [233] P. Bocchiaro and A. Zamperini, *Functional Inorganic Nanohybrids for Biomedical Diagnosis*. INTECH, 2013.
- [234] S. Angkaew and P. Limsuwan, “Preparation of silver-titanium dioxide core-shell (Ag@TiO<sub>2</sub>) nanoparticles: Effect of Ti-Ag mole ratio,” *J.Procedia Eng.*, vol. 32, pp. 649–655, 2012.
- [235] A. Khanna and V. Shetty, “Solar light-driven photocatalytic degradation of Anthraquinone dye-contaminated water by engineered Ag@TiO<sub>2</sub> core-shell nanoparticles,” *J. Desalin. Water Treat.*, vol. 54, pp. 744–757, 2015.
- [236] F. Moreau and G. C. Bond, “Preparation and reactivation of Au/TiO<sub>2</sub> catalysts,” *Catal. Today*, vol. 122, pp. 260–265, 2007.
- [237] B. Muller, J. E. Reseland, H. J. Haugen and H. Tiainen, “Cell growth on pore-graded biomimetic TiO<sub>2</sub> bone scaffolds,” *J. Biomater. Appl.*, vol. 29, pp. 1284–1295, 2015.
- [238] C. Shankar, A. T. N. Dao, P. Singh, K. Higashimine, D. M. Mott and S. Maenosono,

- “Chemical stabilization of gold coated by silver core-shell nanoparticles via electron transfer,” *J. Nanotechnol.*, vol. 23, p. 10, 2012.
- [239] K. D. Wegner and N. Hildebrandt, “Quantum dots: bright and versatile *in vitro* and *in vivo* fluorescence imaging biosensors,” *Chem. Soc. Rev.*, vol. 44, pp. 4792–4834, 2015.
- [240] M. Lubas, J. J. Jasinski, M. Sitarz, L. Kurpaska, P. Podsiad and J. Jasinski, “Raman spectroscopy of TiO<sub>2</sub> thin films formed by hybrid treatment for biomedical applications,” *Spectrochim. Acta Part A Mol. Biomol. Spectrosc.*, vol. 133, pp. 867–871, 2014.
- [241] S. Bao, C. Lei, M. W. Xu, C. J. Cai and D. Z. Jia, “Environment-friendly biomimetic synthesis of TiO<sub>2</sub> nanomaterials for photocatalytic application,” *Nanotechnology*, vol. 23, pp. 0–7, 2012.
- [242] C. Jin *et al.*, “*In vivo* evaluation of the interaction between titanium dioxide nanoparticle and rat liver DNA,” *J. Toxicol. Ind. Heal.*, vol. 29, pp. 235–44, 2013.
- [243] Y. Zhang, K. De La Harpe, A. A. Beckstead, R. Improta and B. Kohler, “UV-induced proton transfer between DNA strands,” *J. Am. Chem. Soc.*, vol. 137, pp. 7059–7062, 2015.
- [244] I. Aiad, M. M. El-Sukkary, E. A. Soliman and M. Y. El-Awady, “*In situ* and green synthesis of silver nanoparticles and their biological activity,” *J. Ind. Eng. Chem.*, vol. 20, pp. 3430–3439, 2014.
- [245] A. Speranza *et al.*, “*In vitro* toxicity of silver nanoparticles to kiwifruit pollen exhibits peculiar traits beyond the cause of silver ion release,” *J. Environ. Pollut.*, vol. 179, pp. 258–267, 2013.
- [246] M. I. Azócar *et al.*, “A systematic study of antibacterial silver nanoparticles: efficiency, enhanced permeability, and cytotoxic effects,” *J. Nanoparticle Res.*, vol. 16, p. 9, 2014.
- [247] A. K. Parmara, N. N. Valandb, K. B. Solankia and S. K. Menona, “Picric acid



- capped silver nanoparticles as a probe for colorimetric sensing of creatinine in human blood and cerebrospinal fluid samples,” *J. Int. Nano Lett.*, vol. 2, p. 31, 2012.
- [248] Q. Dong, H. Su, W. Cao, J. Han, D. Zhang and Q. Guo, “Biogenic synthesis of hierarchical hybrid nanocomposites and patterning of silver nanoparticles,” *J. Mater. Chem. Phys.*, vol. 110, pp. 160–165, 2008.
- [249] J. Moellmann, S. Ehrlich, R. Tonner and S. Grimme, “A DFT-D study of structural and energetic properties of TiO<sub>2</sub> modifications,” *J. Phys. Condens. Matter*, vol. 24, p. 8, 2012.
- [250] F. Regan, *Nanoparticles in Anti-Microbial Materials used and characterisation*. The Royal Society of Chemistry, 2012.
- [251] Z. Sadowski, *Biosynthesis and Application of Silver and Gold Nanoparticles*. INTECH, 2010.
- [252] J. Patel, L. Nemcova, P. Maguire, W. Graham and D. Mariotti, “Synthesis of surfactant-free electrostatically stabilized gold nanoparticles by plasma-induced liquid chemistry,” *J. Nanotechnol.*, vol. 24, p. 11, 2013.
- [253] S. Gupta and M. Tripathi, “A review on the synthesis of TiO<sub>2</sub> nanoparticles by solution route,” *Open Chem.*, vol. 10, pp. 279–294, 2012.
- [254] B. Gipson, M. Moll and L. Kavraki, “SIMS: A hybrid method for rapid conformational analysis,” *J. PLOS*, vol. 8, p. 13, 2013.
- [255] M. Prochazka, M. Stupavska, M. Jerigova and D. Velic, “TiO<sub>2</sub> photocatalytic degradation of cholesterol: SIMS study,” *Surf. Interface Anal.*, vol. 45, pp. 22–26, 2013.
- [256] R. Bhat, V. G. Sharanabasava, R. Deshpande, U. Shetti, G. Sanjeev and A. Venkataraman, “Photo-bio-synthesis of irregular shaped functionalized gold nanoparticles using edible mushroom *Pleurotus florida* and its anticancer evaluation,” *J. Photochem. Photobiol. B Biol.*, vol. 125, pp. 63–69, 2013.

- [257] J. Pulit and M. Banach, "Preparation of nanocrystalline silver using gelatin and glucose as stabilizing and reducing agents, respectively," *Dig. J. Nanomater. Biostructures*, vol. 8, pp. 787–795, 2013.
- [258] M. Kumar *et al.*, "Efficient, green and one Pot synthesis of sodium Acetate functionalized silver nanoparticles and their potential application as food preservative," *Bionanoscience*, vol. 7, pp. 521–529, 2017.
- [259] N. L. Over, *Ruby Glass of the 20th Century*. 1855.
- [260] J. Tan *et al.*, "Controllable Aggregation and Reversible pH Sensitivity of AuNPs Regulated by Carboxymethyl Cellulose," *Langmuir*, vol. 26, pp. 2093–2098, 2010.
- [261] C. Pfeiffer *et al.*, "Interaction of colloidal nanoparticles with their local environment: the (ionic) nanoenvironment around nanoparticles is different from bulk and determines the physico-chemical properties of the nanoparticles," *J. R. Soc. Interface*, vol. 11, p. 13, 2014.
- [262] B. Narasimha, B. Praveen and K. Mallikarjuna, "Mushrooms (*Agaricus bisporus*) mediated biosynthesis of silver nanoparticles, characterization and their antimicrobial activity," *Int. J. Nano Dimens.*, vol. 2, pp. 29–36, 2011.
- [263] P. Mohanpuria, N. K. Rana, and S. K. Yadav, "Biosynthesis of nanoparticles: Technological concepts and future applications," *J. Nanoparticle Res.*, vol. 10, pp. 507–517, 2008.
- [264] A. Karwa, S. Gaikwad, and M. K. Rai, "Mycosynthesis of silver nanoparticles using Lingzhi or Reishi medicinal mushroom, *Ganoderma lucidum* (W. Curt.:Fr.) P. Karst. and their role as antimicrobials and antibiotic activity enhancers.," *Int. J. Med. Mushrooms*, vol. 13, pp. 483–91, 2011.
- [265] J. Huang *et al.*, "Biogenic silver nanoparticles by *Cacumen Platycladi* extract: Synthesis, formation mechanism, and antibacterial activity," *J. Ind. Eng. Chem. Res.*, vol. 50, pp. 9095–9106, 2011.
- [266] M. Malakauskaite-Petruleviciene, A. Beganskien and StankeviciuteZivile, "Sol-gel

synthesis of calcium hydroxyapatite thin films on quartz substrate using dip-coating and spin-coating techniques,” *J.Sol-Gel Sci Technol*, vol. 71, pp. 437–446, 2014.

- [267] P. Roy and R. Sailaja, “Mechanical , thermal and bio-compatibility studies of PAEK-hydroxyapatite nanocomposites,” *J. Mech. Behav. Biomed. Mater.*, vol. 49, pp. 1–11, 2015.
- [268] M. Mirzaee, M. Vaezi and Y. Palizdar, “Synthesis and characterization of silver doped hydroxyapatite nanocomposite coatings and evaluation of their antibacterial and corrosion resistance properties in simulated body fluid,” *J. Mater. Sci. Eng. C*, vol. 69, pp. 675–684, 2016.
- [269] C. Qi, Y. Jie and B.-Q. Lu, “Hydroxyapatite nanosheet-assembled porous hollow microspheres:DNA-templated hydrothermal synthesis, drug delivery and protein adsorption,” *J. Chem.Mater.*, vol. 22, pp. 22642–22650, 2012.
- [270] M. Tlotleng, E. Akinlabi, M. Shukla and S. Pityana, “Microstructures , hardness and bioactivity of hydroxyapatite coatings deposited by direct laser melting process,” *J. Mater. Sci. Eng. C*, vol. 43, pp. 189–198, 2014.
- [271] E. Nordstrom and K. Karlsson, “Carbonate-doped hydroxyapatite,” *J.Materials Sci.*, vol. 1, pp. 182–184, 1990.
- [272] M. H. Uddin, T. Matsumoto and M. Okazaki, *Biomimetic fabrication of apatite related biomaterials*, Amtava Muk. INTECH, 2010.
- [273] L. Berzina-cimdina and N. Borodajenko, *Research of Calcium Phosphates Using Fourier Transform Infrared Spectroscopy*. Materials Science, INTECH, 2012.
- [274] A. Singh, “Hydroxyapatite, a biomaterial : Its chemical synthesis, characterization and study of biocompatibility prepared from shell of garden snail, *Helix aspersa*,” *J. Mater. Lett.*, vol. 35, pp. 1031–1038, 2012.
- [275] N. Roveri, M. Iafisco, A. M. Studiorum and U. Bologna, *The Biomimetic Approach to Design Apatites for Nanobiotechnological Applications*. INTECH, 2010.

- [276] S. Ku, J. Wojnarowicz, A. Chodara, T. Chudoba, S. Gierlotka and W. Lojkowski, "Influence of hydrothermal synthesis parameters on the properties of hydroxyapatite nanoparticles," *J. Nanotechnol.*, vol. 10, pp. 1586–1601, 2016.
- [277] A. C. Mitropoulos, "The Kelvin equation," *J. Colloid Interface Sci.*, vol. 317, pp. 643–648, 2008.
- [278] B. Parker, "On the use of small bone fragment in ununited fracture," *J. Proc. Roy. Soc.*, vol. 7, pp. 275–276, 1914.
- [279] R. K. Brundavanam, G. Eddy, J. Poinern and D. Fawcett, "Modelling the crystal structure of a 30 nm sized particle based hydroxyapatite powder synthesised under the influence of ultrasound irradiation from X-ray powder diffraction data," *J. Materials Sci.*, vol. 3, pp. 84–90, 2013.
- [280] K. P. Tank, P. Sharma, D. K. Kanchan and M. J. Joshi, "FTIR, powder XRD, TEM and dielectric studies of pure and zinc doped nano-hydroxyapatite," *J. Cryst. Res. Technol.*, vol. 46, pp. 1309–1316, 2011.
- [281] S. A. Manafi and S. Jougehdoost, "Synthesis of hydroxyapatite nanostructure by hydrothermal condition for biomedical application," *J. Pharm. Sci.*, vol. 5, pp. 89–94, 2009.
- [282] H. Akazawa and Y. Ueno, "Distinct crystallinity and orientations of hydroxyapatite thin films deposited on C- and A-plane sapphire substrates," *J. Cryst. Growth*, vol. 404, pp. 241–245, 2014.
- [283] A. Haider, S. Haider, S. S. Han and I. Kang, "Recent advances in the synthesis, functionalization and biomedical applications of hydroxyapatite: a review," *RSC Adv.*, vol. 7, pp. 7442–7458, 2017.
- [284] V. Uskokovic, "The role of hydroxyapatite channel in defining selected physicochemical peculiarities exhibited by hydroxyapatite," *RSC Adv.*, vol. 5, pp. 36614–36633, 2015.
- [285] W. Wei, R. Sun, J. Cui and Z. Wei, "Removal of nitrobenzene from aqueous

- solution by adsorption on nanocrystalline hydroxyapatite,” *J.DES*, vol. 263, pp. 89–96, 2010.
- [286] G. Di *et al.*, “Bioinspired synthesis of CaCO<sub>3</sub> superstructures through a novel hydrogel composite membranes mineralization platform : A comprehensive view,” *J.Adv. Mater.*, pp. 610–616, 2016.
- [287] Y. Kim *et al.*, “Structure and Properties of Nanocomposites Formed by the Occlusion of Block Copolymer Worms and Vesicles Within Calcite Crystals,” *J. Adv. Funct. Mater.*, vol. 26, pp. 1382–1392, 2016.
- [288] J. N. Barrows, G. B. Jameson, and M. T. Pope, “ Structure of a heteropoly blue. The four-electron reduced. BETA.-12-molybdophosphate an ion.” vol. 04, no. 7, pp. 1771– 773, 1985.
- [289] E. A. Nagul, I. D. Mckelvie, P. Worsfold and S. D. Kolev, “The molybdenum blue reaction for the determination of orthophosphate revisited : Opening the black box,” *J. Anal. Chim. Acta*, vol. 890, pp. 60–82, 2015.
- [290] D. Dufour, *Clinical diagnosis and management by laboratory methods*, vol. 43. 1997.
- [291] C. Luo, H. Xie, J. Liu and G. Li, “Preparation and characterization of CaCO<sub>3</sub> crystals and CaCO<sub>3</sub>/La<sub>2</sub>(CO<sub>3</sub>)<sub>3</sub>composited fluorescent materials,” *J. Compos. Mater.*, vol. 46(1), pp. 90–97, 2011.
- [292] S. Kunjalukkal, A. Balakrishnan, M. Chu, Y. Jin, T. Nam and S. Cho, “Sol – gel synthesis and characterization of hydroxyapatite nanorods,” *J. Particuology*, vol. 7, pp. 466–470, 2009.
- [293] “Calculated from international centre for diffraction data,” 2017.
- [294] W. Xiao, B. Sonny Bal and M. N. Rahaman, “Preparation of resorbable carbonate-substituted hollow hydroxyapatite microspheres and their evaluation in osseous defects in vivo,” *J. Mater. Sci. Eng. C*, vol. 60, pp. 324–332, 2016.

- [295] L. Han, L. Wang, J. Song, M. C. Boyce and C. Ortiz, “Direct quantification of the mechanical anisotropy and fracture of an individual exoskeleton layer via uniaxial compression of micropillars,” *J.Nano Lett*, vol. 11, pp. 3868–3874, 2011.
- [296] X. Li, D. Pan, S. Lin, Z. Zhuang, and Z. Lin, “Facile *in vitro* hydroxyapatite remineralization of human enamel with remarkable hardness,” *Cryst.EngComm.*, vol. 15, pp. 4351–4356, 2013.
- [297] X. Jing, E. Jin, H. Mi and T. Lih-sheng, “Hierarchically decorated electrospun poly (ε-caprolactone)/nanohydroxyapatite composite nanofibers for bone tissue engineering,” *J. Mater Sci*, vol. 50, pp. 4174–4186, 2015.
- [298] R. A. Perez *et al.*, “Therapeutically relevant aspects in bone repair and regeneration,” *J.Materials Today*, vol. 18, pp. 573–589, 2015.
- [299] C. Shi *et al.*, “Functional hydroxyapatite bioceramics with excellent osteoconductivity and stern-interface induced antibacterial ability,” *J.Biomater.Sci.*, vol. 4, pp. 699–710, 2016.
- [300] C. L. Salgado, L. Grenho, M. H. Fernandes, B. J. Colac and F. J. Monteiro, “Biodegradation, biocompatibility, and osteoconduction evaluation of collagen-nanohydroxyapatite cryogels for bone tissue regeneration,” *J.Soc.Bio.Mat.*, pp. 57–70, 2015.
- [301] U. Anjaneyulu, B. Priyadarshini, A. Nirmala Grace and U. Vijayalakshmi, “Fabrication and characterization of Ag doped hydroxyapatite-polyvinyl alcohol composite nanofibers and its *in vitro* biological evaluations for bone tissue engineering applications,” *J. Sol-Gel Sci. Technol.*, vol. 81, pp. 750–761, 2017.
- [302] M. H. Fathi, A. Hanifi and V. Mortazavi, “Preparation and bioactivity evaluation of bone-like hydroxyapatite nanopowder,” *J. Mater. Process. Technol.*, vol. 2, pp. 536–542, 2008.
- [303] A. Xu, X. Liu, X. Gao, F. Deng, Y. Deng and S. Wei, “Enhancement of osteogenesis on micro/nano-topographical carbon fiber-reinforced polyetheretherketone – nanohydroxyapatite biocomposite,” *J. Mater. Sci. Eng. C*, vol. 48, pp. 592–598,

2015.

- [304] M. del C. García-Rodríguez, A. Altamirano-Lozano and M. Gordillo-García, *The Role of Vitamin C in the Protection and Modulation of Genotoxic Damage Induced by Metals Associated with Oxidative Stress*. INTECH, 2017.
- [305] K. G. H. Desai and H. J. Park, “Encapsulation of vitamin C in tripolyphosphate cross-linked chitosan microspheres by spray drying,” *J. Microencapsul.*, vol. 22, pp. 179–192, 2005.
- [306] P. K. Vemula, U. Aslam, V. A. Mallia and G. John, “*In situ* synthesis of gold nanoparticles using molecular gels and liquid crystals from vitamin-C amphiphiles,” *J.Chem.Mater.*, vol. 19, pp. 138–140, 2007.
- [307] A. Fathi-Azarbayjani, P. L. Tan, Y. Y. Chan and S. Y. Chan, “Ascorbic acid for the safe use of a sunscreen agent: Accumulation of nano zinc oxide and titanium dioxide on the skin,” *J.Scientia Pharm.*, vol. 81, pp. 1141–1150, 2013.
- [308] X. Gao *et al.*, “*In vitro* controlled release of vitamin C from Ca/Al layered double hydroxide drug delivery system,” *J.Materials Sci. Eng. C*, vol. 39, pp. 56–60, 2014.
- [309] R. C. Hardison, “Evolution of hemoglobin and its genes,” *J.Cold Spring Harb. Perspect. Med.*, vol. 2, pp. 1–18, 2012.
- [310] C. Thomas and A. B. Lumb, “Physiology of haemoglobin,” *Contin. Educ. Anaesthesia, Crit. Care Pain*, vol. 12, pp. 251–256, 2012.
- [311] M. Srinivasan, M. Rajabi and S. Mousa, “Multifunctional nanomaterials and their applications in drug delivery and cancer therapy,” *J.Nanomaterials*, vol. 5, pp. 1690–1703, 2015.
- [312] U. Agrawal, R. Sharma, M. Gupta and S. P. Vyas, “Is nanotechnology a boon for oral drug delivery?,” *J.Drug Discov. Today*, vol. 19, pp. 1530–1546, 2014.
- [313] M. A. Mohammed, J. T. M. Syeda, K. M. Wasan and E. K. Wasan, “An overview of chitosan nanoparticles and its application in non-parenteral drug delivery,”

*J.Pharmaceutics*, vol. 9, pp. 1–26, 2017.

- [314] C. Bastiancich, P. Danhier, V. Préat and F. Danhier, “Anticancer drug-loaded hydrogels as drug delivery systems for the local treatment of glioblastoma,” *J. Control. Release*, vol. 243, pp. 29–42, 2016.
- [315] S. R. Soni and A. Ghosh, “Exploring pullulan-poly(vinyl alcohol) interpenetrating network microspheres as controlled release drug delivery device,” *J.Carbohydrate Polym.*, vol. 174, pp. 812–822, 2017.
- [316] S. Maleki Dizaj, M. Barzegar-Jalali, M. H. Zarrintan, K. Adibkia and F. Lotfipour, “Calcium carbonate nanoparticles as cancer drug delivery system,” *J.Expert Opin. Drug Deliv.*, vol. 12, pp. 1649–1660, 2015.
- [317] M. Manzano and M. Vallet-Regí, “Revisiting bioceramics: Bone regenerative and local drug delivery systems,” *J.Progress Solid State Chem.*, vol. 40, pp. 17–30, 2012.
- [318] P. Suresh, A. Kurrey, and M. Singh, “Hollow microspheres as a drug carrier: An overview of fabrication and *in vivo* characterization techniques,” *J.Chronicles Young Sci.*, vol. 5, p. 10, 2014.
- [319] A. Elsayed, “*Recent Advances in Novel Drug Carrier Systems.*” INTECH, 2012.
- [320] S. Zhang, K. Saito, H. Matsumoto, M. Mlnagawa and A. Tanioka, “Characterization of insulin adsorption behavior on amphoteric charged membranes,” *J.Polymer J.*, vol. 40, pp. 837–841, 2008.
- [321] H. K. Elçioğlu and A. D. Sezer, *Nanoparticle insulin drug delivery — applications and new aspects.* INTECH, 2014.
- [322] H. Sato and M. Ikeya, “Organic molecules and nanoparticles in inorganic crystals: Vitamin C in CaCO<sub>3</sub> as an ultraviolet absorber,” *J. Appl. Phys.*, vol. 95, pp. 3031–3036, 2004.
- [323] L. B. Johan and W. L, *Interface phenomena and bioproducts.* 1996.



- [324] R. Ansari, N. Alizadeh and S. M. Shademan, "Application of silica gel/polyaniline composite for adsorption of ascorbic acid from aqueous solutions," *Iran. Polym. J.*, vol. 22, pp. 739–748, 2013.
- [325] J. H. Santos, N. Matsuda, Z. Qi, T. Yoshida, A. Takatsu and K. Kato, "Adsorption behavior of cytochrome c, myoglobin and hemoglobin in a quartz surface probed using slab optical waveguide (SOWG) spectroscopy," *Anal. Sci.*, vol. 19, pp. 199–204, 2003.
- [326] K. Kostarelos, M. Prato, E. Va, S. Merino and C. Martí, "Nanocomposite hydrogels: 3D polymer a nanoparticle synergies for on-demand drug delivery," *ACS Nano*, vol. 9, pp. 4686–4697, 2015.
- [327] D. Behnoodfar, S. Dadbin and M. Frounchi, "PLA microspheres-embedded PVA hydrogels prepared by gamma-irradiation and freeze-thaw methods as drug release carriers," *Int. J. Polym. Mater. Polym. Biomater.*, vol. 62, pp. 28–33, 2013.
- [328] "Insulinum humanum," *Test*, pp. 1–3, 2005.
- [329] E. Caló and V. V. Khutoryanskiy, "Biomedical applications of hydrogels: A review of patents and commercial products," *J. Eur. Polym.*, vol. 65, pp. 252–267, 2015.
- [330] J. S. Son *et al.*, "Porous hydroxyapatite scaffold with three-dimensional localized drug delivery system using biodegradable microspheres," *J. Control. Release*, vol. 153, pp. 133–140, 2011.
- [331] S. Dhivya, J. Ajita and N. Selvamurugan, "Metallic nanomaterials for bone tissue engineering," *J. Biomed. Nanotechnol.*, vol. 11, pp. 1675–1700, 2015.
- [332] J. M. Schierholz and J. Beuth, "Implant infections: A haven for opportunistic bacteria," *J. Hosp. Infect.*, vol. 49, pp. 87–93, 2001.
- [333] F. Wang *et al.*, "Nanoparticle-based antivirulence vaccine for the management of methicillin-resistant staphylococcus aureus skin infection HHS public access," *Adv. Funct. Mater.*, vol. 8, pp. 1628–1635, 2016.

- [334] D. Manikprabhu *et al.*, “Sunlight mediated synthesis of silver nanoparticles by a novel actinobacterium (*Sinomonas mesophila* MPKL 26) and its antimicrobial activity against multi drug resistant *Staphylococcus aureus*,” *J. Photochem. Photobiol. B Biol.*, vol. 158, pp. 202–205, 2016.
- [335] A. Ebrahiminezhad, M. Bagheri, S. M. Taghizadeh, A. Berenjhan and Y. Ghasemi, “Biomimetic synthesis of silver nanoparticles using microalgal secretory carbohydrates as a novel anticancer and antimicrobial,” *Adv. Nat. Sci. Nanosci. Nanotechnol.*, vol. 7, p. 8, 2016.
- [336] V. R. Netala, V. S. Kotakadi, V. Nagam, P. Bobbu, S. B. Ghosh and V. Tarte, “First report of biomimetic synthesis of silver nanoparticles using aqueous callus extract of *Centella asiatica* and their antimicrobial activity,” *Appl. Nanosci.*, vol. 5, pp. 801–807, 2015.
- [337] R. Dobrucka and J. Długaszewska, “Antimicrobial activities of silver nanoparticles synthesized by using water extract of *arnicae anthodium*,” *Indian J. Microbiol.*, vol. 55, pp. 168–174, 2015.
- [338] S. Anjum and B. H. Abbasi, “Biomimetic synthesis of antimicrobial silver nanoparticles using *in vitro*-propagated plantlets of a medicinally important endangered species: *Phlomis bracteosa*,” *Int. J. Nanomedicine*, vol. 11, pp. 1663–1675, 2016.
- [339] J. Manna, S. Goswami, N. Shilpa, N. Sahu and R. K. Rana, “Biomimetic method to assemble nanostructured Ag@ZnO on cotton fabrics: Application as self-cleaning flexible materials with visible-light photocatalysis and antibacterial activities,” *ACS Appl. Mater. Interfaces*, vol. 7, pp. 8076–8082, 2015.
- [340] M. N. Dickson, E. I. Liang, L. A. Rodriguez, N. Vollereaux and A. F. Yee, “Nanopatterned polymer surfaces with bactericidal properties,” *Biointerphases*, vol. 10, p. 8, 2015.
- [341] E. Jackson *et al.*, “Protein-templated biomimetic silica nanoparticles,” *Langmuir*, vol. 31, pp. 3687–3695, 2015.

- [342] X. Y. Cai, N. N. Li, J. C. Chen, E. T. Kang and L. Q. Xu, "Biomimetic anchors applied to the host-guest antifouling functionalization of titanium substrates," *J. Colloid Interface Sci.*, vol. 475, pp. 8–16, 2016.
- [343] H. S. Rathore *et al.*, "Fabrication of biomimetic porous novel sponge from gum kondagogu for wound dressing," *Mater. Lett.*, vol. 177, pp. 108–111, 2016.
- [344] V. K. Sharma, N. Johnson, L. Cizmas, T. J. McDonald and H. Kim, "A review of the influence of treatment strategies on antibiotic resistant bacteria and antibiotic resistance genes," *Chemosphere*, vol. 150, pp. 702–714, 2016.
- [345] G. D. Wright, "Molecular mechanisms of antibiotic resistance," *J. Chem. Commun.*, vol. 47, p. 4055, 2011.
- [346] M. R. Bindhu and M. Umadevi, "Antibacterial activities of green synthesized gold nanoparticles," *Mater. Lett.*, vol. 120, pp. 122–125, 2014.
- [347] A. Muthuvel, K. Adavallan, K. Balamurugan and N. Krishnakumar, "Biosynthesis of gold nanoparticles using *Solanum nigrum* leaf extract and screening their free radical scavenging and antibacterial properties," *J. Biomed. Prev. Nutr.*, vol. 4, pp. 325–332, 2014.
- [348] R. Brayner, "The toxicological impact of nanoparticles," *J. Nano Today*, vol. 3, pp. 48–55, 2008.
- [349] J. J. Giner-Casares, M. Henriksen-Lacey, M. Coronado-Puchau and L. M. Liz-Marzán, "Inorganic nanoparticles for biomedicine: Where materials scientists meet medical research," *Mater. Today*, vol. 19, pp. 19–28, 2016.
- [350] T. Eiampongpaiboon, W. O. Chung, J. D. Bryers, K.-H. Chung and D. C. N. Chan, "Antibacterial activity of gold-titanates on Gram-positive cariogenic bacteria," *Acta Biomater. Odontol. Scand.*, vol. 1, pp. 51–58, 2015.
- [351] S. Dinakar, R. Isacc Fenn Fenn, A. Sobczak-Kupiec and N. Basavegowda, "Bioreduction of chloroaurate ions using fruit extract *Punica granatum* (Pomegranate) for synthesis of highly stable gold nanoparticles and assessment of its

- antibacterial activity,” *J. Micro Nano Lett.*, vol. 8, no. 8, pp. 400–404, 2013.
- [352] J. Lemire, J. J. Harrison and R. J. Turner, “Antimicrobial activity of metals: mechanisms, molecular targets and applications,” *J. Nat. Rev. Microbiol.*, vol. 11, pp. 371–84, 2013.
- [353] Y. Zhang, H. Peng, W. Huang, Y. Zhou, and D. Yan, “Facile preparation and characterization of highly antimicrobial colloid Ag or Au nanoparticles,” *J. Colloid Interface Sci.*, vol. 325, pp. 371–376, 2008.
- [354] S. Sadhasivam, P. Shanmugam, M. Veerapandian, R. Subbiah and K. Yun, “Biogenic synthesis of multidimensional gold nanoparticles assisted by *Streptomyces hygroscopicus* and its electrochemical and antibacterial properties,” *J. BioMetals*, vol. 25, pp. 351–360, 2012.
- [355] M. Koperuncholan, “Bioreduction of chloroauric acid (HAuCl<sub>4</sub>) for the synthesis of gold nanoparticles (GNPs): A special empathies of pharmacological activity,” *J. Int. J. Phytopharm.*, vol. 5, pp. 72–80, 2015.
- [356] Y. Zhao, C. Ye, W. Liu, R. Chen and X. Jiang, “Tuning the composition of AuPt bimetallic nanoparticles for antibacterial application,” *J. Angew. Chemie - Int. Ed.*, vol. 53, pp. 8127–8131, 2014.
- [357] I. N. Kholmanov *et al.*, “Nanostructured hybrid transparent conductive films with antibacterial properties,” *ACS Nano*, vol. 6, pp. 5157–5163, 2012.
- [358] J. Meng *et al.*, “Using gold nanorods core/silver shell nanostructures as model material to probe biodistribution and toxic effects of silver nanoparticles in mice,” *J. Nanotoxicology*, vol. 8, pp. 686–696, 2014.
- [359] C. Zafiu, Z. Hussain, S. Küpcü, A. Masutani, P. Kilickiran and E. K. Sinner, “Liquid crystals as optical amplifiers for bacterial detection,” *Biosens. Bioelectron.*, vol. 80, pp. 161–170, 2016.
- [360] Y. Cai, M. Strømme and K. Welch, “Photocatalytic antibacterial effects are maintained on resin-based TiO<sub>2</sub> nanocomposites after cessation of UV irradiation,”

*J. PLOS ONE*, vol. 8, p. 9, 2013.

- [361] S. Sabella *et al.*, “A general mechanism for intracellular toxicity of metal-containing nanoparticles,” *J. Nanoscale*, vol. 6, p. 7052, 2014.
- [362] W.-C. Hou, P. Westerhoff and J. D. Posner, “Biological accumulation of engineered nanomaterials: a review of current knowledge,” *J. Environ. Sci. Process. Impacts*, vol. 15, pp. 103–122, 2013.
- [363] M. Sirajuddin, S. Ali and A. Badshah, “Drug-DNA interactions and their study by UV-Visible, fluorescence spectroscopies and cyclic voltametry,” *J. Photochem. Photobiol. B Biol.*, vol. 124, pp. 1–19, 2013.
- [364] J. Park, “Endocytosis and exocytosis of nanoparticles in mammalian cells,” *Int J Nanomedicine.*, vol. 1, pp. 51–63, 2014.
- [365] J. Taylor, A. Huefner, L. Li and S. Mahajan, “Nanoparticles and intracellular applications of surface-enhanced Raman spectroscopy,” *RSC*, vol. 141, pp. 5037–5055, 2016.
- [366] L. Shang, K. Nienhaus and G. Nienhaus, “Engineered nanoparticles interacting with cells: size matters,” *J. Nanobiotechnology*, vol. 12, p. 5, 2014.
- [367] N. K. Rajawat, R. Verma and I. Soni, “Median lethal dose (LD 50) estimation of  $\beta$  - cyfluthrin in male and female Swiss albino mice,” *Int. J. Sci. Res.* vol. 5, pp. 22–25, 2015.
- [368] S. H. Mutasher, A. A. Salih and H. S. Al-Lami, “Preparation of some chitosan derivatives and study their effect on human genetic material,” *J. Der. Pharma. Chem.*, vol. 8, pp. 125–134, 2016.
- [369] S. Patel, P. Patel, S. B. Undre, S. R. Pandya, M. Singh and S. Bakshi, “DNA binding and dispersion activities of titanium dioxide nanoparticles with UV/vis spectrophotometry, fluorescence spectroscopy and physicochemical analysis at physiological temperature,” *J. Mol. Liq.*, vol. 213, pp. 304–311, 2016.

- [370] L. Y. T. Chou, F. Song and W. C. W. Chan, "Engineering the structure and properties of DNA-nanoparticle superstructures using polyvalent counterions," *J. Am. Chem. Soc.*, vol. 138, pp. 4565–4572, 2016.
- [371] S. B. Suhani Patel, B. Undre, R. Pandya and M. Singh, "DNA binding and dispersion activities of titanium dioxide nanoparticles with UV/vis spectrophotometry, fluorescence spectroscopy and physicochemical analysis at physiological temperature," *J. Mol. Liq.*, vol. 213, pp. 304–311, 2016.
- [372] C. Jin *et al.*, "In vivo evaluation of the interaction between titanium dioxide nanoparticle and rat liver DNA.," *J. Toxicol. Ind. Heal.*, vol. 29, pp. 235–44, 2013.
- [373] U. Klueh, V. Wagner, S. Kelly, A. Johnson and J. D. Bryers, "Efficacy of silver-coated fabric to prevent bacterial colonization and subsequent device-based biofilm formation," *J. Biomed. Mater. Res.*, vol. 53, pp. 621–631, 2000.
- [374] A. Khanna and V. Shetty, "Solar light-driven photocatalytic degradation of Anthraquinone dye-contaminated water by engineered Ag @ TiO<sub>2</sub> core – shell nanoparticles," *Desalin. Water Treat. ISSN*, vol. 3994, 2015.
- [375] P. Paraskeva and N. J. D. Graham, "Ozonation of municipal waste water effluents," *Water Environ. Res.*, vol. 74, pp. 569–581, 2002.
- [376] N. H. Ince, G. Tezcanli, R. K. Belen and G. Apikyan, "Ultrasound as a catalyzer of aqueous reaction systems: The state of the art and environmental applications," *Appl. Catal. B Environ.*, vol. 29, pp. 167–176, 2001.
- [377] F. Sabin, T. Türk and A. Vogler, "Photo-oxidation of organic compound in the presence of titanium dioxide: determination of the efficiency," *J. Photochem. Photobiol. A Chem.*, vol. 63, pp. 99–106, 1992.
- [378] M. P. Vena, M. Jobbágy and S. A. Bilmes, "Microorganism mediated biosynthesis of metal chalcogenides; a powerful tool to transform toxic effluents into functional nanomaterials," *Sci. Total Environ.*, vol. 565, pp. 804–810, 2015.
- [379] D. Zhang *et al.*, "A bio-inspired inner-motile photocatalyst film: a magnetically

- actuated artificial cilia photocatalyst.," *Nanoscale*, vol. 6, pp. 5516–25, 2014.
- [380] X. y. Liu, N. Li and N. X. Zhang, "Photocatalytic degradation of bisphenol a in water using a visible light-activated biomimetic catalyst," *Fresenius Environ. Bull.*, vol. 23, pp. 523–530, 2014.
- [381] L. Chen *et al.*, "Photocatalytic properties and electrochemical characteristic of a novel biomimetic oxygenase enzyme photocatalyst iron(II) tetrahydroxymethyl tetra(1,4-dithiin) porphyrazine for the degradation of organic pollutants," *J. Mol. Catal. A Chem.*, vol. 372, pp. 114–120, 2013.
- [382] M. Sakai, T. Kato, N. Ishizuka, T. Isobe, A. Nakajima and A. Fujishima, "Bio-inspired highly hydrophobic surface with ecdysis behavior using an organic monolithic resin and titanium dioxide photocatalyst," *J. Sol-Gel Sci. Technol.*, vol. 77, pp. 257–265, 2016.
- [383] W. Li, X. Pei, F. Deng, X. Luo, F. Li and Y. Xiao, "Bio-inspired artificial functional photocatalyst: biomimetic enzyme-like TiO<sub>2</sub>/reduced graphene oxide nanocomposite with excellent molecular recognition ability.," *Nanotechnology*, vol. 26, p. 8, 2015.
- [384] Y. Luo, X. Liu and J. Huang, "Nanofibrous rutile-titania/graphite composite derived from natural cellulose substance.," *J Nanosci. Nanotechnol.*, vol. 13, pp. 582–588, 2013.
- [385] H. Zhou, T. Fan, X. Li, D. Zhang, Q. Guo and H. Ogawa, "Biomimetic photocatalyst system derived from the natural prototype in leaves for efficient visible-light-driven catalysis," *J. Mater. Chem.*, vol. 19, p. 2695, 2009.
- [386] G. Zhang, T. Zhang, B. Li, X. Zhang and X. Chen, "Biomimetic synthesis of interlaced mesh structures TiO<sub>2</sub> nanofibers with enhanced photocatalytic activity," *J. Alloys Compd.*, vol. 668, pp. 113–120, 2016.
- [387] X. Wang, C. Fu, P. Wang, H. Yu and J. Yu, "Hierarchically porous metastable  $\beta$ -Ag<sub>2</sub>WO<sub>4</sub> hollow nanospheres: controlled synthesis and high photocatalytic activity," *J. Nanotechnology*, vol. 24, p. 8, 2013.

- [388] Y. Cheng, L. Courtney and P. Sermon, "Novel routes to stable bio-templated oxide replicas'," *Dev.Porous, Biol.Geopolym.Ceram.*, vol. 28, pp. 209–218, 2008.
- [389] T. Ohno, K. Sarukawa, K. Tokieda and M. Matsumura, "Morphology of a TiO<sub>2</sub> photocatalyst (Degussa, P-25) consisting of anatase and rutile crystalline phases," *J. Catal.*, vol. 203, pp. 82–86, 2001.
- [390] W. R. Siah, H. O. Lintang, M. Shamsuddin and L. Yuliati, "High photocatalytic activity of mixed anatase-rutile phases on commercial TiO<sub>2</sub> nanoparticles," *IOP Conf. Ser. Mater. Sci. Eng.*, vol. 107, p. 8, 2016.
- [391] H. Znad and Y. Kawase, "Synthesis and characterization of S-doped Degussa P25 with application in decolorization of Orange II dye as a model substrate," *J. Mol. Catal. A Chem.*, vol. 314, pp. 55–62, 2009.
- [392] M. Boudart, "Turnover Rates in Heterogeneous Catalysis," *Chem. Rev.*, vol. 95, pp. 661–666, 1995.
- [393] K. Guesh, C. Márquez-Álvarez, Y. Chebude and I. Díaz, "Enhanced photocatalytic activity of supported TiO<sub>2</sub> by selective surface modification of zeolite Y," *Appl. Surf. Sci.*, vol. 378, pp. 473–478, 2016.
- [394] Y. Yang and C. Tian, "Synthesis and characterization of Fe-doped sulfated titania with high photocatalytic activity in visible light," *J. Res. Chem. Intermed.*, vol. 41, pp. 5271–5281, 2015.
- [395] M. A. Lazar and W. A. Daoud, "Selective adsorption and photocatalysis of low-temperature base-modified anatase nanocrystals," *RSC Adv.*, vol. 2, pp. 447–452, 2012.
- [396] Y. Li, C. Liu, P. Xu, M. Li, M. Zen and S. Tang, "Controlled fabrication of ordered mesoporous titania/carbon fiber composites with high photoactivity: Synergistic relationship between surface adsorption and photocatalysis," *Chem. Eng. J.*, vol. 243, pp. 108–116, 2014.
- [397] J. X. Yu, R. A. Chi, Z. Y. He, Y. F. Qi, G. Zhan and J. Guo, "Combination of



- biosorption and photodegradation to remove methyl orange from aqueous solutions,” *Eng. Life Sci.*, vol. 11, pp. 309–315, 2011.
- [398] P. Rahul, S. V. NV, K. S. Ritesh, K. Ashutosh, and S. Sanjay, “Effect of gold nanoparticle size and surface coating on human red blood cells,” *Bioinspired, Biomim. and Nanobiomat.*, vol. 5, pp. 121–131, 2016.
- [399] A. Boni *et al.*, “USPIO-loaded red blood cells as a biomimetic MR contrast agent: A relaxometric study,” *Contrast Media Mol. Imaging*, vol. 9, pp. 229–236, 2014.
- [400] A. C. Anselmo, V. Gupta, B. J. Zern, D. Pan, M. Zakrewsky and V. Muzykantov, “Delivering nanoparticles to lungs while avoiding liver and spleen through adsorption on red blood cells,” *Nano ASC*, vol. 7, pp. 11129–11137, 2013.
- [401] B. Singh, P. Singh, A. J. Sutherland and K. Pal, “Control of shape and size of poly (lactic acid) microspheres based on surfactant and polymer concentration,” *Mater. Lett.*, vol. 195, pp. 48–51, 2017.
- [402] F. Ridi, I. Meazzini, B. Castroflorio, M. Bonini, D. Berti, and P. Baglioni, “Functional calcium phosphate composites in nanomedicine,” *Adv. Colloid Interface Sci.*, vol. 244, pp. 281–295, 2017.
- [403] “Artificial Red Blood Cell Created,” annual meeting of the American Society of Hematology, Renal and Urology news, 2016.
- [404] J. Qu *et al.*, “Preparation of artificial red cell and its application on alleviation of tumor hypoxia,” *Colloids Surfaces B*, vol. 160, pp. 446–454, 2017.
- [405] N. Doshi, A. S. Zahr, S. Bhaskar, J. Lahann, and S. Mitragotri, “Red blood cell-mimicking synthetic biomaterial particles,” *Proc. Natl. Acad. Sci.*, vol. 106, pp. 21495–21499, 2009.
- [406] P. S. Malchesky, “Artificial Oxygen Carriers,” *Artif. Organs*, vol. 41, p. 1, 2017.
- [407] T. M. S. Chang, “From artificial red blood cells, oxygen carriers, and oxygen therapeutics to artificial cells, nanomedicine, and beyond,” *Inf. Health.*, vol. 40, pp.

197–199, 2012.

- [408] M. Amoli-Diva, R. Sadighi-Bonabi and K. Pourghazi, “Switchable on/off drug release from gold nanoparticles-grafted dual light- and temperature-responsive hydrogel for controlled drug delivery,” *Mater. Sci. Eng. C*, vol. 76, pp. 242–248, 2017.
- [409] T. Tanaka and A. Kondo, “Cell-surface display of enzymes by the yeast *Saccharomyces cerevisiae* for synthetic biology,” *FEMS Yeast Res.*, vol. 15, pp. 1–9, 2015.
- [410] K. Zhang, K. Bhuripanyo, Y. Wang and J. Yin, “Yeast Surface Display,” vol. 1319, pp. 245–260, 2015.
- [411] T. Wang, “Engineering Yeast for Cellulosic Ethanol Production,” *Austin J. Chem. Eng.*, pp. 1–5, 2015.

# Appendix 1

## Paper one

*Nanobiosystems: Processing, Characterization and Applications IX; Nanomaterials I; Paper 9928-13; Sunday 28 August 2016; 3:55pm*

### **Biomimetic TiO<sub>2</sub> formation from interfacial sol-gel chemistry leading to new photocatalysts**

Iman A. Jaffer Al-Timini, Uche K. Onwukwe, Myles P. Worsley and Paul A. Sermon\*  
Nanomaterials Laboratory, Wolfson Centre, Brunel University, Uxbridge, Middlesex, UB8 3PH, UK

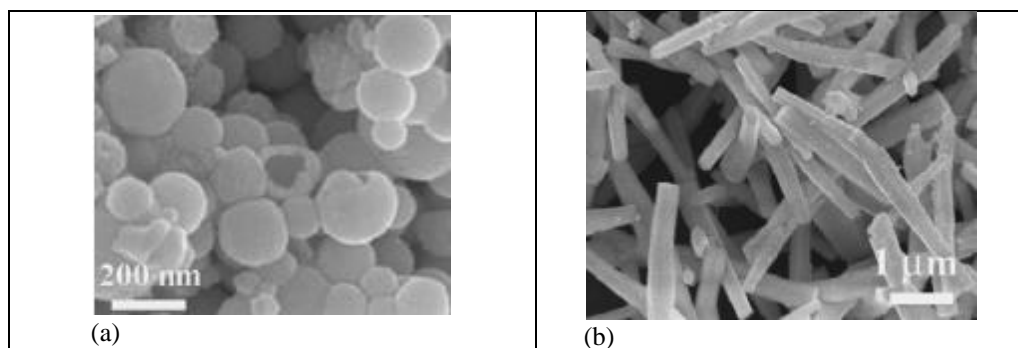
#### **Abstract**

The surfaces of Portobello mushroom spores (PMS) have been used to produce Au and Ag nanoparticles, which are held thereon. They have then been overcoated with TiO<sub>x</sub>. These adsorbed more methyl orange (MO) pollutant from water than commercial P25 TiO<sub>2</sub>. After calcination they form biomimetic TiO<sub>2</sub> (PMS) and removal of the biotemplate, they catalyse faster rates of MO from water (molecules/mg/s) than P25 anatase-rutile. Other biotemplates are now anticipated that will yield biomimetic photocatalysts with higher turnover number (s<sup>-1</sup>) removal of endocrine disruptors from water.

Keyword: titania, photocatalysis, biomimetic, methyl orange, mushroom spores

#### **1. Introduction**

Alternative technologies for control of water pollution by organics include: adsorption on carbon or treatment with O<sub>3</sub> [1], H<sub>2</sub>O<sub>2</sub> [2], ultrasound/cavitation [3] and TiO<sub>2</sub> [4] or biosynthesised functional CdS, CdTe and AgS photocatalysts [5].



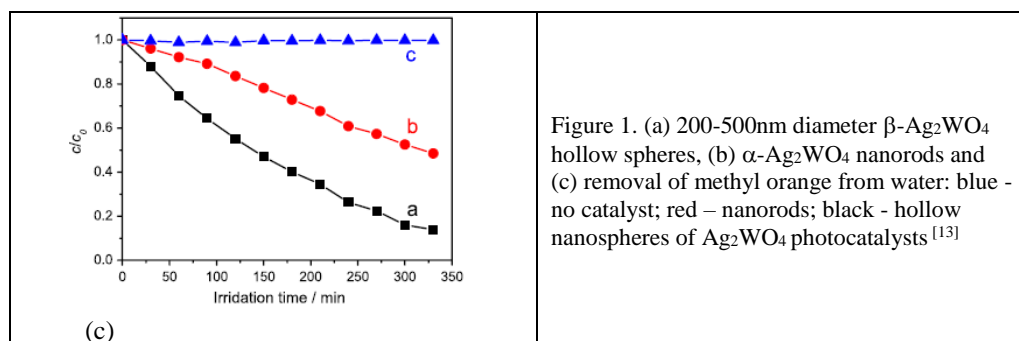


Figure 1. (a) 200-500nm diameter  $\beta$ -Ag<sub>2</sub>WO<sub>4</sub> hollow spheres, (b)  $\alpha$ -Ag<sub>2</sub>WO<sub>4</sub> nanorods and (c) removal of methyl orange from water: blue - no catalyst; red - nanorods; black - hollow nanospheres of Ag<sub>2</sub>WO<sub>4</sub> photocatalysts<sup>[13]</sup>

Bio-inspired<sup>[6]</sup> and biomimetic<sup>[7]</sup> photocatalysts are promising<sup>[8]</sup> for removal of organic pollutants in water. Here bio-inspired photocatalysts based on TiO<sub>2</sub> were most appropriate. Bioinspired<sup>[9]</sup> and biomimetic photocatalysts include TiO<sub>2</sub>/graphene oxide with molecular recognition<sup>[10]</sup> and TiO<sub>2</sub> nanofibers<sup>[11]</sup>. The latter was tested with a 300W lamp when 60mg catalyst was suspended in 100mL of an aqueous solution of 0.18mM methyl orange with magnetic agitation. Leaves have been used to provide a structural inheritance for ZnO photocatalysts<sup>[12]</sup> will be used in our on-going research.

There are two broad experimental approaches available: process illumination at say 300W<sup>[11]</sup> and solar/environmental illumination at say 15W<sup>[13]</sup>. Here we have chosen the latter approach.

It is also especially relevant that others have seen an effect of macroscopic structure on photocatalytic activity<sup>[13]</sup>. UV-absorbance suggested that 50mg metastable  $\beta$ -Ag<sub>2</sub>WO<sub>4</sub> was more active in the photodegradation of 0.06mM methyl orange aqueous solution (10mL) at room temperature when irradiated by a 15W lamp at 365nm without agitation when in the form of hollow spheres (200-500nm diameter; 20nm wall thickness; 165.5m<sup>2</sup>.g<sup>-1</sup> BET area; see Figure 1a) than as solid  $\alpha$ -Ag<sub>2</sub>WO<sub>4</sub> nanorods (Figure 1b). The hollow nanospheres had a band gap energy of 2.88eV that was lower than for the nanorods (3.05eV). We were interested to know whether the photoactivity was structurally dependent or band-gap dependent. We preferred not to use  $\alpha/\beta$ -Ag<sub>2</sub>WO<sub>4</sub>, but rather TiO<sub>2</sub>, that we knew could produce hollow structures on biotemplates<sup>[14]</sup>. One problem with  $\alpha/\beta$ -Ag<sub>2</sub>WO<sub>4</sub> is that the thermodynamically favourable  $\alpha$ - $\beta$  phase transition had to be inhibited. Of course with TiO<sub>2</sub> one has to recognise the potential transformation of anatase to rutile and the effect of any biotemplate-derived impurities. This then was the objective of the present preliminary study that is now reported.

It is interesting that TiO<sub>2</sub>/graphite can be produced from cellulose on 1573K thermal treatment<sup>[15]</sup> since the authors are also working on TiO<sub>2</sub>/C produced from TiO<sub>2</sub>/biotemplates.

## 2. Experimental

### 2.1 Biotemplate and reagents

Spores from fresh Portobello mushrooms (PMS) were harvested.

The reagents are titanium(iv)isopropoxide Ti(OC<sub>3</sub>H<sub>7</sub>)<sub>4</sub> (ACROS organics; 98%), ethanol (Sigma Aldrich; 99.9%), 2-propanol (Fluka; 99.9%; IPA), silver nitrate (AgNO<sub>3</sub>) (Fisher chemical; >99%), gold (III) chloride hydrate (AuCl<sub>3</sub>.xH<sub>2</sub>O) (Sigma Aldrich; 99.9%) and methyl orange (Sigma Aldrich; 85.9%; RMM 327.33; MO). A commercial titania (P25; Sigma Aldrich; 35-65m<sup>2</sup>.g<sup>-1</sup>) was also used.

### 2.2 Biotemplate TiO<sub>x</sub> overcoating and addition of Au/Ag NPs

A 3mM Ti(OC<sub>3</sub>H<sub>7</sub>)<sub>4</sub> solution was made up in 5 mL 2-propanol and filtered (0.22 $\mu$ m). 4-5 mg Portobello mushroom spores (PMS) were washed twice with water and acetone respectively and were then dispersed in 5 mL IPA with magnetic stirring for 1-2h.

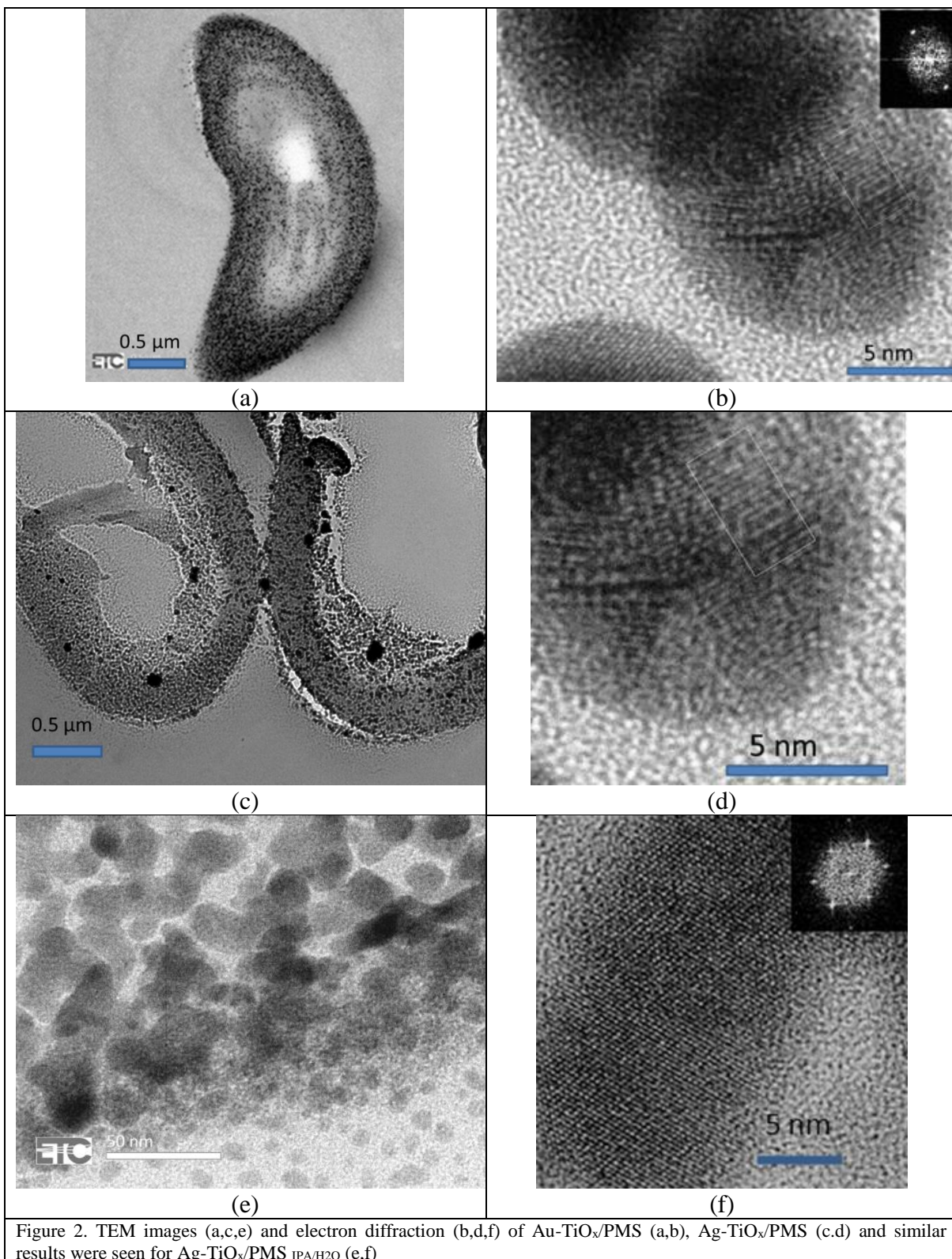
PMS (4-5mg) was dispersed in 5 mL IPA (ultrasonic bath for 15 min). At this point, 5 mL of alcoholic (IPA) AuCl<sub>3</sub> solution (3mM) was added with magnetic stirring at room temperature. The pH of the suspensions was 1.4. Solutions were left for 3h under magnetic stirring. The colour of the solution changed after 1-3h. The

same steps were used to prepare Ag NPs/PMS using 3mM of AgNO<sub>3</sub>. These were considered green methods of synthesis of the Ag and Au NPs using the PMS cell wall.

Ag-TiO<sub>x</sub>/PMS was prepared by ultrasonically dispersing 4-5 mg of PMS in 5mL IPA for 15min. Then, 5mL of alcoholic (IPA) AgNO<sub>3</sub> solution (3mM) was added to the PMS dispersion with magnetic stirring at room temperature for 3h. The Ag/PMS was left overnight. Then to 5mL of Ag NPs/PMS was added Ti(OC<sub>3</sub>H<sub>7</sub>)<sub>4</sub> (3mM) in IPA with magnetic stirring for 3h. The same steps were used to prepare Au-TiO<sub>2</sub>/PMS in IPA.

### **2.3 Biotemplate TiO<sub>2</sub> replica formation**

Overcoated biotemplate samples (TiO<sub>x</sub>/PMS, Ag/PMS, Au/PMS, Ag-TiO<sub>x</sub>/PMS and Au-TiO<sub>x</sub>/PMS) were calcined at 773 K in air for 3h to remove the organic substrate, giving TiO<sub>2</sub> replicas (TiO<sub>2</sub> (PMS), Ag-TiO<sub>2</sub> (PMS) and Au-TiO<sub>2</sub> (PMS)).



## 1.1 Methods of Characterization

The structures of the samples were analysed using transmission electron microscopy (TEM, JEOL JEM 2100f, field emission gun (FEG)) for morphology and particle size using a Gatan camera and imaging software (Gatan microscopy suite, version 3) with an accelerating voltage of 80 and 200kV. Ag, Au and TiO<sub>2</sub> nanoparticles were characterized by UV-Vis spectrophotometer (Perkin Elmer, Lambda 650s) using quartz cuvette. TEM samples were prepared by adding a few mg of the photocatalysts and mixing these with resin (12 g of low viscosity (Taablv), 4 mg low viscosity hardener vH1, 9 mg of low viscosity VH2 hardener and 0.65 mg accelerator). They were left at 330K overnight and then microtomed.

## 2.5 Adsorption and photocatalytic activity towards Methyl Orange (MO)

MO possess an azo group (N=N) conjugated to two phenyl groups leading to a peak in the visible region ( $\lambda_{\max}$  = 464 nm). Samples (P25, PMS, TiO<sub>x</sub>/PMS, Ag/PMS, Au/PMS, Ag-TiO<sub>x</sub>/PMS and Au-TiO<sub>x</sub>/PMS, TiO<sub>2</sub> (PMS), Ag-TiO<sub>2</sub> (PMS) and Au-TiO<sub>2</sub> (PMS)) were tested in duplicate with magnetic stirring at 298K for their (i) rate and extent of adsorption of MO from an aqueous 0.1mM (or 0.01mM) solution over a period of 1h in the dark and (ii) photocatalytic activity over 10h at 298K by UV-Vis spectroscopy under 254 nm, 365 nm and white light (15W) in air. This does not indicate the nature of the products of decolouration, but it is close to solar/environmental levels of UV illumination [13]. Dividing the photocatalytic rate (mmol MO/mg catalyst/s) by the extent of MO adsorption (mmol MO/mg) gave the turnover frequency (TOF) in s<sup>-1</sup> [16]. Some use the turnover rate for photocatalytic reactions [17]. The absorption edge of the biomimetic photocatalysts and replicas was compared to that of rutile (3.0eV; 415nm) and anatase (3.2eV; 380nm).

## 2. Characterization Results

TEM analysis (see Figure 2) of the Au-TiO<sub>x</sub>/PMS and Ag-TiO<sub>x</sub>/PMS showed the Au and Ag NPs 2-10nm in diameter in the wall of the PMS surrounded by TiO<sub>x</sub>. Their nanocrystalline nature was confirmed by the selected area electron diffraction (SAED) pattern with bright circular spots. The lattice fringe spacing for Au-TiO<sub>2</sub> NPs is 0.23nm and 0.27nm corresponding to (111). Further, the (200), (220), (222) and (311) planes of the face central cubic lattice of Au NPs confirm that Au NPs are nanocrystalline. EDX suggested that Au-TiO<sub>x</sub>/PMS contained 7.7at %Ti and 92.3at %Au. In the future this ratio will need to be changed to raise the TiO<sub>x</sub> content.

Table 1 shows that absorption edges of Ag/PMS and Au/PMS move to higher wavelength (i.e. towards the visible) compared to P25, but not when TiO<sub>x</sub> is present. This is beneficial in a solar-environmental sense (i.e. photocatalytic activity under visible light irradiation might be enhanced).

Some have seen a clear correlation between extents of adsorption and rates of photocatalysis on TiO<sub>2</sub>/carbon [18]. Others [19] have looked at the adsorption of MO on P25 and biosorbents; of course here the biotemplate is the biosorbent. A correlation exists between extents of MO adsorption and rates of its photodegradation [20]. P25 adsorbs 16% of MO (when 10mg MO/L and 1g P25/L are used). The adsorption of MO took 1-2h to reach equilibrium; extents of adsorption are also shown in Table 1 [20]. Here the overcoats raised the MO adsorption capacity of PMS by ~300x over that for P25 (4.9 $\mu$ mol/g) [20].

## 4. Photocatalytic Results

Figure 3 shows that the % photocatalytic removal from aqueous solution is higher for Au-TiO<sub>x</sub>/PMS and the Au-TiO<sub>2</sub> (PMS) replica than P25, however the weight of catalyst used varies. Table 2 compares the rates of MO removal from a 0.1mM solution as measured using MO absorbance (464nm) changes. One expected to see plasmonic Ag and Au NPs in combination with semiconductors TiO<sub>2</sub>/PMS offering a new generation of the photocatalysts, but the evidence of this is equivocal. It may be that the chemical communication between the NPs and the TiO<sub>x</sub> is poor, or that TiO<sub>2</sub> has yet to be formed by calcination. On this point, it is clear that pre-calcination to produce TiO<sub>2</sub> replicas gave superior photocatalytic activity. Presumably this is due to their nanocrystalline structure and their hierarchical structure left by the PMS biotemplate/reducing agent. It is possible that the product hollow structure has good specific surface area and probably facilitates multiple reflections of incident light. In addition one sees photocatalytic activity decreasing in the order (but rate constants increasing) Au-TiO<sub>2</sub> (PMS) > Ag-TiO<sub>2</sub> (PMS) > TiO<sub>2</sub> (PMS).

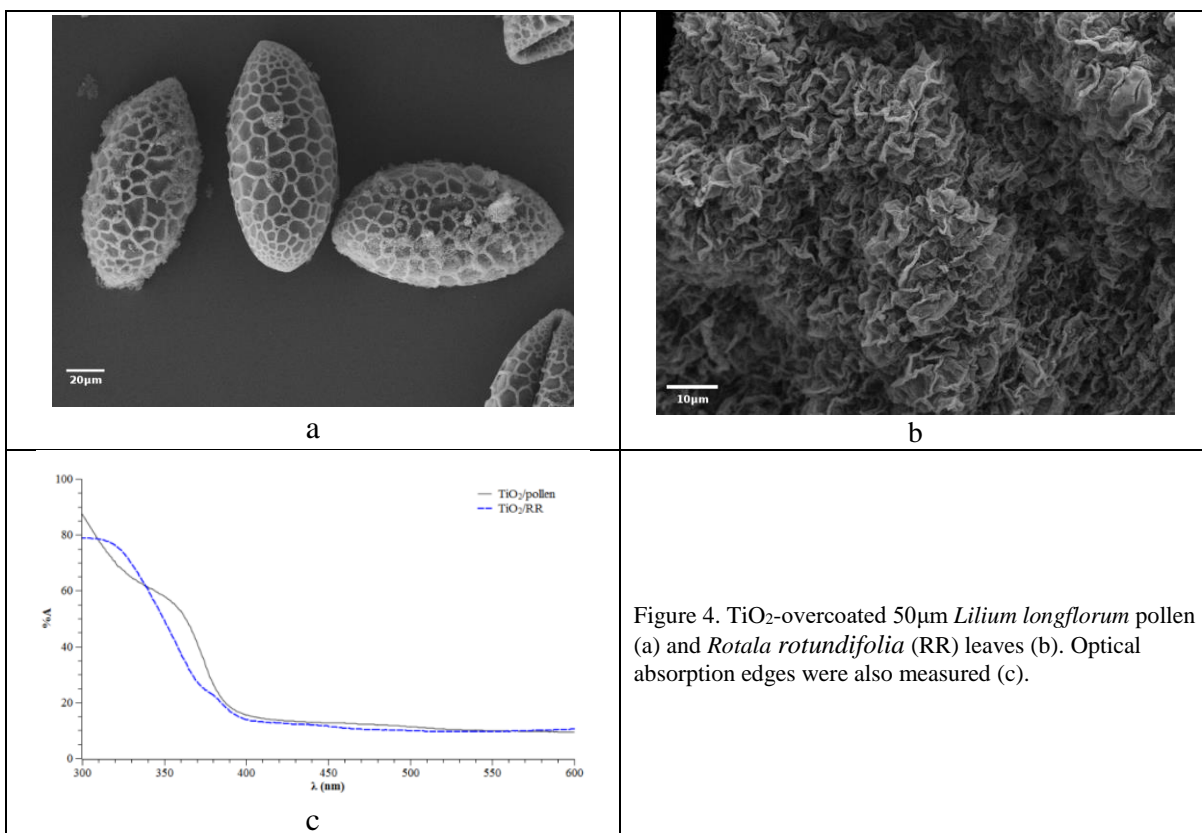
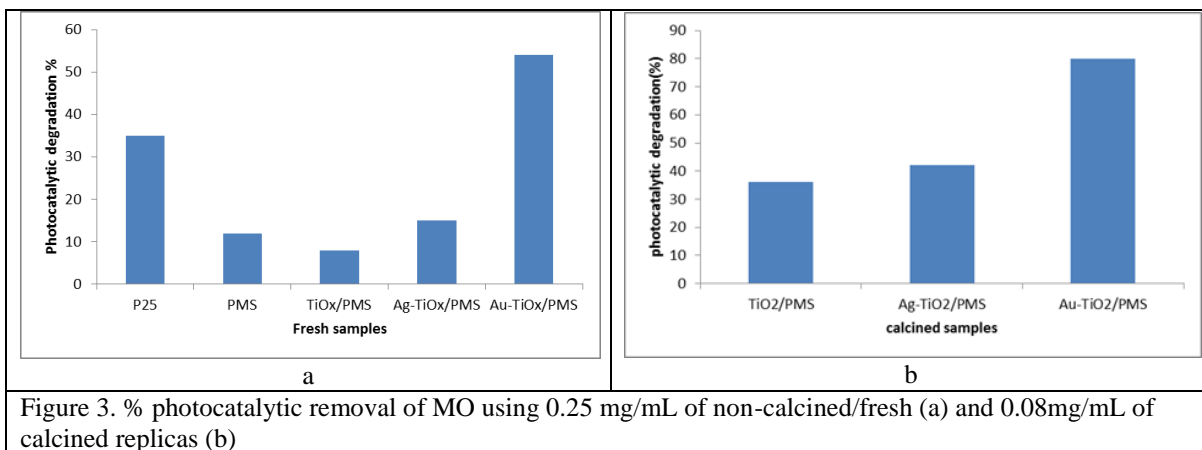




Table 1. Absorption edges ( $\lambda_{\max}$  (nm)) and MO adsorption capacities (n; molecules MO x  $10^{14}$  /mg)

	TiO <sub>x</sub> /PMS	Ag/PMS	Ag-TiO <sub>x</sub> /PMS	Au/PMS	Au-TiO <sub>x</sub> /PMS	P25
$\lambda_{\max}$ (nm)	336	416	333	518	373	
n	89.33		72.00		96.00	0.29 [20]

Table 2. Rates and first-order rate constants of MO removal from 0.1mM aqueous solutions and derived TOFs

Sample	Molecules MO x $10^9$ /mg/s	$k_1$ (min <sup>-1</sup> ) x $10^3$	TOF x $10^5$ (s <sup>-1</sup> )
P25	132	157.7	455.00
PMS	3205	92.7	
TiO <sub>x</sub> /PMS	1748	211.4	19.57
Ag-TiO <sub>x</sub> /PMS	1370	142.8	19.03
Au-TiO <sub>x</sub> /PMS	6090	51.2	63.44
TiO <sub>2</sub> (PMS)	6700	471.2	
Ag-TiO <sub>2</sub> (PMS)	13889	436.1	
Au-TiO <sub>2</sub> (PMS)	11111	355.6	

### 5. Turnover Frequency (TOF), Discussion and Conclusions

The % MO photocatalytic removal is higher for Au-TiO<sub>x</sub>/PMS and Au/TiO<sub>2</sub> (PMS) replicas than for P25, but then measurements are at different catalyst concentrations. Dividing the rate of photocatalytic removal of MO (molecules x  $10^9$ /mg/s) from water in Table 2 by the extent of MO adsorption (n) from Table 1 (molecules MO x  $10^{14}$ /mg) allows one to calculate the TOF [16]. Clearly the TOFs are modest, but for the biomimetic replicas have TOFs that decrease in the order Au-TiO<sub>2</sub> (PMS) > TiO<sub>2</sub> (PMS) > Ag-TiO<sub>2</sub> (PMS) and at their highest are just a factor of x7 lower than for P25 anatase-rutile. This is promising. At present the authors are working on other biotemplates (*Lilium longiflorum* pollen and *Rotala rotundifolia* leaves) and their overcoating with TiO<sub>2</sub> (see Figure 4a,c). However, their absorption edges (see Figure 4c) will need to be raised if they are to be used in sunlight. These may additionally be templated by the target organic water pollutants (e.g. to produce molecular recognition. Such target pollutants include alkylphenol ethoxylates (e.g. TX100) that are endocrine disrupters. Brunel has a strong record in investigating these oestrogen-mimicking pollutants.

### 6. Acknowledgements

The authors gratefully acknowledge sponsorship of IAJAT from Basrah University & the Iraqi Ministry of Higher Education and Scientific Research.

### 7. References

- [1] Paraskeva, P. and Graham, N.J.D. 'Ozonation of municipal wastewater effluents' Water Environ.Res. 74,569-581 (2002)
- [2] Ayling, G. and Castrantas, H. 'Waste treatment with hydrogen peroxide' Chem.Eng. 88,(24),79-82 (1981)
- [3] Ince, N.H., Tezcanli, G., Belen, R.K. and Apikyan, I.G. 'Ultrasound as a catalyser of aqueous reaction systems: the state of the art and environmental applications' Appl.Catal. 29B,167-176 (2001)
- [4] Sabin, F., Turk, T. and Vogler, A. 'Photooxidation of organic compounds in the presence of titanium dioxide – determination of the efficiency' J.Photochem.Photobiol. 63A,99-106 (1992)
- [5] Vena, M.P., Jobbagy, M. and Bilmes, S.A. 'Microorganism mediated biosynthesis of metal chalcogenides; a powerful tool to transform toxic effluents into functional nanomaterials' Sci.Tot.Environ. 565,804-810 (2016)

- [6] Zhang, D.P. et al 'A bio-inspired inner-motile photocatalyst film: a magnetically actuated artificial cilia photocatalyst' *Nanoscale* 6,5516-5525 (2014)
- [7] Yang, Z.H., Yan, S.X., Zhang, Z.Y. and Li, N.X. 'Photocatalytic degradation of bisphenol A in water using a visible light-activated biomimetic catalyst' *Fres. Environ. Bull.* 23,523-530 (2014)
- [8] Chen, L.Q. et al 'Photocatalytic properties and electrochemical characteristic of a novel biomimetic oxygenase enzyme photocatalyst iron(II) tetrahydroxymethyl tetra(1,4-dithiin) porphyrazine for the degradation of organic pollutants' *J.Molec.Catal.* 372A,114-120 (2013)
- [9] Sakai, M., Kato, T., Ishizuka, N., Isobe, T., Nakajima, A. and Fujishima, A. 'Bio-inspired highly hydrophobic surface with ecdysis behavior using an organic monolithic resin and titanium dioxide photocatalyst' *J.Sol.Gel Sci.Technol.* 77,257-265 (2016)
- [10] Li, W.T., Pei, X.L., Deng, F., Luo, X.B., Li, F.C. and Xiao, Y. 'Bio-inspired artificial functional photocatalyst: biomimetic enzyme-like TiO<sub>2</sub>/reduced graphene oxide nanocomposite with excellent molecular recognition ability' *Nanotech.* 26,AR175706 (2015)
- [11] Zhang, G.H., Zhang, T.Y., Li, B., Zhang, X. and Chen, X.W. 'Biomimetic synthesis of interlaced mesh structures TiO<sub>2</sub> nanofibers that have a unique hierarchical mesh with enhanced photocatalytic activity' *J.Alloys.Comp.* 668, 113-120, (2016)
- [12] Zhou, H., Fan, T.X., Li, X.F., Zhang, D., Guo, Q.X. and Ogawa, H. 'Biomimetic photocatalyst system derived from the natural prototype in leaves for efficient visible-light-driven catalysis' *J.Mater.Chem.* 19,2695-2703, (2009)
- [13] Wang, X.F., Fu, C., Wang, P., Yu, H.G. and Yu, J.G. 'Hierarchically porous metastable  $\beta$ -Ag<sub>2</sub>WO<sub>4</sub> hollow nanospheres: controlled synthesis and high photocatalytic activity' *Nanotech.* 24, AR 165602, (2013)
- [14] Cheng, Y., Courtney, L. and Sermon, P.A. 'Novel routes to stable bio-templated oxide replicas' *Dev.Porous. Biol.Geopolym.Ceram.* (ed.Brito, M., Case, E. and Kriven, W.M.) 28,209-218 (2008)
- [15] Luo, Y., Liu, X.Y. and Huang, J.G. 'Nanofibrous rutile-titania/graphite composite derived from natural cellulose substance' *J.Nanosci.Nanotechnol.* 13,582-588 (2013)
- [16] Boudart, M. 'Turnover rates in heterogeneous catalysis' *Chem.Rev.* 95, 661-666 (1995)
- [17] Guesh, K., Marquez-Alvarez, C., Chebude, Y. and Diaz, I. 'Enhanced photocatalytic activity of supported TiO<sub>2</sub> by selective surface modification of zeolite Y' *Appl.Surf.Sci.* 378,473-478 (2016)
- [18] Liu, C., Xu, P., Li, M. and Zen, M. 'Controlled fabrication of ordered mesoporous titania/carbon fiber composites with high photoactivity: Synergistic relationship between surface adsorption and photocatalysis' *Chem.Eng.J.* 243,108-116 (2014)
- [19] Yu, J-X., Chi, R-A., He, Z-Y., Qi, Y-F., Zhan, G. and Guo, J. 'Combination of biosorption and photodegradation to remove methyl orange from aqueous solutions' *Eng.Life Sci.* 11,309-315 (2011)
- [20] Lazar, M.A. and Daoud, W.A. 'Selective adsorption and photocatalysis of low-temperature base-shifted anatase nanocrystals' *RSC Adv.* 2,4470452 (2012)

## Paper two

# Nanoengineering the antibacterial activity of biosynthesized nanoparticles of TiO<sub>2</sub>, Ag and Au and their nanohybrids with Portobello mushroom spores (PMS) (TiO<sub>x</sub>/PMS, Ag/PMS and Au/PMS) and making them optically self-indicating

Iman A. Jaaffer Al-Timimi and Paul A. Sermon\*

Nanomaterials Laboratory, Wolfson Centre, Brunel University, Uxbridge, Middlesex, UB8 3PH, UK

Ahmed A. Burghal, Afrodet A. Salih and Inaam M. N. Alrubaya  
Basrah University, College of Science, Iraq

### Abstract

Results show that nanoparticles (NPs) can be biosynthesized at room temperature on the reductive and chelating surfaces of Portobello mushroom spores (PMS). Using this green approach TiO<sub>x</sub>, Ag, Au, Ag-TiO<sub>x</sub> and Au-TiO<sub>x</sub> NPs have been prepared. These were characterized by TEM, SIMS and  $\mu$ FTIR-FTIR. TiO<sub>x</sub>/PMS, Ag-TiO<sub>x</sub>/PMS, Au-TiO<sub>x</sub>/PMS and Ag/PMS were active in bacterial inhibition towards *Escherichia coli* and *Staphylococcus aureus*, but Au/PMS was not active (suggesting a strong Au-PMS interaction). TiO<sub>x</sub>/PMS, Ag/PMS and Ag-TiO<sub>x</sub>/PMS were equally active in an antibacterial and an antifungal sense when tested against *Asperillus* and *Candide*. All samples (except Ag-TiO<sub>x</sub>/PMS and Au-TiO<sub>x</sub>/PMS) showed an interesting interaction with DNA. We report on the process of fine-tuning these antibacterial properties, progress on making these nanomaterials optically self-indicating and movement towards optical control of their antibacterial activity. Au-TiO<sub>x</sub>/PMS shows a surface plasmon resonance (SPR) with a maximum at 518 nm that might be useful in following its anti-bacterial properties (i.e. making the bionanomaterial self-indicating). The future of such green bio-nanomaterials is strong.

Keywords: mushroom, spores, gold, silver, titania, *Escherichia coli*, *Staphylococcus aureus*, *Asperillus*, *Candide*, DNA

## 1. Introduction

Nanomaterials are used in bone/tissue engineering [1]. Just as importantly, they are also needed to control infections [2] associated with MRSA, antibiotic-resistant bacteria [3] and multi-drug resistant *Staphylococcus aureus* [4]. Microbial infections have become a global health problem, with antibiotic-resistant genes (ABG) and antibiotic-resistant bacteria (ARB) emerging.

It is well established antimicrobials include 5-40nm Ag nanoparticles (NPs) [4] that may be biosynthesized by green routes from

- (i) *Chlorella vulgaris* microalgae cells [5]
- (ii) *Centella asiatica* extract [6]
- (iii) *Arnicae anthodium* extract [7] or
- (iv) *Phlomis bracteosa* plants [8]

In the last case FTIR showed that the polyphenols were mainly responsible for reduction and capping of synthesized Ag NPs were shown to be formed by their characteristic surface plasmon resonance (SPR) peak at 453 nm and TEM. Biomimetic Ag-oxide nanomaterials [9], nanopatterned surfaces [10] and bio-NP composites [11] are also interesting in an antimicrobial sense, as are bioactive Ti-oxide surfaces [12]. It therefore seemed appropriate to investigate PMS-derived Ag NPs, Au NPs and TiO<sub>x</sub>/PMS, Ag/PMS and Au/PMS.

It also seemed suitable to test these against gram positive *Staphylococcus aureus* and gram negative *Escherichia coli* [5,13]; here we wished to measure the diameters of zones of inhibition (mm) on agar plates as previously [8], while also characterizing where the NPs were in relation to the PMS cell wall using TEM [4]. The authors appreciate that anti-microbial strains, that are resistant to conventional anti-microbial agents, have appeared and some agents are unable to access cell membranes, restricting treatment of intracellular pathogens and causing side effects [14,15]. The authors now report a preliminary study of the antimicrobial and antifungal activity of some green Portobello mushroom spore (PMS)-derived NPs in the hope that work at the bio-nanomaterials interface may prove useful.

## 2. Antimicrobial Mechanisms

Bacteria can be classified depending on the structure/functional components of the cell wall into:

- (iii) Gram-positive bacteria (e.g. *Staphylococcus aureus* (*S.aureus*)) whose cell walls contain a thick surrounding layer (20-50 nm) of peptidoglycan (PG) which is attached to specific acids [15] and
- (iv) Gram-negative bacteria (e.g. *Escherichia coli* (*E.coli*)) which is more chemically-structurally complex; here the PG layer is thin and the cell wall tends to be negatively charged [16], with outer membrane containing lipopolysaccharides [53].<sup>17</sup>

Anti-bacterial agents can be (a) bactericidal (killing bacteria) and (b) bacteriostatic (slowing bacterial growth [53]). The mechanism of antibiotic resistance may be innate or may involve prevention of the antibiotic from penetrating the bacterial cell wall or hydrolysis/modification/degradation/inactivation of the antibiotic [18,19].

Most anti-microbial agents exhibit inhibition, affect DNA/RNA synthesis, affect the cell membrane or damage the proteins in the cell [14].

With the development of biomedical nanomaterials, safer and alternative anti-microbial agents have started to emerge; these may be unique or may increase the activity of the conventional anti-microbial agents [19]. Treatment strategies include: (i) photo-disinfection with OH<sup>·</sup> [344], (ii) UV-disinfection at say 264 nm [344], (iii) photo-catalytic disinfection when reactive oxygen species (O<sub>2</sub><sup>-</sup>, ·OH or O<sub>2</sub><sup>-</sup>) are generated [344] (e.g. with TiO<sub>2</sub>/H<sub>2</sub>O) [344] and (iv) nanoparticle disinfection. Nanomaterials can be expected to become more important due to their unique chemical [346], mechanical [347], catalytic [348], electrical, magnetic, optical and biological properties [349]. Such properties make NPs powerful tools for vast and diverse applications (e.g. anti-microbial, diagnosis, imaging, and thereby drug delivery (because NPs provide unprecedented opportunities to molecular process and interrogate cellular clinical application [350])). NPs have recently emerged as unique anti-microbial agents due to their shape, size and high surface area to volume ratio; NPs are of the same dimensions as proteins, nucleic acid, membrane of receptors, antibodies and other biomolecules [351].

Antimicrobial NPs [26] operate by mechanisms that are similar (but slightly different due to their different chemical properties, and their size, surface area, shape, crystallinity, charge, surface energy, chemical composition and aggregation [45]). Such NP properties govern their interaction with/in living cells and the way in which they (i) damage or disrupt the integrity of bacterial membrane, (ii) change the microbial cell wall and nucleic acid pathway, (iii) block the enzyme pathway, and (iv) destruct the cell membrane [46]. Conversely, the cytoplasm of Gram-negative bacteria is a strong reducing environment that can affect the oxidation state for metal NPs [26].

Relevant antimicrobial NPs include (i) TiO<sub>2</sub> that have weak mutagenic potential, but are lethal to *S.aureus* and *E.coli* under UVC in 60 min [19,26], (ii) plasmonic Ag and Au that are chemically stable, non-toxic to human cells, biocompatibility [16] and exhibit localized surface plasmon resonance (LSPR) [36] and colour due to the coherent excitation of all free-electrons with the conduction band causing (SPR) an in-phase oscillation [29].

Ag NPs when coated onto a filter for water purification or coated onto medical devices or in dental resin components reduce infection [27] and can be employed in wound healing and can control vector transmitted infection [14] because they react with biomolecules (like DNA, RNA or enzymes during an electron- release mechanism) weakening DNA replication, combine with proteins (causing denaturation and inactivating them by reducing bacterial proteins levels [30]) and interact with P- or S- containing compounds (like DNA leading to damage the cell wall) and may attach to the cell membrane surface and disturb respiration and permeability [17,29]. Au NPs have a large number of atoms available to attach to the surface of bacteria [31,32].

Biosynthesized Au NPs are promising for many medical applications such as anti-tumor, labeling, imaging, apoptosis and interaction with DNA [33]. They also show good biocompatibility, being compatible with human body cells and being resistance to corrosion [34]. Au NPs show a significant anti-bacterial activity depending on their size and shape and also the type of bacteria [24]. They strongly bind to the bacterial cell wall, allowing them to disrupt the bacterial cell membrane, causing leakage of nucleic acids and cytoplasm [17,35], induce photo-mutagenic processes causing damage to DNA and essential proteins [15], increase in ATP (where ATP generation is a significant part in the respiration chain of bacteria via the  $\text{NAD}^+/\text{NADH}$  reaction) intercellular ATP levels, leading to bacterial death and catalyze oxidation reactions, producing ROS that lead to the death of bacteria [35].

Ag-TiO<sub>x</sub> and Au-TiO<sub>x</sub> nanohybrids show strong anti-microbial activity due to their multi-functionality, e.g. Ag-TiO<sub>2</sub> and Au-TiO<sub>2</sub> NPs exhibit excellent anti-microbial action [36]. Recently, in green bio routes have been used to synthesis NPs (fungi, bacteria, and plants) [32,33] that may have interesting anti-microbial activity.

### 3. Experimental

#### 3.1 Materials

Fresh Portobello mushrooms were harvested. Reagents titanium(iv) isopropoxide  $\text{Ti}(\text{OC}_3\text{H}_7)_4$  (ACROS organics; 98%), ethanol (Sigma Aldrich; 99.9%), 2-propanol (Fluka; 99.9%; IPA),  $\text{AgNO}_3$  (Fisher chemical; >99%), gold (III) chloride hydrate ( $\text{AuCl}_3 \cdot x\text{H}_2\text{O}$ ; Sigma Aldrich; 99.9%) were used as received. Two bacterial strains (pathogenic) were used during the testing: *Staphylococcus aureus* (Gram positive) and *Escherichia coli* (Gram negative). In addition *Aspergellis* and *candida* were used.

#### 3.2 Instruments

FTIR spectra were recorded on an IR-affinity-1 (Shimadzu) with ATR.  $\mu$ -FTIR was undertaken on an FT-IR spectrometer (Perkin Elmer, Spotlight 300). Surface morphology and particle size were examined by scanning electron microscopy (SEM, Supra35 VP) with EDX after Pt or Au coating. Transmission electron microscopy (TEM, Jeol 2100f, field emission gun (FEG) was used to assess morphology and particle size using a Gatan camera/imaging software (Gatan microscopy suite, version 3). Secondary ion mass spectrometry (SIMS, Kore z-7861-M on a silica wafer) was used to investigate surface composition. Ag, Au and TiO<sub>2</sub> nanoparticles were characterized by UV-Vis spectroscopy (Perkin Elmer Lambda 650s).

#### 3.3 Preparations

A 3mM solution of  $\text{Ti}(\text{OC}_3\text{H}_7)_4$  in 5 mL 2-propanol (IPA) was made up and filtered (0.22 $\mu\text{m}$ ). 4-5 mg Portobello mushroom spores (PMS) were washed twice with water and acetone respectively and were then dispersed in 5 mL water and added with magnetic stirring (1-2h) to give TiO<sub>x</sub>/PMS.

PMS (4-5mg) was dispersed in 5 mL water (ultrasonic bath for 15 min). At this point, 5 mL of aqueous 3mM  $\text{AuCl}_3$  solution was added with magnetic stirring at 298K. The pH of the suspensions was 1.4 and adjusted to around 9 - 10 by adding NaOH (0.1 and 0.01M). These Au NP sols were left for 3h under magnetic stirring to give Au/PMS. The colour of the solution changed after 1-3h. The same steps were used to prepare Ag/PMS using 3mM of  $\text{AgNO}_3$ .

Ag-TiO<sub>x</sub>/PMS nanohybrid was prepared by ultrasonically dispersing 4-5 mg of PMS in 5mL water for 15min. Then, 5mL of aqueous  $\text{AgNO}_3$  (3mM) were added to the PMS dispersion with magnetic stirring at 298K for 3h. The Ag/PMS was left overnight. Then to 5mL of Ag NPs/PMS was added  $\text{Ti}(\text{OC}_3\text{H}_7)_4$  (3mM) in IPA with magnetic stirring for 3h. The same steps were used to prepare Au-TiO<sub>x</sub> NPs/PMS in IPA.

#### 3.4 Bio-activity Measurements

Antibacterial activity was determined in duplicate using Mueller Hinton agar. PMS and NP/PMS samples were dispersed in (and diluted with) IPA or H<sub>2</sub>O. The antibacterial activity of NPs/PMS was assessed against two pathogenic bacteria species: *Staphylococcus aureus* (Gram positive) and *Escherichia coli* (Gram negative) in the agar well diffusion method. Overnight cultures were used. After 24 h of incubation, bacterial suspension (inoculum) was diluted with sterile physiological solution, for the diffusion test, to 10<sup>8</sup> CFU/mL (colon forming unit) (turbidity = McFarland barium sulfate standard 0.5) [37]. The control sets (IPA and H<sub>2</sub>O) were maintained at the same condition. The bacterial inoculums were uniformly spread using a sterile cotton swab on a sterile Petri dish containing agar. 50  $\mu\text{L}$  of the PMS or NP/PMS samples were added to each well (6 mm diameter holes cut in the agar gel, 20 mm apart from one another). The plates were incubated for 24 h

at 309K, under aerobic conditions. After incubation, confluent bacterial growth was observed. The diameter of the zone of inhibition can be measured in mm [37].

In the agar diffusion disc-variant measurements, NP/PMS were dispersed in (and diluted with) IPA and were used to impregnated 6 mm filter paper discs (Whatman no. 2) to a loading of 10 $\mu$ L or mg.m<sup>-2</sup>. The discs were maintained at 298K until evaporation was complete and were then kept under refrigeration until the test, when they were placed onto the surface of the agar and incubated overnight at 309 K, at which point the zones of bacterial inhibition were recorded. These measurements were in duplicate [38]. In anti-fungal activity measurements, the NP/PMS samples were assessed against two pathogenic fungi species: *Aspergellis* and *candida* using an agar diffusion disc method. Here the plates were incubated for 72 h at 309 K under aerobic conditions. After incubation, confluent fungi growth was observed. The radii of the regions of inhibition of the fungal growth were again measured (mm); again tests were performed in duplicate [38].

Consideration was also given to PMS and NP/PMS interaction with DNA in a genomic DNA extraction measurement. Nucleic acids from each 200  $\mu$ L of EDTA-whole blood sample were extracted (after cell lysis and protein denaturation according to the procedure 28) and stored frozen (253K) until required. The concentrations of extracted DNA were measured by NanoDrop ND-1000 spectrophotometer that measured absorbance of DNA, RNA, protein and dye at 220-750 nm [39]. 1.5 $\mu$ L of DNA was assessed at 260nm to determine DNA concentration and the optical density (OD) ratio [39]. To study the effect of/on PMS-based samples on genomic human DNA, 10  $\mu$ L of each sample was mixed with 10  $\mu$ L of human genomic DNA. The mixture incubated at 310K for 1 h, then the absorbance of mixture was measured at 260 nm [39] and the DNA concentration was thereby assessed.

## 4. Characterization Results

### 4.1 SIMS (see Table 1)

The positive SIMS for PMS and TiO<sub>x</sub>/PMS showed some intense peaks. PMS peaks at 28, 45 and 68 m/z are decreased in intensity as a result of TiO<sub>x</sub> coating, while peaks at 63 and 64 m/z related to TiO<sup>+</sup> and TiOH<sup>+</sup> respectively appeared. The PMS ion fragments need to be related to surface functional groups seen in FTIR (Table 2).

### 4.2 SEM and TEM

Figures 1-5 illustrate the hollowed oval-shaped morphology of 5 $\mu$ m-sized PMS that was similar to red blood cells and the location of the 10-20nm sized pseudo-spherical discrete Ag and Au NPs and the TiO<sub>x</sub> overlayers in the cell walls. The PMS shape is not changed by heating at 373K, apart from an increase on some concave/convex curvature on fluid loss. When fractured, the cell walls appeared to be ~252 nm thick (i.e. able to accommodate many 10-20nm-sized NPs). Clearly, the Ag and Au NPs were biosynthesized by the functional groups in the PMS cell wall and remain fixed there.

Table 1. Comparison of the intensities of some positive SIMS peaks for the PMS and TiO<sub>x</sub>/PMS.

m/z peak	SIMS intensity for PMS	SIMS intensity TiO <sub>x</sub> /PMS produced from 0.03mM alkoxide solution	Chemical assignment
15	1200	---	CH <sub>3</sub> <sup>+</sup>
23	10000	---	Na <sup>+</sup>
28	50000	14000	C <sub>2</sub> H <sub>x</sub> <sup>+</sup>
29	15000	---	K <sup>+</sup>
40	4000	---	Ca <sup>2+</sup>
45	7500	2000	C <sub>2</sub> H <sub>5</sub> O <sup>+</sup>
63	---	175	TiO <sup>+</sup>
65	---	240	TiOH
68	1400	75	C <sub>x</sub> H <sub>y</sub> O <sup>+</sup>

Table 2. Functional groups seen in PMS samples with FTIR

Functional group	O-H	N-H	C-H	C=O	C-O	C-N	P-C-O
wavenumber (cm <sup>-1</sup> )	3493	3340	2912-2850	1745,1622	1369	1064	1100

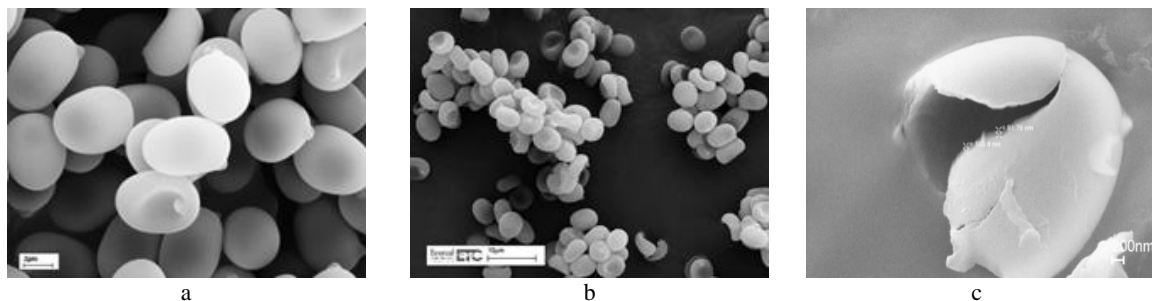


Figure 1. SEM of PMS (a) held at 298K (scale bar=2 $\mu$ m), (b) heated at 373K (scale bar=10 $\mu$ m) and (c) fractured PMS

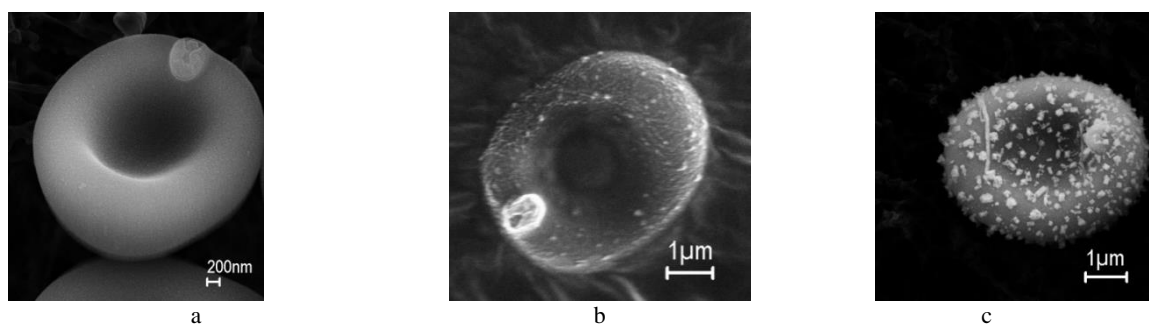


Figure 2. SEM of (a) Au-TiO<sub>x</sub>/PMS<sub>IPA</sub>, (b) Ag-TiO<sub>x</sub>/PMS<sub>IPA</sub> and (c) Au-TiO<sub>x</sub>/PMS<sub>H2O</sub>

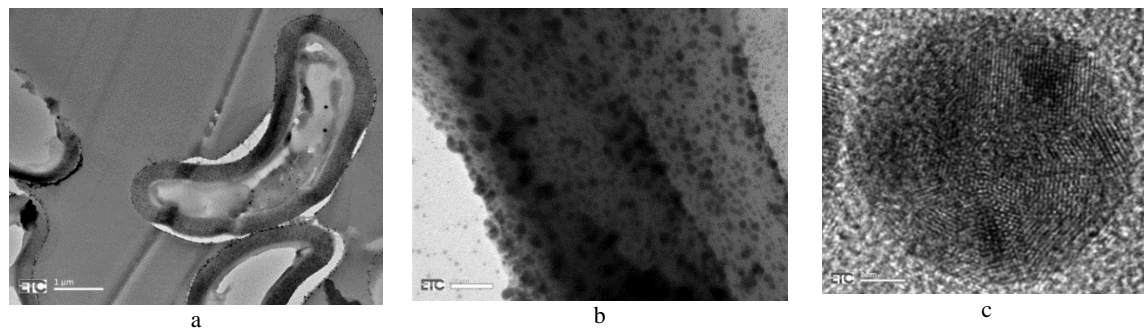


Figure 3. TEM of whole Ag/PMS (a), surface of Ag/PMS (b) and Ag NP within the cell wall of Ag/PMS (c)

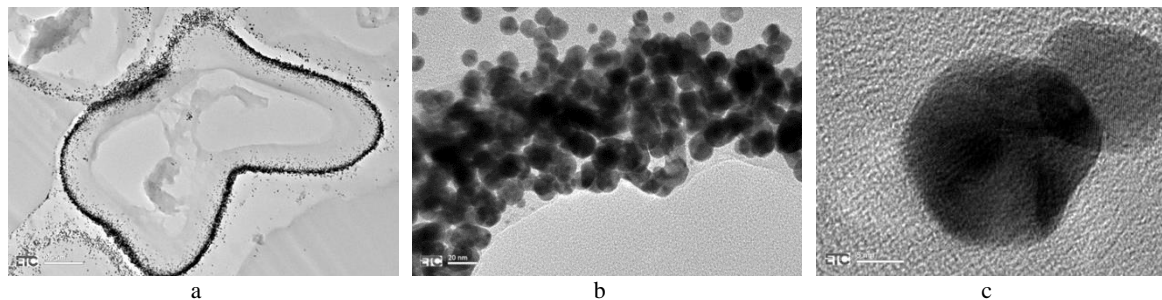


Figure 4. TEM of whole Au/PMS (a), surface of Au/PMS (b) and Au NP within the cell wall of Au/PMS (c)

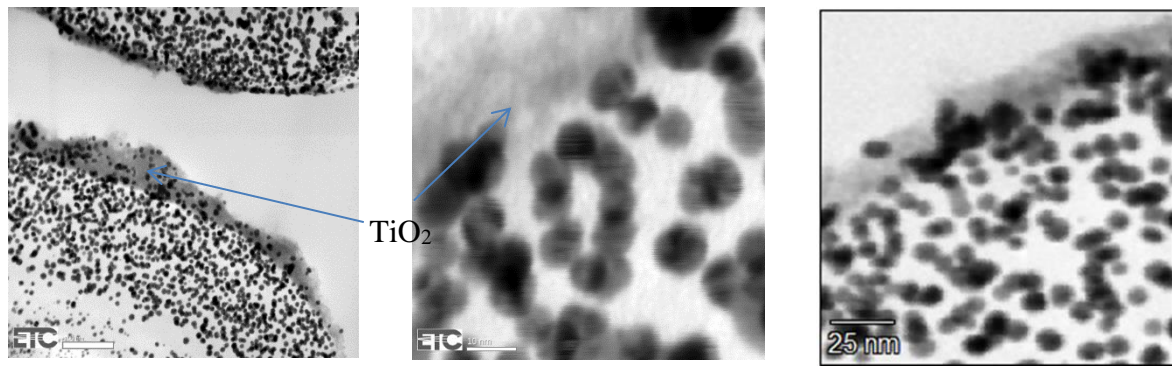


Figure 5. TEM of Au NPs and  $\text{TiO}_x$  layers in the cell walls of Au- $\text{TiO}_x$ /PMSIPA.

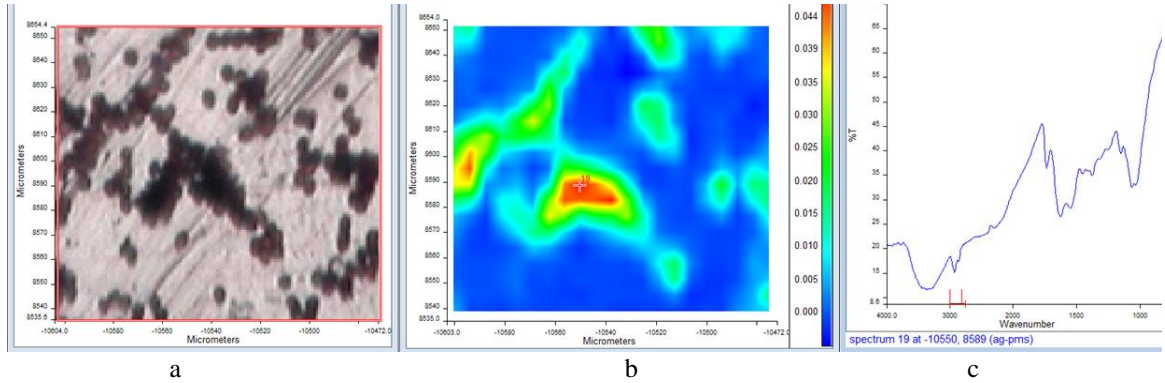


Figure 6. Optical image (a) and total absorbance (b) in  $\mu\text{FTIR}$  and FTIR (c) for Ag/PMS

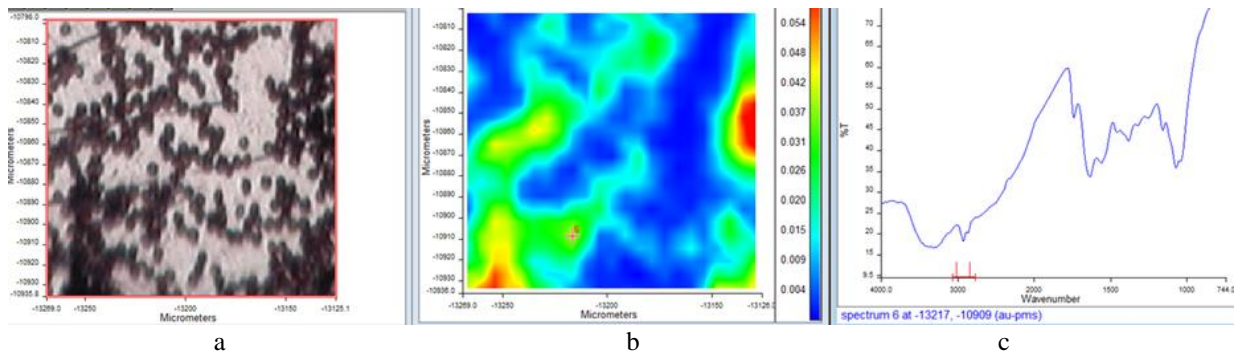


Figure 7. Optical image (a) and total absorbance (b) in  $\mu\text{FTIR}$  and FTIR (c) for Au/PMS

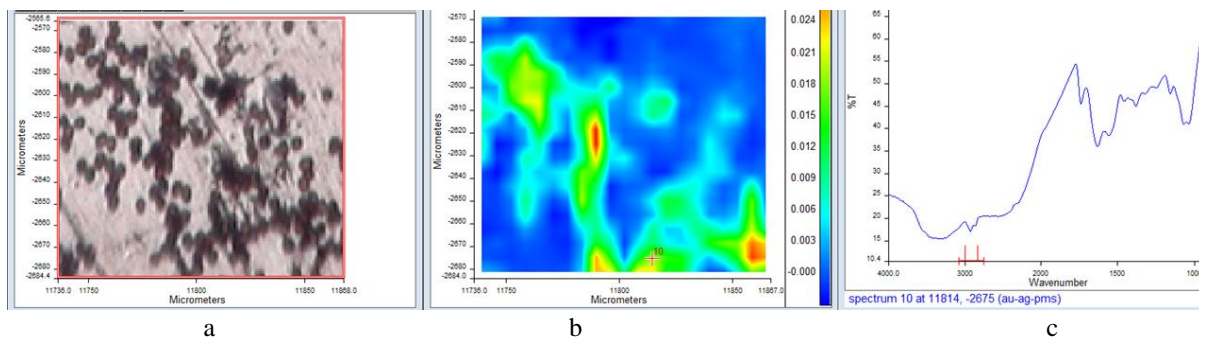


Figure 8. Optical image (a) and total absorbance (b) in  $\mu\text{FTIR}$  and FTIR (c) for Au-Ag/PMS



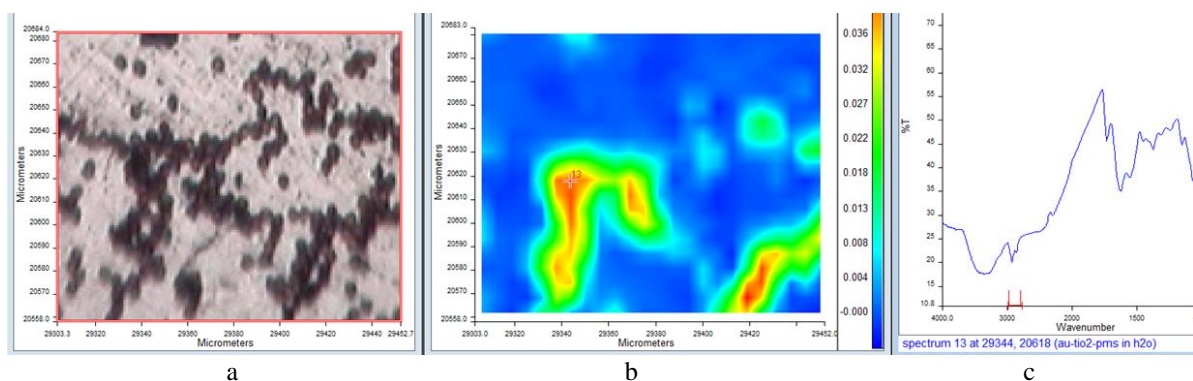


Figure 9. Optical image (a) and total absorbance (b) in  $\mu$ FTIR and FTIR (c) for Au-TiO<sub>x</sub>/PMS

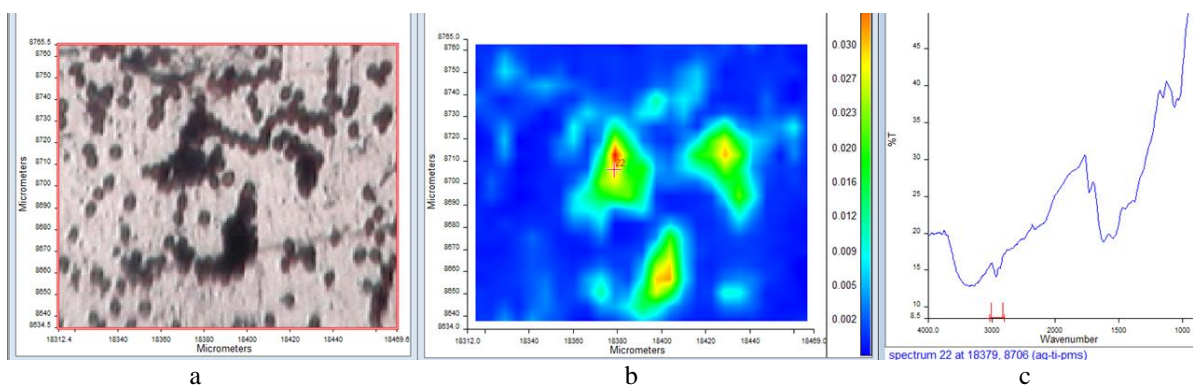


Figure 10. Optical image (a) and total absorbance (b) in  $\mu$ FTIR and FTIR (c) for Ag-TiO<sub>x</sub>/PMS

#### 4.3 Micro-FTIR ( $\mu$ FTIR) and FTIR (Figures 6-10 and Table 2)

Figure 6-10 show optical images,  $\mu$ FTIR and FTIR of Ag/PMS, Au/PMS, Au-Ag/PMS, Au-TiO<sub>x</sub>/PMS and Ag-TiO<sub>x</sub>/PMS.  $\mu$ FTIR allows mapping of chemical functional group mapping in PMS. Figures 6b-10b show some heterogeneity in the total absorbance of microbiological samples (4000-700  $\text{cm}^{-1}$ ). Figures 6-10c show variations in the absorption bands of hydroxyl, carbonyl and amino groups in FTIR spectra of these samples at 1369  $\text{cm}^{-1}$  (C-O) and 1064  $\text{cm}^{-1}$  (C-N). These may be responsible for the reduction of the chloroaurate ions ( $\text{AuCl}_4^-$ ) and silver ions, along with saccharides, thereby biosynthesizing NPs [40].

### 5. Anti-microbial and Anti-fungal Activity Results

Tables 3 and 4 show that IPA,  $\text{Au}^{3+}_{(\text{aq})}$  and  $\text{Ag}^{+}_{(\text{aq})}$  are active in inhibiting both gram positive (*Staphylococcus aureus*) and gram negative (*Escherichia coli*) bacteria, but not water or PMS alone. At the same time TiO<sub>x</sub>/PMS, Ag-TiO<sub>x</sub>/PMS, Au-TiO<sub>x</sub>/PMS and Ag/PMS in water are active in bacterial inhibition. In contrast, Au/PMS is not at all active. The inference must be that this is because there is a strong Au-PMS interaction arising from ready reduction of  $\text{Au}^{3+}_{(\text{aq})}$  by the PMS surface. Conversely there can be no free  $\text{Au}^{3+}_{(\text{aq})}$  after the interaction with dispersed PMS.

Table 5 shows the antibacterial and antifungal activity of five samples produced from a H<sub>2</sub>O suspension. Again Au/PMS was inactive (as in Table 3). Interestingly, Au-TiO<sub>x</sub>/PMS was active in inhibiting *E. coli* and *S. aureus*, but not at all active in inhibiting *Asperillus* and *Candide*. TiO<sub>x</sub>/PMS, Ag/PMS and Ag-TiO<sub>x</sub>/PMS on the other hand were broadly equally active in an antibacterial and an antifungal sense.

Table 6 shows how five PMS-based samples interacted with human blood DNA at 310K in light and dark conditions after samples had been separated into a PMS-sediment and a supernatant liquid. Data are shown as the % of the absorbance (260nm;  $A_{260\text{nm}}$ ) of the added DNA. In almost all supernatant liquid samples and PMS sediment samples (in light and dark conditions),  $A_{260\text{nm}}$  increased greatly beyond the level of the DNA added initially. The only samples that did not show this effect in the supernatant liquid were Ag-TiO<sub>x</sub>/PMS and Au-TiO<sub>x</sub>/PMS, but even then the PMS sediment did show an elevated  $A_{260\text{nm}}$ .

Table 3. Diameter (mm) of inhibition activity against *E.coli* and *S.aureus* by holes samples (9 mm diameter)

	controls			NPs/PMS in IPA			NPs/PMS in H <sub>2</sub> O		
	H <sub>2</sub> O	IPA	PMS	TiO <sub>x</sub> /PMS	Ag-TiO <sub>x</sub> /PMS	Au-TiO <sub>x</sub> /PMS	Au <sup>0</sup> /PMS	Ag <sup>0</sup> /PMS	Au <sup>0</sup> -Ag <sup>0</sup> /PMS
<i>E.coli</i>	0	15	0	15	16	20	0	13	11
<i>S.aureus</i>	0	13	0	18	17	17	0	15	12
NP or PMS concn (mg/100μL)	-	-	4	0.016	0.01/0.007	0.01/0.01	0.039	0.021	-

Table 4. Diameter (mm) of inhibition activity of precursor salts and ions Au against *E.coli* and *S.aureus* (9 mm diameter)

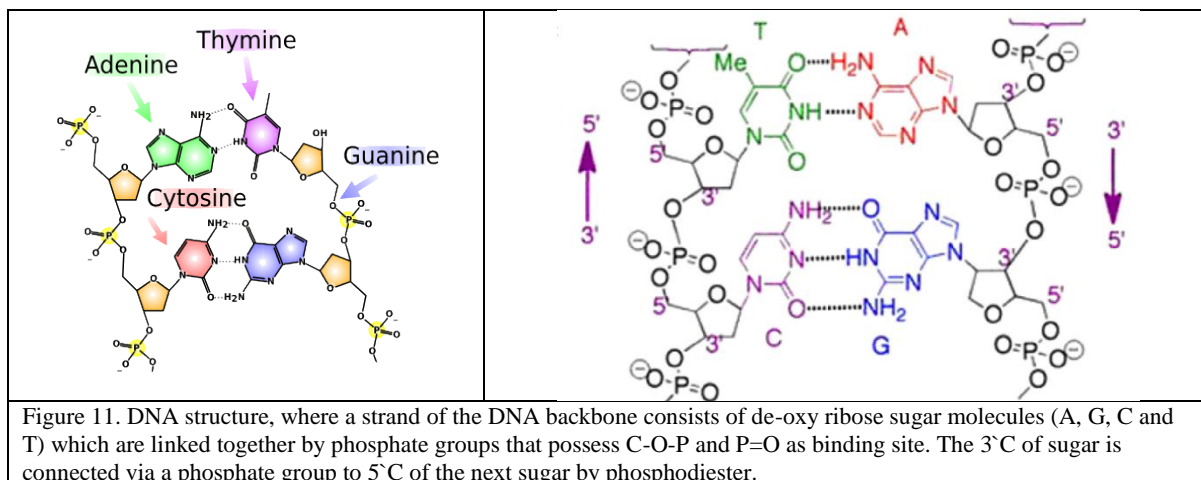
	salts in IPA			salts in H <sub>2</sub> O		
	Au <sup>3+</sup>	Ti <sup>4+</sup>	Ag <sup>+</sup>	Ag <sup>+</sup>	Au <sup>3+</sup>	
<i>E.coli</i>	19	19	24	14	15	
<i>S.aureus</i>	28	22	24	16	17	
Salt or ion concn (mg/100μL)	3.05	2.55	0.05	0.05	3.05	

Table 5. Diameter (mm) of inhibition activity (6mm diameter) of samples dispersed in H<sub>2</sub>O

	TiO <sub>x</sub> /PMS 8μg/50μL	Ag-TiO <sub>x</sub> /PMS 13-21 μg/50μL	Au-TiO <sub>x</sub> /PMS 42-130 μg/50μL	Au/ PMS 25 μg/50μL	Ag/ PMS 13μg/50μL
<i>E.coli</i>	9-7	10-9	8-9	0.00	9-11
<i>S.aureus</i>	20	8-10	7-7	0.00	9-8
<i>Aspergillus</i>	7	8	0.00	0.00	7-9
<i>Candide</i>	11	9-7	0.00	0.00	11-12

Table 6. Effect (%) on original human blood DNA in the light and dark in supernatant liquid about PMS samples and in PMS precipitates

	TiO <sub>x</sub> /PMS	Ag/ PMS	Au/ PMS	Ag-TiO <sub>x</sub> / PMS	Au-TiO <sub>x</sub> / PMS
Supernatant liquid/Dark	1048	133	216	89	50
PMS sediment/Dark	1278	214	294	229	460
Supernatant liquid/Light	659		228	659	194
PMS sediment/Light	917			229	1622



## 6. Discussion and Conclusions

The biosynthesis of NPs/PMS can be explained by an important factor: the nicotinamide adenine dinucleotide NADH and NADH dependent enzyme. The reduction appears to be started by electron transfer as an electron carrier from NADH- dependent enzyme. This process may play a key role in the biosynthesis and bio-transformation reactions<sup>[32]</sup>. The mechanism of formation of NPs/PMS may involve trapping of Ag or Au ions on the surface of PMS and electrostatic interaction between the positive charge of ions and negative charge of carboxylic and hydroxyl groups on the cell wall of PMS in basic solution<sup>[41]</sup>. Furthermore, PMS involves many functional groups and active compounds that can be reacted as both a reducing and capping agent<sup>[32]</sup> ( $\text{NADH} \rightarrow \text{NAD}^+ + \text{e}^-$ ). Proteins and polysaccharides play an important role in any reaction with metal ions, because of the  $\text{COO}^-$  and O-H groups which have a strong ability to chelate/react with Ag and Au ions. PMS contain many functional groups. For example, glucose has carbonyl groups which are highly polar ( $\text{C}^+-\text{O}^-$ ) and namely an aldehyde. This structure is flat (trigonal) and it can be that hydroxyl ions attack the carbonyl group. The mechanism of reaction in an alkaline environment ( $\text{pH} \geq 10$ ) occurs according to:  $2\text{Ag}^+ + -\text{CH}_2\text{OH} (\text{glucose}) + 3\text{OH}^- \rightarrow 2\text{Ag}^0 + -\text{C}=\text{O} + \text{H}_2\text{O}$  or  $\text{Ag}^+ + -\text{CH}_2\text{OH} (\text{glucose}) + \text{OH}^- \rightarrow 2\text{Ag}^0 + -\text{COOH} + 1/2 \text{H}_2$ . It is known that edible mushroom consists of 75% proteins<sup>[42]</sup>. For example, carbonyl group in amino acid, peptides of proteins, enzyme and polysaccharide might have a strong ability to bind with silver and play a role in the reduction of metal ions to atoms by the oxidation of aldehyde group to carboxylic acid<sup>[43]</sup>. So, the proteins probably can form a layer on the Ag or Au NPs which prevents agglomeration of NPs. Therefore, the NPs are stabilized in the mixture<sup>[44]</sup>.

Ag-TiO<sub>x</sub>/PMS is active against an antimicrobial and an antifungal agent, but Au-TiO<sub>x</sub>/PMS is only active against bacteria. This again may reflect on the strength of the Au-PMS interaction. One would expect that NPs/PMS would bind through several metals ions or atoms in the microbial cell<sup>[24]</sup>.

The properties of the bacteria cell wall can play a crucial role in different NPs/PMS because the wall is designed to provide rigidity, shape and strength to protect the cell from osmotic rupture. Gram positive bacteria were found to be more susceptible to the NPs/PMS than Gram negative bacteria because of the difference in their cell wall structure. Gram negative bacteria are considered to be more resistant due to their outer membrane acting as a barrier to many environmental substances including antibiotics<sup>[15]</sup>. In addition, the charge on the membrane of *E.coli* is negative because of the excess number of carboxyl groups, which upon dissociation makes the cell surface negative. The opposite charges of bacteria and nanoparticles are attributed to their bioactivity due to electrostatic forces leading to electrical interaction between the *E.coli* and NPs/PMS increasing the possibility of collisions and decreasing the bacteria growth<sup>[17]</sup>.

Moreover, increasing the surface area/decreasing the particle size, could be helping to improve NP anti-microbial activity<sup>[24]</sup>. NPs have a large surface area available for interaction, which enhance the bactericidal effect more than the large sized particles; hence they impart cytotoxicity to the microorganisms. However, the aggregation of NPs leads to decreasing the property of the interaction of NPs with bacteria cells<sup>[17]</sup>. The size of NPs can give rise to electronic effects which promote their surface reactivity and prevent the aggregation of NPs. For example, NPs with diameter less than 10 nm have anti-microbial activity but NPs with diameter 30-50 nm did not have good anti-microbial activity until NPs reached 20  $\mu\text{g}/\text{mL}$ <sup>[24]</sup>.

TiO<sub>x</sub> NPs/PMS and monohybrid have good anti-bacterial activity against *E.coli*. When the cell of bacteria absorbs the NPs significant oxidative stress happens due to the generation of free radicals like  $\cdot\text{OH}$ ,  $\text{O}_2^-$  and  $\text{H}_2\text{O}_2$  by oxidation of poly unsaturated phospholipids. Hence, these lipids started to submit a peroxidation reaction subsequently leading to:

- glutathione (GSH) depletion
- stress or eventual disruption in the morphology of cell membrane, and
- the electron transfer leading to cellular death<sup>[34]</sup>.

Ag NPs/PMS and monohybrid have excellent anti-bacterial activity against both *E.coli* and *S.aureus* due to the generation of ROS following the administration of NPs. Our results show that Ag NPs/PMS have anti-bacterial activity in lower concentration than other NPs. High activity of silver NPs is attributed to species difference as they dissolve to release  $\text{Ag}^0$ ,  $\text{Au}^0$ ,  $\text{Ag}^+$ ,  $\text{Au}^+$  clusters. Several mechanisms have been suggested leading to the inhibition of bacteria growth:

- Binding Ag NPs with proteins or lipo-poly-saccharide in the cell membrane leading to collapse<sup>[15]</sup>.

- Ag NPs were found to induce phosphate and interaction with atoms which have a high electron density like S, O and N. These are essential biological molecules as thiol group because Ag NPs have an extreme chemical affinity for sulfur group. The interaction with thiol or cysteine in protein leads to denaturation effects, loss of the subsequent of enzyme and changing cytoplasmic components [34].
- Attacking the respiratory chain and inhibition of the respiratory enzymes with the division of cells and causing death [17].
- Starting to act on dehydrogenases of electron transport and reduction of cellular adenosine triphosphate (ATP) level.

Interestingly, Au NPs/PMS do not have any bacterial activity. It can be suggested that:

- Au NPs self-assemble in 4-5  $\mu\text{m}$  long PMS indicating a strong NP-PMS interaction [27].
- Au NPs aggregation caused a decreased inhibitory effect; increasing surface area generates further biophysical interactions [17]
- Au NPs /PMS may be absorbed only on the cell of bacteria but cannot penetrate inside bacteria cells [24].

The ability of biomolecules (like nucleic acid and proteins) to chelate [34] and adsorb [35] Au NPs may direct the NPs to specific sites [34] or change their biological effects [35]. Nevertheless, Au NPs are particularly attractive for target direction diagnostics and therapeutics in the human body [34].

The potent anti-fungal of  $\text{TiO}_x$ /PMS is the most effective catalyst for chemical transformation [35].

Present data suggests that Ag/PMS has a potential as a biocide against *Aspergillus* and *Candida*. Indeed, the disrupting of the structure cell membrane and inhibiting the normal budding process is due to the damage of the membrane integrity [28]. 16).

The results of the present study support the suggestion plant-derived NPs have antibacterial properties that can be utilized as antibacterial agents in new drugs for the therapy of infectious disease caused by pathogens [44].

In addition PMS-based nanomaterials clearly interact with DNA. Figure 11 illustrates the structure of DNA. The base pairs of DNA possess strong absorbance at 260 nm [45]; if the DNA helix is denatured, base stacking is destroyed and UV absorbance goes up. The effect of PMS and most NP/PMS samples was to increase absorbance at 260nm above that for the DNA introduced (both in light and dark conditions and in the supernatant and PMS sediment). The only exception was for the supernatant liquid of Ag- $\text{TiO}_x$ /PMS( $\text{H}_2\text{O}$ , IPA) and Au- $\text{TiO}_x$ /PMS( $\text{H}_2\text{O}$ , IPA). One assumes that all other samples lower base stacking, blocking of DNA replication and causing DNA damage [41]. Figure 12 shows that the absorbance changes in the form of hyperchromism and hypochromism. The present results appear to show that hyperchromism occurs suggesting breakage of the DNA structure. That means a strong interaction between  $\text{TiO}_x$  NPs/PMS and nanohybrid with DNA.

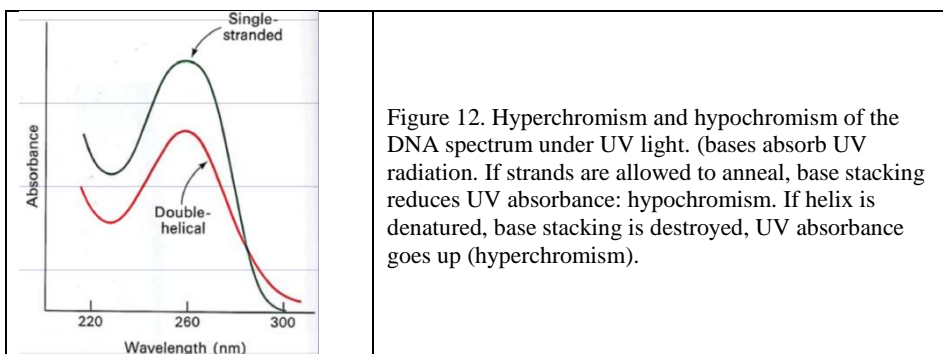


Figure 12. Hyperchromism and hypochromism of the DNA spectrum under UV light. (bases absorb UV radiation. If strands are allowed to anneal, base stacking reduces UV absorbance: hypochromism. If helix is denatured, base stacking is destroyed, UV absorbance goes up (hyperchromism).

Electrostatic interactions can change the conformation/structure of DNA. For example, H-bonds, hydrophobic effect and stacking interactions between complementary bases hold the two strands of DNA together. When NPs/PMS were added, the base-base interaction was reduced in the DNA structure, owing to many bases

becoming free form and H-bond breakage leading to an increase absorbance [45]. Furthermore, the presence of a single stranded DNA will be higher than double stranded DNA in the same concentration.

Moreover, the mechanism of reaction can occur by the phosphate group of DNA which has a negative charge. The positive charge of metals can bind to P=O to form P-O-M via electrostatic reaction [46]. From the results we can see that there are future applications for using these materials as anticancer drugs by destroying the nuclear materials for the tumour cells.

Ag NPs appear to enter the cell and intercalate between the purine and pyrimidine base pairs disrupting the hydrogen bonding between the two anti-parallel strands and denaturing the DNA molecule [47].

In general, all samples can analyze DNA in dark and light. NPs/PMS in mixture and precipitate have an excellent effect which reaches 60 ng/ $\mu$ L. In contrast, NPs/PMS monohybrid supernatant show some decrease in absorbance due to lower NPs/PMS concentration [32]. Explain why DNA was not from PMS.

The interaction between TiO<sub>x</sub> NPs/PMS and monohybrid with human DNA under UV can be explained via the covalent interaction and non-covalent interaction. First, NP/PMS hybrids can bind to alkylation or intra and inter strand crosslinking of DNA as a covalent interaction. Secondly, the non-covalent interaction leads to DNA strands breakage, changing DNA conformation or torsional tension [43]. Additionally, non-covalent interaction involves the following:

- TiO<sub>x</sub>/PMS and hybrids could be interacting between bases pairs.
- they bind to a sugar phosphate group's backbone or the major or minor groove.
- The electrostatic interaction of these NPs includes binding to the exterior of the helix by non-covalent interaction [45].

Several hypotheses can be suggested to explain the increase in absorbance at 260 nm:

- (iii) Exposure of the bases' purine and pyrimidine of DNA when NPs interact with DNA leading to a slight change in the human DNA conformation and
- (iv) NPs release ROS causing DNA damage [48].

Optical amplifiers (e.g. liquid crystals) have been reported [49] to be useful for detection of gram-positive and gram negative bacteria. The authors are considering whether their Au-Ag/TiO<sub>x</sub> bionanomaterials also have useful optical properties. Conversely, UV promotes antibacterial effects in TiO<sub>2</sub> nanocomposites even after cessation of UV irradiation [50].

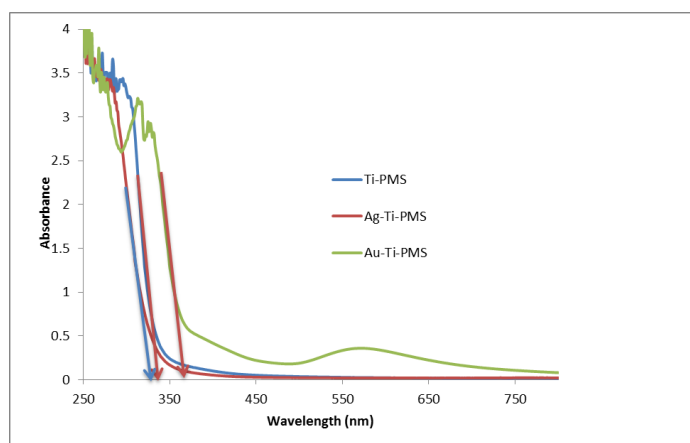


Figure 13. UV-Vis absorbance spectra of TiO<sub>x</sub> NPs/PMS and their monohybrids.

Figure 13 shows that Au-TiO<sub>x</sub>/PMS shows a surface plasmon resonance (SPR) with a maximum at 518 nm, confirming the presence of Au NPs seen in TEM, and this might be used to follow its antibacterial activity, making this nanomaterial self-indicating.

## 7. Acknowledgements

The authors gratefully acknowledge sponsorship of IAJAT from Basrah University & the Iraqi Ministry of Higher Education and Scientific Research.

## 8. References

- [1] Dhivya, S., Ajita, J. and Selvamurugan, N. 'Metallic nanomaterials for bone tissue engineering' *J.Biomed.Nanotech.* 11,1675-1700 (2015)
- [2] Schierholz, J.M. and Beuth, J. 'Implant infections: a haven for opportunistic bacteria' *J.Hosp.Infect.* 49, 87-93, (2001)
- [3] Wang, F. et al 'Nanoparticle-based antivirulence vaccine for the management of methicillin-resistant *Staphylococcus aureus* skin infection' *Adv.Funct.Mater.* 26,1628-1635 (2016)
- [4] Manikprabhu, D. et al 'Sunlight mediated synthesis of silver nanoparticles by a novel actinobacterium (*Sinomonas mesophila* MPKL 26) and its antimicrobial activity against multi drug resistant *Staphylococcus aureus*' *J.Photochem.Photobiol.* 158B,202-205 (2016)
- [5] Ebrahiminezhad, A., Bagheri, M., Taghizadeh, S.M., Berenjian, A. and Ghasemi, Y. 'Biomimetic synthesis of silver nanoparticles using microalgal secretory carbohydrates as a novel anticancer and antimicrobial' *Adv.Nat.Sci.Nanosci.nanotechnol.* 7,AR 015018 (2016)
- [6] Netala, V.R. et al 'First report of biomimetic synthesis of silver nanoparticles using aqueous callus extract of *Centella asiatica* and their antimicrobial activity' *Appl.Nanosci.* 5,801-807 (2015)
- [7] Dobrucka, R. and Dlugaszewska, J. 'Antimicrobial activities of silver nanoparticles synthesized by using water extract of *Arnicae anthodium* Ind.*J.Microbiol.* 55,168-174 (2015)
- [8] Anjum, S. and Abbasi, B.H. 'Biomimetic synthesis of antimicrobial silver nanoparticles using in vitro-propagated plantlets of a medicinally important endangered species: *Phlomis bracteosa*' *Internat.J.Nanomed.* 11,1663-1675 (2016)
- [9] Manna, J., Goswami, S., Shilpa, N., Sahu, N. and Rana, R.K. 'Biomimetic method to assemble nanostructured Ag@ZnO on cotton fabrics: Application as self-cleaning flexible materials with visible-light photocatalysis and antibacterial activities' *ACS Appl.Mater.Interf.* 7,8076-8082 (2015)
- [10] Dickson, K.N., Liang, E.I., Rodriguez, L.A., Vollereaux, N. and Yee, A.F. 'Nanopatterned polymer surfaces with bactericidal properties' *Biointerphas.* 10,AR 021010 (2015)
- [11] Jackson, E. et al 'Protein-templated biomimetic silica nanoparticles' *Lang.* 31,3687-3695 (2015)
- [12] Cai, X.Y., Li, N.N., Chen, J.C., Kang, E.T. and Xu, L.Q. 'Biomimetic anchors applied to the host-guest antifouling functionalization of titanium substrates' *J.Coll.Interf.Sci.* 475,8-16 (2016)
- [13] Rathore, H.S. et al 'Fabrication of biomimetic porous novel sponge from gum kondagogu for wound dressing' *Mater.Lett.* 177,108-111 (2016)
- [14] Yah, C.S. and Simate, G.S. 'Nanoparticles as potential new generation broad spectrum antimicrobial agents.' *Daru*,23,(1),43- (2015)
- [15] Hajipour, M.J. et al 'Antibacterial properties of nanoparticles' *Trends Biotechnol.* 30,499-511 (2012)
- [16] Bankura, K., et al 'Antibacterial activity of Ag-Au alloy NPs and chemical sensor property of Au NPs synthesized by dextran' *Carbohydr.Polym.* 107,151-157 (2014)
- [17] Chen, S.F. et al 'Large scale photochemical synthesis of M@TiO<sub>2</sub> nanocomposites (M = Ag, Pd, Au, Pt) and their optical properties, CO oxidation performance, and antibacterial effect' *Nano.Res.*,1-12 (2010)
- [18] Sharma, V.K., Johnson, N., Cizmas, L., McDonald, T.J. and Kim, H. 'A review of the influence of treatment strategies on antibiotic resistant bacteria and antibiotic resistance genes' *Chemosphere* 150,702-714 (2016)
- [19] Wright, G.D. 'Molecular mechanisms of antibiotic resistance' *Chem.Commun.* 47,4055- (2011)
- [20] Bindhu, M.R. and Umadevi, M. 'Antibacterial activities of green synthesized gold nanoparticles' *Mater. Lett.* 120,122-125 (2014)
- [21] Muthuvel, A., Adavallan, K., Balamurugan, K. and Krishnakumar, N. 'Biosynthesis of gold nanoparticles using *Solanum nigrum* leaf extract and screening their free radical scavenging and antibacterial properties' *Biomed.Prev.Nutr.* 4,325-332 (2014)
- [22] Brayner, R. 'The toxicological impact of nanoparticles' *Nano.Today* 3,48-55 (2008)

- [23] Giner-Casares, J.J., Henriksen-Lacey, M., Coronado-Puchau, M. and Liz-Marzán, L.M. 'Inorganic nanoparticles for biomedicine: Where materials scientists meet medical research' *Mater.Today* 19,page-(2015)
- [24] Eiampongpaiboon, T., Chung, W.O., Bryers, J.D., Chung, K-H. and Chan, D.C.N. 'Antibacterial activity of goldtitanates on Gram-positive cariogenic bacteria' *Acta Biomater.Odontol.Scand.* 1,51–58 (2015)
- [25] Dinakar, S., Isacc Fenn Fenn, R., Sobczak-Kupiec, A. and Basavegowda, N. 'Bioreduction of chloroaurate ions using fruit extract *Punica granatum* (Pomegranate) for synthesis of highly stable gold nanoparticles and assessment of its antibacterial activity' *Micro.Nano.Lett.* 8,400–404 (2013)
- [26] Lemire, J.A., Harrison, J.J. and Turner, R.J. 'Antimicrobial activity of metals: mechanisms, molecular targets and applications.' *Nat.Rev.Microbiol.* 11,371–84 (2013)
- [27] Zhou, Y., Kong, Y., Kundu, S., Cirillo, J.D. and Liang, H. 'Antibacterial activities of gold and silver nanoparticles against *Escherichia coli* and *Bacillus Calmette-Guérin*.' *J.Nanobiotechnol.* 10,19- (2012)
- [28] Tran, Q.H., Nguyen, V.Q. and Le, A.T. 'Silver nanoparticles: synthesis, properties, toxicology, applications and perspectives' *Adv.Nat.Sci.Nanosci.Nanotechnol.* 4,033001 (2013)
- [29] Sharma, V.K., Yngard, R.A. and Lin, Y. 'Silver nanoparticles: green synthesis and their antimicrobial activities' *Adv.Coll.Interf.Sci.* 145,83–96 (2009)
- [30] Guzman, M., Dille, J. and Godet, S. 'Synthesis and antibacterial activity of silver nanoparticles against gram-positive and gram-negative bacteria' *Nanomed.Nanotechnol.Biol.Med.* 8,(1),37–45 (2012)
- [31] Zhang, Y., Peng, H., Huang, W., Zhou, Y. and Yan, D. 'Facile preparation and characterization of highly antimicrobial colloid Ag or Au nanoparticles' *J.Coll.Interf.Sci.* 325,371–376 (2008)
- [32] Sadhasivam, S., Shanmugam, P., Veerapandian, M., Subbiah, R. and Yun, K. 'Biogenic synthesis of multidimensional gold nanoparticles assisted by *Streptomyces hygroscopicus* and its electrochemical and antibacterial properties' *BioMetals* 25,351–360 (2012)
- [33] Koperuncholan, M. 'Bioreduction of chloroauric acid (HAuCl<sub>4</sub>) for the synthesis of gold nanoparticles (GNPs): A special emphathies of pharmacological activity' *Int.J.Phytopharm.* 5,72–80 (2015)
- [34] Chapman, F.R.J. and Sullivan, T. *Nanoparticles in anti-microbial materials: Use and characterisation.* RSC Nanosci.Nanotechnol. 2012.
- [35] Zhao, Y., Ye, C., Liu, W., Chen, R. and Jiang, X. 'Tuning the composition of AuPt bimetallic nanoparticles for antibacterial application' *Angew.Chemie Int.Ed.* 53,8127–8131 (2014)
- [36] Kholmanov, I.N. et al 'Nanostructured hybrid transparent conductive films with antibacterial properties' *ACS Nano* 6,5157–5163 (2012)
- [37] Smania, A., Monache, F.D., Smania, E. de F. A. and Cuneo, R.S. 'Antibacterial activity of steroidal compounds isolated from *Ganoderma applanatum* (Pers.) Pat. (*Aphylllophoromycetidae*) fruit body' *Int.J.Med.Mushrooms* 1,325–330 (1999)
- [38] Vanden Berghe, D.A. and Vlietinck, A.J. 'Screening methods for antibacterial and antiviral agents from higher plants' 6,47–69 (Jan. 1991)
- [39] Sambrood, J.J., Fritsch, E.F. and Maniatis, T., *Molecular cloning: A laboratory manual.* Cold Spring Harbor Laboratory PressNo Title, 1989.
- [40] Huang, J. et al 'Biogenic silver nanoparticles by *Cacumen platycladi* extract: synthesis, formation mechanism, and antibacterial activity' *Ind.Eng.Chem.Res.* 50,9095–9106 (2011)
- [41] Sadowski, Z. 'Biosynthesis and application of silver and gold nanoparticles, silver nanoparticles.' *Intech Open*, 257–277 (2010)
- [42] Bhat, R., Deshpande, R., Ganachari, S.V., Huh, D.S. and Venkataraman, A. 'Photo-irradiated biosynthesis of silver nanoparticles using edible mushroom *Pleurotus florida* and their antibacterial activity studies' *Bioinorg.Chem.Appl.* , 7pages, 2011.
- [43] Sirajuddin, M., Ali, S. and Badshah, A. 'Drug-DNA interactions and their study by UV-Visible, fluorescence spectroscopies and cyclic voltametry' *J.Photochem.Photobiol.* 124B,1–19 (2013)
- [44] Anthony, K.J.P., Murugan, M., Jeyaraj, M., Rathinam, N.K. and Sangiliyandi, G. 'Synthesis of silver nanoparticles using pine mushroom extract: A potential antimicrobial agent against *E. coli* and *B. subtilis*' *J.Ind.Eng.Chem.* 20,2325– 2331 (2013)
- [45] Suhani Patel, S.B., et al 'DNA binding and dispersion activities of titanium dioxide nanoparticles with UV/vis spectrophotometry, fluorescence spectroscopy and physicochemical analysis at physiological temperature' *Mol. Liq.* 213,304–311 (2016)
- [46] Jin, C., et al 'In vivo evaluation of the interaction between titanium dioxide nanoparticle and rat liver DNA.' *Toxicol.Ind.Health* 29,235–44 (2013)
- [47] Klueh, U., Wagner, V., Kelly, S., Johnson, A. and Bryers, J.D. 'Efficacy of silver-coated fabric to prevent bacterial colonization and subsequent device-based biofilm formation' *J. Biomed.Mater.Res.* 53,621–631 (2000)

- [48] El-Said, K., Ali, E., Kanehira, K. and Taniguchi, A. 'Molecular mechanism of DNA damage induced by titanium dioxide nanoparticles in toll-like receptor 3 or 4 expressing human hepatocarcinoma cell lines' J. Nanobiotechnol. 12,(1),48- (2014)
- [49] Zafiu, C. et al 'Liquid crystals as optical amplifiers for bacterial detection' Biosens.Bioelectron. 80,161-170 (2016)
- [50] Cai, Y., Strømme, M. and Welch, K. 'Photocatalytic antibacterial effects are maintained on resin-based TiO<sub>2</sub> nanocomposites after cessation of UV irradiation' PLoS One 8,10- (2013)

Proc. of SPIE Vol. 9930 99300B-13

Downloaded From: <http://proceedings.spiedigitallibrary.org/> on 10/04/2016 Terms of Use: <http://spiedigitallibrary.org/ss/termsofuse.aspx>